Ab initio Modeling of Energy Dissipation during Chemical Reactions at Transition Metal Surfaces

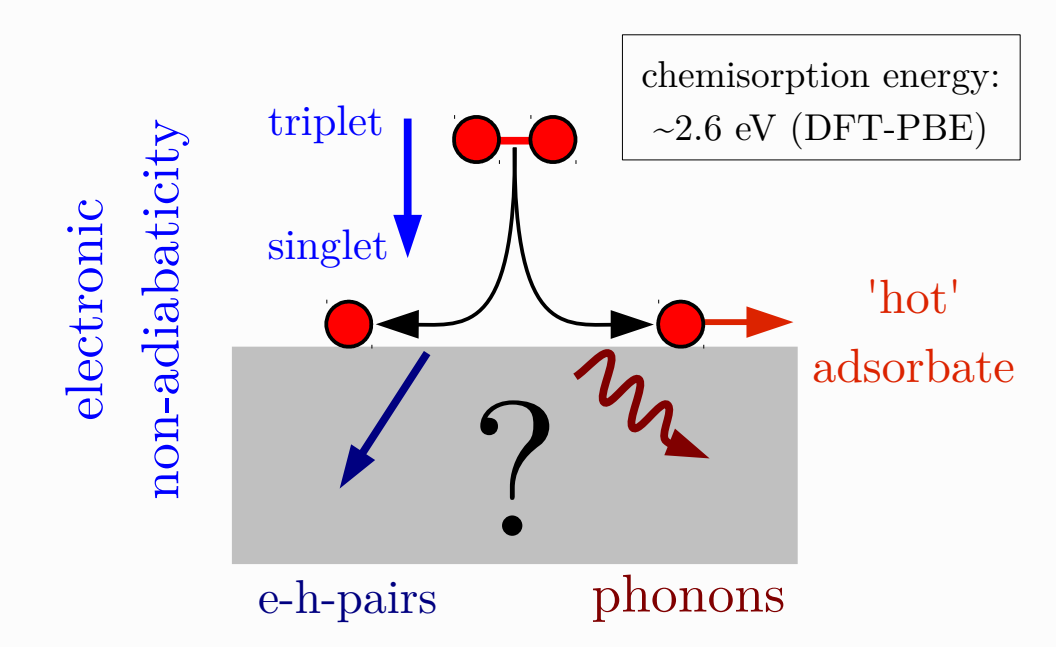

im Fachbereich Physik der Freien Universität Berlin eingereichte Dissertation
zur Erlangung des Akademischen Grades
doctor rerum naturalium

vorgelegt von
Dipl.-Phys. Jörg Meyer

Berlin 2011

MAX-PLANCK-GESELLSCHAFT

Erstgutachter:	Prof. Dr. Karsten Reuter
Zweitgutachter:	Prof. Dr. Daniel Sebastiani
Drittgutachter:	Prof. Dr. Martin E. Garcia
Tag der Disputation:	16. Februar 2012

Colophon

The document constituting this thesis has been typeset with LaTeX 2$_\varepsilon$ using the **KOMA-Script** classes and the AMS-LaTeX packages for arranging formulas, all contained in TeXLive within the GNU/Linux operating system distributions Ubuntu (based on Debian) and gentoo.

The Latin Mordern fonts express the contents in the present, reader friendly typeface and the packages `hyperref` together with `cleveref` and `biblatex` provide the cross references in the electronic version, for which the collection of bibliographic refererences was conveniently supported by cb2Bib.

Plots (both two- and three-dimensional) have been created using the fantastic Python-powered matplotlib package, whereas for other graphics OpenOffice and POV-Ray in combination with the almighty Atomic Simulation Environment (ASE) completely fulfilled the visualization demands.

Altogether, the whole production process was driven by free (as in speech) software only.

Von der einsamen und verzweifelten Suche nach guter Wissenschaft.
Für meine Eltern in schweren Zeiten.

Contents

List of Figures

1. Introduction

Diminishing resources have made energy research become more and more prominent over the recent years. Energy conversion at interfaces is at the center of the rapidly growing field of basic energy science. This concerns desired conversions like solar to chemical energy, but also unavoidable by-products like the dissipation of chemical energy into heat. An atomistic understanding of the involved elementary processes is in all cases only just emerging, but is likely to question established views and macro-scale concepts. With respect to the dissipation of heat freed during exothermic surface chemical reactions, such a prevailing view is that of a rapid equilibration with the local heat bath provided by the solid surface. The view is nurtured by the rare event dynamics resulting from the typically sizably activated nature of surface chemical processes: While the actual elementary processes themselves take place on a picosecond time scale, times between such rare events are orders of magnitude longer. The understanding is then that in these long inter-process time spans any released chemical energy is rapidly distributed over sufficiently many surface phononic degrees of freedom to warrant a description in terms of a mere heat bath with defined local temperature.

At the atomic scale this equilibration with the surface heat bath leads to an efficient loss of memory of the adsorbates about their history on the solid surface between subsequent rare events. This motivates the description in terms of a Markovian state to state dynamics that is e.g. underlying all present-day microkinetic formulations in heterogeneous catalysis.[1–3] In turn, the freed reaction energy only enters the determination of the local heat bath temperature, commonly achieved through a continuum heat balancing equation.[4–6]

In many cases[7–10] this prevalent framework seems to allow for an accurate account e.g. of catalytic conversions. However, particularly for nanostructured surfaces and highly exothermic reactions it is presently unclear whether this effective description is sufficient. With respect to the exothermicity this suspicion comes from recalling that freed enthalpies can well be of the order of several eVs. This is e.g. generally the case for the dissociative adsorption of oxygen molecules at catalytically relevant transition metal surfaces, which is the specific surface chemical reaction this thesis focuses on.

For a number of reasons detailed below, and not least because of the plethora of previous studies of the O-Pd interaction in the context of catalytic CO oxidation[9–16] Pd(100) has been chosen to act as particular showcase. Additionally, most intriguing "different dissociation properties" of O_2 molecules with different rotational orientation relative to the surface (cartwheels and helicopters) have only recently been observed by Rocca and coworkers for this system.[17–19] These results exemplify the limited understanding of the initial stages of oxidation when breaking things down to elementary processes on an atomistic scale.

Of course, in an atomistic picture, the impingement of individual O_2 molecules to undergo dissociation immediately draws a connection to gas-surface dynamics. In this field, the understanding has long been limited by very approximate descriptions of the adsorbate-substrate interactions like those already proposed by Lennard-Jones in 1932 based on potentials named after him.[20] The applicability of first-principles methods due to the enormous increase of computational resources in combination with methodological developments have led to significant progress in the understanding of the adsorption dynamics of diatomic molecules during the last

15 years. Particular focus has been devoted to H_2 adsorption on various metal surfaces,[21,22] as the latter offers a "computationally convenient" electronic structure. The necessity of including all molecular degrees into the dynamics has thus been demonstrated and established. Notwithstanding, arguing with the huge mass mismatch of hydrogen and transition metal atoms, calculations of initial sticking probabilities (a primary quantity of interest as it allows direct comparison with experimental data), have usually relied on a neglect of surface mobility. Only recently, first attempts to go beyond the frozen surface descriptions have been made based on *ab initio* modeling,[23–26] which is considered to be of crucial importance for molecules heavier than H_2 for obvious reasons. However, none of them incorporates a description of phonons and their propagation with the same quality that is used for the adsorbate-substrate interaction.

Several eVs is an enormous amount of energy on the scale of phononic degrees of freedom, which calls for efficient dissipation channels to achieve the assumed quasi-instantaneous local equilibration. At metallic substrates electronic excitations could hereby potentially represent an important additional energy sink. Unfortunately, no consensus has hitherto been reached concerning the role of this additional channel for the gas-surface dynamics and subsequent energy dissipation. The chemicurrent measurements of Nienhaus and coworkers[27,28] Wodtke and coworkers[29,30] as well as state-resolved scattering experiments with highly vibrationally excited NO molecules on from Au(111) provide measurable facts for several systems. Among others Tully and coworkers have frequently stressed that the lack of a band gap in metallic systems should in principle allow for electronic excitations, namely electron-hole (e-h) pairs, of arbitrarily low energies to easily couple with the nuclear motion of a particle impinging from the gas phase.[30–39] According to those general arguments, e-h pair excitations should be particularly facilitated for the Pd(100) substrate because of its extraordinary high density of states at the Fermi level, which is among the highest known among the low-index transition metal surfaces.[40–43] On the other hand, recent comparisons to experimental data for hydrogen and nitrogen molecules on metallic surfaces indicate that electronically adiabatic descriptions provided within the Born-Oppenheimer approximation (BOA) seem to describe the initial interaction dynamics governing the dissociation extremely well.[44–46] In fact, a proper high-dimensional description of the nuclear motion appears hereby to be significantly more important than the effect of e-h pair excitations.[44]

For the particular case of oxygen dissociation the $^3\Sigma_g^-$ spin triplet ground state of gas-phase O_2 brings in another aspect that could require to go beyond an adiabatic BOA treatment. With the spin of adsorbed oxygen atoms at metal surfaces quenched, a spin transition needs to occur at some stage during the adsorption process and could then well affect the gas-surface dynamics. The well-known paradigm system for this is O_2 at Al(111), where only an explicit account of a hindered triplet-singlet transition could reconcile first-principles dynamical simulations with the experimentally measured low sticking coefficient for thermal molecules[47–50] This non-adiabatic hindrance was traced back to the inefficiency of both coupling mechanisms generally discussed to relax the spin selection rules that suppress reactions like oxygen dissociation:[47–51] The low mass number of Al leads to a small spin-orbit coupling and the low Al DOS at the Fermi level prevents efficient spin quenching through the preferred tunneling of minority spin electrons between substrate and adsorbate. Indeed, when going from Al(111) to Ag(111), i.e. switching the substrate from a simple to a coinage metal, a recent study has shown that it is not necessary to invoke a non-adiabatic spin transition.[52] For O_2 on a platinum group metal like palladium on might expect the same as well due to the much larger mass number and DOS at the Fermi level, but this is not clear *a priori*.

Altogether, these challenges for the representative showcase constituted by O_2 dissociation on Pd(100) for chemical reactions at transition metal surfaces in general, are schematically

summarized by the figure on the title page. Aiming at *ab initio* based modeling and quantitative understanding of energy dissipation they will be addressed in the following, based on several new methods and approaches that have been developed as part of this work. It is structured as follows:

In Part I, a concise introduction to the general theory is given which this work is based on, comprising density-functional theory in Chapter 2, molecular dynamics in Chapter 3 and phonons in Chapter 4. Starting from textbook knowledge, specialized aspects are incorporated as needed – if not presented in even more detail in the main chapters due to new theoretical and methodological developments conceived within this work and thus necessarily preceding the results obtained therewith. Computational aspects are briefly touched as well.

Results obtained on a frozen Pd(100) surface are grouped into Part II. First, DFT reference calculations for palladium bulk and surfaces, the oxygen molecule and oxygen adsorbed on Pd(100) are described in Chapter 5, which have served to establish a proper computational setup. Second, statistical properties of O_2 adsorption dynamics on that surface are the topic of Chapter 6. E.g. the initial sticking coefficient is obtained in good agreement with available experimental data. The underlying highly accurate six-dimensional first-principles adiabatic potential energy surface is based on neural network interpolation and a newly devised symmetry adapted coordinate transformation. Third and concluding this part, the importance of electron-hole pair excitations during the adsorption has been investigated in Chapter 7, using and extending a perturbative approach based on TD-DFT. Concomitant non-adiabatic energy losses are small compared to the chemisorption energy, but still offer a mechanism that could be responsible for the adiabatic spin transition of the oxygen molecule.

Part III focuses on surface mobility after the preceding results have clearly pointed towards phonons as main energy dissipation channel. Chapter 8 first reviews energy sinks "from the shelf", i.e. approaches previously appearing in the literature that have been used quite frequently over the last 30 years to go beyond the frozen surface description in an approximative way. A thorough discussion reveals their inherent shortcomings for an accurate description of the release of chemisorption energy to lattice degrees of freedom at a metallic surface. Along those lines, a newly developed embedding approach for metallic systems termed "QM/Me" is then introduced in Chapter 9 and applied to the present system. As indications for a breakdown of the Markov approximation turn out to rather sensitively depend on the description of the substrate bath, the interaction with (surface) phonons and the reliability of the harmonic approximation for the latter are characterized in detail in Chapter 10. In the end, this finally allows to characterize the important role of (surface) phonons during the dissociation dynamics and concomitant energy dissipation with unprecedented first-principles accuracy in Chapter 10. The various methodological developments which are part of this work offer many potential future applications beyond the specific problem of dissociative adsorption. Some of these are surveyed in a concluding outlook in Chapter 11.

As listed at the end of this thesis, so far only the contents of Chapter 7 have been published in a recent special issue of the New Journal of Physics, "Focus on Advances in Surface and Interface Science 2011", and rated among the 10 % most accessed articles in the quarter of publication. In addition, methodological parts of Chapter 6 and Appendix A have enabled a publication addressing non-adiabatic effects of O_2 adsorption on Ag(111), in collaboration with the gas-surface dynamics group in San Sebastian.[52] Preparation of several manuscripts of the remaining chapters is currently under way. It is worth noting that in particular the contents of Chapter 9 and Chapter 10 have already attracted great interest at recent prestigious international conferences.

Part I.

Theoretical Background

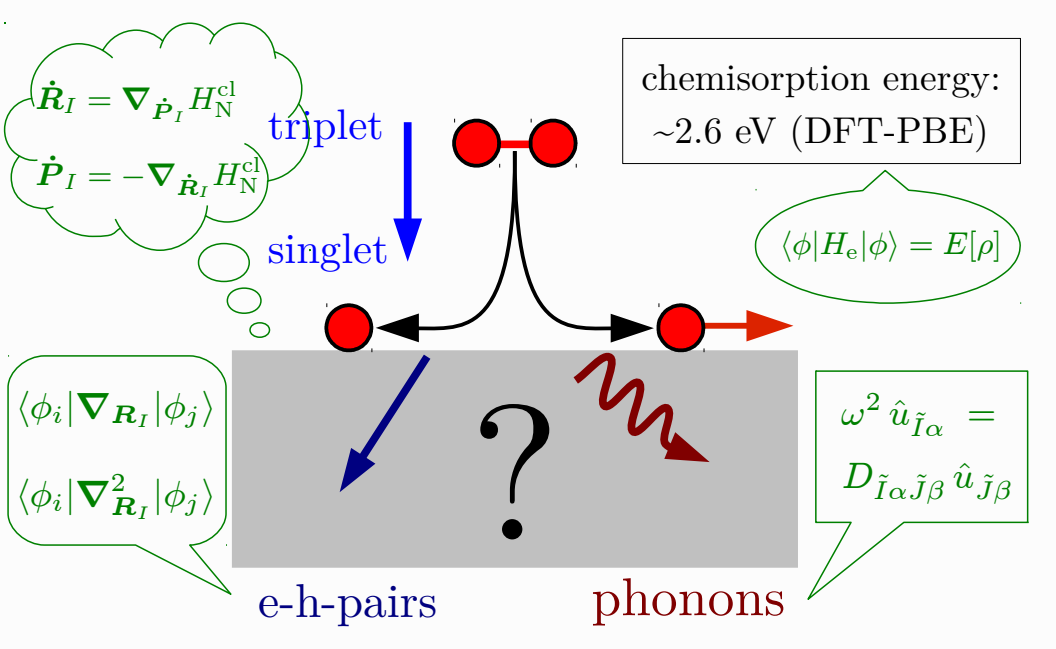

2. Density-Functional Theory

The making and breaking of chemical bonds during chemical reactions calls for quantum mechanics to provide a reliable description on the atomic scale. While the latter allows for exact analytical solutions of small systems only, the treatment of significantly more complex real materials usually requires to make a choice between two options: On the one hand, further approximations to the "first-principles" have to be introduced, resulting in nicely tractable models which include parameters to capture material specific properties. In addition to the underlying approximations, adjustment of these parameters, whose values are unknown *a priori*, might bear the risk of limited predictive power. On the other hand, one can try to tackle quantum mechanics *ab-initio*, heavily relying on numerical techniques, which is the route chosen for this work. When it comes to metals in at least partly periodic systems with large unit cells like surfaces, there is at present no viable alternative to density-functional theory (DFT). This holds even more, when like in the present case, dynamics are involved, i.e. a manifold of energy and force evaluations is required.

2.1. The Many-Body Problem

Solutions of the time-independent Schrödinger equation

$$H\left|\Psi\right\rangle = E\left|\Psi\right\rangle \quad , \tag{2.1}$$

which can be read as an Eigenvalue problem of the Hamilton operator H on the Hilbert space $\mathcal{H}$ of states $|\Psi\rangle$, determine the static properties of a (non-relativistic) quantum mechanical system.[53] Finite systems always have discrete spectra, whereas infinite systems can also yield continous sets of Eigenvalues. Concomitant mathematical subtleties will not be detailed here, also because practical computer calculations lead to discrete spectra in any case due to finiteness of computational resources. Of particular interest is the (potentially degenerate) ground state, i.e. an Eigenstate $|\Psi_0\rangle$, whose (Eigen-)energy E_0 is the lowest possible expectation value

$$E_0 = \left\langle \Psi_0 \right| H \left| \Psi_0 \right\rangle \leq \left\langle \Psi \right| H \left| \Psi \right\rangle \tag{2.2}$$

This is commonly referred to as variational principle and forms the foundations of quantum chemistry: The energy as a functional $E = E\left[|\Psi\rangle\right]$ on the Hilbert space of trial states is to be minimized in order to obtain the ground state. For a system of electrons (e) and nuclei (N), both of which are not assumed to have any substructure here, without any external perturbations, the Hamilton operator can be written as

$$H_{\mathrm{eN}} = \underbrace{T_{\mathrm{e}} + V_{\mathrm{ee}} + V_{\mathrm{eN}}}_{H_{\mathrm{e}}} + T_{\mathrm{N}} + V_{\mathrm{NN}} \quad , \tag{2.3}$$

where the electronic part H_{e} of the total Hamiltonian H will deserve particular attention in the next sections. Contributions of kinetic and potential energy operators are as usual denoted by T and V, respectively. For physical systems consisting of n electrons and N nuclei, with

coordinates $\boldsymbol{r}_i$ and $\boldsymbol{R}_I$, as well as electron mass m_e and nuclear masses M_I, for $i \in \{1, \ldots, n\}$ and $I \in \{1, \ldots, N\}$, respectively, the position space representations of the individual contributions to H_eN are as follows:

Kinetic energy of the electrons
$$T_\mathrm{e} = \sum_{i=1}^{n} \frac{-\hbar^2}{2m_\mathrm{e}} \boldsymbol{\nabla}^2_{\boldsymbol{r}_i} \quad . \tag{2.4a}$$

Electron-electron interaction
$$V_\mathrm{ee} = \sum_{i=1}^{n} \sum_{j>i}^{n} \frac{1}{4\pi\varepsilon_0} \frac{e^2}{\|\boldsymbol{r}_i - \boldsymbol{r}_j\|_2} \quad . \tag{2.4b}$$

Electron-nuclear interaction
$$V_\mathrm{eN} = \sum_{i=1}^{n} \sum_{I=1}^{N} \frac{1}{4\pi\varepsilon_0} \frac{-Z_I\, e^2}{\|\boldsymbol{r}_i - \boldsymbol{R}_I\|_2} \quad . \tag{2.4c}$$

Kinetic energy of the nuclei
$$T_\mathrm{N} = \sum_{I=1}^{N} \frac{-\hbar^2}{2M_I} \boldsymbol{\nabla}^2_{\boldsymbol{R}_I} \quad . \tag{2.4d}$$

Nuclear-nuclear interaction
$$V_\mathrm{NN} = \sum_{I=1}^{N} \sum_{J>I}^{N} \frac{1}{4\pi\varepsilon_0} \frac{Z_I Z_J\, e^2}{\|\boldsymbol{R}_I - \boldsymbol{R}_J\|_2} \quad . \tag{2.4e}$$

SI units have deliberately been chosen over atomic units here and in the following, in order to keep all masses visible and avoid confusion with Rydberg and Hartree atomic units.[i] Only electrostatic interactions are taken into account, for which no doubts have been cast by any experiment that has been carried out so far. As Eq. (2.1) does not take relativistic effects into account, spin does not appear "naturally" and would need to introduced as an additional degree of freedom. For the purposes of this thesis however, interactions resulting from both electron and nuclear spin are too weak to be important. Accordingly, Eqs. (2.4) would not change and hence notation (also in the following) can be kept simple. In Section 2.5 however, spin will be reintroduced for the electronic degerees of freedom.

2.2. Born-Oppenheimer Approximation

Although the Hamiltonian in Eq. (2.1) for chemical systems is as indicated believed to be known very accurately, the $3n + 3N$ degrees of freedom make a solution yet a quite challenging task. However, the "degree of quantum mechanical nature" of electrons and nuclei motivates, in a first step, to save some efforts by restricting the quantum mechanical problem to the electronic sub-Hilbert space $\mathcal{H}_\mathrm{e}$ of the total space $\mathcal{H} = \mathcal{H}_\mathrm{e} \otimes \mathcal{H}_\mathrm{N}$ of electron-nuclear states. An Eigenvalue problem for the electronic Hamiltonian H_e with its $3n$ degrees of freedom thus needs to be solved. There, the nuclear degrees of freedom $\mathcal{R} = \{\boldsymbol{R}_I\}_I$ enter only as parameters in the electron-nuclear interaction $V_\mathrm{eN}(\{r_i\}_i; \mathcal{R})$ given by Eq. (2.4c), which is also referred to as *external potential* in this context.

The total electron-nuclear wavefunction from the original problem Eq. (2.1) is *a priori* not separable into a product of an electronic $|\phi\rangle \in \mathcal{H}_\mathrm{e}$ and a nuclear state $|\psi\rangle \in \mathcal{H}_\mathrm{N}$, but can be

[i] This is particular importance in the context of nuclear dynamics, where no common units for the latter have been established so far in corresponding first-principles computer codes.

written as

$$|\Psi(\mathcal{R})\rangle = \sum_j (|\phi_j(\mathcal{R})\rangle\, |\psi_j(\mathcal{R})\rangle) \tag{2.5}$$

for every set of nuclear coordinates $\mathcal{R}$. The corresponding orthonormal system of Eigenstates $|\phi_j(\mathcal{R})\rangle_j$, obtained as solutions for the electronic Hamiltonian $H_\mathrm{e}(\mathcal{R})$, forms a basis of the subspace $\mathcal{H}_\mathrm{e}$, and $|\psi_j(\mathcal{R})\rangle$ are the concomitant projections in its complement. While the nuclear-nuclear interaction V_NN given by Eq. (2.4e) only acts in $\mathcal{H}_\mathrm{N}$ alone, the nuclear kinetic energy couples the two parts - since motion of the nuclei also changes the electronic Eigensystem $|\phi_j(\mathcal{R})\rangle_j$. Therefore, the nuclear kinetic energy term in Eq. (2.3) as given by Eq. (2.4d) can be responsible for transitions between states in the electronic subsystem, $H^{(1)}_{\mathrm{e},j\to k}$ and $H^{(2)}_{\mathrm{e},j\to k}$:

$$\begin{aligned}
\langle \Psi\, |T_\mathrm{N}|\, \Psi\rangle = &\sum_j \langle \psi_j\, |T_\mathrm{N}|\, \psi_j\rangle \\
&+ \quad 2\sum_{I=1}^{N}\sum_{j,k} \frac{\hbar^2}{2M_I} \langle \psi_k| \underbrace{\langle \phi_k\, |\boldsymbol{\nabla}_{\boldsymbol{R}_I}|\, \phi_j\rangle}_{H^{(1)}_{\mathrm{e},j\to k}} \boldsymbol{\nabla}_{\boldsymbol{R}_I}\, |\psi_j\rangle \\
&+ \quad \sum_{I=1}^{N}\sum_{j,k} \frac{\hbar^2}{2M_I} \langle \psi_k| \underbrace{\left\langle \phi_k \left| \boldsymbol{\nabla}^2_{\boldsymbol{R}_I} \right| \phi_j \right\rangle}_{H^{(2)}_{\mathrm{e},j\to k}} |\psi_j\rangle
\end{aligned} \tag{2.6}$$

In order to keep the notation simple, the parametric dependencies on $\mathcal{R}$ explicitly indicated in Eq. (2.5) have been dropped here. Diagonal contributions $H^{(1)}_{\mathrm{e},j\to j}$ to the so-called *non-adiabatic* coupling vector vanish exactly

$$H^{(1)}_{\mathrm{e},j\to j} = \langle \phi_j\, |\boldsymbol{\nabla}_{\boldsymbol{R}_I}|\, \phi_j\rangle = \frac{1}{2}\boldsymbol{\nabla}_{\boldsymbol{R}_I} \langle \phi_j | \phi_j\rangle = 0 \quad . \tag{2.7}$$

The diagonal matrix elements $H^{(2)}_{\mathrm{e},j\to j}$ can be interpreted as kinetic energy contributions for the electrons due to the motion of the nuclei and hence be estimated against the electronic kinetic energy as given by Eq. (2.4a):

$$\frac{\hbar^2}{2M_I} H^{(2)}_{\mathrm{e},j\to j} = \frac{\hbar^2}{2M_I} \left\langle \phi_j \left| \boldsymbol{\nabla}^2_{\boldsymbol{R}_I} \right| \phi_j \right\rangle \approx \frac{m_\mathrm{e}}{M_\mathrm{I}} \langle \phi_j\, |T_\mathrm{e}|\, \phi_j\rangle \tag{2.8}$$

The mass ratio $\frac{m_\mathrm{e}}{M_\mathrm{I}} < \frac{m_\mathrm{e}}{m_\mathrm{p}} < 6\times 10^{-4}$, where m_p is the proton mass, gives a good motivation to neglect these terms, in particular in a chemical context for elements heavier than hydrogen. The non-diagonal terms of both $H^{(1)}_{\mathrm{e},j\to j}$ and $H^{(2)}_{\mathrm{e},j\to j}$ are difficult to estimate in general. In order to decouple nuclear and electronic systems entirely, they are commonly neglected nevertheless. This is known as Born-Oppenheimer approximation (BOA).[54] From a physical point of view, it assumes that the electrons instantaneously adjust to the current set of nuclear positions, reflecting the different time-scales of nuclear and electronic motion induced by the aforementioned mass ratio. In general, this is believed to be a reasonable assumption though in particular in gas-surface dynamics on metals both experimental and theoretical work has questioned the validity of the BOA.[30]

Within the BOA, the total electron-nuclear wave function becomes a product state

$$|\Psi\rangle = |\phi\rangle\, |\psi\rangle \quad \in \mathcal{H}_\mathrm{e} \otimes \mathcal{H}_\mathrm{N} \quad , \tag{2.9}$$

such that the nuclear part of the Hamiltonian H_N simplifies to

$$H_\mathrm{N} = T_\mathrm{N} + V_\mathrm{NN} + V_\mathrm{e} \quad . \tag{2.10}$$

The BOA thus introduces the concept of a so-called potential energy surface V_e, obtained as expectation value of the electronic Hamiltonian

$$V_\mathrm{e} = V_\mathrm{e}(\mathcal{R}) = \langle \phi(\mathcal{R}) | H_\mathrm{e}(\mathcal{R}) | \phi(\mathcal{R}) \rangle \quad , \tag{2.11}$$

which parametrically depends on the nuclear coordinates. V_e is typically given by the electronic ground state $|\phi_0\rangle$, but depending to the initial conditions can also be another (excited) state. However, the neglect of non-adiabatic coupling described by Eq. (2.6) obviously excludes transitions between electronic states. On the other hand, precisely this decoupling described by Eq. (2.9) allows for a straightforward classical treatment of the nuclear system. The parametric dependence of V_e on $\mathcal{R}$ described by Eq. (2.11) allows to apply the Hellmann-Feynman theorem[55] to conveniently obtain the classical forces: For a set of nuclear positions $\mathcal{R}$ forces F_I on a nucleus I are given by the ground state expectation value of the gradient of the Hamiltonian with respect to the corresponding position parameter

$$\boldsymbol{F}_I(\mathcal{R}) = -\boldsymbol{\nabla}_{\boldsymbol{R_I}} V_\mathrm{e}(\mathcal{R}) = \langle \phi(\mathcal{R}) \, | \boldsymbol{\nabla}_{\boldsymbol{R_I}} H_\mathrm{e}(\mathcal{R}) | \, \phi(\mathcal{R}) \rangle \quad . \tag{2.12}$$

This forms the foundations of the dynamics discussed in Chapter 6 and Chapter 9.

2.3. Hohenberg-Kohn-Sham Theory

2.3.1. The Hohenberg-Kohn Theorems

Even within the Born-Oppenheimer approximation introduced in the last section, the solution of the electronic quantum mechanical problem to be found is a state $|\phi\rangle$ represented by a complicated $3n$-dimensional many-electron wave function $\phi(\{\boldsymbol{r}_i\}_i)$ in position space. Obviously, a three-dimensional function like the electron density

$$\rho(\boldsymbol{r}) = n \cdot \int d\boldsymbol{r}_2 \cdots d\boldsymbol{r}_n \phi^*(\boldsymbol{r}, \boldsymbol{r}_2, \ldots, \boldsymbol{r}_n) \phi(\boldsymbol{r}, \boldsymbol{r}_2, \ldots, \boldsymbol{r}_n) \tag{2.13}$$

would be much simpler to deal with. This object already was the protagonist in Thomas-Fermi theory from 1927.[56–58]

Nevertheless, it took nearly 40 more years before in 1964 Hohenberg and Kohn could rigorously prove that it is indeed sufficient to "only" consider densities instead of wave functions to characterize any physical property of a quantum mechanical system.[59] By *reductio ad absurdum* they could show that the electron density as given by Eq. (2.13) of a non-degenerate ground state uniquely determines an external potential like the one provided by the electron-nuclear interaction V_eN (cf Eq. (2.4c)) as already mentioned in Section 2.2. Since this potential defines the electronic Hamiltonian H_e (cf Eq. (2.3)), which in turn provides electronic states that (according to the foundations of quantum mechanics) contain the entire physical information about the system, the same must also hold for the density. This is commonly referred to as the first Hohenberg-Kohn theorem. Consequently, the ground state energy is not only a functional of wave functions as already indicated in Section 2.1, but can also, at least formally, be written as a functional of the density

$$E = \langle \phi \, | H_\mathrm{e} | \, \phi \rangle = E\,[\rho] \quad . \tag{2.14}$$

For the contribution from V_{eN} to Eq. (2.14), an explicit analytical expression can be easily constructed:

$$\begin{aligned}
\langle \phi \left| V_{\mathrm{eN}} \right| \phi \rangle &= \sum_{I=1}^{N} \frac{1}{4\pi\varepsilon_0} \sum_{i=1}^{n} \int d\boldsymbol{r}_1 \cdots d\boldsymbol{r}_n \phi^*(\boldsymbol{r}_1, \ldots, \boldsymbol{r}_n) \frac{Z_I\, e^2}{\|\boldsymbol{r}_i - \boldsymbol{R}_I\|_2} \phi(\boldsymbol{r}_1, \ldots, \boldsymbol{r}_n) \\
&= \sum_{I=1}^{N} \frac{1}{4\pi\varepsilon_0} \sum_{i=1}^{n} \frac{1}{n} \int d\boldsymbol{r}_i \rho(\boldsymbol{r}_i) \frac{Z_I\, e^2}{\|\boldsymbol{r}_i - \boldsymbol{R}_I\|_2} \\
&= \sum_{I=1}^{N} \frac{1}{4\pi\varepsilon_0} \int d\boldsymbol{r} \rho(\boldsymbol{r}) \frac{Z_I\, e^2}{\|\boldsymbol{r} - \boldsymbol{R}_I\|_2} \\
&\equiv E_{\mathrm{eN}}\left[\rho\right]
\end{aligned} \tag{2.15}$$

Likewise, the respective contributions from the kinetic energy of the electrons and the electron-electron interaction (cf Eqs. (2.4a) and (2.4b)) in principle must also be describable by a functional F_{HK}, such that

$$E\left[\rho\right] = F_{\mathrm{HK}}\left[\rho\right] + E_{\mathrm{eN}}\left[\rho\right] \tag{2.16}$$

F_{HK} is even a *universal* functional since it does not depend on system specific properties like e.g. the number of nuclei in E_{eN} (cf Eq. (2.15)). Unfortunately, an exact explicit analytic representation of F_{HK} is not known.

Notwithstanding, the enormous importance of Eqs. (2.14) and (2.16) is due to the second Hohenberg-Kohn theorem,[59] which establishes a variational principle. Consequently, minimization of Eq. (2.14) with respect to the density under the normalization constraint

$$n = \int d\boldsymbol{r} \rho(\boldsymbol{r}) \tag{2.17}$$

paves the way for practical (computer) calculations by iteratively improving initially chosen trial densities. This brings up the problem of *v-representability*: In general,[ii] not all real-valued functions in three variables are electron densities resulting from electronic Hamiltonians with (one-particle) external potentials as occurring in Eq. (2.15), which has been proved even for physically "reasonable" subsets.[61,62] This complicates the proper mathematical description of the definition range for the minimization as originally proposed by Hohenberg and Kohn.[59] Levy's constrained search approach[61,63] circumvents these difficulties and also lifts the aforementioned restriction to non-degenerate ground states. In practice, a direct minimization of Eq. (2.16) is nowadays known as *orbital free DFT* – the reason for this designation will get obvious in the next paragraph. Unfortunately, good approximations for F_{HK}, in particular the contribution from the kinetic energy of the electrons, are difficult to construct and the accuracy of results can hence be quite limited.[64] Still, orbital free DFT is used within embedding techniques for the description of a larger part of a system for which a more accurate quantum mechanical treatment is then used for a smaller part.[65]

2.3.2. The Kohn-Sham Equations

In order to circumvent the difficulties with the limited knowledge about the kinetic energy functional indicated in the previous paragraph, in 1965 Kohn and Sham proposed a mapping to

[ii] i.e. not only for quantum lattice systems[60]

a non-interacting reference system[66] described by single-particle states $|\varphi_i\rangle$ which are supposed to yield the same density as the interacting system.[iii] These so-called Kohn-Sham orbitals do not have any strict physical meaning. Nevertheless, they can provide similarly good physical insight like molecular orbitals from wave function based electronic structure theories.[67] In Chapter 7, this will be made use of for band structures of periodic metallic systems in particular.

Since electrons are Fermionic particles, the many-electron wave function of such a system is given by a Slater determinant of the (normalized) single particle states

$$\phi^{\mathrm{s}}(r_1, \ldots, r_n) = \frac{1}{n!} \begin{vmatrix} \varphi_1(r_1) & \cdots & \varphi_1(r_n) \\ \vdots & \ddots & \vdots \\ \varphi_n(r_1) & \cdots & \varphi_n(r_n) \end{vmatrix} \tag{2.18}$$

in order to be anti-symmetric under particle exchange

$$\phi^{\mathrm{s}}(\boldsymbol{r}_1, \ldots, \boldsymbol{r}_i, \ldots, \boldsymbol{r}_j, \ldots, \boldsymbol{r}_n) = -\phi^{\mathrm{s}}(\boldsymbol{r}_1, \ldots, \boldsymbol{r}_j, \ldots, \boldsymbol{r}_i, \ldots, \boldsymbol{r}_n) \quad . \tag{2.19}$$

Consequently, the density is simply given by

$$\rho(\boldsymbol{r}) \equiv \rho^{\mathrm{s}}(\boldsymbol{r}) = \sum_i^n \varphi_i^*(\boldsymbol{r})\varphi_i(\boldsymbol{r}) \quad , \tag{2.20}$$

so that the kinetic energy contribution becomes

$$E_{\mathrm{T_e}}^{\mathrm{s}} = \langle \phi^{\mathrm{s}} | T_{\mathrm{e}} | \phi^{\mathrm{s}} \rangle = -\frac{\hbar^2}{2m_{\mathrm{e}}} \sum_{i=1}^n \int d\boldsymbol{r} \varphi_i^*(\boldsymbol{r}) \boldsymbol{\nabla}_{\boldsymbol{r}}^2 \varphi_i(\boldsymbol{r}) \quad . \tag{2.21}$$

The Hohenberg-Kohn functional F_{HK} (cf Eq. (2.16)) is now written as

$$F_{\mathrm{HK}}[\rho] = E_{\mathrm{T_e}}^{\mathrm{s}} + E_{\mathrm{H}}[\rho] + E_{\mathrm{xc}}[\rho] \tag{2.22}$$

Here the Hartree energy E_{H} is the classical electrostatic interaction energy of a ("continuous") electron gas with density ρ

$$E_{\mathrm{H}}[\rho] = \frac{1}{4\pi\varepsilon_0} \frac{1}{2} \int d\boldsymbol{r} d\boldsymbol{r'} \frac{\rho(\boldsymbol{r})\rho(\boldsymbol{r'})\, e^2}{\|\boldsymbol{r} - \boldsymbol{r'}\|_2} \quad . \tag{2.23}$$

The exchange-correlation functional E_{xc} accounts for the missing quantum mechanical interaction of the electrons in the aforementioned non-interacting reference system due to exchange (cf Eq. (2.19)) and correlation effects, i.e. the contributions not captured by both $E_{\mathrm{T_e}}$ and $E_{\mathrm{ee}}[\rho]$. Thus it can formerly be written as

$$E_{\mathrm{xc}}[\rho] = E_{\mathrm{T_e}} - E_{\mathrm{T_e}}^{\mathrm{s}} + E_{\mathrm{ee}}[\rho] - E_{\mathrm{H}}[\rho] \quad , \tag{2.24}$$

where $E_{\mathrm{T_e}} = \langle \phi | T_{\mathrm{e}} | \phi \rangle$. The hope is that these missing parts are "small" and hence can perhaps even be crudely approximated in practice. Minimization of Eq. (2.16) yields single-particle Schrödinger equations

$$\left(-\frac{\hbar^2}{2m_{\mathrm{e}}} \boldsymbol{\nabla}_{\boldsymbol{r}}^2 + \underbrace{v_{\mathrm{H}}(\boldsymbol{r}) + v_{\mathrm{xc}}(\boldsymbol{r}) + v_{\mathrm{ext}}(\boldsymbol{r})}_{v_{\mathrm{eff}}(\boldsymbol{r})} \right) \varphi_i(\boldsymbol{r}) = \varepsilon_i \varphi_i(\boldsymbol{r}) \quad , \tag{2.25}$$

[iii] Tough it appears to be physically plausible that such a non-interacting reference system with the same density can always be found "close enough" to the interacting system of interest, mathematically this is all but clear. Indeed, this aspect has not yet been discussed extensively in the literature.

which are commonly referred to as Kohn-Sham equations. The contributions to the effective potential v_{eff} are given by the functional derivatives with respect to the density of the respective energy contributions:

$$v_{\text{H}}([\rho];\boldsymbol{r}) = \frac{1}{4\pi\varepsilon_0}\int d\boldsymbol{r'}\,\frac{\rho(\boldsymbol{r'})e^2}{\|\boldsymbol{r}-\boldsymbol{r'}\|_2} \tag{2.26a}$$

$$v_{\text{xc}}([\rho];\boldsymbol{r}) = \frac{\delta E_{\text{xc}}[\rho]}{\delta\rho}(\boldsymbol{r}) \tag{2.26b}$$

$$v_{\text{ext}}(\boldsymbol{r}) = \frac{1}{4\pi\varepsilon_0}\sum_{I=1}^{N}\frac{Z_I e^2}{\|\boldsymbol{r}-\boldsymbol{R}_I\|_2} \tag{2.26c}$$

As exact analytic expressions for the exchange correlation energy (cf Eq. (2.24)) are unknown, v_{xc} can likewise only be given formally in Eq. (2.26b) and has to be approximated in practice, as will be detailed in Section 2.5. Most of the computing time spent within the scope of this thesis was used to solve the Eigenvalue problem given by Eq. (2.25), relying on a particular approximation for v_{xc}. Since v_{eff} depends on the density as indicated in Eq. (2.26a) and Eq. (2.26b) and hence via Eq. (2.20) on the to be obtained Kohn-Sham orbitals φ_i themselves, this problem has to be solved self-consistently which complicates the computational procedure. It is typically based on an iterative algorithm as detailed in Section 2.7, with the total energy being calculated in each iteration using the Kohn-Sham Eigenvalues ε_i according to

$$E[\rho] = \sum_{i=1}^{n}\varepsilon_i - E_{\text{H}}[\rho] + E_{\text{xc}}[\rho] - \int d\boldsymbol{r}\, v_{\text{xc}}([\rho];\boldsymbol{r})\,\rho(\boldsymbol{r}) \quad . \tag{2.27}$$

2.4. Time-Dependent Density Functional Theory

In 1984, Runge and Gross have extended the "Hohenberg-Kohn-Sham" theory presented in the previous section to dynamical electronic systems,[68] whose time evolution is described by the time-dependent electronic Schrödinger equation

$$i\hbar\frac{\partial}{\partial t}\,|\phi(t)\rangle = H_{\text{e}}(t)\,|\phi(t)\rangle \quad . \tag{2.28}$$

Analogously to the static case, the time-dependent density $\rho(\boldsymbol{r},t)$ alone is sufficient to completely determine any physical observable, like e.g. (differences of) the total energy. Furthermore, the system can be mapped onto a non-interacting reference system fulfilling single particle equivalents of Eq. (2.28), which, analogously to Eq. (2.25), contain a now time-dependent effective potential

$$v_{\text{TD,eff}}(\boldsymbol{r},t;\,\rho(\boldsymbol{r},t)) = v_{\text{TD,H}}(\boldsymbol{r},t;\,\rho(\boldsymbol{r},t)) + v_{\text{TD,xc}}(\boldsymbol{r},t;\,\rho(\boldsymbol{r},t)) + v_{\text{TD,ext}}(\boldsymbol{r},t;\,\rho(\boldsymbol{r},t)) \quad . \tag{2.29}$$

Like in the static case (cf Eqs. (2.26)), it also depends on the time-dependent density and contains an exchange-correlation part which needs to be approximated in practice. This time-dependent density-functional theory (TD-DFT) is the starting point for a pertubative treatment of (electron-hole pair) excitations of the electronic system due to non-adiabatic effects (cf Eqs. (2.6)) in Chapter 7. Extensions of TD-DFT to the full electron-nuclear dynamics beyond the Born-Oppenheimer approximation are subject of current research.[69–71]

2.5. Exchange-Correlation Functionals

In both the static and dynamic case, the exact exchange-correlation functional (and associated potentials, cf Eqs. (2.26) and (2.29)) are not known and hence need to be approximated in practical calculations. The *local density approximation* (LDA) is inspired by Thomas-Fermi theory[56–58] and takes

$$E_{\mathrm{xc}}^{\mathrm{LDA}}[\rho] = \int d\boldsymbol{r}\ \rho(\boldsymbol{r})\ v_{\mathrm{xc}}^{\mathrm{LDA}}(\rho(\boldsymbol{r})) \quad , \tag{2.30}$$

intrinsically assuming a slowly varying density. This is a purely local functional since the exchange-correlation potential $v_{\mathrm{xc}}^{\mathrm{LDA}}$ at each point in space is taken to be the same as for the homogeneous electron gas

$$v_{\mathrm{xc}}^{\mathrm{HEG}} = v_{\mathrm{x}}^{\mathrm{HEG}} + v_{\mathrm{c}}^{\mathrm{HEG}} \tag{2.31}$$

with the same density $\rho(\boldsymbol{r})$ at that point.

For systems where the spin of the electrons is important – like for example in case of the oxygen molecule – the *local spin density approximation* (LSDA) provides an improvement since the former is taken into account explicitly.

$$E_{\mathrm{xc}}^{\mathrm{LSDA}}\left[\rho^{\uparrow}, \rho^{\downarrow}\right] = \int d\boldsymbol{r}\ \rho(\boldsymbol{r})\ v_{\mathrm{xc}}^{\mathrm{LSDA}}(\rho^{\uparrow}(\boldsymbol{r}), \rho^{\downarrow}(\boldsymbol{r})) \tag{2.32}$$

The exchange and correlation contributions to $v_{\mathrm{xc}}^{\mathrm{LSDA}}$ are obtained just like in case of the LDA from the homogeneous electron gas. This is based on the spin (or also referred to as spin-polarized) density-functional theory generalization by Barth and Hedin.[72] $\rho^{\uparrow}$ and $\rho^{\downarrow}$ represent the charge densities in the two so-called spin channels, $|\uparrow\rangle$ and $|\downarrow\rangle$, respectively, due to a collinear spin treatment, i.e. measuring the spin along an axis which is homogeneously aligned at each point in space. Equivalently, the same information is represented by the electron charge density $\rho = \rho^{\uparrow} + \rho^{\downarrow}$ and spin density $\rho_{\mathrm{s}} = \rho^{\uparrow} - \rho^{\downarrow}$. The total number of unpaired electrons

$$N_{\mathrm{s}} = \int d\boldsymbol{r}\rho_{\mathrm{s}} = \underbrace{\int d\boldsymbol{r}\rho^{\uparrow}(\boldsymbol{r})}_{N^{\uparrow}} - \underbrace{\int d\boldsymbol{r}\rho^{\downarrow}(\boldsymbol{r})}_{N^{\downarrow}} \tag{2.33}$$

is then associated with a total spin $S = \frac{\hbar}{2}|N_{\mathrm{s}}|$, yielding a multiplicity of $\frac{2}{\hbar}S + 1 = |N_{\mathrm{s}}| + 1$. The corresponding magnetic moment of the electronic system, consisting of spin-$\frac{1}{2}$ particles with an electron spin g-factor $g_{\mathrm{e}} \approx -2$, is given by

$$\mu_{\mathrm{s}} = |\boldsymbol{\mu}_{\mathrm{s}}| = |g_{\mathrm{e}}|\frac{S}{\hbar}\mu_{\mathrm{B}} \approx |N_{\mathrm{s}}|\,\mu_{\mathrm{B}} \tag{2.34}$$

in units of the Bohr magneton $\mu_{\mathrm{B}} = \frac{e\hbar}{2m_{\mathrm{e}}}$. To some extent, even ferro- and antiferromagnetic configurations can be mimicked within this picture of collinear spin. A simple way of quantifying the overall spin alignment of parts of a system is to compare the difference between $|N_{\mathrm{s}}| = \left|N^{\uparrow} - N^{\downarrow}\right|$ and $\left|N^{\uparrow}\right| - \left|N^{\downarrow}\right|$. The spatial extent of the spin can also be quantified in more detail by projections of the Kohn-Sham levels in both spin channels onto those obtained for parts of the whole system. In gas surface dynamics, this has been made use of to monitor the spin transition of an incident atom[73,74]. In Chapter 7, this will be extended accordingly to the present case of a molecule instead of a single atom. Furthermore, a charge decomposition

of the spin density according to an "atoms in molecules" approach[75] has allowed to apply a form of (spin-) constrained DFT for the construction of potential energy surfaces for O_2 on the (111) surface of aluminum.[47,76,77] Altogether, apart from improvements of the energetics, spin-polarized DFT can thus also provide additional physical insights for the system under investigation.

While the exchange contribution $v_{\mathrm{x}}^{\mathrm{HEG}}$ can even be given analytically, values for the remaining correlation part $v_{\mathrm{c}}^{\mathrm{HEG}}$ were determined numerically by Ceperly and Alder using quantum Monte Carlo calculations.[78] Different parametrizations of this data due to work by Perdew and Zunger (PZ-LDA)[79] and Perdew and Wang (PW-LDA)[80] have led to the LDA and LSDA implementations found in most present DFT computer codes. Despite its simplicity, it has been very successful in particular for the description of structural and elastic properties of both bulk systems and surfaces.[81]

For small molecules and their adsorption on surfaces, semi-local functionals employing an exchange-correlation potential also depending on the local gradient of the density

$$E_{\mathrm{xc}}^{\mathrm{GGA}}[\rho] = \int d\boldsymbol{r}\ \rho(\boldsymbol{r})\ v_{\mathrm{xc}}^{\mathrm{GGA}}(\rho(\boldsymbol{r}), \boldsymbol{\nabla}_{\boldsymbol{r}}\rho(\boldsymbol{r})) \quad . \tag{2.35}$$

have been found to perform much better, improving the description of adsorption energies in particular.[82] In 1991, the first incarnation of this so-called generalized gradient approximation (GGA) without any empirical parameters was proposed by Perdew and Wang (PW91)[83,84] and has been simplified by Perdew, Burke and Ernzerhof (PBE)[85,86] later on. Furthermore, modifications have been proposed in a comment to the original work (now known as revPBE)[87,88] and in a separate study by Hammer, Hansen and Nørskov aiming to particularly improve adsorption energetics of small molecules on surfaces (resulting in RPBE).[89] Analogously to the LDA, spin-polarized versions of these functionals (for collinear treatment of spin) have been developed alongside.

Further systematic improvement of the exchange-correlation functional is difficult and hence can be seen as one of the drawbacks of density-functional theory. On the other hand, systematically improvable wave function based theories cannot be straightforwardly applied to periodic systems and suffer from poor scaling with system size.[90,91] Similarly, the computational demands of many-body techniques like the random phase approximation (RPA) currently calls for additional simplifications[92] when applied to adsorption systems or restrict the size of the latter.[93,94] Lack of forces further limits the possible application to dynamics at present.

But also non-local functionals have been proposed during the last years,[95–102] particularly motivated by the desire to capture van-der-Waals contributions to chemical binding (hence also referred to as vdW-DF), e.g. for large, organic molecules on surfaces. Due the high computational effort initial, non-self-consistent applications were focused on such systems.[95,96] Recent algorithmic improvements have made evaluations of their performance for a broader range of systems subject of current research.[103]

Finally, non-local effects of exchange and correlation in the electron-electron interaction have also been added *a posteriori* "on top of DFT" via computationally appealing more or less semi-empirical schemes (DFT-D, DFT+vdW).[104–106] This has shown to improve the description of adsorption (of organic molecules) over semi-local functionals, but rather in structural than energetic properties.[107,108] For small molecules (O_2 on Al(111)) an improvement could not yet be verified.[109]

Altogether, DFT-GGA has served as a "work-horse" for the present and many other surface studies in the past decades. Certainly, going beyond the accuracy of GGAs would be desirable, but more accurate electronic structure theory proves to be extremely computationally challeng-

ing when a large number of evaluations is required like in the context of dynamics. Not focusing on the influence of the employed exchange-correlation functional, all density functional calculations in the present study have been carried out using the PBE functional, which is expected to be a reasonable, sufficiently accurate compromise for the present study. At this point, it is important to emphasize that all concepts which are developed within the scope of this work do not rely on a particular choice of E_{xc}. In fact, they can be easily applied to energetics obtained with a "divine" density-functional, should it be obtained in the future, or even yet another electronic structure method allowing to calculate total energies for adsorption systems.

2.6. Periodic Systems

In a perfect solid, the external potential of the electronic problem in Eq. (2.3) is periodic. The corresponding Hamiltonian H_{e} hence commutes with translation operators $T_{\boldsymbol{a}_i}$,

$$[H_{\mathrm{e}}, T_{\boldsymbol{a}_i}] = 0 \quad i \in 1,2,3 \quad , \tag{2.36}$$

which are defined by their effect on (real space) wave functions

$$T_{\boldsymbol{L}}\phi(\boldsymbol{r}) = \langle \boldsymbol{r} \,|T_{\boldsymbol{L}}|\, \phi\rangle = \phi(\boldsymbol{r}+\boldsymbol{L}) \quad . \tag{2.37}$$

$\boldsymbol{L}$ is a lattice vector

$$\boldsymbol{L} = n_1\boldsymbol{a}_1 + n_2\boldsymbol{a}_2 + n_3\boldsymbol{a}_3 \quad (n_1,n_2,n_3) \in \mathbb{N}^3 \quad , \tag{2.38}$$

where $\boldsymbol{a}_i$, $i \in \{1,2,3\}$ are the primitive lattice vectors defining the periodicity.

The translational symmetry allows to classify the electronic Eigenstates by good quantum numbers $\boldsymbol{k}$. As stated in Bloch's famous theorem,[110] the latter can be written as so-called Bloch waves

$$\phi_{\boldsymbol{k}b}(\boldsymbol{r}) = u_{\boldsymbol{k}b} \cdot \mathrm{e}^{i\boldsymbol{k}\boldsymbol{r}} \quad , \tag{2.39}$$

consisting of a lattice periodic function $u_{\boldsymbol{k}b}$ and a plane wave $\mathrm{e}^{i\boldsymbol{k}\boldsymbol{r}}$ with $\boldsymbol{k}$ inside the first Brillouin zone[iv] and additional quantum numbers called band indices b. Due to its periodicity, $u_{\boldsymbol{k}b}$ can be written in form of a Fourier series, resulting in

$$\phi_{\boldsymbol{k}b} = \sum_{\boldsymbol{G}} c_{\boldsymbol{G}}^{\boldsymbol{k}b} \mathrm{e}^{i(\boldsymbol{k}+\boldsymbol{G})\boldsymbol{r}} \quad , \tag{2.40}$$

where $\boldsymbol{G}$ are reciprocal lattice vectors. For each $\boldsymbol{k}$, the discrete set of plane waves $\{\mathrm{e}^{i(\boldsymbol{k}+\boldsymbol{G})\boldsymbol{r}}\}_{\boldsymbol{G}}^{\boldsymbol{k}}$ forms an orthogonal basis set for functions with the lattice periodicity expressed in Eq. (2.37). More precisely, since $\boldsymbol{k}$ belongs to the first Brillouin zone and is hence only a fraction of a reciprocal lattice vector $\boldsymbol{G}$, this even holds for the union set $\bigcup_{\boldsymbol{k}}\{\mathrm{e}^{i(\boldsymbol{k}+\boldsymbol{G})\boldsymbol{r}}\}_{\boldsymbol{G}}^{\boldsymbol{k}}$, yielding

$$\int d\boldsymbol{r}\, \mathrm{e}^{-i(\boldsymbol{k}'+\boldsymbol{G}')\boldsymbol{r}} \cdot \mathrm{e}^{i(\boldsymbol{k}+\boldsymbol{G})\boldsymbol{r}} = 2\pi\, \delta_{\boldsymbol{G}\boldsymbol{G}'}\, \delta(\boldsymbol{k}-\boldsymbol{k}') \quad . \tag{2.41}$$

Equation (2.40) is very appealing for numerical calculations on a computer: Electronic states and other quantities can simply be represented as vectors of their expansion coefficients $C_{\boldsymbol{G}}^{\boldsymbol{k}b}$

[iv] The definition of $u_{\boldsymbol{k}b}$ makes consideration of $\boldsymbol{k}'$ outside the first Brillouin zone pointless: It can always be replaced by $\boldsymbol{k} = \boldsymbol{k}' + \boldsymbol{G}$ inside the latter with the lattice periodic part $\mathrm{e}^{i\boldsymbol{G}\boldsymbol{r}}$ absorbed into $u_{\boldsymbol{k}b}$.

given on (regular) grids – without any further approximations due to the discreteness. The Kohn-Sham equations Eqs. (2.25) thus become matrix equations, which, thanks to the orthogonality, have the simple form:

$$\sum_{\boldsymbol{G'}} \left(\frac{\hbar^2}{2m_\mathrm{e}} \left(\boldsymbol{k}+\boldsymbol{G}\right)^2 + \tilde{v}_\mathrm{eff}(\boldsymbol{G}-\boldsymbol{G'}) \right) c_{\boldsymbol{G'}}^{\boldsymbol{k}b} = \varepsilon^{\boldsymbol{k}b} c_{\boldsymbol{G'}}^{\boldsymbol{k}b} \quad , \tag{2.42}$$

where $\tilde{v}_\mathrm{eff}$ is the Fourier transform of the effective potential. In particular, the kinetic energy operator is diagonal, i.e. just a multiplication. Fourier transformation of Eq. (2.40) yields coefficients of an equivalent real space representation in which the same holds for the effective potential. Fortunately, performing such discrete Fourier transforms to switch between representations is a well developed numerical technique, scaling favorably with $\mathcal{O}(N_\mathrm{FFT}\log(N_\mathrm{FFT}))$ when carried out in form of a so-called *fast Fourier transform*.[v]

Obviously, a representation in form of Eq. (2.40) must be finite on a computer, i.e. only coefficients below a certain cut off, which is conveniently given in form of an energy, can be considered

$$\frac{\hbar^2}{2m_\mathrm{e}} \left(\boldsymbol{k}+\boldsymbol{G}\right)^2 \leq E_\mathrm{cut} \quad . \tag{2.43}$$

The size of this cut off energy E_cut required for numerically converged results thus determines the efficiency of the approach. Squaring the orbitals to obtain the charge density according to Eq. (2.20) results in a representation equivalent to Eq. (2.40) which in principle requires even twice as many coefficients in each direction. In practice, however, a grid which is smaller than one corresponding to $4\,E_\mathrm{cut}$ is used, as the corresponding large wave vector components of the density are typically not of predominant importance.

Unfortunately, the single-particle states of valence electrons oscillate strongly in regions close to the nuclei in order to be preserve orthogonality with respect to the core states, thus resulting in rather large values for E_cut. With increasing mass of the elements, this problem becomes more and more severe, so that transition metals could not be economically treated. The problem can be remedied by introducing so-called pseudopotentials.[111,112] Within a *frozen core approximation*, only valence electrons, which are typically most important for the description of chemical bonding, are treated explicitly. Apart from reducing the number of electrons, this paves the way for replacing the Coulomb potentials, which determine the electron-nuclear interaction in Eq. (2.4c), by suitable "soft" potentials. These pseudopotentials are constructed to reproduce corresponding all-electron results for the scattering properties of single-particle states of spherical atoms outside a certain cut off radius r_c. Inside however, the aforementioned strong oscillations are suppressed, thus reducing the required E_cut. The resulting pseudo-atom replacements in Eq. (2.4c) typically make the external potential in the Kohn-Sham equations non-local[111] which however can be dealt with rather efficiently in a plane wave framework.[113] This construction also allows to incorporate relativistic effects as captured by scalar relativistic extensions to the atomic Schrödinger equation, which also become more and more important with increasing nuclear mass.[114]

In the early days pseudopotentials always were constructed to be *norm-conserving*, i.e. the norm of the pseudo-atomic states was always enforced to be the same as the one of their corresponding all-electron counterparts.[115,116] Consequently, the soft part inside the pseudoization sphere given by r_c was always constrained to yield the same amount of charge as given by the

[v] See e.g. http://www.fftw.org for a free implementation and further reading on FFTs in general.

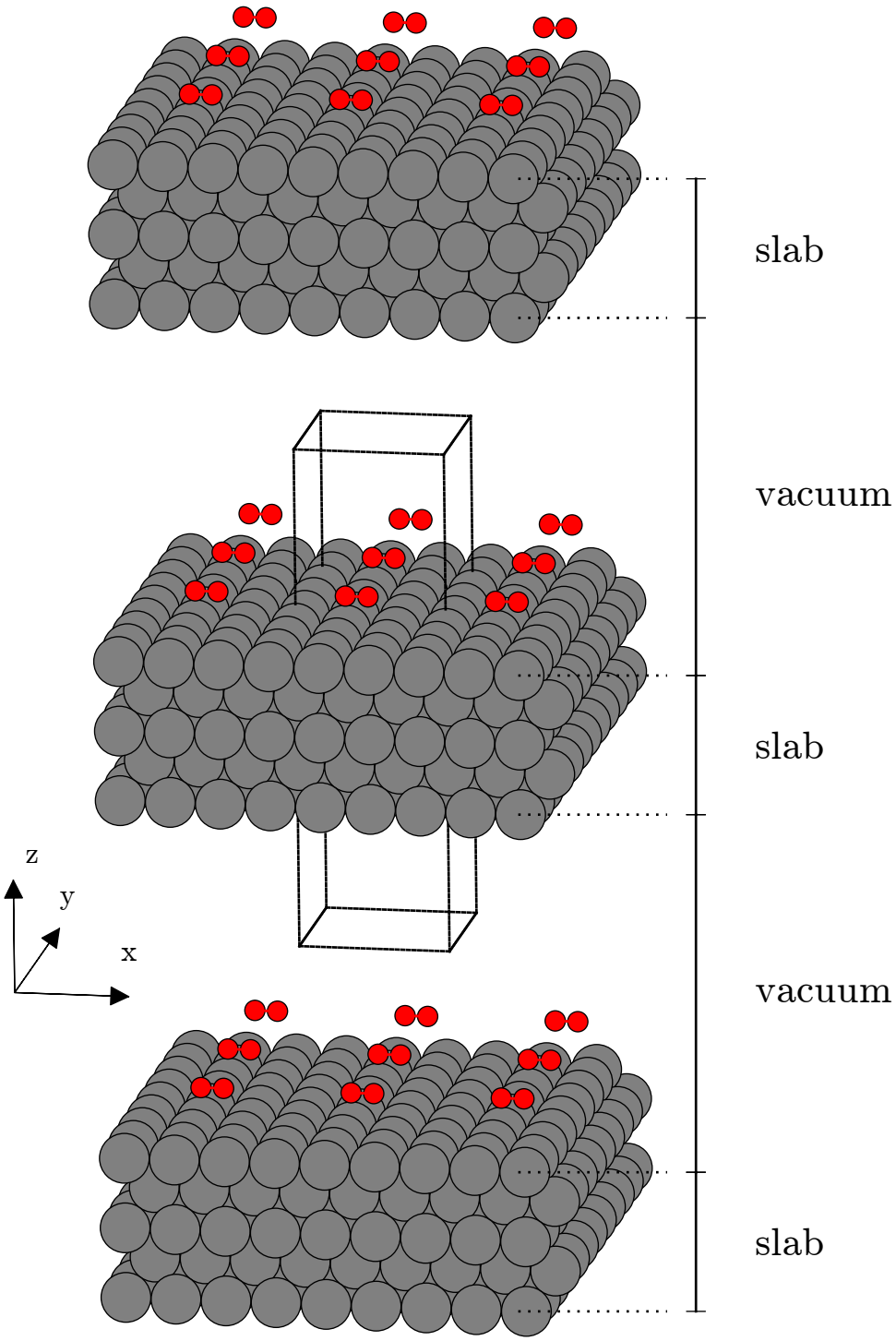

Figure 2.1.: Schematic representation of a 3×3 supercell of the primitive Pd(100) surface unit cell with an O_2 molecule modeled by a slab of five layers which are separated by vacuum along the z direction. The supercell is indicated by the solid black lines. Two images in each direction are shown.

latter. Lifting this constraint lead to the construction of so-called *ultrasoft* pseudopotentials (USPs),[117,118] which allows significant further reduction of the cut off energy required to represent the single-particle Kohn-Sham states of the pseudoelectrons, in particular for transition metals. At the same time, a generalized orthonormality in the sense of a non-canonical scalar product is introduced for the latter, which has to be kept in mind e.g. when defining projection operations[119,120] (also see Section 2.5 and Section 7.3.2). The missing charge is reintroduced by so-called augmentation charges Q, which are also part of the pseudopotential. They are strictly localized in the regions around the cores and can be "harder" than the "ultrasoft" pseudo-atomic states, which is why a representation on an even finer grid than the on used for the pseudo charge density (within a double grid technique[121]) can be highly advisable. Of course, it is beneficial (if not even mandatory) to exploit the reduction of the computational burden offered by the USPs for this work. Nevertheless, a proper description of light elements of the second row of the periodic table of elements still requires a rather large cut off energy. It is thus not surprising that many gas-surface dynamical studies have been focused on hydrogen so far.

Unfortunately, the plane wave expansion given by Eq. (2.40) still contains the continuous index $\boldsymbol{k}$. Practice shows however that the Brillouin zone (with associated volume V_{BZ}) can be sampled quite efficiently by means of discrete and finite $\boldsymbol{k}$-point grids[122,123], i.e. by introducing the approximation

$$\frac{1}{V_{\mathrm{BZ}}} \int_{\mathrm{BZ}} d\boldsymbol{k} \;\approx\; \frac{1}{(2\pi)^3} \sum_{\boldsymbol{k}} w_{\boldsymbol{k}} \quad , \tag{2.44}$$

Since real space symmetry directly translates into reciprocal space, only $\boldsymbol{k}$-points from the irreducible part of the Brillouin zone with symmetry-induced weights $w_{\boldsymbol{k}}$ need to be calculated explicitly. Every periodic Hamiltonian, thus fulfilling Eq. (2.36), also possesses the so-called time reversal symmetry

$$E(\boldsymbol{k}) = E(-\boldsymbol{k}) \quad . \tag{2.45}$$

This is usually exploited in order to only calculate half number of $\boldsymbol{k}$-points on the aforementioned equally spaced grid $\boldsymbol{k}$-point grids, conveniently reducing the computational effort by a factor of two.

When it comes to surfaces, the three-dimensional periodicity assumed so far is broken in one direction. Despite Wolfgang Pauli's famous quote

> *"God made the bulk; surfaces were invented by the devil."*

this not a reason for despair after all the formalism which has been introduced so far: Surfaces can still be treated efficiently within the so-called supercell approach shown schematically in Fig. 2.1. Slabs of sufficient thickness are separated by sufficient amounts of vacuum, which is traditionally chosen to be along the z-axis and supposed to be large enough to decouple adjacent copies. Unfortunately, computational effort is spent also to describe these regions due the basis set expansion given by Eq. (2.40), although a single $\boldsymbol{k}$-point along this direction provides sufficient sampling of the (ideally) two-dimensional Brillouin zone. On the other hand, the truly periodic treatment in lateral directions ensures a proper description of the corresponding band structure, which is of particular importance for metallic surfaces and description of adsorption thereon.[82] To model adsorption of individual molecules, lateral interactions need to be sufficiently decoupled by also choosing appropriate cell sizes in these directions as indicated in Fig. 2.1.

For more, also particularly technical details about the plane wave approach, the interested reader is referred to the excellent review by Payne and coworkers.[124]

2.7. Finding the Ground State

As already indicated in Section 2.3, the self-consistent solution for the Kohn-Sham equations (cf Section 2.3.2) and thus the ground state of the quantum mechanical system is typically obtained iteratively. This self-consistency cycle is usually initialized with a superposition of atomic (pseudo) charge densities defining the initial single-particle Hamiltonian of Eq. (2.25). The latter are obtained from the numerical solution of the spherical (pseudo) atoms, preferentially based on the same exchange-correlation functional.[vi]

Probably the most straightforward way to self-consistency is given by a simple density mixing strategy

1. Solve the Kohn-Sham equations (cf Section 2.3.2) for the given input density ρ^{in}. As indicated in Section 2.6 for a plane wave basis set (cf Eq. (2.42)), this translates into a matrix diagonalization problem.

2. Calculate new output density ρ^{out} according to Eq. (2.20).

3. Stop if ρ^{in} and ρ^{out} are in "sufficiently good agreement", which can be measured according to different criteria. Otherwise, obtain a new input density by forming a mixture of ρ^{in} and ρ^{out} and restart.

Obviously, the last step is the eponym of this strategy, which is necessary in order to avoid too drastic changes in the Eigenstates from iteration to iteration and hence stabilize and accelerate the approach of self-consistency. Apart from simple linear mixing, i.e. $(1-\alpha)\rho^{\text{in}} + \alpha\rho^{\text{out}}$, also more sophisticated and effective mixing schemes have been developed.[125–129] Still, only a cumbersome trial and error procedure of adjusting mixing parameters can ensure to reach self-consistency for particularly "nasty" systems.

Due to the large number of basis functions and hence enormous matrix sizes conventional matrix diagonalization cannot be used for the first step in a plane wave basis set, In fact, the vast majority of the Kohn-Sham states obtained thereby would not even be useful because they would describe unoccupied states. In their seminal work in the middle of the 80s,[130] Car and Parinello (CP) recast the electronic minimization problem into a dynamical one. This allowed to adapt hitherto matured techniques and computational infrastructure for (classical) molecular dynamics (MD, cf Chapter 3). The corresponding CPMD algorithm thus even allows to treat the dynamics of both electrons and nuclei on equal footing and does not rely on matrix diagonalization. Another approach was introduced by Teter and coworkers, targeting (even) larger systems.[131] Applying conjugate gradient optimization techniques,[132] which in principle guarantee convergence, directly to the Kohn-Sham energy functional to be minimized, it has been termed *direct minimization* later on.[124] Relying on that functional, it is to be clearly distinguished from orbital free DFT and thus avoids the problem of finding good approximations for the kinetic energy part of the interacting electrons in the Hohenberg-Kohn functional (cf Section 2.3). In the middle of the 90s, Kresse and Furthmüller demonstrated that a combination of density mixing with an iterative diagonalization technique yields a highly efficient and powerful scheme.[133,134] Only a tiny fraction of the Kohn-Sham states are calculated, naturally

[vi] Here, the initial radial potential is typically taken according to some physically reasonable analytical expression in order to construct the initial Hamiltonian. Any of the algorithms sketched out in the following can be used to achieve self-consistency, but typically a very simple form of density mixing is sufficient for this rather simple problem.

focusing on those with the lowest energies that are to be occupied by electrons. Not surprisingly, this scheme has been adopted and is even used by default in many plane wave DFT codes.

Without further ado, metallic systems pose a (severe) challenge to each of these approaches. Because unoccupied levels are not clearly separated from occupied ones by a band gap, algorithms might get stuck by repeatedly occupying and unoccupying states around the Fermi energy ε_F – resulting in large changes in the density. Such oscillations back and forth without getting any closer to the ground state are also known as charge sloshing. Already very early in the 80s, Fu and Ho[135] introduced an idea to significantly improve the convergence of the self-consistency cycle for metals. It can be nicely formulated[136] by introducing a local density of states (LDOS) including a broadening function $\tilde{\delta}$ with a width σ

$$\tilde{\rho}_\mathrm{LDOS}(\varepsilon, \boldsymbol{r}) = \sum_{i=1}^{n} \frac{1}{\sigma} \tilde{\delta}\left(\frac{\varepsilon - \varepsilon_i}{\sigma}\right) |\varphi_i(\boldsymbol{r})|^2 \quad , \tag{2.46}$$

which yields an equally broadened density of states (DOS)

$$\tilde{\rho}_\mathrm{DOS}(\varepsilon) = \int d\boldsymbol{r}\, \tilde{\rho}_\mathrm{LDOS}(\varepsilon, \boldsymbol{r}) = \sum_{i=1}^{n} \frac{1}{\sigma} \tilde{\delta}\left(\frac{\varepsilon - \varepsilon_i}{\sigma}\right) \tag{2.47}$$

and an electron density

$$\tilde{\rho}(\boldsymbol{r}) = \int_{-\infty}^{\varepsilon_\mathrm{F}} d\varepsilon\, \tilde{\rho}_\mathrm{LDOS}(\varepsilon, \boldsymbol{r}) = \sum_{i=1}^{n} \underbrace{\int_{-\infty}^{\frac{\varepsilon_\mathrm{F}-\varepsilon_i}{\sigma}} d\tilde{\varepsilon}\, \tilde{\delta}(\tilde{\varepsilon})}_{\equiv f_i} |\varphi_i(\boldsymbol{r})|^2 \tag{2.48}$$

with occupation factors f_i. Obviously, for $\tilde{\delta} = \delta$ the aforementioned single-particle electron density $\rho(\boldsymbol{r})$ given Eq. (2.20) and a corresponding "δ-discrete" DOS $\rho_\mathrm{DOS}(\varepsilon)$ are reobtained. If $\tilde{\rho}$ instead of ρ is used in the self-consistency cycle, drastic changes in the density due to the charge sloshing described before are smoothened out – thus stabilizing the convergence. Moreover, because the remaining error in self-consistency appears more strongly in derivatives of the total energy, this might be the only way to obtain properly converged forces that are suitable for *ab initio* molecular dynamics. An energy functional that is consistent with Eqs. (2.46) to (2.48) is obtained when also the so-called band energy term in Eq. (2.27), $\sum_{i=1}^{n} \varepsilon_i = \int_{-\infty}^{\varepsilon_\mathrm{F}} \rho_\mathrm{DOS}(\varepsilon)$, is modified accordingly in addition:

$$\int_{-\infty}^{\varepsilon_\mathrm{F}} d\varepsilon\, \varepsilon\, \tilde{\rho}_\mathrm{DOS}(\varepsilon) = \sum_{i=1}^{n} \underbrace{\int_{-\infty}^{\frac{\varepsilon_\mathrm{F}-\varepsilon_i}{\sigma}} d\tilde{\varepsilon}\, \tilde{\delta}(\tilde{\varepsilon})}_{=f_i} - \sigma \sum_{i=1}^{n} \underbrace{\left[- \int_{-\infty}^{\frac{\varepsilon_\mathrm{F}-\varepsilon_i}{\sigma}} d\tilde{\varepsilon}\, \tilde{\varepsilon}\, \tilde{\delta}(\tilde{\varepsilon}) \right]}_{\equiv S_i} \tag{2.49}$$

As already pointed out by Gillan[137] the corresponding "smeared" functional is equivalent to the Mermin functional[138], which provides a nonzero temperature generalization of the Hohenberg-Kohn functional given in Eq. (2.16), if the occupation factors f_i are taken from a Fermi-Dirac distribution. σ thus corresponds to a temperature. The first moments of the broadening function $\tilde{\delta}$ in the second term of Eq. (2.49), $\{S_i\}_i$, are entropy contributions to this free energy functional. In general and also in this work, the heated electronic system (not in equilibrium with the nuclei) is not of interest – only its positive effect to stabilize convergence as a

numerical trick. Apart from "Fermi smearing" generalized broadening functions $\tilde{\delta}$ have been proposed.[135,139–142] Some of them yield an error only in higher orders of the generalized temperature σ when using correction formulae for the energy to estimate $\sigma \to 0$, i.e. the desired value of the Hohenberg-Kohn functional. They are thus more efficient to correct for smearing. Forces usually cannot be easily corrected,[143] which is why σ should always be kept as small as possible just to still facilitate convergence.

While fractional occupancies are not incorporated at all into the direct minimization scheme by Teter and coworkers described above, the density mixing scheme by Kresse and Furthmüller greatly benefits from or even needs to rely on this finite temperature treatment for metallic systems. However, in addition to the mixing parameters, the smearing width is another parameter that needs to be treated with care: If chosen too large, it can even lead to convergence to a wrong electronic ground state. Quite in contrast, the so-called ensemble DFT scheme proposed by Marzari and coworkers[141,142,144] directly targets the free energy functional discussed in the previous paragraph and thus also explicitly minimizes the latter with respect to the occupancy factors. It can be seen as a sophisticated generalization of direct minimization for metals which carries over the robustness of the former including guaranteed convergence even for small smearing widths. Unfortunately, its underlying algorithm is computationally much more expensive compared to the aforementioned density mixing.

2.8. The CASTEP Code

The CASTEP code[145,146] is a modern implementation of density-functional theory using plane waves as a basis set together with pseudopotentials as described in the previous section and hence particularly suited for the treatment of periodic systems.

The code structure is schematically illustrated in Fig. 2.2, where contributions by the author of this thesis (mainly due to engagement in other projects[107,108]) are indicated accordingly. Paradigms of modern software design and engineering have been used during its development, which nowadays inevitably include ideas and concepts of *object-oriented programing* as much as possible within the employed programing language Fortran 95. The resulting clean and well commented code thus avoids unnecessary duplications, allowing and stimulating code reusability as well as simplifying maintainability and extendability – in particular when multiple developers are involved.[vii] In fact, this code is a complete rewrite of an earlier software package of the same name, initially developed by Mike Payne as "Cambridge Ab-initio Serial Total Energy Program", the complete rewrite of which has been stimulated and influenced by interests in commercial marketing by the company *accelrys*.[viii]

The layers indicated in Fig. 2.2 provide abstraction barriers and therefore "hide" low-level ("Utility") modules like Fourier transformations, input/output or parallelism as much as possible from the high-level algorithms tackling the actual physical problems. Thanks to the hierarchy, this functionality can be exchanged rather easily, e.g. allowing to switch between different implementations of Fourier transformations or plug in effectively non-parallel communication.

[vii] Unfortunately, this aspect is often overlooked in science, resulting in poorly written codes which might be reusable by the original author at best. This can have severe implications on the continuity of research in a world where the complexity of software is growing steadily – to some extent induced by the ongoing trend of increasing parallelization.

[viii] More precisely, CASTEP is an important part of the "Materials Studio" software package from *accelrys*, see `http://accelrys.com/products/materials-studio/quantum-and-catalysis-software.html`, which becomes increasingly popular and wide-spread in industry.

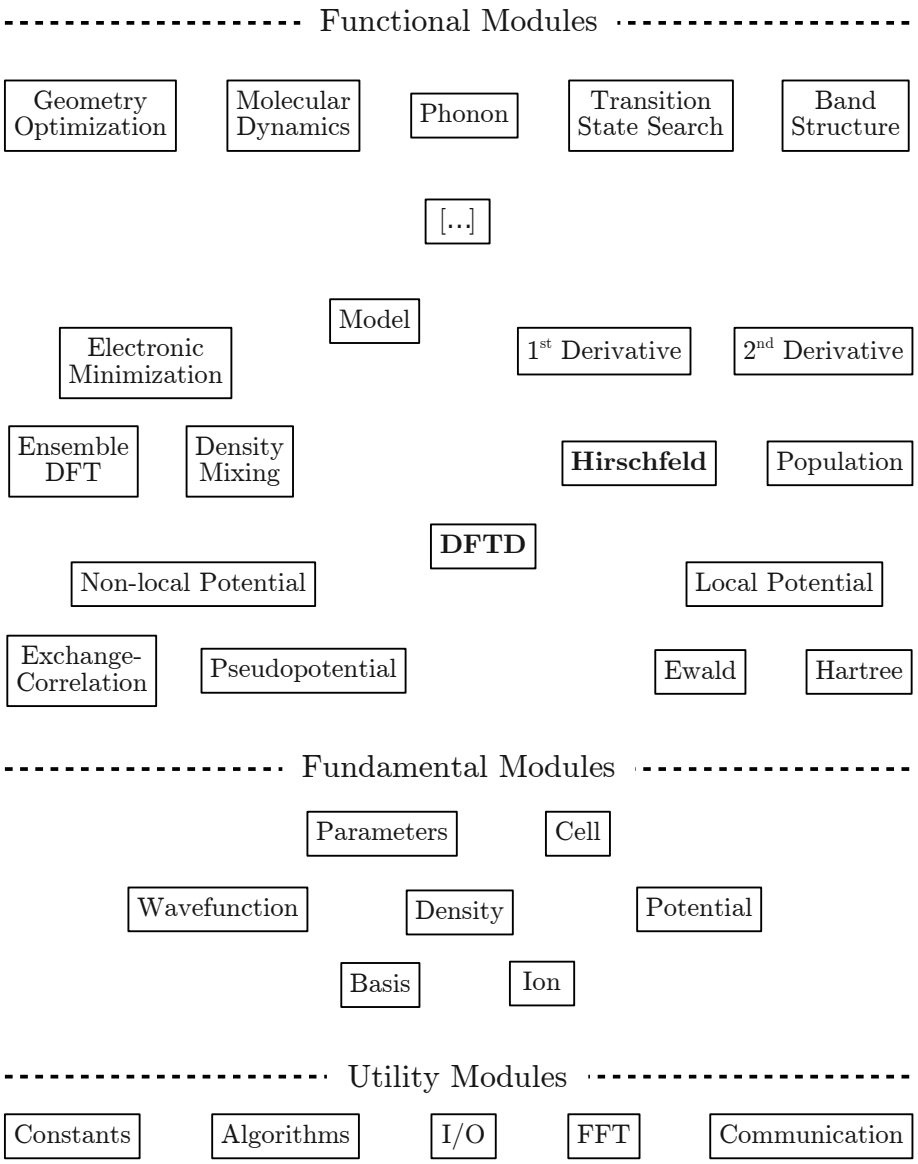

Figure 2.2.: Modular structure of the CASTEP code, grouped into the three abstraction levels "Utility", "Fundamental" and "Functional". Contributions by the author are highlighted by bold letters.

In the middle ("Fundamental") abstraction layer, typical data structures together with rather generic methods operating thereon are provided. They are made use of in high-level ("Functional") modules in particular for the actual self-consistent solution of the Kohn-Sham equations (cf Eq. (2.25)), for which several minimization algorithms are implemented. This includes direct minimization[124,131] ensemble DFT[142,144]) as well as density mixing[133,134] (cf Section 2.7). Thanks to the aforementioned design philosophy, the code structure closely resembles the underlying mathematical expressions and formulae,[145] which greatly simplifies their application in practical tasks like simple (single point) total energy as well as e.g. molecular dynamics or phonon calculations. The same holds for post-processing utilities or special-purpose applications like the perturbative approach for electron-hole pairs in Chapter 7 and its corresponding implementation described in more detail in Appendix C.

Different levels of parallelism are available as well, which is particularly important due to the fact that more computational power is nowadays provided through massively parallel computer architectures rather than increased single processor performance. Message passing as provided by the MPI standard[147] forms the basic communication infrastructure for all parallelism. The availability of MPI implementations on practically all supercomputers currently in use ensures high portability of the CASTEP code. Apart from simple parallelization over symmetry reduced $\boldsymbol{k}$-points, which requires hardly any communication during the solution of the individual corresponding Kohn-Sham problems and hence scales perfectly with the number of CPUs, the plane wave coefficients of a single $\boldsymbol{k}$-point can be parallelized as well. For large supercells and concomitantly smaller Brillouin zones, resulting in (sampling with) fewer $\boldsymbol{k}$-points and reduced grid spacings, this becomes increasingly important. However, it leads to a parallelization of matrix operations, which require an intense amount of communication. Even with state-of-the-art networking infrastructure, the scaling is limited to about a hundred CPU cores. A lot of the calculations in this work have been carried out at this limit, often suffering from shortcomings of bleeding edge technology. Only very recently, an intermediary layer of parallelism was introduced, parallelizing certain operations on bands rather than plane wave coefficients,[148] but unfortunately too late to be of benefit for this work.

3. Molecular Dynamics

Dissipation of energy in any kind of physical system is by definition a dynamical process. If the dynamics of chemical reactions take place on a single potential energy surface (cf Section 2.2) and the involved nuclei are "sufficiently heavy", a classical treatment of the latter is certainly a very good starting point. This chapter is therefore devoted to provide a short overview on the extremely powerful technique of molecular dynamics (MD),[i] which follows the spirit of Richard Feynman's famous quote

> *If we were to name the most powerful assumption of all, which leads one on and on in an attempt to understand life, it is that all things are made of atoms, and that everything that living things do can be understood in terms of the jigglings and wigglings of atoms.*

For a more detailed treatment, the reader is refered to the (respective chapters in) the excellent books by Frenkel and Smit[149] or Marx and Hutter.[150]

3.1. Equations of Motion

Within the Born-Oppenheimer approximation, which was described in Section 2.2, the full quantum mechanical electron-nuclear state separates into a direct product (cf Eq. (2.9)). If the probability amplitudes described by the wave function that represents the nuclear part are "sufficiently" localized, their interference and hence quantum effects like e.g. tunneling are negligible. The latter typically decays exponentially with the nuclear mass, so that a classical description becomes usually adequate for nuclei with masses heavier than hydrogen.[ii] This has e.g been confirmed for the dynamics of N_2 molecules on a Ru(0001) surface by practical calculations.[151]

As can e.g. be demonstrated by virtue of Ehrenfest's theorem, the nuclear Hamilton operator (cf Eq. (2.10)) goes over to a classical Hamilton function

$$H_{\mathrm{N}}^{\mathrm{cl}}(\mathcal{R},\mathcal{P}) = T_{\mathrm{N}}^{\mathrm{cl}}(\mathcal{P}) + V_{\mathrm{N}}^{\mathrm{cl}}(\mathcal{R}) \quad , \tag{3.1}$$

of positions $\mathcal{R} = \{R_I\}_I$ and $\mathcal{P} = \{P_I\}_I$ associated with each of the N nuclei when described

[i] As nicely explained by Wikipedia (http://en.wikipedia.org/wiki/Molecules), the word "molecule" refers to a "extremely minute *particle*", hence implying the second part of the wave-particle duality. In contrast, a time dependent quantum mechanical treatment of the nuclei (as wave functions) hence is usually refered to as quantum dynamics.

[ii] For free molecules in gas phase, a simple estimate is also provided by the de Broglie wavelength $\lambda = \frac{h}{p} \approx 12.8\sqrt{\frac{E}{(\mathrm{meV})}\frac{m}{(\mathrm{u})}}$ Å, where h is Planck's constant, p, E and m the momentum, energy and mass, respectively, of the classical particle. However, for the present purposes of reactions on surfaces, properties of bound states are certainly involved, so that estimates for free particles are misleading.

as point-like classical particles. The kinetic energy $T_{\mathrm{N}}^{\mathrm{cl}}(\mathcal{P})$ and potential energy $V_{\mathrm{N}}^{\mathrm{cl}}(\mathcal{R})$,

$$T_{\mathrm{N}}^{\mathrm{cl}}(\mathcal{P}) = \sum_{I=1}^{N} \frac{\boldsymbol{P}_I}{2M_I} \tag{3.2a}$$

$$V_{\mathrm{N}}^{\mathrm{cl}}(\mathcal{R}) = V_{\mathrm{NN}}^{\mathrm{cl}}(\mathcal{R}) + V_{\mathrm{e}}^{\mathrm{cl}}(\mathcal{R}) \quad , \tag{3.2b}$$

are the classical analogues of T_{N} and $V_{\mathrm{NN}}+V_{\mathrm{e}}$, as given by Eq. (2.4d) and Eqs. (2.4e) and (2.11), respectively. The quantum mechanical complexity of the electron-nuclear interaction is now hidden in $V_{\mathrm{N}}^{\mathrm{cl}}(\mathcal{R})$, after the electronic degrees of freedom have been "integrated out" according to Eq. (2.11). A few examples for approximations for the latter are detailed in the following Section 3.2.

For transformations to other coordinate systems, the Lagrange formalism can be more convenient – a fact that is exploited in Section 6.1. The Legendre transform in velocities $\dot{\mathcal{R}} = \{\dot{\boldsymbol{R}}_I\}_I$ and conjugated momenta $\mathcal{P} = \{\boldsymbol{P}_I\}_I$ relates the Hamiltonian $H_{\mathrm{N}}^{\mathrm{cl}}(\mathcal{R}, \mathcal{P})$ to the corresponding Lagrangian $L(\mathcal{R}, \dot{\mathcal{R}})$

$$H_{\mathrm{N}}^{\mathrm{cl}}(\mathcal{R}, \mathcal{P}) = \sum_{I=1}^{N} \dot{\boldsymbol{R}}_I \cdot \boldsymbol{P}_I - L_{\mathrm{N}}(\mathcal{R}, \dot{\mathcal{R}}) \quad . \tag{3.3}$$

Variational minimization of the latter yields the Euler-Lagrange equations

$$-\boldsymbol{\nabla}_{\boldsymbol{R}_I} V(\mathcal{R}) = \boldsymbol{F}_I = m_I \cdot \ddot{\boldsymbol{R}}_I \quad , \tag{3.4}$$

which are Newton's famous equations of motion. However, from a computational point of view, their pendants obtained within the Hamilton formalism

$$\dot{\boldsymbol{R}}_I = \boldsymbol{\nabla}_{\boldsymbol{P}_I} H_{\mathrm{N}}^{\mathrm{cl}} = \frac{\boldsymbol{P}_I}{M_I} \tag{3.5a}$$

$$\dot{\boldsymbol{P}}_I = -\boldsymbol{\nabla}_{\boldsymbol{R}_I} H_{\mathrm{N}}^{\mathrm{cl}} = -\boldsymbol{\nabla}_{\boldsymbol{R}_I} V_{\mathrm{N}}^{\mathrm{cl}} \tag{3.5b}$$

are typically more convenient: For the system of first order ordinary differential equations (ODEs) given by Eqs. (3.5) rather than the (equivalent) system of second order ODEs in Eq. (3.4), there is a variety of well understood numerical algorithms which allow efficient solutions on a computer. A few examples are described in more detail in Section 3.3.

Since molecular dynamics is often used in order to obtain statistical properties, sampling of phase space distributions other than the microcanonical described by Eqs. (3.5) can be desirable. One possibility to achieve that without sacrificing continuous dynamics is by extending those equations of motion. For the canonical ensemble (NVT), this was done correctly for the first time by Nosé[152–154] and later extended by Hoover[155] as well as Martyna and coworkers,[156]

finally resulting in a so-called Nosé-Hoover chain (of length L):

$$\dot{\boldsymbol{R}}_I = \frac{\boldsymbol{P}_I}{M_I} \tag{3.6a}$$

$$\dot{\boldsymbol{P}}_I = -\boldsymbol{\nabla}_{\boldsymbol{R}_I} V_{\mathrm{N}}^{\mathrm{cl}}(\mathcal{R}) \; - \; \boldsymbol{P}_I \frac{p_{\eta_1}}{Q_1} \tag{3.6b}$$

$$\dot{\eta}_l = \frac{p_{\eta_l}}{Q_l} \qquad , \qquad l \in \{1, \ldots, L\} \tag{3.6c}$$

$$\dot{p}_{\eta_1} = \left[\sum_{I=1}^{N} \frac{\boldsymbol{P}_I^2}{M_I} - 3N k_{\mathrm{B}} T \right] \; - \; p_{\eta_1} \frac{p_{\eta_2}}{Q_2} \tag{3.6d}$$

$$\dot{p}_{\eta_l} = \left[\frac{p_{\eta_{l-1}}^2}{Q_{l-1}} - k_{\mathrm{B}} T \right] \; - \; p_{\eta_l} \frac{p_{\eta_{l+1}}}{Q_{l+1}} \qquad , \qquad l \in \{2, \ldots, L\} \tag{3.6e}$$

$$\dot{p}_{\eta_L} = \left[\frac{p_{\eta_{L-1}}^2}{Q_{L-1}} - k_{\mathrm{B}} T \right] \tag{3.6f}$$

The L auxiliary variables η_l with associated momenta p_{η_l} are the so-called thermostat variables. Similar extensions to Eqs. (3.5) called barostats can also be constructed in order to sample the isobaric ensemble (NPE), as introduced by Parrinello and Rahman.[157,158] In the literature, individual trajectories generated by such extended dynamics are very often also ascribed physical reality, which does not have any theoretical justification. For thermostats, this will be discussed more extensively within the context of energy dissipation in Section 8.5 of Chapter 8.

3.2. Interaction Potentials

As described in the previous section (cf Eq. (3.2b)), the influence of the electronic structure with all its quantum mechanical complexity on the interaction between the nuclei is hidden in $V_{\mathrm{N}}^{\mathrm{cl}}(\mathcal{R})$, An exact analytic representation of the latter is generally impossible. A realistic description of a physical system within a molecular dynamics simulation therefore strongly depends on how well the complexity of this many-body problem is captured by the actual choice for this interatomic potential $V_{\mathrm{N}}^{\mathrm{cl}}(\mathcal{R})$. In the following, a few popular choices for the latter, which are particularly relevant for this thesis, are described.

3.2.1. Pair Potentials

The contribution of $V_{\mathrm{NN}}^{\mathrm{cl}}(\mathcal{R})$ to $V_{\mathrm{N}}^{\mathrm{cl}}(\mathcal{R})$ in Eqs. (3.2) is by definition a sum of pair potentials – the Coulomb potentials according to Eq. (2.4e). However, in general, this does not hold for $V_{\mathrm{e}}^{\mathrm{cl}}(\mathcal{R})$, resulting in

$$V_{\mathrm{N}}^{\mathrm{cl}}(\mathcal{R}) \approx \frac{1}{2} \sum_{A,B} V_{AB}^{\mathrm{pair}}(\boldsymbol{R}_A, \boldsymbol{R}_B) \quad . \tag{3.7}$$

to be a generally crude but probably simplest choice for $V_{\mathrm{N}}^{\mathrm{cl}}(\mathcal{R})$ for more than two atoms.

For (partly) periodic systems like bulk and surfaces, this sum is typically evaluated for a single unit cell within periodic boundary conditions (cf Section 2.6). To save computational effort, a cut-off radius R_{cut} is employed

$$V^{\mathrm{pair/cut}}(\boldsymbol{R}_{AB}) = \begin{cases} V^{\mathrm{pair}}(\boldsymbol{R}_{AB}) & , \; \|\boldsymbol{R}_{AB}\|_2 < R_{\mathrm{cut}} \\ 0 & , \; \|\boldsymbol{R}_{AB}\|_2 \geq R_{\mathrm{cut}} \end{cases} \quad . \tag{3.8}$$

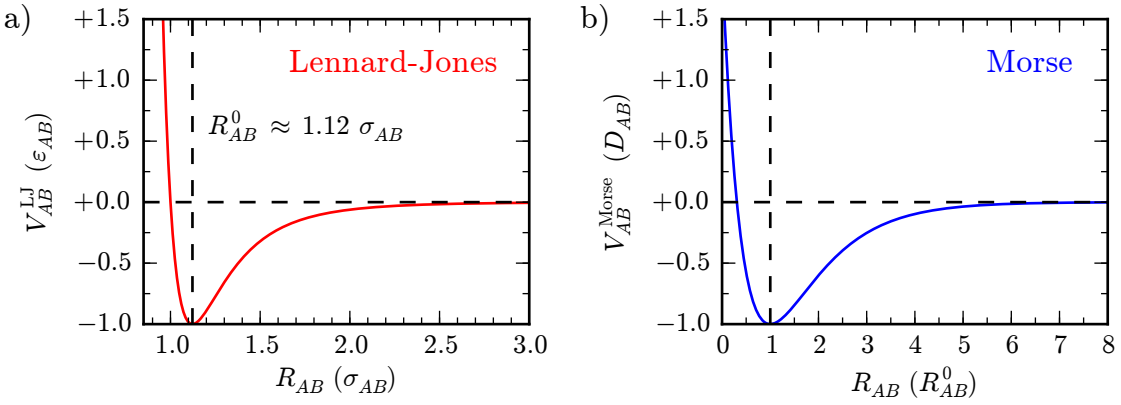

Figure 3.1.: a) Lennard-Jones and b) Morse potentials. Distances and energies are conveniently given in the usual dimensionless units as indicated in the axis labels.

This avoids the computation of pair interactions with negligible contributions – assuming a sufficiently strong decay of the underlying pair potential with distance. If this is not the case, methods like Ewald summation or particle mesh approaches can be used to efficiently deal with the long range part.[149]

One of the earliest but still very popular functional forms was proposed in 1924 by Lennard-Jones (in a similar form)[159]

$$V^{\mathrm{LJ}}_{AB}(R_{AB}) = 4\varepsilon_{AB}\left[\left(\frac{\sigma_{AB}}{R_{AB}}\right)^{12} - \left(\frac{\sigma_{AB}}{R_{AB}}\right)^{6}\right] \quad , \tag{3.9}$$

where R_{AB} denotes the distance between two atoms A and B. Forces are given by

$$F^{\mathrm{LJ}}_{AB}(R_{AB}) = -\frac{\partial V^{\mathrm{LJ}}_{AB}(R_{AB})}{\partial R_{AB}} = -\frac{4\varepsilon_{AB}}{R_{AB}}\left[\left(12\frac{\sigma_{AB}}{R_{AB}}\right)^{12} - \left(6\frac{\sigma_{AB}}{R_{AB}}\right)^{6}\right] \tag{3.10}$$

The equilibrium bond distance, where V^{LJ}_{AB} has its minimum, is given by $R^0_{AB} = \sqrt[6]{2}\sigma_{AB}$ and the bond strength or well depth is described by ε_{AB} as indicated in the plot shown in Fig. 3.1a, thus illustrating the meaning of the two parameters σ_{AB} and ε_{AB}. A famous choice for the latter is $\sigma^{\mathrm{Ar}}_{AB} = 120 k_{\mathrm{B}}\mathrm{K}$ and $\varepsilon^{\mathrm{Ar}}_{AB} = 3.4\text{Å}$,[iii] which quite successfully describe correlation functions of liquid Argon as was shown in one of the first molecular dynamics simulations.[160] The dominating van-der-Waals bonds in this system are captured rather well by the sum of R^{-6} pair terms contained in the Lennard-Jones potential. For that reason, many more complicated approximations for $V^{\mathrm{cl}}_{\mathrm{N}}(\mathcal{R})$ that are in use for the description of biological systems, like e.g. proteins,[iv] contain contributions from Lennard-Jones potentials. Likewise, as already indicated in Section 2.5, within modern semi-empirical DFT-D approaches, Born-Oppenheimer potential energy surfaces are augmented by similar sums of pair potentials containing R^{-6} terms. They are supposed to capture otherwise not included long-range parts due to van-der-Waals interactions, where parameters are either fixed[104,105] or obtained directly from the

[iii] See http://www.sklogwiki.org/SklogWiki/index.php/Argon for more details and an overview about other choices for $\sigma^{\mathrm{Ar}}_{AB}$ and $\varepsilon^{\mathrm{Ar}}_{AB}$.

[iv] In the bio-community they are commonly referred to as "force-fields".

electronic structure of the system under investigation.[106,107] However, often parameters are only available for interactions between atoms of type A $(\varepsilon_A, \sigma_A)$ and B $(\varepsilon_B, \sigma_B)$ seperately. Then, the parameters for the interaction between two atoms of types A and B $(\varepsilon_{AB}, \sigma_{AB})$ are very commonly devised according to completely empircial mixing rules employing geometric and arithmetic means:

$$\varepsilon_{AB} = \sqrt{\varepsilon_A \varepsilon_B} \tag{3.11a}$$

$$\sigma_{AB} = \frac{\sigma_A + \sigma_B}{2} \tag{3.11b}$$

Attempts were also made to parametrize generalized versions of Lennard-Jones potentials for an improved pair potential description of metals.[161] Due to the particular importance for this thesis, it is worth noting that also the peculiarities of phonons at surfaces have first been extensively investigated by Allen and coworkers based on a Lennard-Jones potential[162–169] as detailed in Chapter 4.

Another still very popular pair potential is the one proposed by Morse[170]

$$\begin{aligned} V_{AB}^{\text{Morse}}(R_{AB}) &= D_{AB}^0 \left[1 - \exp\left(-\alpha_{AB}(R_{AB} - R_{AB}^0)\right)\right]^2 - D_{AB}^0 \\ &= D_{AB}^0 \left[\exp\left(-2\alpha_{AB}(R_{AB} - R_{AB}^0)\right) - \right. \\ &\qquad \left. 2\exp\left(-\alpha_{AB}(R_{AB} - R_{AB}^0)\right)\right] \quad , \end{aligned} \tag{3.12}$$

which also (like the Lennard-Jones potential) only depends on the distance R_{AB} between two atoms A and B. Of course, the constant shift D_{AB}^0 in the first expression is not of any physical relevance and hence is often also simply dropped. Forces are given by

$$\begin{aligned} F_{AB}^{\text{Morse}}(R_{AB}) &= -\frac{\partial V_{AB}^{\text{Morse}}(R_{AB})}{\partial R_{AB}} \\ &= -2D_{AB}^0\alpha_{AB} \left[\exp\left(-2\alpha_{AB}(R_{AB} - R_{AB}^0)\right) - \right. \\ &\qquad \left. \exp\left(-\alpha_{AB}(R_{AB} - R_{AB}^0)\right)\right] \end{aligned} \tag{3.13}$$

The parameters D_{AB}^0 and R_{AB}^0 describe the well depth and equilibrium bond length, respectively, as shown by the plot in Fig. 3.1b. α is related to the vibrational properties which Morse originally tried to model for diatomic molecules with this choice of the potential:[170] The force constant is given by $k = 2\alpha^2 D_{AB}^0$. Indeed, nowadays with parameters determined by first-principles calculations, a Morse potential can describe covalently bound simple diatomic systems rather well. The interaction of single atoms on a fixed site on a surface can be modeled to some extent by combination of (two) Morse potentials (cf Appendix C). Along these lines, it is quite self-evident that also the first attempts to model the interaction of diatomics on surfaces were essentially based on a decomposition into pair contributions described by Morse potentials – with the lateral corrugation however being very difficult to capture properly. A more detailed discussion of the corresponding so-called LEPS and EDIM potentials can be found at the beginning of Chapter 6. Finally, also an application to metals has been reported,[171] long before more quantitative alternatives became tractable, like the one detailed in the next section.

3.2.2. Embedded Atom Method

While the metal-adsorbate interaction is very difficult or perhaps even impossible to describe at a first-principles level of accuracy by simple potential forms – hence deserving special attention in Chapter 6, more successful semi-empirical attempts exist for "bare" metals. Lacking

tractable alternatives for the computational resources available at the time, simple pair potentials like those described in the previous section have been (ab-)used initially according to Eq. (3.7).[162–169,171] However, when it comes to elastic properties, pair potentials are generally insufficient due to the delocalized, many-body character of the chemical binding in metals.[172,173] This can be rationalized by the so-called bond order (BO) conservation principle, stating that the total amount of bond strength is typically conserved for different coordinations and hence must be shared differently for the individual bonds.[174] Obviously, this cannot be fulfilled by construction with a sum of pair potentials according to Eq. (3.7).

With the embedded atom method (EAM),[172,175] the Finnis Sinclair potential,[173] the effective medium theory (EMT)[176,177] or the glue model[178] – just to name a few – different attempts have been made to address this problem, which all add a many-body correction to a basic pair potential description. Probably the most widespread[179–181] and therefore straightforward choice for the purposes detailed in Part III[v] is the EAM. It has its foundations in the aforedescribed density-functional theory (cf Section 2.3). As first discussed by Stott and Zaremba,[182] the Hohenberg-Kohn theorem can be generalized to also yield the (electronic) energy of an impurity in a solid

$$E_{\mathrm{e}}^{\mathrm{imp}} = F_{\mathrm{imp}}\left[\rho^{\mathrm{host}}\right] \quad , \tag{3.14}$$

where F_{imp} is a functional of the electron density of the *unperturbed* host ρ^{host}. It is to be distinguished from the Hohenberg-Kohn functional F_{HK} (cf Eq. (2.16)),[vi] but for a given impurity type and position it is universal with its exact form unknown just like the latter. Now, each atom of a solid can be seen as an impurity in the host electron density of all the other atoms. This *quasiatom* concept[182] motivates the following ansatz for an interatomic potential[172,175]

$$\begin{aligned} V_{\mathrm{N}}^{\mathrm{cl}}(\mathcal{R}) \approx V^{\mathrm{EAM}}(\mathcal{R}) &= \sum_I V_I^{\mathrm{EAM}}(\mathcal{R}) \\ &= \sum_I \left[\frac{1}{2} V_I^{\mathrm{EAM,pair}}(\mathcal{R}) + F^{\mathrm{EAM}}\left(\bar{\rho}_I^{\mathrm{EAM}}(\mathcal{R})\right)\right] \quad , \end{aligned} \tag{3.15}$$

where I denotes a summation over atoms.[vii] The pair potential contribution,

$$V_I^{\mathrm{EAM,pair}} = \sum_{J \neq I} V^{\mathrm{EAM,pair}}\left(R_{IJ}\right) \quad , \tag{3.16}$$

with R_{IJ} denoting the distance between atoms I and J, is motivated by the electrostatic interaction $V_{\mathrm{NN}}^{\mathrm{cl}}(\mathcal{R})$ (cf Eqs. (3.2) in Section 3.2.1). F^{EAM} is the so-called *embedding* function, motivated by Eq. (3.14) and supposed to capture the quantum mechanical many-body nature of the "embedding" of each atom into the host. In the spirit of the local density approximation of density-functional theory (cf Eq. (2.30) in Section 2.5), it only depends on the background electron density $\bar{\rho}_I$ at the site of the (quasi-)atom I, for which this is to be taken as contribution in Eq. (3.15). Thus the latter is given by

$$\bar{\rho}_I^{\mathrm{EAM}} = \sum_{J \neq I} \rho^{\mathrm{EAM}} R_{IJ} \quad , \tag{3.17}$$

[v] More precisely, its modified successor (MEAM) as detailed below is employed therein.

[vi] For example, it is not variational with respect to the host electron density,[175] which however is of no practical concern for what follows.

[vii] It is interesting to note that also state-of-the-art high-dimensional interatomic potentials typically use such an atomic decomposition of the energy.[183,184]

where ρ^{EAM} are atomic electron densities. To turn the embedded atom method into an interatomic potential in practice, originally different functional forms have been proposed and used for $V^{\mathrm{EAM,pair}}$, F^{EAM} and $\rho^{\mathrm{EAM}}(R)$, where the latter is typically taken to be spherically symmetric. Parameters in these forms have then been related to physical properties for which experimental data was available and fitted to reproduce the latter. Increasing feasibility and accuracy of first-principles calculations have allowed to avoid this detour by adjusting parameters directly in order to match calculated reference forces.[185] Within this force matching procedure, to accommodate a much larger amount of data – exploiting the inherent flexibility and ambiguities of $V^{\mathrm{EAM,pair}}$, F^{EAM} and $\rho^{\mathrm{EAM}}(R)$ – more general, numerical forms have been introduced. The actual fitting procedure thus becomes a much bigger effort and challenge in turn, as nicely exemplified by the work of Brommer and coworkers[186] whose potfit code is specifically dedicated to these purposes.[viii]

In contrast, in the modified embedding atom method (MEAM), more stringent forms for the pair potential, embedding function and density are used. The effort for a parametrization from first principle calculations is therefore significantly reduced, as e.g. discussed by van Beurden and coworkers.[187,188] The MEAM was originally developed by Baskes to also properly capture covalent bonding in materials like silicon[189,190] by trying to put in more physical insights into the aforementioned underlying functions. Later, the modification has also been formulated and proven useful for metals and in particular improved the description of metal surfaces.[191] This introduces several canonical parameters capturing material specific properties, marked accordingly in the formulae that follow, thus simplifying recognition and reference. For the embedding function, a form which has already proven to be reasonable within the EAM is chosen:

$$F^{\mathrm{MEAM}}\left(\bar{\rho}_I\right) = AE_0 \frac{\bar{\rho}_I}{\rho_0} \ln\left(\frac{\bar{\rho}_I}{\rho_0}\right) \tag{3.18}$$

A is a scaling parameter and E_0 is the cohesive energy of the bulk material. ρ_0 depends on the reference structure of the latter by its nearest neighbor coordination number Z_0 and hence is 12 for a fcc crystal. The background electron density is given by

$$\bar{\rho}_I = \bar{\rho}_I^{(0)}\, G(\Gamma_I) \quad , \tag{3.19}$$

Originally, the function G was taken to be $G(\Gamma) = \sqrt{1+\Gamma}$.[ix] Other forms, $G(\Gamma) = \exp(\frac{\Gamma}{2})$ or $G(\Gamma) = 2\,(1 + exp(-\Gamma))^{-1}$, have been used and discussed as well, but no clear improvements were found.[192]

$$\Gamma_I = \sum_{k=1}^{3} t^{(k)} \frac{\bar{\rho}_I^{(k)}}{\bar{\rho}_I^{(0)}} \tag{3.20}$$

is supposed to capture a directional dependance of the latter by means of the partial densities $\bar{\rho}_I^{(k)}$. The concomitant better description of directed chemical bonds represents the main physical insight and hence ascribed improvement of the MEAM. When the weights $t^{(k)}$ are set to

[viii] The resulting potfit code is available under *GPL* from http://www.itap.physik.uni-stuttgart.de/~imd/potfit.

[ix] The square root bares the risk of imaginary values for the background electronic density if some the weight parameters $t^{(k)}$ below in Eq. (3.20) are negative.

zero, the background electron density becomes spherical again (as will become clear from what follows), and hence the EAM is recovered. The partial densities are given by

$$\bar{\rho}_I^{(0)} = \sum_{J \neq I} S_{IJ} \rho^{(0)}\left(R_{IJ}\right) \tag{3.21a}$$

$$\left(\bar{\rho}_I^{(1)}\right)^2 = \sum_{\alpha=1}^{3} \left[\sum_{J \neq I} S_{IJ} \rho^{(1)}\left(R_{IJ}\right) \frac{R_{IJ\alpha}}{R_{IJ}} \right]^2 \tag{3.21b}$$

$$\begin{aligned} \left(\bar{\rho}_I^{(2)}\right)^2 = & \sum_{\alpha=1}^{3} \sum_{\beta=1}^{3} \left[\sum_{J \neq I} S_{IJ} \cdot \rho^{(2)}\left(R_{IJ}\right) \cdot \frac{R_{IJ\alpha} R_{IJ\beta}}{R_{IJ}^2} \right]^2 - \\ & \frac{1}{3} \left[\sum_{J \neq I} S_{IJ} \cdot \rho^{(2)}\left(R_{IJ}\right) \right]^2 \end{aligned} \tag{3.21c}$$

$$\left(\bar{\rho}_I^{(3)}\right)^2 = \sum_{\alpha=1}^{3} \sum_{\beta=1}^{3} \sum_{\gamma=1}^{3} \left[\sum_{J \neq I} S_{IJ} \cdot \rho^{(3)}\left(R_{IJ}\right) \cdot \frac{R_{IJ\alpha} R_{IJ\beta} R_{IJ\gamma}}{R_{IJ}^3} \right]^2 \tag{3.21d}$$

In more recent versions of the MEAM, the expression for $\bar{\rho}_I^{(3)}$ (Eq. (3.21d)) has been modified to[193]

$$\left(\widetilde{\bar{\rho}_I^{(3)}}\right)^2 = \left(\bar{\rho}_I^{(3)}\right)^2 - \frac{3}{5} \left[\sum_{J \neq I} S_{IJ} \cdot \rho^{(3)}\left(R_{IJ}\right) \cdot \frac{R_{IJ\alpha}}{R_{IJ}} \right]^2 \quad . \tag{3.22}$$

Here, the atomic electron densities $\rho^{(k)}$ are physically motivated taken as exponentially decaying

$$\rho^{(k)}(r) = \exp\left(\beta^{(k)} \left(\frac{r}{R^0} - 1 \right) \right) \quad , \quad k \in \{0, 1, 2, 3\} \quad , \tag{3.23}$$

introducing the decay parameters $\beta^{(k)}$ and the nearest neighbor distance R^0. Similar to Eq. (3.7), S_{IJ} in Eqs. (3.21) encapsulate a cut off function f_c and a screening function construction S_{IKJ} and C_{IKJ} as introduced by Baskes in a slight revision of the theory:[194]

$$S_{IJ} = f_\mathrm{c}\left(\frac{R_\mathrm{c} - R_{IJ}}{\Delta R} \right) \cdot \prod_{K \notin \{I,J\}} \bar{S}_{IKJ} \tag{3.24a}$$

$$S_{IKJ} = f_\mathrm{c}\left(\frac{C_{IKJ} - C_\mathrm{min}}{C_\mathrm{max} - C_\mathrm{min}} \right) \tag{3.24b}$$

$$C_{IKJ} = 1 + 2 \frac{R_{IJ}^2 R_{IK}^2 + R_{IJ}^2 R_{KJ}^2 - R_{IJ}^4}{R_{IJ}^4 - \left(R_{IK}^2 - R_{KJ}^2\right)^2} \tag{3.24c}$$

$$f_\mathrm{c}(x) = \begin{cases} 1 & , \quad x \geq 1 \\ \left[1 - (1-x)^4\right] & , \quad 0 < x \leq 1 \\ 0 & , \quad x \leq 0 \end{cases} \tag{3.24d}$$

Typical values are $R_\mathrm{c} = 4\,\text{Å}$ for the cut off radius and $\Delta R = 0.1\,\text{Å}$ for the cut off region, though they can be made element specific during parametrization. In the original formulation,[194]

dimensionless parameters $C_{\max}$ and $C_{\min}$, which are for the ellipses measuring the "direct line of sight" between two atoms when determining the screening, are taken to be 2.8 and 2.0, respectively. The sums in Eqs. (3.21) thus become limited to nearest neighbors and remain computationally tractable. Restriction to nearest neighbors is also implicitly included in the construction of the pair potential. While in the EAM, there is a certain ambiguity what to put into the pair potential on the one hand and the embedding function and background density on the other, a clear prescription is given for the former in the MEAM. First, usually the so-called "*universal equation of state*" as proposed by Rosé[195] is employed for the energy per atom in the bulk reference structure already mentioned in the context of the embedding function Eq. (3.18):

$$V^{\text{Rosé}}(R) = -E_0 \left[1 + a^*(R)\right] \mathrm{e}^{-a^*(R)} \quad , \tag{3.25}$$

Here,

$$a^*(R) = \alpha \left(\frac{R}{R_0} - 1 \right) \tag{3.26}$$

introduces

$$\alpha = \sqrt{\frac{9B\Omega}{E_0}} \quad , \tag{3.27}$$

where B and Ω are the bulk modulus and atomic (i.e. primitive cell) volume, respectively – the parameters E_0 and R_0 have already been explained above (cf Eq. (3.18) and Eq. (3.23)). When only nearest neighbors are considered, equating $V^{\text{Rosé}}$ as given by Eq. (3.25) and V^{MEAM} yields

$$V^{\text{MEAM,pair}}\left(R_{IJ}\right) = S_{IJ} \cdot \frac{2}{Z_0} \left[V^{\text{Rosé}}\left(R_{IJ}\right) - F^{\text{MEAM}}\left(\bar{\rho}_I\right) \right] \quad . \tag{3.28}$$

for the pair potential. As already indicated before (cf Eq. (3.18)), Z_0 is the nearest neighbor coordination number of the reference structure. The latter is considered to be symmetric, which is the reason for the prefactor in Eq. (3.28) – dividing out identical terms $V_I^{\text{MEAM,pair}}$ in the MEAM analogue of Eq. (3.15)). Extension to second nearest neighbors as discussed by Lee and Baskes[196] require to modify this expression. In addition, in that case, it turned out to be beneficial to also make the screening parameter $C_{\min}$ (cf Eq. (3.24b)) materials specific.[197]

Obviously, the interatomic potential defined by Eqs. (3.18) to (3.20), (3.21a) to (3.21d), (3.23), (3.24a) to (3.24d), (3.25), (3.26) and (3.28) is already quite complex *per se*. Its implementation from scratch, also including forces which as required for most practical applications like molecular dynamics simulations, is thus a rather time consuming task, also requiring careful testing in the end. Therefore, the implementation by Greg Wagner,[198] which is available as part of the LAMMPS code (cf Section 3.4), is used in Part III.

From the many applications of the EAM and MEAM, highly successful calculations of material specific phonons,[199] also and in particular for metal surfaces,[200–202] deserve special attention within the scope of this thesis. Extensions to more than one atom type have also been discussed, in particular for alloys,[191] but also for the treatment of adsorbates.[188] Transferability to a proper description of the dissociation of an adsorbate is certainly limited by the amount of quantum mechanics built into the method and hence does not constitute a state-of-the-art treatment. Therefore, the MEAM will not be used for description of multi-component systems within this work.

3.2.3. Potentials with *ab*-initio Quality

Even if parametrized from first-principles calculations, semi-empirical potentials generally show limited transferability and hence accuracy outside a "regime of trust" for which the parameters were obtained. The underlying functional form of the former often poses an unsurmountable limit, systematically not being able to capture with the desired accuracy the underlying quantum mechanical complexity of $V_{\mathrm{N}}^{\mathrm{cl}}(\mathcal{R})$. In the current context, the interaction of diatomics with a surface poses a particular challenge, as a potential must be able to properly capture the strong corrugation of the latter and the breaking and making of chemical bonds during the dissociation of the former. Trying to obtain "the accuracy of quantum mechanics without the electrons",[184] more general and flexible functional forms are the subject of current research.[183,184] One of these are neural networks as also discussed and further developed in this context in Chapter 6. Obviously, the more degrees of freedom are supposed to be described with the aforementioned quantum mechanical accuracy, the more difficult and challenging the construction of these "modern" potentials becomes. The availability of typically several ten thousands of reference data sets is a prerequisite, even for simple bulk systems consisting of a single atomic species.[203–206] For more computationally demanding surface calculations also involving several elements (as it is the case within the present work), a successful applicability of these methods at reasonable computational cost without reducing the number of degrees of freedom is therefore yet to be demonstrated.

A pragmatic way that avoids most of the aforementioned problems is to directly evaluate $V_{\mathrm{N}}^{\mathrm{cl}}(\mathcal{R})$ by *ab initio* calculations "on-the-fly" during a molecular dynamics simulation (AIMD). First steps into this direction have already been taken in 1985, when Car and Parrinello reformulated the many-body Hamiltonian introduced by Eq. (2.3) in Section 2.1. They recast the latter into an effective Lagrangian treating both electronic and nuclear degrees of freedom on an equal footing within the Born-Oppenheimer approximation and employing density-functional theory for the electrons (cf Chapter 2).[130,207] In fact, it was even the computational experience with molecular dynamics obtained in the years before which made the treatment of the electronic part tractable, thus greatly stimulating the development modern electronic structure techniques. While being enormously successful and still frequently used for systems with a gap between occupied and unoccupied states, metals pose a severe challenge for Car-Parrinello molecular dynamics (CPMD): In contrast to what is nowadays usually referred to as *ab initio* molecular dynamics (AIMD), there are no electronic self-consistency cycles during the propagation ensuring that each step is based on the electronic ground state. This tremendously reduces the computational burden but tends to drift away the electronic system from the Born-Oppenheimer surface for systems without a gap. Along those lines, some strategies have been devised over the recent years to make AIMD less computationally demanding, none of which has yet been shown to work for metallic systems however.[208–211]

Aiming at an *ab initio* quality modeling, in this work, a mixed strategy is pursued instead – carefully considering the desired purposes: In Part II, a neural network based potential is developed and parametrized using a large number of DFT calculations for O_2 on a frozen Pd(100) surface. Afterwards, running a plethora of molecular dynamics trajectories thus comes at low computational cost and hence allows to obtain reliable statistics for the initial encounter of the molecule with the surface. For the subsequent dynamics close to the surface, in Part III, the increased dimensionality of the problem when considering energy dissipation into realistic phonons of an extended substrate required to base the development of an embedding scheme on *ab initio* molecular dynamics.

3.3. Integrators

In order to obtain a numerical solution of the Hamiltonian equations of motion given by Eqs. (3.5) for certain initial conditions $\{(\boldsymbol{R}_I, \boldsymbol{P}_I)(t = t_0)\}_I$, they need to be discretized in time. The corresponding numerical algorithms are typically referred to as integrators when used in this context.

3.3.1. The Verlet Algorithm

The basic idea for the Verlet algorithm[212] is a simple Taylor expansion in the time step Δt:

$$\boldsymbol{R}_I(t+\Delta t) = \boldsymbol{R}_I(t) + \frac{\boldsymbol{P}_I(t)}{M_I}\Delta t + \frac{1}{2}\frac{\boldsymbol{F}_I(t)}{M_I}\Delta t^2 + \frac{1}{6}\dddot{\boldsymbol{R}}_I(t)\,\Delta t^3 + \mathcal{O}\left(\Delta t^4\right) \tag{3.29a}$$

$$\boldsymbol{R}_I(t-\Delta t) = \boldsymbol{R}_I(t) - \frac{\boldsymbol{P}_I(t)}{M_I}\Delta t + \frac{1}{2}\frac{\boldsymbol{F}_I(t)}{M_I}\Delta t^2 - \frac{1}{6}\dddot{\boldsymbol{R}}_I(t)\,\Delta t^3 + \mathcal{O}\left(\Delta t^4\right) \tag{3.29b}$$

Adding Eqs. (3.29a) and (3.29b) then yields

$$\boldsymbol{R}_I(t+\Delta t) = 2\boldsymbol{R}_I(t) - \boldsymbol{R}_I(t-\Delta t) + \frac{\boldsymbol{F}_I(t)}{M_I}\Delta t^2 + \mathcal{O}\left(\Delta t^4\right) \quad , \tag{3.30}$$

which has the nice property of being exact up to fourth order in Δt without third order terms appearing explicitly. Neither do the momenta (or equivalently velocities, cf Eq. (3.5b)), which can be obtained up to second order according to

$$\boldsymbol{P}_I = M_I\frac{\boldsymbol{R}_I(t+\Delta t) + \boldsymbol{R}_I(t-\Delta t)}{2\Delta t} + \mathcal{O}\left(\Delta t^2\right) \quad . \tag{3.31}$$

In order to estimate the positions $\boldsymbol{R}_I(t_0 - \Delta t)$ required in the first step, Eq. (3.29b) can be used with $\boldsymbol{P}_I(t_0)$, dropping the (usually unknown) third order term. Swope and coworkers have shown that Eq. (3.30) can be recast into into the mathematically equivalent but numerically advantageous form commonly referred to as velocity Verlet[213], which is hence nowadays typically used rather than the original formulation:

$$\boldsymbol{R}_I(t+\Delta t) = \boldsymbol{R}_I(t) + \frac{\boldsymbol{P}_I(t)}{M_I}\Delta t + \frac{1}{2}\frac{\boldsymbol{F}_I(t)}{M_I}\Delta t^2 + \mathcal{O}\left(\Delta t^4\right) \tag{3.32a}$$

$$\boldsymbol{P}_I(t+\Delta t) = \boldsymbol{P}_I(t) + \frac{\boldsymbol{F}_I(t) + \boldsymbol{F}_I(t+\Delta t)}{2}\Delta t + \mathcal{O}\left(\Delta t^2\right) \quad , \tag{3.32b}$$

The standard implementation of Eqs. (3.32) is according to the following algorithm for a step starting at time t with known positions and momenta $\boldsymbol{R}_I(t)$ and $\boldsymbol{P}_I(t)$, respectively, advancing the time by Δt:

1. Intermediary update of momenta:

$$\boldsymbol{P}_I\left(t + \frac{\Delta t}{2}\right) = \boldsymbol{P}_I(t) + \frac{1}{2}\boldsymbol{F}_I(t)\,\Delta t \tag{3.33a}$$

2. Final update of positions:

$$\boldsymbol{R}_I(\Delta t) = \boldsymbol{R}_I(t) + \frac{\boldsymbol{P}_I\left(t + \frac{\Delta t}{2}\right)}{M_I}\Delta t \tag{3.33b}$$

3. Calculation of forces at final positions:

$$\boldsymbol{F}_I\left(t+\Delta t\right) = -\boldsymbol{\nabla}_{\boldsymbol{R}_I} V_{\mathrm{N}}^{\mathrm{cl}}\left(\{\boldsymbol{R}_I\left(t+\Delta t\right)\}_I\right) \tag{3.33c}$$

4. Final update of momenta:

$$\boldsymbol{P}_I\left(t+\Delta t\right) = \boldsymbol{P}_I\left(t+\frac{\Delta t}{2}\right) \; + \; \frac{1}{2}\boldsymbol{F}_I\left(t+\Delta t\right)\Delta t \tag{3.33d}$$

Afterwards, positions and momenta as well as forces are thus known at time $t+\Delta t$.

Because the velocity Verlet integrator is symplectic,[149] it in principle yields for excellent conservation of the energy according to the Hamiltonian given by Eq. (3.1),[x] allowing to conveniently monitor the accuracy of the integration. Of course, this only holds if the time step Δt is not too large and forces are sufficiently accurate, which can be a problem if an analytic representation for the latter is not available – like typically in case of *ab initio* molecular dynamics.

3.3.2. The Bulirsch-Stoer Method

The key feature of the method proposed by Bulirsch and Stoer[214] for the integration of ordinary differential equations is that it aims for extremely large time steps Δt, that would never yield accurate solutions with e.g. the Verlet algorithm presented in the previous section. In brief, such a step starting at time t with known positions and momenta $\boldsymbol{R}_I(t)$ and $\boldsymbol{P}_I(t)$, respectively, is attempted in the following way:

1. The time step Δt is equally divided into S substeps $\Delta\tau_S = \frac{\Delta t}{S}$, which are used to carry out an approximate integration according to the modified midpoint method[132]

$$\boldsymbol{r}_I^s = \begin{cases} \boldsymbol{R}_I(t) & , \quad s=0 \\ \boldsymbol{r}_I^0 \; + \; \Delta\tau_S \, \frac{\boldsymbol{p}_I^0}{M_I} & , \quad s=1 \\ \boldsymbol{r}_I^{s-2} \; + \; 2\,\Delta\tau_S \, \frac{\boldsymbol{p}_I^{s-1}}{M_I} & , \quad s\in\{2,\ldots,S\} \end{cases} \tag{3.34a}$$

$$\boldsymbol{p}_I^s = \begin{cases} \boldsymbol{P}_I(t) & , \quad s=0 \\ \boldsymbol{p}_I^0 \; - \; \Delta\tau_S \, \boldsymbol{\nabla}_{\boldsymbol{R}_I} V_{\mathrm{N}}^{\mathrm{cl}}\left(\{\boldsymbol{r}_I^0\}_I\right) & , \quad s=1 \\ \boldsymbol{p}_I^{s-2} \; - \; 2\,\Delta\tau_S \, \boldsymbol{\nabla}_{\boldsymbol{R}_I} V_{\mathrm{N}}^{\mathrm{cl}}\left(\{\boldsymbol{r}_I^{s-1}\}_I\right) & , \quad s\in\{2,\ldots,S\} \end{cases} \quad , \tag{3.34b}$$

finally resulting in estimates for $\boldsymbol{R}_I(t+\Delta t)$ and $\boldsymbol{P}_I(t+\Delta t)$

$$\boldsymbol{R}_I^S(t+\Delta t) = \frac{1}{2}\left[\boldsymbol{r}_I^S + \boldsymbol{r}_I^{S-1} \; + \; \Delta\tau_S \, \frac{\boldsymbol{p}_I^S}{M_I}\right] \tag{3.35a}$$

$$\boldsymbol{P}_I^S(t+\Delta t) = \frac{1}{2}\left[\boldsymbol{p}_I^S + \boldsymbol{p}_I^{S-1} \; - \; \Delta\tau_S \, \boldsymbol{\nabla}_{\boldsymbol{R}_I} V_{\mathrm{N}}^{\mathrm{cl}}\left(\{\boldsymbol{r}_I^S\}_I\right)\right] \quad . \tag{3.35b}$$

The number of substeps can be increased according to the following sequence

$$S_k = 2,4,6,8,10,12,14,16,\ldots,[S_k=2k],\ldots \tag{3.36}$$

[x] More precisely, of a Hamiltonian which is slightly perturbed from the original one.

2. $\boldsymbol{R}_I^S(t+\Delta t)$ and $\boldsymbol{P}_I^S(t+\Delta t)$ are interpolated as a function of substep size, allowing to obtain a so-called Richardson extrapolation to $\boldsymbol{R}_I^\infty(t+\Delta t)$ and $\boldsymbol{P}_I^\infty(t+\Delta t)$, i.e. infinitely small substep size, together with an error estimate. Bulirsch and Stoer have originally proposed to use rational functions for this step,[215] but polynomials can be more efficient for "smooth" problems.[132] In either case, only powers of t_S^2 need to be used, because one nice property of the integration according to the modified midpoint method used in the previous step is that it can be shown to be an even function.[132]

3. Each time after the previous two steps have been completed, a decision must be made based on the error estimate whether to further increase the number of substeps according to Eq. (3.36), or, if the latter is already considered to be large enough, the (total) time step Δt itself ought to be reduced.

For *ab initio* molecular dynamics, this procedure bears the risk of a large number of "unused" computationally expensive force evaluations, in particular as their numerical uncertainty if not being analytic introduces an additional complicating element. This can outweigh potential gains due to large step sizes Δt, so that the velocity Verlet algorithm described in the previous section is typically a safer and more efficient choice.

3.3.3. The Liouville Operator Approach

When extended equations of motion like the Nosé-Hoover chains for continuous sampling of the canonical ensemble given by Eqs. (3.6) are considered, time derivatives of the momenta typically depend on the momenta themselves (cf Eqs. (3.6b), (3.6d) and (3.6e)). Using the integrators which have been described so far, this has first been dealt with by iterative solution of the momenta equations in order to obtain "self-consistency" during every time step.[156] Fortunately, this rather inconvenient procedure can be avoided by a very elegant and extremely beneficial application of the Liouville operator formalism as first proposed by Martyna and coworkers.[216,217]

Formally, the solution $\boldsymbol{\Gamma}(t) = (\Gamma_\alpha(t))_\alpha$ of any system of first order ordinary differential equations can be written with the help of an exponential operator as

$$\Gamma_\alpha(t) = \exp(iL_{\boldsymbol{\Gamma}} t)\ \Gamma_\alpha(0) \quad , \tag{3.37}$$

where the operator $L_{\boldsymbol{\Gamma}}$ is defined according to

$$\begin{aligned} \dot{\Gamma}_\alpha &= \underbrace{\left(\sum_\beta \dot{\Gamma}_\beta \frac{\partial}{\partial \Gamma_\beta} \right)}_{iL_{\boldsymbol{\Gamma}}} \Gamma_\alpha \\ &= \qquad iL_{\boldsymbol{\Gamma}} \qquad \Gamma_\alpha \quad . \end{aligned} \tag{3.38}$$

In the context of molecular dynamics, it is important to emphasize that the equations of motion represented by $\dot{\boldsymbol{\Gamma}}$ enter into this definition.

In the simple case of Hamilton's equation of motion for the microcanonical ensemble (cf Eqs. (3.5)), $iL_{\boldsymbol{\Gamma}}$ becomes the Liouville operator corresponding to the Hamiltonian given by

Eq. (3.1).

$$\begin{aligned} iL &= \sum_{I=1}^{N} \left[\dot{\boldsymbol{R}}_I \cdot \boldsymbol{\nabla}_{\boldsymbol{R}_I} + \dot{\boldsymbol{P}}_I \cdot \boldsymbol{\nabla}_{\boldsymbol{P}_I} \right] \\ &= \sum_{I=1}^{N} \left[\boldsymbol{\nabla}_{\boldsymbol{P}_I} H \cdot \boldsymbol{\nabla}_{\boldsymbol{R}_I} - \boldsymbol{\nabla}_{\boldsymbol{R}_I} H \cdot \boldsymbol{\nabla}_{\boldsymbol{P}_I} \right] \\ &= \underbrace{\sum_{I=1}^{N} \frac{\boldsymbol{P}_I}{M_I} \cdot \boldsymbol{\nabla}_{\boldsymbol{R}_I}}_{\equiv iL_1} \underbrace{- \sum_{I=1}^{N} \boldsymbol{F}_I \cdot \boldsymbol{\nabla}_{\boldsymbol{P}_I}}_{\equiv iL_2} \end{aligned} \tag{3.39}$$

When the analogue of the initially introduced exponential operator is now approximated by a so-called Trotter factorization using the operators L_1 and L_2 as defined in Eq. (3.39)

$$\exp\left(iL\Delta t\right) = \underbrace{\exp\left(iL_2 \frac{\Delta t}{2}\right)}_{\equiv O_1} \underbrace{\exp\left(iL_1 \Delta t\right)}_{\equiv O_2} \underbrace{\exp\left(iL_2 \frac{\Delta t}{2}\right)}_{\equiv O_1} + \mathcal{O}(\Delta t^3) \quad , \tag{3.40}$$

the velocity Verlet integrator can be obtained: Sequential application of the exponential operators O_1, O_2 and O_1 defined in Eq. (3.40) yields Eqs. (3.33a), (3.33b) and (3.33d) from the update steps 1, 2 and 4, respectively, described in Section 3.3.1.[xi]

As already indicated initially, this technique can also be applied in the same way to e.g. the equations of motion for Nosé-Hoover chains (cf Eqs. (3.6)) greatly simplifying their numerical solution. A symmetric Trotter factorization ensures the symplecticity of the obtained integrator, which in fact can be translated directly into computer code from the sequential application of the exponential operators. Examples for factorizations and resulting discretizations can be found in the work by Martyna and coworkers.[216,217]

3.4. Practical Aspects and Implementations

Within *ab initio* molecular dynamics as described in the previous section, the electronic structure part to obtain the forces dominates the computational cost and hence limits the the system sizes to about 1000 atoms at present (depending on available computational resources). Therefore, molecular dynamics implementations that typically come with first-principles codes are not very sophisticated. When it comes to molecular dynamics with (semi-) empirical potentials however, calculation of individual force components according to the corresponding analytic forms usually do not comprise the most expensive part. For pair potentials (and more complicated potentials building on top of them) rather the iteration over pairs as indicated in Eq. (3.7) leads to a formal $\mathcal{O}(N^2)$ scaling with system size (for $N \gg 1000$) which becomes the bottleneck. As already indicated in Section 3.2, the introduction of a cut off distance (cf Eq. (3.8)) zeros out many contributions which hence do not need to be considered during the iteration. This can be achieved by iterating over so-called neighbor lists instead, which only contain its the neighbors closer than a certain distance for each atom. This brings down the scaling to essentially $\mathcal{O}(N)$. Of course, neighbor list generation still scales as $\mathcal{O}(N^2)$. As initially proposed by Verlet,[212]

[xi] Here the identity $\exp\left(c\frac{\partial}{\partial x}\right) f(x) = f(x+c)$ is useful to be kept in mind. The force update according to Eq. (3.33c) in the third step is of course implied by Eq. (3.33d)

the introduction of a so-called skin distance on top of the cut off distance allows to avoid the necessity of neighbor list rebuilds during every time step, thus still leading to a net gain in performance.

The advent of massively parallel computers has had a particularly tremendous impact on molecular dynamics simulations. As discussed by Plimpton[218], the latter can be parallelized very efficiently based on atom, force and spatial decomposition.[xii] The availability of cheap graphic cards equipped with graphics processing units (GPUs) due the wide public popularity of more and more realistic computer games has thus led to the "GPU-revolution": Thanks to slight adaptations of the algorithms accounting for the specific technical properties of these devices,[219–223] MD simulations, which have required computing clusters before, can now be performed on desktop computers. Apart from MD codes specifically developed for these purposes like e.g. *HOOMD-blue*,[222] the corresponding functionality has also found its way more and more into most of the "large" and popular MD codes focused on biological systems, like e.g. *GROMACS* or *NAMD*.

The LAMMPS code, a modern MD code written in C++,[218] on the other hand does not only include force fields for such systems, but also numerous specimens from materials science like EAM type potentials described in Section 3.2.2.[198] This is one of the reasons why it has been chosen as a starting point for the extensions and applications presented in Part III.[xiii] Furthermore, its overall design employs object orientation to allow for great and simple both maintainability and extendability. Several different algorithms for the generation of neighbor lists are conveniently provided this way,[218] as well as parallelization based on spatial decomposition[218] relying on MPI for communication.[147] GPU-based parallelism is also available for some parts, but still in its infancy – and neither required nor used for the present work. Numerical parts, like the interaction potentials in particular, are implemented according to a procedural paradigm in plain C, allowing not to sacrifice numerical efficiency.

[xii] This holds for MD based on semi-empirical potentials – parallelization of the dominating *ab initio* part within AIMD is an issue for itself, strongly depending on the intrinsic properties of the employed first-principles technique.

[xiii] Licensed under *GPL* and available from `http://lammps.sandia.gov`.

4. Phonons

On a macroscopic scale, the Wiedemann-Franz law[i] empirically connects thermal and electrical conductivity of metals. However, when the electronic system is not forcibly driven significantly out of equilibrium, e.g. by laser irradiation, on the atomic scale the involvement of phonons in heat conduction cannot be denied even for metallic systems. Their importance in gas-surface dynamics is hence an ongoing debate,[224] as most contemporary, commonly used models (like the one used in Part II) do not incorporate phonons at all or in a very approximative way at most. This will be detailed in Part III, together with results of accurate, first-principles simulations using a newly developed computational methodology. The goal of this chapter is therefore to briefly recapture essential aspects of phonons and their specifics at surfaces. More detailed presentations of the bulk related parts (i.e. in particular Section 4.1) can be found in any textbook about solid state physics.[225]

4.1. The Harmonic Solid

Just like for vibrations of finite systems (i.e. molecules or clusters), the starting point for lattice dynamics and hence the description of phonons is a Taylor expansion up to second order of the interatomic potential (cf Chapter 3) of the (infinite) solid around the equilibrium positions $\mathcal{R}_0 = \{\boldsymbol{R}_I^0\}_I$ of the nuclei in the lattice:

$$\begin{aligned} V_\mathrm{N}^\mathrm{cl}(\mathcal{R}) = V_\mathrm{N}^\mathrm{cl}\big|_{\mathcal{R}_0} &+ \underbrace{\sum_I \sum_{\alpha=1}^{3} \left.\frac{\partial V_\mathrm{N}^\mathrm{cl}}{\partial R_{I\alpha}}\right|_{\mathcal{R}_0} \left(R_{I\alpha} - R_{I\alpha}^0\right)}_{=0} \\ &+ \frac{1}{2} \sum_{I,J} \sum_{\alpha=1}^{3} \sum_{\beta=1}^{3} \left(R_{I\alpha} - R_{I\alpha}^0\right) \underbrace{\left.\frac{\partial^2 V_\mathrm{N}^\mathrm{cl}}{\partial R_{I\alpha} \partial R_{J\beta}}\right|_{\mathcal{R}_0}}_{\equiv \Phi_{I\alpha J\beta}} \left(R_{J\beta} - R_{J\beta}^0\right) \\ &+ \mathcal{O}\left(\left\|\boldsymbol{R}_I - \boldsymbol{R}_I^0\right\|_2^3\right) \end{aligned} \tag{4.1}$$

Here, nuclei are enumerated by I and J and individual Cartesian components by α and β. Obviously, the first order term vanishes, as forces $\boldsymbol{F}_I(\mathcal{R}_0) = -\boldsymbol{\nabla} V_\mathrm{N}^\mathrm{cl}{}_{\boldsymbol{R}_I}$ at the equilibrium positions are zero. When terminating the expansion given by Eq. (4.1) after the second order term, the resulting harmonic solid

$$V_\mathrm{N}^\mathrm{cl}(\mathcal{R}) - V_\mathrm{N}^\mathrm{cl}(\mathcal{R}_0) \;\approx\; V^\mathrm{harmsol}(\mathcal{R}) = \frac{1}{2} \sum_{I,J} \left(\boldsymbol{R}_J - \boldsymbol{R}_J^0\right)^\dagger \boldsymbol{\Phi}_{IJ} \left(\boldsymbol{R}_I - \boldsymbol{R}_I^0\right) \tag{4.2}$$

[i] See e.g. http://en.wikipedia.org/wiki/Wiedemann-Franz_law.

is held together by the eponymous term.[ii] The symmetric force constant matrix Φ (and the positive semi-definite form associated therewith) naturally defines a pair potential, which, however, in contrast to the potentials discussed in the previous chapter (cf Section 3.2.1), involves the full vectorial character of the displacement vectors $\boldsymbol{U}_I = \boldsymbol{R}_I - \boldsymbol{R}_I^0$ and not only their absolute value. Splitting sums over atoms into those within a central primitive unit cell (here and in the following indicated by a tilde over the index) and their equivalent periodic images translated by lattice vectors (cf Eq. (2.38) in Section 2.6) leads to

$$V^{\mathrm{harmsol}}(\mathcal{U}) = \frac{1}{2} \sum_{\tilde{I},\tilde{J}}^{\text{cell}} \sum_{\boldsymbol{L}_{\tilde{I}}\boldsymbol{L}_{\tilde{J}}}^{\text{images}} \sum_{\alpha=1}^{3} \sum_{\beta=1}^{3} \left[U_{\tilde{J}\beta}\left(\boldsymbol{L}_{\tilde{J}}\right)\right]^* \Phi_{\tilde{I}\alpha\tilde{J}\beta}\left(\boldsymbol{L}_{\tilde{I}}, \boldsymbol{L}_{\tilde{J}}\right) U_{\tilde{I}\alpha}\left(\boldsymbol{L}_{\tilde{I}}\right) \quad , \tag{4.3}$$

where $\mathcal{U} = \{\boldsymbol{U}_I\}_I = \{\boldsymbol{U}_{\tilde{I}\alpha}\}_{\tilde{I}\alpha}$. Consequently, Newton's equations of motion (cf Eq. (3.4)) read as follows:

$$M_{\tilde{I}} \ddot{U}_{\tilde{I}\alpha}\left(\boldsymbol{L}_{\tilde{I}}\right) = -\sum_{\tilde{J}}^{\text{cell}} \sum_{\boldsymbol{L}_{\tilde{J}}}^{\text{images}} \sum_{\beta=1}^{3} \Phi_{\tilde{I}\alpha\tilde{J}\beta}\left(\boldsymbol{L}_{\tilde{I}}, \boldsymbol{L}_{\tilde{J}}\right) U_{\tilde{J}\beta}\left(\boldsymbol{L}_{\tilde{J}}\right) \tag{4.4}$$

An ansatz for solutions for the displacements in Eq. (4.4) is a plane wave with wave vector $\boldsymbol{q}$ and (angular) frequency $\omega(\boldsymbol{q})$:

$$U_{\tilde{I}\alpha}\left(\boldsymbol{L}_{\tilde{I}}, t; \boldsymbol{q}\right) = \frac{1}{\sqrt{M_{\tilde{I}}}} A(\boldsymbol{q})\, \hat{u}_{\tilde{I}\alpha}(\boldsymbol{q})\, \mathrm{e}^{i\left(\boldsymbol{q}\cdot\boldsymbol{L}_{\tilde{I}} - \omega(\boldsymbol{q})t\right)} \quad , \quad \hat{u}_{\tilde{I}\alpha}(\boldsymbol{q}) \in \mathbb{C} \quad . \tag{4.5}$$

$A(\boldsymbol{q})$ is a real valued amplitude and $\hat{u}_{\tilde{I}\alpha}(\boldsymbol{q})$ the component α of atom $\tilde{I}$ in the aforementioned primitive unit cell of a $3N_{\mathrm{cell}}$-dimensional complex-valued unit vector, where N_{cell} denotes the total number of atoms in that cell. Of course, physical solutions are only the real or the imaginary part of $U_{\tilde{I}\alpha}\left(\boldsymbol{L}_{\tilde{I}}, \boldsymbol{q}\right)$ given by Eq. (4.5). Similar to Bloch states (cf Section 2.6), $\boldsymbol{q}$-values outside the first Brillouin zone can be folded back to equivalent counterparts inside the latter which describe the same physical displacement wave. Inserting Eq. (4.5) into Eq. (4.4) leads to

$$\omega^2(\boldsymbol{q})\, \hat{u}_{\tilde{I}\alpha}(\boldsymbol{q}) = \sum_{\tilde{J}}^{\text{cell}} \sum_{\beta=1}^{3} D_{\tilde{I}\alpha\tilde{J}\beta}(\boldsymbol{q})\, \hat{u}_{\tilde{J}\beta}(\boldsymbol{q}) \quad , \tag{4.6}$$

where the dynamical matrix has been defined as

$$\begin{aligned} D_{\tilde{I}\alpha\tilde{J}\beta}(\boldsymbol{q}) &= \sum_{\boldsymbol{L}_{\tilde{I}}\boldsymbol{L}_{\tilde{J}}}^{\text{images}} \frac{1}{\sqrt{M_{\tilde{I}} M_{\tilde{J}}}} \Phi_{\tilde{I}\alpha\tilde{J}\beta}\left(\boldsymbol{L}_{\tilde{I}}, \boldsymbol{L}_{\tilde{J}}\right) \mathrm{e}^{i\boldsymbol{q}\left(\boldsymbol{L}_{\tilde{J}} - \boldsymbol{L}_{\tilde{I}}\right)} \\ &= \sum_{\boldsymbol{L}}^{\text{images}} \frac{1}{\sqrt{M_{\tilde{I}} M_{\tilde{J}}}} \Phi_{\tilde{I}\alpha\tilde{J}\beta}\left(\boldsymbol{0}, \boldsymbol{L}\right) \mathrm{e}^{i\boldsymbol{q}\boldsymbol{L}} \end{aligned} \tag{4.7}$$

[ii] Adding higher order terms obviously captures more and more "many-body" effects, but also gets more and more difficult in computational practice. Nevertheless, it has been proposed only recently to construct systematically improvable interatomic potentials.[226]

More precisely, the formulation after the first equality sign gets obvious when inserting Eq. (4.5) into Eq. (4.3) yielding the contribution of a single mode $\boldsymbol{q}$ to the potential energy:

$$\begin{aligned} V^{\mathrm{harmsol}}(\boldsymbol{q}) &= \frac{1}{2} \sum_{\tilde{I},\tilde{J}}^{\mathrm{cell}} \sum_{\alpha=1}^{3} \sum_{\beta=1}^{3} \left[\hat{u}_{\tilde{I}\alpha}(\boldsymbol{q})\right]^* \\ &\qquad \left[\sum_{\boldsymbol{L}_{\tilde{I}}\boldsymbol{L}_{\tilde{J}}}^{\mathrm{images}} \frac{1}{\sqrt{M_{\tilde{I}} M_{\tilde{J}}}} \Phi_{\tilde{I}\alpha\tilde{J}\beta}\left(\boldsymbol{L}_{\tilde{I}}, \boldsymbol{L}_{\tilde{J}}\right) \mathrm{e}^{i\boldsymbol{q}\left(\boldsymbol{L}_{\tilde{J}} - \boldsymbol{L}_{\tilde{I}}\right)} \right] \hat{u}_{\tilde{J}\beta}(\boldsymbol{q})\, A^2(\boldsymbol{q}) \\ &= \frac{1}{2}\, A^2(\boldsymbol{q}) \sum_{\tilde{I},\tilde{J}}^{\mathrm{cell}} \sum_{\alpha=1}^{3} \sum_{\beta=1}^{3} \left[\hat{u}_{\tilde{I}\alpha}(\boldsymbol{q})\right]^* D_{\tilde{I}\alpha\tilde{J}\beta}(\boldsymbol{q})\, \hat{u}_{\tilde{J}\beta}(\boldsymbol{q}) \end{aligned} \tag{4.8}$$

To keep this energy contribution real-valued and hence physical, the complex conjugation already foresightedly included in Eqs. (4.2) and (4.3) leads to differences of lattice vectors in the exponential. Since these are lattice vectors again, the second equality sign just implies a different way of summing over the latter.

For every $\boldsymbol{q}$, Eq. (4.6) is an eigenvalue equation for the dynamical matrix as given by Eq. (4.7), with $3N_{\mathrm{cell}}$ different solutions. These solutions are called phonons – deferred from a quantum mechanical description of lattice dynamics where they appear as excitations treated as quasiparticles. The orthonormal system of Eigenvectors $\{(\hat{u}_{\tilde{I}\alpha})\,(\boldsymbol{q}, b)\}_b$ with corresponding Eigenvalues $\{\omega^2(\boldsymbol{q}, b)\}_b$, where $b \in 1, \ldots, N_{\mathrm{cell}}$ is the phonon band index, describe displacement patterns inside the unit cell and angular frequencies of the lattice distortion waves, respectively. Obviously, it follows directly from Eq. (4.7) that the dynamical matrix is hermitian in the atom indices,

$$D_{\tilde{J}\beta\tilde{I}\alpha}(\boldsymbol{q}) = \sum_{\boldsymbol{L}}^{\mathrm{images}} \frac{1}{\sqrt{M_{\tilde{I}} M_{\tilde{J}}}} \underbrace{\Phi_{\tilde{J}\beta\tilde{I}\alpha}\left(\boldsymbol{L}, \boldsymbol{0}\right)}_{=\Phi_{\tilde{I}\alpha\tilde{J}\beta}(\boldsymbol{0},\boldsymbol{L})} \mathrm{e}^{-i\boldsymbol{q}\boldsymbol{L}} = \left[D_{\tilde{I}\alpha\tilde{J}\beta}(\boldsymbol{q})\right]^* \quad , \tag{4.9}$$

keeping in mind that the force constant matrix is symmetric and the lattice vector $\boldsymbol{L}$ turns into its negative when switching the indices of the atoms. The Eigenvalues $\{\omega^2(\boldsymbol{q}, b)\}_b$ thus are real, and, as the potential energy is expanded around a minimum, also non-negative, this makes their square roots $\{\omega(\boldsymbol{q}, b)\}_b$ well defined physical oscillation frequencies. For $\boldsymbol{q} = \boldsymbol{0}$, Eigenvectors are real as well, since according to Eq. (4.7) the dynamical matrix entirely consists of real-valued elements. Furthermore, another immediate consequence of Eq. (4.7) is the relation of dynamical matrices at $\boldsymbol{q}$ and $-\boldsymbol{q}$:

$$D_{\tilde{I}\alpha\tilde{J}\beta}(-\boldsymbol{q}) = \left[D_{\tilde{I}\alpha\tilde{J}\beta}(\boldsymbol{q})\right]^* \quad . \tag{4.10}$$

Insertion into the complex conjugated version of Eq. (4.6) yields

$$\omega^2(\boldsymbol{q}, b)\, \left[\hat{u}_{\tilde{I}\alpha}(\boldsymbol{q}, b)\right]^* = \sum_{\tilde{J}}^{\mathrm{cell}} \sum_{\beta=1}^{3} D_{\tilde{I}\alpha\tilde{J}\beta}(-\boldsymbol{q}) \left[\hat{u}_{\tilde{J}\beta}(\boldsymbol{q}, b)\right]^* \quad , \tag{4.11}$$

i.e. the Eigenvectors at $-\boldsymbol{q}$ are identical to those at $\boldsymbol{q}$, $\omega^2(-\boldsymbol{q}, b) = \omega^2(\boldsymbol{q}, b)$, with corresponding Eigenvectors being the complex conjugates of each other $(\hat{u}_{\tilde{I}\alpha})\,(-\boldsymbol{q}, b) = \left[(\hat{u}_{\tilde{I}\alpha})\,(\boldsymbol{q}, b)\right]^*$.[iii] More

[iii] This is similar to the time reversal symmetry of a Hamiltonian of periodic systems as given Eq. (2.45) in Section 2.6.

symmetry properties of the dynamical matrix have been extensively discussed in the review by Maradudin and Vosko.[227]

Similar to normal modes in non-periodic systems, the linearity of Eq. (4.6) allows to describe more complex displacement patterns by superposition of these solutions, which individually can be seen as "Fourier modes". In fact, a macroscopic solid practically allows for infinitely large wave lengths $\lambda = \frac{2\pi}{\|\boldsymbol{q}\|_2}$ and thus leads to continuous $\boldsymbol{q}$. The ansatz given by Eq. (4.5) thus becomes a (reciprocal space) component of a regular spatial Fourier integral transformation, which can be constructed as the continuum limit of discrete Fourier transforms in infinitely large supercells. Any displacement pattern can be represented by the latter, as will be detailed and made use of in Section 10.1 in order to devise a phonon projection scheme.

For different band indices b, $\omega(\boldsymbol{q}, b)$ (as a function of $\boldsymbol{q}$) along paths through the Brillouin zone defines the dispersion relation of different branches of the phonon spectrum, which are typically measured in neutron scattering experiments.[iv] The corresponding phonon density of states (i.e. number of phonon modes per volume) both of each branch and total are given by counting the respective number of phonons with a particular frequency $\omega(\boldsymbol{q}, b)$ within the Brillouin zone:

$$\rho_{\text{phon}}(\omega) = \sum_b \rho_{\text{phon}}(\omega, b) = \sum_b \frac{1}{(2\pi)^3} \int_{\text{BZ}} d\boldsymbol{q}\, \delta(\omega - \omega(\boldsymbol{q}, b)) \tag{4.12}$$

Nowadays, dynamical matrices and hence accurate dispersion relations can be calculated – at best from first-principles as detailed in the following (cf Section 4.2). Otherwise, $\omega(\boldsymbol{q}, b)$ needs to be approximated, like e.g. in the Debye model.[225] Here, all phonon branches are replaced by a total of three (acoustic) counterparts, each with linear dispersion

$$\omega(\boldsymbol{q}, b) = c_b \|\boldsymbol{q}\|_2 \quad , \quad b \in \{1, 2, 3\} \quad , \tag{4.13}$$

where the c_b are *a priori* unknown phase and (due to the linearity also) group velocities. This is a good approximation for the description of isotropic crystals with a mono-atomic basis in the limit of long wave lengths. The c_b then correspond to the dispersion of the one longitudinal and two transversal acoustic phonon branches, c_l and c_t, respectively. Furthermore, in integrals over phonon modes, the Brillouin zone is replaced by a simple sphere in reciprocal space with radius q_D, so that insertion of Eq. (4.13) into Eq. (4.12) leads to

$$\rho_{\text{phon}}^{\text{Debye}}(\omega) = \begin{cases} \frac{3}{2\pi^2}\frac{\omega^2}{c^3} = 9\frac{N_\text{cell}}{V_\text{cell}}\frac{\omega^2}{\omega_\text{D}^3} & , \quad \omega \leq \omega_\text{D} \\ 0 & , \quad \omega > \omega_\text{D} \end{cases} \quad . \tag{4.14}$$

Here, the effective velocity of sound

$$\frac{1}{c^3} = \frac{1}{3}\sum_{b=1}^{3} \frac{1}{c_b^3} \tag{4.15}$$

has been defined as an average over the aforementioned (one longitudinal and two transversal) acoustic phonon branches. Furthermore, the cut off at the Debye frequency ω_D assures that Eq. (4.14) yields the right number of phonon modes, i.e. three times the number of atoms in the unit cell N_cell, per unit cell volume V_cell

$$\frac{3N_\text{cell}}{V_\text{cell}} = \int_0^{\omega_\text{D}} \rho_{\text{phon}}^{\text{Debye}}(\omega) = \frac{1}{2\pi^2}\frac{\omega_\text{D}^3}{c^3} = \frac{q_\text{D}^3}{2\pi^2} \quad . \tag{4.16}$$

[iv] See e.g. http://www.neutron.anl.gov.

This defining equation for ω_D has already been used in Eq. (4.14) in order to simplify the non-vanishing part of the expression for the phonon density of states within the Debye model. Obviously, according to Eq. (4.16), the Debye wave vector q_D is completely defined by geometric properties of the unit cell of the crystal. Therefore, in order to obtain the best Debye model "closest" to a given phonon dispersion or density of states (e.g. calculated from first principles, *vide infra*), c must be obtained by fitting Eq. (4.13) or Eq. (4.14), respectively, to the former. The latter is usually more convenient, but both yields ω_D or equivalently the Debye temperature Θ_D:

$$k_\mathrm{B}\Theta_\mathrm{D} = \hbar\omega_\mathrm{D} = \hbar c q_\mathrm{D} \tag{4.17}$$

By measuring (e.g.) specific heats or elastic constants of a material, Θ_D and thus the only unknown parameter of the Debye model can also be obtained experimentally. As detailed in Chapter 8 of Part III, this simple model is commonly used to "guess characteristic frequencies" appearing as parameters in simple models for energy dissipation employed within the context of gas-surface dynamics. Apart from using Debye frequencies directly, the average frequency of the Debye spectrum (cf Eq. (4.14))

$$\bar{\omega}_\mathrm{D} = \frac{V_\mathrm{cell}}{3N_\mathrm{cell}} \int\limits_0^{\omega_\mathrm{D}} d\omega\, \omega\, \rho_\mathrm{phon}^\mathrm{Debye}(\omega) \;=\; \frac{3}{4}\omega_\mathrm{D} \tag{4.18}$$

is sometimes used instead.

To go beyond the harmonic solid as described by Eqs. (4.2) and (4.3), spectral densities Eq. (4.12) can also be obtained from extensive molecular dynamics simulations (cf Section 3.2) employing interatomic potentials which go beyond the former, like e.g. pair or embedded atom method potentials described in Section 3.2.1 or Section 3.2.2 respectively. As a standard theoretical tool, the velocity autocorrelation function (VACF)

$$C_\mathrm{VAC}(t) = \lim_{\tau\to\infty} \frac{1}{\tau} \int\limits_0^{\tau} dt'\, \dot{\boldsymbol{U}}(t') \cdot \dot{\boldsymbol{U}}(t'+t) \tag{4.19}$$

is used to obtain such a DOS by Fourier transform over the time domain

$$\rho_\mathrm{phon}^\mathrm{VAC}(\omega) = \lim_{\tau\to\infty} \int\limits_{-\tau}^{+\tau} dt\, C_\mathrm{VAC}(t)\, \mathrm{e}^{i\omega t} \tag{4.20}$$

No additional information about the (harmonic) phonon modes is required. On the other hand, displacement patterns are not obtained as straightforwardly as in form of the Eigenvectors $\hat{u}_{\tilde{I}\alpha}(\boldsymbol{q}, b)$ by the solution of Eq. (4.6), though accessible in principle via spatial Fourier transformation. Typically, frequency shifts as obtainable by comparison of harmonic and anharmonic density of states are of most prominent interest. However, recently, within the scope of thermal transport in materials, Eigenvectors have obtained a lot of attention as well: Population of phonon modes according to a Boltzmann distribution allows to minimize[v] inconvenient thermalization efforts in molecular dynamics simulations[228–231] typically required otherwise when using thermostats (cf Sections 3.1 and 8.5). In practice, Eqs. (4.19) and (4.20) are evaluated

[v] or even avoid when within the validity range of the harmonic approximation

based on velocity fields of the displacements from molecular dynamics trajectories. Discrete time steps of these trajectories (cf Section 3.3) naturally lead to discrete sums instead of integrals. Furthermore, convergence of the sampling of initial conditions over an infinitely long time interval in Eq. (4.19) can result in total integration times of the aforementioned trajectories that is computationally very expensive if not prohibitive.

4.2. Phonons from First-Principles

Since extended *ab initio* molecular dynamics simulations (cf Section 3.2.3) which are long enough to reliably obtain phonons according to Eqs. (4.19) and (4.20) are computationally very intensive, first-principles methods typically aim at solving the Eigenvalue problem of lattice dynamics of the harmonic solid as given by Eq. (4.6). In that case, obtaining the second derivatives of the total energy (cf Eq. (4.1)) is the task at hand.

One possible route to address this challenge is by determining elements of the force constant matrix $\mathbf{\Phi}$ numerically, which has also been termed the *direct method* – implying finite displacements of atoms. However, using the primitive cell as simulation cell within the usually employed periodic boundary conditions for first-principles modeling of bulk materials (cf Section 2.6), displacements are repeated accordingly throughout the entire solid. This corresponds to phonons (in potentially different branches) with infinite wave lengths λ and hence zero wave vector $\|\boldsymbol{q}\|_2 = \frac{2\pi}{\lambda}$ i.e. the Γ point at the center of the Brillouin zone. Going to $N_1 \times N_2 \times N_3$ supercells allows for possible displacement patterns describing phonons at points

$$\boldsymbol{q}(n_1, n_2, n_3) = \sum_{i=1}^{3} \left[\frac{n_i}{N_i} - \frac{1}{2} \right] \boldsymbol{b}_i \quad , \quad (n_1, n_2, n_3) \in \prod_{i=1}^{3} \{0, \ldots, N_i - 1\} \tag{4.21}$$

in the (original) Brillouin zone, where the $\boldsymbol{b}_i$ denote the corresponding reciprocal lattice vectors.[vi] Equivalently, these points fulfill the condition

$$\left| \exp\left(2\pi i \, \boldsymbol{q}(n_1, n_2, n_3) \cdot [N_1 \boldsymbol{a}_1 + N_2 \boldsymbol{a}_2 + N_3 \boldsymbol{a}_3]\right) \right| = 1 \quad , \tag{4.22}$$

where $\boldsymbol{a}_1$, $\boldsymbol{a}_2$ and $\boldsymbol{a}_3$ are the primitive lattice vectors. By increasing the size of the supercell, phonons throughout the entire Brillouin zone can thus be sampled more and more accurately.

If the displacement pattern and hence the normalized displacement Eigenvector $\hat{\boldsymbol{u}}(\boldsymbol{q}; b)$ for a certain phonon wave vector $\boldsymbol{q}$ and branch b (cf Eq. (4.6)) are known e.g. due to symmetry reasons, Eq. (4.8) simplifies to

$$V^{\text{harmsol}}(\boldsymbol{q}; b) = \frac{1}{2} \omega^2(\boldsymbol{q}; b) A^2(\boldsymbol{q}; b) \quad . \tag{4.23}$$

Fitting a parabola to the results of total energy calculations obtained for different displacement amplitudes $A(\boldsymbol{q}; b)$ along $\hat{\boldsymbol{u}}(\boldsymbol{q}; b)$, then allows to obtain the corresponding phonon frequencies $\omega(\boldsymbol{q}; b)$. Before sufficiently accurate forces could be obtained, this was the first variant of the direct method which has been used in the context of first-principles calculations.[232] Because of the required knowledge about the phonon displacement Eigenvector it is commonly referred to as frozen-phonon approach, which also hints at its limited general applicability.

[vi] These phonons can be realized in different branches at the Γ point of the Brillouin zone of the supercell and can be folded back to the (original) Brillouin zone of the primitive cell accordingly.

Nowadays, elements of the force constant matrix can be calculated directly using difference quotients obtained from finite displacements around the equilibrium crystal geometry according to (cf Eq. (4.1))

$$\Phi_{I\alpha J\beta} \;=\; \frac{\partial F_{J\beta}}{\partial R_{I\alpha}} \;\approx\; \frac{F_{J\beta}}{u_{I\alpha}} \quad . \tag{4.24}$$

As in most first-principles codes for periodic systems, the numerical convergence of forces $F_{J\beta} = \frac{\partial V_{\mathrm{N}}^{\mathrm{cl}}}{\partial R_{J\beta}}$ is typically worse by an order of magnitude compared to total energies (cf Section 5.3), care must still be taken when choosing the size of these displacements: When too small, a better description of the harmonic regime can be annihilated by the limited accuracy of the forces, while when too large, one might already be outside that regime. In principle, the ensuing diagonalization of the dynamical matrix given by Eq. (4.7) yields both phonon displacement patterns and frequencies – without the requirement of any *a priori* knowledge about the system. However, as already indicated in the second to last paragraph, the periodic boundary conditions limit the distance between atoms which are displaced independently according to the size of the employed supercells. If the elements of the force constant decay to zero as a function of atomic distance $R_{IJ} = \|\boldsymbol{R}_I - \boldsymbol{R}_J\|_2$ between atoms I and J, then this systematic error in the practical evaluation of Eq. (4.24) can be neglected for sufficiently large supercells. Of course, this is system dependent and hence convergence needs to be checked with respect to supercell size. Frank and coworkers, who reported the first application of this incarnation of the direct method in a first-principles context,[233] could indeed observe such a behavior for the bulk alkali metals which were the subject of their study: Rather small supercells allowing for "independent" fifth nearest neighbors turned out to be sufficient. This can be attributed to an efficient screening of elastic deformations in metallic systems, in contrast to semi-conductors and insulators as also predicted by the nearsightedness principle introduced by Walter Kohn.[234,235] Phonon calculations via finite displacements thus are very suitable in the present context.

In general, as already pointed out by Kresse and coworkers,[236] the practical evaluation of Eq. (4.24) within supercells always implicitly includes a summation over periodic images of the latter, which therefore have been termed cumulant force constants

$$\Phi^{\mathrm{cum}}_{\tilde{I}\alpha\tilde{J}\beta}\left(\boldsymbol{L}_{\tilde{I}}, \boldsymbol{L}_{\tilde{J}}\right) = \sum_{\boldsymbol{L}^{\mathrm{S}}}^{\substack{\text{supercell}\\ \text{images}}} \Phi_{\tilde{I}\alpha\tilde{J}\beta}\left(\boldsymbol{L}_{\tilde{I}}, \boldsymbol{L}_{\tilde{J}} + \boldsymbol{L}^{\mathrm{S}}\right) \tag{4.25}$$

by Parlinski and coworkers in the following.[237] Their work also provides a formal framework to include symmetry when obtaining $\boldsymbol{\Phi}^{\mathrm{cum}}$ from calculated forces. This can not only reduce the number of required displacement calculations substantially, but also remedy violations of the symmetry due to the aforementioned limited numerical accuracy of the latter.[vii] Based on the cumulant force constants as given by Eq. (4.25), an approximate dynamical matrix is defined as

$$D^{\mathrm{cum}}_{\tilde{I}\alpha\tilde{J}\beta}(\boldsymbol{q}) = \sum_{\boldsymbol{L}}^{\substack{\text{extended}\\ \text{supercell}}} \frac{w_{\boldsymbol{L}}}{\sqrt{M_{\tilde{I}} M_{\tilde{J}}}}\, \Phi^{\mathrm{cum}}_{\tilde{I}\alpha\tilde{J}\beta}\left(\boldsymbol{0}, \boldsymbol{L}\right)\, \mathrm{e}^{i\boldsymbol{q}\cdot\boldsymbol{L}} \quad . \tag{4.26}$$

[vii] More precisely, by virtue of a singular value decomposition, an optimal fit for the cumulant force constant matrix to the calculated force field data is obtained, as the symmetry-independent elements of the former are typically overdetermined by the latter.

Special care needs to be taken in order to guarantee the Hermicity of $D^{\mathrm{cum}}_{\tilde{I}\alpha\tilde{J}\beta}$: An extended supercell is constructed which ensures that the central atoms are embedded into an environment with the correct local symmetry, i.e. periodic images at the surface of the former might have to be added. The summation then only runs over "original" lattice vectors $\boldsymbol{L}$ of the primitive cell within this extended supercell, with weight factors $w_{\boldsymbol{L}} \leq 1$ properly compensating for the added atoms. Comparison of Eqs. (4.25) and (4.26) with Eq. (4.7) for the exact dynamical matrix confirms that $D^{\mathrm{cum}}_{\tilde{I}\alpha\tilde{J}\beta}$ is identical to $D_{\tilde{I}\alpha\tilde{J}\beta}$, for those $\boldsymbol{q}$ fulfilling Eq. (4.22), i.e. those phonons the wave vectors of which are commensurate and hence representable with the chosen supercell. Altogether, the Parlinski method represents the present state-of-the-art within the direct method, and can simply be understood as a clever form of "Fourier interpolation" of the dynamical matrix between exact $\boldsymbol{q}$ according to the underlying first-principles calculations. Of course, the faster the aforementioned decay of elements of the force constant matrix with distance, the smaller will be the difference between the former as well as the dynamical matrix and their cumulant counterparts.

Nevertheless, it should be briefly noted that some inherent systematic problems of the direct approach still remain: The splitting of longitudinal and transversal optical modes at the Γ point (LO/TO-splitting) in polar materials (implying a basis consisting of more than one atom) cannot be obtained directly, as supercells cannot describe the correct boundary conditions for the associated macroscopic electric field. Parlinski and coworkers proposed to remedy this by adding so-called "non-analytical" terms to the dynamical matrix for $\boldsymbol{q} = \boldsymbol{0}$,[238] requiring additional parameters characterizing dielectric properties of the material obtained separately by linear response theory.[239] In fact, as only recently pointed out by Wang and coworkers, it is also possible (and even apparently more accurate) to enrich the force constants by a corresponding real-space contribution capturing the long range electrostatic interaction.[240] On the other hand, to avoid these problems entirely, density-functional perturbation theory (DFPT) as developed by Baroni and coworkers[241,242] can also be used to calculate the dynamical matrix directly. But in contrast to the various flavors of the direct method, DFPT obviously cannot be used when the interaction between atoms in the crystal is described with a classical force field model.[viii] Therefore, and since metallic systems do not suffer from these difficulties, in the present work, the Parlinski method will be used throughout as the method of choice in order to solve Eq. (4.6).

4.3. Surface Phonons

When it comes to surfaces, the three-dimensional periodicity of the bulk solid is broken, and the Brillouin zone thus becomes two-dimensional. In this context, the notation convention is to label high symmetry points within the latter by the same symbol as their bulk counterparts plus adding a bar on top. Already in 1887 Lord Rayleigh could show using elastic continuum theory, i.e. assuming large wave lengths compared to the interatomic spacings in the crystal, that phonons with smaller frequencies than found in bulk exist at the surface, with their displacement patterns including components along the surface normal.[244] With the advent of helium atom scattering (HAS) in the 1970s as an experimental technique in surface science,

[viii] Furthermore, the DFPT implementation in the CASTEP code by Keith Refson[243] currently does neither feature gapless systems nor ultrasoft pseudopotentials, and is hence not applicable to the current purposes, i.e. the desired calculations of surface phonons (cf Section 4.3) of Pd(100) and their implications for the dissociation dynamics of O_2.

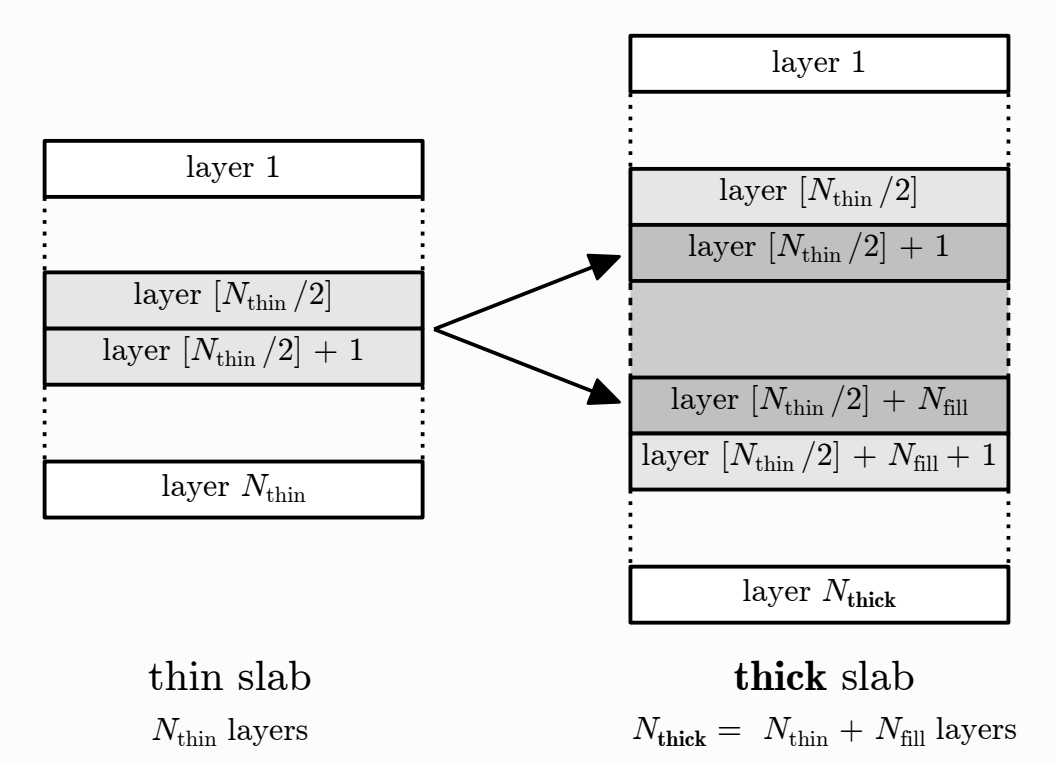

Figure 4.1.: Schematic illustration of the slab filling approach as typically used in first-principles calculations of surface phonons in order to reduce the computational burden: First, force constants for a thin slab (left) consisting of N_{thin} layers are obtained. Then, the Eigenvalue problem of lattice dynamics (cf Eq. (4.6)) is solved for a slab with N_{fill} layers inserted in the middle, whose dynamical matrix (cf Eq. (4.7)) is constructed by adding additional force constants which are taken to be bulk-like. This yields a total of $N_{\text{thick}} = N_{\text{thin}} + N_{\text{fill}}$ layers (right) and implicitly assumes that the thin slab was thick enough for this to make physical sense. Here, $[x]$ denotes the floor function, i.e. the largest integer smaller than x.

lattice dynamics of surfaces became a hot topic, but it took until 1981 until the first surface phonon spectra including the aforementioned Rayleigh modes could be measured with HAS for the insulator surface of LiF(100) by Toennies and coworkers.[245,246] Only two years later, the same group also published corresponding data for Ag(111) – the first metal surface.[247] Meanwhile also energy electron loss spectroscopy (EELS) allows to resolve surface phonons[248] – a technique whose improved high resolution descendant (HREELS) has also been applied for according measurements on Pd(100) by Chen and Kesmodel,[249] which still form the reference data for this surface.

Theoretical and computational efforts into this direction had already been stimulated before. Low-energy electron diffraction (LEED) experiments raised questions about structural and dynamical properties of crystal surfaces. Long before modern electronic structure methods were available and hence the special electronic properties of surfaces could be theoretically studied, de Wette and coworkers used Lennard-Jones potentials Section 3.2.1 for interatomic interactions. By carrying out both lattice dynamics and molecular dynamics simulations with the latter (cf Section 4.1) – tremendously challenging on the super computers available at the time due to the summation over neighbors which need to be carried out (cf Eq. (3.7)) –

they could provide a (first) theoretical perspective on properties like surface relaxation, mean square amplitudes of vibration of surface atoms or surface vibrational density of states.[163–165] It is important to emphasize that they introduced and established slabs (cf Section 2.6) to model surfaces in their pioneering work.[162–169] In such a slab model, for each (two-dimensional) phonon wave vector $\boldsymbol{q}$ in the surface Brillouin zone, the continua of bulk bands of a "real" semi-infinite crystal is approximated by the discrete number of $3N_{\text{layers}}$ branches due to the finite number of layers N_{layers} in the former (cf Section 4.1).[ix] This makes the slab thickness a very important convergence parameter – in particular when studying surface phonons, rather thick slabs are required to describe the latter correctly (or even at all!). Therein, surface phonon modes are using the calculated displacement Eigenvectors (cf Eq. (4.6)). If the vibrational weight in the surface layers at the top and the bottom of the slab exceeds a certain threshold S

$$\sum_{\tilde{I}}^{\substack{\text{surface}\\ \text{layers}}} \sum_{\alpha=1}^{3} \left|\hat{u}_{\tilde{I}\alpha}(\boldsymbol{q}, b)\right|^2 \geq S \tag{4.27}$$

the corresponding mode with phonon wave vector $\boldsymbol{q}$ and band index b (cf Section 4.1) is classified as surface phonon mode. Of course, in Eq. (4.27) the displacement Eigenvector $\hat{u}_{\tilde{I}\alpha}(\boldsymbol{q}, b)$ is assumed to be properly normalized

$$\sum_{\tilde{I}=1}^{N_{\text{cell}}} \sum_{\alpha=1}^{3} \left|\hat{u}_{\tilde{I}\alpha}(\boldsymbol{q}, b)\right|^2 = 1 \quad . \tag{4.28}$$

The number of surface layers to consider and the size of the threshold S are not sharply defined. Heid and Bohnen have e.g. used the first two layers and $S = 20\,\%$ in their work,[250] which provides a physically reasonable description.

De Wette and coworkers also introduced the notation to label and enumerate surface phonon modes by S_i, which is still commonly used nowadays. Apart from the aforementioned "traditional" Rayleigh mode S_1 with out-of-surface-plane polarization close to the $\bar{\Gamma}$-point, they also "discovered" surface phonon modes at boundaries of the Brillouin zone[162] as well as even within the bulk bands.[166] Their thorough theoretical analysis could also rationalize the latter and still provides the framework for the treatment of surface phonons until today.[168] Furthermore, within their Lennard-Jones based model, they also discussed different low index surfaces of the corresponding crystals[169] and the effect of adsorbate layers with different masses,[167] which, with proper choice of the parameters, might provide a reasonable description for the corresponding noble gas systems (cf Section 3.2.1).

Obviously, the simplicity of this model for the interatomic interactions limits the ability to describe other, "more realistic" materials. While the simple analytic form of the Lennard-Jones potential (cf Eqs. (3.9) and (3.10)) is computationally appealing, as a central force potential it is unable to capture the full vectorial nature of the pair potential given by Eq. (4.2) which makes up the harmonic solid. This systematic shortcoming and its significance in particular for metals and their surfaces has been pointed out already very early by Musser and Rieder.[251] It can be remedied by using interatomic potentials that account for the many-body character of the chemical binding in metals, like e.g. those resulting from the embedded atom method (EAM) and its modified descendant (MEAM) described in Section 3.2.2. Indeed, for the present system,

[ix] The indices of atoms inside the supercell, $\tilde{I}$ and $\tilde{J}$ in Section 4.1, are hence conveniently decomposed into a layer index and a "remainder" uniquely denoting the lateral position.[168]

the surface phonon spectrum of Pd(100) could be modeled by Chulkov and coworkers in quite good agreement with the aforementioned experimental data[249] by using a home-made EAM potential.[252] But also for surfaces a first-principle description of the interatomic interactions has become possible in order to treat their vibrational properties. Typically, density-functional theory in the local density approximation (LDA, cf Section 2.5) is used, as it is commonly considered to provide a slightly better description of elastic properties of clean surface compared to gradient corrected exchange-correlation functionals.[253] Combined with DFPT for the actual lattice dynamics part, this represents the current "state of the art".[254–256] In order to ease the computational burden of dealing with thick slabs, the concept of "slab filling", which is schematically depicted in Fig. 4.1 has proven extremely useful in this context.[257] The force constants of N_{fill} inner layers of a thick(er) slab are taken from computationally less expensive bulk calculations[x] or by repeating those of the inner layers of a thinner slab, thus "filling" the N_{thin} layers of a thin slab, for which actual *ab initio* calculations have been performed, yielding the force constant matrix for a slab with a total of $N_{\text{thick}} = N_{\text{thin}} + N_{\text{fill}}$ layers in the end. In principle, "slab filling" can also be used together with the Parlinski flavor of the direct method, since a DFPT treatment is not mandatory for metallic systems, as detailed in Section 4.2 – though it certainly adds more complexity to the calculation of forces for the displacements.

More details, both about the "early" experimental and theoretical aspects about surface phonons can be found in the book of the same title edited by Kress and de Wette.[258] In addition, for more recent methodological aspects including first-principles calculations as well as results for individual surfaces the reader is referred (e.g.) to the excellent review articles by Fritsch and Schröder[257] as well as Heid and Bohnen.[250] While the former addresses semiconductors, the latter is particularly interesting in the context of this thesis as it focuses on metal surfaces. Very recent advances are detailed in the work by Benedek and coworkers.[259]

4.4. Implementations

Exploiting the respective technical infrastructure of the underlying electronic structure code, it is not surprising that implementations of DFPT (cf Section 4.2) are typically tightly integrated into the former (CASTEP, VASP, PWSCF, ...). Unfortunately, the same also holds for several implementations of the direct method which also enable phonon calculations for classical force fields as required in Part III. The stand-alone code PHON by Dario Alfè[260] is hence a noteworthy exception written in Fortran 90. Conveniently employing and extending the high-level infrastructure provided by the Atomic Simulation Environment (ASE), for the phonon calculations carried out in the aforementioned part of this thesis, the PHONOPY-code[xi] by Atsushi Togo[261] has been used and coupled to both CASTEP (cf Section 2.8) and LAMMPS (cf Section 3.4). In contrast to PHON, this coupling has been greatly simplified by the former. Furthermore, PHONOPY fully implements the Parlinski method[237] and provides proper handling for all symmetry space groups via an external C library. Building thereon, the code was extended to allow for a treatment of surface phonons using the slab filling as described in Section 4.3.

[x] Of course, the corresponding matrix elements have to be transformed properly when changing the lattice basis from the primitive bulk to primitive unit cell of the slab modeling the surface.

[xi] Licensed under *GPL* and hence freely available from `http://phonopy.sf.net`.

Part II.

Gas-Surface Dynamics of Oxygen on a Frozen Pd(100) Surface

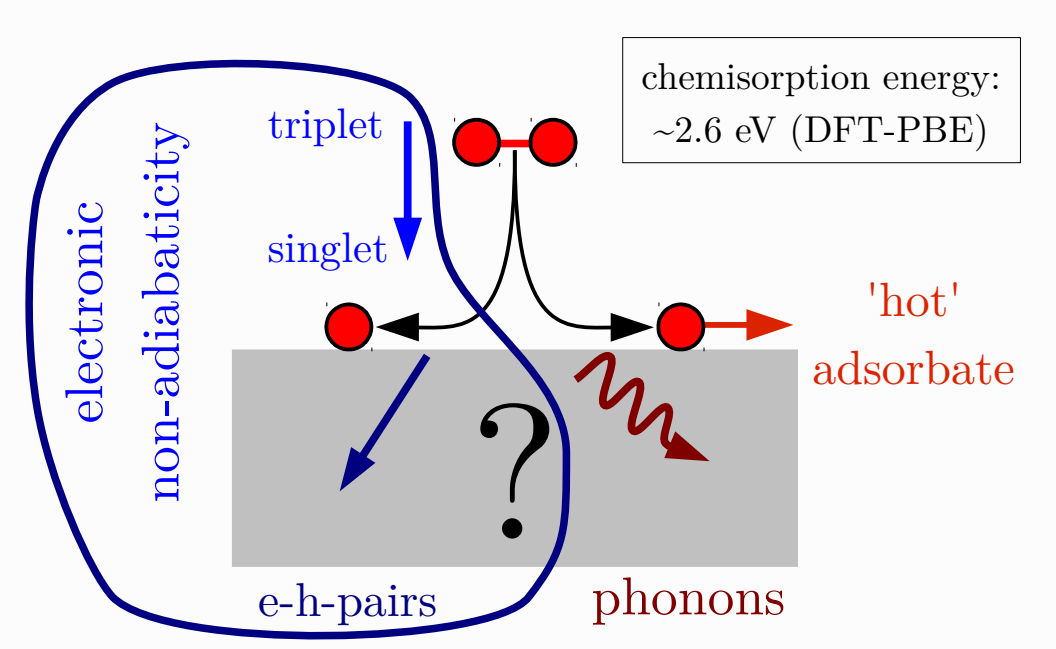

5. DFT Reference Calculations

A plethora of previous work has shown that the semi--local exchange-correlation functionals proposed by Perdew, Burke and Enzerhof (PBE)[85,86] as well as by Hammer, Hansen and Nørskov (RPBE)[89] provide a substantial if not even mandatory improvement over the local density approximation (LDA)[79,80] for both the description of the O_2 molecule[48,76] and the interaction of oxygen with palladium surfaces,[12,15,16,262–264] i.e. they yield results in good agreement with a lot of available experimental data. As already discussed in Section 2.5, lacking readily available alternatives providing comparable quality at the same computational price, PBE serves as a "work-horse" for the present study. The goal of this chapter is thus to establish a reliable computational setup used throughout the rest of this work based on the plane-wave pseudopotential code CASTEP(cf Section 2.8), comparing against highly accurate data, either available from the literature or obtained in this context from more computationally expensive first-principles calculations. All of the numbers reported in the following have been carefully checked for convergence with respect to the relevant technical parameters (see e.g. Chapter 2), in the same fashion as documented extensively (also using the CASTEP code) by McNellis.[265] Along the lines of this whole thesis to focus on methodological aspects, a similarly extensive account is not repeated here, but rather the particular (much bigger) challenges faced for the present system are pointed out.

5.1. Palladium Bulk and Surfaces

In 1978, King and Manchester carried out high-precision X-ray diffraction experiments,[266] providing the most accurate values for the lattice constant of clean bulk palladium in its natural face-centered cubic (fcc) phase: At 5.9 K, the lowest temperature which could be considered, it is (3.8782 ± 0.0001) Å. This has been extrapolated to 3.8779 Å at absolute zero by Giri and Mitra[267]. The value given in Table 5.1 can thus be taken as a reliable experimental reference, differing slightly from other such values which have found their way into the literature.[15,253,268] Table 5.1 also shows that the reference values obtained from highly accurate all-electron cal-

	Exp.[266,269]	PBE[263]	PBE[253]	PBE[262]	PBE (CL)	PBE (OTF)
$a_{0,\mathrm{Pd}}$ (Å)	3.88	3.94	3.95	3.95	3.93	3.99
$B_{0,\mathrm{Pd}}$ (Mbar)	1.95	1.63	1.63	1.57	1.74	1.63

Table 5.1.: Comparison of bulk lattice constant $a_{0,\mathrm{Pd}}$ and modulus $B_{0,\mathrm{Pd}}$ of palladium. Experimental data has been rounded to the second digit which is beyond measurement uncertainty in both cases. Values from all-electron calculations using the PBE exchange-correlation functional carried out by Todorova[263], DaSilva[253] and Zhang[262], serve as reference for those calculated with the CASTEP code within the present work using two different pseudopotentials (CL and OTF) as detailed in the text.

culations (neglecting corrections for the zero point energy),[253,262,263] overestimates the experimental value, thus following the well-known trend of PBE to underbind, i.e. overcorrecting the overbinding obtained by LDA for many materials.[253] Using a cut off energy $E_{\text{cut}} = 350\,\text{eV}$, a $12 \times 12 \times 12$ Monkhorst-Pack grid together with a simple Gaussian smearing (employing a width of 0.1 eV) for the Brillouin zone sampling of the electronic states (cf Sections 2.6 and 2.7), those values are fairly well reproduced by both ultrasoft pseudopotentials from the Cambridge library (CL) and the ones produced by the so-called "on-the-fly" pseudopotential generator (OTF).[i] Standard settings for the sizes of the grids on which the (pseudo-)charge density and the augmentation charges are represented have been verified to yield converged results. The same holds for the bulk modulus also given in Table 5.1: The experimental value extrapolated to absolute zero[269,270], is underestimated by PBE, which is again nicely reproduced within the present computational setup.

On a technical note, values for both the equilibrium lattice constant $a_{0,\text{Pd}}$ and the bulk modulus $B_{0,\text{Pd}}$ obtained by both unit cell optimization and fitting Murnaghan's equation of state[271]

$$\Delta E(V) = E(V) - E(V_0) = \frac{B_0 V}{B_0'}\left[\frac{1}{B_0' - 1}\left(\frac{V_0}{V}^{B_0'}\right) + 1\right] - \frac{B_0 V_0}{B_0' - 1} \tag{5.1}$$

to total energies are in perfect agreement. Of course, this is to be expected from a proper implementation of the stress tensor which unit cell optimization relies on[272] – conveniently calculated analytically at negligible computational cost within CASTEP. For computational efficiency, the primitive unit cell of the fcc crystal is used, as it only contains a single atom. Its lattice vectors $\left(\boldsymbol{a}_1^{\text{prim}}\boldsymbol{a}_2^{\text{prim}}\boldsymbol{a}_3^{\text{prim}}\right)$, written in the matrix form according to common crystallographic conventions, are related to those of the conventional cubic unit cell with edge length a $(\boldsymbol{a}_1^{\text{conv}}\boldsymbol{a}_2^{\text{conv}}\boldsymbol{a}_3^{\text{conv}})$, which contains four atoms, according to

$$(\boldsymbol{a}_1^{\text{conv}}\boldsymbol{a}_2^{\text{conv}}\boldsymbol{a}_3^{\text{conv}}) = a \cdot \mathbb{1}_{3\times 3} = \underbrace{\begin{pmatrix} -1 & 1 & 1 \\ 1 & -1 & 1 \\ 1 & 1 & -1 \end{pmatrix}}_{\equiv \boldsymbol{M}} \cdot \left(\boldsymbol{a}_1^{\text{prim}}\boldsymbol{a}_2^{\text{prim}}\boldsymbol{a}_3^{\text{prim}}\right) \tag{5.2a}$$

$$\Longleftrightarrow$$

$$\left(\boldsymbol{a}_1^{\text{prim}}\boldsymbol{a}_2^{\text{prim}}\boldsymbol{a}_3^{\text{prim}}\right) = \frac{1}{2} \cdot \underbrace{\begin{pmatrix} 0 & 1 & 1 \\ 1 & 0 & 1 \\ 1 & 1 & 0 \end{pmatrix}}_{\equiv \boldsymbol{M}^{-1}} \cdot (\boldsymbol{a}_1^{\text{conv}}\boldsymbol{a}_2^{\text{conv}}\boldsymbol{a}_3^{\text{conv}}) \quad . \tag{5.2b}$$

With

$$V^{\text{conv/prim}} = \boldsymbol{a}_1^{\text{conv/prim}} \cdot \boldsymbol{a}_2^{\text{conv/prim}} \times \boldsymbol{a}_3^{\text{conv/prim}} \tag{5.3}$$

the total energies $E(V)$ to fit Eq. (5.1) to thus become $E^{\text{PBE}}(V^{\text{prim}}(a))$, where

$$V_{(0)}^{\text{conv}} = a_{(0)}^3 = 4V_{(0)}^{\text{prim}} \quad . \tag{5.4}$$

[i] Without going into any details, the built-in default settings of the "on-the-fly" pseudopotential generator for palladium from CASTEP 4.0 were used here, which are abbreviated in the generation string `1|2.4|5|7|15|50:425s0.1,4d9.9[]` which is explained in detail in the documentation of the former. Also see the footnote in Section 5.4.

The equilibrium volume of the unit cell $V_0 = V_0^{\text{prim}}$, the bulk modulus B_0 as well as its partial derivative with respect to pressure $B_0' = \left.\frac{\partial B}{\partial p}\right|_{V_0}$ are the obvious fit parameters.[ii]

When moving beyond the frozen surface approximation in Part III, elastic properties of the solid come into focus. Therefore, results of phonon calculations, both all-electron using the FHI-aims code[iii] and with Castep for the aforementioned pseudopotentials all based on PBE, are presented in Fig. 5.1. The direct method (cf Section 4.2) has been employed using supercells containing 32 atoms, consisting of $2 \cdot \mathbb{1}_{3\times3}$ the conventional or equivalently $2 \cdot \boldsymbol{M}$ times the primitive unit cell at the respective equilibrium lattice constants given in Table 5.1, where $\boldsymbol{M}$ has been defined in Eqs. (5.2). The cubic and hence more compact shape of these supercells yields a size convergence that is advantageous compared to multiples of the rhombohedral primitive cell of the fcc lattice as given by Eq. (5.2b). Thanks to the exploitation of symmetry as proposed by Parlinski and coworkers,[237] only a single atom needed to be displaced along one direction. A displacement distance $d = 0.1\,\text{Å}$ has proven to be a good compromise, both small enough to stay within the harmonic regime and yet large enough to yield forces beyond numerical noise after reducing the smearing and tightening the electronic convergence (cf Section 2.7). Both the phonon band structure and density of states shown in Fig. 5.1a and Fig. 5.1b, respectively, are obtained based on the implementation available within phonopy after loosely interfacing with both Castep and FHI-aims (cf Section 4.4)[iv] Differences in the curves in Fig. 5.1 can thus be reliably traced back to the underlying all-electron and pseudopotential force calculations, which would not have been possible with results from the literature.[277–279] Along the path through the Brillouin zone indicated in the inset of Fig. 5.1a, experimental data for the phonon dispersion was obtained by Miiller and Brockhouse using neutron scattering (lowest investigated temperature: 120 K)[273,274] The former is defined by the reciprocal lattice vectors

$$(\boldsymbol{b}_1\boldsymbol{b}_2\boldsymbol{b}_3) = \frac{2\pi}{a} \cdot \underbrace{\begin{pmatrix} -1 & 1 & 1 \\ 1 & -1 & 1 \\ 1 & 1 & -1 \end{pmatrix}}_{\equiv \boldsymbol{M}} \tag{5.5}$$

with

$$\boldsymbol{a}_i^{\text{prim}} \cdot \boldsymbol{b}_j^{\text{prim}} = \delta_{ij} \quad , \quad i,j \in \{1,2,3\} \quad . \tag{5.6}$$

The all-electron PBE reference slightly underestimates that data in particular at the boundaries of the Brillouin zone. This is very accurately reproduced by the PBE(OTF) pseudopotential, while PBE(CL) is accidentally closer to experiment – which is not surprising when considering the bulk moduli given in Table 5.1. In fact, based on an all-electron generalization of density functional perturbation theory (DFPT, cf Section 4.2) to the full-potential linear muffin-tin-orbital (LMTO) method,[280] Takezawa and coworkers have compared LDA and PBE phonon

[ii] It is interesting to point out that Murnaghan himself has not given Eq. (5.1) directly. Instead, the basic idea for its derivation, see e.g.
http://en.wikipedia.org/wiki/Birch-Murnaghan_equation_of_state,
to expand the bulk modulus up to second order in pressure $B(p) = B_0 + B_0'p + \mathcal{O}(p^2)$ can be traced back to his work.

[iii] Default settings at the "light" level turn out to yield converged results. As expected, the optimized lattice constant perfectly reproduces the all-electron values previously reported in the literature (Table 5.1).

[iv] It is worth noting at this place that the author of this thesis has contributed a convenient front end to phonopy and the FHI-aims code called "phonopy-FHI-aims", which also simplified the present calculations.

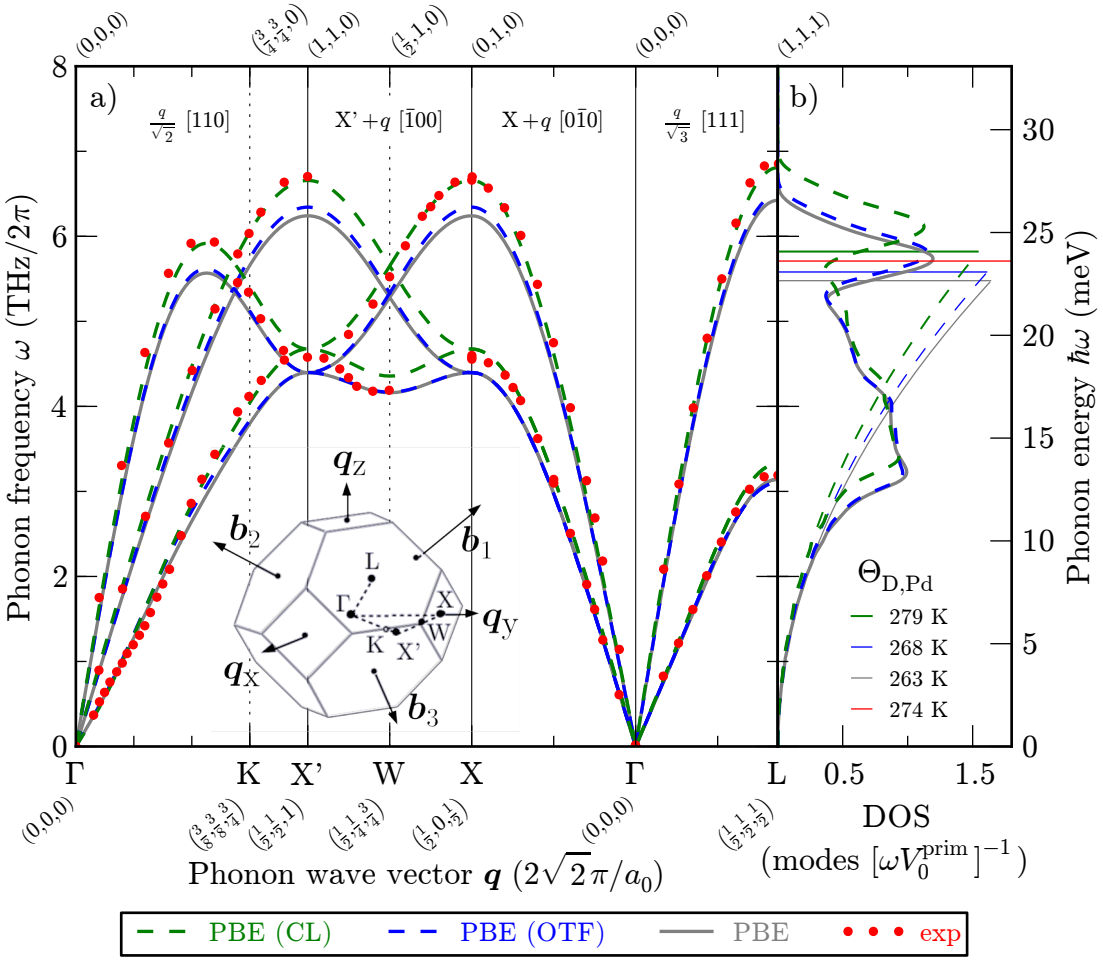

Figure 5.1.: a) Phonon dispersion of bulk palladium along the path in the Brillouin zone indicated in the inset. At the lower axis, special points are labeled according to common notation and given together with their fractional coordinates with respect to the primitive vectors of the reciprocal lattice $\boldsymbol{b}_1, \boldsymbol{b}_2, \boldsymbol{b}_3$, which are defined in Eqs. (5.5) and (5.6). Labels at the upper axis show the corresponding absolute coordinates in reciprocal space with respect to the Cartesian coordinate system defined by $\boldsymbol{q}_\text{x}, \boldsymbol{q}_\text{y}, \boldsymbol{q}_\text{z}$. Parametrizations of the path segments are given below, employing the usual crystallographic notation to indicate directions (with respect to the conventional unit cell of the face-centered cubic lattice). b) Phonon density of states corresponding to the phonon dispersions in a) (thick lines), together with fits to a Debye model (thin lines) and resulting Debye temperatures $\Theta_{\text{D,Pd}}$ obtained therefrom. Areas under the curves are equal to three times one atom in the primitive cell, since the densities of states have been divided by the volumes $V_0^{\text{prim}} = \frac{1}{4}a_0^3$ of the latter (cf Section 4.1), resulting from the respective lattice constants a_0 given in Table 5.1 Results from all-electron calculations using FHI-AIMS (PBE, gray) are compared against CASTEP calculations with two different pseudopotentials (PBE (CL) and PBE (OTF) in green and blue, respectively) and experimental data (red). The latter is taken from the work of Miiller and Brockhouse[273,274] in case of the dispersion. Debye temperatures were obtained by Rajput[275] as well as Veal and Rayne.[276]

	PBE[263]	PBE[253]	PBE[262]	PBE (CL)	PBE (OTF)
$\sigma_{\mathrm{Pd}}^{100}\,(\mathrm{J\,m^{-2}})$	1.33		1.55	1.61	1.45
$\sigma_{\mathrm{Pd}}^{111}\,(\mathrm{J\,m^{-2}})$	1.15	1.33	1.39	1.47	1.30

Table 5.2.: Surface energies of Pd(100) and Pd(111). PBE reference data from all-electron calculations of Todorova[263], DaSilva[253] and Zhang[262] are compared to those calculated with the CASTEP code within the present work using two different pseudopotentials (CL and OTF) as detailed in the text.

band structures for bulk palladium and found that the former are in better agreement with the experimental data.[278] Such good agreement has also been found in other studies relying on LDA.[277,279] However, as already indicated in the beginning of this section, the description of oxygen adsorption demands to go beyond the former within this context. Turning to the phonon density of states shown in Fig. 5.1b, by fitting the first quarter of the first principles curves to Eq. (4.14) the "closest" Debye models have been obtained – as already sketched out in Section 4.1. This fraction has been chosen and verified to nicely cover the linear regime of the dispersion of all three phonon branches shown in Fig. 5.1a). where the essential assumption of the Debye model is thus fulfilled. The resulting Debye temperatures $\Theta_{\mathrm{D,Pd}}$ agree reasonably well with those that have been obtained from experiments: The ultrasonic elasticity measurements by Rayne resulted in $(275 \pm 8)\,\mathrm{K}$.[269] Similarly, calorimetry carried out by Hoare and Yates[281] as well as Veal and Rayne[275] have led to $(274 \pm 3)\,\mathrm{K}$ and, slightly more accurate, $(273.6 \pm 1.4)\,\mathrm{K}$, respectively.

Finally, it is noted in passing that a comparison of the electronic density of states in the energy range of the valence electrons with one obtained from an all electron calculation[263] also yields excellent agreement, which is important with respect to Chapter 7.

Turning to surfaces, surface energies $\sigma_{\mathrm{Pd}}^{100}$ and $\sigma_{\mathrm{Pd}}^{111}$ are given in Table 5.2 for both Pd(100) and Pd(111) as a sensitive indicator for the quality of their description. They are calculated according to the commonly applied strategy

$$\sigma = \frac{1}{2A}\left(E_{\mathrm{slab}} - \frac{N_{\mathrm{slab}}}{N_{\mathrm{bulk}}} \cdot E_{\mathrm{bulk}}\right) \quad , \tag{5.7}$$

where E^{slab} and E^{bulk} are total energies from a slab (cf Section 2.6) and a comparable bulk calculation, and the factor $\frac{N_{\mathrm{slab}}}{N_{\mathrm{bulk}}}$ scales both to the same number of atoms used in the former. In a plane wave calculation, using simulation cells of the same size and thus the same basis set is recommended, as it provides a beneficial cancellation of numerical errors. The factor of $\frac{1}{2}$ accounts for the fact that the surfaces come in pairs in the slab calculations. A is the surface area of the slabs used in the calculations: $A^{100} = \left(a^{100}\right)^2 = \frac{1}{2}\left(a_0\right)^2$ and $A^{111} = \frac{\sqrt{3}}{2}\left(a^{111}\right)^2 = \frac{\sqrt{3}}{4}\left(a_0\right)^2$ for (100) and (111) surfaces of fcc crystals with surface lattice constants $a^{100} = a^{111} = \frac{\sqrt{2}}{2}a_0$, respectively. The initial interlayer distances of truncated bulk, $d^{100} = \frac{1}{2}a_0$ and $d^{111} = \sqrt{\frac{2}{3}}a^{111} = \frac{1}{\sqrt{3}}a_0$, were relaxed with the Broyden-Fletcher-Goldfarb-Shanno algorithm[132] as implemented in the CASTEP code.[272] The PBE (CL) and PBE (OTF) values presented in Table 5.2 have been obtained based on 1×1 slabs of the surface unit cell (i.e. one atom per layer), consisting of 5 layers and a vacuum distance $> 10\,\text{Å}$ corresponding to six interlayer distances d^{100} and d^{111} for the respective surface. $12 \times 12 \times 1$ Monkhorst-Pack grids have been used together with further reduced smearing in order to obtain sufficiently converged forces

for the relaxation. The negligible changes are in good agreement with low energy electron diffraction (LEED) experiments[282–284] and also nicely reproduce those obtained within the all-electron calculations[253,263] from which the corresponding surface energies are mentioned in Table 5.2. Once more, Table 5.2 shows that both pseudopotentials (CL and OTF) used in this work not only reproduce the right energetic ordering, i.e. attribute the Pd(111) to be more stable than the more open Pd(100) surface, but also yield a fair quantitative agreement with the all-electron calculations. In fact, in case of Pd(100) the disagreement of the former are even within the scatter of the latter values Todorova[263], Da Silva and coworkers[253] and Zhang[262].

5.2. O_2 Molecule

Table 5.3 summarizes properties of the oxygen molecule and their DFT-PBE description which are of particular relevance for the present thesis. More extensive collections of reference values can be found in the work by Behler[76] and Carbogno[109]. However, the most exact all-electron PBE reference values presented in Table 5.3 were obtained with the FHI-aims code, using a basis set of numerically tabulated atom-centered orbitals from the `really_tight` collection from the FHI-aims "workshop version" of 2009,[285] and hence cannot be found in either of those collections. The Castep values are calculated as "molecule in a box", based on ultrasoft pseudopotentials for oxygen from the aforementioned sources (CL and OTF),[v] that require a cut off energy of 400 eV and 500 eV, respectively. The grid size for the (ultrasoft pseudo-)charge density needs to be increased so that the expansion coefficients of all squared plane waves are described exactly (cf Section 2.6), which also makes the calculations considerably more expensive. Beyond that, further enlargement of the grid used to represent the augmentation charges does not have a significant effect on the calculated values. The boxes were tested to be sufficiently large to suppress any interaction of images through the inherent periodic boundary conditions, consequently sampling the negligible dispersion of electronic states only via a single $\boldsymbol{k}$-point. On the contrary, the FHI-aims calculations are truly aperiodic thanks to the atom-centered basis set. In order to more adequately describe the spin triplet of the ground state ($^3\Sigma_g^-$) of the O_2 molecule within PBE, spin-polarized calculations are required with a fixed number of two excess electrons in one of the spin channels. ($N_s = 2$, cf Section 2.5)

As shown in Table 5.3, the pseudopotential calculations nicely reproduce the equilibrium bond length d_{0,O_2} and the vibrational frequency of the stretch mode ω_{0,O_2} in the harmonic approximation from the all-electron PBE calculations, which are also in good agreement with the experimental data.[288]

However, they perform worse for energetic properties: The binding energy E_{b,O_2} is closer to the one obtained in experiments, but only due to fortuitous canceling of errors with opposite sign, induced by both the PBE exchange-correlation functional and the pseudopotentials. On the other hand, for $\Delta E_{O_2}^{t\to s}$, both of these errors add up, so that the Castep values are even further away from the spectroscopically measured value for the energy difference between the ground state of the O_2 molecule and its first electronically excited state.[287] They are denoted by $^3\Sigma_g^-$ and $^1\Delta_g$, respectively, reflecting their triplet and singlet electronic spin configurations. Therefore, $\Delta E_{O_2}^{t\to s}$ is also referred to as singlet-triplet gap.

Since the spin is quenched for adsorbed oxygen (see below in Section 5.3) due to the metal

[v] As before, the latter were generated with the "on-the-fly" pseudopotential generator using the default settings for oxygen built into Castep 4.0, compactly encoded in the generation string `2|1.3|5|7|15|20:21(qc=7.5)[]` which is not addressed in detail here.

	Exp.[286–288]	PBE[48,76]	PBE	PBE (CL)	PBE (OTF)
d_{0,O_2} (Å)	1.21	1.22	1.22	1.24	1.22
E_{b,O_2} (eV)	5.12	6.10	6.23	5.64	5.90
ω_{0,O_2} (meV)	196	189	193	194	196
$\Delta E_{O_2}^{t\to s}$ (eV)	0.98	1.14	1.15	1.26	1.22

Table 5.3.: Comparison of the equilibrium bond length d_{0,O_2}, binding energy E_{b,O_2} (without zero point energy corrections), (harmonic) vibrational frequency ω_{0,O_2} and singlet-triplet gap $\Delta E_{O_2}^{t\to s}$of O_2. Experimental reference data[286–288] is compared against results from all-electron calculations (PBE) and those obtained with CASTEP calculations using two different pseudopotentials (PBE,CL and PBE,OTF). The former were done by Behler[48,76] and, aiming at even tighter convergence with FHI-AIMS, like the CASTEP calculations as part of this work as detailed in the text.

surface acting as "spin bath", a spin transition must occur during the dynamics of the adsorption process. $\Delta E_{O_2}^{t\to s}$ is thus an important quantity for the description of the two two diabatic potential energy surfaces corresponding to triplet and singlet states of O_2 at the starting point of the dynamics. The non-adiabaticity of that spin transition has been discussed extensively on Al(111)[48–50,76] and will also be picked up for the Pd(100) surface in Chapters 6 and 7. In the former work, it has also been reasoned that $\Delta E_{O_2}^{t\to s}$ is best described by

$$\Delta E_{O_2}^{t\to s} \approx E_{O_2}^{sp} - E_{O_2}^{nsp} \tag{5.8}$$

within density-functional theory with PBE as approximate exchange-correlation functional. Here $E_{O_2}^{sp}$ and $E_{O_2}^{nsp}$ are the total energies of an O_2 molecule from a non-spin polarized and spin polarized calculation, respectively. This "recipe" has also been adopted for the values for $\Delta E_{O_2}^{t\to s}$ calculated within this work as given in Table 5.3.

On an important technical note, special care must be taken for the calculations of $E_{O_2}^{nsp}$ with CASTEP: Though traditionally recommended for systems with a gap between occupied and unoccupied states, like e.g. (small) molecules, using direct minimization[131] to obtain self-consistency leads to a different electronic ground state than that obtained by other electronic minimization schemes, which allow for fractional occupancies naturally occurring when introducing smearing according to a generalized finite temperature (cf Section 2.7): Already at a smearing width of 0.1 eV, the total energy estimate for zero smearing obtained by density mixing (DM)[133] is about 0.5 eV lower. Unfortunately, though not surprising, no mixing settings could be found for this scheme to yield self-consistent solutions for smearing widths $\ll 0.1$ eV, which would be required for reliable results with negligible error due to smearing.[vi] Fortunately, ensemble DFT (EDFT)[142,144] reliably allows to obtain total energies for the PBE ground state of non- spin polarized O_2 even for a smearing width of 1×10^{-3} eV, used to calculate the values for $\Delta E_{O_2}^{t\to s}$ given in Table 5.3 according to Eq. (5.8). The reason behind the aforementioned significant energy difference is that, as indicated above, only within both DM and EDFT the frontier levels

[vi] In case of FHI-AIMS, adjusting the mixing settings still allows density mixing, which is the only electronic minimization scheme currently available in this code, to converge for such appropriately reduced smearing. The much smaller basis set apparently leaves much less room for oscillations which prevent convergence within the same electronic minimization scheme in CASTEP.

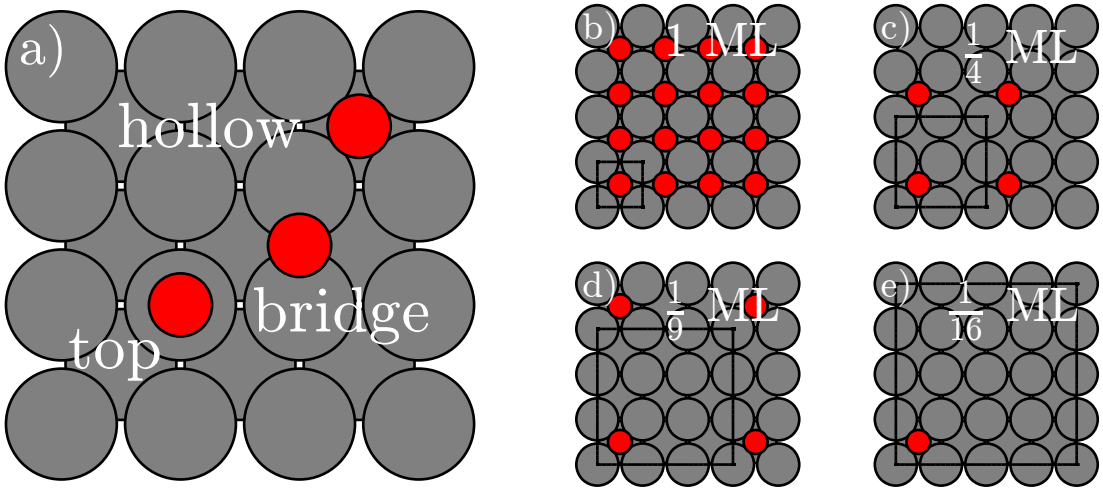

Figure 5.2.: a) Adsorption sites of a atomic oxygen on the Pd(100) surface. b) to e) 1×1 to 4×4 overlayer structure of oxygen adsorbed in the hollow site, corresponding to coverages Θ of 1 ML to $^1/_{16}$ ML, respectively. The unit cells for each structure are indicated by the black squares.

corresponding to the $2\pi^*$ orbitals of the oxygen molecule can each be half occupied. This has been found in agreement with previous work,[48–50,76] and is crucial for a DFT-PBE description to better mimic the $^1\Delta_g$ singlet state as argued therein.

Improving the agreement between the all-electron and the pseudopotential calculations for the energetic quantities in Table 5.3 would require to construct a replacement pseudopotential, which outperforms the two which have been used here (CL and OTF) and possesses similarly low computational demands. Before turning to such a non-trivial, time-consuming endeavor right away, it is first checked how the errors of the present pseudopotentials propagates to the description of the interaction of oxygen with the Pd(100) surface. This is, after all, of central interest for the present work, and detailed in the next section.

5.3. Pd-O Interaction

Now, combining both pseudopotentials from both sets (CL and OTF, see previous sections), adsorption energies E_{ads} have been calculated for various coverages Θ with respect to an O_2 molecule to be dissociated according to

$$E_{\mathrm{ads}}(\mathrm{site},\Theta) = E^{100}_{\mathrm{O@Pd}}(\mathrm{site},\Theta) - \left[E^{100}_{\mathrm{Pd}}(\Theta) + \tfrac{1}{2}E_{\mathrm{O_2}}\right] \quad . \tag{5.9}$$

Here, $E_{\mathrm{O_2}}$ is the total energy of an isolated oxygen molecule in gas phase in its spin triplet ground state (cf Section 5.2). $E^{100}_{\mathrm{O@Pd}}(\mathrm{site},\Theta)$ and E^{100}_{Pd} are the total energies of geometry optimized slab calculations of oxygen adsorbed at a particular surface site and a clean Pd(100) surface, respectively, using the surface unit cell of the periodic overlayer structure induced by the coverage Θ in order to minimize the computational effort. This is illustrated in Fig. 5.2 for the high-symmetry adsorption sites (hollow, bridge, top, cf Fig. 5.2a) and coverages with corresponding unit cells (1×1 to 4×4, Figs. 5.2b to 5.2e) considered in this work, where one monolayer (ML) of coverage is defined by the 1×1 overlayer structure. Obviously, these

E_{ads}(site, Θ)	(1 × 1)-O 1 ML	(2 × 2)-O 1/4 ML	(3 × 3)-O 1/9 ML	(4 × 4)-O 1/16 ML
hollow				
PBE[16,262]	−0.34	−1.35	−1.25	
PBE			−1.11	
PBE,CL	−0.27	−1.35	−1.27	−1.23
PBE,OTF	−0.04	−1.18	−0.94	
bridge				
PBE[16,262]	−0.38	−0.96	−1.02	
PBE			−0.90	
PBE,CL	−0.23	−0.87	−0.90	−0.91
PBE,OTF	+0.07	−0.70	−0.94	
top				
PBE			+0.23	
PBE,CL	+0.77	+0.34	+0.32	+0.33
PBE,OTF	+1.03	+0.42	+0.56	

Table 5.4.: Oxygen adsorption energies on Pd(100) for different coverages Θ given in fractions of a monolayer (ML), where 1 ML is defined by the 1 × 1 overlayer structure. Results from all-electron calculations from Zhang[16,262] and those selectively carried out within this work for Θ = 1/9 ML using FHI-aims, are compared against Castep calculations with two different pseudopotentials (PBE,CL and PBE,OTF) as detailed in the text.

calculations get more expensive with decreasing coverage as the unit cells become larger. The sign in Eq. (5.9) has been chosen such that for negative values the combined system of oxygen on the Pd(100) surface is energetically favored over the two separate systems, indicating an exothermic reaction with accompanying release of binding or chemisorption energy.

For the results presented in Table 5.4, all calculations have been carried out without spin polarization based on the more accurate and computationally demanding technical parameters found to be required for O_2 and the same $\boldsymbol{k}$-point sampling as for the clean surfaces – both detailed in the previous sections. In order to obtain forces which are accurate enough for the relaxations, the smearing width and the electronic convergence accuracy need to be slightly reduced. Five-layer slabs with oxygen adsorbed on one side where used. Lacking a dipole correction as proposed by Neugebauer and Scheffler[289] to compensate for artificial adsorbate induced electrostatic interactions between adjacent slabs through the vacuum of the employed supercells (cf Section 2.6) also slabs consisting of seven layers with oxygen adsorbed on both sides were tested in case of the Castep calculations. The dipole is clearly visible in the electrostatic potentials averaged along the surface normal, but work functions extracted therefrom are in very good agreement with all-electron calculations including the aforementioned dipole correction.[290] No significant difference for the resulting adsorption energies have been found within the accuracy of the numerical convergence, which is estimated to be about ±50 meV within both given pseudopotentials. Again, using a basis set from the `really_tight` settings and without going into more technical details, the values obtained within the FHI-aims all-electron calculations have been verified to be converged by an order of magnitude better and can thus be considered as the most accurate reference. Due their high computational cost and aiming at the low coverage limit, they have only been carried out for the 3 × 3 overlayer

structures, for which the lateral interactions between periodic images are already negligible.

Altogether, Table 5.4 shows the agreement between the pseudopotential and all-electron calculations to be quite good, with the CL potentials performing slightly better. It is thus the choice for all subsequent CASTEP calculations for the present system.

Using the CL potential and the computational settings thus established here, the energy difference between oxygen adsorbed on bridge and hollow sites was found to yield the barrier for oxygen diffusing from one to another another hollow site via the bridge site. Mapping the potential energy surface to obtain a minimum energy path, the bridge site was confirmed to be the transition state – just as expected also by symmetry arguments.

Furthermore, motivated by experiments of Rocca and coworkers,[17–19] also oxygen located at several sites below the surface has been studied. Following the same trend as observed for other transition metal surfaces including the Pd(111),[11] corresponding absorption energies (defined in complete analogy to Eq. (5.9)) all show absorption to be endothermic due to the distortions of the lattice closely around the subsurface oxygen needed to maintain bond distances of about 2 Å. These are found to be similar to those reported by Todorova and coworkers for the Pd(111) surface.[14]

For the dynamics of oxygen dissociation and hence the remainder of this work, energetics (and forces) of arbitrary configurations of an O_2 molecule above the Pd(100) surface are the key quantity of interest. For a few selected highly symmetric such configurations[vii] further comparisons have been performed, resulting in similarly good agreement between the CL pseudopotential and all-electron calculations[290] as before.

However, as detailed in Section 5.2, in general these calculations have to be spin polarized. This brings up a deficiency of the PBE functional (cf Section 2.5) to properly describe the paramagnetic ground state of bulk palladium which has first been discussed in the magnetism community only recently.[279,291,292] "Spin-polarized PBE-Pd", as obtained from bulk calculations otherwise identical to those described in Section 5.1, is ferromagnetic, favored by $\Delta E_{\mathrm{Pd}}^{\mathrm{PBE}} \approx 5\,\mathrm{meV}$ and and with a magnetic moment of $\mu_{\mathrm{Pd}}^{\mathrm{PBE}} \approx 0.4\,\mu_{\mathrm{B}}$ per atom according to all-electron calculations.[291,292] This is "correctly" reproduced by the CL pseudopotential, albeit with a larger energetic preference ($\Delta E_{\mathrm{Pd}}^{\mathrm{PBE,CL}} = 35\,\mathrm{meV}$ and $\mu_{\mathrm{Pd}}^{\mathrm{PBE,CL}} = 0.48\,\mu_{\mathrm{B}}$). In the context of this work, these aforementioned values have also been confirmed by other all-electron calculations, and in addition it has been verified that RPBE unfortunately performs even slightly worse.[290] The corresponding "spin polarized equilibrium lattice constant" only differs by a few mÅ from the non-spin polarized case. In slab calculations, the magnetic moment ranges from $0.4\,\mu_{\mathrm{B}}$ to $0.5\,\mu_{\mathrm{B}}$, slightly decreased for atoms in the surface layer, increasing towards bulk-like layers at the center of the slab. Recalculating the adsorption energies with CASTEP using the CL pseudopotentials for the 3×3 case based on spin polarized slabs, which are most relevant for this work (cf Chapter 6), revealed that they only differ within the numerical uncertainty estimated above. Consequently, although the aforementioned deficiency certainly leads to a qualitatively wrong physical description on the small meV energy scales important for magnetic properties, a good description of chemical dynamics can still be expected.

However, the artificial PBE-induced ferromagnetism severely complicates achieving self-consistency at all and always converge to comparable ground states (cf Section 2.7). Within density mixing, the latter can be helped by putting non-zero local spin densities (formed by scaling the atomic charge densities accordingly in both spin channels) onto individual atoms during initialization. For an O_2 molecule far away from the surface it is even imperative, as it is

[vii] owing to the urge to keep the computational burden for the WIEN2K code as small as possible

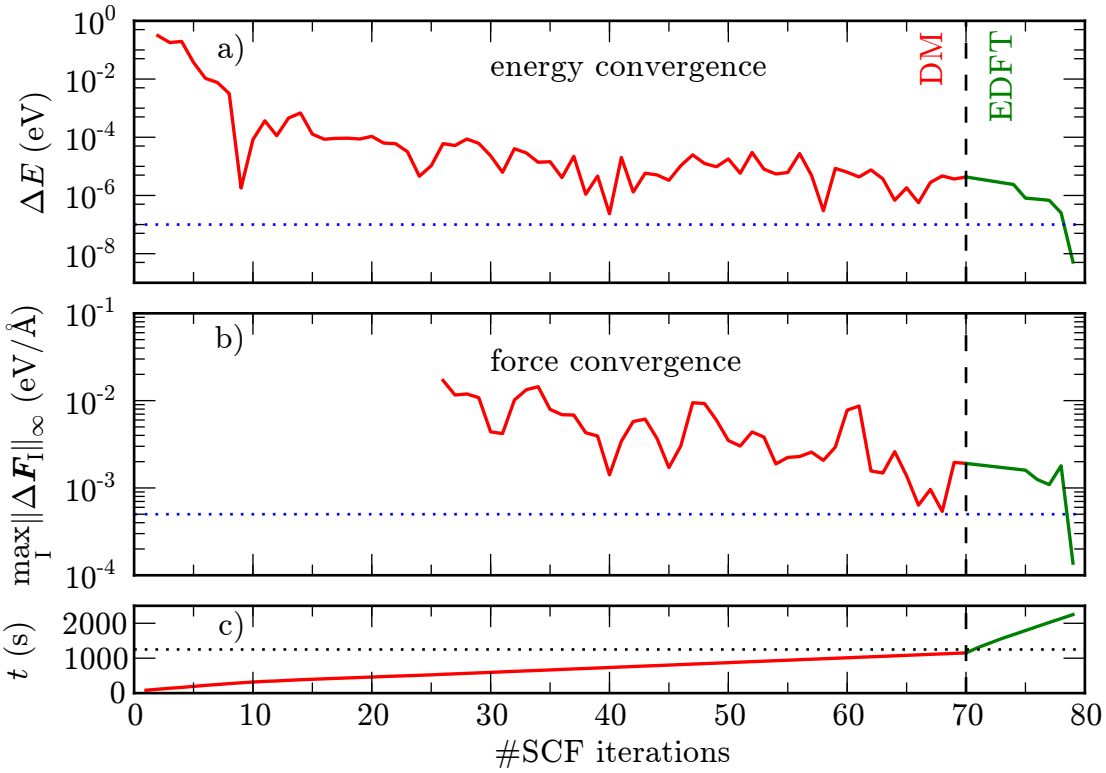

Figure 5.3.: a) Changes of the total energy ΔE and b) maximum force component $\|\boldsymbol{F}_I\|_\infty$ on any atom I as a function of the number of self-consistent field (SCF) cycles. c) Total time of the calculation. The vertical dashed lines indicate the (maximum) number of SCF cycles after which the electronic minimization scheme was switched from density mixing (DM) to ensemble DFT (EDFT), because the electronic convergence criteria (*hmm* in a) and *hmm* in b), indicated by the horizontal dotted lines) have not been met by the former. These tight values had to be chosen for *ab initio* molecular dynamics in the remainder of this work in order to ensure energy conservation over several picoseconds (cf Chapter 9 and Chapter 10). Note that the few EDFT iterations take almost the same time those using DM, as illustrated by the horizontal dotted line in c). For details and further discussion see text.

described in its "spin-polarized" singlet state otherwise.[47,50] For arbitrary configurations on a large scale as required to map a potential energy surface (cf Chapter 6) or *ab initio* molecular dynamics (cf Chapter 9 and Chapter 10), also its superior computational demands make it the clear favorite. Unfortunately, self-consistency cannot be achieved for numerous configurations – despite increase of smearing to unphysically large values (cf Section 5.2) and testing of a variety of mixing settings, for which an overall optimal choice of parameters simply does not exist. Picking up the trail of Marzari and coworkers, who were also targeting dynamics involving metal surfaces,[142,293] brings up ensemble DFT as an interesting alternative for the electronic minimization that guarantees convergence also at reasonably small smearing (cf Section 2.7). However, its CASTEP implementation does not enable the aforementioned crucial local spin density initialization and poses prohibitive large computational demands for the present application if used for entire self-consistency cycles on a large scale. Of course, the "best of both worlds" can be combined as follows:

1. Use density mixing (DM) including the desired initialization of local spin densities around atoms for a maximum number of $N_{\mathrm{SCF}}^{\mathrm{DM}}$ self-consistency iterations.

2. If self-consistency has not been achieved, switch to ensemble DFT (EDFT), the Kohn-Sham orbitals (and resulting charge and spin density) obtained so far.

The performance of this hybrid scheme (DM/EDFT), after the CASTEP code was extended accordingly by the author of this thesis, is illustrated for $N_{\mathrm{SCF}}^{\mathrm{DM}} = 70$ in Fig. 5.3, Though conceptually trivial – it can be seen as a somewhat extended and enhanced initialization of EDFT in particular for spin polarized systems – it is important to emphasize that these changes have proven essential for further parts of this work (typically using values for $N_{\mathrm{SCF}}^{\mathrm{DM}}$ between 60 and 70). Its application and concomitant improvement for other systems shows its general value.

5.4. Conclusions and Outlook

Altogether, the ultrasoft pseudopotentials from the Cambridge library (CL) perform better than their counterparts from the "on-the-fly" pseudopotential generator of the CASTEP code (OTF) for the application that this work focuses on:[viii] Not only do they yield results much closer to the all-electron reference calculations for the adsorption energies presented in the previous subsection, but they also come at computational price that still allows to study dynamics with the available resources.

Furthermore, the preceding subsections have also shown a remarkable spread in the properties obtained from all-electron calculations. Though not suffering from approximations beyond the exchange-correlation functional in principle, apparently it has not always been possible to afford proper convergence in computational practice – at least in those days when the calculations were performed – or other convergence behavior (e.g. only in relative energetics) was of relevance for these studies. Resulting deviations can even come close to those achieved with the pseudopotentials favored here.

Notwithstanding, the pseudopotential approximation has to be seen critically. This holds in particular in the context of new first-principles based methods like the perturbative approach in Chapter 7 to calculate electron-hole pair spectra, which therefore also includes a corresponding discussion.

Finally, as detailed in the following, the focus of this work has not been devoted to pseudopotential optimization – also keeping the advent of further developed, highly efficient all-electron methods and corresponding implementations, like e.g. FHI-AIMS[285,294], in mind, which show good scaling on the massively parallel computer platforms of the future. Consequently, the computational setup established within the PBE-CL slab calculations for the interaction of oxygen with the Pd(100) surface is used as basis for a "sufficiently accurate" first-principles

[viii] It is important to note that the built-in OTF default settings employed here have been revised within CASTEP versions >4.0, which this work has been started with. Again without going into any details, the new default generation strings for the former (sill valid in the currently latest version 5.5) are `2|1.0|1.3|0.7|13|16|18|20:21(qc=7)` for oxygen and `3|2.0|2.0|1.5|10|12|13|40U:50U:41:42(qc=5.5)5s0.05` for palladium. The resulting ultrasoft pseudopotentials are harder (i.e. have smaller pseudoization radii) than those employed here, and in case of palladium also pseudoize the semi-core states (i.e. $4s^2 4p^6 4d^{10} 5s^{0.05}$ instead of $4d^{9.9} 5s^{0.1}$). Better agreement with all-electron calculations can thus be expected. However, the compromise between speed and accuracy will not be improved over the one offered by the pseudopotentials employed in the remainder of this work.

methodology in the remainder of this work. Deviations therefrom will be specified and discussed in place. Also and in particular for the *ab initio* molecular dynamics in the following chapters, the DM/EDFT "hybrid" electronic minimization scheme turns out to be crucial. Without it, forces that are accurate enough to ensure a proper conservation of motion integrals (like e.g. energy in the microcanonical ensemble) could not have been obtained reliably.

6. Statistical Properties

Before molecules from the gas phase can undergo reactions on surfaces they first have to get in contact with the latter. From a theoretical point of view, one is faced with a Maxwell-Boltzmann distribution of the former which immediately brings up the problem of statistics. The impingement of molecules onto the surface thus occurs with randomly distributed initial molecular orientation and lateral position, facing the corrugation of the surface potential. To obtain quantities which can be compared to measured data even if obtained from molecular beam experiments, where the initial velocity (both its absolute value and direction) are rather well defined, averaging over a huge number of impingement events is usually necessary. Therefore, a discussion of gas-surface dynamics must inevitably consider statistical aspects.

The strength of scattering theories is to directly include these aspects into the analytical expressions which typically provide access to "final state" properties. Indeed, surface scattering experiments have been successfully modeled with such approaches.[295] However, details of the gas-surface interaction are only considered by (though few) effective parameters, which can be adjusted to fit experimental data. Not only is this rather dissatisfying from an *ab initio* perspective, but in fact too many details of the interaction might be lost in the description of molecules which are not "quickly reflected" from the surface. A generalization to chemical reactions *on* the surface (like e.g. dissociation) hence is difficult if not yet impossible,[296] and scattering theories are consequently not further considered here.

Rather, nowadays standard theoretical tool for capturing reaction probabilities on the atomic scale is employed: Individual impingement events are "trajectorized", following the time evolution of the reacting molecule via molecular dynamics (MD). Within the Born-Oppenheimer approximation, both classical mechanics and quantum dynamics can be used for the nuclei.[297] The former has been questioned in the context of gas-surface dynamics on metal surfaces both by experiments[29,30] and theory,[44–47,298–300] but an electronically adiabatic description of the adsorbate-substrate interaction has nevertheless always formed the starting point and an important reference for extended investigations. Therefore, non-adiabatic electron dynamics are neglected here in a first step as well.

The key challenge is to obtain a realistic description of the aforementioned interaction potential between molecule and surface – even for small adsorbates like diatomics. Qualitative ideas about dissociation on surfaces have already been discussed in the pioneering work by Lennard-Jones from 1932.[20] Still, only in the 1970s, when McCreery and Wolken adapted a semi-empirical parametrization based on Morse potentials according to the London-Eyring-Polanyi-Sato (LEPS) recipe, a quantitative treatment became possible.[301–305] As LEPS has its origin in the description of molecules, it is not surprising that the advent of semi-empirical descriptions of metals according to the effective medium theory (EMT)[176] or the (related) embedded atom method (EAM) in the 1980s[175,181] have stimulated applications[306] or triggered adaptations to gas-surface dynamics called embedded diatomics in molecules (EDIM).[307–309]

When *ab initio* techniques started to become available in the 1990s also for the treatment of adsorption on metallic surfaces, attempts have been made to adjust the parameters in the popular LEPS model according to the latter.[310–315] However, it has soon been realized that such "simple" semi-empirical parametrizations are generally not flexible enough to capture

the quantum mechanical complexity of bond formation with the surface and bond breaking within the adsorbate. On the other hand, each calculated trajectory requires a huge number of evaluations of the interaction potential, which was far too computationally expensive even for computationally most accessible systems with molecular hydrogen as adsorbate. Fortunately, the Born-Oppenheimer approximation allows to decouple the dynamics from the expensive first-principles calculations: Within a so-called "divide-and-conquer" strategy, first a representation of the potential energy surface describing the adsorbate-substrate interaction is obtained whose evaluation comes at a much lower computational cost. Then, in a second step, extensive dynamical calculations can be carried out. Apart from its computational advantages, the availability of a plethora of experimental data let first such *ab initio* studies of dynamics focus on H_2, in particular on copper surfaces. As nicely reviewed by Darling and Holloway,[297] only two or three degrees of freedom of the interaction potential had been included for computational convenience, with the nuclei of the hydrogen atoms being treated both classically and quantum mechanically.

The first six-dimensional treatment based on a first-principles description of the adsorbate-substrate interaction on a frozen surface within a "divide-and-conquer" approach has been presented by Groß and coworkers for H_2 on Pd(100).[316–320] These studies showed that "dimensionality matters". Reducing the number of degrees of freedom in the phase space underlying the dynamics neglects "important parts" so that dramatically wrong results for statistical properties can be extracted out of it.[82] For example, reaction rates cannot be obtained reliably out of static considerations as typically done by means of transition state theory for reactions on a surface.[3,8] Facing the six-dimensional problem is hence an absolute necessity and can be more important than a quantum mechanical treatment of the nuclei – even in case of hydrogen.[22]

Consequently, now the accurate representation of the "full-dimensional" (within the frozen surface approximation) adsorbate-substrate interaction became the key concern. The analytical expressions that had first been chosen by Groß and coworkers[316–320] even contained artificial symmetries and showed significant deviations from the underlying first-principles data. The latter also held for the six-dimensional potential energy surface constructed by Kroes and coworkers to model H_2 on copper.[312,313,321] The corrugation reducing procedure (CRP), originally sketched out by Kresse[322] and further developed by Busnengo and coworkers,[323,324] provides a robust interpolation technique, that has been frequently and successfully applied to model six-dimensional potential energy surfaces of various systems in gas-surface dynamics.[325–329] Key idea of the CRP is to reduce the corrugation of the six-dimensional PES of a diatomic by first subtracting a three-dimensional PES of both its constituent atoms to smoothen the target of the interpolation. However, for a spin-polarized system like the present (O_2 has a triplet ground state when it is far way from the surface), this might be less effective than for a non-spin-polarized system like H_2. Furthermore, the CRP typically requires a rather large number of *ab initio* data points on regular grids to be computed. In contrast, a modified Shepard (MS) interpolation works with irregularly spaced points along prominent reaction paths and has proven successful for the description of reaction dynamics in gas phase.[330] It has been adapted to gas-surface dynamics,[331–333] but its dependance on second derivatives of the PES has limited its applications:[334,335] In most periodic first-principles codes, these Hessians can only be calculated numerically and hence are computationally very expensive. A recent comparison to the CRP has shown that some scattering properties can be obtained at a similar quality but based on less *ab initio* input data – if the interpolation is "steered" accordingly.[335] Therefore, it might be possible to tackle higher dimensional systems with MS interpolation. The quality of the results will strongly depend on the statistical observable, since the shape of the interpolated potential is much worse compared to the CRP. Another alternative in form

of a tight binding model has hitherto only been applied to one system, O_2 on Pt(111),[336,337] because despite the physical insights incorporated therein, the number of parameters and concomitant fitting effort is enormous. Neural networks on the other hand do not incorporate any physical properties of the system, but offer a large flexibility to describe PESs. Accordingly, accurate models could be obtained with modest effort, not only for systems with H_2,[338–341] but also with the computationally more demanding O_2 as an adsorbate.[47,48,50,298,299,342]

Apart from these state-of-the-art approaches aiming for an *ab initio* quality description of the interaction potential, simpler and accordingly significantly less accurate parametrizations are still in wide-spread use today: For NO on Au(111), a model primarily addressing the validity of the Born-Oppenheimer approximation[36,37,39] relies on combinations of simple Morse potentials. For oxygen on palladium surfaces, similar Morse potential constructions have relied on parameters from unrealistically small cluster models of the surface[343,344] or even only a few numbers of empirical data.[345,346] More promising is the recently proposed flexible periodic (FP) LEPS model. It introduces additional physically motivated parameters to the original LEPS prescription. With less calculated data points as input than the CRP model used as reference, it allows to improve the interpolation quality significantly over the former. However, the difference to the latter is still quite notable.[347,348]

Going beyond the frozen surface approximation and keeping an *ab initio* quality model for the potential proves to be a severe challenge, as the interpolation problem becomes increasingly difficult with each degree of freedom that is added. Recent work has combined a many-body expansion with a neural network treatment and demonstrated a successful description of PESs of simple gas-phase systems with directed, short-ranged bonds.[349] For bulk systems consisting of a single element, high-dimensional interatomic potentials could also be constructed based on neural networks thanks to a representation of first-principles input data via generalized symmetry functions.[183,350,351] However, even for "simple" systems, the amount of data that is required for an accurate description is enormous.[204–206,351] Lately, an extensive overview about attempts to fit potential energy surfaces by neural networks has been given by Handley and Popelier.[352] Promising progress in this direction has also been achieved only very recently with a slightly different approach: By combining Gaussian processes with a sophisticated transformation of atomic coordinates, so-called Gaussian approximation potentials (GAPs) were demonstrated to provide "the accuracy of quantum mechanics, without the electrons" with a significantly reduced amount of first-principles input data.[184] GAPs for both non-metallic and metallic, but only single-element bulk systems have been introduced so far. Consequently, it is at present unclear at present whether gas-surface dynamical problems, including multiple elements and a large corrugation of the adsorbate-substrate potential, can be successfully tackled with this method.

Giving up the idea of interpolation altogether, one of the "drosophilas" of gas-surface dynamics, H_2 on palladium surfaces, has recently been subject of AIMD i.e. evaluating the gas-surface interaction potential "on-the-fly" for each classical trajectory.[25,353–356] Even for this computationally very appealing system and with deliberately reduced accuracy for the description of the electronic structure, only on the order of a hundred trajectories could be obtained for selected initial conditions (i.e. impingement energies, angles, vibrations, rotations etc.). Whether this provides a sufficient amount of statistics depends on the intrinsic complexity of the observables and general properties of the interaction potential of the system – and is thus unclear *a priori*. Of course, previous studies employing state-of-the-art techniques within the frozen surface approximation allow for an extensive statistical sampling and hence are of great help to focus on interesting aspects. Guided accordingly, pioneering AIMD studies were therefore able to show that substrate mobility (within the limitations of the employed periodic boundary conditions)

can be very important for the dissociation dynamics even for very light molecules such as H_2. The still limited statistics might be improved by the steady increase of computational power and further improvements in first-principles codes. In addition, several acceleration schemes for AIMD have been recently developed, which however unfortunately do not work for metallic systems,[210] rely on reduced integration accuracy due to less converged forces,[208,209] or are tailored for statistical sampling in equilibrium situations only.[357] Therefore, it has to be seen how quickly the amount of trajectories accessible within AIMD can be increased by the necessary several orders of magnitude.

Accordingly, with the dynamics of the present system not having been subject to *first-principles* theoretical modeling before, a direct AIMD treatment is not a prudent choice. Rather, a "divide-and-conquer" strategy is chosen, using an efficient state-of-the-art interpolation technique like neural networks mentioned above to obtain a six-dimensional interaction potential with *ab initio* quality. This provides a first impression of the dynamics of the system for arbitrary observables, based on reliable statistical sampling. In principle, the resulting PES can also be "reused" for a quantum mechanical treatment of the nuclei, but is not considered to be necessary for the present system: For a "heavy" diatomic adsorbate (compared to H_2) like N_2 on Ru(0001), van Harrevelt and coworkers have found that a quantum mechanical treatment of the nuclei has negligible effects on the reaction rates. Instead, substrate mobility is a crucial aspect and certainly to be addressed in a further step discussed in more detail in Chapter 8.

This chapter begins with an introduction of the relevant theoretical aspects in Section 6.1. Although the underlying physics are essential to what follows, very much to the author's own surprise a concise presentation is hard (if at all) to find in the literature of the field. After briefly presenting the relevant details about neural networks, particular focus is on a coordinate transformation scheme. This is crucial to face the rather challenging six-dimensional interpolation problem, correctly incorporating and exploiting the translational and fourfold symmetry of the frozen Pd(100) surface during its interaction with the O_2 molecule. Transferability to other low-index surfaces of both fcc and bcc crystals is demonstrated in Appendix A. Thereafter, in Section 6.3, technical details on the neural network interpolation of the potential energy for the present system and subsequent MD runs are described, followed by the resulting statistical properties obtained therewith. Apart from the (initial) sticking of the molecules, this also includes the identification of entrance channels for dissociation.

6.1. Theory

6.1.1. Coordinate Systems

Apart from Cartesian coordinates, a center of mass centered spherical coordinate system is very convenient for the description of the dynamics of a diatomic molecule above a (frozen) surface. Both are illustrated in Fig. 6.1. The latter quite naturally allows to depict and follow dissociation pathways due to the interaction with the surface potential, which has been done traditionally[301,302] in terms of so-called elbow-plots. This will also be adapted for the present system (*vide infra*).

Here and in the following, the origin is located in the surface plane on a top site. The diatomic consists of two atoms A and B with masses m_A and m_B, respectively, and has a total mass $M = m_\mathrm{A} + m_\mathrm{B}$. A molecular configuration is given by Cartesian coordinates

$$\boldsymbol{R}^\mathrm{cart} = \boldsymbol{R}_\mathrm{A} \oplus \boldsymbol{R}_\mathrm{B} = (X_\mathrm{A}, Y_\mathrm{A}, Z_\mathrm{A}) \oplus (X_\mathrm{B}, Y_\mathrm{B}, Z_\mathrm{B}) \tag{6.1}$$

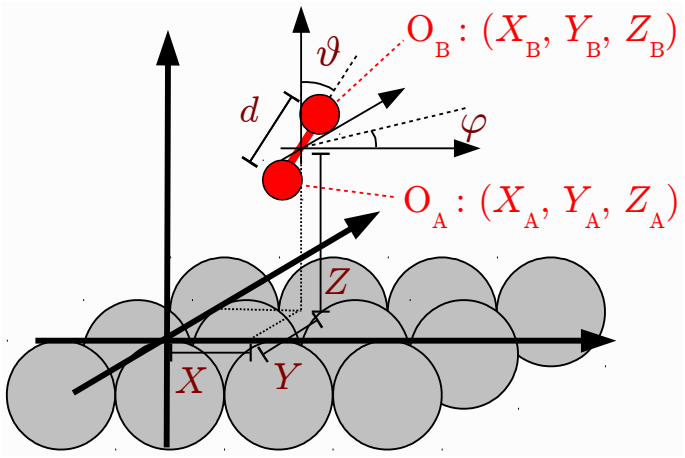

Figure 6.1.: Illustration of convenient coordinate systems used for the description of six-dimensional dynamics of diatomics on (frozen) surfaces. Position and orientation of the molecule can be equivalently described by standard Cartesian coordinates $\boldsymbol{R}^{\text{cart}} = (X_\text{A}, Y_\text{A}, Z_\text{A}) \oplus (X_\text{B}, Y_\text{B}, Z_\text{B})$ or center of mass centered spherical coordinates $\boldsymbol{R}^{\text{sph}} = (X, Y, Z, d, \vartheta, \varphi)$. The origin is located in the surface plane on a top site.

of the two atoms A and B or the equivalent spherical description

$$\boldsymbol{R}^{\text{sph}} = (X, Y, Z, d, \vartheta, \varphi) \tag{6.2}$$

with center of mass coordinates $\boldsymbol{R} = (X, Y, Z)$, internuclear distance d, polar angle ϑ,[i] and azimuth angle φ. Accordingly, the transformation $\mathbb{R}^6 \to \mathbb{R}^6 : \boldsymbol{R}^{\text{cart}} \mapsto \boldsymbol{R}^{\text{sph}}$ from the former to the latter is

$$X = \frac{m_\text{A}}{M} X_\text{A} + \frac{m_\text{B}}{M} X_\text{B} \tag{6.3a}$$
$$Y = \frac{m_\text{A}}{M} Y_\text{A} + \frac{m_\text{B}}{M} Y_\text{B} \tag{6.3b}$$
$$Z = \frac{m_\text{A}}{M} Z_\text{A} + \frac{m_\text{B}}{M} Z_\text{B} \tag{6.3c}$$
$$d = \sqrt{(X_\text{B} - X_\text{A})^2 + (Y_\text{B} - Y_\text{A})^2 + (Z_\text{B} - Z_\text{A})^2} \equiv \sqrt{d_\parallel^2 + d_\perp^2} \tag{6.3d}$$
$$\vartheta = \arccos\left(\frac{d_\perp}{d}\right) \tag{6.3e}$$
$$\varphi = \arccos\left(\frac{X_\text{B} - X_\text{A}}{d_\parallel}\right) = \arcsin\left(\frac{Y_\text{B} - Y_\text{A}}{d_\parallel}\right) \quad . \tag{6.3f}$$

Of course, Eq. (6.3f) is only valid for $d_\parallel \neq 0$, which is equivalent to $\vartheta \neq 0$. In other words, for a diatomic molecule with its molecular axis perpendicular to the surface, an azimuth angle is not defined. The reverse transformation $\mathbb{R}^6 \to \mathbb{R}^6 : \boldsymbol{R}^{\text{cart}} \mapsto \boldsymbol{R}^{\text{sph}}$ of Eq. (6.3) reads as follows:

[i] ϑ is also commonly referred to as zenith or inclination angle.

$$X_A = X - \frac{m_B}{M}\, d\, \sin(\vartheta)\, \cos(\varphi) \tag{6.4a}$$
$$Y_A = Y - \frac{m_B}{M}\, d\, \sin(\vartheta)\, \sin(\varphi) \tag{6.4b}$$
$$Z_A = Z - \frac{m_B}{M}\, d\, \cos(\vartheta) \tag{6.4c}$$
$$X_B = X + \frac{m_A}{M}\, d\, \sin(\vartheta)\, \cos(\varphi) \tag{6.4d}$$
$$Y_B = Y + \frac{m_A}{M}\, d\, \sin(\vartheta)\, \sin(\varphi) \tag{6.4e}$$
$$Z_B = Z + \frac{m_A}{M}\, d\, \cos(\vartheta) \quad . \tag{6.4f}$$

Finally, for a homonuclear diatomic with $m_\mathrm{A} = m_\mathrm{B} = m$ as considered here, Eqs. (6.3) and (6.4) do simplify accordingly by inserting $\frac{m_\mathrm{A}}{M} = \frac{m_\mathrm{B}}{M} = \frac{1}{2}$.

6.1.2. Equations of Motion

The Born-Oppenheimer approximation and the assumption of classical nuclei leads to dynamics given by classical mechanics. From a computational point of view, the Hamiltonian formalism (i.e. as a system of first order differential equations) is preferable because excellent methods exist for their numerical solution. In Cartesian coordinates, with the momenta

$$\boldsymbol{P}_\mathrm{A} = m_\mathrm{A} \dot{\boldsymbol{R}}_\mathrm{A} \tag{6.5a}$$
$$\boldsymbol{P}_\mathrm{B} = m_\mathrm{B} \dot{\boldsymbol{R}}_\mathrm{B} \quad , \tag{6.5b}$$

the classical Hamiltonian is given by

$$H^\mathrm{cart} = \frac{\boldsymbol{P}_\mathrm{A}}{2m_\mathrm{A}} + \frac{\boldsymbol{P}_\mathrm{B}}{2m_\mathrm{B}} + V_\mathrm{6D}^\mathrm{cart}(\boldsymbol{R}^\mathrm{cart}) \quad . \tag{6.6}$$

This leads to the usual equations of motion

$$\dot{\boldsymbol{R}}_\mathrm{A} = \frac{\boldsymbol{P}_\mathrm{A}}{m_\mathrm{A}} \tag{6.7a}$$
$$\dot{\boldsymbol{R}}_\mathrm{B} = \frac{\boldsymbol{P}_\mathrm{B}}{m_\mathrm{B}} \tag{6.7b}$$
$$\dot{\boldsymbol{P}}_\mathrm{A} = -\boldsymbol{\nabla}_{\boldsymbol{R}_\mathrm{A}} V_\mathrm{6D}^\mathrm{cart}(\boldsymbol{R}^\mathrm{cart}) \tag{6.7c}$$
$$\dot{\boldsymbol{P}}_\mathrm{B} = -\boldsymbol{\nabla}_{\boldsymbol{R}_\mathrm{B}} V_\mathrm{6D}^\mathrm{cart}(\boldsymbol{R}^\mathrm{cart}) \quad . \tag{6.7d}$$

In order to transform to the center of mass centered spherical coordinates described in Section 6.1.1 the respective conjugate momenta need to be obtained. Applying the transformation Eq. (6.4) to the Lagrangian corresponding to Eq. (6.6) yields

$$\boldsymbol{P} = (P_X, P_Y, P_Z) = M(\dot{X}, \dot{Y}, \dot{Z}) = M\dot{\boldsymbol{R}} \tag{6.8a}$$
$$p_d = \mu \dot{d} \tag{6.8b}$$
$$p_\vartheta = \mu d^2 \dot{\vartheta} \tag{6.8c}$$
$$p_\varphi = \mu d^2 \sin(\vartheta)^2 \dot{\varphi} \quad . \tag{6.8d}$$

Here the reduced mass $\mu = \frac{m_A m_B}{m_A+m_B} = \frac{m_A m_B}{M}$ has been introduced, which simplifies to $\mu^{\text{homo}} = \frac{m^2}{2m} = \frac{1}{2}m$ for a homonuclear diatomic molecule. The resulting Hamiltonian is

$$H^{\text{sph}} = \frac{\boldsymbol{P}}{2M} + \frac{1}{2\mu}\left(p_d^2 + \frac{1}{d^2}p_\vartheta^2 + \frac{1}{d^2\sin(\vartheta)}p_\varphi^2\right) \tag{6.9}$$

$$V_{6\text{D}}^{\text{sph}}(\boldsymbol{R}, d, \vartheta, \varphi) \quad . \tag{6.10}$$

The equations of motion in this coordinate system keep their usual form, since the transformation given by Eq. (6.3) is canonical – as can be easily verified.

$$\dot{\boldsymbol{R}} = \frac{1}{M}\boldsymbol{R} \tag{6.11a}$$

$$\dot{d} = \frac{1}{\mu}p_d \tag{6.11b}$$

$$\dot{\vartheta} = \frac{1}{\mu d^2}p_\vartheta \tag{6.11c}$$

$$\dot{\varphi} = \frac{1}{\mu d^2\sin(\vartheta)^2}p_\varphi \tag{6.11d}$$

$$\dot{\boldsymbol{P}} = -\boldsymbol{\nabla}_{\boldsymbol{R}}V_{6\text{D}}^{\text{sph}}(\boldsymbol{R}, d, \vartheta, \varphi) \tag{6.11e}$$

$$\dot{p}_d = -\frac{\partial}{\partial d}V_{6\text{D}}^{\text{sph}}(\boldsymbol{R}, d, \vartheta, \varphi) + \frac{1}{\mu}\frac{1}{d^3}p_\vartheta^2 + \frac{1}{\mu}\frac{1}{d^3\sin(\vartheta)^2}p_\varphi^2 \tag{6.11f}$$

$$\dot{p}_\vartheta = -\frac{\partial}{\partial \vartheta}V^{\text{sph}}(\boldsymbol{R}, d, \vartheta, \varphi) + \frac{1}{\mu}\frac{\cos(\vartheta)}{d^2\sin(\vartheta)^3}p_\varphi^2 \tag{6.11g}$$

$$\dot{p}_\varphi = -\frac{\partial}{\partial \varphi}V_{6\text{D}}^{\text{sph}}(\boldsymbol{R}, d, \vartheta, \varphi) \quad . \tag{6.11h}$$

Equations (6.7) and Eqs. (6.11) nicely underline the advantages of a "divide-and-conquer" approach: The dynamics of the nuclei given by these equations due to the classical Hamiltonians in Eqs. (6.6) and (6.9) can be completely decoupled from *ab initio* evaluations of the potential energy surface (PES) given by the adsorbate-substrate interaction within the frozen surface approximation $V_{6\text{D}}$, either in the Cartesian or spherical formulation, $V_{6\text{D}}^{\text{cart}}$ in Eq. (6.7) or $V_{6\text{D}}^{\text{sph}}$ in Eqs. (6.7) and (6.11), respectively. Obtaining an accurate interpolation of the latter, which allows fast evaluation during the dynamics, is now the task at hands. To face this challenge of high-dimensional interpolation for the six molecular degrees of freedom, neural networks are employed as a sophisticated and efficient interpolation technique.

6.1.3. Neural Networks

Artificial neural networks have been inspired by neuroscience. They consist of a network of *nodes* (also called *perceptrons*), which is trying to mimic the way how biological neurons (e.g. in the brain) process information: As soon as incoming connections exceed a certain threshold, a node "fires" on all its outgoing links to other nodes it is connected with. For the representation of PESs, the subclass of certain topologies called *multi-layer feed-forward* networks have proven to be very beneficial as nicely summarized in a recent review article by by Handley and Popelier.[352]

A particular example of this kind of neural network is shown in Fig. 6.2. In general, they consist of an *input* layer, one or more *hidden* layers and an *output* layer, each containing N_0, N_l

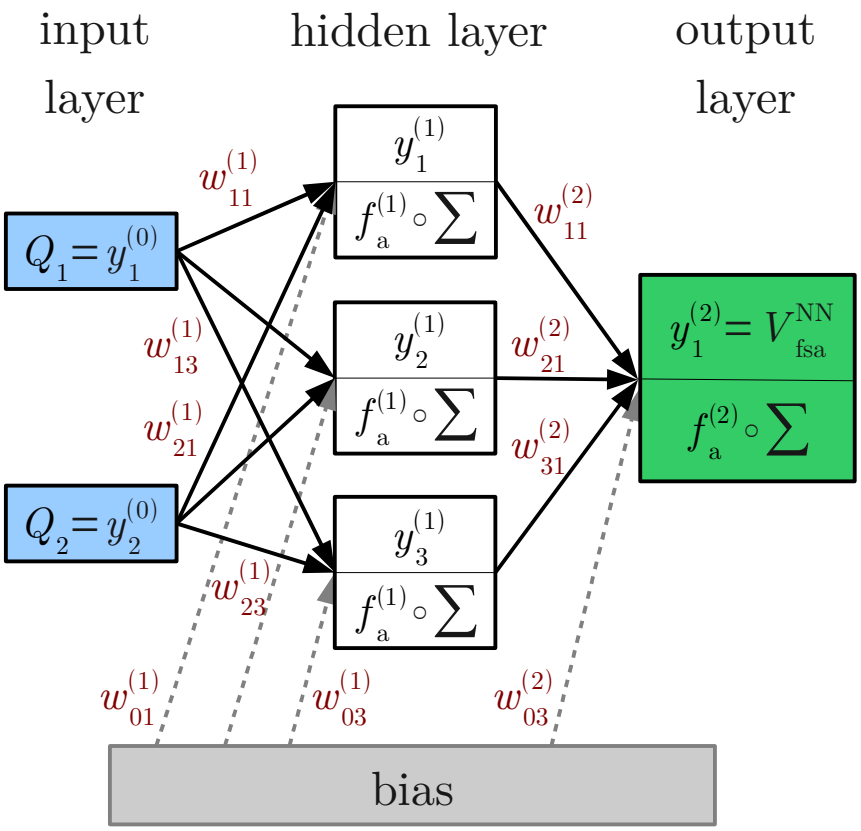

Figure 6.2.: Schematic illustration of a neural network with $L = 1$ hidden layer, $N_0 = 2$ nodes in the input, $N_1 = 3$ in the hidden and $N_2 = 1$ node in the output layer whose values are denoted by $y_j^{(l)}$ for $l \in \{0, 1, 2\}$ and $j \in 1, \ldots, N_l$. Together with the bias this results in a total of 13 weights $w_{ij}^{(l)}$ for $l \in \{1, 2\}$, $i \in \{0, \ldots, N_{l-1}\}$ and $j \in \{1, \ldots, N_l\}$, which are to be obtained by neural network training. For details see text.

for $l \in \{1, \ldots, L\}$ and $N_{L+1} = 1$ nodes, respectively, where L is the number of hidden layers. The values of the nodes in the input layer, represented by a vector $\boldsymbol{Q} = (Q_1, \ldots, Q_{N_0})$, denotes a molecular configuration, for which the (therefore single) node in the output layer then gives the interpolated value $V_{6D}^{NN}(\boldsymbol{Q})$ of the PES. Each node i in layer $l-1$ only has forward connections to nodes j in layer l (resulting in the name of this subclass), where now and in the following $l \in \{1, \ldots, L+1\}$. These connections are associated with weights $w_{ij}^{(l)}$. In addition, bias weights $w_{0k}^{(l)}$ with $k \in \{1, \ldots, N_l\}$ further extend the flexibility. *Activation functions* $f_a^{(l)}$ (also termed 'squashing' functions in mathematical literature) model the aforementioned "firing" in a smoothened way: In each node, they map the summed input weights in a monotonic way to a certain output interval, typically $[0; 1]$. Different types of activation functions can be used in different layers. In the following, a hyperbolic tangent $f_a^{(l)}(x) = \tanh(x)$ for $l \in \{1, \ldots, L\}$[ii] and

[ii] More precisely, $f_a^{(l)}(x) = a \tanh(bx)$, with recommended values[358] for the parameters $a = 1.7159$ and $b = \frac{2}{3}$,

a linear function $f_{\mathrm{a}}^{(L+1)}(x) = x$, are used throughout in the hidden layers and output layer and denoted by t and l, respectively – the latter conveniently allows unrestricted output values for $V_{\mathrm{6D}}^{\mathrm{NN}}$. Sticking to a common notation convention,[76,77,338,339,342,358] the topology of a particular neural network is then denoted by $\{N_0 - \ldots - N_{L+1}\ \left(\prod_{l=1}^{L} \mathrm{t}\right) \mathrm{l}\}$ The following recursion formula gives the value $y_j^{(l)}$ of the j-th node in layer l for $l \in \{1, \ldots, L+1\}$

$$y_j^{(l)} = w_{0j}^{(l)} + f_{\mathrm{a}}^{(l)} \left(\sum_{i=1}^{N_{l-1}} w_{ij}^{(l)} y_i^{(l-1)} \right) \quad , \quad j > 1 \quad , \tag{6.12}$$

where $y_j^{(0)} = Q_j$ are the input values and $y_1^{(L+1)} = V_{\mathrm{6D}}^{\mathrm{NN}}$ the interpolated PES in the output layer. Accordingly, the explicit structure of the simple $\{2 - 3 - 1\ \mathrm{tl}\}$ network with only one hidden layer ($L = 1$) shown in Fig. 6.2 is given by

$$V_{\mathrm{6D}}^{\mathrm{NN}} = f_{\mathrm{a}}^{(2)} \left(w_{01}^{(2)} + \sum_{j=1}^{N_1=3} w_{j1}^{(1)} f_{\mathrm{a}}^{(1)} \left(w_{0j}^{(1)} + \sum_{i=1}^{N_0=2} w_{ij}^{(1)} Q_i \right) \right) \quad , \tag{6.13}$$

where $f_{\mathrm{a}}^{(1)}$ and $f_{\mathrm{a}}^{(2)}$ are the aforementioned hyperbolic tangent and linear functions, respectively.

For "well-suited" (but arbitrary) activation functions, neural networks with at least a single hidden layer and a sufficiently large number of nodes N_1 therein are so-called universal approximators. Mathematically rigid proofs have been given by both Cybenko[359] as well as Hornik and coworkers,[360] – the work of the latter including a bigger class of functions to be approximated than the former. For the present purposes, this means that any kind of physical PES[iii] can in principle be described exactly by a neural network. Compared to other interpolation approaches, this is an extremely valuable property, which by far does not hold for e.g. commonly employed spline interpolation techniques. The latter might lack the flexibility to properly account for the strong corrugation exhibited by PESs of a typical gas-surface dynamics problems. As a neural network like the one illustrated in Fig. 6.2 is described by a composition of functions, for differentiable activation functions $f_{\mathrm{a}}^{(l)}$ for $l \in \{1, \ldots, L+1\}$ the interpolation function corresponding to Eq. (6.13) is differentiable both with respect to its inputs $\boldsymbol{Q} = (Q_1, \ldots, Q_{N_0})$ and weights $w_{ij}^{(l)}$. In fact, analytical derivatives $\frac{\partial V_{\mathrm{6D}}^{\mathrm{NN}}}{\partial Q_i}$ for $i \in \{1, \ldots, N_0\}$ can be calculated easily,[358] so that forces which are exactly consistent with the interpolated $V_{\mathrm{6D}}^{\mathrm{NN}}$ are obtained, allowing to ensure excellent energy conservation in molecular dynamics.[iv]

In practice, for an database of calculated (*ab initio*) data points $\{(\boldsymbol{Q}, V_{\mathrm{6D}}(\boldsymbol{Q}))\}_{\boldsymbol{Q}}$, the quite non-trivial task of neural network *training* or *learning* has to be carried out first: For a particular topology, an optimal set of weights needs to be determined, starting from random values. To do so, the database is usually first split into a *training* and a *test set*. Then, *examples*, i.e. elements from the training set, are presented to the neural network. Iteratively (in so-called

is used for $l \in \{1, \ldots, L\}$.

[iii] *Natura non facit saltus*: A function representing a PES of any physical system should even be differentiable. This mathematically "nice" property already limits the class of functions to be approximated.

[iv] Quite in contrast, in *ab initio* molecular dynamics, forces obtained "on-the-fly" alongside with potential energies are much less numerically converged than the latter. Obtaining "sufficiently conservative" forces requires a numerical effort that is usually not afforded, resulting in comparably poor energy conservation during microcanonical MD trajectories. Current (unconfirmed) hope is that this error vanishes when averaging over trajectories.[361]

epochs) the weights are adjusted to minimize a *cost function*. Here, the root mean square error

$$\mathrm{RMSE} = \sqrt{\sum_{\boldsymbol{Q}} \left(V_{\mathrm{6D}}(\boldsymbol{Q}) - V_{\mathrm{6D}}^{\mathrm{NN}}(\boldsymbol{Q})\right)^2} \tag{6.14}$$

is conveniently used for the latter, where $V_{\mathrm{6D}}(\boldsymbol{Q})$ are input energies and $V_{\mathrm{6D}}^{\mathrm{NN}}(\boldsymbol{Q})$ the corresponding neural network output given by the current set of weights, and the sum is over all molecular configurations $\boldsymbol{Q}$ in the training set. In order to monitor the transferability of the fit to data which is not directly targeted by the cost function, Eq. (6.14) is concomitantly evaluated for the test set as well. Typically, this RMSE of the test set does not decrease any more after a certain number of epochs, since further improvements of the fitting quality can only be obtained at the cost of transferability, which is commonly referred to as *overfitting*. Obviously, this is the optimal point to terminate the learning procedure. In principle, any algorithm for non-linear fitting problems is suitable for the weight adjustment – potentially exploiting the fact that even derivatives with respect to the latter are available as indicated above. However, according to previous experiences, an extended adaptive Kalman filter[358] has proven particularly useful for this purpose when fitting potential energy surfaces.[76,183,339,358,362]

Unfortunately, it is unclear *a priori* for which topology training might yield the result with best interpolation quality. For a given database, several topologies hence need to be tested and compared. In regions of the PES for which different fits yield most different results, the database needs to be extended accordingly, starting the whole training process all over again. This is iterated until a satisfactory interpolation has been obtained at last.

For more details on neural networks and their application to interpolation of potential energy surfaces, the reader is primarily referred to Sönke Lorenz's PhD thesis,[358] but also the one by Jörg Behler[76] as well as corresponding publications.[338,339,342] This section only provides a brief overview about those aspects which are directly relevant for this thesis in the following.

6.1.4. Symmetry Adapted Coordinates

6.1.4.1. Neural Network Input

As detailed in the previous sections, neural networks are a mere mathematical interpolation tool that do not incorporate any available physical properties of the target function. On a frozen surface, symmetry is certainly one such property to take into account: First and most important, unphysical outcomes of observables might be obtained during the dynamics if the underlying PES does not have the correct symmetry. Furthermore, a proper account of the latter should also simplify the interpolation procedure itself and increase its accuracy, since it limits the freedom of the interpolation function. Unfortunately, such a symmetry constraint cannot be enforced during neural network training directly. In that respect, the high flexibility of neural networks can also become a curse, since obtaining a fit which (accidentally) obeys the right symmetry properties gets infinitesimally unlikely.

The symmetry of a (100) surface is illustrated in Fig. 6.3: In addition to the two-dimensional translational symmetry of the fcc(100) surface lattice, point group symmetry at the high symmetry sites (fourfold on top and hollow sites, twofold on bridge sites) leads to a symmetry irreducible wedge of triangular shape whose vertices are formed by the latter. When the O_2 molecule is added (as an isolated, non-periodic "perturbation"), the symmetry operations of the pure surface allow to produce symmetry equivalent molecular configurations. Additionally, for a homonuclear diatomic like O_2, there is the exchange symmetry of its two constituent atoms A and B: Swapping their coordinates must leave the total energy of the system invariant. Inside

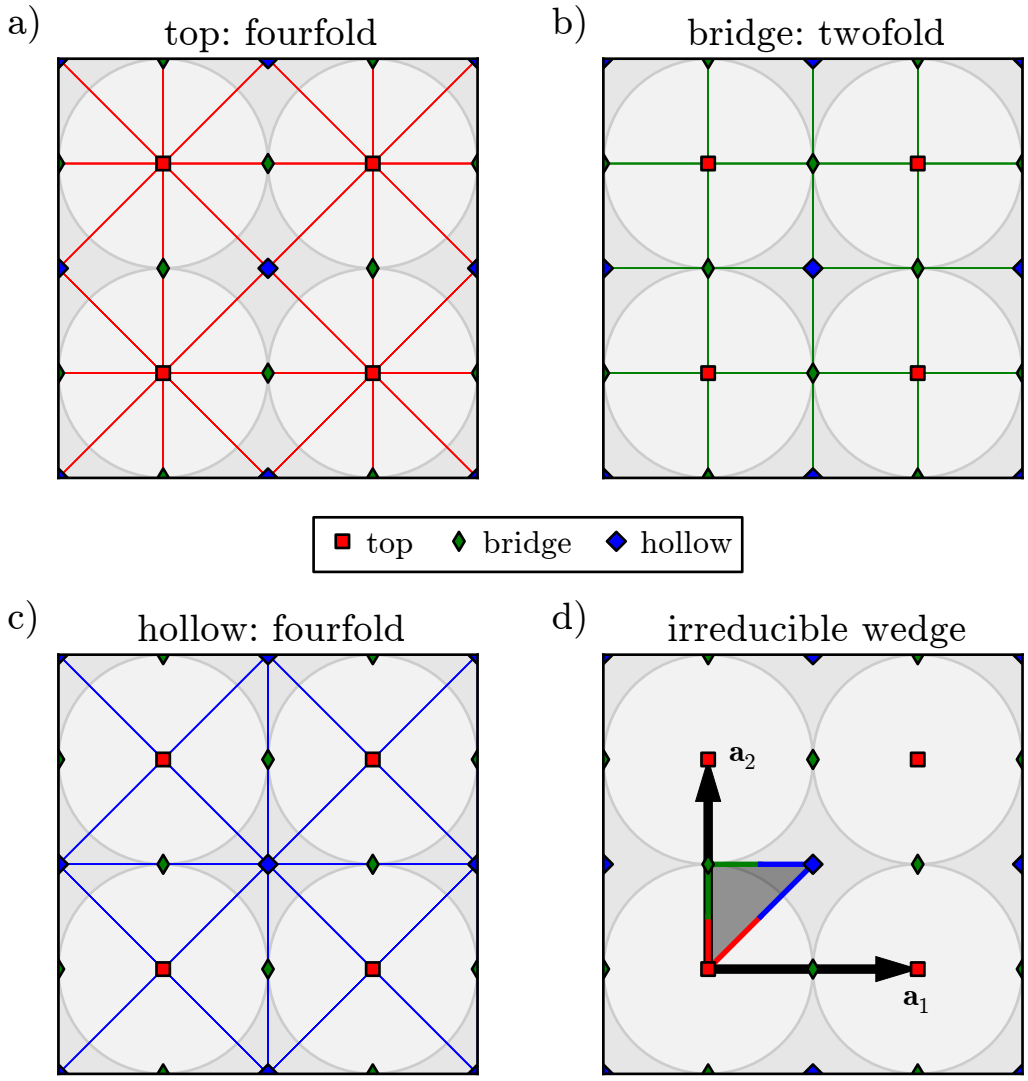

Figure 6.3.: Symmetry and irreducible wedge of a fcc(100) surface: Top and hollow sites have fourfold symmetry, as shown in a) and c), respectively. In contrast, b) illustrates the twofold symmetry of bridge sites. This results in an irreducible wedge of triangular shape indicated in d), together with the primitive vectors $\boldsymbol{a}_1$ and $\boldsymbol{a}_2$ of the surface lattice.

the irreducible wedge, only the latter is left, whereas at the boundaries, each molecular configuration is equivalent to many others due to point group symmetry of the surface. This holds in particular at the vertices (less so at the edges), making them particularly and interesting candidates for which actual *ab initio* calculations most efficiently should be carried out first.

Of course, the most straightforward way to account for symmetry of calculated molecular configurations is by manually applying the symmetry operations to the former, using their proper representations in the respective coordinate systems (cf Section 6.1.1). In several interpolation strategies, most prominently the corrugation-reducing procedure,[323,324] or a Shepard method[330–333] such an unfolding is intrinsically required to ensure the right symmetry properties of the analytical interpolation functions. However, in contrast to finite systems, translational symmetry renders the symmetry group (denumerable) infinite, which can lead to problems if not taken special care of in the lateral coordinates[333] – unless the dynamics are artificially constrained to the "unfolded range". In case of dynamical trapping on the surface, this range can be rather large. Hence, the database of calculated configurations has to be "flooded" with symmetry equivalent replicas, easily increasing its size by factors typically between 10 and 100. As Ludwig and Vlachos have noted,[340] this quickly increases the training time of the neural network by orders of magnitude. More severely, this does enforce symmetry here in general: Arbitrary (i.e. non-calculated) molecular configurations which ought to be equivalent by symmetry can still yield different neural network interpolated total energies. Therefore, this brute force unfolding is not a viable option in this context.

On the contrary, the interpolation could also be restricted to the irreducible wedge only. Then, any arbitrary molecular configuration outside the latter has to be explicitly folded back first by applying the corresponding symmetry operation (translation composed with proper or improper rotation and/or swapping of constituent atoms of the diatomic). The lateral periodicity is practically filtered out before the interpolation step. Therefore, this simple approach is particularly appealing for the transfer of interpolation techniques which originally have been developed to treat non-periodic (gas-phase) systems to gas-surface dynamics, like in case of the modified Shepard interpolation by Crespos and coworkers.[331,332] It his can be quite cumbersome to implement, however, and requires a large number of comparison operations which typically become a computational bottleneck during the dynamics, as they have to be performed for each MD step. Even worse, symmetry can no longer automatically induce the right values of energy and forces at the boundaries of the irreducible wedge, as has been extensively discussed by Abufager and coworkers.[333] For these reasons, this approach is not followed here.

A more elaborate concept is to prefix the actual interpolation step by a coordinate transformation that is more abstract than the simple backfolding discussed before. The actual interpolation could then be carried out in symmetry "filtered" (i.e. adapted or constrained) coordinates, but would automatically have the correct symmetry properties. An interpolated PES would then be evaluated according to

$$V_{6\mathrm{D}} \approx V_{6\mathrm{D}}^{\mathrm{NN}}(\boldsymbol{Q}(\boldsymbol{R}^{\mathrm{cart}}, \boldsymbol{R}^{\mathrm{sph}})) \tag{6.15}$$

Most straightforward, a symmetry reduced lateral position could be defined by giving the distances to the closest translationally equivalent vertices of the symmetry irreducible wedge. As Behler and coworkers have already discussed and illustrated,[342] this minimum distance convention leads to kinks in the distances when the reference vertices change, destroying differentiability – similar to what happens within the back-folding strategy described before. Proper differentiability is necessary to obtain well-defined forces from the PES for the ensuing MD simulations.

Within their work concerning O_2 on Al(111),[47,48,298,299] Behler and coworkers have proposed a way to incorporate the symmetry based on a generalized triangulation for fcc(111) surfaces.[342] The basic idea is to "measure" generalized distances to the vertices of the symmetry irreducible wedge by a triple of three numbers, which are obtained via what is termed symmetry functions by the authors. They are formed by a single periodic function of the lateral surface coordinates ($\mathbb{R}^2 \rightarrow \mathbb{R}$), which is shifted to the three vertices of the symmetry irreducible wedge of the (111) surface Essentially, this function is a differentiable alternative to the (using a minimum distance convention) periodically placed circles – avoiding the problems mentioned before. It is based on some of the first odd terms of a Fourier series defined by the lattice vectors of the surface with expansion coefficients of absolute value one. The idea to use such first terms of Fourier series expansions is not all new in the context of six-dimensional PESs in gas-surface dynamics.[312–318,320,322–324] However, it is important to emphasize that they are supposed to serve merely as a tool for the incorporation of symmetry, not limiting the flexibility of the actual interpolation function within the symmetry constraint. Quite in contrast, in previous interpolation attempts the expansion coefficients have been parameters which needed to be determined within the respective fitting procedures.[312–315,320,323,324] Accordingly, even when fcc(100) surfaces had been addressed, the corresponding expressions were not directly useful for the present purposes.

The same holds for the pioneering methodological work by Lorenz and coworkers,[338,339] which constitutes the first neural network interpolation for a six-dimensional PES in gas-surface dynamics. Although they have also addressed a homonuclear diatomic on a fcc(100) surface (H_2 on Pd(100)), unfortunately their neural network input allowed for the same "artificial features" (i.e. unphysical properties) which had also been present in the reference PES.[316–318] Therefore, the approach by Behler and coworkers demonstrated for homonuclear diatomics on fcc(111) surfaces[342] is clearly superior. Unluckily, they do neither discuss how to generally construct their symmetry functions nor give explicit expressions for the latter for other surfaces. Closer inspection reveals that the claimed "straightforward" generalizability is not that straightforward after all: In fact, the vertices of the irreducible wedge of the fcc(111) surface are the top, fcc and hcp hollow sites, which all have the same threefold (point group) symmetry. In that respect, this surface is simpler than the present (100) surface where only two of the three vertices of the irreducible wedge, top and hollow, have the full fourfold symmetry, whereas the bridge site is only twofold (cf Fig. 6.3). This has to be kept in mind and further complicates an adaption of their approach.

Within their extended neural network interpolation scheme and focusing on H_2 on Cu(111), Ludwig and Vlachos also rely on a transformation of lateral coordinates based on the first few terms of a Fourier series to account for translational symmetry of the surface.[340,341] These terms are different compared to those used by Behler and coworkers[342] and exchange symmetry of the two hydrogen atoms is not included at all. Yet again, infelicitously, no helpful methodological insights for the present system could be gained.

In principle, the coordinate transformations tailored for high-dimensional neural network interpolation,[183] which were published in full detail only very recently,[350] could (now) be adapted, but they were shown not be efficient for lower dimensional problems even when a plethora of reference data is available.[350] The multi-component nature of the present system together with the strong corrugation of the adsorbate-substrate potential pose an additional challenge. This makes a a proper, specifically optimized coordinate transformation scheme for the six molecular coordinates along the lines of previous work (still) much more desirable if not imperative for the present problem – as future work might show.

Altogether, a suitable scheme to perform symmetry adapted neural network interpolation of

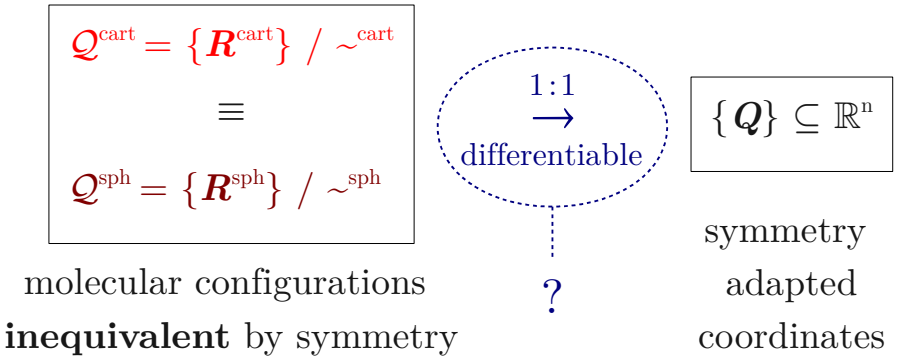

Figure 6.4.: Schematic illustration of a function which uniquely transforms molecular configurations as contained in the quotient spaces $\mathcal{Q}^{\text{cart}} = \{\boldsymbol{R}^{\text{cart}}\}/\sim^{\text{cart}}$ or $\mathcal{Q}^{\text{sph}} = \{\boldsymbol{R}^{sph}\}/\sim^{\text{sph}}$ to symmetry adapted coordinates $\{(Q_1, \ldots, Q_n)\} \subset \mathbb{R}^n$. In the present context this required to obtain input values for the neural network interpolation of the PES according to Eq. (6.15). Differentiability is mandatory to allow for subsequent molecular dynamics runs (cf Eq. (6.23)).

the six-dimensional PES for a homonuclear diatomic on fcc(100) surfaces does not exist and hence needs to be developed. Its importance should not be underestimated: The way how sampled data from a high-dimensional PES is presented to the interpolation scheme might even be more important than the sophistication of the interpolation scheme itself, as very recent work has shown.[183,184] In fact, recent work has exemplified how dramatically wrong a neural network interpolation can become due to a misconstructed coordinate transformation. The systematically wrong description of the underlying physical system was reflected by a reduction of the heuristically observed interpolation quality by two orders of magnitude.[350] What follows has been inspired by the pioneering work by Behler and coworkers,[342] but starts by phrasing the problem in proper mathematical terms first – as illustrated in Fig. 6.4: A differentiable (coordinate) transformation is required that uniquely maps elements of the quotient spaces $\mathcal{Q}^{\text{cart}} = \{\boldsymbol{R}^{\text{cart}}\}/\sim^{\text{cart}}$ or $\mathcal{Q}^{\text{sph}} = \{\boldsymbol{R}^{sph}\}/\sim^{\text{sph}}$ to tuples of real numbers. The equivalence relations $\sim^{\text{sph}}$ or $\sim^{\text{cart}}$ are defined via the respective representations of the symmetry group of the adsorbate-substrate system: Two molecular configurations are considered to be equivalent if there is a symmetry operation that allows to transform one to the other. Consequently, different elements of the quotient spaces are only those molecular configurations which cannot be further related by symmetry. The two transformations given by Eqs. (6.3) and (6.4) also induce a bijection between the two quotient spaces such that they can be used equivalently and exchangeably as starting point for the construction of the required coordinate transformation. Injectivity is crucial to avoid unphysical ambiguities: Molecular configurations which are not equivalent by symmetry must in principle be allowed to have different potential energies. Finally, as has already been indicated before, differentiability is required to obtain well-defined forces for molecular dynamics to be performed on the interpolated PES. Such a coordinate transformation is constructed in the following as systematically as possible, carefully verifying the desired properties.

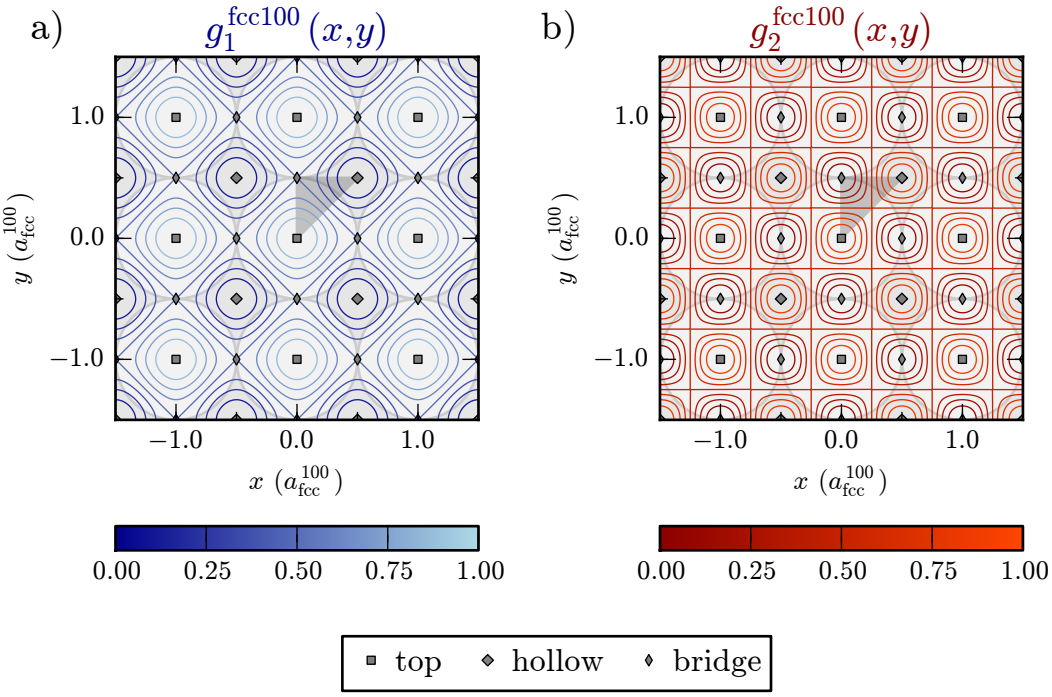

Figure 6.5.: Contour plots of the coordinate transformations a) g_1^{fcc100} and b) g_2^{fcc100} as defined by Eq. (6.17) for lateral coordinates (x, y) given in units of the surface lattice constant a_{fcc}^{100}. The spacing of the contour lines is $\frac{1}{8}$.

6.1.4.2. Coordinate Transformation

Since the lateral position of the adsorbate is subject to the full surface induced part of the symmetry of the problem, the construction of symmetry reduced coordinates is started here. The key idea is to represent the whole discrete but infinite set $[(x_0, y_0)]$ of symmetry equivalents of a single point (x_0, y_0) on the surface by the intersection of inverse images of two functions g_1^{fcc100} and g_2^{fcc100}, $\mathbb{R}^2 \to \mathbb{R}$ with appropriate periodicity and symmetry, in the following way:

$$\begin{aligned}[(x_0, y_0)] &= \left[g_1^{\mathrm{fcc100}}\right]^{-1}\left(g_1^{\mathrm{fcc100}}(x_0, y_0)\right) \cap \left[g_2^{\mathrm{fcc100}}\right]^{-1}\left(g_2^{\mathrm{fcc100}}(x_0, y_0)\right) \\ &= \left\{(x, y) \;\middle|\; \begin{array}{l} g_1^{\mathrm{fcc100}}(x, y) = g_1^{\mathrm{fcc100}}(x_0, y_0) \wedge \\ g_2^{\mathrm{fcc100}}(x, y) = g_2^{\mathrm{fcc100}}(x_0, y_0) \end{array}\right\} \subset \mathbb{R}^2\end{aligned} \tag{6.16}$$

This is shown graphically in Figs. 6.6a to 6.6d for several example points with coordinates (x_0, y_0) inside the irreducible wedge. By giving the two contour values $g_1^{\mathrm{fcc100}}(x_0, y_0)$ and $g_2^{\mathrm{fcc100}}(x_0, y_0)$, the intersection points of the corresponding plotted contour lines obviously yield the equivalence class $[(x_0, y_0)]$. Instead of a *tri*angulation with generalized distances mentioned above, this "*bi*angulation" is thus completely sufficient to describe symmetry equivalent points on the surface. The following terms of the (two-dimensional) Fourier series induced by the

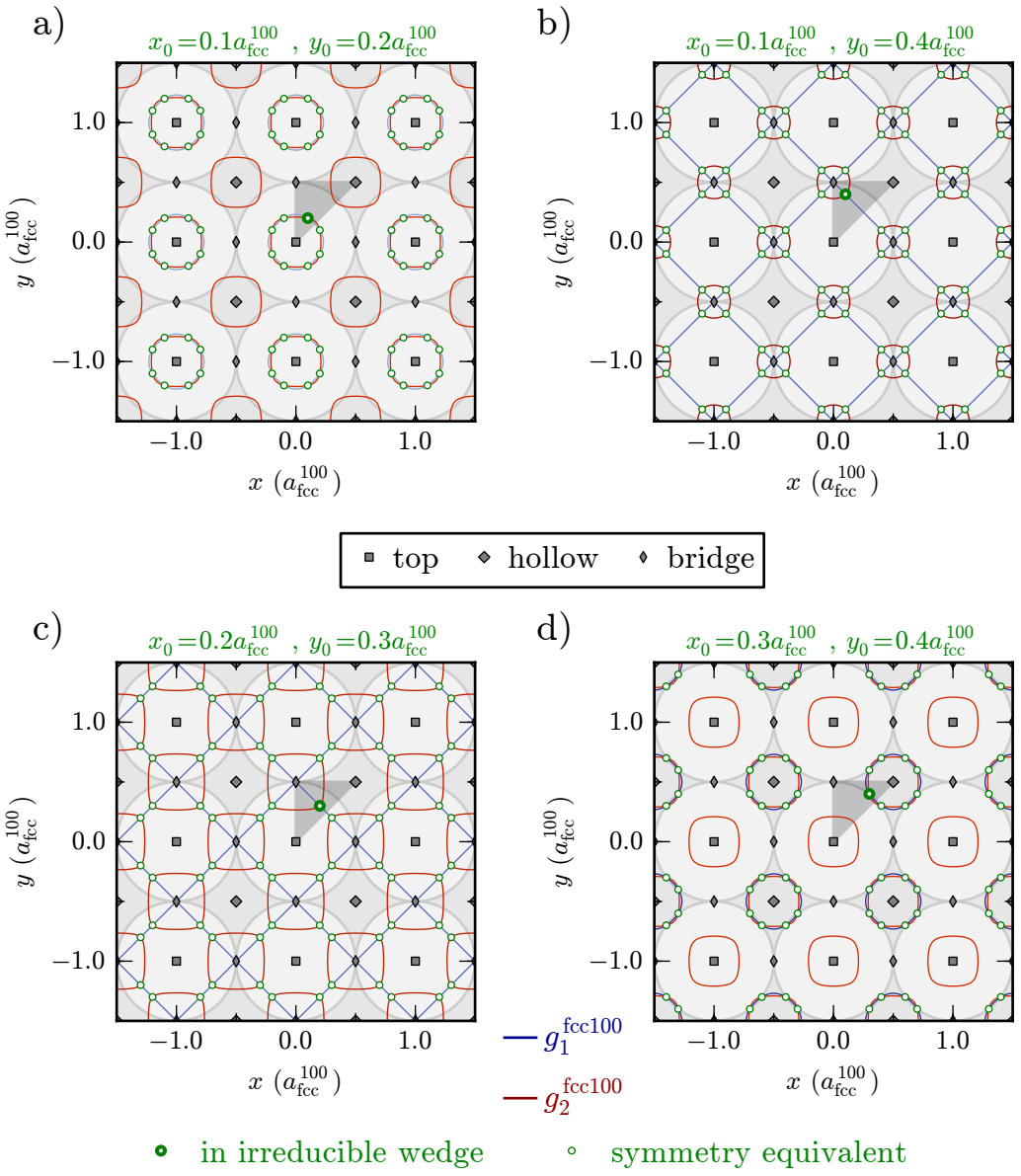

Figure 6.6.: Examples for symmetry equivalent lateral coordinates given in units of the surface lattice constant a_{fcc}^{100}. In a) to d), for different points (x_0, y_0) in the indicated triangular irreducible wedge (thick green circle), the respective equivalents are the intersection points (thin green circles) of contour lines of g_1^{fcc100} (blue) and g_2^{fcc100} (red) as defined by Eqs. (6.17) (cf Eq. (6.16)). Contour values are given by $g_1^{\mathrm{fcc100}}(x_0, y_0)$ and $g_2^{\mathrm{fcc100}}(x_0, y_0)$, respectively.

surface lattice are a both convenient and appropriate choice for g_1^{fcc100} and g_2^{fcc100}:

$$\begin{aligned} g_1^{\mathrm{fcc100}}(x,y) &= \frac{1}{4}\left[\cos\left(\boldsymbol{G}_{01}^{\mathrm{fcc100}} \cdot \begin{pmatrix} x \\ y \end{pmatrix}\right) + \cos\left(\boldsymbol{G}_{10}^{\mathrm{fcc100}} \cdot \begin{pmatrix} x \\ y \end{pmatrix}\right)\right] + \frac{1}{2} \\ &= \frac{1}{4}\left[\cos\left(\frac{2\pi}{a_{\mathrm{fcc}}^{100}} x\right) + \cos\left(\frac{2\pi}{a_{\mathrm{fcc}}^{100}} y\right)\right] + \frac{1}{2} \end{aligned} \tag{6.17a}$$

$$\begin{aligned} g_2^{\mathrm{fcc100}}(x,y) &= \frac{1}{4}\left[\cos\left(\boldsymbol{G}_{11}^{\mathrm{fcc100}} \cdot \begin{pmatrix} x \\ y \end{pmatrix}\right) + \cos\left(\boldsymbol{G}_{1\bar{1}}^{\mathrm{fcc100}} \cdot \begin{pmatrix} x \\ y \end{pmatrix}\right)\right] + \frac{1}{2} \\ &= \frac{1}{4}\left[\cos\left(\frac{2\pi}{a_{\mathrm{fcc}}^{100}} x\right) \cdot \cos\left(\frac{2\pi}{a_{\mathrm{fcc}}^{100}} y\right)\right] + \frac{1}{2} \quad . \end{aligned} \tag{6.17b}$$

Equation (6.17a) and Eq. (6.17b) are plotted in Figs. 6.5a and 6.5b, respectively, as contour lines. Here, the common choice of primitive lattice vectors,

$$\boldsymbol{a}_1^{\mathrm{fcc100}} = a_{\mathrm{fcc}}^{100} \begin{pmatrix} 1 \\ 0 \end{pmatrix} \tag{6.18a}$$

$$\boldsymbol{a}_2^{\mathrm{fcc100}} = a_{\mathrm{fcc}}^{100} \begin{pmatrix} 0 \\ 1 \end{pmatrix} \quad , \tag{6.18b}$$

has been assumed, with a_{fcc}^{100} denoting the surface lattice constant. The corresponding primitive vectors of the corresponding reciprocal lattice,

$$\boldsymbol{b}_1^{\mathrm{fcc100}} = \frac{2\pi}{a_{\mathrm{fcc}}^{100}} \begin{pmatrix} 1 \\ 0 \end{pmatrix} \tag{6.19a}$$

$$\boldsymbol{b}_2^{\mathrm{fcc100}} = \frac{2\pi}{a_{\mathrm{fcc}}^{100}} \begin{pmatrix} 0 \\ 1 \end{pmatrix} \quad , \tag{6.19b}$$

then define reciprocal lattice vectors

$$\boldsymbol{G}_{ij}^{\mathrm{fcc100}} = i\boldsymbol{b}_1^{\mathrm{fcc100}} + j\boldsymbol{b}_2^{\mathrm{fcc100}} \tag{6.20}$$

used in the aforementioned Fourier series. Following the usual crystallographic convention, a bar over an index number indicates a minus sign.

With both the translational and point group symmetry of lateral degrees of freedom properly incorporated in g_1^{fcc100} and g_2^{fcc100}, the following transformation from the physical coordinate systems introduced in Section 6.1.1 could now be chosen to represent an entire class of symmetry equivalent molecular configurations:

$$\tilde{Q}_1 = g_1^{\mathrm{fcc100}}(X_{\mathrm{A}}, Y_{\mathrm{A}}) \tag{6.21a}$$

$$\tilde{Q}_2 = g_2^{\mathrm{fcc100}}(X_{\mathrm{A}}, Y_{\mathrm{A}}) \tag{6.21b}$$

$$\tilde{Q}_3 = g_1^{\mathrm{fcc100}}(X_{\mathrm{B}}, Y_{\mathrm{B}}) \tag{6.21c}$$

$$\tilde{Q}_4 = g_2^{\mathrm{fcc100}}(X_{\mathrm{B}}, Y_{\mathrm{B}}) \tag{6.21d}$$

$$\tilde{Q}_5 = Z_{\mathrm{A}} \tag{6.21e}$$

$$\tilde{Q}_6 = Z_{\mathrm{B}} \tag{6.21f}$$

$$\tilde{Q}_7 = d \quad . \tag{6.21g}$$

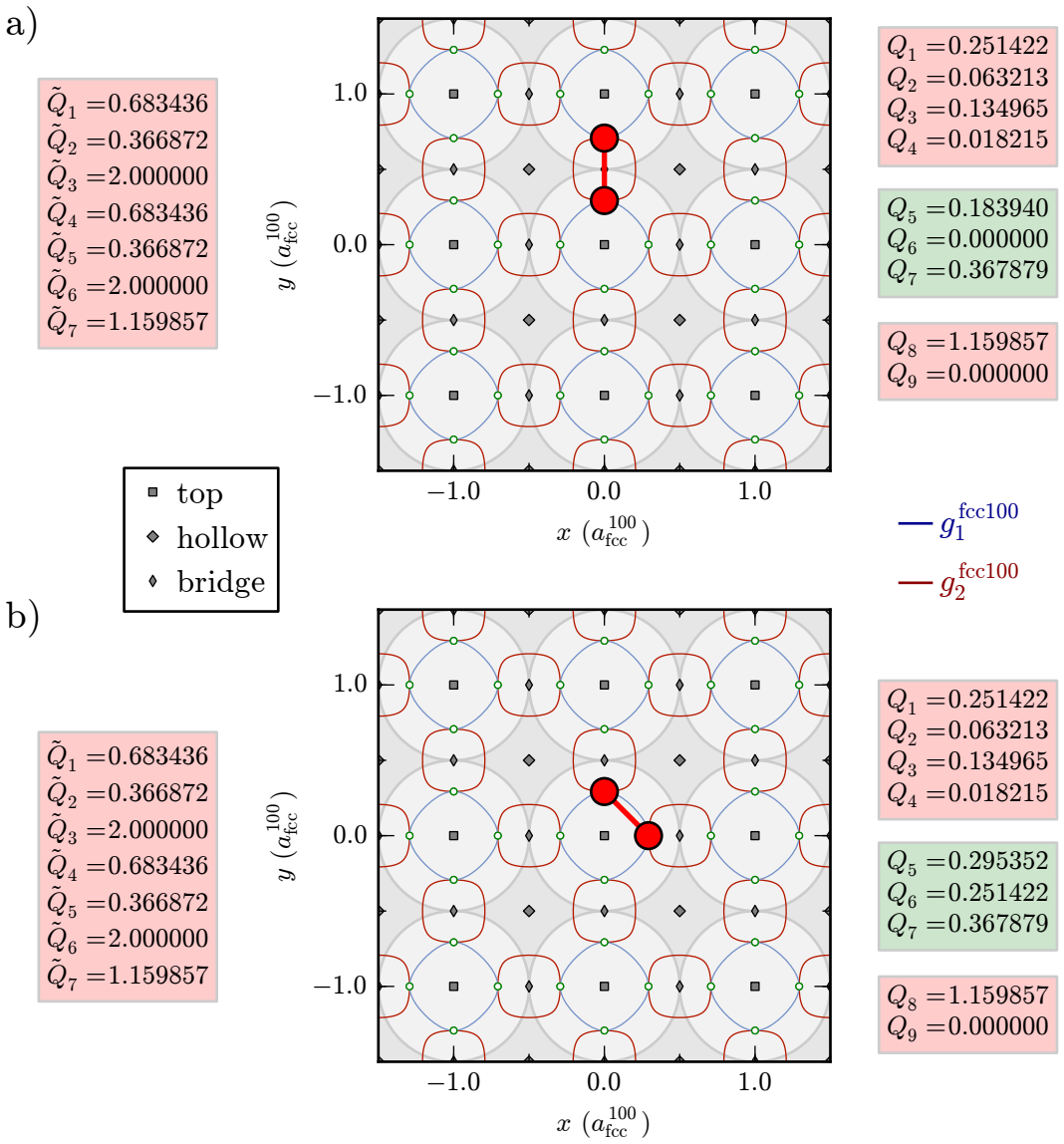

Figure 6.7.: Accidental degeneracies in symmetry adapted coordinates. Obviously, the two molecular configurations $\boldsymbol{R}_{\mathrm{a}}^{\mathrm{cart}} = (0\,\text{Å}, u \cdot a_{\mathrm{fcc}}^{100}, 2\,\text{Å}, 0\,\text{Å}, (1-u) \cdot a_{\mathrm{fcc}}^{100}, 2\,\text{Å})$ and $\boldsymbol{R}_{\mathrm{b}}^{\mathrm{cart}} = (0\,\text{Å}, u \cdot a_{\mathrm{fcc}}^{100}, 2\,\text{Å}, u \cdot a_{\mathrm{fcc}}^{100}, 0\,\text{Å}, 2\,\text{Å})$, where $u = (2+\sqrt{2})^{-1}$, illustrated in a) and b) together with their lateral coordinate transformations g_1^{fcc100} and g_2^{fcc100} (cf Eq. (6.17)), respectively, are not equivalent by symmetry. The transformed coordinates $\tilde{\boldsymbol{Q}}$ as given by Eq. (6.21), however, do not allow to distinguish between both configurations. Thanks to proper inclusion of (symmetry adapted) center of mass coordinates (Q_5, Q_6, Q_7) in $\boldsymbol{Q}$ as defined in Eq. (6.22), this undesired degeneracy is broken. For the numbers shown a realistic value of the surface lattice constant of Pd(100)$a_{\mathrm{fcc}}^{100} = (\sqrt{2})^{-1} \cdot 3.96\,\text{Å}$, has been used – emphasizing the relevance of the problem for accessible bond lengths d of the O_2 molecule.

The internuclear distance d needed to be added here as $\tilde{Q}_7$ because placing two atoms A and B with heights above the surface given by $\tilde{Q}_5$ and $\tilde{Q}_6$, respectively, on any of the set of symmetry equivalent lateral positions encoded in $(\tilde{Q}_1, \tilde{Q}_2, \tilde{Q}_3, \tilde{Q}_4)$ leaves this undefined otherwise (cf Fig. 6.6). Hence, Eq. (6.21) maps the six physical degrees of freedom to a seven-dimensional vector $\tilde{\boldsymbol{Q}} = (\tilde{Q}_1, \ldots, \tilde{Q}_7)$ of redundant symmetry reduced coordinates. Ludwig and Vlachos have used an analogous transformation for the neural network input within their PES interpolations of H_2 on Cu(111) and Pt(111), properly adjusted to the symmetry of fcc(111) surfaces.[340,341] Unfortunately, both in their case and here, this has several disadvantages and problems:

1. Far the worst for the reasons explained above, $\tilde{\boldsymbol{Q}}$ is obviously not invariant when swapping atoms A and B, i.e. exchange symmetry is not incorporated.

2. Equations (6.21) introduce additional symmetry when both atoms of the diatomic are located on symmetry equivalent lateral positions, i.e. $\tilde{Q}_1 = \tilde{Q}_3$ and $\tilde{Q}_3, \tilde{Q}_4$: As illustrated in Fig. 6.7, nonequivalent *molecular* configurations are mapped to the same $\tilde{\boldsymbol{Q}}$, so that the injectivity of the desired transformation illustrated in Fig. 6.4 is violated. Only very recently, Groß has shown how severely such an accidental symmetry in the underlying PES can affect the sticking coefficient calculated therewith: The latter is falsified by more than a factor of two for certain incidence energies.[363] Of course, depending on the kind of degeneracy and its importance for particular entrance channels this cannot easily be generalized, i.e. the systematic error may even be be larger for other systems.

3. The neural network interpolation quality has been found empirically to largely benefit when a physically motivated decay of corrugation with increasing distance towards the surface is directly incorporated into the transformed lateral coordinates. This is completely in line with experiences of Lorenz, Behler and coworkers.[338,339,342]

All of these shortcomings of Eqs. (6.21) are taken care of by the following transformation to symmetry adapted coordinates $\boldsymbol{Q} = (\tilde{Q}_1, \tilde{Q}_9)$:

$$Q_1 = \frac{1}{2}\left[f(Z_\mathrm{A}) \cdot g_1^{\mathrm{fcc100}}(X_\mathrm{A}, Y_\mathrm{A}) + f(Z_\mathrm{B}) \cdot g_1^{\mathrm{fcc100}}(X_\mathrm{B}, Y_\mathrm{B})\right] \tag{6.22a}$$

$$Q_2 = f(Z_\mathrm{A}) \cdot g_1^{\mathrm{fcc100}}(X_\mathrm{A}, Y_\mathrm{A}) \cdot f(Z_\mathrm{B}) \cdot g_1^{\mathrm{fcc100}}(X_\mathrm{B}, Y_\mathrm{B}) \tag{6.22b}$$

$$Q_3 = \frac{1}{2}\left[f(Z_\mathrm{A}) \cdot g_2^{\mathrm{fcc100}}(X_\mathrm{A}, Y_\mathrm{A}) + f(Z_\mathrm{B}) \cdot g_2^{\mathrm{fcc100}}(X_\mathrm{B}, Y_\mathrm{B})\right] \tag{6.22c}$$

$$Q_4 = f(Z_\mathrm{A}) \cdot g_2^{\mathrm{fcc100}}(X_\mathrm{A}, Y_\mathrm{A}) \cdot f(Z_\mathrm{B}) \cdot g_2^{\mathrm{fcc100}}(X_\mathrm{B}, Y_\mathrm{B}) \tag{6.22d}$$

$$Q_5 = f(Z) \cdot g_1^{\mathrm{fcc100}}(X, Y) \tag{6.22e}$$

$$Q_6 = f(Z) \cdot g_2^{\mathrm{fcc100}}(X, Y) \tag{6.22f}$$

$$Q_7 = f(Z) \tag{6.22g}$$

$$Q_8 = d \tag{6.22h}$$

$$Q_9 = \cos(\vartheta)^2 \quad , \tag{6.22i}$$

where $f(x) = \exp(-\frac{1}{2}x)$ like in previous work[338,339,342] takes care of damping the sensitivity to corrugation of the surface potential to be interpolated for increasing distances from the surface. Exchange symmetry has been included by symmetrizing $(\tilde{Q}_1, \tilde{Q}_3)$ and $(\tilde{Q}_2, \tilde{Q}_4)$ to (Q_1, Q_2) and (Q_3, Q_4), respectively. The same could have been done with $(\tilde{Q}_3, \tilde{Q}_6)$, but $Q_8 = \tilde{Q}_7$ together with Q_9 already fully include the distances of both atoms from the surface

invariant under exchange symmetry in a much simpler way. Accordingly, the six-dimensional vector $\boldsymbol{Q}^6 = (Q_1, Q_2, Q_3, Q_4, Q_8, Q_9)$ already constitutes a better and simpler (since lower dimensional) map than $\tilde{\boldsymbol{Q}}$ from Eqs. (6.21). However, properly symmetry transformed center of mass coordinates (Q_5, Q_6, Q_7) need to be added in order to resolve the injectivity problem described before as illustrated in Fig. 6.7. Thus, Eq. (6.22) constitutes the desired map with the properties sketched out in Fig. 6.4. Unfortunately, a proper mathematical prove is not trivial. Obviously, $\boldsymbol{Q}$ is differentiable with respect to both Cartesian and spherical coordinates. An inverse transformation for Eqs. (6.22) cannot be easily constructed. It could be useful in practice but is not necessary here as only forward evaluations are required to evaluate energies and forces of the PES to be interpolated. Hence, injectivity on the quotient spaces $\mathcal{Q}^{\text{cart}}$ or $\mathcal{Q}^{\text{sph}}$ is difficult to show. Therefore, this has been verified only numerically by calculating $\boldsymbol{Q}$ for a very large number of sets of points representing different symmetry classes, i.e. elements of the quotient spaces. No duplicates of $\boldsymbol{Q}$ or indications thereof have been found.[v]

One reason why this received so much attention is that transformations, which do not have the desired properties, can easily go unnoticed during neural network training and evaluations. As mentioned before, this appears to be the case in the work of Ludwig and Vlachos[340,341] – with unknown consequences for statistical properties obtained therewith. On the other hand, Behler and coworkers did even observe a significantly better interpolation quality only after adding transformed center of mass coordinates according to their "symmetry functions".[342] They did not analyze the reasons though, which in fact can also be related to a "restoration of injectivity" of their map. Hence, a correct description of the physical system – apart from being desirable from a theoretical point of view – may even yield practical benefits, too.

Generalization to heteronuclear diatomics is simple: In Eqs. (6.22), only the symmetrization of (Q_1, Q_2, Q_3, Q_4) needs to be removed, i.e. they simply can be replaced by the raw values of $g_1^{\text{fcc100}}(x, y)$ and $g_2^{\text{fcc100}}(x, y)$ for both atoms. Obviously, the only surface specific part of Eqs. (6.22) are the lateral coordinate transformations $g_1^{\text{fcc100}}(x, y)$ and $g_2^{\text{fcc100}}(x, y)$. Since the idea behind them is not *tri*angulation, only two of them are required for each atom. Instead of eleven "symmetry functions" which have been used by Behler and coworkers in their work for fcc(111) surfaces,[342] only a nine-dimensional input vector for the neural network is required here. This diminishes the number of weights quite considerably (cf Section 6.1.3), reducing the complexity of NN training and accelerating its evaluation. Further improvement along these lines brings up the mathematically challenging question whether a coordinate transformation can be constructed with properties as sketched out in Fig. 6.4, but whose image is embedded in a $\mathbb{R}^n$ with dimension $n < 9$, and if so what might be the smallest n possible. Within the scope of this thesis, this question remains unanswered. Even if perhaps not yet the optimal choice, Eqs. (6.22) can easily be used for other surfaces if proper replacements for Eqs. (6.17) can be found. In principle, only two proper linearly independent truncations of the corresponding Fourier series with the right symmetry properties are required. Indeed, stimulated by ongoing work,[52] such truncations are given in Appendix A for each of the low-index surfaces ((100), (110), (111)) of fcc and bcc crystals[vi] – with reciprocal lattice vectors $\boldsymbol{G}_{ij}$ among $i, j \in \{0, 1, 2\}$ in each case. Their constructions have been guided and hence greatly simplified by intersection plots equivalent to Figs. 6.5 and 6.6, which are included in Appendix A as well. These plots

[v] Applying the implicit function theorem might a starting point, but only locally for an environment around a point. Accordingly, the numerical treatment might even be the best way to address global injectivity from a mathematical point of view.

[vi] Even a fcc(111) surface with "artificial" six-fold symmetry, tailored for PESs with practically degenerate energies on fcc and hcp hollow sites, is included.

allow to check adherence to the right lateral (i.e translational and point group) symmetry of the underlying surface "at a glance", which is then automatically carried forward to the more complicated resulting total transformation based on Eqs. (6.22).

Altogether, the transformation to symmetry adapted coordinates is completely independent of the interpolation scheme which is employed, i.e. other methods might benefit thereof as well. For a concise comparison of different interpolation methods currently in use in gas-surface dynamics, which addresses both accuracy and efficiency, this should be taken into account. Such a comparison, albeit very desirable, is still missing.

6.1.4.3. Forces

For the molecular dynamics trajectories calculated in the following, forces, i.e. derivatives of the interpolated potential energy surface with respect to the (physical) coordinates of the adsorbate $\boldsymbol{R}^{\mathrm{ph}} \in \{\boldsymbol{R}^{\mathrm{cart}}, \boldsymbol{R}^{\mathrm{sph}}\}$, are needed. According to Eq. (6.15), they are given analytically by application of the chain rule

$$\boldsymbol{\nabla}_{\boldsymbol{R}^{\mathrm{ph}}} V_{6\mathrm{D}} \approx \boldsymbol{\nabla}_{\boldsymbol{Q}} V_{6\mathrm{D}}^{\mathrm{NN}} \cdot \frac{\partial(Q_1, \ldots, Q_9)}{\partial(R_1^{\mathrm{ph}}, \ldots, R_6^{\mathrm{ph}})} \quad , \tag{6.23}$$

where the Jacobian of the symmetry adapted coordinates $\boldsymbol{Q}$ with respect to the physical coordinates $\boldsymbol{R}$ is required.[vii]

6.2. Technical Details

6.2.1. DFT Calculations

In generalization of the adsorption energies given by Eq. (5.9) discussed in Section 5.3, the interaction potential $V_{6\mathrm{D}}$ for selected molecular configurations is calculated according to

$$V_{6\mathrm{D}}(\boldsymbol{R}^{\mathrm{ph}}) = \left[E^{100}_{\mathrm{O_2@Pd}}(\boldsymbol{R}^{\mathrm{ph}}) - \left(E^{100}_{\mathrm{Pd}} + E_{\mathrm{O_2}}\right)\right] \quad , \tag{6.24}$$

where all terms on the right-hand side are obtained from corresponding DFT calculations. The sign has been chosen such that for negative values the combined system of both oxygen atoms in contact with the Pd(100) surface is more energetically favorable than the two separate systems, i.e. an (isolated) O_2 molecule in gas phase and the clean metal surface. It hence indicates an exothermic reaction with accompanying release of (binding or chemisorption) energy.

Based on the computational setup established in Chapter 5, 3×3 slabs of the primitive unit cell of the Pd(100) surface consisting of five layers and a vacuum distance of 15 Å (cf Section 2.6) are used for the evaluation of $V_{6\mathrm{D}}$. Spin polarized calculations with the exchange-correlation functional due to Perdew, Burke and Ernzerhof (PBE)[85,86] for about 3500 configurations have been performed, heavily relying on the DM/EDFT hybrid scheme for electronic minimization described in Section 5.3 and reusing charge densities and wave functions from those close by wherever possible. The latter proved to be of particular importance in the vicinity of the spin transition from the O_2 triplet to a singlet state, which will be discussed in more detail in Chapter 7.

[vii] In principle, this Jacobian can also be obtained by automatic differentiation (see e.g. http://www.autodiff.org) as commonly employed in computer algebra systems. Within the present approach, the respective derivatives could be easily written down and were quickly coded explicitly.

The generation of the DFT data was started with a systematic mapping of configurations as a function of (Z, d) over different lateral high-symmetry sites $\{X_i, Y_i\}_i$ in the irreducible wedge of the surface unit cell and for different angular orientations $\{\varphi_i, \vartheta_i\}_i$. The corresponding 33 elbow plots are shown in Appendix B.1 of Appendix B. Consistent with the lack of long range dispersive interactions in the PBE functional (cf Section 2.5), for $Z > 5\,\text{Å}$, corrugation has been found to be below the numerical uncertainties of the underlying DFT calculations (cf Section 5.3), resulting in $V_{6D}(X, Y, Z > 5\,\text{Å}, d, \vartheta, \varphi) \approx V_{O_2}(d)$. The database has thus been extended by further values for $Z > 5\,\text{Å}$ from the calculated binding energy $V_{O_2}(d)$ of a free oxygen molecule in the gas phase.

With increasing knowledge about the PES as obtained from dynamics on different neural network interpolations (*vide infra*) more configurations have been added also in lateral and angular directions at particular heights and intermolecular distances $\{Z_i, d_i\}_i$, which the former showed to be frequently visited. These are listed in detail within the (X, Y) and (φ, ϑ) contour plots, i.e. other, less frequently considered two-dimensional cuts through $V_{6D}(\boldsymbol{R}^{ph})$, in Appendix B.2 and Appendix B.3 of Appendix B, respectively. Consistent with the results from Section 5.3, no indications for subsurface oxygen were found to be of relevance for the energy regime of interest here. In order to ensure that the neural network interpolation thus reliably yields $Z > 0\,\text{Å}$ in the trajectories, highly repulsive values $V_{6D}^{max}(Z = 0\,\text{Å}) = 5\,\text{eV}$ were finally added to the database – consistent with the damping according to Eq. (6.25) discussed in Eq. (6.25). The calculation of precise values from DFT (typically showing exponentially increasing energies towards $Z = 0\,\text{Å}$) would have required a significant computational effort, and would only have complicated the interpolation procedure, but not have changed the actual dynamics. A similar procedure was applied for $d \leq 1.0\,\text{Å}$ as well, which also typically yields exponentially increasing energies. In the end, the input data set for the interpolation finally consists of more than 6000 values for $V_{6D}(\boldsymbol{R}^{ph})$ altogether.

6.2.2. Neural Network Interpolation

Along the lines of previous work[47,342] neural network training (cf Section 6.1.3) has been simplified by limiting highly repulsive energies to $V_{6D}(\boldsymbol{R}^{ph}) \leq V_{6D}^{max} = 5\,\text{eV}$, which is still much larger than the energy range of interest for the ensuing molecular dynamics trajectories discussed below. The input data has thus been preprocessed through a damping function

$$V_{6D}^{damped}(V_{6D}) = \begin{cases} V_{6D} & \text{for } V_{6D} \leq V_{6D}^{thresh}, \\ V_{6D}^{max} - \Delta \cdot \exp\left[-\frac{(V_{6D} - V_{6D}^{thresh})}{\Delta}\right] & \text{for } V_{6D} > V_{6D}^{thresh}, \end{cases} \tag{6.25}$$

where $\Delta = \left(V_{6D}^{max} - V_{6D}^{thresh}\right)$. For the present system, the threshold energy has been set to $V_{6D}^{thresh} = 4\,\text{eV}$. In contrast to the "cutoff function" used before[47,342] the one given by Eq. (6.25) is also properly differentiable at the onset of the damping at V_{6D}^{thresh} – ensuring conceptually consistent forces.

Using the adaptive extended Kalman filter (EKF) algorithm including the modifications described introduced by Lorenz and coworkers[339] for neural network training, the sensitivity is further focused on the most relevant parts of the PES, where also the validity of the frozen surface approximation is least impaired, by assigning training weights to the input data according to

$$\omega_{train}(Z, d, V_{6D}^{damped}) = \begin{cases} 1.0 & \text{if } d < 0.99\,\text{Å or } Z = 0\,\text{Å} \\ \omega_Z(Z) \cdot \omega_V(V_{6D}^{damped}) & \text{otherwise} \end{cases}, \tag{6.26a}$$

where

$$\omega_Z(Z) = \begin{cases} 500 & \text{if } Z \leq 0.5\,\text{Å} \\ 1000 & \text{if } 0.5\,\text{Å} < Z \leq 1.0\,\text{Å} \\ 2000 & \text{if } 1.0\,\text{Å} < Z \leq 1.5\,\text{Å} \\ 2500 & \text{if } 1.5\,\text{Å} < Z \leq 2.0\,\text{Å} \\ 3000 & \text{if } 2.0\,\text{Å} < Z \leq 2.5\,\text{Å} \\ 4000 & \text{if } 2.5\,\text{Å} < Z \leq 3.5\,\text{Å} \\ 5000 & \text{if } Z > 3.5\,\text{Å} \end{cases} \tag{6.26b}$$

and

$$\omega_V(V_{6\text{D}}^{\text{damped}}) = \begin{cases} \frac{1}{20} & \text{if } V_{6\text{D}}^{\text{damped}} > 4.0\,\text{eV} \\ \frac{1}{10} & \text{if } 1.5\,\text{eV} \leq V_{6\text{D}}^{\text{damped}} \leq 4.0\,\text{eV} \\ \frac{1}{5} & \text{if } 1.0\,\text{eV} \leq V_{6\text{D}}^{\text{damped}} < 1.5\,\text{eV} \\ \frac{1}{2} & \text{if } 0.5\,\text{eV} \leq V_{6\text{D}}^{\text{damped}} < 1.0\,\text{eV} \\ 1 & \text{otherwise} \end{cases} . \tag{6.26c}$$

Several values for the parameters of the forgetting schedule employed within the EKF, which help to avoid early trapping in local minima during neural network training, have been tried. The best fit quality has been obtained with $\lambda(0) = 0.98$ and $\lambda_0 = 0.99670$ for the present system, using the same notation as in the aforementioned work. Hyperbolic tangents were used as activation functions (cf Section 6.1.3). Between 1 % to 2 % of each input data set have first been randomly selected for the test set. Over 20 neural networks with different topologies have then been trained in each case, focusing on two and three hidden layers with different numbers of nodes. Training has been stopped after 150 epochs as the error of both training and test set did not decrease significantly any more and overfitting was not yet observed.

Unfortunately, in contrast to O_2 on Al(111), a good reproduction of the DFT data could not be primarily focused on a well-defined barrier region rather far away from the surface.[48,76] When focusing on a rather benign quantity like the initial sticking coefficient, which is dominantly decided by the passing through and being reflected at the barrier in such a region, this a perfectly viable strategy. Instead, when the results of much less benign, more detailed statistical quantities like lateral and angular distributions (cf Section 6.3.2) are to be trusted, a much more careful global verification of the quality of the obtained PES is required. In addition to the global mean average deviations (MADs) and root mean square errors (RMSEs), the latter has thus been carefully monitored by numerous two-dimensional (d, Z), (X, Y) and (ϑ, φ) cuts through the obtained neural network fits, including information about the errors of individual data points as exemplified by Fig. 6.8, Fig. 6.9 and Fig. 6.10 and collected in Appendix B for the best fit that has finally been obtained. Together with the evaluation of MADs and RMSEs for selected regions, this has enabled the selective iterative improvement indicated in Section 6.2.1 before by performing DFT calculations for specific points as needed.

The aforementioned finally obtained best fit is based on a neural network with a $\{9-29-29-29-1ttttl\}$ topology. The RMSE for relevant energies is less than 20 meV. Regions which turn out to be particularly important for the dynamics (*vide infra*) are typically even better described as illustrated in the contours plots shown in Fig. 6.8, Fig. 6.9 and Fig. 6.10 – in comparison

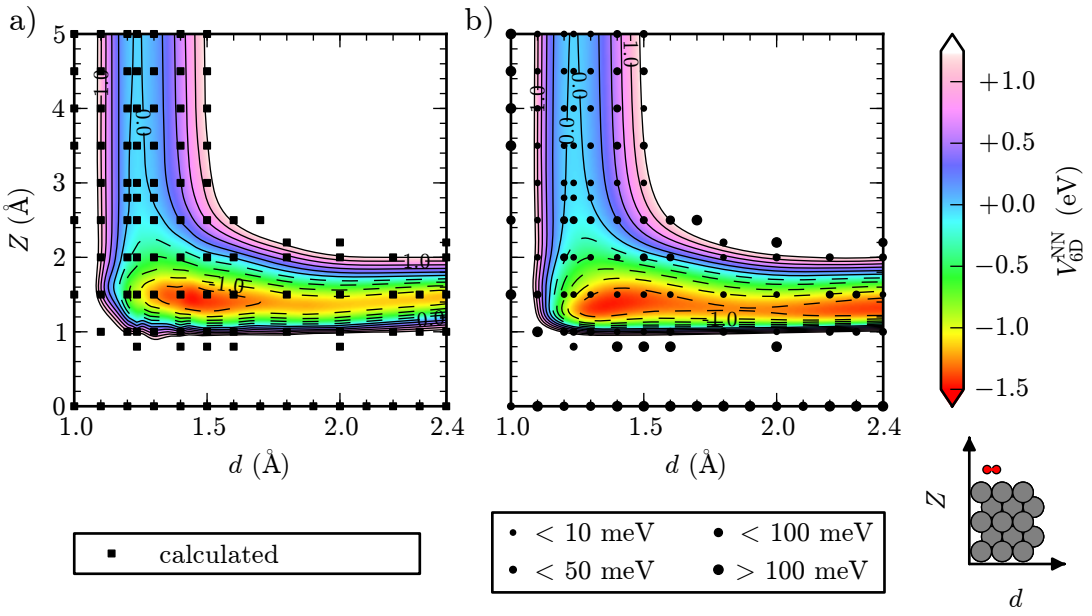

Figure 6.8.: Two-dimensional (Z, d) cuts through the six-dimensional PES for $X = 0.5a_{\mathrm{Pd}}^{100}$, $Y = 0.5a_{\mathrm{Pd}}^{100}$, $\vartheta = 90°$ and $\varphi = 0°$ as indicated by the inset. a) Contouring is based on a two-dimensional interpolation with thin plate splines.[364] Only the indicated (calculated) points from the NN data base in this particular cut plane are used and matched exactly by the resulting interpolation spline. b) The continuous description underlying the contouring is based on the best six-dimensional NN fit (using all of the several thousands of configurations in the training set) as detailed in the text. For each of the points of the whole NN input data set which are in the cutting plane the respective errors of the NN description is illustrated by the marker size. The spacing of the contour lines is 0.25 eV in both cases.

with "simple" spline interpolation [viii] in the two respective dimensions. As indicated before, a comprehensive account of the fitting quality is given in Appendix B. Results presented below in Section 6.3 have also been recalculated for a different, slightly worse interpolation, but no significant changes were found.

6.2.3. Molecular Dynamics Simulations

The MD simulations relied on a Bulirsh-Stoer integrator as described in Section 3.3.2 for the classical equations of motion in their spherical formulation in Eq. (6.11). A large number of trajectories can this way be reliably obtained based on the neural network interpolated V_{6D} with negligible computational effort. The Jacobian of the coordinate transformation has been carefully checked against numerical derivatives using simple finite differences in order to ensure analytically correct forces according to Eq. (6.23). Numerical difficulties due to singularities for $\sin(\vartheta) \to 0$ have not been encountered. The integration accuracy has been adjusted to ensure energy conservation within 5 meV even for the longest trajectories.

[viii] So-called *thin plate splines*[364] have been employed, a Fortran 77 implementation of which is freely available through (e.g.) http://gams.nist.gov/serve.cgi/Module/CMLIB/LOTPS/838

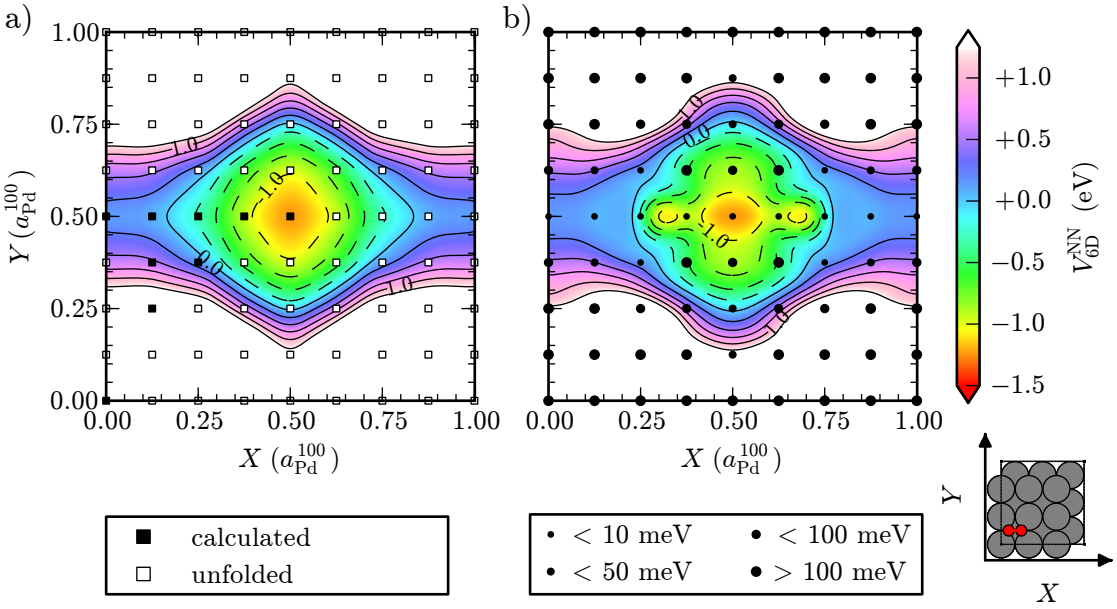

Figure 6.9.: Two-dimensional (X, Y) cuts through the six-dimensional PES for $Z = 1.5\,\text{Å}$, $d = 1.3\,\text{Å}$, $\vartheta = 90°$ and $\varphi = 0°$ as indicated by the inset. a) and b) have been obtained by two-dimensional spline and six-dimensional NN fit as detailed in the caption of Fig. 6.8. Symmetry equivalent configurations in the NN data set have been unfolded for the former to fill the whole cut plane.

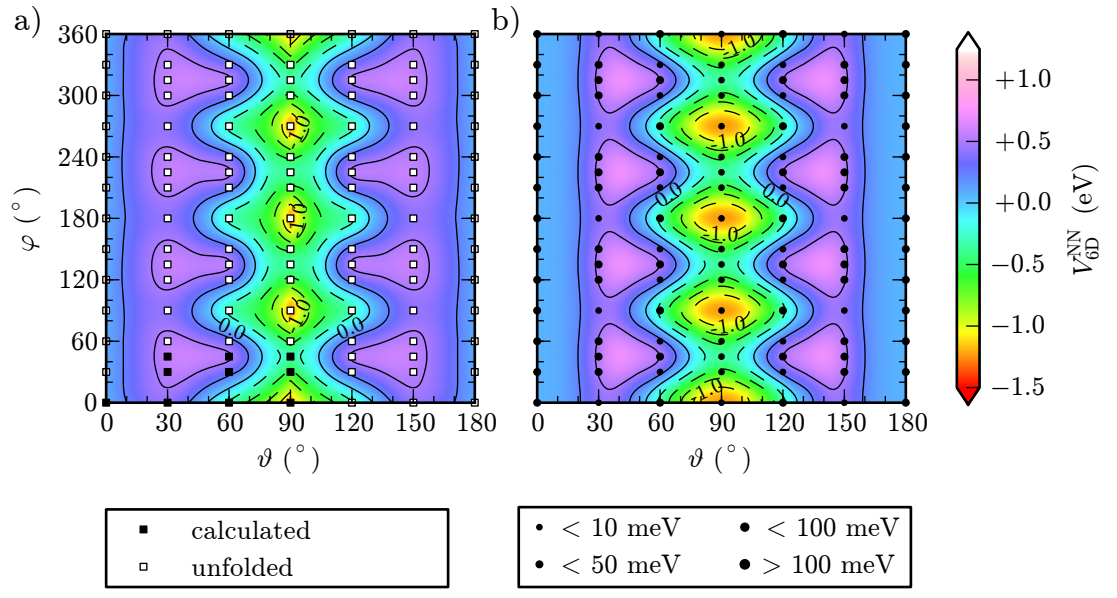

Figure 6.10.: Two-dimensional (ϑ, φ) cuts through the six-dimensional PES for $X = 0.5a_{\mathrm{Pd}}^{100}$, $Y = 0.5a_{\mathrm{Pd}}^{100}$, $Z = 1.5\,\text{Å}$ and $d = 1.3\,\text{Å}$. a) and b) have been obtained in the same fashion as detailed in Fig. 6.8 and Fig. 6.9.

Initial conditions are chosen such that trajectories start at $Z_0 = 6\,\text{Å}$ above the surface, corresponding to a free O_2 molecule as described in Section 6.2.1 at its equilibrium bond length d_0 (cf Section 5.2). Any classical representation of the zero point energy is neglected, i.e. molecules do not initially rotate or vibrate. For different initial kinetic energies E_i, lateral positions (X_0, Y_0) in the surface unit cell and angular orientations (ϑ_0, φ_0) are sampled using a conventional Monte Carlo procedure based on a uniform distribution U, thus resulting in random values to be drawn from the distribution

$$f(X_0, Y_0, \vartheta_0, \varphi_0) = U(X_0)\; U(Y_0)\; |\sin(\vartheta_0)|\, U(\vartheta_0)\; U(\varphi_0) \quad . \tag{6.27}$$

Here, equal distribution of molecular configurations on the unit sphere $S_0^2(\vartheta_0, \varphi_0)$ in $\mathbb{R}^3$ according to

$$U(S_0^2)\; dS_0^2 = |\sin(\vartheta_0)|\, U(\vartheta_0)\, U(\varphi_0) \quad , \tag{6.28}$$

has been properly taken into account.[ix] Focusing on normal incidence, the initial momentum is completely defined, with the only non-zero component given by

$$P_Z = M\dot{Z} = \sqrt{2ME_\text{i}} \;\approx\; 311 \sqrt{\frac{M}{\text{u}}} \sqrt{\frac{E_\text{i}}{\text{meV}}}\; 10^{-23}\,\text{u}\,\text{m}\,\text{s}^{-1} \tag{6.29}$$

Equally, since $\dot{Z} = \dot{Z}_\text{A} = \dot{Z}_\text{B}$,

$$\boldsymbol{P}_\text{A} = m_\text{A}(0, 0, \dot{Z}) \tag{6.30a}$$

$$\boldsymbol{P}_\text{B} = m_\text{B}(0, 0, \dot{Z}) \quad , \tag{6.30b}$$

where $\frac{1}{2}M = m_\text{A} = m_\text{B} = m_\text{O} \approx 16\,\text{u}$, with m_O denoting the atomic mass of oxygen.

6.3. Results and Discussion

6.3.1. Initial Sticking

Figure 6.11 shows the first-principles *ab initio* sticking coefficient $S_0(E_\text{i})$ as a function of initial kinetic energy E_i, obtained from classical dynamics on the previously obtained adiabatic six-dimensional PES. For each value of E_i, 2000 trajectories were first calculated, and one of the following possibilities was considered for their individual outcomes:

1. A trajectory is counted as dissociative sticking event when the O_2 bond length d is stretched beyond 2.4 Å, i.e. twice the gas-phase distance, and the associated velocity component $\dot{d}$ is still positive. This is a rather conservative criterion, as some variation of the critical bond distance has shown to have no effect on the sticking curve.

[ix] The reader is reminded that the surface element

$$dS_0^2 = \left| \frac{\partial \mathbf{e}_{r,0}}{\partial \vartheta_0} \times \frac{\partial \mathbf{e}_{r,0}}{\partial \varphi_0} \right| d\vartheta_0\, d\varphi_0 = |\sin(\vartheta_0)\, \mathbf{e}_{r,0}|\, d\vartheta_0\, d\varphi_0$$

is defined based on the radial unit vector in spherical coordinates

$$\mathbf{e}_{r,0} = (\sin(\vartheta_0)\cos(\varphi_0),\, \sin(\vartheta_0)\sin(\varphi_0),\, \cos(\vartheta_0)) \quad .$$

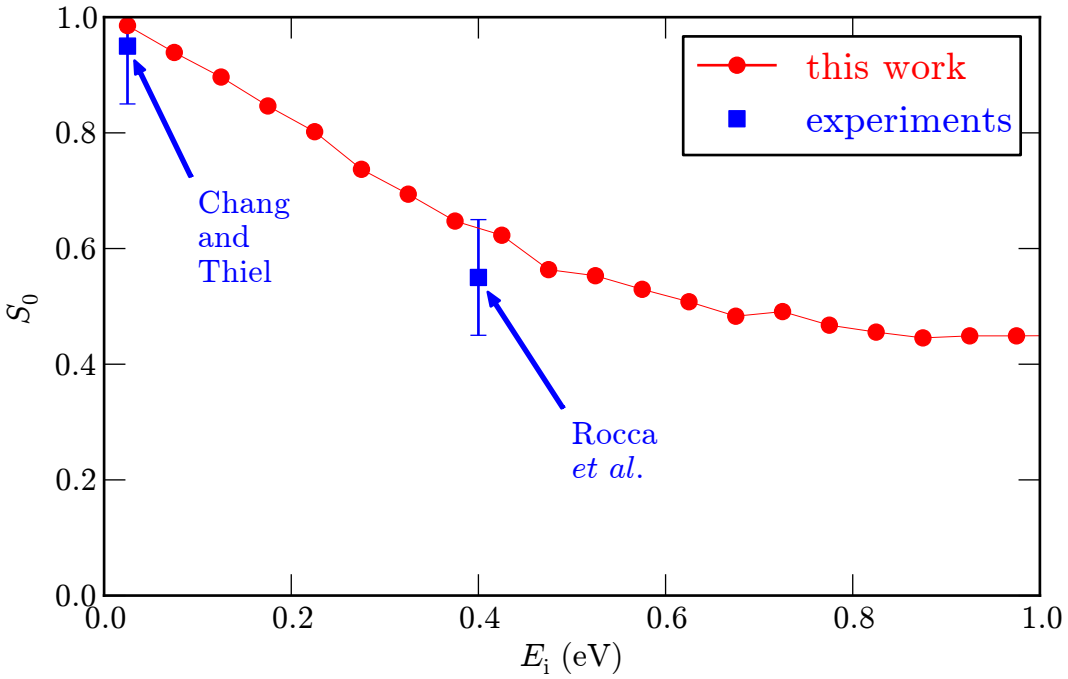

Figure 6.11.: Initial sticking coefficient S_0 for O_2 on Pd(100) based on trajectory calculations on the six-dimensional PES developed within this chapter. The scarce experimental data from Chang and Thiel[365] as well as Rocca and coworkers[366] is also plotted (with realistic error bars) for comparison. As detailed in the text, only dissociative sticking has been observed.

2. A molecule is counted as reflected when its center of mass reaches the initial starting distance of 6 Å with a positive velocity component $\dot{Z}$. The results were equally found to be insensitive to reasonable variations of this criterion.

3. Should a trajectory neither have yielded dissociation or reflection after 6 ps, it is counted as trapped. This maximum integration time has to be treated with particular care: On the one hand, if chosen too long, trajectories will become systematically wrong due to the neglect of energy transfer to the frozen surface. On the other, if too short, slow passages around early barriers might not be properly captured. Fortunately, for the present system, dissociation or reflection is obtained within 2 ps for more than 99.995 % of the trajectories. even for lowest initial kinetic energy of 25 meV that has been considered.

The statistical convergence of the curve shown in Fig. 6.11 was verified by doubling the number of trajectories thereafter.

Considering the scarcity of the of available experimental data,[365,366] the theoretical curve agrees excellently. This has to be seen in light of e.g. the preceding work on O_2 at Al(111), where a similarly calculated S_0 deviated by up to two orders of magnitude in particular for lowest incidence energies as discussed in more detail in Chapter 7. For that system, experiment and theory could only be reconciled by assuming a strongly non-adiabatic spin transition of the oxygen molecule.[47–50,183,299] In turn, the present results indicate that the latter is not necessarily a general effect during dissociative adsorption of O_2 on metal surfaces. This is further corroborated by other indications based on the results obtained in Section 7.3.2 in the context of electron-hole pair excitations in the substrate. In fact, only recently, an adiabatic

description has also been found to yield good agreement with experimental data for the sticking of O_2 on Ag(111) as well.[52] The dominant role of non-adiabatic effects might thus indeed be limited to the adsorption dynamics of O_2 on surfaces of simple metals like aluminum.

The aforementioned "quick decision" about the outcome of a trajectory after 2 ps already indicates that the obtained dissociative sticking occurs directly, i.e. without preceding trapping in a so-called precursor state. This is in agreement with results from recent molecular beam experiments for O_2 on Pd(100): Initial sticking was observed to be depending on coverage, but independent of surface temperature, which contradicts a precursor dominated mechanism at least for temperatures higher than 273 K considered in that study.[17] Quite in contrast, for the (111) surfaces of both palladium and platinum, an indirect, precursor related mechanism has been proposed based on the measured decrease of S_0 for low incidence energies, which is similar to what has been obtained in Fig. 6.11, and results from high-resolution energy loss spectroscopy (EELS).[367–369] There, this decrease is a dynamical result of the so-called steering effect:[316,320,363] Inspection of individual trajectories shows that faster molecules do not have the time to find a path leading to dissociation within the surface potential, and thus are simply reflected before.[x] This will be further corroborated in Section 6.3.2. It has also been observed in dynamical simulations for O_2 on Pt(111) based on a high-dimensional PES, albeit for molecular trapping instead.[337] In addition to adsorbed oxygen atoms, HREELS measurements for O_2 adsorbed on Pd(100) at 80 K also indicate the presence of molecular oxygen,[370–372] which could act as a potential precursor state in the dynamics. In fact, the elbow plot shown in Fig. 6.8 also shows a shallow local minimum indicative for such a state. Vibrational frequencies calculated in this minimum based on both the interpolated PES and DFT directly yield indeed excellent agreement with the measure energy loss peak at 90 meV.[370–372] Of course, the frozen surface approximation might artificially limit the importance of a precursor dominated dissociation mechanism. However, the fact that a sticking curve very similar to the measured one for O_2 on Pd(111) can be obtained without invoking the latter might also stimulate a closer reexamination of the conclusions reached for that system based on a state-of-the-art high-dimensional dynamical model like the present one.

6.3.2. Entrance Channels

In order to characterize the entrance channels to dissociation, phase space distributions caused by the adsorption dynamics at various heights above the surface have been extracted. Since these are less benign than the simple initial sticking coefficient, more extensive sampling is required. Thanks to the negligible computational cost of the trajectory calculations on the interpolated PES, 1,000,000 trajectories could be integrated easily.

Starting with proper randomly distributed initial conditions in X, Y, ϑ and φ as detailed in Section 6.2.3 and an initial kinetic energy of $E_\mathrm{i} = 50$ meV, (i.e. still thermal molecules in the high-energy Boltzmann tail), Fig. 6.12 shows the resulting distributions in these coordinates at $Z = 1.5$ Å during their initial encounter with the surface. As verified in Section 6.3.3, the frozen surface approximation can still be trusted there.

First of all, all plots in Fig. 6.12 show the corresponding perfect fourfold symmetry of the (frozen) Pd(100) surface – as to be expected due to proper incorporation of symmetry into the PES according to Section 6.1.4. The distributions clearly peak at $X = Y = 0.5a_\mathrm{Pd}^{100}$ together with $\vartheta = 90°$ and $\varphi = 0°$, i.e. oxygen molecules centered above the hollow site with their

[x] Eventually, for even higher incidence energies (not shown in Fig. 6.11), sticking increases again.

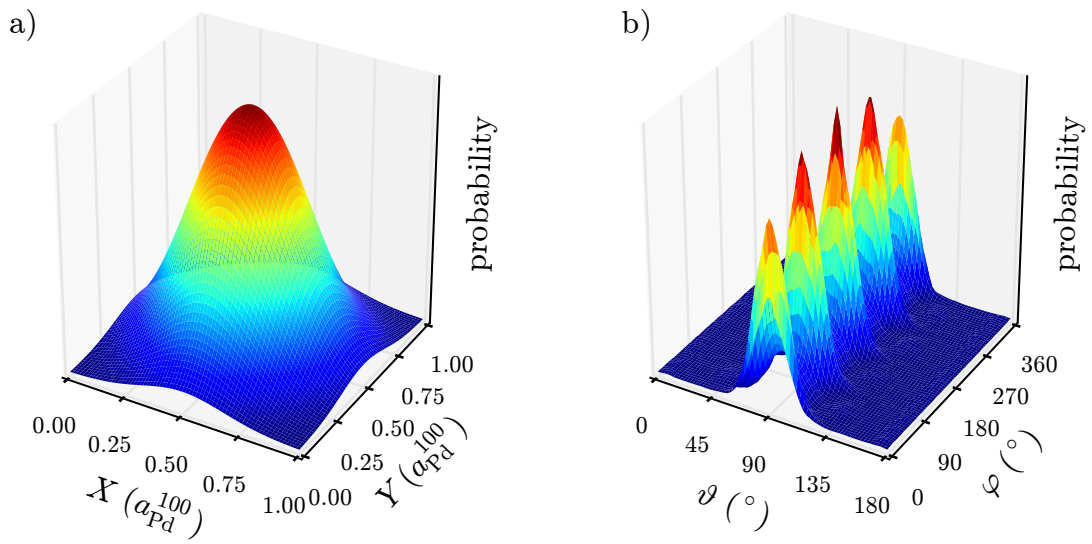

Figure 6.12.: Probability distributions of a) (X, Y) and b) (ϑ, φ) coordinates during the initial encounter of O_2 molecules with the Pd(100) surface at a height $Z = 1.5\,\text{Å}$ above the latter. Results were obtained from extensive phase space sampling by $1,000,000$ MD trajectories and were slightly broadened by two-dimensional Gaussians, whose widths were carefully chosen to about three times the spacing of the plotting grid.

molecular axis oriented parallel to the surface along a [100] direction. According to Fig. 6.11 in Section 6.3.1 essentially all of the molecules stick dissociatively for the selected initial kinetic energy. Therefore, second, and more importantly, the aforementioned configuration is revealed as the dominant entrance channel for dissociation. This can be easily understood by returning to the properties of the underlying PES: Figure 6.9 and Fig. 6.10 clearly reflect the properties of the obtained distributions. Qualitatively identical distributions have also been obtained for several values of E_i in a range between 25 meV to 400 meV. Their absolute magnitude is reduced with increasing E_i in the same way as the initial sticking coefficient plotted in Fig. 6.11. This clearly corroborates what has already been invoked before in Section 6.3.1: The O_2 molecules are thus less efficiently steered into the dominant entrance channel identified here.

6.3.3. Surface Mobility

Finally, the influence of surface mobility has been investigated based on a few AIMD trajectories that were obtained based on the same computational setup as described in Section 6.2.1 within the microcanonical ensemble. The implementation of the velocity Verlet algorithm available within CASTEP was used for the time integration with a time step of 2.5 fs (cf Chapter 3). Energy conservation within a few meV could only be achieved by again heavily relying on the DM/EDFT electronic minimization scheme described in Section 5.3. The AIMD trajectories are started from $Z(t = 0\,\text{fs}) = 6\,\text{Å}$ above the surface like in the frozen surface description based on the interpolated potential energy surface, and the initial velocity of $\dot{Z} = 5.5\,\text{Å}\,\text{ps}^{-1}$ of the O_2 molecule is perpendicular to the surface (cf Section 6.2.3). The latter corresponds to an initial kinetic energy of $E_\text{i} = 50\,\text{meV}$ according to Eq. (6.29) as before for the analysis presented in Section 6.3.2, while the palladium atoms in the slab forming the surface are initially at rest.

As illustrated by Fig. 6.13 for one of these trajectories, the resulting displacements of the

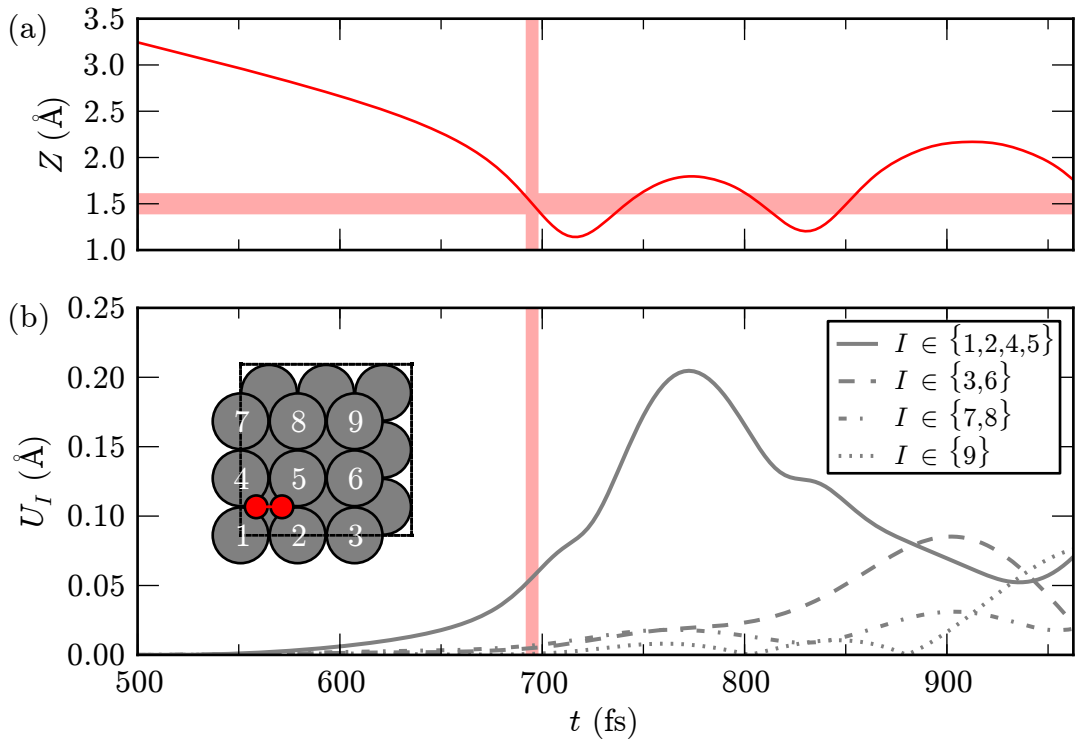

Figure 6.13.: a) Center of mass distance $Z(t)$ of an oxygen molecule from the surface with its molecular axis oriented parallel to the surface and centered above the hollow site (as shown in the inset below). b) Absolute values of displacements of the palladium atoms $U_I(t)$ in the top layer of the surface. Atoms are numbered as indicated by the inset. Starting from $Z(t = 0\,\text{fs}) = 6\,\text{Å}$ above the surface the first 500 fs of the trajectory are not shown. The O_2 molecule moves with constant initial velocity $\dot{Z}(t = 0\,\text{fs}) = 5.5\,\text{Å}\,\text{ps}^{-1}$ during that time corresponding to an initial kinetic energy $E_\text{i} = 50\,\text{meV}$ according to Eq. (6.29). As no energy has thus been transferred to the surface atoms, no deviation from their initial equilibrium positions can be observed meanwhile.

palladium atoms in the top layer of the surface set in rather late during the initial encounter with the O_2 molecule, and do not exceed 0.1 Å even when the latter is at a height of $Z = 1.5\,\text{Å}$. Qualitatively identical results have been obtained for the other AIMD trajectories as well. The steering into the dominant entrance channel identified before according to the statistics obtained in Section 6.3.2 is thus very unlikely affected by the neglected surface mobility. However, as discussed in further detail in Part III, the latter becomes crucial for the ensuing dissipative dissociation dynamics on the surface. Even in the rather small 3×3 simulation cell used here, Fig. 6.13 shows significantly larger displacements for $t > 700\,\text{fs}$.

Since the frozen surface description based on an interpolated PES is computationally very appealing, an extension by a suitable "energy sink" that mimics the influence of the substrate on the adsorbate dynamics would be very interesting. Adding a friction term depending linearly on the velocity, which appears in several models in the literature, very often even only with a

scalar friction coefficient (cf Chapter 8), is a very simple and straightforward ansatz to do so.

$$\begin{aligned} \boldsymbol{F}_I^{\mathrm{AIMD}} &= \boldsymbol{F}_I^{\mathrm{6D}} + \boldsymbol{F}_I^{\mathrm{fric}} \\ &= -\boldsymbol{\nabla}_{\boldsymbol{R}_I} V_{\mathrm{6D}} + \boldsymbol{\eta}_I^{\mathrm{fric}}\, \dot{\boldsymbol{R}}_{\boldsymbol{I}} \end{aligned} \qquad \text{for } I \in \{A, B\} \tag{6.31}$$

Fitting attempts for the friction tensors $\boldsymbol{\eta}_I^{\mathrm{fric}}$ using the available data for the forces from the neural network fit $\boldsymbol{F}_I^{\mathrm{6D}}$, the velocities of both oxygen atoms $\dot{\boldsymbol{R}}_{\boldsymbol{I}}$ ($I \in \{A, B\}$) and the $\boldsymbol{F}_I^{\mathrm{AIMD}}$ target force from the AIMD trajectories starting from identical initial conditions have turned out to be a hopeless endeavor: Huge deviations larger than $1\,\mathrm{eV\,\AA^{-1}}$ remain between the left-hand side of Eq. (6.31) and its right-hand side. Probably not surprising considering the generalized Langevin equations (GLEs) approach described in Section 8.1, the influence of the complex many-body system constituted by the metal surface (without even considering potential electronic non-adiabatic effects) cannot be condensed into simple friction tensors for the description of individual trajectories. Whether this prevails also on a statistical level, i.e. for observables which are (sufficiently) averaged over the fine grained microscopic details of the time evolution of the system is topic of current research.

6.4. Summary and Outlook

A first-principles based statistical treatment of the initial adsorption dynamics has been carried out according to a "divide and conquer" strategy relying on the Born-Oppenheimer approximation. In this step, the substrate has been kept frozen, resulting in a six-dimensional potential energy surface (PES).

Neural networks (NN) have been used as a very adaptive mathematical tool to obtain a continuous PES model from DFT data calculated for over 3000 molecular configurations above the surface including the strong corrugation of the latter. For an accurate NN-PES based on this rather small input data set with less than 4^6 members (which would be the number of points on a regular cubic with only four points per direction), the development of a proper symmetry adapted coordinate transformation turned out to be an essential key challenge. The resulting scheme has even been generalized to other low-index surfaces in Appendix A and already allowed to obtain another high-quality NN-PES for O_2 on Ag(111).[52] It is not tied to neural networks and therefore can also allow to overcome problems encountered with other interpolation schemes, e.g. the modified Sheppard method, in future applications.

The initial sticking coefficient S_0 for O_2 on Pd(100) was calculated based on classical dynamics on the aforementioned adiabatic NN-PES and shows good agreement with presently available sparse experimental data. An extensive sampling of phase space revealed that the oxygen molecules are steered into a single entrance channel that dominates the dissociation dynamics: Predominantly, the latter thus occurs with the molecular axis parallel to the surface, along a [100] direction and centered over the fourfold hollow site. As picked up below this will greatly simplify further investigations in the remainder of this work. Comparison with *ab initio* molecular dynamics trajectories verifies that substrate motion is still negligible during this initial steering and that a simple friction model cannot mimic the influence of the latter on the ensuing adsorbate dynamics.

Finally, the obtained NN-PES opens perspectives for interesting future dynamical studies for this system – in particular in light of the intriguing recent results of experiments by Rocca and coworkers with beams of rotationally polarized oxygen molecules impinging on a Pd(100) surface.[17–19] They have observed that so-called helicopters and cartwheels, i.e. rotationally

excited O_2 molecules with their molecular axis aligned perpendicular and parallel to the surface, respectively, yield different initial sticking and seem to form adsorbed species of different reactivity towards CO oxidation. Although obviously strongly indicating a dynamical cause, at the moment, however, no conclusive explanation can be offered based on the present theoretical model. Further experimental data, which is currently under way, might help "steering" further theoretical efforts in order to elucidate the previous observations.

Building upon the firm background of a dominant entrance channel for dissociation the goal of the remaining parts of this thesis is to investigate different energy dissipation channels in detail, accurately qualifying their importance for the dissociation dynamics. In Chapter 7, the role of electron-hole pair excitations is estimated based on trajectories from the here obtained NN-PES, benefiting greatly from the knowledge about their individual statistical relevance. Thereafter in Part III, details and trends of the interplay of adsorbate and phonon dynamics come into focus. First discussed therein are simple extensions to a six-dimensional PES, which would certainly be desirable given the thus enabled statistical treatment at very modest computational cost (once the PES is obtained). However and along the lines of the failure of the simple friction model, it turns out that for molecules which are significantly heavier than H_2 and have a more complicated electronic structure, a more accurate reference within the spirit of first-principles modeling is required. In the end, the results obtained in this chapter are simply used to define realistic initial conditions "closer to the surface" from where a detailed dynamical treatment including substrate mobility is started.

7. Electronic Non-Adiabaticity

Notwithstanding all the efforts detailed in the previous chapter to obtain a quantum mechanical, i.e. high-quality, description of the (initial) interaction of O_2 molecules with a frozen Pd(100) surface, the obtained potential energy surface (PES) and all concomitant results are still based on the Born-Oppenheimer approximation (BOA) combined with a classical treatment of the nuclei. (cf Section 2.2 in Part I).

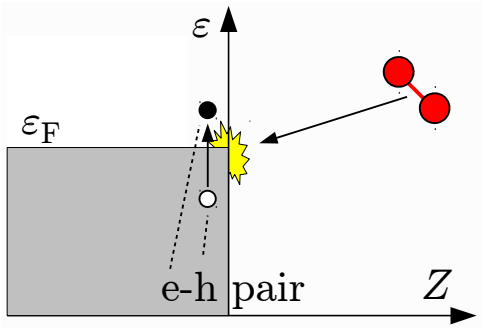

Figure 7.1.: Schematic illustration of electron-hole pair excitation during the impingement of a gas particle on a metal surface. An electron is excited from an occupied state below the Fermi level ε_F to an unoccupied state above, resulting in an excited state commonly referred to as electron-hole (e-h) pair.

This second approximation is usually not considered to be severe in gas-surface dynamics.[22] Even for H_2, with its de Broglie wave-length considerably smaller than that of O_2, a quantum mechanical description of the nuclei (within the BOA) has only very limited influence on the dynamics on the very same[320] or the (111) low-index surface of palladium.[373] For heavier atoms like e.g. nitrogen, a similar treatment has confirmed tunneling to have negligible influence on the reaction rate of N_2 molecules on a (stepped) Ru(0001) surface – the quality of the interpolation of the Born-Oppenheimer PES having in fact a much bigger influence on the latter.[151] Accordingly, there is no obvious necessity to deal with the complete electron-nuclear wave function, fundamental time-dependent properties of which are a topic of present active research even yet from a theoretical point of view.[71,374]

However, the validity of the BOA in particular for dynamics on metal surfaces has been lively discussed for quite a long time. As for example Tully[30–35,38,39] (but also many others) have frequently pointed out, the lack of a band gap in metallic systems should allow electronic excitations (i.e. electron-hole pairs) of arbitrarily low energies to easily couple with the nuclear motion a particle impinging from the gas phase. This is depicted schematically in Fig. 7.1. On the other hand, recent comparisons to experimental data for hydrogen[375] but also nitrogen molecules[44] on metallic surfaces indicate that electronically adiabatic descriptions provided within the BOA (i.e. neglecting any electronic excitations) seem to work extremely well in those cases. The reader is referred to more references in a very recent mini-review by Luntz.[376] It is worth pointing out that a high-dimensional description of the nuclear motion of the impinging adsorbate has been found to be significantly more important than the effect of electron-hole pair excitations[44] – even though the description of the latter in that work has been criticized to lack the necessary accuracy.[45,46] Here, high-dimensional means the inclusion of all adsorbate degrees of freedom on a frozen substrate surface into an interpolated *ab initio* PES governing the dynamics, i.e. a state-of-the-art model as used in Chapter 6.

7.0.1. Non-adiabaticity due to Adsorbate Degrees of Freedom

Quite in contrast, when using such a description for O_2 on Al(111), even one of the simplest statistical properties characterizing the dynamics is not properly described: Six-dimensional adiabatic dynamics on PESs obtained with the PBE and RPBE exchange-correlation functionals yield an initial sticking which is several orders of magnitude higher compared to experiment, at least for low energies.[47,48] Proposing a highly non-adiabatic transition from the spin-triplet state of the free O_2 molecule in the gas phase to the singlet ("quenched" spin) state when adsorbed on the surface has allowed to reconcile DFT-based PESs with the experimental data.[47,48] This can further be improved by actually allowing for transitions between a singlet and a triplet potential energy surface[49,50] obtained within constrained DFT[77] according to "surface hopping" within the "fewest switches" algorithm originally proposed by Tully.[377] Therefore, *not* accounting for excitations of the electronic degrees of freedom of the *substrate* in those models seems to be reasonable – in this respect similar to the other systems mentioned before. It is "only" the spin degrees of freedom of the *adsorbate* which apparently are responsible for the strongly non-adiabatic behavior.

For the present system, the situation is quite different. The sticking curve presented in Section 6.3.1 is in excellent agreement at least with the sparse experimental data. This can be rationalized by considering the two coupling mechanisms that have been discussed for the non-adiabatic spin transition of O_2 on Al(111): Spin-orbit coupling and tunneling of electrons between substrate and adsorbate. The former has been estimated to be to weak for that system.[50] However, it scales with mass, getting significantly stronger when heavier elements are involved. In fact, from small cluster systems in the gas phase, spin-orbit coupling is well known to strongly relax the "spin-forbiddeness" of reactions like oxygen dissociation.[51] When going from a finite to an infinite size system like a surface, spin-orbit coupling is therefore expected to favor increased adiabaticity for O_2 on Pd(100) compared to Al(111). As to the second mechanism, tunneling of two electrons effectively allows to perform the spin-transition from singlet to triplet within the continuum of states provided by the metal surface. Hence the latter acts as a "spin bath", quenching the spin during adsorption.[47,109] The probability for electron tunneling is generally proportional to the density of states (DOS) close to the Fermi level at the surface. The latter is extraordinary high in case of Pd(100),[40–43,378] which is not surprising, since bulk palladium is even close to fulfill Stoner's criterion for band ferromagnetism.[225] Therefore, spin transition due to tunneling, which is already perceived as the more dominant mechanism in case of O_2 on Al(111), should be even more efficient on Pd(100) compared to the simple metal. In fact, for this system, it should be even among the highest of all transition metals. Altogether, for the present system, both mechanisms are expected to be significantly enhanced. This rationalizes the aforementioned good agreement of the adiabatic dynamics presented in Chapter 6 with the experimental data *a posteriori* and hence gives no indications requiring to specially account for of adsorbate induced non-adiabaticity.

7.0.2. Non-adiabaticity due to Substrate Degrees of Freedom

Nevertheless, precisely the large number of states close to the Fermi level could also facilitate very efficient electron-hole pair excitations. Their role in the adsorption dynamics of the present system might not be visible for a rather benign quantity like sticking or might even simply be hidden due to fortuitous error cancelation e.g. with the underlying DFT energetics. From the perspective of energy dissipation, however, they might be very important. Within this perspective, the primary focus of this chapter is to obtain a reasonable estimate of the

energy dissipated to electron-hole pairs. Most importantly, this will allow to judge the relative importance of the electronic energy dissipation channel for the total amount of chemisorption energy of about 2.6 eV to be dissipated and allow to address further channels if necessary.

Looking for a suitable possibility to obtain this estimate, several approaches reported in the literature have to be ruled out however: The time-dependent Newns–Anderson model developed of Mizielinski and coworkers has never been applied to other adsorbates than (atomic) hydrogen.[379–382] Even if parametrized based on DFT in the same way as in that work, it bears the risk of relying upon a too approximate description of the electronic structure for the semi-quantitative estimate desired here. Very accurate "direct" *ab initio* simulation of electron-hole pair excitations within time-dependent (TD-) DFT and Ehrenfest dynamics for the nuclei have only been applied to hydrogen atoms impinging on the (111) surface of aluminum.[74,383,384] The computational settings used have been very much at the "convergence limit", resulting nevertheless in reasonable agreement with available experimental data from so-called "chemi-currents" experiments.[28] However, even with such settings the run-times for the dynamics were about a year. Within current abilities of both hardware and available codes,[385] the computationally much more demanding present system hence cannot (yet) be treated this way. Contrarily, the computational effort of approaches based on electronic friction theory[32,386–388] depends on the way how friction coefficients are calculated. One study already mentioned uses the local density friction approximation (LDFA), and hence can easily afford an according incorporation into six-dimensional dynamical studies of diatomics interacting with rigid surfaces.[44] This has been criticized to not be sufficiently accurate.[45,46] Indeed, more accurate calculations of electronic friction coefficients are possible[389] and have proven very successful for the description of electronic damping of adsorbate vibrational motion.[390] They have never been used so far together with a high-dimensional adsorbate-substrate PES of *ab initio* quality though.[300,391] More severely, already first applications within a forced oscillator model (FOM) for the electrons of the substrate have revealed the proper description of spin transitions as an intrinsic shortcoming of electronic friction theory.[73,392] This, of course, makes any method based on the latter highly problematic when trying to describe the dissociation of oxygen molecules.[i]

Recently, a new approach based on ("simple") perturbation theory applied to a TD-DFT framework has been proposed by Timmer and Kratzer.[393] It does not suffer from any troubles with spin, as the authors have demonstrated convincingly, both through theoretical considerations and good agreement with the full TD-DFT data for hydrogen atoms on Al(111) already mentioned above.[383] In fact, the scheme even allows to use separate non-spin-polarized calculations to describe the electronic structure of the substrate, while treating the interaction with the adsorbate fully spin-polarized. Hence, for the present system this paves the way for an ideal (if not even unique) workaround against the artificial ferromagnetism of the substrate within the description with the PBE exchange-correlation functional. Computationally very appealing is the fact that only ground state DFT calculations are required, so that a lot of electronic structure data already generated during the calculations performed for the previous chapter can conveniently be reused directly.[ii] For these reasons, this approach is considered

[i] Also the simple pragmatic workaround (fixing the total spin of the DFT simulation cell) proposed by Trail and coworkers[73] might not be easily applicable to the present system: In a spin-polarized description with the PBE exchange-correlation functional, the latter attributes artificial ferromagnetism to the palladium substrate.

[ii] Of course, this imposes certain storage demands: Calculations for the previous chapters were focused on total energies only. Hence the several terabytes of accompanying electronic structure data would otherwise simply have been deleted.

to be the method of choice for the present system to obtain the aforementioned reasonable estimate for energy dissipation into electron-hole pairs.

This chapter is structured as follows: First, a recapitulation of the theory developed by Timmer and Kratzer[393] is given, enriched by some clarifications and more detailed definitions. It is compared to electronic friction theory where of relevance, to (also mathematically) emphasize the aforementioned problems of the latter for the present system. Then, details about an improved implementation created independently within the present work are described, allowing to efficiently treat more numerically demanding systems like oxygen on palladium. As previous work has mainly been focused on purely one-dimensional trajectories (of mono-atomic adsorbates), the generalization to curved trajectories (of multi-atomic adsorbates) is pointed out. Finally, results for O_2 on Pd(100) are presented and discussed in comparison to experimental work, together with conclusions about the importance of electron hole pair excitation for the dissipation of the chemisorption energy.

7.1. Theory

7.1.1. Trajectories

The starting point for the following derivation is a classical trajectory $\boldsymbol{Q}(t)$ of a particle (a single atom or a molecule consisting of N atoms) from the gas phase impinging on the metal surface. In general, $\boldsymbol{Q}$ is a $3N$ dimensional vector of Cartesian coordinates of the atoms, which might be replaced by a suitable reaction coordinate description. It is assumed that the particle collides with the surface and is reflected, which is commonly referred to as a "full round trip". Consequently, for very small and very large times t the particle is assumed to be infinitely far away from the surface. This is meant in a physical sense such that the particle-surface interaction vanishes. As originally proposed by Timmer and Kratzer,[393] energy loss due to interaction with the surface is neglected for the trajectory in the following. Accordingly, a rigid surface, not allowing for any phonon excitations, is considered and energy dissipation into the electronic degrees of freedom of the surface is assumed to be sufficiently small not to change the trajectory significantly. If the latter is true (*vide infra*), these are reasonable approximations for the aforementioned present purposes.

7.1.2. Time-Dependent Perturbation Theory

Thanks to the Runge-Gross theorem,[68] the time dependent electronic many-body problem can be mapped onto an effective single particle Hamiltonian

$$h^\sigma(t) = t_\mathrm{e} + v^\sigma_{\mathrm{TD,eff}}(t) \quad , \tag{7.1}$$

where t_e is the kinetic energy contribution and the time-dependent effective potential (cf Eq. (2.29)) is given by

$$v^\sigma_{\mathrm{TD,eff}}(t) = v^\sigma_{\mathrm{TD,H}}(t) + v^\sigma_{\mathrm{TD,xc}}(t) + v_{\mathrm{TD,ext}}(t) \; . \tag{7.2}$$

σ denotes collinear spin in two different channels within the framework of spin density-functional theory (cf Section 2.5),[72] and in general the same (or a compatible) notation as in Part I is used. v^σ_ext describes the electron-ion interaction and explicitly depends on time due to the motion of the impinging particle along its trajectory $\boldsymbol{Q}(t)$. The dependence of the Hartree potential v^σ_H and exchange-correlation potential v^σ_xc on the time-dependent density $\rho(\boldsymbol{r}, t)$ is dropped in

order to simplify readability.[iii] At the "beginning" and the "end" of the full round trip, the (stationary) potential

$$v^{\sigma}_{\mathrm{TD,eff}}(t) \xrightarrow[\|\boldsymbol{Q}(t\to\pm\infty)\|_2\to\infty]{t\to\pm\infty} v^{\sigma}_{\mathrm{eff;\,non-int}} \tag{7.3}$$

describes vanishing particle-surface interaction as mentioned before yielding a (time-independent) Hamiltonian

$$h^{\sigma}(t) \xrightarrow{t\to\pm\infty} t_{\mathrm{e}} + v^{\sigma}_{\mathrm{eff;\,non-int}} \quad \equiv \quad h^{\sigma}_{(0)} \tag{7.4}$$

So far, no approximations have been made. However, to obtain a scheme that is more computationally tractable than the direct TD-DFT approach used (e.g.) by Lindenblatt and coworkers,[74,383,384] the time-dependent effective potential is now approximated by its counterparts in a "series of snapshots" of respective separate non-time-dependent ground state problems along the considered trajectory $\boldsymbol{Q}(t)$ as described by non-time-dependent DFT (cf Section 2.3),

$$v^{\sigma}_{\mathrm{TD,eff}}(t) \;\approx\; v_{\mathrm{H}}(\boldsymbol{Q}(t)) + v^{\sigma}_{\mathrm{xc}}(\boldsymbol{Q}(t)) + v_{\mathrm{ext}}(\boldsymbol{Q}(t)) \;\equiv\; \underbrace{v^{\sigma}(\boldsymbol{Q}(t)) + v^{\sigma}_{\mathrm{eff;\,non-int}}}_{\equiv v^{\sigma}_{\mathrm{eff}}(\boldsymbol{Q}(t))} \quad , \tag{7.5}$$

with the interaction part of the approximated effective potential $v^{\sigma}(t)$ vanishing at the boundaries of the considered trajectory

$$v^{\sigma}(t) \xrightarrow[\|\boldsymbol{Q}(t\to\pm\infty)\|_2\to\infty]{t\to\pm\infty} 0\,. \tag{7.6}$$

Following the arguments of Timmer and Kratzer,[393] the concomitant neglect of deviations from the instantaneous ground state charge density can only be justified for systems where the densities associated with excited electrons and holes are small compared to the overall charge density. If emission of light or electrons during the adsorption of O_2 molecules had ever been reported in experiments for the present system, such a justification would certainly be difficult. From a theoretical point of view, this can of course be confirmed *a posteriori* if the calculated electron-hole pair spectra are sufficiently small (*vide infra*).

Equations (7.4) and (7.5) define an approximation for Eq. (7.1),

$$h^{\sigma}(t) \approx h_{(0)} + v^{\sigma}(\boldsymbol{Q}(t))\,, \tag{7.7}$$

which is a quantum mechanical textbook example for a starting point of time-dependent perturbation theory:[53] The unperturbed Hamiltonian $h_{(0)}$ gets acted on by a (implicitly) time- (and spin-) dependent perturbation potential $v^{\sigma}(\boldsymbol{Q}(t))$. This potential might not be small, but should only be non-zero, cf Eq. (7.6), during a short time interval, given by the time of "intense interaction" (collision) of the impinging particle with the surface. As detailed by Timmer and Kratzer,[393] this motivates a perturbative treatment. Up to first order, the transition rate p_{ij} for an excitation within one spin channel σ from an occupied state $|\varepsilon^{\sigma}_i\rangle$ into an unoccupied

[iii] Real space representations of $v^{\sigma}_{\mathrm{TD,eff}}(t)$ and its contributions will simply be denoted by $v^{\sigma}_{\mathrm{TD,eff}}(\boldsymbol{r},t)$ and so on, as already used in Eqs. (2.26) and Eq. (2.29) within Part I. The kinetic energy contribution in Eq. (7.1) is given by $t_{\mathrm{e}} = -\frac{\hbar^2}{2m_{\mathrm{e}}}\boldsymbol{\nabla}^2_{\boldsymbol{r}}$ in real space (cf Eqs. (2.26)).

state $|\varepsilon_j^\sigma\rangle$ (i.e. $i \neq j$), which belong to the part of $h_{(0)}$ that describes the (clean) surface, is given by

$$p_{ij}^\sigma(t) = \frac{1}{i\hbar}\,\langle\varepsilon_j^\sigma|v^\sigma(\boldsymbol{Q}(t))|\varepsilon_i^\sigma\rangle\,\exp\left(\frac{i}{\hbar}(\varepsilon_j^\sigma - \varepsilon_i^\sigma)\,t\right)\,. \tag{7.8}$$

States associated with the impinging particle (spanning the other part of the Hilbert space which $h_{(0)}$ acts on) are not considered here as the electron-hole pair excitations to be described are supposed to be located within the substrate. For closer contact with actual calculations, discrete sets of initial and final substrate states rather than continuous band structures are denoted by indeces i and j, respectively, in the following. In practice, these indeces hence encapsulate $\boldsymbol{k}$-point and band indices of the Kohn-Sham states of the clean surface (cf Eq. (2.39) in Section 2.6).

7.1.3. Electron-Hole Pair Spectra

The excitation spectrum for a complete round trip is obtained accordingly from Eq. (7.8) by integrating over time and summing over allowed transitions:

$$\tilde{P}_{\mathrm{ex}}^\sigma(\hbar\omega) = \sum_{ij}\left|\int_{-\infty}^{+\infty} dt\; p_{ij}(t)\right|^2\,\delta\left(\hbar\omega - (\varepsilon_j^\sigma - \varepsilon_i^\sigma)\right)\,. \tag{7.9}$$

Here $\hbar\omega$ are positive and non-zero excitation energies. Furthermore, here and in the following, for these kind of sums over transitions appropriate weight factors (depending on symmetry) for the $\boldsymbol{k}$-point part of the indices i and j are implicitly considered.

Integrating Eq. (7.9) by parts leads to

$$\begin{aligned}\int_{-\infty}^{+\infty} dt\; p_{ij}^\sigma(t) = &\underbrace{\left[-\frac{1}{\varepsilon_j^\sigma - \varepsilon_i^\sigma}\,\left\langle\varepsilon_j^\sigma\,|\,v^\sigma\,|\,\varepsilon_i^\sigma\right\rangle\,\exp\left(\frac{i}{\hbar}(\varepsilon_j^\sigma - \varepsilon_i^\sigma)\,t\right)\right]_{t\to-\infty}^{t\to+\infty}}_{=0}\\ &+\frac{1}{\varepsilon_j^\sigma - \varepsilon_i^\sigma}\,\underbrace{\int_{-\infty}^{+\infty} dt\,\left\langle\varepsilon_j^\sigma\left|\frac{dv^\sigma}{dt}\right|\varepsilon_i^\sigma\right\rangle\,\exp\left(\frac{i}{\hbar}(\varepsilon_j^\sigma - \varepsilon_i^\sigma)\,t\right)}_{=\lambda_{ij}^\sigma}\,.\end{aligned} \tag{7.10}$$

The boundary term vanishes due to the properties of the interaction potential v^σ as given by Eq. (7.6). Reinserting the result of Eq. (7.10) back into Eq. (7.9) gives

$$\tilde{P}_{\mathrm{ex}}^\sigma(\hbar\omega) = \sum_{ij}\left|\frac{\lambda_{ij}^\sigma}{\varepsilon_j^\sigma - \varepsilon_i^\sigma}\right|^2\,\delta\left(\hbar\omega - (\varepsilon_j^\sigma - \varepsilon_i^\sigma)\right)\,. \tag{7.11}$$

Here the "dressed" (transition) matrix elements

$$\lambda_{ij}^\sigma = \int_{-\infty}^{+\infty} dt\,\left\langle\varepsilon_j^\sigma\,|\,\boldsymbol{\nabla}_{\boldsymbol{Q}}v^\sigma(\boldsymbol{Q}(t))\,|\,\varepsilon_i^\sigma\right\rangle\cdot\dot{\boldsymbol{Q}}(t)\;\cdot\;\exp\left(\frac{i}{\hbar}(\varepsilon_j^\sigma - \varepsilon_i^\sigma)\,t\right) \tag{7.12}$$

have been defined, which is one of the key ingredients to be calculated.

Generalization to Finite Temperatures

Up to now, only occupations of substrate states corresponding to zero temperature have been considered in Eqs. (7.8), (7.9) and (7.11). Generalization to finite electronic temperatures is easily possible by introducing Fermi occupation factors

$$f(\varepsilon) = \frac{1}{\exp\left(\frac{\varepsilon-\varepsilon_\mathrm{F}}{k_\mathrm{B}T}\right)+1} \,. \tag{7.13}$$

Not allowing for de-excitations of "thermally smeared" electrons, Eq. (7.11) then gets extended to the following expression for the electron-hole pair spectrum:

$$P^\sigma_\mathrm{ex}(\hbar\omega) = \underbrace{\sum_{ij} \left|\frac{\lambda_{ij}}{\varepsilon^\sigma_j - \varepsilon^\sigma_i}\right|^2 \delta\left(\hbar\omega - (\varepsilon^\sigma_j - \varepsilon^\sigma_i)\right)}_{\tilde{P}^\sigma_\mathrm{ex}(\hbar\omega)} \left[f\left(\varepsilon^\sigma_i\right) - f\left(\varepsilon^\sigma_j\right)\right] \theta\left(\hbar\omega\right) \,. \tag{7.14}$$

Individual spectra for electrons and holes can be obtained consistently by considering respective transitions only relative to the Fermi level,

$$P^\sigma_\mathrm{ex,el}(\hbar\omega) = \sum_{ij} \left|\frac{\lambda_{ij}}{\varepsilon^\sigma_j - \varepsilon^\sigma_i}\right|^2 \delta\left(\hbar\omega - (\varepsilon^\sigma_j - \varepsilon_\mathrm{F})\right) \left[f\left(\varepsilon^\sigma_i\right) - f\left(\varepsilon^\sigma_j\right)\right] \theta\left(\hbar\omega\right) \,, \tag{7.15a}$$

$$P^\sigma_\mathrm{ex,ho}(\hbar\omega) = \sum_{ij} \left|\frac{\lambda_{ij}}{\varepsilon^\sigma_j - \varepsilon^\sigma_i}\right|^2 \delta\left(\hbar\omega - (\varepsilon^\sigma_i - \varepsilon_\mathrm{F})\right) \left[f\left(\varepsilon^\sigma_i\right) - f\left(\varepsilon^\sigma_j\right)\right] \theta\left(-\hbar\omega\right) \,, \tag{7.15b}$$

where, as before, the excitation energies $\hbar\omega$ are positive and non-zero. As pointed out by Timmer and Kratzer[393] Eqs. (7.14), (7.15a) and (7.15b) stay mathematically well defined even for $|\varepsilon_j - \varepsilon_i| \to 0$. Nevertheless, numerical evaluations have difficulties in these regions, which is why they are omitted in plots of calculated spectra (*vide infra*).

7.1.4. Comparison to Electronic Friction Theory

When electronic friction theory[386–388] is combined with the forced oscillator model[73,392] introducing further approximations to obtain excitation spectra,[394,395] the equations directly comparable to Eqs. (7.15a) and (7.15b) read as follows when adapted to the present notation:

$$P^\sigma_\mathrm{FOM;\,el}(\hbar\omega) = \frac{1}{\pi\hbar} \int_{-\infty}^{\varepsilon^\sigma_\mathrm{F}} d\varepsilon \left|\frac{\lambda^\sigma_\mathrm{fric}(\varepsilon^\sigma_\mathrm{F} + \hbar\omega - \varepsilon)}{(\varepsilon_\mathrm{F} + \hbar\omega) - \varepsilon}\right|^2 \left[f(\varepsilon) - f(\varepsilon^\sigma_\mathrm{F} + \hbar\omega)\right] \theta\left(\hbar\omega\right) \tag{7.16a}$$

$$P^\sigma_\mathrm{FOM;\,ho}(\hbar\omega) = \frac{1}{\pi\hbar} \int_{\varepsilon^\sigma_\mathrm{F}}^{+\infty} d\varepsilon \left|\frac{\lambda^\sigma_\mathrm{fric}(\varepsilon - \varepsilon^\sigma_\mathrm{F} + \hbar\omega)}{\varepsilon - (\varepsilon^\sigma_\mathrm{F} + \hbar\omega)}\right|^2 \left[f(\varepsilon^\sigma_\mathrm{F} + \hbar\omega) - f(\varepsilon)\right] \theta\left(-\hbar\omega\right) \,, \tag{7.16b}$$

with

$$\lambda^\sigma_\mathrm{fric}(\varepsilon) = \int_{-\infty}^{\infty} dt \, \sqrt{\eta^\sigma(Q(t))} \, \dot{Q}(t) \, \exp\left(\frac{i}{\hbar}\varepsilon t\right) \tag{7.17}$$

based on the electronic friction coefficient

$$\eta^{\sigma}(Q(t)) = \pi\hbar \sum_{ij} \left| \left\langle \varepsilon_j^{\sigma}(t) \left| \frac{dv_{\mathrm{eff}}^{\sigma}(Q(t))}{dQ} \right| \varepsilon_i^{\sigma}(t) \right\rangle \right|^2 \delta(\varepsilon_j^{\sigma}(t) - \varepsilon_{\mathrm{F}}^{\sigma})\, \delta(\varepsilon_i^{\sigma}(t) - \varepsilon_{\mathrm{F}}^{\sigma}) \quad . \tag{7.18}$$

For the sake of simplicity and better readability but without loss of generality, a one-dimensional description via a reaction coordinate $Q(t)$ is employed here.

Comparing Eq. (7.12) and Eqs. (7.17) and (7.18), the key ingredient to be calculated for both theories is obviously very similar: Matrix elements of the type

$$\left\langle \varepsilon_j^{\sigma}(t) \left| \frac{dv_{\mathrm{eff}}^{\sigma}(Q(t))}{dQ} \right| \varepsilon_i^{\sigma}(t) \right\rangle$$

with $v_{\mathrm{eff}}^{\sigma}(\boldsymbol{Q}(t))$ as defined in Eq. (7.5).[iv] In fact, due to the energy difference entering $\lambda_{\mathrm{fric}}^{\sigma}$ in Eqs. (7.16) can also be understood as representing matrix elements for electronic transitions corresponding to λ_{ij}^{σ}. Their dependance on the electronic structure is less direct, i.e. "only" due to the forced oscillator model connected to the electronic friction coefficient η^{σ}. Additionally, it is important to note, that instantaneous Eigenstates $|\varepsilon_i^{\sigma}(t)\rangle$, $|\varepsilon_j^{\sigma}(t)\rangle$ are used to obtain the latter. Obviously, the present theory can be modified in a straightforward way to use instantaneous Eigenstates as well in Eq. (7.12). This has also been termed Gunnarsson-Schönhammer (GS)-like perturbation theory,[396] inspired by work of the eponyms.[397] However, this leads to conceptual issues with shifts of Eigenvalues in the DFT calculations at different points of a trajectory and technical problems with (relative) phase shifts of the instantaneous Eigenstates. The latter are obtained only up to an arbitrary unitary transformation, which can be dealt with via a mapping scheme in practice. However, experiences of Timmer and Kratzer have shown that (GS)-like perturbation theory leads to unphysical results.[396] Therefore, this approach is not followed here any further.

Apart from that, the main difference between the present and electronic friction theory comes from the fact that squared moduli of the (respective) matrix elements appear before the time integration is carried out in Eqs. (7.17) and (7.18). As discussed extensively by Timmer and Kratzer,[393] this is the reason why Eqs. (7.12), (7.14), (7.15a) and (7.15b) also remain mathematically well defined even in case of an adiabatic spin transition: According to the underlying density-functional theory and corresponding practical calculations, the spin population assigned to the impinging adsorbate typically (at least for hydrogen atoms impinging on different substrates)[73,74,383,384,392,393] is proportional to $\sqrt{|\boldsymbol{Q}(t) - \boldsymbol{Q}_0|}$ around the transition point $\boldsymbol{Q}_0$. This leads to a $\left(\sqrt{|\boldsymbol{Q}(t) - \boldsymbol{Q}_0|}\right)^{-1}$ singularity of $\frac{dv_{\mathrm{eff}}^{\sigma}(Q(t))}{dQ}$, for which the aforementioned main difference is of crucial (mathematical) importance. Nevertheless, in the spirit of mimicking non-adiabatic dynamics, different attempts (based on introduction of a "local" magnetic field or simply constraining total spin of the simulation cell along the same lines as Trail and coworkers[73,392]) have already been investigated to smoothen the spin transition within the present theory.[396]

[iv] The fact that the constant part $v_{\mathrm{eff;\,non-int}}^{\sigma}$ (cf Eq. (7.5)) is not subtracted here obviously does not matter for the derivatives in Eq. (7.12) and Eq. (7.18).

7.1.5. Dissipated Energy

Finally, the energy dissipated into electron-hole pair excitations, which is of key interest here, is obtained as energy-weighted integral over the excitation spectrum Eq. (7.14):

$$E_{\mathrm{eh}}^{\sigma} = \int_{0}^{+\infty} d\varepsilon \; \varepsilon \, P_{\mathrm{ex}}^{\sigma}(\varepsilon) \; . \tag{7.19}$$

(7.20)

Again, a comparable expression is also obtained within electronic friction theory,

$$E_{\mathrm{eh;\,fric}}^{\sigma} = \int_{\boldsymbol{Q}} dQ \; \eta^{\sigma} = \int_{\underline{\tau}\to-\infty}^{\overline{\tau}\to+\infty} dt \; \eta^{\sigma}(\boldsymbol{Q}(t)) \; \dot{\boldsymbol{Q}}(t) \; , \tag{7.21}$$

which additionally would allow to "measure" the dissipated energy for only a part of the considered trajectory $\boldsymbol{Q}(t)$. However, with friction theory not being (directly) applicable, Eq. (7.19) should serve well for providing the desired estimate of energy dissipated into electron-hole pairs.

7.2. Implementation

7.2.1. Trajectory Description: Reaction Coordinate

In previous work, typically strictly one dimensional trajectories $Q(t)$ along the surface normal (conventionally the z-axis) have been considered by studying adsorption of mono-atomic adsorbates with perpendicular impingement over high symmetry sites.[73,74,383,384,392–395] The motion of multi-atomic incoming particles (like the homo-nuclear diatomic molecule O_2) is in contrast less likely to be reducible to a single spatial dimension. To keep the input of the present implementation scalar, an effectively one-dimensional description of coordinates and velocities, i.e. a suitable reaction coordinate Q, is employed. A canonical choice is the arc length associated with a given trajectory $\boldsymbol{Q}(t)$:

$$Q(t) = \int_{\underline{\tau}}^{t} d\tau \; \|\Delta \boldsymbol{Q}(\tau)\|_2 \tag{7.22}$$

However, in case of negligible changes of relative coordinates within the adsorbate, Eq. (7.22) does not provide immediately obvious physically meaningful information about the trajectory of an adsorbate as it scales with the number of atoms of the latter. For a stiff diatomic molecule like O_2 such dominantly rigid motion is rather common unless considering large vibrational excitations e.g. during scattering at high kinetic energies. Therefore, it is interesting to note that Eq. (7.12) and all its descendants obviously remain invariant if trajectories are described by scaled and shifted coordinates and consistent velocities

$$\boldsymbol{Q}(t) \quad \longrightarrow \quad \tilde{\boldsymbol{Q}}(t) \equiv \boldsymbol{Q}_0 + \alpha \, \boldsymbol{Q}(t) \tag{7.23a}$$

$$\dot{\boldsymbol{Q}}(t) \quad \longrightarrow \quad \dot{\tilde{\boldsymbol{Q}}}(t) \equiv \alpha \, \dot{\boldsymbol{Q}}(t) \quad . \tag{7.23b}$$

When $\alpha = \frac{1}{\sqrt{N_{\mathrm{ads}}}}$ for an adsorbate consisting of N_{ads} atoms, the corresponding arc length $\tilde{Q}(t)$ then conveniently corresponds to the absolute distance traveled by the center of mass of the adsorbate (or likewise any of its constituents). Furthermore, the reaction coordinate description

also allows to include motion of the substrate atoms if the frozen surface approximation would eventually be lifted.[396] In practice, trajectories are typically obtained via molecular dynamics on a (Born-Oppenheimer) potential energy surface (PES) based on an interpolation to DFT energies – here as detailed in Chapter 6. This is computationally much less involved (once the PES has been obtained) than anything related to the calculation of the required matrix elements. Coordinates $\boldsymbol{Q}(t)$ and velocities $\dot{\boldsymbol{Q}}(t)$ as a function of time can hence be easily obtained on a rather dense grid. The thus induced discretization of the reaction coordinate Q as given by Eq. (7.22) (potentially using the aforementioned transformation)

$$Q(t_n) \approx \sum_{t_i \leq t_n} \|\boldsymbol{Q}(t_{i+1}) - \boldsymbol{Q}(t_i)\|_2 \tag{7.24}$$

is hence accordingly accurate. For the velocities $\dot{Q}$ simple projections along directions of coordinate differences,

$$\dot{Q}(t_n) \approx \frac{\boldsymbol{Q}(t_{n+1}) - \boldsymbol{Q}(t_n)}{\|\boldsymbol{Q}(t_{n+1}) - \boldsymbol{Q}(t_n)\|_2} \cdot \dot{\boldsymbol{Q}}(t) \tag{7.25}$$

have been used in the following and found to be sufficiently accurate for present purposes. In principle, higher order correction to the latter can be taken into account by also including the influence of instantaneous accelerations $\ddot{\boldsymbol{Q}}\Delta t$ via the calculated forces.[396] Due to the choice of MD integrator, the discretization grid might neither be uniform nor contain the exact points (but normally more and others) for which electronic structure data (allowing the calculation of matrix elements) is explicitly available. This can be easily remedied via interpolation, since reaction coordinate Q and velocity $\dot{Q}$ typically vary rather smoothly with time. Therefore, t_n, $Q(t_n)$ and $\dot{Q}(t_n)$ are expected to be given as input, allowing to relate and interpolate the latter two as required for the evaluation of the time integrals defining λ_{ij} in Eq. (7.12). The trajectory input needs to end at the turning point (defining a half round trip), easily identified for example by change of sign of the velocities $\dot{Q}$.

7.2.2. Matrix Elements

The key computational challenge is the evaluation of the matrix elements occurring in Eq. (7.12) along trajectories which are parametrized by reaction coordinates $Q(t)$ as described in the previous section. While the Hellmann-Feynman theorem (cf Eq. (2.12)) allows for a convenient evaluation of parametric derivatives of the *total energy* (e.g. with respect to nuclear degrees of freedom resulting in forces), a similarly straightforward procedure is no longer possible for matrix elements

$$\begin{aligned}\left\langle \varepsilon_j^\sigma \middle| \frac{dv^\sigma(\boldsymbol{Q}(t))}{dt} \middle| \varepsilon_i^\sigma \right\rangle &= \left\langle \varepsilon_j^\sigma \middle| \boldsymbol{\nabla}_{\boldsymbol{Q}} v^\sigma(\boldsymbol{Q}(t)) \middle| \varepsilon_i^\sigma \right\rangle \cdot \dot{\boldsymbol{Q}}(t) \\ &= \left[\frac{\partial}{\partial Q} v_{ij}^\sigma\right](Q(t)) \cdot \underbrace{\frac{\dot{\boldsymbol{Q}}(t)}{\|\dot{\boldsymbol{Q}}(t)\|_2} \cdot \frac{\dot{\boldsymbol{Q}}(t)}{\|\dot{\boldsymbol{Q}}(t)\|_2}}_{=1} \cdot \dot{Q}(t) \quad ,\end{aligned} \tag{7.26}$$

involving (a derivative of) the potential only. Also in density-functional perturbation theory (DFPT),[242,398] higher order derivatives of the *total energy* are the target quantity. In those cases, the response of the density and wave functions need to be considered, leading to a "plethora of new terms" which do not occur when the Hellmann-Feynman theorem is

applicable.[243] Therefore, the derivative of the potential appearing in Eq. (7.26) has to be evaluated numerically.

In the nowadays widely used theory of inelastic tunneling (IET), originally developed by Lorente and Persson,[119,399] the matrix elements $\frac{\partial}{\partial Q} v_{ij}^{\sigma}$ appearing in Eq. (7.26) are required as well. This is not surprising, as one of the ingredients of the former is electronic friction theory,[386–388] whose similarities to the present approach have already been pointed out in the previous section. In the rapidly growing IETS community,[390,400–405] these matrix elements are usually calculated with the original VASP[v] implementation of Lorente and Persson:[119,399]

$$\frac{\partial}{\partial Q} v_{ij}^{\sigma} \approx \begin{cases} 0 & \boldsymbol{k}_{\parallel,i} \neq \boldsymbol{k}_{\parallel,j} \\ \Delta\varepsilon_i^{\sigma} & \boldsymbol{k}_{\parallel,i} = \boldsymbol{k}_{\parallel,j} \ , \ n_i = n_j \\ (\varepsilon_i^{\sigma} - \varepsilon_j^{\sigma}) \left\langle \varepsilon_j^{\sigma} | \Delta\varepsilon_i^{\sigma} \right\rangle & \boldsymbol{k}_{\parallel,i} = \boldsymbol{k}_{\parallel,j} \ , \ n_i \neq n_j \end{cases} \tag{7.27}$$

Here n_i and $\boldsymbol{k}_{\parallel,i}$ are the explicit band index n and explicit components parallel to the surface of the $\boldsymbol{k}$-point index, respectively, of the (Bloch) state $|\varepsilon_i\rangle$ otherwise collectively denoted by i as indicated before in Section 7.1.2 (see also Section 2.6, in particular Eq. (2.39)). Eq. (7.27) is motivated by understanding $\frac{\partial}{\partial Q} v_{ij}^{\sigma}$ as the non-adiabatic couplings in the electronic system due to the kinetic energy operator for the nuclei, which are neglected within the Born-Oppenheimer approximation. They are given by Eq. (2.6) in Section 2.2 and discussed there in more detail. A linear approximation in the displacements along Q yields Eq. (7.27), relating $\frac{\partial}{\partial Q} v_{ij}^{\sigma}$ approximately to first order changes in (Kohn-Sham) Eigenstates and Eigenvalues (as indicated by Δ),[vi] which was originally proposed by Head-Gordon and Tully.[31,406] The neglect of *inter*-$\boldsymbol{k}$-point transitions is detailed in the following paragraph as addressed by Trail and coworkers.[389] Obviously, Eq. (7.27) incorporates changes of the electronic structure along Q and hence cannot be applied in the present context relying on unperturbed substrate states. Accordingly, a convenient reuse of the aforementioned implementation, hence saving own tedious efforts if it was available, is not possible. A comparison to other approaches described in the following, addressing both systematic and practical approximations inherent to this ansatz might thus be interesting and important future work.

When applying electronic friction theory in the context of gas-surface dynamics, Trail and coworkers have chosen a more direct way[389] to obtain the required matrix elements

$$\frac{\partial}{\partial Q} v_{ij}^{\sigma} \approx \left\langle \varepsilon_j^{\sigma} \left| \frac{\Delta V(\boldsymbol{Q})}{\|\Delta \boldsymbol{Q}\|_2} \right| \varepsilon_i^{\sigma} \right\rangle \quad . \tag{7.28}$$

Here derivatives of the potential are approximated by finite differences and overlaps mediated by the such obtained field are calculated. When using periodic boundary conditions, apart from the electronic states $|\varepsilon_i^{\sigma}\rangle$ and $\left|\varepsilon_j^{\sigma}\right\rangle$ also $\frac{dv^{\sigma}}{dt} = v^{\sigma\prime}$ obviously has the periodicity of the employed simulation cell. The matrix elements $\frac{\partial}{\partial Q} v_{ij}^{\sigma}$ can thus be written without any approximation in

[v] See http://cms.mpi.univie.ac.at/vasp.

[vi] In practice, the latter are obtained via finite differences, and proper care must be taken when using ultrasoft pseudopotentials,[119] and for potentially different phases of equivalent Eigenstates obtained from the different DFT calculations used to obtain the finite differences.[403]

the following (discrete) plane wave representation (cf Eq. (2.40) in Section 2.6):

$$\begin{aligned}\left\langle \varepsilon_j^\sigma \left| v^{\sigma\,\prime} \right| \varepsilon_i^\sigma \right\rangle &= \sum_{\boldsymbol{G}_i}\sum_{\boldsymbol{G}_j}\sum_{\boldsymbol{G}_v} \int d\boldsymbol{r} \left(c_{\boldsymbol{G}_j}^{\sigma\,\boldsymbol{k}_j\,n_j}\right)^* \; c_{\boldsymbol{G}_i}^{\sigma\,\boldsymbol{k}_i\,n_i} \; v_{\boldsymbol{G}_v}^{\sigma\,\prime} \; \mathrm{e}^{-i(\boldsymbol{G}_j+\boldsymbol{k}_j)\boldsymbol{r}+i(\boldsymbol{G}_i+\boldsymbol{k}_i)\boldsymbol{r}+i\boldsymbol{G}_v\boldsymbol{r}} \\ &= \sum_{\boldsymbol{G}_i}\sum_{\boldsymbol{G}_j}\sum_{\boldsymbol{G}_v} \left(c_{\boldsymbol{G}_j}^{\sigma\,\boldsymbol{k}_j\,n_j}\right)^* \; c_{\boldsymbol{G}_i}^{\sigma\,\boldsymbol{k}_i\,n_i} \; v_{\boldsymbol{G}_v}^{\sigma\,\prime} \; 2\pi\delta\left(\underbrace{(\boldsymbol{G}_i-\boldsymbol{G}_j+\boldsymbol{G}_v)}_{\text{lattice vector}} - (\boldsymbol{k}_i-\boldsymbol{k}_j)\right) \\ &\neq 0 \quad , \quad \text{only if } \boldsymbol{k}_i \neq \boldsymbol{k}_j\end{aligned} \tag{7.29}$$

As before, $\boldsymbol{k}_i$ and n_i are the explicit $\boldsymbol{k}$-point and band index, respectively, of the (Bloch) state $|\varepsilon_i\rangle$ otherwise collectively denoted by i. The inequality sign holds strictly since $\boldsymbol{G}_i-\boldsymbol{G}_j+\boldsymbol{G}_v$ is a reciprocal lattice vector and $\boldsymbol{k}_i$ and $\boldsymbol{k}_j$ are out of the first Brillouin zone, only the center of which within the common choice is a reciprocal lattice vector.[vii] Therefore, as Trail and coworkers pointed out,[389] only *inter*-, but no *intra*-$\boldsymbol{k}$ transitions contribute when considering $\frac{\partial}{\partial Q}v_{ij}^\sigma$ for a periodic overlayer. They also proposed a way to obtain the corresponding matrix elements for an isolated adatom according to a perturbation ansatz.[389] For the rather small simulation cells they used, this indeed makes a considerable difference. Timmer and Kratzer have used (in the beginning) the same basic numerical evaluation given by Eq. (7.28), but within larger periodic simulation cells,[393] hence not taking such transitions into account. This is completely in line with previous work e.g. within the approach of Lorente and coworkers as indicated in the previous paragraph (see Eq. (7.27)), or the TD-DFT calculations by Lindenblatt and coworkers.[74,383,384])

Along those lines, in this work, only *inter*-$\boldsymbol{k}$ transitions are considered. For a general trajectory $\boldsymbol{Q}(t)$, Eq. (7.26) is evaluated using the reaction coordinate description $Q(t)$ via

$$\left\langle \varepsilon_j^\sigma \left| \frac{dv^\sigma(\boldsymbol{Q}(t))}{dt} \right| \varepsilon_i^\sigma \right\rangle \approx \frac{\partial}{\partial Q} M_{ij}^\sigma(Q)\cdot\dot{Q}(t) \quad , \tag{7.30}$$

where discretizations of Q and $\dot{Q}$ are obtained using Eq. (7.24) and Eq. (7.25), respectively. $\frac{\partial}{\partial Q}M_{ij}^\sigma(Q)$ is obtained by first calculating matrix elements $\left\langle \varepsilon_j^\sigma \,|\, v_{\text{eff}}^\sigma(Q) \,|\, \varepsilon_i^\sigma \right\rangle$ directly at points $Q(t_n)$ for which electronic structure data is available, which hence needs to be specified accordingly in the input. Afterwards, each matrix element is interpolated along Q and finally, the analytical derivative of the interpolation gives $\frac{\partial}{\partial Q}M_{ij}^\sigma(Q)$. According to Eq. (7.5), this also leads to the required matrix elements $\frac{\partial}{\partial Q}v_{ij}^\sigma$ in the end, allowing evaluation at arbitrary $Q(t)$ as required in the time integrals defining λ_{ij} in Eq. (7.12). The quality of the interpolation can be easily checked by trying different one-dimensional interpolation schemes and calculating electronic structure data for more points along the trajectory in order to increase the number of explicitly available matrix elements. The crucial advantage of this strategy is that it allows for efficient use of existing infrastructure in most plane wave codes, because the derivative of the potential does not need to be constructed in a form which can be used for acting on the states directly – contrary to Eq. (7.28). This is particularly useful (if not essential) when dealing with non-local and/or ultrasoft pseudopotentials. Of course, the matrix elements calculated for all $Q(t_n)$ have to be kept in memory first before the interpolation and its derivative are formed, resulting in higher memory demands than for the other schemes. In fact, part of the initial

[vii] This can also be understood as conservation of crystal momentum.

motivation for the application of the forced oscillator model in combination with electronic friction theory has been to avoid this.[73,392] At least nowadays, however, this can be efficiently dealt with also by the virtue of (memory) parallelization (cf Appendix C.1.2). This might still be technically inconvenient, but is no longer a conceptual problem.

After proposing these practical improvements to the original authors,[407] they have been gratefully accepted, stimulated a rewrite from scratch of their first implementation[396] and acknowledged in their latest study.[394] They emphasize a performance improvement by about a factor of three with their (not explicitly parallelized) implementation in the plane wave code PWscf,[407] part of the Quantum ESPRESSO[viii] suite of programs. Additionally, they also report reduced numerical instabilities in the problematic regions of the spectra given by Eqs. (7.14), (7.15a) and (7.15b) in Eq. (7.12) above and apparently did not encounter any troubles with memory.

Meanwhile, the improved approach has already been implemented into the Castep code and parallelized to efficiently calculate electron-hole pair spectra for several different trajectories for the present system, which are presented in Section 7.3.1. Details about this implementation are described in Appendix C.1 in Appendix C.

7.2.3. Tests

In order to test the present implementation, it was applied to the system originally studied by Timmer and Kratzer: A half round trip of a hydrogen atom impinging on a top site on Al(111).[393] Compared to the present case, this system is rather benign, resulting in modest computational effort to recalculate everything from scratch. This effort has been reduced further by switching from norm-conserving pseudopotentials (as originally used) to ultrasoft pseudopotentials. In principle, the loss of orthonormality of the numerical representation of the substrate Kohn-Sham Eigenstates could lead to problems with the potential mediated overlaps in Eq. (7.26). Therefore, the application to the H on Al(111) can also be seen as a pragmatic test of this issue, before spending additional conceptual and/or implementation efforts.[ix] Furthermore, valuable experiences with the numerical stability of the several numerical integration schemes in combination with the density of calculated matrix elements along a trajectory and concomitant interpolation quality could be obtained. Details about the numerical integration in the present implementation are given in Appendix C.1.1 in Appendix C. Therein, Appendix C.2 also illustrates extensively that the results of the original authors are excellently reproduced – as to be expected from *ab initio* calculations when numerical errors are well controlled and a straightforward application of the method with ultrasoft pseudopotentials does not seem to be problematic in general. During this testing, the `QAGS` adaptive integrator has been found to be numerically more stable than the direct (analytical) integration of the interpolation splines for the integrand in Eq. (7.12) employed by Timmer and Kratzer. (also see Appendix C.1.1, in particular Eq. (C.1)) Thanks to the algorithmic improvements described in Section 7.2.2 and parallelism, the evaluation of all properties given by Eqs. (7.14), (7.15a), (7.15b) and (7.19) for the aforementioned system could be reduced from about a week within the original implementation[407] to a few hours. Therefore, after having gained trust in the present efficient implementation, it is now applied to the computationally more demanding

[viii] Licensed under GPL and available from `http://www.quantum-espresso.org`.

[ix] Such efforts could go along the lines of special treatment with the S-operator as vaguely indicated by Lorente and Persson[119] or even include a PAW-like reconstruction of all-electron wave functions for the states following Blöchl.[408]

case of present interest: O_2 on Pd(100).

7.3. Results and Discussion

7.3.1. Electron-Hole Pair Spectra and Dissipated Energies

Using the interpolated six-dimensional potential energy surface V_{6D} presented in Chapter 6, trajectories starting over four different high symmetry sites have been calculated. For each trajectory, the starting point is at a center of mass distance of $Z_0 = 6\,\text{Å}$ above the surface, where the adsorbate-substrate interaction $v^\sigma(\boldsymbol{Q})$ has already well decayed to essentially zero. In all cases, the molecules are reflected, such that a half round trip as described in Section 7.1.1 can be consistently defined.

As already indicated initially in Section 7.0.2, electronic structure data obtained during the interpolation of the six-dimensional potential energy surface could largely be reused. It has been calculated for an increasing point density along the trajectories until resulting spectra did not change significantly any more. Since ultrasoft pseudopotentials have been used throughout, it has been verified first whether their effect on the resulting dissipated spectra and (even more important) dissipated energies is as negligible for this system as for H on Al(111) detailed in the Appendix C. As to be expected, a quantitative inspection shows that the overlap of the Kohn-Sham states of the clean palladium surface is larger than in case of aluminum. Therefore, for one trajectory, excitation spectra have been calculated based on non-spin polarized electronic structure once obtained with the ultrasoft and once obtained with a norm-conserving pseudopotential for the Pd atoms. The latter has been obtained with the internal "on-the-fly" pseudopotential generator available within CASTEP. With reasonable efforts, a "good" potential could only be obtained by including the $4s$ and $4p$ semi-core states as valence resulting in a total of 18 pseudized electrons. According to common practice the local component has been put into the f-channel. Several pseudization radii r_c and projector optimization settings have been tested. Finally, pseudization radii $r_c^{\text{local}} = r_c^{\text{non-local}} = 2.1\,\text{Bohr}$ for the local and non-local components and $r_c^{\text{inner}} = r_c^{\text{core}} = 1.6\,\text{Bohr}$ for the augmentation functions and pseudo-core charge together with a suitable kinetic energy based projector optimization have been chosen as best result.[x] This pseudopotential is harder than the otherwise employed ultrasoft potential and hence requires a plane wave cut off energy of 500 eV. It yields a lattice constant of $a^{NC}_{\text{Pd-fcc}} = 3.92\,\text{Å}$, slightly smaller than the one obtained with the latter ($a^{NC}_{\text{Pd-fcc}} = 3.93\,\text{Å}$), which has not been compensated for in the slab geometries. Of course, the trajectories themselves are artificial, as electronic structure data is obtained for a different Born-Oppenheimer surface inconsistent with the one used for the motion of the nuclei. Nevertheless, this allows to scrutinize the effect of ultrasoft pseudopotentials for the present purposes. While the shape of the spectra is qualitatively very similar in both cases, resulting dissipated energies differ by several millielectron volts in case of the norm-conserving pseudopotential (i.e. 20 % to 40 % for the considered trajectory). Therefore, for the present system the initial concern hence appears to be justified *a posteriori* and has to be kept in mind. Nevertheless, for the desired order of magnitude estimate of energy dissipated into electron-hole pair excitations, this error margin is still be sufficient without further ado.

In particular, when switching to the actual spin-polarized calculations, it turns out that the

[x] Corresponding "generation string" for the internal "on-the-fly" pseudopotential generator available within CASTEP: `3|2.1|2.1|1.6|20|22|23|40N:50N:41N:42N(qc=6){5s0.05}[]`

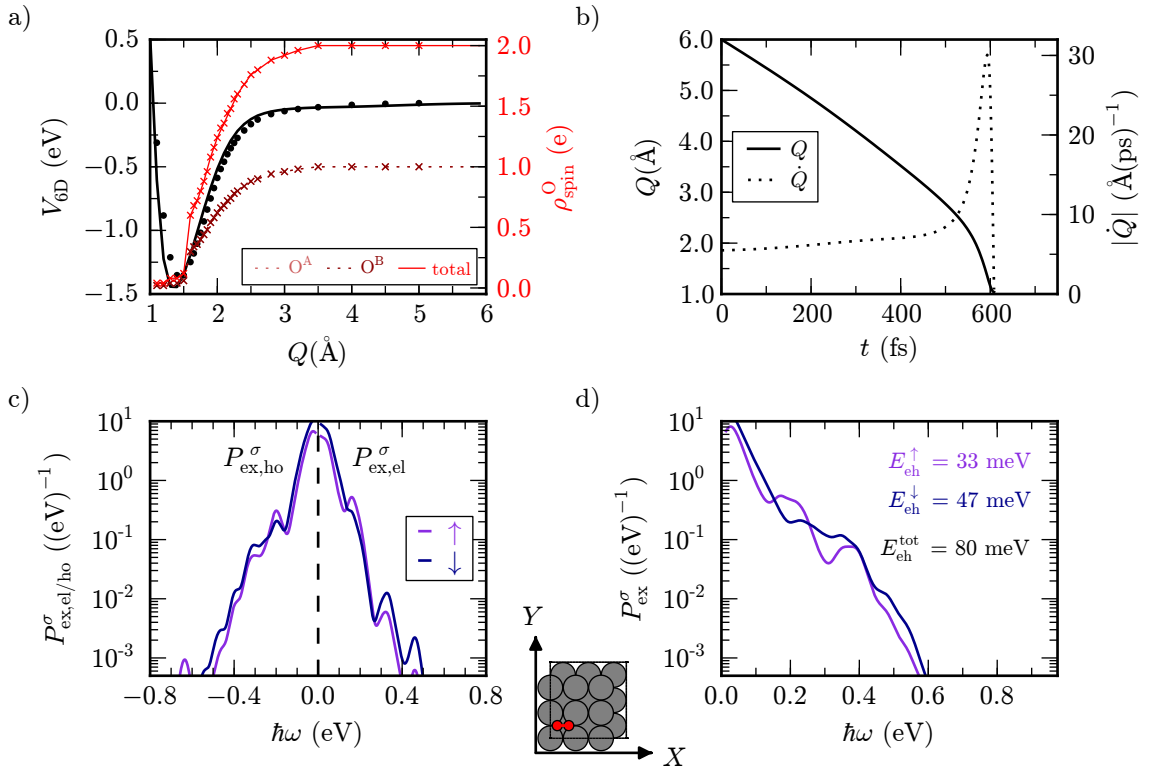

Figure 7.2.: Electron-hole pair excitations for an O_2 molecule starting at a height of 6 Å above a *hollow* site of the Pd(100) surface with the molecular axis oriented parallel to the latter in X direction (cf inset). The initial kinetic energy is 50 meV corresponding to an initial velocity $\dot{Q}(t=0) = 5.5\,\text{Å}\,\text{fs}^{-1}$. a) Interaction potential of molecule and surface in the frozen surface approximation V_{6D} along the trajectory given by the reaction coordinate Q (left axis). Black dots indicate points for which electronic structure data has been calculated and employed for the determination of the spectra in c) and d). The black line indicates the six-dimensional neural network interpolation used to obtain the trajectory shown in b) (solid line, left axis) and (absolute value of) the corresponding velocity (dotted line, right axis). Furthermore, the adiabatic spin transition of the oxygen molecule along the former is shown in red (right axis) via projections of the spin density onto the two constituting oxygen atoms O^A and O^B (dotted lines, shades of dark red) and their sum (solid line, light red). Projections (calculated at points indicated by crosses) are based on the plane-wave implementation[409,410] of the population analysis scheme due to Mulliken[411] available in CASTEP. Lines are only to guide the eye. c) Separate electron (right) and hole (left) spectra $P^{\sigma}_{ex,el}(\hbar\omega)$ and $P^{\sigma}_{ex,ho}(\hbar\omega)$ according to Eqs. (7.15a) and (7.15b). d) Electron-hole pair spectrum $P^{\sigma}_{ex}(\hbar\omega)$ given by Eq. (7.14) together with resulting dissipated energies according to Eq. (7.19) (rounded to full meV). All spectra are for a half round trip with energies $\hbar\omega$ relative to the Fermi energy. Both majority (↑, violet) and minority (↓, blue) spin channels are shown. For details see text.

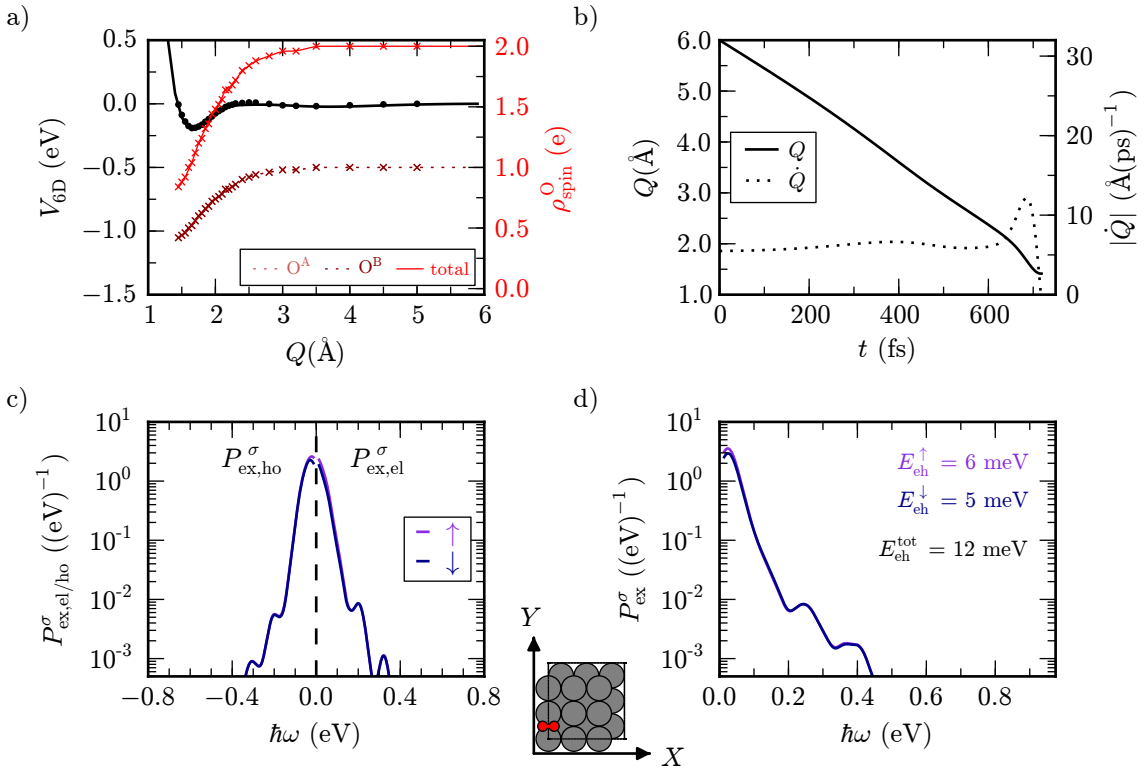

Figure 7.3.: Electron-hole pair excitations for an O_2 molecule starting at a height of 6 Å above a *bridge* site of the Pd(100) surface with the molecular axis oriented parallel to the latter in X direction (cf inset). The initial kinetic energy is 50 meV corresponding to an initial velocity $\dot{Q}(t=0) = 5.5\,\text{Å}\,\text{fs}^{-1}$. For details see text and caption of Fig. 7.2, which contains equivalent data to those shown here.

description of the substrate states is even more important: Dissipated energies can be larger by several hundreds of millielectron volts (i.e. even several 100 % in relative terms) when the unphysical electronic structure corresponding to a ferromagnetic substrate is used compared to calculations with non-spin-polarized description of the latter. This holds in particular if changes of the spin-density due to the adsorbate-substrate interaction along a trajectory are large. Therefore, for all the results presented in the following, matrix elements have been evaluated using the Kohn-Sham states of a non-spin polarized clean Pd(100) surface "cloned" into both spin channels of the (spin-polarized) adsorption calculations including the O_2 molecule. The fact that only the derivative of the potential enters Eq. (7.12) can be seen as particular (additional) virtue of the employed scheme for this specific system: It allows to exploit cancellation of errors in differences (as already in case of the energetics) – quite in contrast to a conventional treatment even within TD-DFT (should it become computationally tractable).

The results for the four considered trajectories of an oxygen molecule with an initial kinetic energy of 50 meV, initially aligned parallel to the surface over hollow (*h-para*) and bridge (*b-para*) site and perpendicular over hollow (*h-perp*) and top (*t-perp*) site are shown in Figures 7.2 to 7.5, respectively. Their corresponding reaction coordinates Q and velocities $\dot{Q}$ as a function of time are depicted in Figs. 7.2b to 7.5b The excellent quality of the six-dimensional interpolation of the (nuclear) frozen surface potentials V_{6D} used to determine the latter is underscored (once

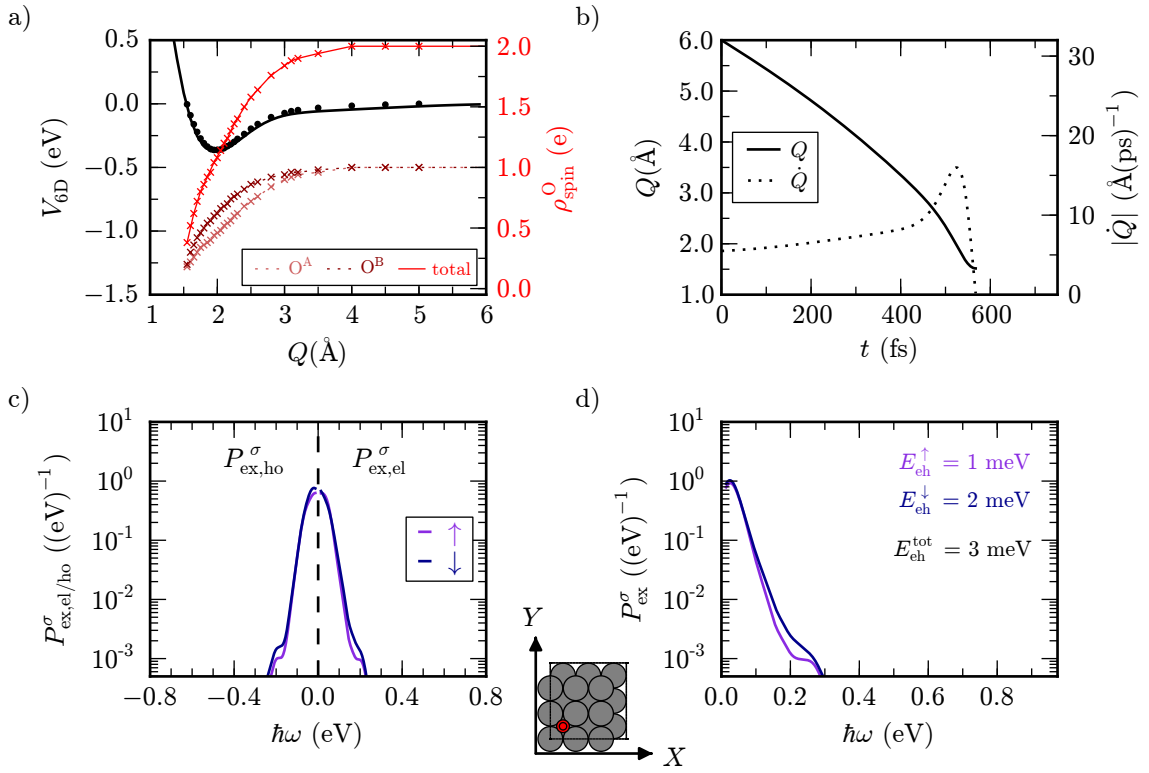

Figure 7.4.: Electron-hole pair excitations for an O_2 molecule starting at a height of 6 Å above a *hollow* site of the Pd(100) surface with the molecular axis oriented perpendicular to the latter. The initial kinetic energy is 50 meV corresponding to an initial velocity $\dot{Q}(t=0) = 5.5\,\text{Å}\,\text{fs}^{-1}$. For details see text and caption of Fig. 7.2, which contains equivalent data to those shown here.

more) by Figs. 7.2a to 7.5a: Energetics of points where the electronic structure data is used for the calculation of matrix elements for the electron-hole pair spectra have not necessarily been included in the training set of the neural network interpolation, but are matched extremely well – except for highly repulsive areas not affecting the dynamics. The same subset of figures also illustrates that the spin transition of the oxygen molecule in the adiabatic picture not only depends on the penetration depth, but also strongly on lateral position and orientation. In particular, only the two trajectories starting over the hollow site (*h-para* and *h-perp*) seem to cross the spin transition point Q_0 (cf Figs. 7.2a and 7.4a), resulting in a $\sqrt{Q-Q_0}$-like decay of the oxygen-projected spin density $\rho^{O}_{spin} = \rho^{O}_{\uparrow} - \rho^{O}_{\downarrow}$ like in case of hydrogen described above in Section 7.1.4. On the other hand, *b-para* reaches a minimum Z-height comparable to *h-perp* (cf Figs. 7.3b and 7.4b), but the projected spin density on both oxygen atoms remains nearly twice as large (cf Figs. 7.3b and 7.4b). In the plots of the separate spectra for electrons and holes in Figs. 7.2c to 7.5c the range of $\hbar\omega \leq 10\,\text{meV}$ corresponding to the width of the employed Fermi broadening in the electronic self-consistency has been omitted for numerical reasons – as already indicated in Eq. (7.12), The same holds for the electron-hole pair spectra according to Eq. (7.14), which are shown in Figs. 7.2d to 7.5d, together with the dissipated energies consequently obtained using Eq. (7.19).

Turning to the energy dissipation in more detail, first of all it is important to note that E^{tot}_{eh}

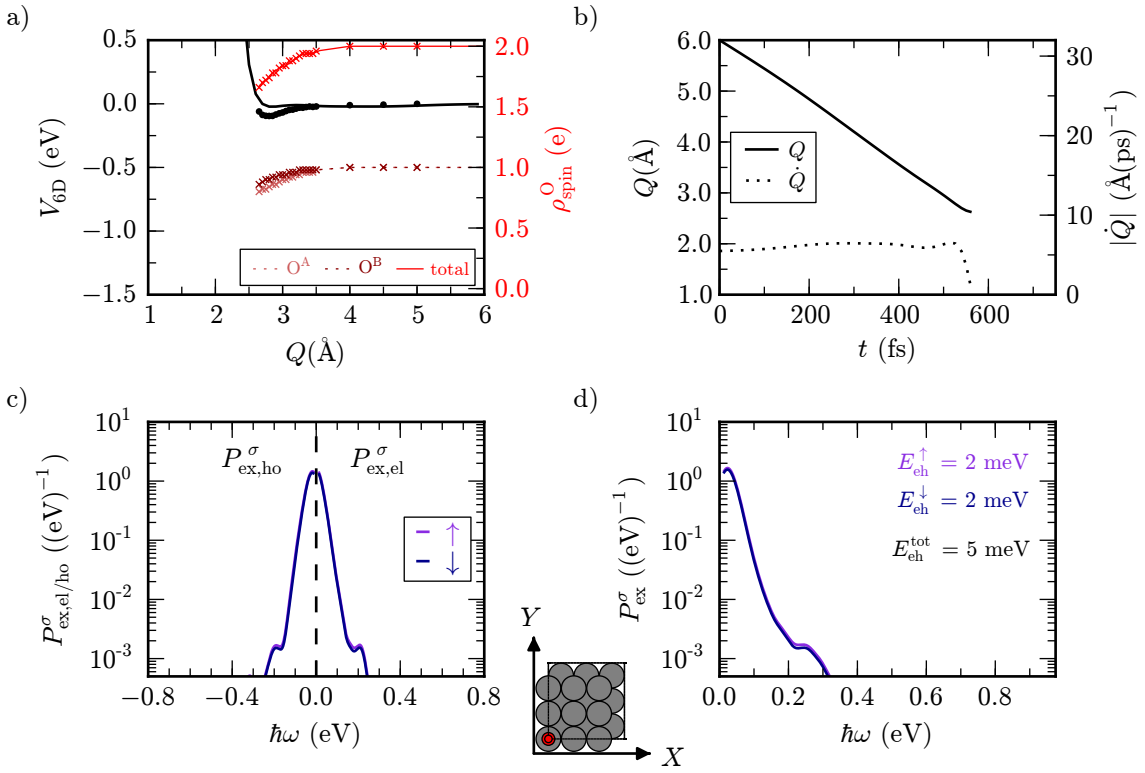

Figure 7.5.: Electron-hole pair excitations for an O_2 molecule starting at a height of 6 Å above a *top* site of the Pd(100) surface with the molecular axis oriented perpendicular to the latter. The initial kinetic energy is 50 meV corresponding to an initial velocity $\dot{Q}(t=0) = 5.5\,\text{Å fs}^{-1}$. For details see text and caption of Fig. 7.2, which contains equivalent data to those shown here.

does not exceed at most 5 % of the chemisorption energy of 2.6 eV for all trajectories considered here. This apparently weak perturbation justifies the use of unperturbed trajectories and substrate states a posteriori. According to the analysis presented in Section 6.3.2 the trajectory *h-para* propagates into the main entrance channel for dissociation. Although it is reflected, it can be considered of biggest statistical relevance in the context of energy dissipation. Among the four trajectories considered here, the total dissipated energy of 80 meV per half round trip is largest for this trajectory. Hereby, dissipation in the minorty spin channel (spin ↓) is significantly stronger, which will be discussed in more detail in Section 7.3.2. The absolute value for the total dissipated energy is similar to what has been obtained for atomic hydrogenon various substrates (and by various theoretical methods) impinging at an on-top site[74,382,393]. This is remarkable, since Lindenblatt and co-workers have obtained an absolute value of about one order of magnitude larger for the impingement of H on the chemically much more favored fcc site on Al(111) by non-spin polarized TD-DFT calculations.[384] The same general trend is observed when comparing all the other trajectories with considerably less attractive interaction potential V_{6D} to *h-para*, resulting in correspondingly lower dissipated energies altogether. However, comparing *b-para* and *h-perp* shows that also the orientation of the molecule matters: Both trajectories result from a similarly repulsive interaction potential, but energy dissipation to electron hole pairs is by a factor of four less for the latter. This constitutes an important

confirmation of one of the key results of Juaristi and coworkers[44] obtained within electronic friction theory combined with LDFA for other systems including diatomics: The importance of the "high" dimensionality of the molecule-substrate-interaction also prevails with the present (more accurate) model of electron-hole pair excitations.

Finally, the velocity dependence has been tested for *h-para* by raising the initial kinetic energy to 400 meV corresponding to a nearly tripled initial velocity of $\dot{Q}(t = 0) = 15\,\text{Å}\,\text{fs}^{-1}$. The corresponding trajectory and spectra (not shown) do not change qualitatively. Energies dissipated into electron-hole pairs are increased by around a factor of 1.3, resulting in a total of about 100 meV. Hence this seems to a reasonable estimate for the "most interesting" trajectory within a thermally accessible range of impinging molecules. There also remains a higher amount of energy dissipation in the minority spin channel (spin ↓) at practically the same ratio as in Fig. 7.2d. Compared to the results for N_2 on W(110) based on electronic friction theory with friction coefficients obtained from LDFA,[44] the relative increase of the total dissipated energy is much less. A similar increase of the incidence kinetic energy leads (on average) to a much larger energy dissipation there, more similar to the increase of the initial kinetic energy. This might indicate caution also when determining dissipated energies based on electronic friction theory and LDFA – but of course a more extensive comparison would be required to solidify this statement.

7.3.2. Spin Transition

Having a closer look at the electron-hole pair spectra for *h-para* as shown in Figs. 7.2c and 7.2d, the already mentioned slight asymmetry between electrons and holes deserves further attention. The fact that excitations are stronger in the spin minority channel (spin ↓) is particularly interesting in light of the spin transition of the O_2 molecule, which, according to Fig. 7.2a, is complete in case of *h-para*. The same effect also seems to be present, albeit much weaker, for *h-perp* – correlating with the aforementioned similar degree of spin transition in this case.

Timmer and Kratzer have obtained nothing comparable for the spectra of H on Al(111).[393] Only the spectra for the same system in the work of Lindenblatt and Pehlke[74] show something along the same lines: Abundances of excited electrons and holes in the spin majority and minority channel, respectively. However, since the TD-DFT based dynamics are intrinsically non-adiabatic and the spectra are obtained *a posteriori* by relaxation back to the electronic ground state, this is not surprising. It can be easily understood by propagation on excited potential energy surfaces during the non-instantaneous spin transition. In contrast, the present description is adiabatic, and transitions are evaluated based on unperturbed substrate states. Nevertheless, a closer look at the electronic structure can provide further insights – in particular for *h-para* because of its aforementioned large statistical relevance for adsorption.

The electronic structure of an O_2 molecule including its appearance in a density-functional theory picture of Kohn-Sham orbitals has been extensively discussed e.g. by Behler[48,76] and Carbogno.[109] Briefly, from the highest Kohn-Sham orbitals, the $2\sigma_\text{p}$ and the doubly-degenerate $2\pi_\text{p}$ are filled in both spin channels with six electrons in total. The also doubly-degenerate $2\pi_\text{p}^*$ on the other hand is occupied by two electrons in the majority spin channel only, which is spin ↑ in the present case, thus resulting in the spin-polarized "triplet" ground state within the picture of Kohn-Sham DFT. In the present work, this picture is reproduced at the beginning of a trajectory when the interaction with the substrate is negligible as illustrated in Fig. 7.6. The 1s state of each oxygen atom is part of the frozen core of the pseudopotential, so that the $1\sigma_\text{s}$ and $1\sigma_\text{s}^*$ orbitals of the oxygen molecule with the total of four paired electrons contained therein do not appear explicitly in the present calculations. Furthermore, the $2\sigma_\text{s}$ and $2\sigma_\text{s}^*$ are

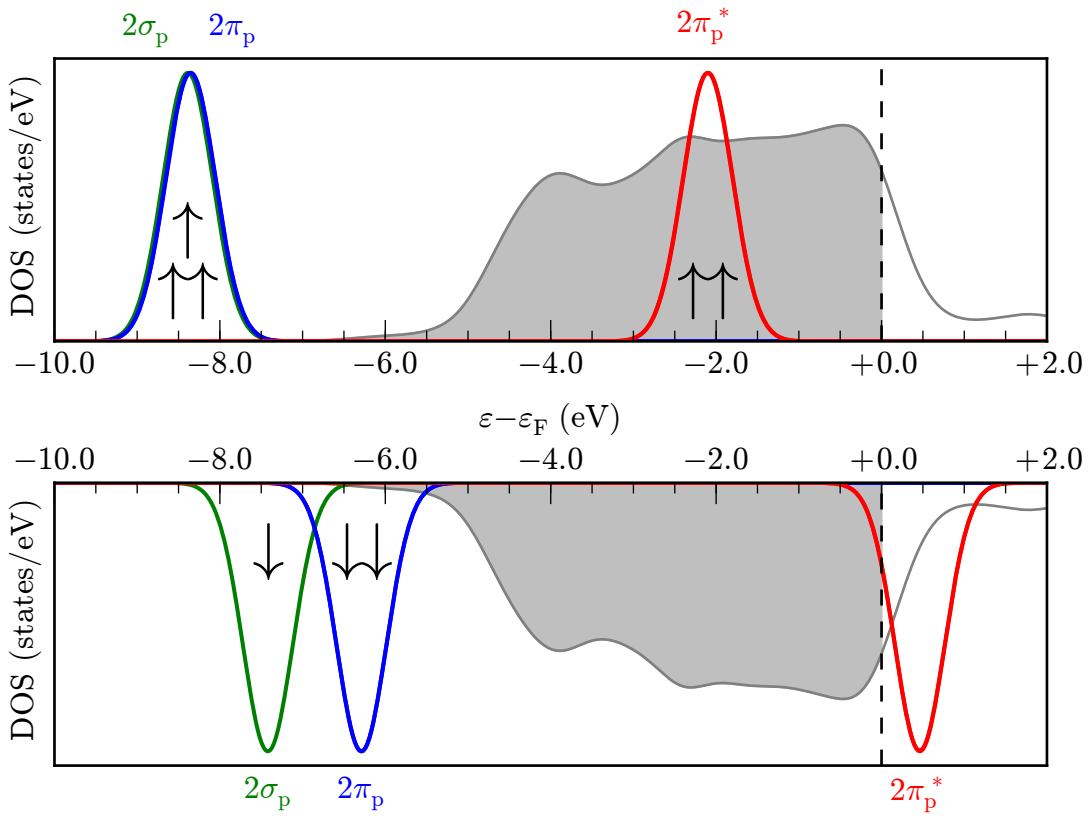

Figure 7.6.: Density of states including projections onto molecular orbitals of the O_2 molecule at the beginning ($t = 0$) of the *h-para* trajectory (cf Fig. 7.2) for both spin ↑ (majority spin channel, upper panel) and spin ↓ (minority spin channel, lower panel). The projections have been obtained according to Eq. (7.31) for $|2\sigma_p\rangle \otimes \{|\uparrow\rangle, |\downarrow\rangle\}$ (green), $|2\pi_p\rangle \otimes \{|\uparrow\rangle, |\downarrow\rangle\}$ (blue) and $\left|2\pi_p^*\right\rangle \otimes \{|\uparrow\rangle, |\downarrow\rangle\}$ (red), and broadened by a Gaussian with a width of 0.3 eV. The total density of states for a clean surface (as obtained from a non-spin polarized calculation) is shown in gray and has been downscaled by a factor of 50. Filled states below the Fermi level ε_F are indicated by the filled gray curve.

too low in energy and thus always filled with the "missing" four of the total of 16 electrons of the O_2 molecule. Consequently, they are not important for the spin transition discussed below and hence not shown in Fig. 7.6.

The molecular levels along a trajectory with reaction coordinate Q can be identified via a projected density of the states (PDOS). For an O_2 state $|\varphi^\sigma_{O_2}(Q)\rangle$, the molecular PDOS is given by

$$\rho^\sigma_{\varphi_{O_2}}(\varepsilon; Q) = \sum_n \left|\langle\varphi^\sigma_{O_2}(Q)|\varepsilon^\sigma_n(Q)\rangle\right|^2 \delta(\varepsilon - \varepsilon_n) \quad , \tag{7.31}$$

as first used by Lorente and Persson.[119] They also emphasized that projecting onto molecular states rather than those of the individual constituent atoms is obviously a better choice for a detailed analysis of the electronic structure, when, like in the present case, the O_2 molecule strongly interacts with the surface. Completely consistent with the transitions for the calculation of electron-hole pair spectra (cf Section 7.1.2), Kohn-Sham states are used in order to

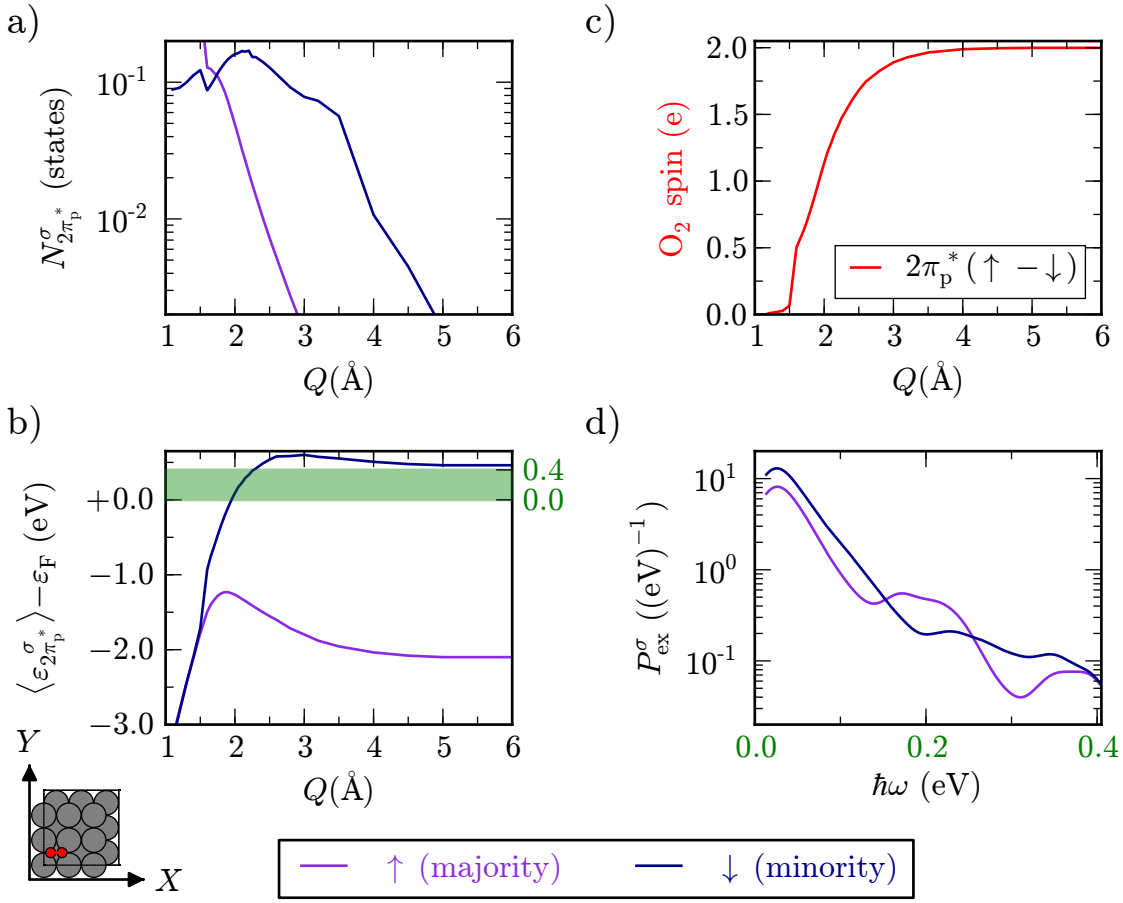

Figure 7.7.: Comparison of spin transition and electron-hole pair excitations for the *h-para* trajectory (cf Fig. 7.2). a) Number of states projected onto the $2\pi_p^*$ orbital $N^{\sigma}_{2\pi_p^*}(Q)$ of the oxygen molecule in an energy interval from ε_F to $\varepsilon_F + 0.4\,\text{eV}$ as given by Eq. (7.36). b) Center of the $2\pi_p^{*\sigma}$ molecular projected density of states (PDOS) $\langle \varepsilon^{\sigma}_{2\pi_p^*}(Q) \rangle$ as given by Eq. (7.35). The integration interval used for a) is indicated by the green shaded area. c) Spin projected onto the O_2 molecule using the molecular PDOS according to Eq. (7.33). To be compared with Fig. 7.2a, which is based on atomic projections, showing that both yield an identical description of the spin transition. d) Electron-hole pair excitations $P^{\sigma}_{ex}(\hbar\omega)(Q)$ given by Eq. (7.14) as already shown in Fig. 7.2d, but zoomed in to a smaller interval of excitation energies from 0.0 to 0.4 eV, identical to the integration interval used for a).

evaluate Eq. (7.31). This has been implemented by the author of this thesis as a post-processing tool for CASTEP,[xi] and the corresponding code has already been carefully tested and successfully used within another project.[120,265]

As already indicated in the next to last paragraph, the molecular PDOS analysis along the *h-para* trajectory focuses on the orbitals

$$|\varphi^{\sigma}_{\mathrm{O}_2}\rangle \in \left\{ |2\sigma_\mathrm{p}\rangle, |2\pi_\mathrm{p}\rangle, \left|2\pi^*_\mathrm{p}\right\rangle \right\} \otimes \{|\uparrow\rangle, |\downarrow\rangle\} \tag{7.32}$$

as shown in Fig. 7.6 for its beginning ($t = 0$). Using the molecular PDOSs, the projected spin on the O_2 molecule is straightforwardly defined as

$$\begin{aligned} S_{\{\varphi_{\mathrm{O}_2}\}}(Q) &= n^{\uparrow}_{\{\varphi_{\mathrm{O}_2}\}}(Q) - n^{\downarrow}_{\{\varphi_{\mathrm{O}_2}\}}(Q) \\ &= \sum_{\varphi_{\mathrm{O}_2}} \int_{-\infty}^{\infty} d\varepsilon \, \left[f^{\uparrow}(\varepsilon;Q)\rho^{\uparrow}_{\varphi_{\mathrm{O}_2}}(\varepsilon;Q) - f^{\downarrow}(\varepsilon;Q)\rho^{\downarrow}_{\varphi_{\mathrm{O}_2}}(\varepsilon;Q) \right] \quad , \end{aligned} \tag{7.33}$$

where $f^{\sigma}(\varepsilon;Q)$ are occupation numbers which ensure to obtain proper electron numbers $n^{\sigma}_{\{\varphi_{\mathrm{O}_2}\}}(Q)$ for $\sigma \in \{\uparrow,\downarrow\}$. In this picture, it also turns out numerically that it is completely sufficient to only consider filling of the projected $2\pi^*_\mathrm{p}$ orbital, i.e.

$$S_{\mathrm{tot}} = S_{\{2\pi^*_\mathrm{p}\}} \quad , \tag{7.34}$$

where S_{tot} considers projections onto all O_2 states – as to be expected for a reasonable choice of projections. $S_{\{2\pi^*_\mathrm{p}\}}$ is plotted in Fig. 7.7c and furthermore practically identical to its pendant based on atomic projections as shown in Fig. 7.2a.

Consequently, for the comparison of the adiabatic spin transition of the O_2 molecule *along* to the calculated electron-hole pair excitations for the *total h-para* trajectory, which is illustrated in Fig. 7.7, it is completely sufficient to focus on the $2\pi^*_\mathrm{p}$ orbital: Figure 7.7d zooms in from Fig. 7.2d electron-hole pair excitations within an interval from 0 to 0.4 eV, which is just below the location of the $2\pi^*_\mathrm{p}$ at the begin of the trajectory as illustrated by Fig. 7.7b. The latter plot shows the center of the $2\pi^{*\sigma}_\mathrm{p}$ molecular PDOS, $\rho^{\sigma}_{2\pi^*_\mathrm{p}}(\varepsilon;Q)$, in both spin channels (i.e. $\sigma \in \{\uparrow,\downarrow\}$) along the trajectory, as given by

$$\langle \varepsilon^{\sigma}_{2\pi^*_\mathrm{p}} \rangle(Q) = \int_{-\infty}^{\infty} d\varepsilon \; \varepsilon \; \rho^{\sigma}_{2\pi^*_\mathrm{p}}(\varepsilon;Q) \quad . \tag{7.35}$$

This is a rough measure of the orbital position relative to the Fermi energy, not including the width due to hybridization with the substrate states. Above $Q = 2$ Å, $\varepsilon^{\downarrow}_{2\pi^*_\mathrm{p}}$ is above the Fermi level while $\varepsilon^{\uparrow}_{2\pi^*_\mathrm{p}}$ is far below, thus leading to minority and majority spin channels as described before. At about $Q = 3.5$ Å, in the aforementioned energy interval (unoccupied!) substrate states which overlap with $2\pi^*_\mathrm{p}$ become available in this spin channel as the width of that Kohn-Sham orbital increases, while in the majority spin channel, a similar amount only becomes

[xi] As in practically all plane wave DFT codes, the Kohn-Sham orbitals of the individual free atoms are directly available together with some form of corresponding population analysis – the latter being an adapted[409,410] Mulliken[411] analysis in case of the CASTEP code. As indicated before, the spin projections shown in Figs. 7.2a to 7.5a are based thereon. In contrast, projections onto molecular orbitals according to Eq. (7.31) require more efforts: Code must be written for its evaluation, and $\{\langle \varphi^{\sigma}_{\mathrm{O}_2}(Q)|\}$ need to be calculated separately. This is probably the reason why they are by far not as widespread in the literature, often resulting in questionable electronic structure anaylses.

available at $Q = 2\,\text{Å}$. The number of those projected states along the trajectory

$$N^{\sigma}_{2\pi^*_\text{p}}(Q) = \int_{\varepsilon_\text{F}}^{\varepsilon_\text{F}+0.4\,\text{eV}} d\varepsilon\ \rho^{\sigma}_{2\pi^*_\text{p}}(\varepsilon; Q) \tag{7.36}$$

is plotted in Fig. 7.7a. At this point, it is important to note that reducing the $\varepsilon_\text{F} + 0.4\,\text{eV}$ integration range to 0.1 eV only leads to quantitative but not qualitative changes.

Altogether, stronger electron-hole pair excitations in the minority spin channel (cf Fig. 7.7d) for excitation energies between 0 and 0.4 eV coincide with a larger amount of states that overlap with the $2\pi^*_\text{p}$ orbital of the O_2 molecule. A tempting interpretation is therefore to see this as a strong indication for an efficient compensation mechanism of the spin-density associated with the adsorbate by the (forcibly non-spin polarized!) electronic structure of the substrate. This goes by the assumption also inherent to the perturbative treatment for the electron-hole pairs, namely that the electronic structure during the "real" spin transition does not behave in a radically different fashion. In that case, this can also be seen as a confirmation for efficient electron tunneling to the O_2 molecule as hypothesized previously in Section 7.0.1 – rationalizing and justifying an adiabatic description in turn. In order to finally exclude that it is no remaining "artifact" of the artificial spin polarization of the substrate in the perturbation potential $v^\sigma(\boldsymbol{Q}(t))$, a comparison to other transition metal surfaces (with lower density of states at the Fermi level) would be interesting.

7.3.3. Indications from Experiments

Despite of all the uncertainties in the obtained electron-hole pair spectra, they are consistent with experiments: Nienhaus and coworkers have not been able to successfully detect so-called *chemicurrents* during O_2 adsorption on polycrystalline palladium so far.[412] Using Si-based Schottky-diodes with a thin substrate metal film as second electrode as detectors, they could measure very weak currents for the first time when exposing silver and copper films to beams of atomic hydrogen and deuterium.[27] According to current understanding, these currents are generated due to creation of electron-hole pairs, and up to now, corresponding experiments are the most direct way to measure the generation of the latter during chemical reactions at surfaces. Using the same experimental setup, such chemicurrents have been successfully detected for various other adsorbate-substrate combinations,[28,413] among which in particular O_2 on polycrystalline silver is probably most important to mention here.[414,415] This strongly suggests that the calculated spectra and concomitant non-adiabatic energy dissipation estimate are based on reasonable approximations for the present system.

7.3.4. Critical Assessment and Outlook

Apart from differences among different trajectories, the present perturbative approach certainly comes with its own error bars. For H_2 on Al(111), a comparison with TD-DFT results of Lindenblatt and coworkers,[74,383,384] neglecting any errors of the latter which have been obtained at (or perhaps even) below the numerical convergence limit, shows a pronounced underestimation of the dissipated energy and highlights the importance of the treatment of spin.[393,396] This is perfectly along the same lines as what has been observed in the present case when (in a straightforward fashion) unperturbed substrate states have been taken from the artificially ferromagnetic palladium substrate as obtained within a PBE description. As already indicated in Section 7.1.4, Timmer and Kratzer have investigated modifications and extensions of their approach for H_2 on Al(111): Employing a "GS-like" description and smoothening the

spin transition to mimic a "more non-adiabatic" situation, they could obtain better agreement with the aforementioned TD-DFT results.[396] However, according to the arguments given in Section 7.0.1, there is no reason why a strongly non-adiabatic spin transition should be expected for the present system. Even if the dissipated energy was wrong by a similar amount as Timmer and Kratzer estimate in their case,[393,396] be it due to choice of the trajectories or the inherent approximations of the method, the importance for the dissipation of the total mount of chemisorption energy of $\sim 2.6\,\mathrm{eV}$ would still not be dominant – and this is, of course, most important for the present thesis. In fact, Mizielinski and Bird have demonstrated only very recently that the total amount of dissipated energy, quite in contrast to the actual electron-hole pair spectra, is very robust when considering different orders in *their* perturbation ansatz.[395] However, based on the adsorbate velocity and combined with simple "model electronic structure", the latter is not directly comparable to the present approach.

Furthermore, the very low amount of energy dissipated into the electron-hole pairs observed for this system seems to be perfectly in line not only with the experiments described in Section 7.3.3, but also with trends observed in other recent studies beyond single atoms on metal surfaces, no matter if the impinging diatomic carries a permanent dipole moment (HCl on Al(111))[416] or not (H_2 on Cu(110), W_2 on W(110)).[44] Compared to the former, which employs TD-DFT within Ehrenfest dynamics for the nuclei (considered to be state-of-the art in this context),[74,383,384] the latter study has been criticized[45,46] for using electronic friction theory with friction coefficients obtained from the local density friction approximation (LDFA).[387,388] The reason for choosing LDFA was driven by its appealing simplicity and (nowadays) very light computational cost for obtaining atomic friction coefficients (neglecting any correlations due to the binding in the molecule). Nevertheless, the work by Juaristi and coworkers[44] has shown that apart from electronic matrix elements of the type given by $\frac{\partial}{\partial Q} v_{ij}^{\sigma}$ the velocity factors in Eqs. (7.12) and (7.17), i.e. the present and electronic friction theory, certainly do become important in a statistical treatment. Along those lines, differences of about one order of magnitude in the dissipated energies have also been observed here for the different trajectories studied. Therefore, also in order to make closer contact to experiment, the next step after development of a viable theory should be its application to more than a single trajectory. After a trivial modification of the present efficient implementation as described in Section 7.2, the aforementioned matrix elements required to obtain the friction coefficient within electronic friction theory (cf Eq. (7.18)) could be easily "produced on a large scale" when sampling a high-dimensional potential energy surface. With the same techniques used to interpolate corresponding potential energy surfaces (cf Chapter 6), the latter could then be represented continously and employed in ensuing molecular dynamics simulations. The otherwise discarded electronic structure data from the underlying DFT calculations would be put to good use this way – the challenging storage requirements typically in the order of terabytes can easily be mastered nowadays thanks to the steady decrease of hard disk prices over the last years. Hence the aforementioned criticism[45,46] on the work by Juaristi and coworkers[44] could be easily taken into account and lifted in corresponding future applications. Of course, this goes under the assumption that also techniques for high-dimensional interpolation get a more wide-spread use.

Finally, since the present state-of-the art treatment only considered non-reactive trajectories on a frozen surface, the question arises how important non-adiabatic effects might be during actual dissociation events involving a mobile substrate. Though having been addressed in the literature,[300,376] from an accurate first-principles point of view, a definite answer is yet to be found. It might be provided by a TD-DFT description, as has been endeavored for a few systems,[74,416] perhaps even going beyond the approximation of classical nuclei.[71] Unfortunately, computational cost with available codes make this an extremely cumbersome effort

– in particular if not crowned with significantly higher scientific insights than both more approximate but also more computationally tractable models. Very promising along those lines is the so-called "independent-electron surface hopping" model proposed only very recently by Shenvi and coworkers.[38] Like TD-DFT, it can in principle capture both adsorbate and substrate related non-adiabaticity. For the scattering of highly vibrationally excited NO on Au(111), non-adiabatic transitions between different charge states of the molecules have been included when evaluating energy dissipation to the substrate.[36,37,39] Available experimental data, which has already provided strong indications for the importance of electronically non-adiabatic effects several years ago,[29,30] could be nicely reproduced at least qualitatively. However, the underlying potential energy surfaces are based on extended Morse potentials and a simple nearest neighbor harmonic potential for the substrate, both parametrized based on *ab initio* data. Hence, a straightforward application to a dissociation problem with an accompanying release of a high amount of chemisorption energy like in the present case is questionable due to the limited transferability of the hitherto employed potentials. Given the results already obtained for the present system, efforts for an according extension and application of the model might hence better be spent for the gas-surface dynamics of different systems. Coming back to the initial question of this paragraph, at least for the present system the experimental findings (or better lack thereof) as described in Section 7.3.3 do provide valuable guidance for further modeling: If non-adiabaticity was important during the dissociation of O_2 molecules on Pd(100), sizable chemicurrents should be detectable. Turning to a completely adiabatic description hence appears to be a well justified approximation – at least for the present system.

7.4. Summary

After a thorough discussion of good reasons to neglect potential non-adiabaticity induced by the spin transition O_2 molecules undergo during adsorption on the Pd(100) surface, non-adiabatic effects in form of electron-hole pair excitations of the substrate have been addressed. Due to the exceptionally high density of states of palladium at the Fermi-level, the importance of these excitations for the dissipation of the chemisorption energy has called for a state-of-the art first-principles estimate.

Among approaches available in the literature, a very recent one based on time-dependent perturbation theory in the adsorbate-substrate interaction potential has been chosen, allowing to obtain such an estimate for the present system (with all its challenges) by reusing efficiently results of the conventional ground state DFT calculations from Chapter 6.

Therefore, a very efficient parallel implementation has been done within the CASTEP code, whose underlying algorithm has already been gratefully adopted by the original authors of the theoretical of approach. Numerical accuracy has been verified by comparison to their reference data, including straightforward general applicability to ultrasoft pseudopotentials. Results are in perfect agreement, but can be obtained more than an order of magnitude faster than with the original implementation. This allows a computationally efficient treatment of more demanding systems like the present one. Furthermore, matrix elements which pose the key computational challenge are very similar to those required within electronic friction theory, which is nowadays applied to model a plethora of non-adiabatic phenomena. Therefore, further applications in the future are straightforwardly envisioned.

Application to O_2 on Pd(100) based on an adiabatic spin transition has shown that electron-hole pair excitations play a negligible role for energy dissipation. Several reflected trajectories on a frozen substrate, including one which can be considered statistically most representative

according to the results of Section 6.3.2, yield less than 100 meV to be dissipated into this channel during the initial encounter of the molecule with the surface. For other trajectories, dissipated energies are up to two orders of magnitude less, confirming the importance of a six-dimensional treatment also in this context. This rationalizes the lack of detectable chemicurrents in unpublished attempts with polycrystalline palladium. Given the (initial) sticking in the order of one (cf Section 6.3.1), these unsuccessful attempts allow in turn to consistently rule out a significantly increased importance during actual dissociation.

A strong asymmetry between the two spin channels has been identified for the most statistically relevant trajectory, and compared to a thorough analysis of the electronic structure changes related to the spin transition in the adiabatic picture. As expected, the latter is due to a filling of the $2\pi_{\mathrm{p}}^{*}$ orbital of the oxygen molecule. Stronger electron-hole pair excitations are present in the spin minority channel in an energy range where this orbital overlaps with the substrate states during the course of the trajectory. This suggests tunneling of excited electrons as an efficient mechanism for the quenching of the spin and justifies the adiabatic picture in turn.

Most importantly, this shifts the focus of this thesis away from electronic to non-electronic degrees of freedom in order to address energy dissipation. Therefore, detailed investigations of phonon excitations are the topic of the following chapters in Part III.

Part III.

Gas-Surface Dynamics of Oxygen on a Mobile Pd(100) Surface

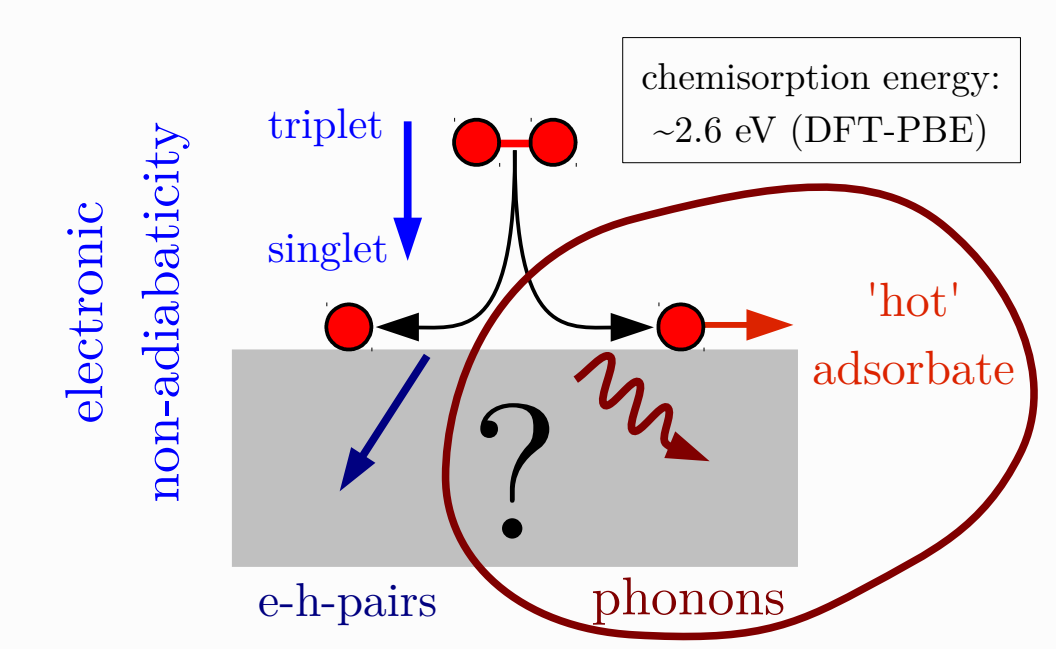

8. Energy Sinks "from the Shelf": An Overview

In the preceding Part II of this thesis, dynamical properties have been addressed, for which an accurate modeling of the dissociation and the accompanying release of chemisorption energy was not of central conceptual concern: As discussed in Chapter 6, steering of incident oxygen molecules occurs at a distance above the surface where the interaction between adsorbate and substrate is yet too weak to inflict considerable movement of the substrate atoms. Since the precise details of how the two oxygen atoms on the surface reach the threshold distance beyond which a trajectory is counted as stuck are not important, the initial sticking curve obtained in Section 6.3.1 will hardly be affected by inclusion of substrate mobility. The same holds for the major entrance channel for dissociative adsorption identified in Section 6.3.2. Furthermore, in Chapter 7, non-adiabatic effects in form of electron-hole pair excitations have been addressed using perturbation theory based on unperturbed trajectories on the frozen surface. Completely in line with indications from experiments[412] the concomitant energy loss has been estimated as negligibly small compared to the total chemisorption energy of about 2.6 eV in the low coverage regime (cf Section 5.3), justifying the perturbative treatment in turn. Obviously, this also excludes electron-hole pair excitations as predominant energy dissipation channel and strongly points at phonons to constitute the latter.

To estimate the implications thereof, at this point, it is instructive to consider a typical velocity with which phonons propagate: A frequently quoted value for the speed of sound in bulk palladium c_{Pd}[i] is approximately 31 Å ps^{-1} at 290 K.[417] Within the present theoretical model, values at 0 K have been implicitly obtained from fitting Debye models to phonon density of states as shown in Fig. 5.1 in Section 5.1 of Chapter 5. These effective velocities of sound given by Eq. (4.15) in Section 4.1 of Chapter 4 range from 22 Å ps^{-1} to 23 Å ps^{-1} for the FHI-aims all-electron and Castep pseudopotential calculations, respectively. They nicely agree with approximately 20 Å ps^{-1} resulting from Eq. (4.15) when inserting the ultrasonic velocities at 4 K, which Hsu and Leisure obtained for the crystallographic direction considered during their measurements of elastic constants.[270] Of course, this is not surprising, given the excellent agreement of the calculated phonon dispersion with the experimental data from Miiller and Brockhouse[273] in the linear regime (cf Fig. 5.1), which for itself also accurately reproduces data from earlier elasticity measurements.[269] From the dynamics on the frozen surface in Part II, the relevant time during which a dissociation event occurs, can be estimated to be (at least) 1 ps to 2 ps.[ii] With the lattice constant of palladium of about 3.9 Å (cf Section 5.1) a phonon wave packet travels more than 10 bulk lattice constants during this time. In an atomistic

[i] See e.g. http://en.wikipedia.org/wiki/Palladium or http://www.webelements.com/palladium/physics.html. Unfortunately, traces of the original value, which even appears to have been calculated based on an unknown model,[417] vanish in (at least here in Germany) unretrievable Soviet Russian literature.

[ii] This estimate is based on typical dissociative trajectories obtained in Chapter 6. According to the results from Section 6.3.3, phonon excitations lacking in the frozen-surface dynamics are expected to set in noticeably when center of mass distance of the oxygen to the Pd(100) surface is about 2 Å. The time it typically takes from then until complete dissociation is the time given above.

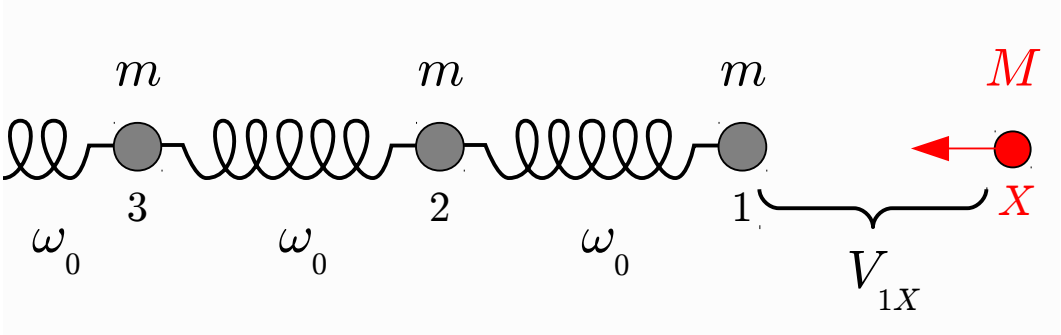

Figure 8.1.: Zwanzig's linear chain model for gas-surface dynamics.[422] A single gas atom interacts via an interaction potential V_{1X} with a semi-infinite chain of harmonic oscillators coupled by nearest neighbor force constants $m\omega_0$ only.

simulation where this is supposed to be captured and unphysical reflections due to commonly employed periodic boundary conditions or surface effects in finite-size cluster models are to be avoided, models encompassing at least 30 surface lattice constants, i.e. 15 in each direction, and more than 20 layers along a [100] direction then need to be considered. Although, as indicated before, phonons are even quantitatively captured by the present level of theory, such sizes are way too large for a direct dynamical treatment of the whole system within DFT, as detailed in Section 8.3. In addition, the detailed electronic structure of such a large model might not even provide additional insight for adsorbate-substrate systems like the present. Keeping this in mind, the goal of this chapter is to critically review more effective (and approximate) heat sink approaches found in the literature, which can be combined with an atomistic first-principles modeling to reach a quantitative description of energy dissipation during dissociative adsorption.[iii]

8.1. Generalized Langevin Equations

One of the earliest discussions of energy dissipation in gas-surface dynamics was given by Zwanzig.[422]. He approximated the surface by a semi-infinite linear chain, only considering nearest neighbor interactions with identical force constants between the one-dimensional harmonic oscillators as illustrated in Fig. 8.1. With additional approximations concerning the interaction of the single gas atom with the topmost surface atom, he could obtain analytical solutions for classical trajectories in two limiting cases. Despite its simplicity, this model could rationalize dynamical events like trapping and inelastic scattering.

Very general developments in non-equilibrium statistical mechanics led by (again) Zwanzig,[423] Mori[424] and Kubo[425] conceived the idea of so-called *Generalized Langevin Equations* (GLEs), which, in contrast to traditional phenomenological Langevin equations used e.g. to describe Brownian Motion, had a rigorous theoretical justification. In these stochastic equations of motion for macroscopic observables, the large number of microscopic degrees of freedom of an interacting many-body system are captured by their elimination into well-defined effective

[iii] This excludes Billing's semiclassical atomistic model due its intrinsic approximations concerning the adsorbate-substrate interaction potential.[418–421] Though being considered as current state of the art, Manson's theory of inelastic surface scattering is not considered either.[295] Details about the adsorbate-substrate interaction are only considered by effective parameters, and chemical reactions are not meant to be modeled.[296]

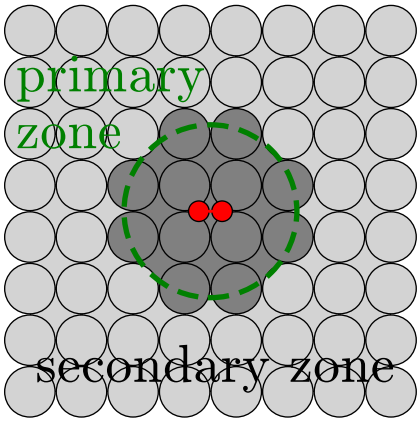

Figure 8.2.: Primary and secondary zones for applications of generalized Langevin equations (GLEs) in gas-surface dynamics. Atoms with coordinates $\mathcal{R}_P$ within the former (dark gray) are located within a certain area around the impingement point of the gas atoms (red) with coordinates $\mathcal{R}_X$, which is taken to be of the usual circular shape (dashed green line) here. The remaining atoms (light gray) belong to the secondary zone and their degrees of freedom $\mathcal{R}_Q$ are "integrated out" by the GLE formalism as described in the text.

statistical properties. This reduction of complexity of the underlying dynamical problem stimulated Adelman and Doll to combine the GLE approach with Zwanzig's original linear chain model for the gas-surface dynamical systems.[426,427] An extension to arbitrary but still harmonic surface lattices succeeded,[428] while ideas to go beyond the harmonic approximation by a rather complicated transformation back to an effective but fictitious nearest neighbor collinear harmonic chain model followed thereafter.[429]

In practice, however, the previous "simple" GLE formulation[428,430–432] is still mostly used. It divides the gas-surface system into gas atoms as well as substrate atoms in a *primary* and *secondary zone* with coordinates $\mathcal{R}_X = \{\boldsymbol{R}_X\}_X$, $\mathcal{R}_P = \{\boldsymbol{R}_P\}_P$ and $\mathcal{R}_Q = \{\boldsymbol{R}_Q\}_Q$, and masses $\{m_X\}_X$, $\{m_P\}_P$, $\{m_Q\}_Q$ respectively, as illustrated in Fig. 8.2. The gas atoms interact according to a potential $V_X(\mathcal{R}_X)$ to be specified – if more than a single gas atom is considered. The primary zone is the impingement region of the gas atoms, in which the chemical interactions between gas and surface atoms occur and which is assumed to be small. Atoms contained therein hence directly interact with the gas atoms via an unknown potential $V_{XP}(\mathcal{R}_X, \mathcal{R}_P)$, whereas the interactions among themselves are assumed to be harmonic according to force constant matrices $\boldsymbol{\Phi}_{PP}$ and displacement coordinates $\boldsymbol{U}_P = \boldsymbol{R}_P - \boldsymbol{R}_P^0$. Secondary zone atoms with coordinates $\mathcal{R}_Q$ are supposed to form the heat bath given by the surrounding bulk material, i.e. the associated region is macroscopically large allowing to associate a certain temperature T. Interaction with the gas atoms is only considered by an effective background potential $V_{XQ}(\mathcal{R}_X)$ which is conveniently absorbed into V_X. All other interactions are those of the assumed harmonic lattice and hence described by the symmetric force constant matrices $\boldsymbol{\Phi}_{QP} = \boldsymbol{\Phi}_{PQ}$ and $\boldsymbol{\Phi}_{QQ}$ and displacement coordinates $\boldsymbol{U}_Q = \boldsymbol{R}_Q - \boldsymbol{R}_Q^0$. This leads to the following (classical)

equations of motion:

$$m_X \ddot{\boldsymbol{R}}_X = -\boldsymbol{\nabla}_{\boldsymbol{R}_X} V_X(\mathcal{R}_X) - \boldsymbol{\nabla}_{\boldsymbol{R}_X} V_{XP}(\mathcal{R}_X, \mathcal{R}_P) \tag{8.1a}$$

$$m_P \ddot{\boldsymbol{R}}_P = -\boldsymbol{\nabla}_{\boldsymbol{R}_P} V_{XP}(\mathcal{R}_X, \mathcal{R}_P) - \sum_Q \boldsymbol{\Phi}_{PQ} \boldsymbol{U}_Q \tag{8.1b}$$

$$m_Q \ddot{\boldsymbol{R}}_Q = -\sum_P \boldsymbol{\Phi}_{QP} \boldsymbol{U}_P - \sum_Q \boldsymbol{\Phi}_{QQ} \boldsymbol{U}_Q \tag{8.1c}$$

Following Adelman and Doll,[428] by formally solving Eq. (8.1c) for the secondary atoms and eliminating them from Eq. (8.1b) afterwards, Eqs. (8.1b) and (8.1c) can be recast into a generalized Langevin equation for the primary zone atoms only:

$$m_X \ddot{\boldsymbol{R}}_X(t) = -\boldsymbol{\nabla}_{\boldsymbol{R}_X} V_X(\mathcal{R}_X) - \boldsymbol{\nabla}_{\boldsymbol{R}_X} V_{XP}(\mathcal{R}_X, \mathcal{R}_P) \tag{8.2a}$$

$$\begin{aligned} m_P \ddot{\boldsymbol{R}}_P(t) = & -\boldsymbol{\nabla}_{\boldsymbol{R}_P} V_{XP}(\mathcal{R}_X, \mathcal{R}_P) \\ & - \int_0^t d\tau\, m_P \underbrace{\boldsymbol{\Gamma}_{PP'}(t-\tau)}_{\text{friction kernel}} \dot{\boldsymbol{R}}_{P'}(\tau) + \underbrace{\boldsymbol{F}^{\mathrm{r}}_P(t)}_{\text{random force}} \end{aligned} \tag{8.2b}$$

Equations (8.2) are in principle still exact in a stochastic sense, hiding the complexity of the many-body system in the *friction kernel* $\boldsymbol{\Gamma}_{PP'}$, and the *random force* $\boldsymbol{F}^{\mathrm{r}}_P$. The memory provided by the former in the friction integral is precisely what distinguishes GLEs from simple Langevin equations and also obviously complicates their solution. $\boldsymbol{\Gamma}_{PP'}$ and $\boldsymbol{F}^{\mathrm{r}}_P$ are well defined but rather involved functions of the neglected secondary zone degrees of freedom and hence not given here explicitly. One immediate consequence in combination with the assumed harmonic lattice is that the probability distribution for the random force is Gaussian with a width related to the vibrational properties of the lattice. Furthermore, both Adelman and Doll[428] and Kantorovich[432] – only very recently in a mathematically more rigorous way – have shown how a manifestation of the fluctuation-dissipation theorem[424,425] follows, relating friction kernel and (probability distribution of the) random force:

$$\boldsymbol{\Gamma}_{PP'}(t) = k_{\mathrm{B}} T \, \langle \boldsymbol{F}^{r}_P(t) \boldsymbol{F}^{\mathrm{r}\,\dagger}_{P'}(0) \rangle^{\text{secondary zone}}_{NVT} \tag{8.3}$$

Here k_{B} is the Boltzmann constant, and in a consistent treatment the canonical average is taken over the secondary zone only, as Kantorovich emphasized.[432] Equation (8.3) ensures that energy dissipation out of the primary zone described by the friction integral in Eq. (8.2b) is on average balanced by a back-flow of energy, allowing to maintain or restore the secondary zone (bath) temperature T in the primary zone.

The big advantage of the GLE approach is that only the "interesting" dynamics of gas phase and primary zone atoms given by Eq. (8.2a) and Eq. (8.2b), respectively, need to be followed explicitly, resulting in a greatly reduced number of coupled differential equations. This comes at the prize that individual trajectories have lost their physical meaning, since the statistical treatment of the bath gives rise to the discontinuous random force. Additionally, an exact representation of the friction integral including all the memory contained therein would require to evaluate the detailed dynamics of the bath and hence nullify the advantages of its statistical treatment. Therefore, a suitable approximation for the friction kernel needs to be employed to make the GLE approach in its original formulation tractable in practice.

The first to make practical use of the latter to model gas-surface dynamics of a realistic system were Tully and coworkers.[433] Still for Zwanzig's original chain model, they employed a very

simple approximation of the friction kernel in Eq. (8.2b) together with a few parameters chosen to mimic the collision of He atoms with a tungsten surface, where the latter was represented through a Debye phonon spectrum of bulk tungsten. By appropriate numerical evaluation of the system of stochastic differential equations given by Eq. (8.2), they calculated about ten thousand stochastic trajectories to obtain statistical quantities like (initial) sticking probabilities and energy transfer. Hence, for the first fime in that work, they were probably to treat energy dissipation in gas-surface dynamics atomistically in a materials-specific fashion at a very simple semi-empirical level. Shortly after, Tully proposed more sophisticated and complicated parametrizations for the friction kernel, specific to low index surfaces of fcc and bcc crystal.[434] He incorporated some insight from the molecular dynamics studies of the corresponding surfaces of Lennard-Jones crystals by deWette and coworkers,[165] which certainly belonged to the most sophisticated theoretical work on surface vibrational properties at the time. Further applications followed, e.g. to surface diffusion,[435] focusing on improved empirical potentials for the gas-surface interaction,[436–439] in particular of the well-known LEPS kind,[301,302] but also discussing simplified parametrizations of the friction kernel.[440] Despite arguments against the inconvenient numerical treatment of GLEs and in favor of simplified descriptions of energy dissipation for example via simple (and entirely empirical) Langevin equations,[441,442] finally also electronic non-adiabaticity was tried to be captured by the friction integral within a GLE description,[32,443] and is still applied in very recent studies.[300,391] Combination with the very simple surface oscillator model[444–446] as detailed in the next section is another reason why the GLE approach is yet commonly invoked as convenient extension to frozen surface *ab initio* potential energy surfaces in state-of-the-art work.[447] The same holds for slightly more advanced models in which a primary zone of about 80 surface atoms is coupled to bulk oscillators. Nearest neighbor harmonic interactions among those atoms have been used with a single force constant obtained from a fit to one high-symmetry direction of corresponding measured bulk phonon dispersions. The interaction with the gas atoms are approximated by a sum of pair potentials with a single global parameter fitted to *ab initio* data, hence neglecting any many-body effects in the gas-surface interaction by construction.[326,448]

Interest in the evolving field of multiscale modeling gave a new impulse on the development of both accurate and practical friction kernels. Cai and coworkers proposed a way how to efficiently calculate the kernel numerically.[449] The Green's function molecular dynamics method as proposed and implemented by Müser and coworkers also relies on integrating out harmonic degrees of freedom in the spirit of the GLE approach and obtains the response of the bath system by a numerical representation of the associated elastic Green's functions.[450–452] In contrast, E took ideas from his *absorbing boundary conditions* framework, which aims at the minimization of phonon reflections,[453] and combined the latter with the GLE formulation to obtain approximate GLEs with simpler integration kernels termed *variational boundary conditions*.[454] Earlier work by Moseler and coworkers was along the same lines, but more physically motivated by focusing on energetic-particle solid collisions. They also proposed links to continuum mechanics in form of elasticity theory.[455] Only recently, Kantorovich[432] revisited the basic theoretical formulation of Adelman and Doll[428,453] to correct the inconsistencies indicated in the preceding paragraph above. Additionally, he could demonstrate that the same GLE as given by Eq. (8.2b) can still be constructed even when primary zone atoms interact via any kind of anharmonic potential. However, harmonicity is still required (at least in practice) for interactions among and with secondary zone atoms forming the bath. In succeeding work[456] he and his coworker could demonstrate that for sufficiently short range interactions and some further approximations the GLE description can be recast into so-called *stochastic boundary conditions*: Atoms within a boundary layer of the primary zone with coordinates $\{R_B\}_B$ and masses $\{m_B\}_B$ are propagated

according to even only a conventional Langevin equation

$$m_B \ddot{\boldsymbol{R}}_B(t) = -\sum_P \boldsymbol{\Phi}_{PB}\,\boldsymbol{U}_B(t) - \sum_B \boldsymbol{\Phi}_{BB}\,\boldsymbol{U}_B(t) - m_B\,\gamma\,\dot{\boldsymbol{R}}_B(t) - \boldsymbol{F}^{\mathrm{r}}_B(t)\,, \tag{8.4}$$

while the remainder follows simple Newtonian dynamics. Force constant matrices $\boldsymbol{\Phi}_{PB}$ and $\boldsymbol{\Phi}_{BB}$ as well as displacement coordinates $\boldsymbol{U}_B$ are defined accordingly as before in the preceding paragraphs. The simple friction coefficient γ is related to the width σ of the Gaussian distribution of the random force $\boldsymbol{F}^{\mathrm{r}}_B$ by

$$\sigma = \frac{2\,m_B\,\gamma\,k_{\mathrm{B}}T}{\delta t}\,. \tag{8.5}$$

This is a result of approximations made for the friction integral, where a discrete time interval δt has been introduced, which gets the meaning of the time step used in practical molecular dynamics calculations.[456,457]

To summarize, the significant reduction of the bath degrees of freedom into a friction kernel and a random force is of course appealing. It comes at the prize that individual trajectories lose their physical meaning though still correct in stochastic sense even for systems which are far away from thermal equilibrium. This is quite in contrast to thermostats discussed in one of the following sections. For the present purposes, *a priori* it is unclear whether the harmonic approximation made implicitly (at least for the bath and the coupling to it) in GLEs is reasonable when the release of several electron Volts of chemisorption energy is to be described. Finally, the GLE approach has not yet been employed within a framework of realistic interactions at a first-principles level between gas and primary zone atoms *and* among the latter.

8.2. Surface Oscillator

Starting with the dynamics of molecular hydrogen on surfaces, quantum mechanical treatment both of electrons and ions demanded a reduction of the degrees of freedom. Therefore, the frozen surface approximation resulting in a six-dimensional potential energy surfaces $V^{6\mathrm{D}}$ as constructed and employed in Part II became quite popular and was conveniently justified by the large mass mismatch of gas and surface atoms. Indeed, early "high-dimensional" studies based on LEPS potentials and a harmonic oscillators for the substrate (the latter parameterized based on Debye models of the bulk substrate) showed less than 10 % energy transfer to the substrate,[304] or negligible influence of surface temperature on sticking.[438,439]

Nevertheless, in order to have some ingredient in the model which can be claimed to represent a certain surface temperature, the surface is taken to be rigid and represented by a harmonic oscillator as illustrated in Fig. 8.3 – like an even simplified version of Zwanzig's collinear chain model Fig. 8.1. It is usually coupled to the previously constructed six-dimensional potential $V^{6\mathrm{D}}$ in the following way:[445,446,458–467]

$$V^{6\mathrm{D+SO}}(X,Y,Z,d,\theta,\varphi) = V^{6\mathrm{D}}(X,Y,Z-Z_{\mathrm{S}},d,\theta,\varphi) + \frac{1}{2}m_{\mathrm{S}}\,\omega_{\mathrm{S}}^2\,Z_{\mathrm{S}}^2 \tag{8.6}$$

Here, the spherical coordinates of a diatomic molecule X,Y,Z,d,θ,φ are defined in the same way as in Section 6.1.1 of Chapter 6, Z_{S}, m_{S} and ω_{S} are (displacement) coordinate, mass and characteristic frequency of the surface oscillator, respectively. With Fig. 8.3 in mind, the coupling to the Z distance (of the center of mass) of the molecule from the surface via

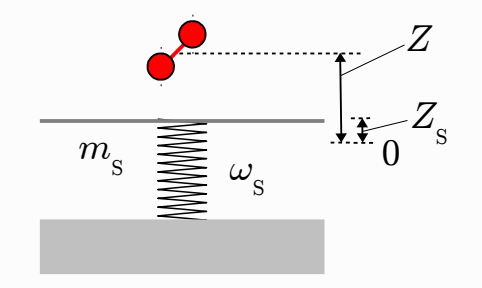

Figure 8.3.: Schematic illustration of the one-dimensional surface oscillator model, for the usual coupling along the surface normal leading to a rigid up and down-shift of the latter. Z is the center of mass distance of the molecule with respect to the rest position of the surface, Z_S is the surface oscillator displacement coordinate, m_S and ω_S are the mass and characteristic frequency parameters of the latter.

a shift of coordinates appears intuitively natural. In fact, in this form the surface oscillator had already appeared even earlier in the literature in a study of gas-surface scattering.[444] Yet, other couplings, for example perpendicular to specific reaction paths,[468] including an exponential decay with surface distance (termed *modified* surface oscillator)[461] or finally even three dimensional surface oscillators[23,447]

$$V^{6D+SO^3}(\boldsymbol{R}_A, \boldsymbol{R}_B) = V^{6D}(\boldsymbol{R}_A - \boldsymbol{R}_S, \boldsymbol{R}_B - \boldsymbol{R}_S) + \frac{1}{2} m_S \boldsymbol{R}_S^\dagger \boldsymbol{\Omega}_S^2 \boldsymbol{R}_S \tag{8.7}$$

have been proposed as well. In the latter case, the surface oscillator coordinates $\boldsymbol{R}_S$ were coupled to the Cartesian coordinates $\boldsymbol{R}_A$ and $\boldsymbol{R}_B$ of the two atoms of the diatomic, and the frequency matrix $\boldsymbol{\Omega}_S$ was taken to be diagonal. Surface oscillator parameters, i.e. mass and characteristic frequencies, are usually chosen based on the atomic masses of the surface atoms and experimentally determined vibrational properties, e.g. the Debye frequency of the corresponding bulk material. Changes in these parameters by orders of magnitude are usually found not to have any significant influence on statistical properties (typically sticking or scattering properties) that have been studied.[23,447,461,466,467] To model energy flow from the surface into the bulk, the surface oscillator degrees of freedom have been treated like the primary zone in a traditional generalized Langevin equation (cf Section 8.1), which of course leads to further parameters to be specified.[445–447]

In summary, there are two major approximations in the "somewhat suspect" surface oscillator model, as Kroes nicely points out in his recent review:[469] First, all substrate degrees of freedom are reduced to a single (at best three-dimensional) harmonic oscillator, whose connection to the bulk is furthermore assumed to be describable by a generalized Langevin equation. Second, the coupling to the gas-surface interaction as given by Eqs. (8.6) and (8.7) is chosen intuitively convenient for a pre-existing potential energy surface obtained within the frozen surface approximation, but is otherwise completely arbitrary. Both of these approximations are hence not constructed systematically out of the (even classical) many-body Hamiltonian of the interacting gas-surface system. The concomitant simplicity of the model might be the reason for its insensitivity to the actual choice of parameters in many of the applications, and the influence of surface temperature might indeed be captured qualitatively correct when forming averages for statistical properties concerning sticking and scattering. However, it is highly questionable, how much insight can be gained when as in the present case the energy release during a single dissociation event is to be followed.

8.3. *ab initio* Molecular Dynamics

The apparently simple and straightforward way to go beyond the simple surface oscillator model described in the previous section is to include a mobile substrate. When using interaction potentials between and among gas and surface atoms which are entirely empirical[304] or "empirically augmented" interpolated *ab initio* potentials obtained on a frozen surface.[326,448] the corresponding molecular dynamics simulations are at least nowadays no longer a big computational challenge. On the other hand, calculating the quantum mechanical interactions "on-the-fly" during the dynamics from first-principles is commonly referred to as *ab initio* Molecular Dynamics (AIMD) and by several orders of magnitude computationally more demanding.

In DFT codes based on plane waves (cf Section 2.6) the computational cost also strongly depends on what element is used as adsorbate, due to the different plane-wave cut-offs that are required. Hydrogen is a particular attractive choice, and hence it is not surprising that this (on different substrates) has often been a convenient starting point for first-principles based investigations in gas-surface dynamics employing new methodologies.[74,316–318,383,384] The AIMD studies of sticking and adsorbate dynamics by Groß and coworkers for H_2 adsorption on Pd(100)[353,354] are yet another good example for this. However, even then the still enormous computational burden required to jeopardize accuracy for speed, resulting in a computational cost which is more than one order of magnitude less compared to the present system O_2 on Pd(100). The current hope is inflicted inaccuracies do average out and hence statistical quantities are not affected,[361] though this is not guaranteed from a theoretical point of view. Nevertheless, for that study it took more than a year to obtain 100 trajectories with a supercell containing about 100 substrate atoms. This is of course nowhere close to what has been estimated as required by considering phonon propagation in the introduction of this chapter to avoid unphysical reflections at boundaries of the latter. However, for hydrogen, the same arguments which have already been used in favor of the frozen substrate (cf Section 8.2), could be invoked here as well: The large mass mismatch between adsorbate and surface atoms, should result in a weak coupling and hence only mild excitation of substrate vibrations. Nevertheless, this does not correct the physical quality of the model as far as the description of phonons is concerned.

Altogether, for O_2 at Pd(100), direct AIMD simulations in sufficiently large cells are impossible within present computational abilities. Apart from the fact that nearly three times as much chemisorption energy is released compared to the dissociative adsorption of H_2 on the same surface, the mass ratio of oxygen and palladium atoms leads to the anticipation of much stronger phonon excitations. This is further corroborated by earlier studies: During the adsorption of atomic oxygen on Cu(100), modeled with an "empirically augmented" interpolated frozen-surface *ab initio* potential, 8 eV are dissipated to a substrate of 80 copper atoms in 1 ps.[448] Scattering of O_2 on Pt(111) leads to a transfer of on average 40 % of the initial kinetic energy to substrate vibrations. In this work by Groß and coworkers, a tight-binding Hamiltonian is used, which is parametrized based on DFT calculations, resulting in an effective description of the Pt-O-interaction at the tight-binding level.[337] It is interesting to note that platinum atoms are even nearly twice as heavy as palladium atoms. Hence for the present system, a method to properly account for phonon excitation is still to be found.

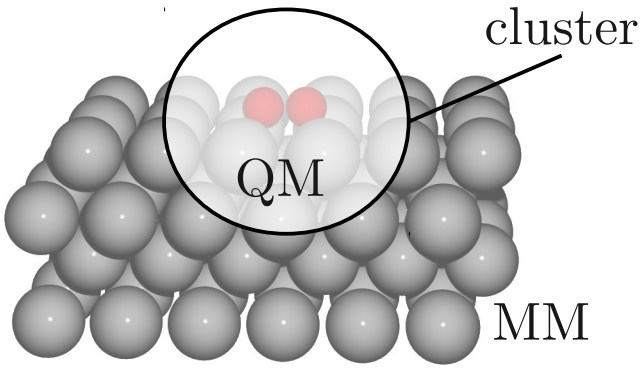

Figure 8.4.: Schematic illustration of QM/MM embedding: In a region of interest, a cluster is cut out and treated with higher, i.e. quantum mechanical (QM) accuracy. The remainder of the model is treated with a simpler, less accurate and computationally less demanding force field, also referred to as molecular mechanics (MM). Note that cluster sizes required to yield a realistic band structure of a surface are enormous (i.e. several hundred to thousand atoms). Therefore, QM/MM based embedding cannot be applied to the present system.

8.4. Embedding

The general idea of embedding is to subject only a certain region to an accurate and computationally expensive quantum mechanical (QM) treatment (too expensive to apply to the whole system), while the remainder of the simulated system is treated using less exact, but also much cheaper so-called "molecular mechanics" (MM), hence the common acronym QM/MM. The latter refers to a description by a less exact, but also much cheaper interatomic potential, which does not consider the electronic degrees of freedom explicitly.

For the present system, the impingement region of the O_2 molecule is the obvious choice for the QM treatment, to describe the bond breaking and formation during the dissociation reaction at high accuracy. This is illustrated schematically in Fig. 8.4. The designated QM region then needs to be cut out to allow the separate treatment, i.e. an artificial cluster needs to be constructed according to the geometrical criteria that define this region. However, for metallic systems, this is a big problem, as the cluster does not have a metallic band structure which plays a fundamentally important role for the accordingly delocalized adsorbate-substrate interaction.[82] This is the reason why periodic boundary conditions are commonly used for a proper description of the metal-adsorbate binding – an excellent description of the band structure is naturally contained therein. Cluster sizes which are required to get in good agreement to the periodic limit are so humongously large (several hundred to thousands atoms) that the advantages of any embedding are annihilated.

Furthermore, the boundary region needs special care in order to achieve a good matching of the two different theoretical descriptions. For molecular dynamics simulations, this is either done directly on the level of forces or indirectly by constructing an embedding energy expression from which forces then can then be derived. For the former, the following is quite common:

$$V_{\text{tot}}^{\text{QM/MM}} = V_{\text{sys}}^{\text{MM}} + V_{\text{cluster}}^{\text{QM}} - V_{\text{cluster}}^{\text{MM}} \tag{8.8}$$

The potential energy of the whole system $V_{\text{sys}}^{\text{MM}}$ is corrected by the difference of the QM (higher quality) and MM (lower quality) methods for the chosen embedding cluster. This is also referred

to as ONIOM method.[470] Since in principle, a hierarchy of methods with increasing quality can be stacked within the scheme, the name reminds of the layered skin structure of an onion.

Both approaches are particularly popular in the biophysical community. To treat large biomolecules in solution and include the effect of the environment, there is hardly any other way than embedding. Cutting out clusters around reactive centers usually works very nicely here, as bonds are predominantly covalent and hence very localized. Bonds which are cut when forming the cluster are usually saturated by hydrogen atoms. Only recently, the effect of the embedding error due to the boundary region gets investigated.[471]

In material science, an embedding scheme termed "learn on-the-fly" (LOTF) has only recently been developed and applied to crack propagation in silicon.[472–475] Again, due to the strong covalent character of the bonds in bulk silicon, a description based on clusters with dangling bonds properly terminated by hydrogen is very successful. On the other hand, for the reasons outlined in the preceding paragraph, the situation is quite different for metallic systems. Three recent reviews about applications of QM/MM schemes do not mention any in heterogeneous metal catalysis.[476–478] In fact, there is one attempt to apply ONIOM for hydrogen adsorption on Li(110) surfaces. Clusters sizes up to about 50 atoms are employed without embedding, making the obtained energetics highly questionable.[479] Choly and coworkers have proposed another QM/MM scheme for bulk metals which in the end arrives at the same energy expression like for a (one-layered) ONIOM scheme (including the cluster treatment).[480] This has been extended by a buffer region by Liu and coworkers in order to reduce the embedding error.[481] In both cases, the embedded atom method is applied as lower quality method for the treatment of the large bulk metal part.[172,175,181] Still, it remains higly questionable (and unchecked), how large the wrong to non-existing description of the metallic band structure in the embedding clusters is in those two studies even for the investigated bulk properties.

A detailed overview about embedding techniques and their applications in particular in materials science can be found in the excellent and very recent review by Bernstein and coworkers.[482] However, despite of the appeal that an embedding treatment might have for a problem involving a metallic substrate like the one under investigation here, no appropriate solution can be found therein.

8.5. Thermostats

Originally, molecular dynamics has become popular as an appealing alternative to Monte Carlo techniques, aiming at the calculation of partition functions for classical systems. Relying on ergodicity, the calculation of time averages along MD trajectories instead of ensemble averages by solution of high-dimensional integrals becomes more and more favorable as system size increases. However, moving through phase space according to trajectories given by Newton's equations of motion corresponds to sampling (if ergodicity is fulfilled) the microcanonical ensemble (NVE) only. Going beyond the latter is usually much more interesting – being concerned about heat release and dissipation in the present context certainly favors the canonical ensemble (NVT). Of course, in principle a bath with a large number of additional degrees of freedom could be included explicitly in the dynamics and would allow to keep a sub-part at a consistently defined a temperature. However, depending on the computational cost of the employed interaction potential, for most applications, the numerical effort for the integration of motions simply gets too large. The GLE approach, as detailed in the preceding Section 8.1, provides one way to deal with this problem, but assumes harmonic system-bath interactions and leaves the friction kernel to be dealt with in practice. Focusing on the calculation of sta-

tistical properties in thermodynamic equilibrium, so-called *thermostats* have been developed alternatively – without making any *a priori* assumptions about the underlying interactions.

Andersen proposed to maintain a certain desired temperature in a molecular dynamics simulation by redrawing particle velocities from the corresponding Maxwell-Boltzmann distribution within certain time intervals. The latter are rationalized as collision with a fictitious heat bath and determined by a Poisson process with prescribed frequency, resulting in a stochastic thermostat.[483] In contrast, the thermostat developed by Berendsen and coworkers provides continuous dynamics via the introduction of a velocity dependent friction term into Newton's equations of motion. This is in fact motivated by a Langevin equation (cf Eq. (8.4)), whose random force term gets dropped. The friction coefficient is constructed such that velocities are globally rescaled to enforce the desired target temperature T.[484] In a MD simulation of N particles with coordinates $\{\boldsymbol{R}_I\}_{I\in\{1,\dots,N\}}$, the latter is usually obtained as so-called instantaneous temperature based on the average kinetic $\bar{E}_{\mathrm{kin}}$ energy, which can be conveniently calculated:

$$\frac{3}{2}k_{\mathrm{B}}T = \bar{E}_{\mathrm{kin}} = \frac{1}{2}\langle m_I \dot{\boldsymbol{R}}_I^2\rangle_I \quad , \quad I \in \{1,\dots,N\} \tag{8.9}$$

Consequentially, the Berendsen thermostat practically aims at keeping $\langle E_{\mathrm{kin}}\rangle_I$ constant. In the canonical ensemble, however, this is supposed to fluctuate with a variance of $\frac{2}{3N}$ as can be easily shown.[149] As a result, the Berendsen thermostat does not describe the canonic ensemble correctly – the smaller N is, the worse the description gets. This certainly is one of the reasons why thermostats based on Nosé's ideas are more popular nowadays: By considering an extended system with fictitious degrees of freedom, equations of motion can be constructed that yield a canonical distribution for the original, physical variables, which is contained in the microcanonical distribution of the extended set of variables. Nosé originally achieved this via the introduction of time rescaling in the physical system.[152–154] Hoover provided a simplified reformulation which does not require the somewhat awkward rescaling of time and its concomitant inconveniences in practice.[155] Unfortunately, he also demonstrated for a simple system like a one-dimensional harmonic oscillator that the resulting dynamics are not ergodic.[155] Therefore, harmonic systems in general tend to suffer from poor sampling of the canonical ensemble when molecular dynamics trajectories produced by this Nosé-Hoover thermostat are considered. A solution was proposed by Martyna and coworkers.[156] They showed that ergodicity is improved by "thermostatting the thermostat" and hence arrived at what they termed *Nosé-Hoover chains*. The equations of motion are

$$m_I \ddot{\boldsymbol{R}}_I = -\boldsymbol{\nabla}_{\boldsymbol{R}_I} V(\{\boldsymbol{R}_{I'}\}) - m_I\, \dot{\boldsymbol{R}}_I\, \dot{\eta}_1 \quad , \quad I \in \{1,\dots,N\} \tag{8.10a}$$

$$Q_1\, \ddot{\eta}_1 = \left[\sum_{I=1}^{N} m_I \dot{\boldsymbol{R}}_I^2 - 3Nk_{\mathrm{B}}T\right] - Q_1\, \dot{\eta}_1\, \dot{\eta}_2 \tag{8.10b}$$

$$Q_i\, \ddot{\eta}_i = \left[Q_{i-1}\, \dot{\eta}_{i-1}^2 - k_{\mathrm{B}}T\right] - Q_i\, \dot{\eta}_i\, \dot{\eta}_{i+1} \quad , \quad i \in \{2,\dots,M-1\} \tag{8.10c}$$

$$Q_M\, \ddot{\eta}_M = \left[Q_{M-1}\, \dot{\eta}_{M-1}^2 - k_{\mathrm{B}}T\right] \ , \tag{8.10d}$$

where the M additional, fictitious coordinates $\{\eta_i\}_i$ together with thermostat masses $\{Q_i\}_i$ have been introduced. As indicated before, the case of $M = 1$ is identical to what Hoover had proposed originally It is interesting to note that the velocity dependent terms in Eqs. (8.10) couple in a very similar way to the dynamics like in case of the Berendsen thermostat,[484] thanks to the difference enforcing the instantaneous temperature in the "chain", Eqs. (8.10b)

to (8.10d). Equations (8.10) give rise to trajectories with a microcanonical distribution

$$f(\{\boldsymbol{R}_I\}_I, \{\dot{\boldsymbol{R}}_I\}_I, \{\eta_i\}_i, \{\dot{\eta}_i\}_i) \quad \propto \underbrace{\exp\left(-\frac{1}{k_\mathrm{B}T}\left[V(\{\boldsymbol{R}_I\}_I) + \sum_{I=1}^{N}\frac{1}{2}m_I\dot{\boldsymbol{R}}_I^2\right]\right)}_{\equiv f_\mathrm{c}(\{\boldsymbol{R}_I\}_I, \{\dot{\boldsymbol{R}}_I\}_I)} \cdot \exp\left(-\frac{1}{k_\mathrm{B}T}\left[\sum_{i=1}^{M}\frac{1}{2}Q_i\,\dot{\eta}_i^2\right]\right) \tag{8.11}$$

in the phase of the extended system, as can be proven by showing that Eq. (8.11) is stationary.[156] As indicated before, the canonical distribution f_c for the physical system is obviously contained therein. Thanks to the coupling of the fictitious and the physical degrees of freedom in Eqs. (8.10), each of the two factors in Eq. (8.11) can still vary during the course of the dynamics. This results in the sampling of the canonical distribution of the physical system, if the dynamics of the total system is ("sufficiently") ergodic. Furthermore, along a trajectory, the following quantity is conserved

$$\tilde{H}^\mathrm{NHC}(\{\boldsymbol{R}_I\}_I, \{\dot{\boldsymbol{R}}_I\}_I, \{\eta_i\}_i, \{\dot{\eta}_i\}_i) \quad = V(\{\boldsymbol{R}_I\}_I) + \sum_{I=1}^{N}\frac{1}{2}m_I\dot{\boldsymbol{R}}_I^2 + \sum_{i=1}^{M}\frac{1}{2}Q_i\,\dot{\eta}_i^2 + 3Nk_\mathrm{B}T\,\eta_1 + \sum_{i=2}^{M}k_\mathrm{B}T\,\eta_i \tag{8.12}$$

Evidently, $\tilde{H}$ is not a Hamiltonian that generates the dynamics given by Eqs. (8.10). The thermostat masses control the coupling strength to the fictitious bath. It can be shown that the thermostat coordinates oscillate approximately with an average characteristic frequency

$$\omega_\mathrm{NHC} = \sqrt{\frac{3Nk_\mathrm{B}T}{Q_1}} = \sqrt{\frac{k_\mathrm{B}T}{Q_i}} \quad , \quad i \in \{2, \ldots, M\}\,. \tag{8.13}$$

It is common practice to choose ω_NHC according to vibrational properties of the physical system, e.g. phonon frequencies.[156] However, very often this choice is also guided by numerical convenience when integrating Eqs. (8.10) and is hence completely arbitrary. Again, just like in case of the surface oscillator described in Section 8.2, the bath is condensed into a single parameter.

Finally, thermostats are still an active field of research and latest developments incorporate both stochastic and velocity rescaling elements,[485] again in contrast to the continuous dynamics provided by the Nosé-Hoover based types. In any case, individual trajectories lose their physical meaning. This is obvious when stochastic elements are involved, just like in the case of (generalized) Langevin equations. In fact, without the systematic construction described in Section 8.1, the latter are often considered as stochastic thermostats as well. On the other hand, as Jellinek has pointed out as generalization of the Nosé-Hoover approach[486]

> *"[...] there are infinitely many different dynamics capable of mimicking the canonical ensemble [...]"*

By construction, same initial conditions can hence produce different deterministic continuous trajectories, only supposed to yield the right ensemble properties as time averages, if there are no problems due to ergodicity. The former are mere sampling tools, i.e. it is highly questionable whether a real physical trajectory in the large statistical system is correctly described by any of them. This has been seen as a chance to also capture properties of systems which are not in thermal equilibrium by non-equilibrium molecular dynamics (NEMD) simulations,[487–489]

as it is undoubtedly the case during an exothermic chemical reaction on a surface due to the concomitant release of chemisorption energy. However, the whole construction targets thermal equilibrium, quite in contrast to that of generalized Langevin equations (cf Section 8.1), which is, following Kantorovich,[456,457] a good argument in favor of stochastic boundary conditions as described at the end of Section 8.1 for the present NEMD purposes. Nevertheless, "thermostatting" a "boundary zone" to represent a heat bath and maintain a certain temperature is quite common in practice, in particular in simulations of thermal conductivity.[490] Quite so, it has also been employed in studies of surface dynamics recently, in combination with *ab initio* molecular dynamics (cf Section 8.3) – the latter becoming more feasible and popular in this field as well.[491,492]

8.6. Summary

Altogether, none of the previously employed models does include a realistic surface phonon band structure of the substrate and describes the adsorbate-substrate interaction at a first-principles level of theory. Therefore, it is not surprising that in his recent review Kroes considers an accurate description of the energy dissipation to phonons as one of the key challenges in contemporary theoretical modeling of gas-surface dynamics.[469] In particular, as discussed above, there are strong arguments for phonons to constitute the predominant energy dissipation channel for O_2 dissociation on Pd(100) studied here. Recent gas-surface dynamical studies for several other systems including electron-hole pair excitations on different levels of theory[44,46,74,384,393,394,493] suggest that this might be rule rather than exception. Even for the scattering of highly vibrationally excited NO molecules from a Au(111) surface, a system for which experiments have suggested electronic non-adiabatic effects to be of major importance,[29] Shenvi *et al.* have shown only recently by state-of-the-art simulations that still a large fraction (more than 30 %) of the energy dissipated into phonons.[38] In general, when adsorbates heavier than hydrogen are involved and chemisorption energies in the order of several electron volts are released, classical theory obviously becomes more and more appropriate and trivially ascribes an increasing importance to energy dissipation into phonons. A more accurate approach to describe the latter hence seems to be highly desirable.

Therefore, in the following chapter, first a new embedding scheme termed 'QM/Me' for metallic substrates in general is developed. Its ensuing application then allows to model the heat release (i.e. energy dissipation to phonons) during O_2 dissociation on Pd(100) from the highly desirable *ab initio* perspective – without the need for any parameters from experiment. Contrary to all approaches described above, it neither requires any fundamental physical approximations beyond Born-Oppenheimer *per se*, nor does it imply dynamics in which individual trajectories lose their physical meaning. In Chapter 9, these approaches are revisited in light of the new model, and in Chapter 10, its hitherto unrivaled accuracy is made use of in order to investigate the importance of two conceptually important aspects: The role of both surface phonons and substrate anharmonicity during exothermic surface chemical reactions are quantified on an *first-principles* basis for the first time.

9. "QM/Me" - a Novel Embedding Approach for Metallic Systems

As has been detailed in the previous chapter, there are no adequate "energy sinks from the shelf" allowing to model the energy dissipation into phonons during the exothermic dissociative adsorption of O_2 on Pd(100) from a state-of-the-art first-principles perspective.

Despite the also for present purposes very appealing spatially motivated combination of different levels of theory and concomitant accuracy, traditional "Quantum Mechanics/Molecular Mechanics" (QM/MM) based embedding treatments have never been successfully applied to adsorption problems on Metals. Therefore, a new method allowing embedding for such systems is the topic of this chapter – and consequently christened "QM/Me". After details about its construction have been laid out in Section 9.1, first results from its application to O_2 dissociation on Pd(100) are presented in Section 9.2, which are finally summarized thereafter in Section 9.3, together with an outlook to a variety of straightforward further applications.

9.1. Embedding within Periodic Boundary Conditions

9.1.1. Embedding Ansatz

In order to keep a proper description of the adsorbate-substrate interaction during the adsorption,[82] the following embedding ansatz employing periodic boundary conditions (PBCs) for the quantum mechanical energies is proposed:

$$V^{\mathrm{QM/Me}}(\mathcal{R}) = V^{\mathrm{Me}}(\mathcal{R}_{\mathrm{bath}}) + \underbrace{\left[E^{\overline{\mathrm{QM}}}(\mathcal{R}_{\mathrm{slab}} \cup \mathcal{R}_{\mathrm{ads}}) - E^{\overline{\mathrm{QM}}}(\mathcal{R}_{\mathrm{slab}})\right]}_{\equiv V^{\Delta\overline{\mathrm{QM}}}(\mathcal{R}_{\mathrm{slab}} \cup \mathcal{R}_{\mathrm{ads}})} \tag{9.1}$$

where the coordinate sets $\mathcal{R}$, $\mathcal{R}_{\mathrm{bath}}$, $\mathcal{R}_{\mathrm{slab}}$ and $\mathcal{R}_{\mathrm{X}}$ are defined as

$$\mathcal{R}_{\mathrm{ads}} = \{\boldsymbol{R}_X\}_{X \in \{\text{adsorbate atoms in embedding cell}\}} \tag{9.2a}$$

$$\mathcal{R}_{\mathrm{slab}} = \{\boldsymbol{R}_M\}_{M \in \{\text{metal atoms in embedding cell}\}} \tag{9.2b}$$

$$\mathcal{R}_{\mathrm{env}} = \{\boldsymbol{R}_M\}_{M \in \{\text{metal atoms in environment}\}} \tag{9.2c}$$

$$\mathcal{R}_{\mathrm{bath}} = \{\boldsymbol{R}_M\}_{M \in \text{bath}} = \mathcal{R}_{\mathrm{slab}} \cup \mathcal{R}_{\mathrm{env}} \tag{9.2d}$$

$$\mathcal{R} = \{\boldsymbol{R}_I\}_{I \in \text{model}} = \mathcal{R}_{\mathrm{bath}} \cup \mathcal{R}_{\mathrm{X}}\,. \tag{9.2e}$$

$\mathcal{R}_{\mathrm{env}}$ has been defined in addition conveniently collecting the coordinates of all the atoms in the environment added due to the embedding. Both Eq. (9.1) and the definitions Eq. (9.2) are illustrated in Fig. 9.1.

$V^{\overline{\mathrm{QM}}}$ is obtained from two quantum mechanical calculations within identical PBCs, defined by the embedding cell, using density functional theory according to the previously employed setup (cf Chapter 5). The associated region is the impingement area around the molecule, i.e. the same supercell which could also have been used in a treatment via conventional *ab initio* molecular dynamics as detailed in Section 8.3.

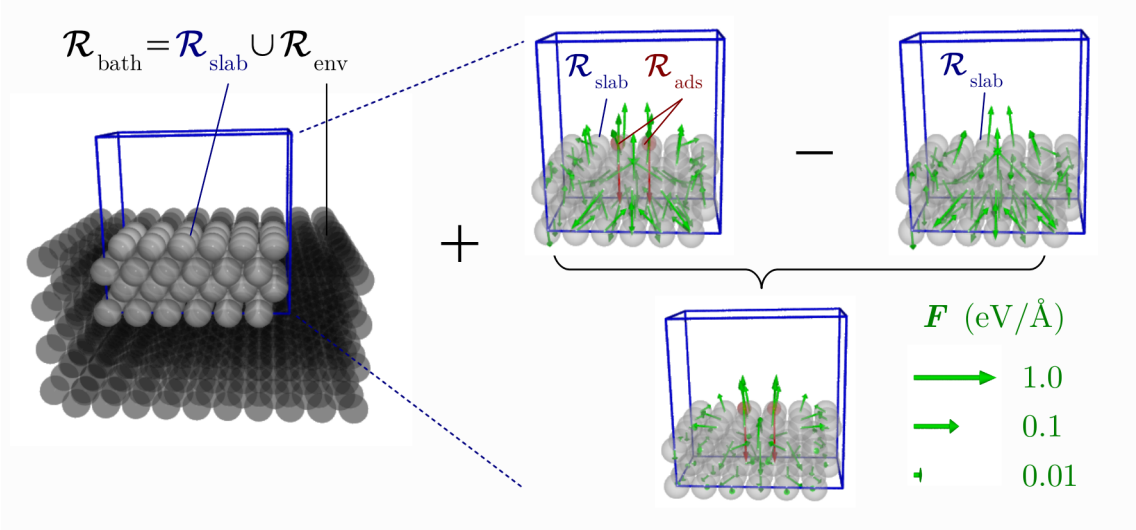

Figure 9.1.: Schematic illustration of the novel QM/Me embedding scheme as defined in Eq. (9.1) for the example of O_2 adsorption on Pd(100). A possible embedding cell for the periodic quantum mechanical calculations is indicated in blue. Palladium atoms ($\mathcal{R}_{\text{slab}}$) and an oxygen molecule ($\mathcal{R}_{\text{ads}}$) contained therein are shown in gray and red, respectively. In the left part, a few additional palladium atoms in the environment ($\mathcal{R}_{\text{env}}$) formed by the bath ($\mathcal{R}_{\text{bath}}$) are indicated in black. (Sets of respective coordinates given in parentheses are defined by Eqs. (9.2).) Note that this image is only schematic, i.e. sizes of bath and embedding cells employed in actual calculations differ from what is shown here. In the right, Hellman-Feynman forces on the atoms in the embedding cell are visualized in green. Resulting force differences $\boldsymbol{F}_I^{\Delta\overline{\text{QM}}}(\mathcal{R}_{\text{slab}} \cup \mathcal{R}_{\text{ads}})$ according to Eq. (9.4) are shown in the bottom part. As discussed in the text (in more detail in Section 9.1.2), they decay quickly with increasing distance from the adsorbate.

V^{Me} indicates an energy from an interatomic potential (cf Section 3.2) suitable for the description of metals, which should be computationally much less expensive compared to DFT but nevertheless on par in its accuracy with the latter for bath atoms which are only slightly distorted from their equilibrium lattice sites. Despite these low demands on transferability, a seamless match is still required, which is achieved in this context by an adaption of the modified embedded atom method (MEAM),[189–191] as described in detail in the following Section 9.1.3.

Inside the supercell used for the periodic quantum mechanical calculations, the difference term $V^{\Delta\overline{\text{QM}}}$ cancels elastic contributions provided on the DFT level for the metals atoms $\mathcal{R}_{\text{slab}}$, which are already taken care of by V^{Me}, and thus acts as a correction that (e.g.) properly captures the bond breaking constituting the "origin" of a concomitant energy release in course of an exothermic chemical reaction. It properly extends the interatomic potential by adding the missing contributions due to the adsorbate-substrate interaction and any direct interactions between "multicomponent adsorbates" like e.g. an O_2 molecule. Thanks to the description of the latter on a quantum mechanical level, all the important many-body effects are included, contrary to descriptions of even only monoatomic adsorbates with parametrized potentials in the past.[304,326,448]

Obviously, $V^{\Delta\overline{\text{QM}}}$ has been motivated by the usual way how binding energies of adsorbates on surfaces are calculated, as given by e.g. Eq. (5.9) or Eq. (6.24). In those cases, however, all

energies are minimized individually with respect to the corresponding nuclear coordinates, and a constant reference is used when energies of different configurations are compared (energy of the O_2 molecule in the two aforementioned cases). The latter could be introduced to $V^{\Delta\overline{\mathrm{QM}}}$ here as well, but evidently is of no importance for the dynamics discussed in the following.

Of course, Eq. (9.1) is based on the assumption that $V^{\Delta\overline{\mathrm{QM}}}$ provides well-defined quantum mechanical adsorbate-substrate and adsorbate-adsorbate interaction augmentations to V^{Me} in the sense that they are effectively localized around the adsorbates. In fact, on the level of energies it is rather well known from DFT adsorption studies relying on the aforementioned expressions, that in particular for small adsorbates like atoms or diatomics on metal surfaces adsorption energies reach a constant value on a meV scale for moderately sized supercells and corresponding rather small minimum distances between periodic images within the PBCs (3×3 supercells for the present system, see e.g. Section 5.3 or the work by Zhang and Reuter[16]). This can be seen as a natural consequence of the nearsightedness principle[234,235] which is particularly effective due the efficient screening properties of metallic systems.[494] The generalization to arbitrary configurations implied by $V^{\Delta\overline{\mathrm{QM}}}$ will be discussed in detail in Section 9.1.2, focusing on the forces (*vide infra*) which are employed in the ensuing dynamics. Finally, for oxygen adsorption on Pd(100), Zhang and Reuter have also observed that energy differences like those in $V^{\Delta\overline{\mathrm{QM}}}$ seem to cancel a part of the exchange-correlation error at least when comparing local and semi-local functionals.[16] Though by no means part of the original and primary goals of the embedding ansatz proposed by Eq. (9.1) above, its overall description might thus even go beyond the DFT level of accuracy originally to be expected should this trend prevail – but of course also depending on the quality of V^{Me}).

It is interesting to note that Eq. (9.1) bears similarities to the energy function used within the ONIOM embedding approach[470] as given by Eq. (8.8), but with the crucial difference that the construction of clusters is avoided entirely, thus allowing to overcome the inapplicability of the latter to metallic systems (cf Section 8.4). In addition, the embedding region is treated twice at the same level of theory, each containing a different set of atoms, which is supposed to suppress boundary effects and yields a many-body augmentation of an interatomic potential. It might be interesting to explore whether the latter aspect could also be beneficially applied to traditional cluster based embedding.

In order to make the above embedding ansatz become practical within (classical) molecular dynamics simulations (MD), forces resulting from the potential energy given by Eq. (9.1) are required (cf Chapter 3). Just like for the ONIOM scheme they are easily obtained according to

$$\boldsymbol{F}_I^{\mathrm{QM/Me}}(\mathcal{R}) = \boldsymbol{F}_I^{\mathrm{Me}}(\mathcal{R}_{\mathrm{bath}}) \;+\; \boldsymbol{F}_I^{\Delta\overline{\mathrm{QM}}}(\mathcal{R}_{\mathrm{slab}} \cup \mathcal{R}_{\mathrm{ads}}) \quad \text{with } I \in \text{model}\,, \tag{9.3}$$

where the individual contributions are

$$\boldsymbol{F}_I^{\mathrm{Me}}(\mathcal{R}_{\mathrm{bath}}) = \begin{cases} -\boldsymbol{\nabla}_{\boldsymbol{R}_I} V^{\mathrm{Me}}(\mathcal{R}_{\mathrm{bath}}) & \text{if } I \in \text{bath} \\ 0 & \text{otherwise} \end{cases} \tag{9.4a}$$

and

$$\boldsymbol{F}_I^{\Delta\overline{\mathrm{QM}}}(\mathcal{R}_{\mathrm{slab}} \cup \mathcal{R}_{\mathrm{ads}}) = \begin{cases} -\boldsymbol{\nabla}_{\boldsymbol{R}_I} E^{\overline{\mathrm{QM}}}(\mathcal{R}_{\mathrm{slab}} \cup \mathcal{R}_{\mathrm{ads}}) & \text{if } I \in \text{adsorbate atoms} \\ -\Big[\boldsymbol{\nabla}_{\boldsymbol{R}_I} E^{\overline{\mathrm{QM}}}(\mathcal{R}_{\mathrm{slab}} \cup \mathcal{R}_{\mathrm{ads}}) & \\ \qquad -\boldsymbol{\nabla}_{\boldsymbol{R}_I} E^{\overline{\mathrm{QM}}}(\mathcal{R}_{\mathrm{slab}})\Big] & \text{if } I \in \text{metal atoms in environment} \\ 0 & \text{otherwise} \end{cases} \tag{9.4b}$$

Using the flexible self-developed interface extension to the LAMMPS code, which is described in detail in Appendix D.2, corresponding trajectories are easily obtained, triggering two CASTEP calculations to evaluate both $\{-\boldsymbol{\nabla}_{\boldsymbol{R}_I} E^{\overline{\mathrm{QM}}}(\mathcal{R}_{\mathrm{slab}} \cup \mathcal{R}_{\mathrm{ads}})\}_I$ and $\{-\boldsymbol{\nabla}_{\boldsymbol{R}_I} E^{\overline{\mathrm{QM}}}(\mathcal{R}_{\mathrm{slab}})\}_I$ in each MD step, whereas the remaining forces $\{-\boldsymbol{\nabla}_{\boldsymbol{R}_I} V^{\mathrm{Me}}(\mathcal{R}_{\mathrm{bath}})\}_I$ are obtained analytically within LAMMPS directly. Employing a velocity Verlet integrator (cf Section 3.3) with a time step of 2.5 fs, the total energy is typically conserved by less than 1×10^{-3} meV per atom for a simulation containing 125,002 atoms when enforcing and assuring accurate force convergence up to $5 \times 10^{-4}\,\mathrm{eV\,\AA^{-1}}$ during the self-consistency cycles thanks to the DM/EDFT scheme introduced in Section 5.3. Of course, this is to be expected since Eqs. (9.4) are the exact derivatives of the potential energy contribution of the aforementioned total energy given by Eq. (9.1) – as long as a correct implementation and proper handling of the accuracy of the numerically determined force components is taken care of.

At last, concluding this introduction of QM/Me embedding, its two intrinsic principle sources of embedding related errors are summarized:

1. The effective localization of the force differences resulting from $V^{\Delta\overline{\mathrm{QM}}}$.

2. The description of the bath according to the "cheaper" level theory given by V^{Me}.

Both will be discussed individually in more detail in the following two subsections.

Evidently, the second error source is intrinsic to any kind of embedding technique. As indicated before, in the present case, interatomic potentials should generally be able to describe the expected small displacements from equilibrium positions in the bath outside the embedding region rather accurately. "Force matching" the DFT description still requires some attention as described in Section 9.1.3.

The first source of error one can, of course, be systematically controlled and monitored by changing the size of the embedding region. As already indicated in Fig. 9.1 and detailed in Section 9.1.2, the force differences resulting from $V^{\Delta\overline{\mathrm{QM}}}$ decay rather quickly as a function of distance (within the minimum image convention in PBCs) from the center of strong chemical interaction. Errors due to unphysical reflections of phonon propagations at the cell boundaries are thus avoided for moderately sized embedding supercells and do not have to be carefully suppressed like e.g. in the absorbing boundary conditions approach (cf Section 8.1).[449,453,454]

As proclaimed before, this provides a huge conceptual advantage compared to conventional *ab initio* molecular dynamics (cf Section 8.3). As long as the latter are not run routinely with the same stringent convergence settings as single point calculations,[25,363] resulting systematic errors due to badly converged (numerical) forces must be seen with the same concern as the two aforementioned sources of errors for the embedding. With the rather tight settings chosen here as mentioned above and in the remainder of this work, it was not necessary to extend that

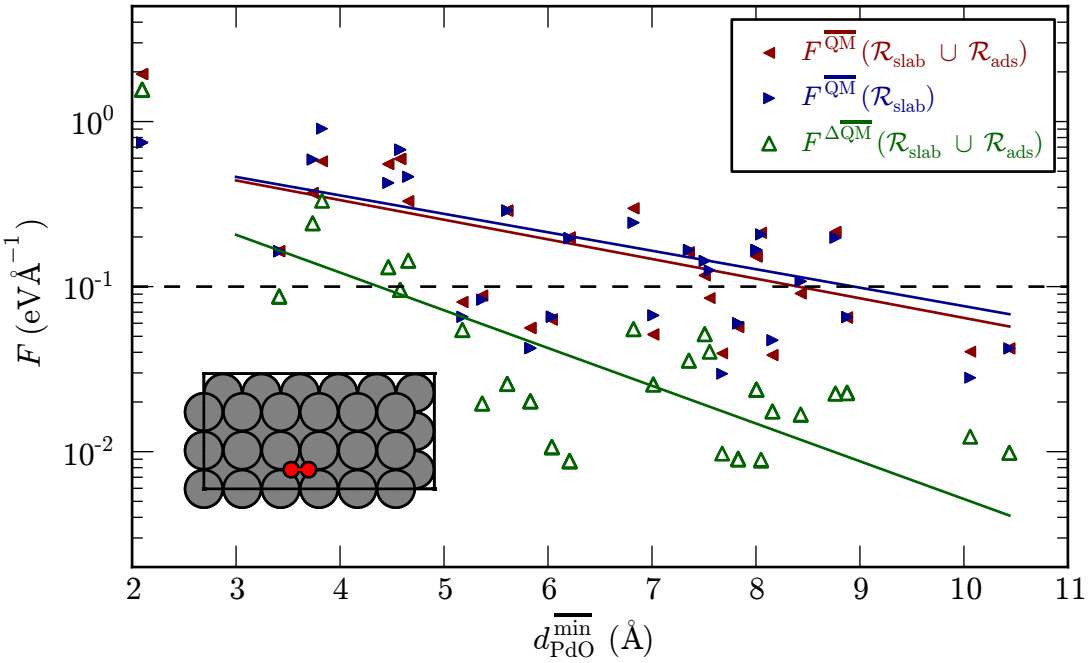

Figure 9.2.: Decay of force differences obtained for QM/Me embedding with increasing distance from the adsorbates. Results shown are for the snapshot displayed in Fig. 9.1, with equivalent trends also found for all other time steps along the trajectory. Lines are only meant to guide to the eye and are based on a fit of an exponential function. It it interesting to note that the corresponding decay constant for the absolute values of $\boldsymbol{F}_I^{\Delta\overline{\mathrm{QM}}}$ (green) is twice as large as those for the other two "raw" forces (red and blue) from the periodic DFT calculations.

list accordingly. In addition, again the use of differences might provide some additional error canceling which however has not yet been explored here.

Compared to other applications of traditional QM/MM-based embedding in materials science 0.1 meV Å^{-1} can be taken as a typical "good" accuracy estimate for the embedding induced force error.[482] This can also be achieved in applications in the bio-community,[471] but systematic error estimates are not routinely included in most corresponding studies. Finally, when doing "quantum mechanics without the electrons" for large systems, by using only recently developed interatomic potentials based on sophisticated interpolation techniques (neural networks[183] or Gaussian processes[184]), hitherto reported force errors are even higher. 0.1 meV Å^{-1} is thus taken as a target and comparison value in the following two subsections.

9.1.2. Force Differences

The effective localization of the force differences arising from $V^{\Delta\overline{\mathrm{QM}}}$ in Eq. (9.1) is crucial for the QM/Me embedding scheme introduced in the previous section and has already been visualized in Fig. 9.1 by force fields for a snapshot of a trajectory using a 6×3 with four layers embedding cell. In order to further quantify the anticipated "decay" from the center of strong chemical interaction, i.e. the location of both oxygen atoms, Fig. 9.2 plots absolute values of forces (and their differences) corresponding to the snapshot in the former figure. The distance

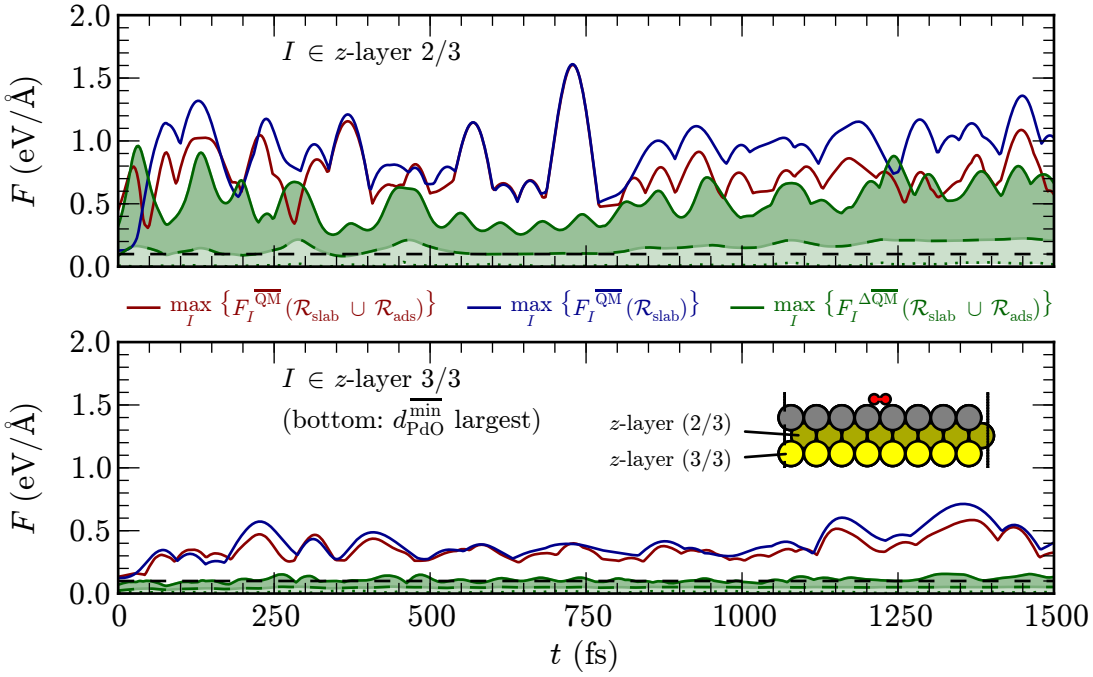

Figure 9.3.: Forces and their differences (same coloring as in Fig. 9.2) along the entire trajectory for atoms in the two bottommost layers of an 8×3 embedding cell with three layers as indicated in the inset of the lower panel. For the force difference F_I, maxima, averages and minima are shown at each time step as well by the different shades of green. As to be expected from Fig. 9.2, these differences on atoms in the third (bottommost) layer, which are most distant from the two oxygen adsorbates, are much smaller compared to those in the second one. Their maxima are nearly always smaller than 0.1 meV Å^{-1}, which is further discussed in the text. It is expected that a reduction far below this value would have been found in fourth layer if it had been included.

to the aforementioned center is defined according to

$$d_{\mathrm{PdO}}^{\overline{\mathrm{min}}} = \min_{\boldsymbol{R}_\mathrm{I} \in \overline{\mathcal{R}_\mathrm{Me}}} \min_{\boldsymbol{R}_\mathrm{J} \in \mathcal{R}_\mathrm{O}} \|\boldsymbol{R}_I - \boldsymbol{R}_J\|_2 \quad . \tag{9.5}$$

Here, $\overline{\mathcal{R}_\mathrm{Me}}$ includes all periodic images so that the definition of $d_{\mathrm{PdO}}^{\overline{\mathrm{min}}}$ is based on the minimum image convention. As to be expected from the concept of nearsightedness due to the efficient screening in metallic systems,[234,235] exponential decay of the absolute values of the forces with respect to $d_{\mathrm{PdO}}^{\overline{\mathrm{min}}}$ provides a reasonable fit. With the elastic contributions canceled and thus only focusing on the chemical interaction between the Pd(100) surface and the two oxygen atoms in the force differences, this decay is significantly faster and thus very beneficial for QM/Me embedding. In this respect, Fig. 9.2 is representative, i.e. qualitatively identical results have been obtained for a plethora of other snapshots as well.

In order to systematically check the decay for different embedding cells along entire trajectories, the size of the former has been selectively increased in x, y and z directions. This allows to monitor the maximum absolute values of forces and their differences in these additional slices or layers and compare their decay with those "already" included in the accordingly smaller embedding cells. Building upon a 8×3 cell with three layers, which has come into particular

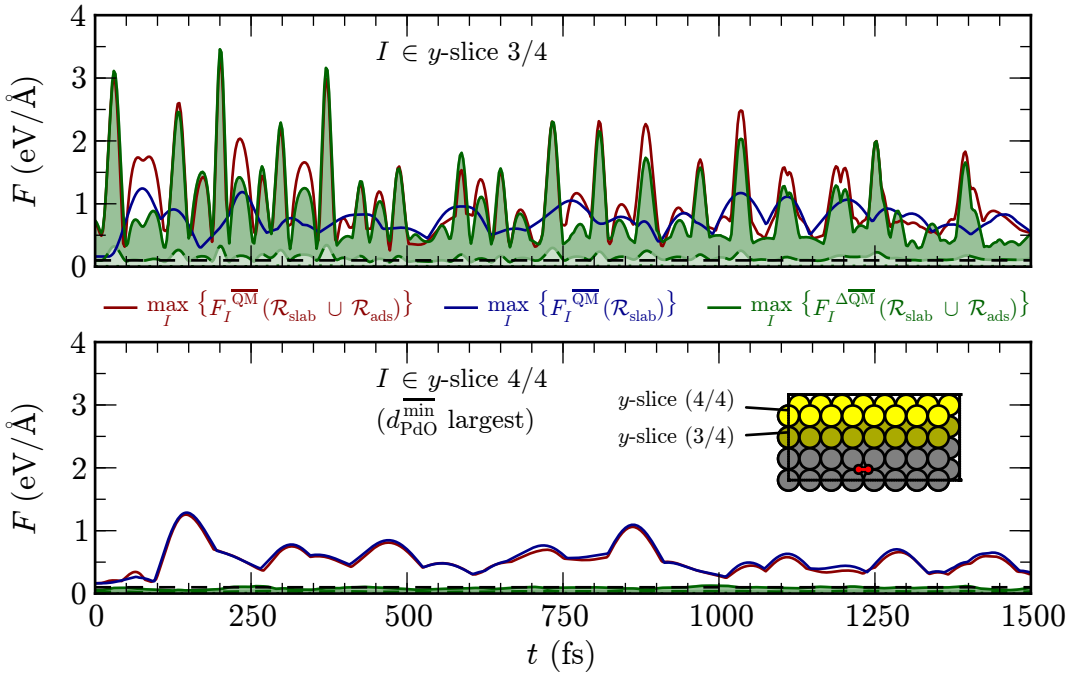

Figure 9.4.: Same as Fig. 9.3, but for the y-slices most distant from the oxygen adsorbates in an 8×4 embedding cell with three layers as indicated in the inset of the lower panel. Again, force differences in the fourth y-slice, which is most distant from the two oxygen adsorbates along the entire trajectory, are significantly smaller than those in the third.

focus after first indications of the results presented in Section 9.2.3, Figure 9.3, Fig. 9.4 and Fig. 9.5 show those quantities as a function of time based on the aforementioned embedding cell itself as well as a three-layer 8×4 and a three-layer 10×3 counterpart, respectively. Of course, as the slices are still "fairly close" to both oxygen atoms, distances according to Eq. (9.5) for atoms contained therein vary quite significantly. Since "distance plots" like the one shown in Fig. 9.2 are always based on the cuboid QM/Me embedding cells, which contain full neighbor shells only up to certain values of $d_{\mathrm{PdO}}^{\overline{\mathrm{min}}}$ always smaller than the largest ones, the "layers and slices" plots provide a good practical estimate of the embedding error due to force differences. This can be compared against the "typical" criterion of $0.1\,\mathrm{meV\,Å^{-1}}$ set out in Section 9.1.1. According to these plots it can be expected to be fulfilled in a 8×3 embedding cell with three layers in both y and z directions. In x this is not the case at the end of the trajectory, but this is not surprising due to the adsorbate motion detailed in Section 9.2.3 and, as extensively discussed therein, this by no means affects the concomitant results.

Finally, it has to be noted that the system behaves very chaotically with respect to the adsorbate dynamics. Trajectories resulting from the different embedding cells mentioned above do still deviate after several hundred femtoseconds – without however the main results presented in Section 9.2 being affected, as carefully discussed therein.

9.1.3. Bath Description

Following the spirit of embedding techniques, also for their extension to metallic systems proposed above obviously a computationally cheaper method is required for the description of the

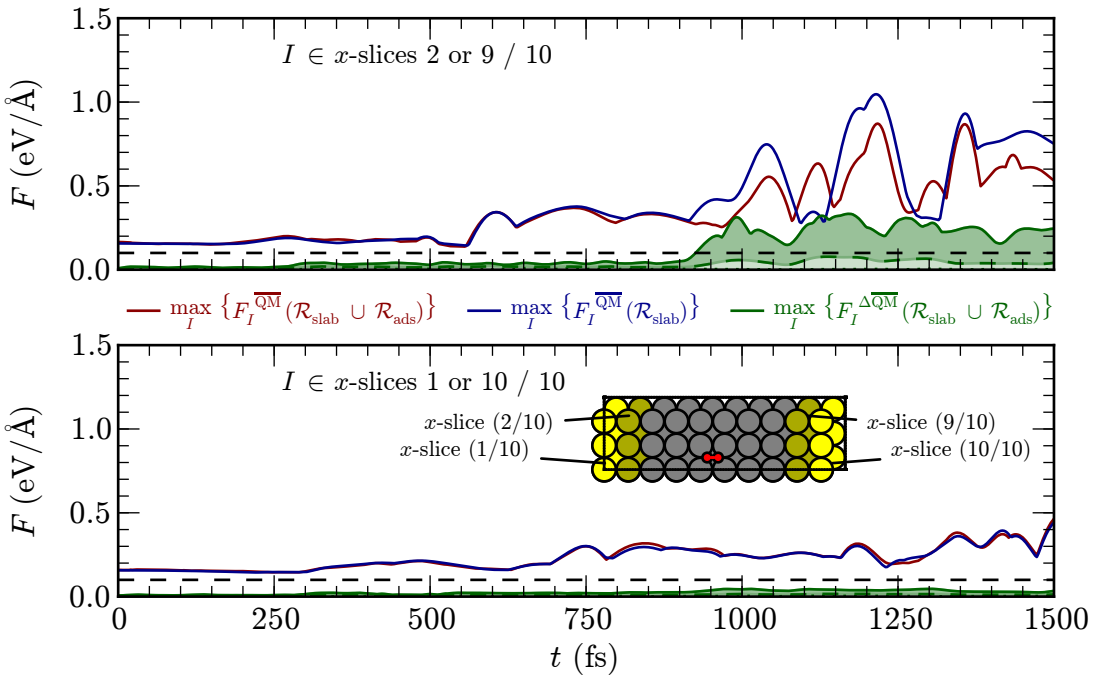

Figure 9.5.: Same as Fig. 9.4, but for the x-slices initially most distant from the oxygen adsorbates in a 10×3 embedding cell with three layers as indicated in the inset of the lower panel. Force differences in these slices only gain significant sizes as the oxygen adsorbates move towards them as detailed in the remainder of this chapter (cf Section 9.2.3).

	E_0	R_0	α	A	$\beta^{(0)}$	$\beta^{(1)}$	$\beta^{(2)}$	$\beta^{(3)}$	$t^{(0)}$	$t^{(1)}$	$t^{(2)}$	$t^{(3)}$
Baskes[191]	3.91	2.75	6.43	1.01	4.98	2.2	6.0	2.2	1.0	2.34	1.34	4.48
Beurden[187]	3.68	2.80	6.24	1.0	5.28	4.07	4.93	2.18	1.0	2.27	6.22	3.68
this work	3.88	2.78	6.18	1.0	4.30	4.77	0.89	0.0	1.0	8.68	5.11	−10.93

Table 9.1.: Parameters for the optimized MEAM potential (MEAMopt) obtained in this work by force matching DFT data as described in the text. Their meaning is explained in detail in Section 3.2.2. Values obtained and used by Baskes[191] as well as van Beurden and Kramer[187] are shown for reference.

	d_{12}	d_{23}	d_{34}
PBE(CL)	1.948	1.970	1.965
MEAMopt	1.943	1.968	1.964

Table 9.2.: Comparison of interlayer distances d_{ij} between layers i and j of the Pd(100) surface obtained from DFT-PBE(CL) (cf Section 5.1 and the optimized MEAM potential (MEAMopt).

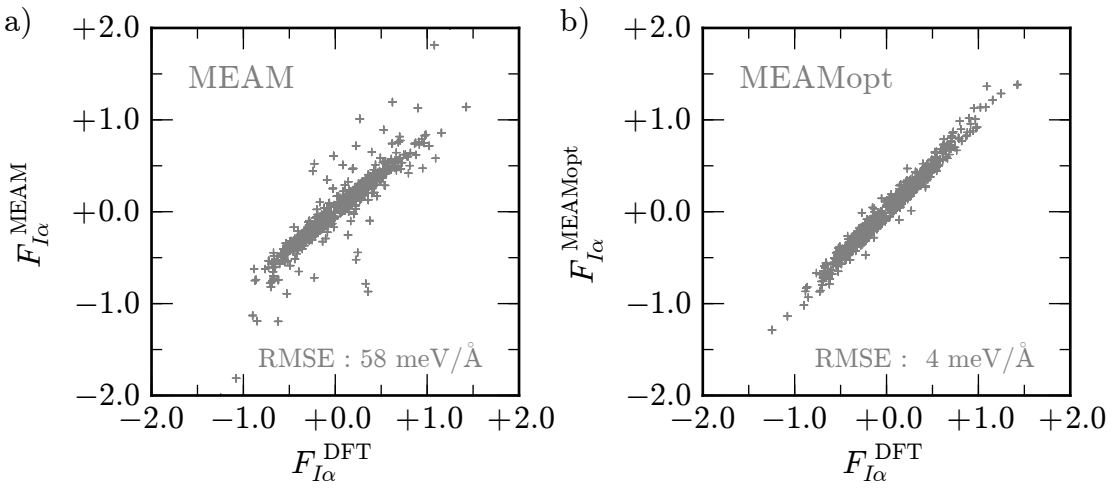

Figure 9.6.: Force errors a) before and b) after optimization of the MEAM potential by force matching. The former is based on the parametrization by Baskes[191], which is given together with the one constituting MEAMopt in Table 9.1.

environment, i.e. a large, bulk-like bath. At least for "low" substrate temperatures and perfect, defect-free surfaces considered here the essential demand to mimic first-principles quality for "small" displacements, with a realistic description of phonons in particular, can generally be met by interatomic potentials that have been developed during the last decades (cf Section 3.2.2).[i] Unfortunately, in order to seamlessly match the DFT description of the embedding region, none can be "taken from the shelf" directly. The aforementioned requirements might also be fulfilled by a harmonic potential according to Eq. (4.2), which is implicitly obtained from phonon calculations. This has been done before starting from a bulk reference,[36,434,448] thus lacking a good description of surface phonon modes. The latter have been ascribed an important role for the energy uptake,[23] but are quite cumbersome to include within a corresponding harmonic force field in the dynamics (cf Section 10.3 and Appendix D.4. Furthermore, given the amount of energy to be dissipated, it is not clear *a priori* how important anharmonic couplings might be. These aspects are investigated in great detail in Chapter 10. Here however, alternatives which do not suffer from these limitations and are yet simple(r) to (re)parameterize are sought out. Starting point for the latter process are snapshots taken from a O_2 dissociation trajectory obtained with conventional *ab initio* molecular dynamics, whose results will also be discussed in the following (cf Section 9.2), recalculated with the adsorbate atoms deleted as in the previous section.

Simple pair potentials, like most prominently the forms proposed by Lennard-Jones or Morse, are not well suited to describe bulk metals or their surfaces at all. Instead, forms incorporating many-body effects have been proposed in the literature to account for the (non-covalent) nature of metallic bonding. (cf Section 3.2). Indeed, simple rescaling of coordinates to account for the difference between the PBE and experimental lattice constants used in the original parametrization (together with other empirical data) of the embedded atom method (EAM)

[i] It is interesting to note in this context that one possible future application of the QM/Me approach might be to straightforwardly "correct" the description of interatomic potentials around defects.

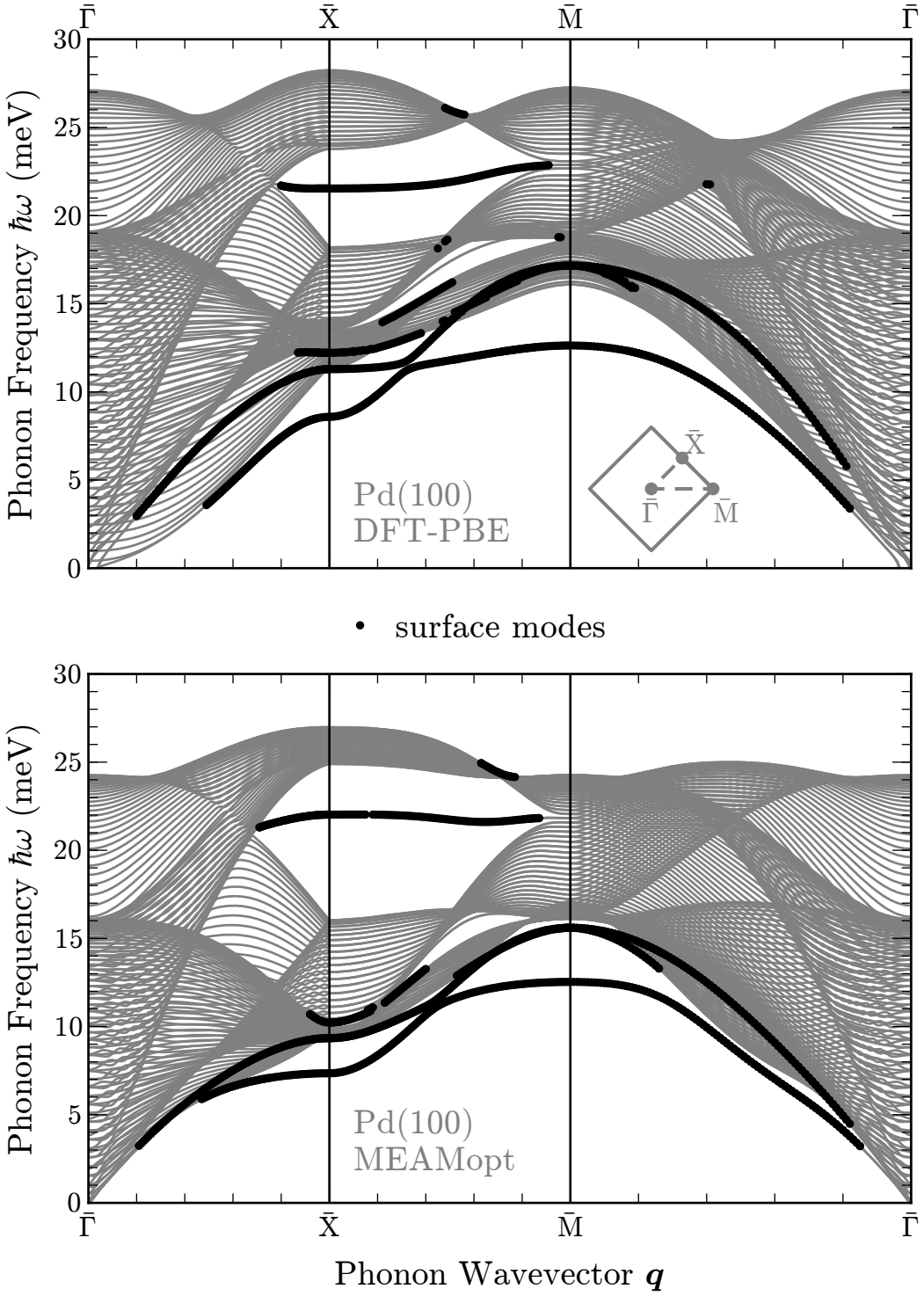

Figure 9.7.: Surface phonon dispersion of Pd(100) as obtained by DFT-PBE(CL) (cf Section 5.1) and the optimized MEAM potential (MEAMopt). Modes whose vibrational weight according to their displacement Eigenvector exceeds 20 % in the first two layers (cf Section 4.3) were identified as surface modes and are indicated by the small black circles.

potential for palladium[175] already yields remarkable agreement. However, despite specialized tools like the potfit code[186] which have been developed over recent years, further systematic optimization of the underlying pair potential, electron density and embedding functions (cf Section 3.2.2) remains a rather complex fitting problem.[495,496] Given the similarities of EAM to other approaches like the effective medium theory[176,177] or the glue model[178] the same holds for those as well.

On the other hand, the modified embedded atom method (MEAM) incorporates physical properties of surfaces in its functional form, which is (thus) more rigorously defined – and relies only on a rather modest set of parameters as detailed in Section 3.2.2. Force matching (cf Section 3.2.2) via a least squares fit according to a Levenberg-Marquardt algorithm with adequately imposed boundaries[497] yields the desired improvement over previous parameterizations[187,191] as shown in Fig. 9.6.[ii] Nevertheless, the latter provided several useful starting values simplifying the fitting procedure and are thus given together with the optimized parameters obtained here in Table 9.1. For slabs with six and more layers, which are obviously of particular interest in the present context, both surface relaxation and phonon dispersion, presented in Table 9.2 and Fig. 9.7, respectively, are reasonably well reproduced compared to the DFT-PBE reference, without having been actively incorporated into the fit. The surface phonon calculations have been carried out by an extension of the direct method as detailed in Section 4.2, based on a version of PHONOPY which has been modified accordingly by the author of this thesis (cf Section 4.4). As to be expected from the bulk phonon calculations presented in Section 5.1, laterally converged results are obtained based on 3×3 multiples of the surface unit cell. Slabs with eight layers then assure convergence with respect to the latter and are still "affordable" for the finite displacement calculations within the first-principles reference. Using slab filling, the dispersion for the 50 layer equivalents shown in Fig. 9.7 are then obtained. For what follows in Chapter 10 it is important to emphasize that surface modes are reasonably well described – meeting the demands formulated above.

9.2. Results and Discussion

The QM/Me implementation based on LAMMPS and CASTEP, which has already silently served its purpose in the previous section, is employed to obtain the results presented in the following as well. The LAMMPS code drives the MD integration via a newly developed interface, which is described in full technical detail in Appendix D.2 of Appendix D. Given the experiences concerning energy conservation from Section 9.1.1 trajectories are integrated according to the velocity Verlet algorithm using a time step of 2.5 fs.

According to the error estimates discussed in Section 9.1.2, an (8×3) supercell of the surface unit cell of the Pd(100) surface with three layers is used as embedding cell, which is described with the same DFT setup based on CASTEP that has been described and used before in Chapters 5 and 6 (> 10 Å of vacuum, PBE, $E_{\text{cut}} = 400$ eV, equivalent of $2 \times 4 \times 1$ $\boldsymbol{k}$-points). Thanks to the DM/EDFT scheme introduced in Section 5.3, very tight electronic convergence settings can be maintained along entire trajectories, allowing to obtain extremely well converged forces

[ii] Based on the C routines by Manolis Lourakis, which are freely available under *GPL* from `http://www.ics.forth.gr/~lourakis/levmar`, and provide an excellent implementation of the Levenberg-Marquardt methods including convex constraints as proposed by Fukushima and coworkers[497] a rather general purpose command line utility was written: It allows to perform the aforementioned optimization by coupling to the MEAM implementation of Greg Wagner provided within the LAMMPS code using shell scripts and files.

(5×10^{-4} eV Å^{-1}), which are not routinely afforded in *ab initio* molecular dynamics for metallic systems. This is of particular importance for the results presented in Sections 9.2.2 and 9.2.3 and will also be picked up again in Section 10.3 of the next chapter.

The extended surface and bulk forming the bath is described by the optimized MEAM potential seamlessly matching the DFT data described in Section 9.1.3. Based on the simple estimate in Chapter 8 using the speed of sound in bulk palladium plus a generous safety margin (computational cost does not impose significant limitations here), a (50×50) surface unit cell with 50 layers, i.e. a total of 125,000 Pd atoms, is used for the bath. Periodic boundary conditions are employed in lateral directions for convenience, but, as verified below, do not restrict the propagation of excited phonons. For the sake of simplicity, the bath is initially kept at 0 K. Interlayer distances of the topmost layers are thus relaxed to their equilibrium values before the dynamics are started. In principal, also pre-equilibration to a particular surface temperature is straightforward by using standard molecular dynamics techniques, and would only require computationally inexpensive classical dynamics for the substrate. Future applications might ideed exploit the intriguing possibility of the present approach to model the former without any *a priori* simplifications.

Initial conditions are taken from the single entrance channel for dissociation identified in Chapter 6 beyond the spin transition point when the O_2 molecule is about 1.8 Å away from the surface with its molecular axis oriented parallel to the latter above a fourfold hollow site. This safely allows to perform non-spin polarized calculations, reducing the computational cost of the DFT part by a factor of two. As the entrance channel is very narrow (cf Chapter 6), trajectories starting from these conditions can be expected to be of exceptionally large statistical relevance.

Still, the dominant fraction of the CPU time, i.e. more than 95 %, is spent for the DFT force evaluations within the present computational setup including the efficient, state-of-the-art implementation of both the MEAM force field and the MD integration based on neighbor lists.[218] If found to be necessary (*vide infra*), the bath size could thus be easily increased further before the break-even point is reached (cf Appendix D.2).

9.2.1. Heat Dissipation

Since within the QM/Me approach the environment acting as bath is treated fully atomistically, an unprecedented both realistic and detailed quantification of heat dissipation can be obtained from a first-principles perspective. In contrast to all the "energy sinks from the shelf" described in Chapter 8, no *a priori* simplifications are implied, and heat transfer can directly be monitored by simply watching the dissemination of kinetic energy away from the impingement point of the O_2 molecule.

This is the origin of the chemical reaction which generates the heat by converting the 2.6 eV chemisorption energy (cf Chapter 5) accordingly. Figure 9.8 shows that both oxygen atoms equilibrate as expected while doing so, but are not yet fully in equilibrium with the bath after 1.5 ps, i.e. the end of the integration time that has been afforded for the trajectory: More than 75 meV still reside with each adsorbed oxygen atom, and the total kinetic energy of palladium atoms still fluctuates around less than $\frac{1}{2} \cdot 2.6\,\text{eV} = 1.3\,\text{eV}$ as would be expected in thermal equilibrium according to the equipartition theorem.

Focusing on the substrate, the kinetic energy that has left the embedding cell is of particular interest, as it provides a quantitative *a posteriori* characterization of the importance of the embedding itself. Figure 9.8 shows that after 1.5 ps only one fifth of the kinetic energy still

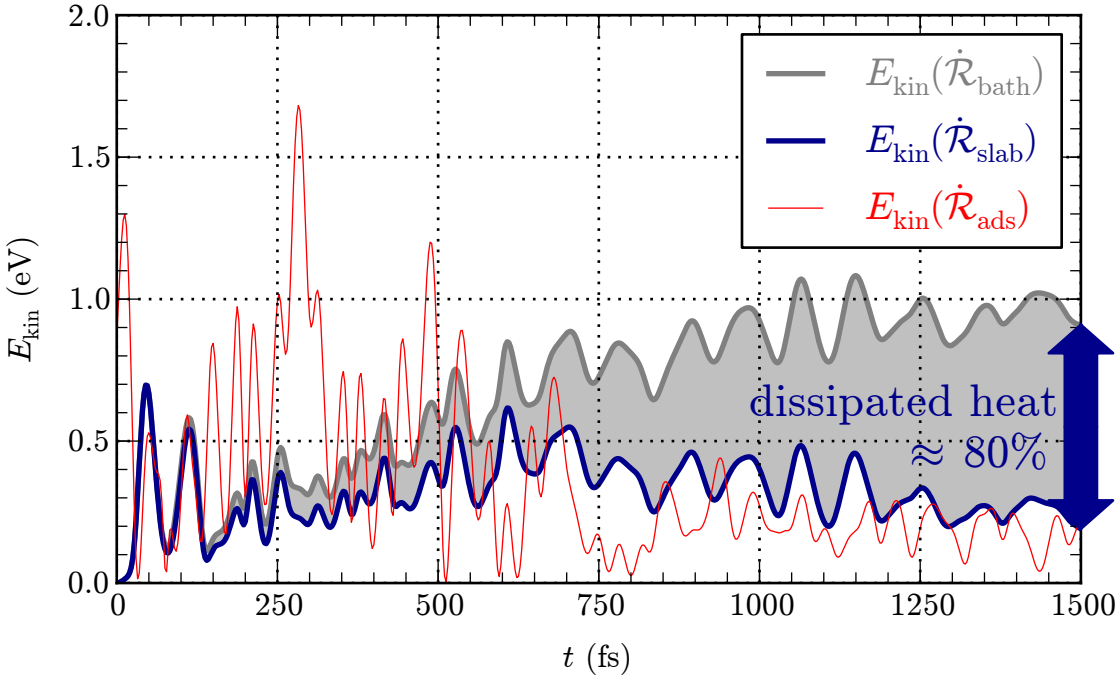

Figure 9.8.: Total kinetic energy of all palladium atoms in the bath (thick gray line) as well as those in the QM/Me embedding cell contained therein (thick blue line) as a function of time. The area between these two curves is a measure for the dissipated heat. In addition, the kinetic energy of the dissociating oxygen molecule is also shown (thin red line).

resides therein,

$$E_{\mathrm{kin}}(\dot{\mathcal{R}}_{\mathrm{slab}};t)\Big|_{t=1.5\,\mathrm{ps}} = \sum_{\dot{\boldsymbol{R}}_I \in \dot{\mathcal{R}}_{\mathrm{slab}}} \tfrac{1}{2} m_{\mathrm{Pd}}\, \dot{\boldsymbol{R}}_I^2(t)\Big|_{t=1.5\,\mathrm{ps}} \approx 0.2 \cdot E_{\mathrm{kin}}(\dot{\mathcal{R}}_{\mathrm{bath}};t)\Big|_{t=1.5\,\mathrm{ps}} \quad , \tag{9.6a}$$

while about 80 %

$$E_{\mathrm{kin}}(\dot{\mathcal{R}}_{\mathrm{env}};t)\Big|_{t=1.5\,\mathrm{ps}} = \sum_{\dot{\boldsymbol{R}}_I \in \dot{\mathcal{R}}_{\mathrm{env}}} \tfrac{1}{2} m_{\mathrm{Pd}}\, \dot{\boldsymbol{R}}_I^2(t)\Big|_{t=1.5\,\mathrm{ps}} \approx 0.8 \cdot E_{\mathrm{kin}}(\dot{\mathcal{R}}_{\mathrm{bath}};t)\Big|_{t=1.5\,\mathrm{ps}} \tag{9.6b}$$

of the total kinetic energy of all palladium atoms $E_{\mathrm{kin}}(\dot{\mathcal{R}}_{\mathrm{slab}};t)\Big|_{t=1.5\,\mathrm{ps}} \approx 0.9\,\mathrm{eV}$ has been transferred to "bath atoms" in the environment of the embedding cell. In other words, Eq. (9.6b) and Fig. 9.8 quantify the inherent, systematic error for this representative trajectory when no bath is included – like e.g. in conventional *ab initio* molecular dynamics, as all this energy would have been erroneously reflected back into the simulation cell by the periodic boundary conditions (cf Section 8.3). As the largely dominant fraction of the total atomistically resolved heat cannot be correctly accounted for thereby, an even only qualitatively correct description of the dissipation energetics thus forcibly demands to go beyond such conventional simulations. Although the simple back-of-the-envelope calculation based on the speed of sound in bulk palladium made in Chapter 8 already hinted into this direction, this might in its quantification yet still be a surprising and so much the more very important result.

Of course, it has been verified that the chosen bath size is large enough. boundaries of the latter. It turns out that a cuboid region centered below the impingement point containing only $20 \times 20 \times 20$ atoms already accommodates about 95 % of the total kinetic energy $E_{\mathrm{kin}}(\dot{\mathcal{R}}_{\mathrm{bath}})$ defined as before through Eq. (9.6b) after 1.5 ps of simulation time. So the dissipation dynamics with the $(50 \times 50 \times 50)$-atom bath chosen before certainly does not suffer from any lack of size convergence as far as the latter is concerned. Since the DFT calculations largely dominate the computational cost as already indicated before, no significant amount of CPU time has been wasted by the inclusion of this "safety margin" (also see Appendix D.2). On the other hand, due to the correspondingly finer sampling of reciprocal space, this provides an excellent starting point for the detailed phonon excitation analysis presented in Chapter 10.

9.2.2. Comparison with "Energy Sinks from the Shelf"

As QM/Me embedding does not imply any *a priori* simplifications for the dissipation dynamics, the results presented in the previous section can be seen as a reference which sets the benchmark for the more approximate "energy sinks from the shelf" described in Chapter 8.

Before turning to the results of the corresponding comparison shown in Fig. 9.9, several issues need to be clarified first in order ascertain proper comparability. Of course, the initial positions and momenta of the nuclei were all chosen to be exactly the same as for QM/Me before. But, after all, in very chaotic systems with large Lyapunov coefficients like the present one,[iii] numerically integrated trajectories can easily diverge from the "real" deterministic path[149] for mere technical reasons:

1. The surface oscillator (SO) could in principle have been coupled to the frozen surface potential energy surface obtained in Chapter 6 based on neural network interpolation (NN-PES) in the usual way[23,447] given by Eq. (8.6) or Eq. (8.7) in Section 8.2. However, the latter has never been trained for regions of large interatomic distances beyond the dissociation threshold on the surface, as this was never part of the original purpose detailed in that chapter. The accuracy of the finally obtained fit is thus highly uncertain in those areas. For that reason, a three-dimensional surface oscillator as described by Eq. (8.7) has been implemented into LAMMPS as detailed in Appendix D.3. This allows to employ the exact same MD integration infrastructure within LAMMPS (most notably velocity Verlet[213] instead of Bulirsch-Stoer[214] used for the dynamics on the NN-PES, cf Section 3.3) as for the QM/Me results.

2. Of course, also the implementations of the Langevin and Nosé-Hoover chains (NHC) thermostats (cf Sections 8.1 and 8.5) available in LAMMPS make use of that infrastructure.[iv] More precisely, the latter includes its own integrator based on the Liouville operator approach following Tuckerman and coworkers[216,217] as described in Section 3.3.3 in Part I. Both implementations have been thoroughly checked before their application in the present context by running dynamics with the optimized MEAM potential obtained before (cf Section 9.1.3), carefully monitoring the conservation of the respective conserved

[iii] Not evaluated quantitatively like e.g. in the work by Martyna and coworkers,[156] but experiences collected "along the way" already with the dynamics on the frozen surface have clearly revealed their chaotic character, which is well-known for other gas-surface dynamics systems as well.

[iv] See `http://lammps.sandia.gov/doc/fix_langevin.html` and `http://lammps.sandia.gov/doc/fix_nh.html`, respectively.

quantity.[v]

3. Forces are always obtained on-the-fly from CASTEP calculations with identical computational settings via the same coupling interface (cf Appendix D.2) for the same slab that has been used as embedding cell in Section 9.2.1 before. As already described in the beginning of this section, the former are "very conservative", i.e. very close to the "exact" derivatives of the DFT total energies, thanks to the tight electronic minimization enabled by the DM/EDFT scheme introduced in Section 5.3. Together with the small time step for the trajectory integration, not only excellent energy conservation is obtained, but also "very numerically deterministic" trajectories: By starting from slightly different numerically converged electronic ground states for identical initial positions and momenta of the nuclei, it has been verified that resulting trajectories even after 2 ps (800 integration steps) only differ insignificantly for the comparisons presented in the following. This is also holds for and is exemplified further by the results in Section 10.3 of the ensuing chapter.

Altogether, the effect of different energy sinks can thus be properly distinguished and compared.

In order to make this comparison as fair as possible, the frequency parameters have been chosen according to the Debye frequency $\frac{\omega_\mathrm{D}}{2\pi} = 5.82\,\mathrm{THz}$ obtained from the calculations of the bulk phonon spectra in Section 5.1 (CASTEP PBE-CL value). Though usually based on empirical data, the common practice for the surface oscillator[465,468] to use the average frequency of the Debye spectrum $\bar{\omega}_\mathrm{D} = \frac{3}{4}\omega_\mathrm{D}$ (cf Eq. (4.18)) together with the atomic mass of a surface atom was then followed.[vi] With thermostats set to $T = 0.1\,\mathrm{K}$, which aims to reproduce the non-pre-equilibrated bath used for QM/Me embedding before and is still numerically stable, all required parameters are then defined. The trajectory calculations have also been repeated with the resulting frequency parameters varied by a factor of two in both directions, but indeed, as has been observed for other systems before no qualitative differences were found thereby.[23,24,465] On the one hand, this insensitivity of the results with respect to the actual values of the parameters can be seen as comforting reassurance not to worry too much about the latter, on the other, it might already indicate the limited power of those models to capture the actual physics.

For the two thermostat approaches (Langevin and NHC) it is more important how many atoms are subject to the corresponding modified equations of motion. Of course, in the spirit of stochastic boundary conditions (cf Section 8.1) it appears to be most reasonable and in order to avoid any interference with the periodic boundaries of the underlying DFT calculations in lateral directions it is most straightforward only to abuse the latter for atoms in the bottommost layer. Thanks to the MD infrastructure provided by LAMMPS, trajectories with such mixed simple Newtonian and thermostat enriched equations of motions are straightforward to obtain.

In order to judge the ability of the "energy sinks from the shelf" to mimic the dissipation dynamics of QM/Me reference, Fig. 9.9 shows the kinetic energy of both oxygen atoms $E_\mathrm{kin}^{\mathrm{O}_2}$ as

[v] Here it is important to note that a patch by Aidan Thompson from April 7th, 2010, see `http://lammps.sandia.gov/bug2010.html`, was applied. Among other things, it updated the equations of motion for Nosé-Hoover chains according to the formulation given by of Shinoda and coworkers,[498] resulting in a transparent implementation of the state-of-the-art integrator mentioned above. Having not yet been part of the last official release version of LAMMPS at the time, particularly careful testing procedures thus became mandatory.

[vi] More precisely, $m_\mathrm{S} = m_\mathrm{Pd}$ and $\Phi_{ij} = m_\mathrm{Pd}\,\bar{\omega}_\mathrm{D}^2\,\delta_{ij} \approx 5.31\,\mathrm{eV\,\AA^{-2}}\delta_{ij}$ were used as input parameters for the self-written LAMMPS extension implementing the surface oscillator (cf Appendix D.3). The damping parameters of the LAMMPS implementations of the Nosé-Hoover chains and Langevin thermostats[iv] were set to $\frac{2\pi}{\bar{\omega}_\mathrm{D}} \approx 0.2\,\mathrm{ps}$.

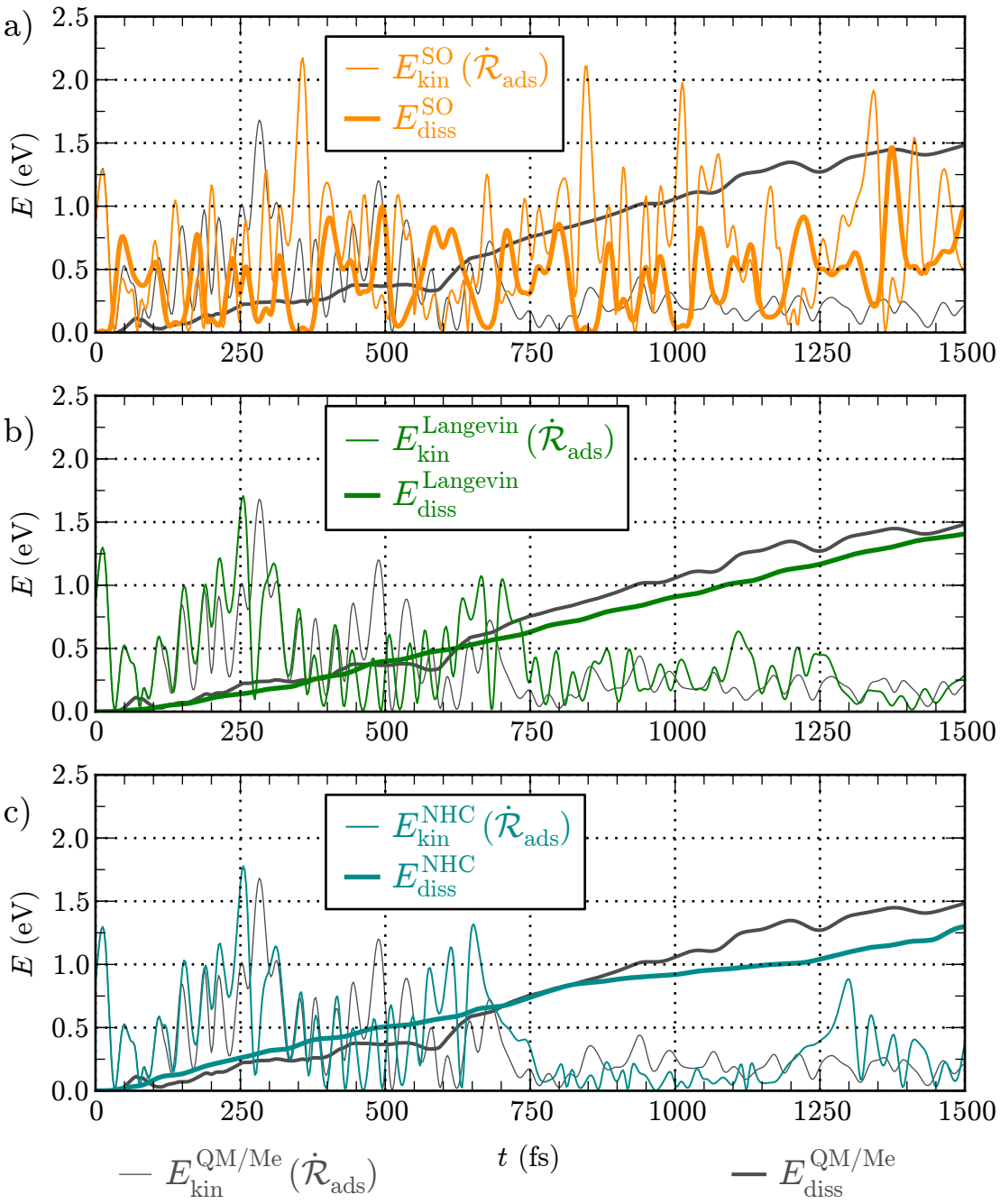

Figure 9.9.: Energy dissipation as described by "energy sinks from the shelf" compared with QM/Me. Dissipated energies for a) the surface oscillator b) the Langevin thermostat and c) Nosé-Hoover chains as given by Eq. (9.9), Eq. (9.11) and Eq. (9.10), respectively, are shown (thick orange, green and blue lines, respectively). The corresponding kinetic energies of the two oxygen atoms are plotted as well (thin orange, green and blue lines, respectively). In addition, the QM/Me references are shown in each plot as well: The dissipated energy defined by Eq. (9.7) (thick gray lines) and the kinetic energy of the oxygen atoms (thin gray lines), which is identical to the one plotted in Fig. 9.8.

in Fig. 9.8 and the dissipated energies which have been removed from the quantum mechanically treated region. Kinetic energies including the latter as before in Fig. 9.8) show different amounts of fluctuations due to the different complexity of the models and are thus more difficult to compare. However, it is important to keep in mind that this region needs to be included in order to fulfill the total energy balance of the approximately 2.6 eV of chemisorption energy that is freed and conserved in the respective extended systems. For QM/Me embedding, the dissipated energy can be defined as

$$E_{\mathrm{diss}}^{\mathrm{QM/Me}}(t) \;=\; E^{\mathrm{env}}(t) \;-\; E^{\mathrm{env}}(0) \quad , \tag{9.7}$$

where

$$\begin{aligned} E^{\mathrm{env}}(t) \;&=\; V^{\mathrm{MEAMopt}}(\mathcal{R}_{\mathrm{bath}};t) \;-\; E^{\overline{\mathrm{QM}}}(\mathcal{R}_{\mathrm{slab}};t) \\ &=\; E_{\mathrm{tot}}(t) \;-\; E_{\mathrm{kin}}(\mathcal{R}_{\mathrm{ads}};t) \;-\; E_{\mathrm{kin}}(\mathcal{R}_{\mathrm{slab}};t) \;-\; E^{\overline{\mathrm{QM}}}(\mathcal{R}_{\mathrm{slab}}\cup\mathcal{R}_{\mathrm{ads}};t) \quad , \end{aligned} \tag{9.8}$$

to avoid problems with counting potential energy contributions between the embedding cell and the rest of the bath on the level of the optimized MEAM potential. In Eq. (9.8), $E_{\mathrm{tot}}(t)$ denotes the (conserved) total energy along the trajectory, whereas $E^{\overline{\mathrm{QM}}}(\mathcal{R}_{\mathrm{slab}};t)$ and $E^{\overline{\mathrm{QM}}}(\mathcal{R}_{\mathrm{slab}}\cup\mathcal{R}_{\mathrm{ads}};t)$ are the energies resulting from the quantum mechanical calculations within the embedding as introduced in Eq. (9.1).

For the surface oscillator it is simply given by the total energy of the added oscillator degrees of freedom (cf Eq. (8.7))

$$E_{\mathrm{diss}}^{\mathrm{SO}}(t) = \frac{1}{2}m_{\mathrm{S}}\dot{\boldsymbol{R}}_{\mathrm{S}}^{2}(t) + \frac{1}{2}m_{\mathrm{S}}\boldsymbol{R}_{\mathrm{S}}^{\dagger}(t)\boldsymbol{\Omega}_{\mathrm{S}}\boldsymbol{R}_{\mathrm{S}}(t) \quad . \tag{9.9}$$

Thanks to the conserved quantity in the NHC formalism as given by Eq. (8.12), an equivalent definition involving only the additional dynamic variables $\{\eta_i\}_{i=1,\ldots,M}$ introduced by the thermostat provides the dissipated energy:

$$E_{\mathrm{diss}}^{\mathrm{NHC}}(t) = \sum_{i=1}^{M}\frac{1}{2}Q_i\,\dot{\eta}_i^2 \;+\; 3Nk_{\mathrm{B}}T\,\eta_1 \;+\; \sum_{i=2}^{M}k_{\mathrm{B}}T\,\eta_i \tag{9.10}$$

The influence of the length of the Nosé-Hoover chains has been tested and values beyond $M = 3$, for which results are shown in Fig. 9.9, have been found not to influence the trajectories. Finally, the energy changes due to the friction and random forces imposed by the Langevin thermostat (cf Eqs. (8.2)) are simply kept track of along MD time steps Δt and thus provide the corresponding dissipated energy

$$E_{\mathrm{diss}}^{\mathrm{Langevin}}(t) = \sum_{I}\Big[\underbrace{\boldsymbol{F}_I^{\mathrm{fric}}(t)+\boldsymbol{F}_I^{\mathrm{rand}}(t)}_{\boldsymbol{F}_I^{\mathrm{Langevin}}(t)}\Big]\cdot\dot{\boldsymbol{R}}_I(t)\cdot\Delta t \;-\; E_{\mathrm{diss}}^{\mathrm{Langevin}}(t-\Delta t) \tag{9.11}$$

starting from $E_{\mathrm{diss}}^{\mathrm{Langevin}}(0) = 0$.

Apart from the surface oscillator, the dissipated energies of both the Langevin and NHC thermostats are in quite good agreement with QM/Me. The same also holds for the "cooling down" of the oxygen atoms as illustrated by their kinetic energy. With the physically motivated choice of parameters, but unfortunately also others within a certain range as detailed above, these two energy sinks are indeed able to suck energy out of simulation cell in a "realistic" fashion. On the one hand, this can be seen as a promising numerical validation in a realistic

system for the approximations leading to the stochastic boundary conditions as constructed out of the generalized Langevin approach (GLE) approach (Section 8.1) by Kantorovich and Rompotis.[456] On the other, apart from being standing on better theoretical grounds, they hardly seem to provide any practical advantages over the abuse of NHC in this respect.

In contrast, even within quite a range around physically motivated parameters, the three additional degrees of freedom of the simple surface oscillator provide a very poor description of the energy dissipation. Obviously, the lack of mobility of the surface atoms imposes quite a severe limitation in this respect. Altogether, optimistically, the combination of SO and GLE termed "generalized Langevin oscillator" (GLO)[444] might thus be advocated as a reasonable choice for augmenting a frozen surface potential – in particular for brief adsorbate-substrate interactions like e.g. during scattering. However, the results of the following section and Chapter 10 will make it clear why it has not been considered worthwhile to extend the LAMMPS implementation of the surface oscillator accordingly and include the GLO approach in the comparison presented here.

9.2.3. Hot Adatoms

After the apparent success of the thermostats to mimic the "global" energy uptake of the solid compared to the QM/Me reference, focus is now shifted quite naturally to less benign quantities involving dynamical properties of the adsorbates. Unfortunately, this brings the immediate disillusion.

The motion of the two oxygen adatom fragments immediately after the dissociation of their parent O_2 molecule is characterized by an increasing distance along the former's molecular axis as illustrated by Fig. 9.10. Interpretations of experimental data (*vide infra*) have indicated such a phenomenon before[499,500] and have thus coined the term "hot adatom motion" to clearly distinguish the latter from thermal diffusion. In addition to the comparison presented in the previous section, also results from simulations with no energy uptake by the substrate (frozen surface) or only within the periodic boundary conditions of the simulated slab (AIMD) are included. Again, proper comparability of the resulting trajectories is ascertained in the same fashion as detailed before.

Obviously, the adsorbate motion is significantly influenced by the description of the substrate and its abilities to dissipate energy. Considering the latter, deviations from the QM/Me reference might not be surprising for the two models newly added here, but come rather unexpected for those using the Langevin and Nosé-Hoover chains (NHC) thermostats. In those cases, both oxygen adatoms are unlikely to make yet another jump to a neighboring fourfold hollow site after the integration time afforded here. Since this is the equilibrium adsorption site with respect to which the chemisorption energy of about 2.6 eV for the dissociative adsorption of O_2 on Pd(100) is calculated and the bridge-hollow diffusion barrier on the frozen surface amounts to approximately 300 meV (cf Section 5.3), the residual average kinetic energy of the oxygen atoms during the last steps of the trajectory as shown in Fig. 9.9 is probably not sufficient.

However, this hints at an important practical advancement of QM/Me embedding for more extensive applications like e.g. the collection of statistics: Similar to what has already been proposed by Tully within his stochastic trajectory approach based on a Langevin model,[434] an embedding region could be defined around each adsorbate and follow its motion dynamically. As soon as these "hot zones", which according to Section 9.1.2 could each be much smaller than the single embedding region used here, do no longer overlap, the embedding is continued based on them. The present implementation is already flexible enough to treat multiple embedding regions even concurrently (cf Appendix D.2), but fully automatic determination would

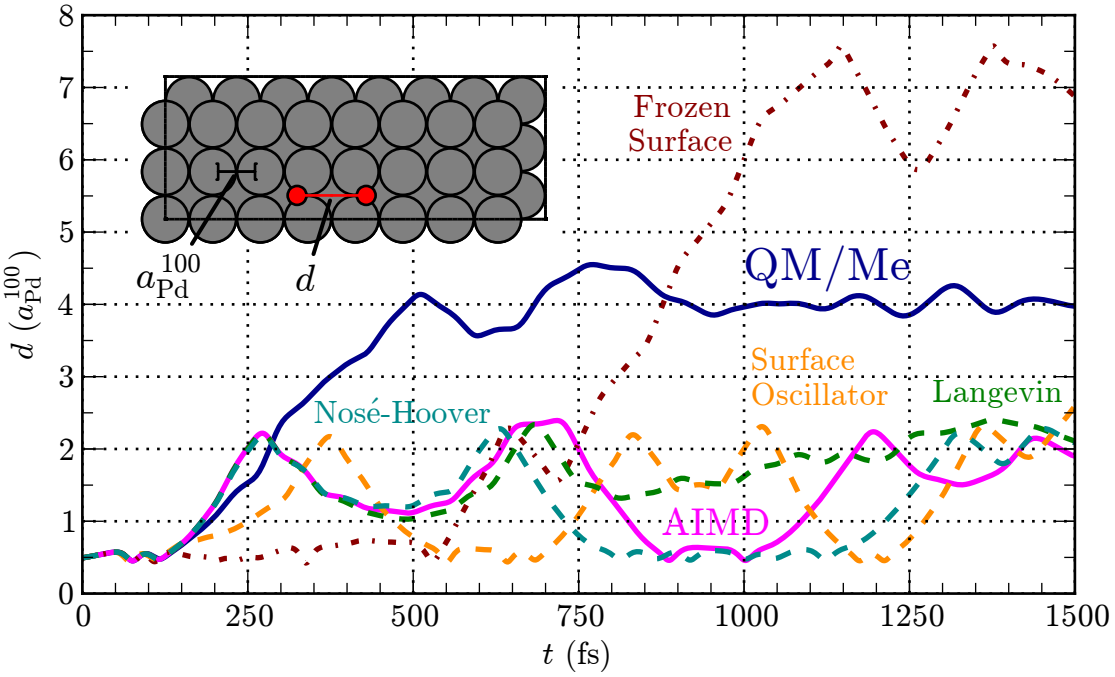

Figure 9.10.: Separation distance of oxygen atoms on the Pd(100) surface following dissociation of O_2 resulting from different energy sinks as detailed in the text.

require some further attention. Due to the typically non-linear scaling of the underlying DFT calculations with respect to supercell size, the computational cost can be reduced accordingly. What is even more important in the present context is that this allows to further check the influence of the embedding region for the observed adsorbate motion: After all, a distance of four surface lattice constants is the maximum distance within the lateral periodic boundary conditions of the quantum mechanically treated region, for which, however, according to the work by Zhang and Reuter[16] substrate mediated oxygen-oxygen interactions are expected to have largely vanished. Indeed, such a continuation of the QM/Me trajectory after about 500 ps (based on two 3×3 supercells with 3 layers centered around each oxygen atom), reproduces the original trajectory fairly well. No further increase of the separation distance is observed in particular. Potential unphysical substrate mediated oxygen-oxygen interactions through periodic images have been systematically suppressed thereby as the two supercells are completely independent on the DFT level and only still coupled via the substrate motion described on the level of the optimized MEAM potential. This provides further trust in both the embedding approach and the resulting hot adatom separation distance.

Of course, given the chaotic behavior of the present system, trajectories will differ for other initial conditions than the ones focused on here. but as already emphasized at the beginning of this section, these initial conditions are of exceptional statistical relevance. Groß on the other hand did perform statistics for H_2 dissociation on Pd(100) based on about 100 trajectories for hot adatom dynamics,[354] but relying on conventional AIMD. Given the smaller mass of the former adsorbate, limitations of the former should also be less severe than for O_2 due to the expected concomitant less intense energy transfer. According to Groß, the calculated average H_2 separation distances thus provide an upper limit for hot adatom motion of heavier adsorbates as they couple more strongly to the substrate, resulting in more rapid energy dissipation.

However, this argument does not consider that the latter might also free a much higher amount of chemisorption energy: E.g. $E_{\mathrm{chem}}^{\mathrm{H_2 \rightarrow 2H_{(ads)}}} \approx 1.0\,\mathrm{eV}$, vs $E_{\mathrm{chem}}^{\mathrm{O_2 \rightarrow 2O_{(ads)}}} \approx 2.6\,\mathrm{eV}$ for adsorption on Pd(100). Of course, the present data lacks statistical averaging and does (thus) not confute that argument for the present system. Still, it does show that (at least) for heavier adsorbates trajectories can yield a radically different separation distance when phonon propagation and concomitant energy uptake are included properly like in QM/Me embedding. Therefore, it yet remains to be seen if this trend is "washed out" by statistics and whether that upper boundary estimate does indeed prevail.

In fact, for oxygen there is also some experimental data available which can provide important benchmarks for dynamical first-principles calculations like those presented here – similar to what static properties (i.e. lattice constants etc.) have served for during the last three decades. Pair distance distributions have been counted by scanning tunneling microscopy (STM) in ultra-high vacuum (UHV) experiments "right after" dissociation, i.e. following exposure and adsorption of O_2 introduced into the UHV chamber as background gas. In contrast to hydrogen, oxygen adatoms are much simpler to detect by almost any established surface science technique. For O_2 on Al(111), extraordinarily large distances of over 14 surface lattice constants have been observed,[500,501] but are more likely to be related to be the result of a "cannon-ball" abstraction mechanism according to current theoretical understanding (cf Chapter 7). Later, apart from simple metals, much smaller pair separations peaking at two surface lattice constants were observed for O_2 on Pt(111), i.e. on another fcc(111) surface of a member (like palladium) of the platinum group metals.[502] More open fcc(100) surfaces, which provide a straight minimum energy path between multiple highest coordinated equilibrium adsorption sites (via bridge sites), have only been studied for the coinage metals silver[503,504] and copper[505,506] up to now. Larger peak distances of seven and fourteen surface lattice constants have been observed for the oxygen adatoms in the first case, while the latter has yielded only two, similar to Pt(111). For the present system, no such STM experiments have been carried out so far. Notwithstanding, hot adatoms have been invoked as one possible explanation for the formation of a metastable c(2×2) ordered phase of adsorbed oxygen on Pd(100) under "extreme conditions", i.e. high pressure and low surface temperature, by Chang and Thiel.[365,499,507] Altogether, the separation distance obtained here by QM/Me is similar to those obtained by experiments for similar surfaces. For Pd(100), it confirms previous assumptions, and might even be seen as a first prediction of the outcome of corresponding STM experiments.

Finally, it has to be emphasized that the implications for modeling the kinetics of chemical reactions on surfaces are much deeper – with obvious consequences e.g. for heterogeneous catalysis. Relying on the Markov approximation, present state-of-the-art first-principles kinetic Monte Carlo (1p-kMC) simulations[7–10] treat adsorption and diffusion as two decoupled, statistically unrelated elementary processes. The rate for the latter, i.e. the diffusion of oxygen adatoms from one equilibrium binding site to another, is obtained based on transition state theory by the corresponding diffusion barrier alone, which is given by the energy difference between bridge and hollow sites of about 300 meV, cf Chapter 5). As in the present case this yields a time scale of microseconds, the inclusion of memory of the dissociation event as achieved through the present QM/Me simulations can obviously lead to changes of six orders of magnitude in time. Reactions with neighboring CO molecules might even yield "hot chemistry", somewhere "between" the Eley-Rideal and Langmuir-Hinshelwood mechanisms (i.e. reactants directly reacting with adsorbates from the gas phase versus surface mediated reactions of adsorbates), that are conventionally used to depict heterogeneous catalysis in textbooks.[1,2] Furthermore, also the implications for the "mere" detailed arrangement of adsorbates with increasing coverage might

be crucial for many surface functionalities. Given the aforementioned experimental indications for the present system, Liu and Evans have thus enriched some of their kMC modeling for the formation and ordering of oxygen adlayers by a hot adatom process, with a crude rate estimate based on available empirical data.[508] On the way to first-principles based multiscale modeling, the present approach thus paves the way to investigate the effect of the enormous amounts of heat released by exothermic elementary reaction steps on the atomistic scale, and obtain kinetic parameters to be incorporated into more coarse-grained simulations.

9.3. Summary

In this chapter, a new embedding technique termed "QM/Me" has been developed in order to overcome the inapplicability of conventional QM/MM embedding to metallic systems. The adsorbate-adsorbate and adsorbate-substrate interactions are described entirely on a quantum mechanical level within periodic boundary conditions, taking the metallic band structure and its crucial importance for the binding fully into account. Past attempts based on parametrized pair potentials are of much inferior accuracy as they miss the flexibility and many-body effects naturally included in here by the proper description of the electronic structure. A huge bulk-like bath of substrate atoms is described by the modified embedded atom method (MEAM), which has been adapted to seamlessly match the DFT description and implicitly includes anharmonic effects. QM/Me thus provides several conceptual advantages over previous approaches that have been used to model "energy sinks" (cf Chapter 8): For example, suppression of unphysical phonon reflections due to artificial boundary effects as e.g. proposed in the absorbing boundary conditions approach is not necessary. Contrary to generalized Langevin equations and thermostats, no statistical elements are introduced on a conceptual level, so that classical trajectories do not lose their physical meaning, as long as Newton's equations of motions capture the essential physics of the system under investigation. This certainly is only of mild concern for any adsorbates heavier than hydrogen, like the present showcase system O_2 on Pd(100).

Errors specifically introduced due to the embedding were demonstrated to be very small because of the effective localization within the scheme. Recently developed direct high-dimensional interpolation attempts (cf Section 3.2.3) appear to perform worse or at best comparable for systems with "only" covalent interactions according to what has been reported in the literature until now. In fact, using the *ab initio* based embedding part of QM/Me might become a very interesting and successful starting point for such approaches in the future – extending their applicability to the description of more complicated potential energy surfaces like e.g. those typically encountered in gas-surface dynamics. Altogether, there are no approximations which cannot be well controlled in practice – beyond those for the description of the electronic structure which are not in the focus of the present study.

The scheme can be easily implemented using existing classical molecular dynamics (also providing a "metal potential") and quantum mechanical codes, since the at present dominating cost of the quantum mechanical force calculations allows for an efficient coupling by casting instructions into simple (shell) scripts and realizing data exchange via files. According to the present experiences, the computational cost is less than twice that of conventional *ab initio* molecular dynamics simulations for the same system, allowing to treat any system which is treatable with the former nowadays. Combinations with ideas from the literature to accelerate those dynamics (cf Section 3.2.3) are straightforward in principle, but might demand more sophisticated implementations (i.e. direct integration) of the coupling, resulting in an even broader range of applicability. To make the coupling as seamless as possible from a systematical

point of view, an according adjustment of the "metal potential" is typically required. More sophisticated approaches than the one employed here can certainly be used to improve the description of the bath even further. Finally, embedding regions which dynamically follow a "hot zone" can be introduced, which is nastier from a technical point of view, but conceptually straightforward.

A QM/Me embedded simulation for O_2 dissociation on Pd(100) shows that the great majority of the energy freed during that exothermic chemical reaction is dissipated out of the embedding cell before the two adsorbate atoms have fully equilibrated with the substrate. Accordingly, within conventional *ab initio* molecular dynamics (AIMD), where typically simulation cells of the same size as the embedding cells used here are used for the description of the total system, are not reliable to capture energy dissipation to substrate phonons. Although "energy sinks from the shelf" more sophisticated than a simple surface oscillator (cf Chapter 8) can indeed successfully augment AIMD to mimic the energy drain, their effect on the adsorbate dynamics can still be enormous. This holds in particular for "hot adatom motion", for which strong indications are predicted for the present system according to QM/Me – in good agreement with experimental data from STM experiments for O_2 dissociation on other metal surfaces. On a broader scope, this prediction has ground-shaking consequences for microkinetic models of heterogeneous catalysis: The Markov approximation, which forms one of the foundations of coarse-grained microkinetic models is thus substantially questioned from a first-principles perspective.

Future applications of QM/Me gas-surface dynamics might in particular encompass an unprecedented realistic modeling of surface temperature. This could elucidate its role e.g. during O_2 dissociation on Ag(100), which might be crucial to reconcile theoretical modeling[328] and experimental observations.[503,504] Since the atomistic details of the redistribution of energy are of crucial importance not only for heterogeneous catalysis, but also for the rapidly-growing field of basic energy research, further applications of QM/Me can facilitate to gain fundamental insights also there. Finally, also studies of static properties might benefit, for example long-ranged elastic effects at interfaces in general or even around bulk defects.

Having established a new technique with unpreceded accuracy, this now allows to systematically scrutinize approximations of previous attempts to account for energy dissipation (as detailed in Chapter 8) from a first-principles point of view. In particular, the role of surface phonons and the harmonic approximation for the solid are investigated in the following chapter – continuously showcased for O_2 on Pd(100).

10. Role of Phonons

In the previous chapter the QM/Me embedding approach has been introduced and applied to gas-surface dynamics in order to model energy dissipation during exothermic chemical reactions into phononic degrees of freedom of a metal surface.

In principal, there are now two main routes that could be followed: First, this scheme could be taken and used to accumulate statistics by calculating many trajectories. Of course, this is more a (and quite substantial) computational rather than an actual scientific challenge. Nevertheless, similar to what Groß has shown only recently relying on conventional *ab initio* molecular dynamics for H_2 dissociation on Pd(100), this can yield e.g. averaged atomic separation distances for the hot oxygen adatoms observed here, which could be compared to corresponding data from STM experiments. Since the few such studies, which have obtained distance distributions of equilibrated adatoms "right after" dissociation of a diatomic, have all been done for oxygen dissociation[500–506], this might allow for a much closer comparison than the one based on the calculations for H_2.[354] It would still involve a different substrate, however, as no experimental data is available for O_2 on Pd(100). In addition, the present system is also computationally much more demanding than the system addressed by Groß, because of the presence of oxygen and the related notoriously bad electronic convergence behavior (cf Section 5.3). Following a common recipe, this could be addressed by decreasing the accuracy below the standard used for single point DFT calculations and reducing the computational cost accordingly. In this approach is then argued that the reduced convergence does average out and might even provide further entropy to the sampling of phase space, hence not affecting the statistical quantities in a way to be concerned about.[361] However, to the best of the author's knowledge there are not yet any deeper theoretical arguments relating numerical errors concerning the integration of MD trajectories to systematic problems of statisical sampling. Therefore, it remains to be seen in the future, when more efficient algorithms and implementations of electronic structure codes as well as increased computational power will allow to obtain accurately converged *ab initio* MD trajectories more routinely, whether such an argument prevails.

Second, a systematic, quantitative analysis of the phonon excitations for the obtained trajectories could be worked out. Due to the large number of degrees of freedom which are treated explicitly on the level of the semi-empirical interatomic potential, the QM/Me Hamiltonian incorporates a realistic "phononic fine structure" of that bath (cf Section 9.1.3). It is only this what lays the foundations for such an analysis which could provide important information about the details of the energy dissipation into the dominant dissipation channel (cf Chapter 7). For the first time, the QM/Me approach thus provides the unique opportunity to obtain valuable input for more coarse grained theoretical models like scattering theories relying on assumptions about concomitant phonon excitations[295] or ultimately to include energy dissipation into kinetic Monte Carlo models in heterogeneous catalysis.[3]

With the focus on the physics of energy dissipation, this thesis centers on the second route. Correspondingly, this chapter starts with the development of a projection scheme which is suitable for instantaneous application at each time step *along* trajectories – without the need for any averaging over time. Its application allows subsequently to address and unravel the importance of surface phonons for the energy dissipation. Finally, the validity of the harmonic

approximation for the substrate is investigated by comparing to dynamics obtained with the best possible harmonic force field implicitly obtained from phonon calculations. This thesis thus concludes with an important, pioneering first principles perspective on a commonly used starting point for other models (cf Sections 8.1 and 8.2).

10.1. Projection onto Phonon Modes

The large embedding supercells with which the QM/Me Hamiltonian allows to follow the dynamics of chemical reactions on surfaces implicitly provide an accurate description of the underlying phonons. Therefore, in principle, trajectories propagated according to this Hamiltonian should enable a detailed analysis which phonon modes are excited during an exothermic chemical reaction on the surface. For finite systems like molecules or clusters, a projection onto harmonic Eigenmodes for a molecular dynamics trajectory is mathematically well defined and simple to carry out. In periodic systems on the other hand, for every phonon wave vector $\boldsymbol{q}$ the solution of the corresponding Eigenvalue problem given by the dynamical matrix (cf Eq. (4.6) in Section 4.1) yields a corresponding Eigensystem of phonon modes, i.e. uncountably many in total. Therefore, such an identification of excited phonon modes is all but trivial.

Recently, research on atomistic details of thermal transport has attracted a lot of interest, triggered by e.g. industrial interest in thermal coatings. At least in non-metallic materials the former is dominated by phononic contributions and characterized by phonon relaxation times in a scattering picture. Since molecular dynamics is the obvious computational tool to follow the phonon dynamics, a mode decomposition along a corresponding trajectory is required here as well in order to "measure" the decay of individual phonon modes. McGaughey and Kaviany have given[509] and used[510,511] a formula for the monatomic primitive cell of their Lennard-Jones model crystals, based on phonon Eigenvectors and a spatial Fourier transformation. Employing more sophisticated potentials for more complicated systems, Henry and Chen have made use thereof.[512–514] Their primitive cell contains more than one atom, just like the slab models of Pd(100) do in the present case (cf Section 2.6 and Section 4.3). Nevertheless, they do not comment on any modifications. Apart from that, unfortunately neither the original, nor the following work gives a clear derivation (or an according reference) on how this formula has been obtained – despite its fundamental importance for all the ensuing analyses building thereon.

Perhaps it is for this reason that Estreicher and coworkers do not refer to McGaughey's and Kaviany's original work[509] when calculating vibrational lifetimes of impurities in Si[515,516] and their consequences for thermal conductivities in the same material.[229–231,517] Instead, they only indicate a transformation of nuclear coordinates to the normal modes of the system in their employed supercell description, without going into detail.[229,516] As indicated in Section 4.2, the modes at the Γ-point of the supercell, do naturally contain information about non-Γ-point modes in the larger Brillouin zones of smaller cells. In addition, the dynamical matrix (cf Eq. (4.7)) is a real symmetric matrix at Γ and hence so must be its Eigenvectors, which perfectly fits with the entirely real-valued phonon description focusing on frequency space that Estreicher and coworkers employ in their work.[229–231,515–517] However, in order to make contact with phonon dispersion relation and thus identify modes by their actual phonon wave vector, a back-folding operation of the Γ-point modes in the small Brillouin zone of the supercell into the larger Brillouin zones of the underlying smaller cells would be required, which might not be entirely straightforward. A more severe limitation is due to the fact that the dynamical matrix of the supercell needs to be obtained and diagonalized, which is avoided in usual lattice

dynamics calculations (cf Section 4.2).[i] For supercells containing on the order of at most a thousand atoms, this might still be possible, though computationally rather involved when symmetry is not exploited while setting up displacements for the direct method. However, when dealing with supercells containing two orders of magnitude more atoms as is easily the case in embedding situations like the present one, the cubic scaling of matrix diagonalization alone renders this approach impractical or even impossible.

Only very recently, de Koker has published yet a different first-principles based approach to thermal conductivity.[518,519] He uses the phonon density of states Eq. (4.20) as obtained by the velocity autocorrelation Eq. (4.19) to obtain mode-resolved phonon lifetimes along molecular dynamics trajectories. While this is appealing in order to avoid the aforementioned projection schemes and their "uncertainties", the non-continuous and non-equilibrium nature of the dissociation process obviously forbids time-averaging over a long molecular dynamics trajectory. In other words, it is clearly imperative for the present purposes to obtain phonon populations "on-the-fly", i.e. instantaneously for every time step.

Therefore, a general phonon projection scheme is now derived, which not only allows to treat the present problem, but is also perfectly suited for all of the aforementioned cases. This instantaneous phonon mode decomposition can be applied to any problem containing "phononic details" beyond the Γ-point by employing a description based on $\prod_{i=1}^{N_\mathrm{p}} N_i$ supercells, where $N_\mathrm{p} \in \{1,2,3\}$ denotes the number of periodic directions. The formalism is thus deliberately kept general, allowing for an easy specialization to slabs, i.e. $N_\mathrm{p} = 2$, in the end as required for the present purposes. $N_i \in \mathbb{N} \setminus \{0\}$ characterizes the size of the supercell in direction i as multiples of the respective primitive cell. This defines a grid of the latter

$$\boldsymbol{L}_n = \sum_i n_i \boldsymbol{a}_i \quad , \quad n = (n_i) \in \prod_{i=1}^{N_\mathrm{p}} \{0, \ldots, N_i - 1\} \quad , \tag{10.1}$$

where the $\{\boldsymbol{a}_i\}_{i=1}^{N_\mathrm{p}}$ are real space lattice vectors as defined by the primitive cell. With the concomitant reciprocal space lattice vectors $\{\boldsymbol{b}_i\}_{i=1}^{N_\mathrm{p}}$ a corresponding grid in the Brillouin zone

$$\boldsymbol{q}_n = \sum_i \left[\frac{n_i}{N_i} - \frac{1}{2}\right] \boldsymbol{b}_i \quad , \quad n = (n_i) \in \prod_{i=1}^{N_\mathrm{p}} \{0, \ldots, N_i - 1\} \tag{10.2}$$

is given. As already mentioned in Section 4.2 (cf Eqs. (4.21) and (4.22) for $N_\mathrm{p} = 3$) the latter grid describes the $\boldsymbol{q}$-points where periodicity of the phonons is commensurate with the chosen supercell and which hence are described exactly.

The same notation as in Part I is employed, building on the theoretical background described in Chapter 4. In particular, atoms in the supercell are indexed by a number $\tilde{I}$ in the primitive cell and a lattice vector $\boldsymbol{L}$ leading to the desired periodic image, with vector components denoted by lowercase Greek letters. Starting point is the atomic displacement field $\{U^{\mathrm{MD}}_{\tilde{I}\alpha}(\boldsymbol{L}_n;t)\}_{\tilde{I}\alpha,\boldsymbol{L}_n}$ at a time t with respect to equilibrium positions $\{R^0_{\tilde{I}\alpha}(\boldsymbol{L}_n)\}_{\tilde{I}\alpha,\boldsymbol{L}_n}$. Generalization to the corresponding velocity field $\{\dot{R}^{\mathrm{MD}}_{\tilde{I}\alpha}(\boldsymbol{L}_n;t)\}_{\tilde{I}\alpha,\boldsymbol{L}_n}$ is then straightforward in the end.

[i] As detailed in Section 4.2, displacement calculations within the direct method in a $N_1 \times N_2 \times N_3$ supercell of a primitive cell with N_cell atoms provides access to $\prod_{i=1}^{3} N_i$ exact $\boldsymbol{q}$-points in the Brillouin zone of the latter by solving Eigenvalue problems given by the corresponding dynamical matrices of dimension $(3N_\mathrm{cell})^2$ for each of them. In general, this is computationally much more feasible than the diagonalization of a single $(3N_\mathrm{cell}\prod_{i=1}^{3} N_i)^2$ dimensional dynamical matrix at the Γ-point of the supercell.

Both of these time-dependent quantities are "naturally" obtained from a molecular dynamics trajectory. Now, the ansatz

$$\begin{aligned} U^{\mathrm{MD}}_{\tilde{I}\alpha}(\boldsymbol{L}_n;t) &= \frac{1}{\prod_{i=1}^{N_\mathrm{p}} N_i} \sum_{\boldsymbol{q}_{n'}}^{\mathrm{grid}} \frac{\prod_{i=1}^{N_\mathrm{p}} \sqrt{N_i}}{\sqrt{M_{\tilde{I}}}} \, \bar{C}_{\tilde{I}\alpha}(\boldsymbol{q}_{n'};t) \, \mathrm{e}^{i\boldsymbol{q}_{n'}\cdot\boldsymbol{L}_n} \\ &= \frac{1}{\prod_{i=1}^{N_\mathrm{p}} \sqrt{N_i}} \frac{1}{\sqrt{M_{\tilde{I}}}} \sum_{\boldsymbol{q}_{n'}}^{\mathrm{grid}} \sum_{b'=1}^{3N_\mathrm{cell}} C(\boldsymbol{q}_{n'},b';t) \, \hat{u}_{\tilde{I}\alpha}(\boldsymbol{q}_{n'},b') \, \mathrm{e}^{i\boldsymbol{q}_{n'}\cdot\boldsymbol{L}_n} \end{aligned} \tag{10.3}$$

first transforms the displacement field on the real space described by Eq. (10.1) onto the corresponding reciprocal grid given by Eq. (10.2) of exact phonon wave vectors, component-wise by means of a (generalized or shifted) discrete Fourier transform.[ii] At every point $\boldsymbol{q}_{n'}$, the resulting $3N_\mathrm{cell}$-dimensional vector of generally complex-valued expansion coefficients $\bar{C}_{\tilde{I}\alpha}(\boldsymbol{q}_{n'};t)$ is then represented in the orthonormalized basis $\{(\hat{u}_{\tilde{I}\alpha})\,(\boldsymbol{q}_{n'},b')\}_{b'} \subset \mathbb{C}^{3N_\mathrm{cell}}$ of displacement Eigenvectors, where b is the phonon band index. The resulting phonon mode expansion coefficients $C(\boldsymbol{q}_{n'},b';t)$ are the quantity of interest to obtain in the following.

It is important to emphasize that Eq. (10.3) is mathematically well-defined with physically induced uniqueness for a given choice of a supercell description. Obviously, both are required properties for a properly defined projection scheme. The fact that the displacement field on the left-side is real-valued leads to the following properties of the expansion coefficients:

$$\bar{C}_{\tilde{I}\alpha}(\boldsymbol{q}_{n'};t) = \left[\bar{C}_{\tilde{I}\alpha}(-\boldsymbol{q}_{n'};t)\right]^* \tag{10.4a}$$

$$C(\boldsymbol{q}_{n'},b';t) = \left[C(-\boldsymbol{q}_{n'},b';t)\right]^* \quad . \tag{10.4b}$$

Furthermore, masses have been separated out of the latter in form of $\frac{1}{\sqrt{M_{\tilde{I}}}}$, following the conventional treatment in lattice dynamics employing mass weighted coordinates (cf Eq. (4.5)). The grid factor $\prod_{i=1}^{N_\mathrm{p}} \sqrt{N_i}$ has been added to simplify the relation between the length (measured in the corresponding 2-norms, $\|\cdot\|_2$) of the original displacement field vector and its Fourier transformed counterparts according to Parseval's theorem, thus resulting in

$$\begin{aligned} \sum_{\tilde{I}=1}^{N_\mathrm{cell}} \sum_{\alpha=1}^{3} \sum_{\boldsymbol{L}_{n'}}^{\mathrm{grid}} M_{\tilde{I}} \left[U^{\mathrm{MD}}_{\tilde{I}\alpha}(\boldsymbol{L}_n;t)\right]^2 &= \sum_{\tilde{I}=1}^{N_\mathrm{cell}} \sum_{\alpha=1}^{3} \sum_{\boldsymbol{q}_{n'}}^{\mathrm{grid}} \left|\bar{C}_{\tilde{I}\alpha}(\boldsymbol{q}_{n'}\right|^2 \\ &= \sum_{\boldsymbol{q}_{n'}}^{\mathrm{grid}} \sum_{b'=1}^{3N_\mathrm{cell}} \left|C(\boldsymbol{q}_{n'},b';t)\right|^2 \quad . \end{aligned} \tag{10.5}$$

Finally, Eq. (10.3) also has a natural continuum limit representing the infinite solid, obtained for infinite supercell size: A conventional Fourier transform

$$\frac{1}{V_\mathrm{BZ}} \sum_{\boldsymbol{q}_{n'}}^{\mathrm{grid}} \frac{V_\mathrm{BZ}}{\prod_{i=1}^{N_\mathrm{p}} N_i} C(\boldsymbol{q}_{n'}) \xrightarrow{N_i\to\infty} \frac{1}{V_\mathrm{BZ}} \int_\mathrm{BZ} d\boldsymbol{q} C(\boldsymbol{q}) \quad . \tag{10.6}$$

[ii] The corresponding article in the English wikipedia
http://en.wikipedia.org/wiki/Discrete_Fourier_transform
currently recapitulates the underlying theory in concise way. For implementations in practice it is useful to remind the reader that the scalar product $\boldsymbol{q}_{n'} \cdot \boldsymbol{L}_n$ is dimensionless, i.e. lattice constants of real space and reciprocal space lattice vectors cancel accordingly.

Moreover, this also provides a systematic and sound mathematical foundation of the interpretation of the plane wave ansatz (cf Eq. (4.5)) of lattice dynamics with continuous wave vectors as "Fourier modes" – as already vaguely indicated in Section 4.1.[iii]

As indicated above, the desired phonon mode decomposition is given by the coefficients $C(\boldsymbol{q}_{n'}, b'; t)$. The orthonormality relations for the discrete Fourier transformation

$$\sum_{\boldsymbol{L}_{n''}}^{\text{grid}} \mathrm{e}^{-i\boldsymbol{q}_n \cdot \boldsymbol{L}_{n''}} \, \mathrm{e}^{i\boldsymbol{q}_{n'} \cdot \boldsymbol{L}_{n''}} = \left(\prod_{i=1}^{N_\mathrm{p}} N_i \right) \, \delta_{\boldsymbol{q}_n \boldsymbol{q}_{n'}} \tag{10.7}$$

and the displacement Eigenvectors

$$\sum_{\tilde{I}=1}^{N_\mathrm{cell}} \sum_{\alpha=1}^{3} \left[\hat{u}_{\tilde{I}\alpha}(\boldsymbol{q}_n, b) \right]^* \hat{u}_{\tilde{I}\alpha}(\boldsymbol{q}_n, b') = \sum_{\tilde{I}=1}^{N_\mathrm{cell}} \left[\hat{\boldsymbol{u}}_{\tilde{I}}(\boldsymbol{q}_n, b) \right]^* \cdot \hat{\boldsymbol{u}}_{\tilde{I}}(\boldsymbol{q}_n, b') = \delta_{bb'} \tag{10.8}$$

greatly simplify the task to obtain the latter. Applying both Eq. (10.7) and Eq. (10.8) to Eq. (10.3) in this order yields

$$\begin{aligned} C(\boldsymbol{q}_n, b; t) &= \sum_{\tilde{I}=1}^{N_\mathrm{cell}} \left[\hat{\boldsymbol{u}}_{\tilde{I}}(\boldsymbol{q}_n, b) \right]^* \cdot \sum_{b'=1}^{3N_\mathrm{cell}} C(\boldsymbol{q}_n, b'; t) \, \hat{\boldsymbol{u}}_{\tilde{I}}(\boldsymbol{q}_n, b') \\ &= \sum_{\tilde{I}=1}^{N_\mathrm{cell}} \sum_{\alpha=1}^{3} \left[\hat{u}_{\tilde{I}\alpha}(\boldsymbol{q}_n, b) \right]^* \sum_{\boldsymbol{L}_{n'}}^{\text{grid}} \frac{\sqrt{M_{\tilde{I}}}}{\prod_{i=1}^{N_\mathrm{p}} \sqrt{N_i}} \, U^{\mathrm{MD}}_{\tilde{I}\alpha}(\boldsymbol{L}_{n'}; t) \, \mathrm{e}^{-i\boldsymbol{q}_n \cdot \boldsymbol{L}_{n'}} \\ &= \frac{1}{\prod_{i=1}^{N_\mathrm{p}} \sqrt{N_i}} \sum_{I=1}^{N_\mathrm{supercell}} \sqrt{M_{\tilde{I}(I)}} \, \left[\hat{\boldsymbol{u}}_I(\boldsymbol{q}_n, b) \right]^* \cdot \boldsymbol{U}^{\mathrm{MD}}_I(t) \, \mathrm{e}^{-i\boldsymbol{q}_n \cdot \left(\boldsymbol{R}^0_I - \boldsymbol{R}^0_{\tilde{I}(I)} \right)} \quad . \end{aligned} \tag{10.9}$$

The terms following the last equality sign are obtained by iterating over atoms in the supercell directly instead of using the combined index plus lattice vectors notation as introduced above

$$\sum_{\tilde{I}=1}^{N_\mathrm{cell}} \sum_{\boldsymbol{L}_{n'}}^{\text{grid}} \longrightarrow \sum_{I=1}^{N_\mathrm{supercell}} \quad . \tag{10.10}$$

Hereby, the map $\tilde{I}(I)$ gives the index $\tilde{I}$ of the respective image inside the primitive cell for an atom with supercell index I. If that cell only contains a single atom, $\boldsymbol{R}^0_{\tilde{1}}$ can be set as the origin so that only $\boldsymbol{R}^0_I$ appears in the exponential. Equation (10.9) then simplifies to the expression that has been given by McGaughey and Kaviany[509] for this case. Moreover, Eq. (10.9) also illustrates in turn how this expression needs to be modified when the primitive cell is not monatomic – which Henry and Chen hopefully have used internally without clearly saying so in their published work.[512–514]

It is illustrative to consider a displacement field corresponding to a single phonon mode with

[iii] Restriction of the reciprocal space integration domain to the Brillouin zone is thereby also systematically constructed.

wave vector $\boldsymbol{q}_{n'}$ and band index b', as used as ansatz in the context of lattice dynamics.

$$\begin{aligned} U^{\text{single}}_{\tilde{I}\alpha}(\boldsymbol{L}_n;t) &= \frac{1}{\sqrt{M_{\tilde{I}}}}\, A\left(\boldsymbol{q}_{n'},b'\right)\ \Re\left(\hat{u}_{\tilde{I}\alpha}(\boldsymbol{q}_{n'},b')\ \mathrm{e}^{i[\boldsymbol{q}_{n'}\cdot\boldsymbol{L}_n-\omega(\boldsymbol{q}_{n'},b')t]}\right) \\ &= \frac{1}{\sqrt{M_{\tilde{I}}}}\,\frac{A\left(\boldsymbol{q}_{n'},b'\right)}{2}\ \Big(\hat{u}_{\tilde{I}\alpha}(\boldsymbol{q}_{n'},b')\ \mathrm{e}^{i[\boldsymbol{q}_{n'}\cdot\boldsymbol{L}_n-\omega(\boldsymbol{q}_{n'},b')t]}\ + \\ &\qquad \underbrace{\left[\hat{u}_{\tilde{I}\alpha}(\boldsymbol{q}_{n'},b')\right]^*}_{=\hat{u}_{\tilde{I}\alpha}(-\boldsymbol{q}_{n'},b')}\ \mathrm{e}^{-i[\boldsymbol{q}_{n'}\cdot\boldsymbol{L}_n-\omega(\boldsymbol{q}_{n'},b')t]}\Big) \end{aligned} \tag{10.11}$$

Here $A\left(\boldsymbol{q}_{n'},b'\right)$ is a real-valued amplitude just like in Section 4.1 (cf Section 4.1). Since Eq. (10.11) solves the equations of motion of the harmonic solid as given by Eq. (4.6), the implied time dependence is correct for the latter, but generally cannot be split off from the amplitude as a simple exponential phase factor. In fact, as already indicated in the beginning, Eq. (10.9) provides a means to calculate the time-dependence of phonon populations in molecular dynamics trajectories based on "real", anharmonic interatomic interactions – including the scattering effects induced thereby. The indicated symmetry property of the displacement Eigenvector $\hat{u}_{\tilde{I}\alpha}(\boldsymbol{q}_{n'},b')$ under inversion of $\boldsymbol{q}_{n'}$ (also see Eqs. (4.10) and (4.11)) simplifies the extraction of the phonon mode expansion coefficients and verification of their properties according to Eqs. (10.4). They are given by

$$\begin{aligned} C^{\text{single}}(\boldsymbol{q}_n,b;t) = \prod_{i=1}^{N_\text{p}}\sqrt{N_i}\ \frac{A\left(\boldsymbol{q}_{n'},b'\right)}{2} \\ \left[\delta_{\boldsymbol{q}_n\boldsymbol{q}_{n'}}\ \delta_{bb'}\ \mathrm{e}^{-i\omega(\boldsymbol{q}_{n'},b')t}+\delta_{\boldsymbol{q}_n,-\boldsymbol{q}_{n'}}\ \delta_{bb'}\ \mathrm{e}^{+i\omega(\boldsymbol{q}_{n'},b')t}\right] \quad . \end{aligned} \tag{10.12}$$

At the Γ-point, i.e. $\boldsymbol{q}_{n'}=\boldsymbol{0}$, Eq. (10.11) and Eq. (10.12) reduce to

$$U^{\Gamma}_{\tilde{I}\alpha}(\boldsymbol{L}_n;t) = \frac{1}{\sqrt{M_{\tilde{I}}}}\ A\left(\boldsymbol{0},b'\right)\ \underbrace{\hat{u}_{\tilde{I}\alpha}(\boldsymbol{0},b')}_{\in\mathbb{R}}\ \cos\left(\omega(\boldsymbol{0},b')t\right) \tag{10.13}$$

and

$$C^{\Gamma}(\boldsymbol{q}_n,b;t) = \prod_{i=1}^{N_\text{p}}\sqrt{N_i}\ A\left(\boldsymbol{0},b'\right)\ \cos\left(\omega(\boldsymbol{0},b')t\right)\ \delta_{\boldsymbol{q}_n\boldsymbol{0}}\,\delta_{bb'} \quad , \tag{10.14}$$

respectively, as all displacement Eigenvectors $(\hat{u}_{\tilde{I}\alpha}(\boldsymbol{0},b'))_{\tilde{I}\alpha}$ are real. When the Γ-point of a supercell is used, $\hat{u}_{\tilde{I}\alpha}(\boldsymbol{0},b')$ describes a "modulation" beyond the simple displacement of entire crystal net planes, which, as indicated above, could be back-folded to wave vectors $\boldsymbol{q}_{n'}\neq\boldsymbol{0}$ in the Brillouin zone of the primitive cell. Since Eq. (10.13) and Eq. (10.14) are equivalent to the expressions used by Estreicher and coworkers,[229–231,515–517] their "phonon picture" is thus fully contained as a special case in the decomposition which has been presented here. In other words, the latter provides a more powerful generalization of the latter as already indicated above.

Inserting Eq. (10.3) into the potential energy of the harmonic solid given by Eq. (4.2) in Section 4.1, a phonon mode decomposition thereof can be obtained, using the previously obtained expansion coefficients $C(\boldsymbol{q}_n,b;t)$ and phonon frequencies $\omega^2(\boldsymbol{q}_n,b)$.

$$\begin{aligned} V^{\text{harmsol}}(t) &= \sum_{\boldsymbol{q}_{n'}}^{\text{grid}}\ \sum_{b'=1}^{3N_\text{cell}}\ V^{\text{harmsol}}(\boldsymbol{q}_{n'},b';t) \\ &= \sum_{\boldsymbol{q}_{n'}}^{\text{grid}}\ \sum_{b'=1}^{3N_\text{cell}}\ \frac{1}{2}\,\omega^2(\boldsymbol{q}_{n'},b')\left|C(\boldsymbol{q}_{n'},b';t)\right|^2 \end{aligned} \tag{10.15}$$

Obviously, as long as the harmonic approximation is good, this also holds reasonably well for the actual potential energy. Using the same decomposition as introduced with Eq. (10.3) and the ensuing formalism also for the velocity field $\{\dot{R}^{\mathrm{MD}}_{\tilde{I}\alpha}(\boldsymbol{L}_n;t)\}_{\tilde{I}\alpha,\boldsymbol{L}_n}$ yields corresponding expansion coefficients $\dot{C}(\boldsymbol{q}_{n'},b;t)$. They allow to decompose the nuclear kinetic energy in the same way.

$$\begin{aligned} T^{\mathrm{cl}}_{\mathrm{N}}(t) &= \sum_{\boldsymbol{q}_{n'}}^{\mathrm{grid}} \sum_{b'=1}^{3N_{\mathrm{cell}}} E^{\mathrm{ph}}_{\mathrm{kin}}(\boldsymbol{q}_{n'},b;t) \\ &= \sum_{\boldsymbol{q}_{n'}}^{\mathrm{grid}} \sum_{b'=1}^{3N_{\mathrm{cell}}} \frac{1}{2}\left|\dot{C}(\boldsymbol{q}_{n'},b;t)\right|^2 \end{aligned} \tag{10.16}$$

In the following, the combination of both decompositions Eq. (10.15) and Eq. (10.16)

$$E^{\mathrm{ph}}(\boldsymbol{q}_n,b;t) = E^{\mathrm{ph}}_{\mathrm{kin}}(\boldsymbol{q}_n,b;t) + V^{\mathrm{harmsol}}(\boldsymbol{q}_n,b;t) \tag{10.17}$$

forms the foundation for the characterization of the total energy uptake of surface phonons in particular (i.e. $N_{\mathrm{p}} = 2$) and their role during the dissociation dynamics. Of course, to obtain the energy density along the continuous directions within the sampling of the surface Brillouin zone latter given by Eq. (10.2) (e.g. in Fig. 10.5 in Section 10.3), the preceding energy decompositions need to be divided by the respective numbers of grid points accordingly.

10.2. Surface Phonons

A first practical application of the formalism derived in the previous section comes with the calculation of energy resolved excitation spectra.

$$E^{\mathrm{ph}}(\hbar\omega;t) = \sum_{\boldsymbol{q}_n}^{\mathrm{grid}} \sum_{b=1}^{3N_{\mathrm{cell}}} E^{\mathrm{ph}}(\boldsymbol{q}_n,b;t)\ \delta(\omega-\omega(\boldsymbol{q}_n,b)) \quad , \tag{10.18}$$

where $\hbar\omega$ are the phonon excitation energies. This reduction to the energy axis simplifies visualization. Still, it is the mode selectivity naturally provided by the underlying formalism which allows to focus on certain groups of modes in the excitation spectra given by Eq. (10.18). In particular the surface phonon modes obviously form a very prominent group in this context, to which attention is thus focused on in the following. After all, the present developments allow to shed light on their role in gas-surface dynamics from a first-principles perspective for the first time. As described before (cf Section 4.3 and Section 9.1.3), modes are classified as surface phonons if their displacement Eigenvectors are localized to at least 20 % in the outermost layers of the slab It has been verified that none of the results presented in the following change qualitatively if degree of localization is increased to 30 % and 40 %. But of course, the expected quantitative changes have been observed, simply because less modes are identified as surface modes in those cases. Since 20 % has been commonly used in the literature before,[250] this "convention" has been finally adapted here as well.

Picking up the trajectory obtained via QM/Me embedding as discussed in Chapter 9, Fig. 10.1 shows spectra for $t = 200\,\mathrm{fs}$, i.e. when the dissociation of the O_2 molecule is right in progress with the oxygen-oxygen distance having reached about one surface lattice constant. The spectra result from a straightforward discretization of Eq. (10.18) based on a $(40\times40\times40)$ grid (cf Eq. (10.1) and Eq. (10.2)). Intriguingly, despite their negligible spectral weight illustrated by the phononic density of states in Fig. 10.1, surface modes have taken up about one quarter of

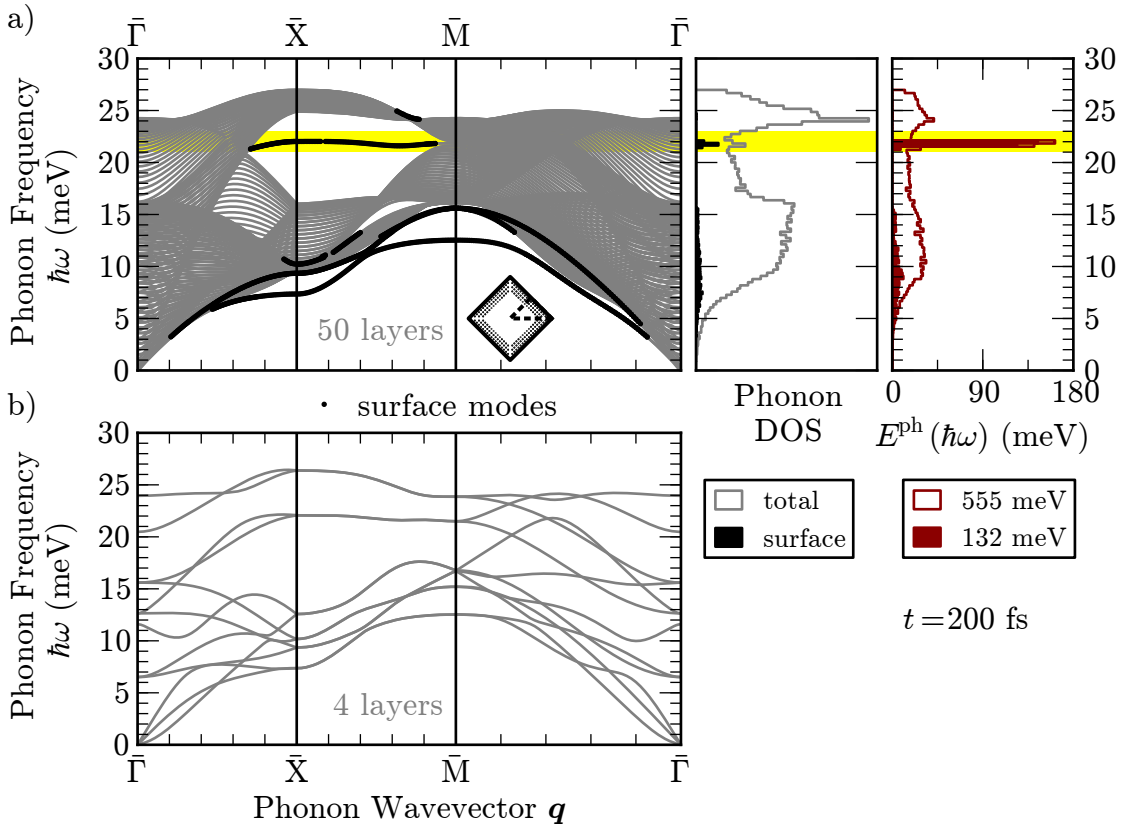

Figure 10.1.: a), rightmost panel: Excitations of surface phonon modes at $t = 200\,\mathrm{fs}$ according to Eq. (10.18). The total amount of energy together with the fraction assigned to surface modes is given below. a), middle and leftmost panel: The corresponding density of states (DOSs) are shown for reference together with the surface phonon dispersion, respectively. As before (cf Fig. 9.7b), modes whose vibrational weight according to their displacement Eigenvector exceeds 20 % in the first two layers (cf Section 4.3) were identified as surface modes and are indicated by the small black circles. Their locations in the surface Brillouin zone is visualized in the inset. The surface phonon band structure of a four layer slab (presently accessible to *ab initio* molecular dynamics) is shown in b) for comparison.

the total energy that has been dissipated into the substrate phonons at that time. Furthermore, it is not the Rayleigh modes that become dominantly excited, although lying energetically below the onset of the bulk part of the spectrum (cf Section 4.3) – quite in contrast to what has been assumed in model Hamiltonians before which are still in frequent use.[520–525] The dominant part of the energy in the phononic system resides instead in the surface band between 21 meV to 23 meV as marked in the dispersion plot in Fig. 10.1 and further detailed in its inset. Looking at the mode Eigenvectors, this is not surprising: As expected, the Rayleigh modes dominantly involve transversal displacements along the surface normal, which are not compatible with the "widening" of the lattice in the surface plane observed during the impingement and subsequent dissociation of the O_2 molecule. In fact, the latter is much better described by the corresponding longitudinal and transversal displacement patterns of the modes belonging to the aforementioned surface phonon band.

Given these insights about the importance of the "right" surface phonon modes, the largely

varying results from Chapter 9, which have been obtained with several more approximate "energy sinks from the shelf" mimicking the energy uptake by the substrate (cf Sections 9.2.2 and 9.2.3), can be rationalized by their different and insufficient description of these particular modes. These conclusions cannot be reached based on conventional *ab initio* molecular dynamics (AIMD): The "small" slabs with typically less than four layers do not allow to describe clearly distinguishable surface phonons as illustrated by the phonon dispersion for a four layer slab in Fig. 10.1 – which is already more than what can typically be afforded in AIMD. In addition, the lateral propagation of the surface modes obviously has to be taken good care of. Attempts to modify the boundary conditions of the slab models thus should not only consider their aperiodic directions like the thermostats in Sections 9.2.2 and 9.2.3 only acting on atoms in the bottom layer, but in particular the periodic, lateral "boundaries". Further emphasizing its advantages, the massive bath employed within the QM/Me approach thus not only provides a more realistic description of the dynamics, but also allows to obtain vital new physical insights about the importance of underlying physical properties for chemical reactions on surfaces.

Finally, the excitation spectrum shown in Fig. 10.1 for one particular time step motivates to further discuss thermalization. The population of the aforementioned surface modes is obviously far away from thermal equilibrium – both for a Bose-Einstein or a Maxwell-Boltzmann distribution in a quantum mechanical or classical picture for the harmonic oscillators constituting the phonons, respectively.[iv] Yet also the rest of the modes are not close to the latter.

10.3. Harmonic Solid

Already when recapitulating the theory behind lattice dynamics in Section 4.1, the harmonic solid was obviously a very important concept for the description of phonons. Likewise, also the analysis scheme presented in Section 10.1 relies on the resulting normal modes. Furthermore, as described in Chapter 8, a lot of the dynamical models employed in the context of gas-surface dynamics make use of this concept – implicitly assuming that the interaction with adsorbates involves only single phonon excitations and leads only to a weak perturbation away from equilibrium. As the results of the previous section already confute the latter assumption, QM/Me is now put forward in order to offer a first-principles perspective on the former.

Even at the level of the optimized MEAM force field obtained in Section 9.1.3 (MEAMopt), this description of the substrate goes beyond the harmonic approximation (cf Section 3.2.2 in Chapter 3), which, in principle, allows to test the validity of the latter during the exothermic reaction investigated here. Conceptually, this can be done in a straightforward fashion by comparing to trajectories obtained with the best possible harmonic description of the substrate, implicitly obtained from lattice dynamics as described in Chapter 4. Technically, the implementation of the corresponding simple analytical force field is challenging when including force constants from a sufficiently large number of neighbor shells and aiming at molecular dynamics for more than 10^5 substrate atoms as used for QM/Me embedding (cf Chapter 9) to ensure proper phonon propagation. The corresponding extension to the LAMMPS code which is suitable for these purposes is detailed in Appendix D.4 and used in the following. The required force constants are taken from phonon calculations using the aforementioned optimized MEAM force field after extending the PHONOPY infrastructure that has already been employed before as needed. Again, the accuracy of the trajectory integration is sufficiently high in order to al-

[iv] Since the nuclear dynamics are based on Newton's equations of motion, it would of course be more consistent to use a classical Maxwell-Boltzmann distribution if this was analyzed in more quantitative detail.

low for a meaningful comparison. As already pointed out in Section 9.2.2, in particular rather stringent criteria for the electronic self-consistency (enabled along entire trajectories thanks to the DM/EDFT scheme introduced in Section 5.3) are required to obtain well converged forces.

Given the additional complexity introduced by surface phonons, it is not surprising that previous models have rather obtained the force constants from bulk phonon properties and used them also for the surface calculations.[36,434,448,465,468] This has been chosen as a starting point here as well – aiming at a discussion of potentially concomitant limitations. Of course, for each pair of atoms I and J, the corresponding force constant matrix $\mathbf{\Phi}_{IJ}^{\text{bulk}}$ has to be properly transformed to yield the corresponding surface constant matrix

$$\mathbf{\Phi}_{IJ}^{100} = \begin{pmatrix} \cos(45°) & -\sin(45°) & 0 \\ \sin(45°) & \cos(45°) & 0 \\ 0 & 0 & 1 \end{pmatrix} \cdot \mathbf{\Phi}_{IJ}^{\text{bulk}} \quad . \tag{10.19}$$

This accounts for the rotation of the reference coordinate systems with respect to each other, which are commonly used to describe bulk and surface unit cells. As directly inferred from the convergence of the bulk phonon properties with respect to the supercell size within the direct method (cf Section 4.2), an accurate bulk harmonic force field (BHFF) is then formed by including force constants up to third nearest neighbors, corresponding to a cut off distance of about 5 Å and resulting in more than 50 force constant matrices $\mathbf{\Phi}_{IJ}^{100}$. Fig. 10.2 shows a comparison of the results obtained based on QM/Me embedding for trajectories starting from identical initial conditions (same as in Chapter 9), using MEAMopt as originally for the substrate description (cf Section 9.2) and substituting the latter by BHFF. It is important to note that the DFT-based part of the embedding is exactly the same in both cases . As to be expected, the original dynamics employing MEAMopt are reproduced precisely within the first 150 fs. Thereafter, however, the trajectories start to deviate very strongly – similar to what has been observed for the "energy sinks from the shelf" in Section 9.2.1 Emphasizing again that the numerical uncertainties in the non-analytical DFT forces are too small for causing this deviation within the trajectory integration and thus cannot be blamed therefor, this does raise severe doubts about the harmonic approximation in the context of gas-surface dynamics.

Notwithstanding, the use of bulk force constants might still come to the former's rescue. Figure 10.3 illustrates the phonon dispersion resulting from the BHFF when used for the description of the Pd(100) surface compared against the MEAMopt reference. Unlike in the bulk case, the latter is not matched exactly, since changes of the force constants due to the presence of the surface are not accounted for. As shown by Fig. 10.3, this leads in particular to an extremely poor description of the surface phonon modes.

Since surface phonons have been found to play a crucial role for the adsorbate dynamics in Section 10.2, the strong deviations of the trajectories shown in Fig. 10.2 on a rather short time scale might not appear to be so surprising any more. Furthermore, it is thus interesting to include a proper description of the former into a harmonic force field. Of course, this is achieved completely naturally when force constants are obtained from the surface phonon calculations – the resulting surface harmonic force field (SHFF) then by construction yields a dispersion that is indistinguishable from the optimized MEAM reference shown in Fig. 10.3. Technically, this is significantly more complicated as the layer dependance of the force constants needs to be properly considered (cf Appendix D), multiplying the number of force constant matrices $\mathbf{\Phi}_{IJ}^{100}$ accordingly. For the atoms in each layer, again up to third nearest neighbors are considered as for BHFF before. The plots in Fig. 10.4 show the same comparison as in Fig. 10.4, but with SHFF instead of BHFF. Indeed, the trajectories start to deviate much later only after 300 fs, thus confirming that the surface phonons have been correctly identified as culprit before.

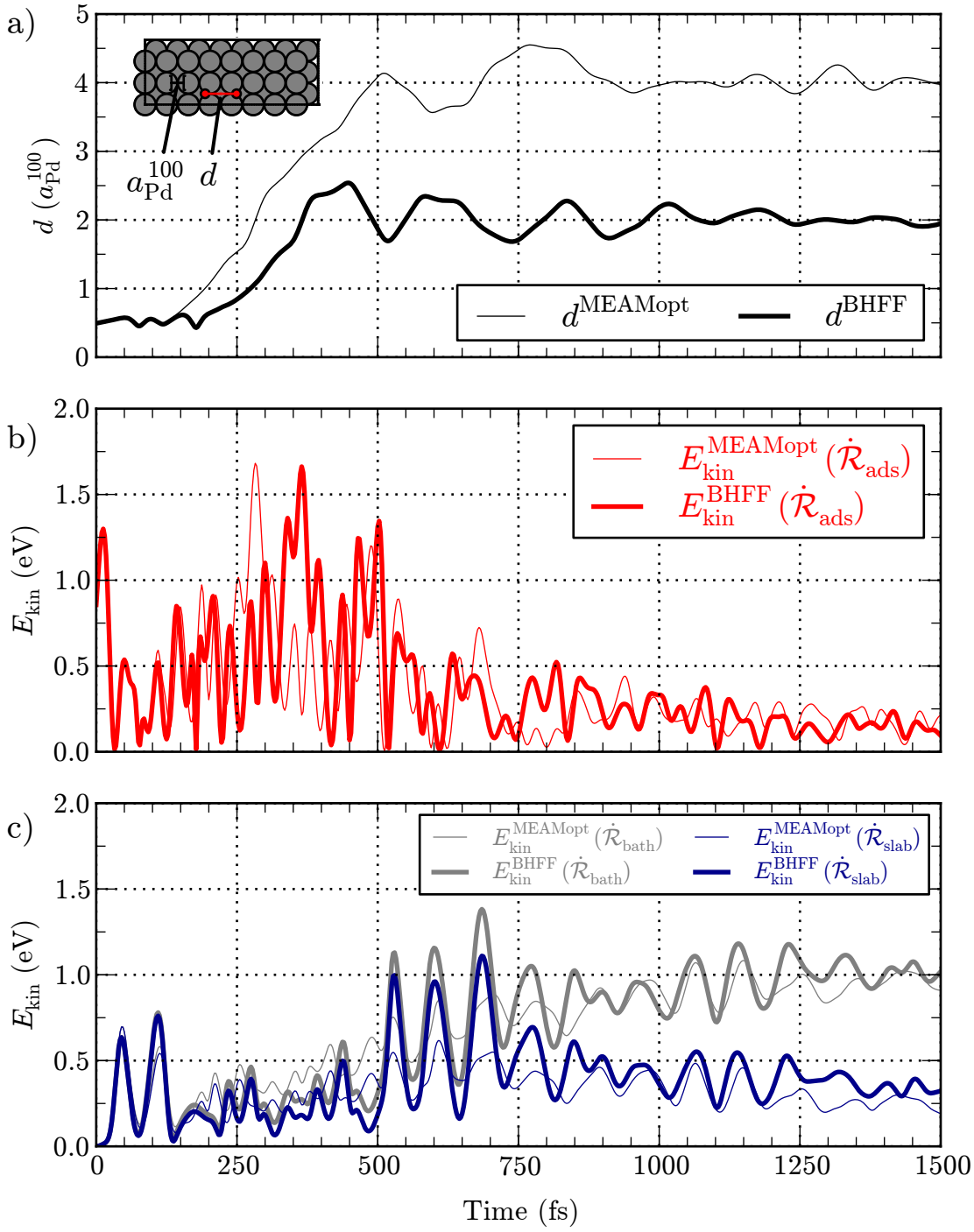

Figure 10.2.: Dissociation dynamics including energy dissipation for O_2 dissociating on a Pd(100) surface described by a harmonic force field based on bulk force constants (BHFF, thick lines) together with the reference results obtained in Chapter 9 (MEAMopt, thin lines) as explained in the text. a) Separation distance $d(t)$ of both oxygen atoms on the surface like in Fig. 9.10. b) and c) Kinetic energies of both oxygen atoms as well as the palladium atoms in the embedding cell (indicated in the inset in a)) and the bath as a function of time, respectively, like in Fig. 9.8.

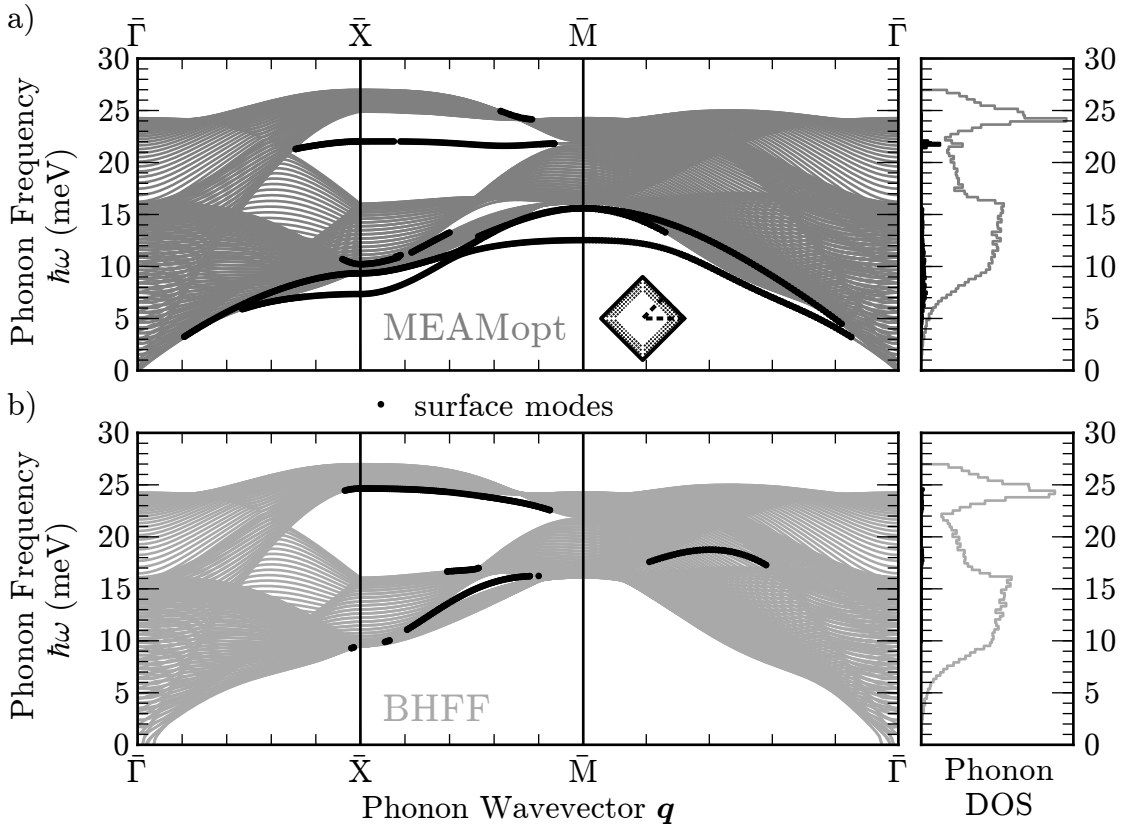

Figure 10.3.: Comparison of phonon dispersions and density of states obtained from (a) MEAMopt and (b) BHFF as explained in the text. Since the latter lacks a proper description of surface features, it is not surprising that it reproduces surface modes (indicated by the small black circles) only very poorly. In both cases, as before in Fig. 9.7 and Fig. 10.1, these modes were identified as such if the vibrational weight according to their displacement Eigenvector exceeds 20 % in the first two layers (cf Section 4.3).

Still, the fact that there are deviations confirms the suspicions about the harmonic solid, as the SHFF represents the best possible corresponding force field for the description of the Pd(100) surface based on MEAMopt.

In order to further scrutinize these important findings, important insights can be gained from the projection scheme worked out at the beginning of this chapter. For $t = 200\,\mathrm{fs}$ (as already used for the surface phonon analysis presented in Section 10.2) Fig. 10.5 visualizes the distribution of phonon excitations over the surface Brillouin zone for substrate descriptions with both MEAMopt and SHFF, summed over all bands according to

$$\tilde{E}^{\mathrm{ph}}(\boldsymbol{q}_n; t) = \sum_{b=1}^{3N_{\mathrm{cell}}} E^{\mathrm{ph}}(\boldsymbol{q}_n, b; t) \quad , \tag{10.20}$$

where $E^{\mathrm{ph}}(\boldsymbol{q}_n, b; t)$ is defined in Eq. (10.17). Like in Section 10.2, projection weights have been calculated using a $(40 \times 40 \times 40)$ grid (cf Eq. (10.1) and Eq. (10.2)), resulting in the dense sampling of reciprocal space indicated in Fig. 10.5. Qualitatively, the same results can already be obtained for a $(20 \times 20 \times 20)$ grid, which, however, does not yield a significant reduction of

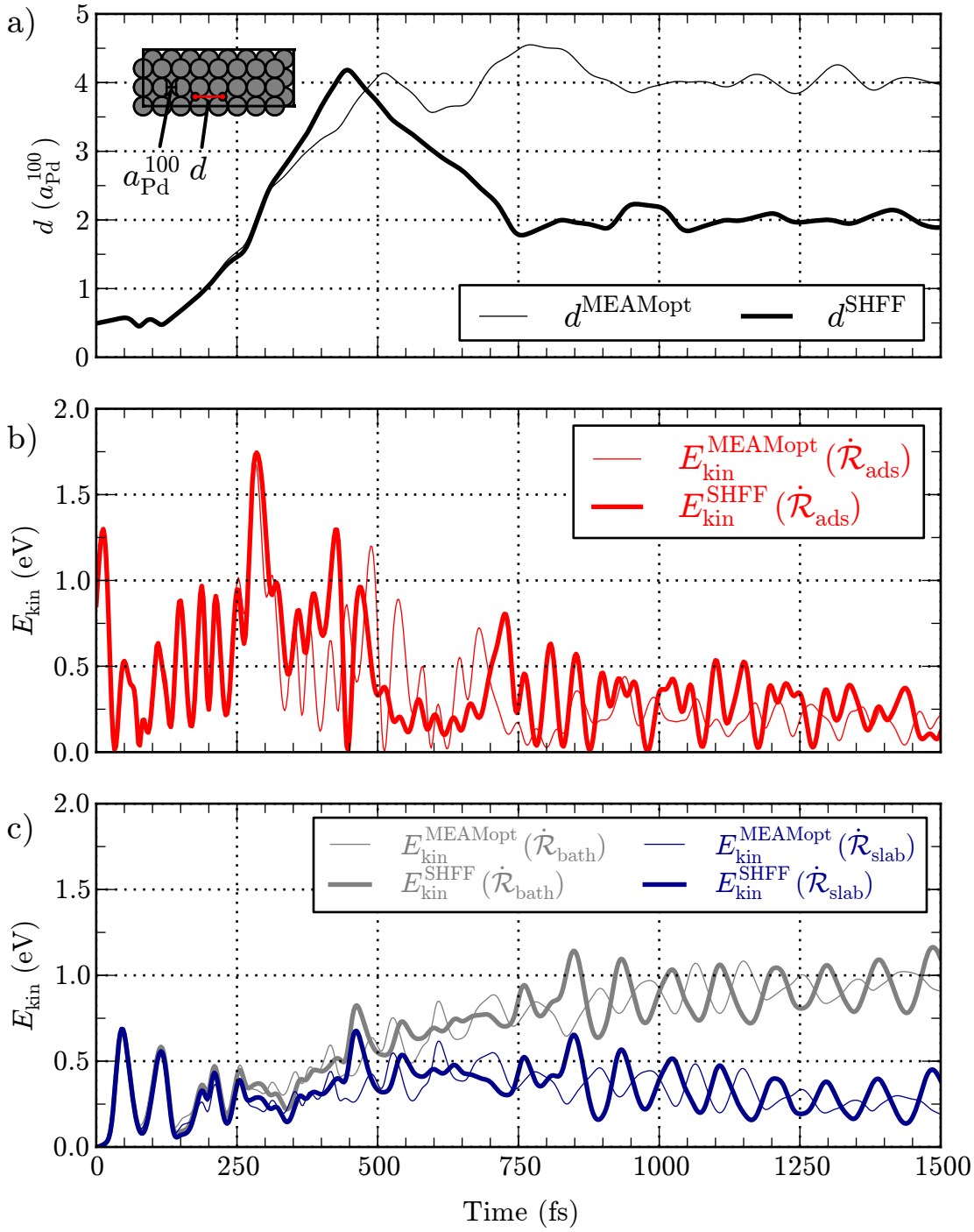

Figure 10.4.: Same as Fig. 10.2, but for a harmonic force field based on surface force constants (SHFF, thick lines) together with the reference results obtained in Chapter 9 (MEAMopt, thin lines) as explained in the text.

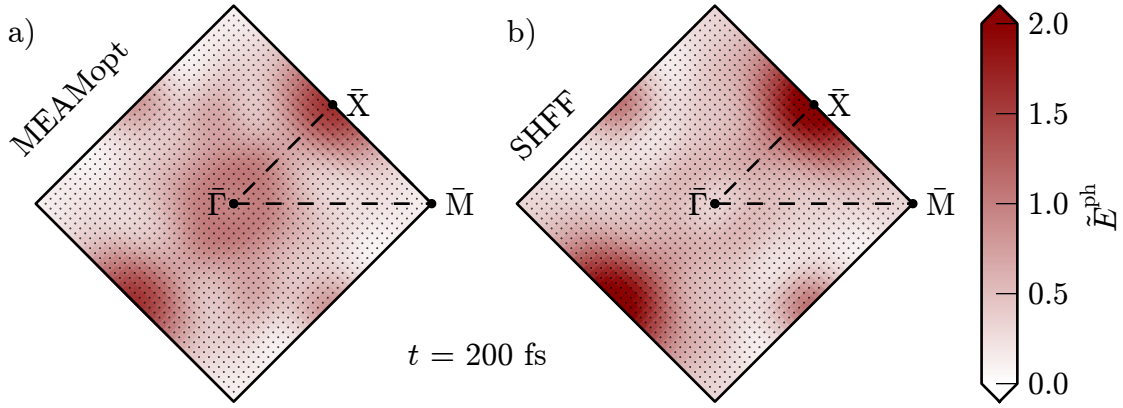

Figure 10.5.: Phonon excitations at $t = 200\,\mathrm{fs}$ over the entire surface Brillouin zone of Pd(100) according to Eq. (10.20) for the a) MEAMopt and b) SHFF force fields described in the text. The blacks dots indicate modes with wave vectors $\boldsymbol{q}$ for which exact results according to the analysis devised in Section 10.1 are obtained using a $(40 \times 40 \times 40)$ grid. At each $\boldsymbol{q}$, all corresponding bands have been summed. The coloring is based on a linear interpolation between these values.

computational effort – in particular in comparison with the integration of a QM/Me trajectory. As clearly shown by Fig. 10.5, this analysis directly targeting phonons reveals differences already at a much earlier time step than perceivable from the trajectory data depicted in Fig. 10.4: Anharmonic couplings, which are present in MEAMopt but absent by construction in SHFF, are of paramount importance to excite phonons with long wavelengths in the vicinity of the Γ point, that obviously do not (predominantly) result from the interaction with the adsorbate alone. The multiphonon nature of the excitations visualized in Fig. 10.5 rationalizes the importance of anharmonicity and thus the breakdown of the harmonic approximation. Finally, as quantum effects become negligible for harmonic oscillator containing many quanta, the former also nicely corroborates the present classical description of the phonon excitations

10.4. Summary and Outlook

This chapter aimed at unraveling details about phonon excitations which are "hidden" in the dynamics and now explicitly accessible thanks to the novel QM/Me embedding approach as introduced in the previous chapter. For this, first a projection scheme has been derived to "count phonons" instantaneously and in a mode-selective fashion at each molecular dynamics time step. To the best of the author's knowledge this has never been worked out in a similarly rigid fashion before. Apart from the specific applications in the present context, it can also straightforwardly offer very beneficial insights into problems of thermal transport, e.g. to characterize the role of defect modes for the Boltzmann transport equation often used for modeling thermal conductivity.

Using this newly introduced phonon projection scheme surface phonons were identified to be of crucial importance for the dissociation dynamics of the O_2 at Pd(100) showcase – rationalizing the vastly different results obtained by using "energy sinks from the shelf" in Chapter 9. Unlike what has been assumed before, it is not the Rayleigh, but surface modes within an energetically higher band in a gap between bulk modes at the boundaries of the surface Brillouin zone

which predominantly get excited. During the dissociation of the oxygen molecule, these modes carry about a quarter of the total energy in the phononic system. The latter is thus strongly perturbed and equilibration is still very much in progress even after 1.5 ps – again in contrast to assumptions made within previous models.

Attention next turned to the harmonic solid frequently employed in modeling of gas-surface dynamics by substituting the description of the substrate in QM/Me embedding by the former based on bulk force constants leads to quite different dynamics. With the best possible harmonic force field resulting from the anharmonic description of the surface as originally employed within the QM/Me embedding approach, deviations set in later – confirming the importance of the surface phonon modes once more. Nevertheless, the fact that trajectories still do deviate considerably, marks a breakdown of the harmonic approximation in the present context. This is rationalized by again invoking the phonon projection scheme: It reveals the multiphonon nature of the excitations, which leads to long-wavelength phonons being predominantly excited by anharmonic decay already much earlier than deviations become apparent in the dynamics. Furthermore, also the classical description of the phonon excitations is corroborated thereby.

Despite all these important theoretical insights, altogether, the analyses worked out in this chapter stand for itself for the time being. Although a plethora of experimental efforts (also) in surface science are currently focused on producing "molecular movies" (e.g. by means of free electron lasers), the difficult experimental challenge of obtaining detailed time-resolved data about phonon excitations during individual adsorbate-substrate interaction events has not yet been mastered. Therefore, at present, comparison to experiments can only be done indirectly based on experimentally accessible observables that demand statistics, i.e. obtaining and analyzing sufficiently many trajectories. As already indicated in the introduction to this chapter this is left for future work – which "only" requires to apply the concepts that have been laid out here on a (computationally) larger scale.

11. Outlook

As typical for scientific work in general, also this thesis has aimed to answer many questions and inspired many new ones at the same time. A detailed discussion of the specific insights gained with respect to energy dissipation during dissociative adsorption has already been presented in the end of the various chapters. The following outlook comprises therefore only a loose collection of additional ongoing effort and future perspectives which have already been stimulated through this work.

Interest in the symmetry adapted coordinates conceived in the context of the interpolation of the six-dimensional potential energy surface (PES) (cf Chapter 6 and generalizations in Appendix A) has already been expressed for an application with the modified Sheppard method, as it should allow to overcome the problem with discontinuities encountered therewith before.[333]

In fact, a neural network based PES relying on the proper variant of these coordinate transformations (cf Appendix A.3) has already been successfully used to obtain a neural network-based PES for O_2 on Ag(111) and investigate the adsorption dynamics for this system.[52] Since, in that case, the initial sticking coefficient is extremely low, several millions of trajectories needed to be calculated for its statistically reliable evaluation, which at present can only be routinely obtained with first-principles quality based on a divide and conquer strategy. A study comparing the extensive statistics concomitantly obtained for scattering to the wealth of experimental data is presently under way.

An application of the perturbative approach for the calculation of electron-hole pair excitation spectra (cf Chapter 7) to other "large" systems, for which chemicurrents have actually been detected,[28] would of course be interesting. Such efforts are planned for O_2 on Ag(100), i.e. a coinage metal surface with the same symmetry as the one investigated here.

Since very similar matrix elements, which pose the central computational challenge, are also required for electronic friction theory (cf Section 7.1.4), the present highly-efficient implementation can easily be adapted. As the community has long relied essentially on a single particular implementation,[119,399] this can offer "fresh" perspectives: For example, together with an ensuing interpolation, this could provide high-dimensional (electronic) friction tensors, allowing to settle the controversy about the accuracy of friction coefficients.[44–46] and thus offer an important contribution to the ongoing debate about the importance of non-adiabatic effects for dissociation dynamics on metal surfaces. In addition, these matrix elements could also serve as a natural starting point to investigate the role of electron-phonon coupling within the substrate for the adsorbate dynamics.[277]

As already indicated above, many systems or experimental observables less benign than sticking can easily require an extensive amount of statistics. Divide and conquer strategies provide a computational efficiency that seems to be difficult to beat in this respect once the PES obtained, implying a frozen substrate as present state of the art. It remains an open question whether the corresponding potential energy surfaces can also be easily extended successfully to accurately account for substrate motion. Only recently, Bonfanti and coworkers have tried another step into that direction, which already clearly hints at the complexity and challenges introduced thereby.[26]. For H_2 on Cu(111), they have extended frozen surface interaction potentials to seven dimensions by inclusion of substrate motion along conveniently preselected displacement

directions, not corresponding to phonon Eigenvectors by construction. Their underlying DFT calculations are based on (2×2) supercells of the surface unit cell, so that phonons could at best have been sampled only at two points in the surface Brillouin zone. Apart from the implied harmonic approximation, in light of the results of this work (cf Chapter 10), it would be interesting to verify whether the implications for the adsorbate dynamics are captured properly, even for a significantly lighter molecule than O_2.

On the contrary, the QM/Me approach introduced in Chapter 9 of this work does not suffer from any of those shortcomings, and could provide theoretical reference data. Still, at present it is unclear how much of the phononic details propagate into also experimentally observable quantities, i.e. are not "washed out" by statistics. To obtain the latter, "on-the-fly" force evaluations with first-principles codes still form a significant computational burden. The latter varies obviously depending on the employed DFT implementation, the system investigated therewith and the (numerical) convergence quality that is aimed for. In general, any system which can treated by *ab initio* molecular dynamics (AIMD) also qualifies for an application of QM/Me. This burden might even be overcome routinely and automatically in practice, during the next few years by the exponential growth of available computational power or even potential further algorithmic improvements of first-principles codes. Special AIMD acceleration schemes that have been conceived in recent years[208–210,357,526] could already be exploited today also with QM/Me – if they are applicable to metallic systems.

Another possibility is to apply techniques currently developed in the context of interatomic potentials based on high-dimensional interpolation.[183,184] As published, these schemes currently try to approximate *direct results* of the underlying quantum mechanical reference calculations. Targeting a difference term as introduced by QM/Me instead results in a "simpler" high-dimensional function to be interpolated and should hence simplify the interpolation procedure. In a first step, the description of the interactions between metal atoms could even be left to an established, more traditional interatomic potential (similar to the MEAM-based one employed here). Behler and coworkers have already made first steps in such a direction by augmenting a "pure" NN description of a polar material (ZnO) with analytical expressions for long-range electrostatics.[527]

Either way, a calculation of pair distributions resulting from the hot adatoms (cf Section 9.2.3) for this or another system, for which corresponding experimental data from scanning tunneling microscopy experiments is already available, would enable an important benchmark for theory. It would also provide another important contribution to the aforementioned debate about the importance to go beyond the Born-Oppenheimer approximation for the description of dynamics on surface.

Ultimately, coarse-grained modeling of heterogeneous catalysis based on first-principles kinetic Monte Carlo simulations[3,7,8] might be extended "beyond the Markov approximation" by including a suitable description of heat dissipation, using kinetic parameters obtained from (QM/Me-based) dynamics. Ideas along those lines have been proposed only recently[528] but base their extensions on the validity of Fourier's law on the atomistic scale. In fact, more extensive evaluations of kinetic energies than in Chapter 9 will allow to verify this assumption.

This would be of obvious interest and importance for the description of thermal transport in general – not only in the context of energy conversion at interfaces. In addition, the former can also benefit from the phonon analysis as presented in Chapter 10. It allows to quantify phonon scattering e.g. at defects, thus providing important input for coarse grained description via the Boltzmann transport equation and the determination of thermal conductivities from first-principles.[509,512–514]

Finally, in principle anything that breaks periodicity of a metal surface or even a bulk crystal

can be subjected to the QM/Me embedding treatment. Its application even in a "static context" might thus provide important insights about long range elastic effects, e.g. for defects, dislocations or steps.

Appendices

Overview

Appendix A practically demonstrates generalizability of the concept behind the symmetry adapted coordinates developed in the scope of Chapter 6 to other common low-index surfaces. The six-dimensional potential energy surface constructed in the same chapter is characterized in comprehensive detail in Appendix B. Motivated by its rather general applicability, implementation details of the code written to obtain electron-hole pair spectra described in Chapter 7 (based on the CASTEP DFT code) together with convergence and consistency checks are assembled into Appendix C. Lastly, the design decisions and implementation of several extensions to the classical MD code LAMMPS, which have been required in Chapter 9 and Chapter 10 and might also have straightforward future applications, are documented in Appendix D.

A. Symmetry Adapted Coordinates for Diatomics on Low-Index Surfaces

In Chapter 6, the six-dimensional potential energy surface of a homonuclear diatomic molecule on a fcc(100) surface is interpolated according to

$$V_{6D} \approx \mathcal{V}_{6D}(\boldsymbol{Q}(\boldsymbol{R}^{ph})) \quad , \tag{A.1}$$

where the physical coordinates $\boldsymbol{R}^{ph}$ are first transformed to symmetry adapted coordinates. Neural networks have been used as interpolation function $\mathcal{V}_{6D}$ in the present work, but the general ansatz given by Eq. (A.1) can also be beneficially used together with any other sophisticated scheme for high-dimensional interpolation.[i] Thus, at the same time, the complexity of the interpolation problem is significantly reduced and symmetry correctly incorporated. In the following, the surface specific parts of this concept (as developed in Section 6.1.4) are given for common low-index surfaces of both fcc and bcc crystal typically encountered in applications. For the sake of completeness, first the essential definitions are briefly recapitulated.

Typical physical coordinates $\boldsymbol{R}^{ph}$ to describe molecular configurations of a (in general heteronuclear) diatomic molecule consisting of two atoms A and B, with masses m_A and m_B, respectively, and a total mass $M = m_A + m_B$, are Cartesian

$$\boldsymbol{R}^{cart} = \boldsymbol{R}_A \oplus \boldsymbol{R}_B = (X_A, Y_A, Z_A) \oplus (X_B, Y_B, Z_B) \tag{A.2}$$

or center of mass centered spherical coordinates

$$\boldsymbol{R}^{sph} = (X, Y, Z, d, \vartheta, \varphi) \quad , \tag{A.3}$$

with center of mass coordinates $\boldsymbol{R} = (X, Y, Z)$, internuclear distance d, polar angle ϑ and azimuth angle φ. Here and in the following, the origin is located in the surface plane on a top site. An illustration of these two coordinate systems above a fcc(100) surface is given in Section 6.1.1 by Fig. 6.1. The transformation from Cartesian to spherical coordinates is given by

$$X = \frac{m_A}{M} X_A + \frac{m_B}{M} X_B \tag{A.4a}$$

$$Y = \frac{m_A}{M} Y_A + \frac{m_B}{M} Y_B \tag{A.4b}$$

$$Z = \frac{m_A}{M} Z_A + \frac{m_B}{M} Z_B \tag{A.4c}$$

$$d = \sqrt{(X_B - X_A)^2 + (Y_B - Y_A)^2 + (Z_B - Z_A)^2} \equiv \sqrt{d_\parallel^2 + d_\perp^2} \tag{A.4d}$$

$$\vartheta = \arccos\left(\frac{d_\perp}{d}\right) \tag{A.4e}$$

$$\varphi = \arccos\left(\frac{X_B - X_A}{d_\parallel}\right) = \arcsin\left(\frac{Y_B - Y_A}{d_\parallel}\right) \tag{A.4f}$$

[i] Interest has already been signaled[529] in conjunction with the so-called corrugation reducing procedure quite frequently used in the gas-surface dynamics community nowadays.[323]

Of course, Eq. (A.4f) is only valid for $d_{\parallel} \neq 0$, which is equivalent to $\vartheta \neq 0$. In other words, for a diatomic molecule with its molecular axis perpendicular to the surface, an azimuth angle is not defined. The reverse transformation from spherical to Cartesian coordinates reads

$$X_A = X - \frac{m_B}{M}\, d\, \sin(\vartheta)\, \cos(\varphi) \tag{A.5a}$$
$$Y_A = Y - \frac{m_B}{M}\, d\, \sin(\vartheta)\, \sin(\varphi) \tag{A.5b}$$
$$Z_A = Z - \frac{m_B}{M}\, d\, \cos(\vartheta) \tag{A.5c}$$
$$X_B = X + \frac{m_A}{M}\, d\, \sin(\vartheta)\, \cos(\varphi) \tag{A.5d}$$
$$Y_B = Y + \frac{m_A}{M}\, d\, \sin(\vartheta)\, \sin(\varphi) \tag{A.5e}$$
$$Z_B = Z + \frac{m_A}{M}\, d\, \cos(\vartheta) \tag{A.5f}$$

For a homonuclear diatomic, the above expression simplify accordingly since $m_\mathrm{A} = m_\mathrm{B} = m$, which e.g. results in $\frac{m_\mathrm{A}}{M} = \frac{m_\mathrm{B}}{M} = \frac{1}{2}$.

In Section 6.1.4, the construction of the following symmetry adapted coordinates $\boldsymbol{Q}^{\mathrm{hom}}$ for a homonuclear diatomic is extensively discussed.

$$Q_1^{\mathrm{hom}} = \frac{1}{2}\left[\exp\left(-\tfrac{Z_\mathrm{A}}{2}\right)\cdot g_1(X_\mathrm{A}, Y_\mathrm{A}) + \exp\left(-\tfrac{Z_\mathrm{B}}{2}\right)\cdot g_1(X_\mathrm{B}, Y_\mathrm{B})\right] \tag{A.6a}$$
$$Q_2^{\mathrm{hom}} = \exp\left(-\tfrac{Z_\mathrm{A}}{2}\right)\cdot g_1(X_\mathrm{A}, Y_\mathrm{A}) \cdot \exp\left(-\tfrac{Z_\mathrm{B}}{2}\right)\cdot g_1(X_\mathrm{B}, Y_\mathrm{B}) \tag{A.6b}$$
$$Q_3^{\mathrm{hom}} = \frac{1}{2}\left[\exp\left(-\tfrac{Z_\mathrm{A}}{2}\right)\cdot g_2(X_\mathrm{A}, Y_\mathrm{A}) + \exp\left(-\tfrac{Z_\mathrm{B}}{2}\right)\cdot g_2(X_\mathrm{B}, Y_\mathrm{B})\right] \tag{A.6c}$$
$$Q_4^{\mathrm{hom}} = \exp\left(-\tfrac{Z_\mathrm{A}}{2}\right)\cdot g_2(X_\mathrm{A}, Y_\mathrm{A}) \cdot \exp\left(-\tfrac{Z_\mathrm{B}}{2}\right)\cdot g_2(X_\mathrm{B}, Y_\mathrm{B}) \tag{A.6d}$$
$$Q_5^{\mathrm{hom}} = \exp\left(-\tfrac{Z}{2}\right)\cdot g_1(X, Y) \tag{A.6e}$$
$$Q_6^{\mathrm{hom}} = \exp\left(-\tfrac{Z}{2}\right)\cdot g_2(X, Y) \tag{A.6f}$$
$$Q_7^{\mathrm{hom}} = \exp\left(-\tfrac{Z}{2}\right) \tag{A.6g}$$
$$Q_8^{\mathrm{hom}} = d \tag{A.6h}$$
$$Q_9^{\mathrm{hom}} = \cos(\vartheta)^2 \tag{A.6i}$$

For a heteronuclear molecule, the symmetrization in Eqs. (A.6a) to (A.6d) has to be removed accordingly:

$$Q_1^{\mathrm{het}} = \exp\left(-\tfrac{Z_\mathrm{A}}{2}\right)\cdot g_1(X_\mathrm{A}, Y_\mathrm{A}) \tag{A.7a}$$
$$Q_2^{\mathrm{het}} = \exp\left(-\tfrac{Z_\mathrm{A}}{2}\right)\cdot g_2(X_\mathrm{A}, Y_\mathrm{A}) \tag{A.7b}$$
$$Q_3^{\mathrm{het}} = \exp\left(-\tfrac{Z_\mathrm{B}}{2}\right)\cdot g_1(X_\mathrm{B}, Y_\mathrm{B}) \tag{A.7c}$$
$$Q_4^{\mathrm{het}} = \exp\left(-\tfrac{Z_\mathrm{B}}{2}\right)\cdot g_2(X_\mathrm{B}, Y_\mathrm{B}) \tag{A.7d}$$
$$Q_i^{\mathrm{het}} = Q_i^{\mathrm{hom}} \quad , \quad i \in \{5, 6, 7, 8, 9\} \tag{A.7e}$$

g_1 and g_2 are surface specific functions $\mathbb{R}^2 \to \mathbb{R}$ determining symmetry equivalent lateral positions as discussed in detail in the context of Eq. (6.16) in Section 6.1.4. For a surface lattice with primitive vectors $\boldsymbol{a}_1$ and $\boldsymbol{a}_2$, they are typically based on appropriate combinations of lowest order terms of the corresponding Fourier series, given by the corresponding reciprocal lattice vectors

$$\boldsymbol{G}_{ij} = i\boldsymbol{b}_1 + j\boldsymbol{b}_2 \quad . \tag{A.8}$$

The crystallographic convention to indicate a negative direction by a bar over the corresponding number is adopted. As usual, the primitive vectors $\boldsymbol{b}_1$ and $\boldsymbol{b}_2$ of the reciprocal lattice are defined by

$$\boldsymbol{a}_i \cdot \boldsymbol{b}_j = 2\pi\delta_{ij} \quad i,j \in \{1,2\} \quad . \tag{A.9}$$

In the following Appendices A.1 to A.6, examples are given for (100), (110) and (111) surfaces of both fcc and bcc crystals.

A.1. fcc(100)

Equations and plots presented in this section are identical to those in Section 6.1.4 and are only included here for the sake of completeness.

Primitive vectors of the surface lattice (cf Fig. A.1.1 for illustration):

$$\boldsymbol{a}_1^{\mathrm{fcc100}} = \frac{\sqrt{2}}{2} a_{\mathrm{fcc}} \begin{pmatrix} 1 \\ 0 \end{pmatrix} = a_{\mathrm{fcc}}^{100} \begin{pmatrix} 1 \\ 0 \end{pmatrix} \tag{A.10a}$$

$$\boldsymbol{a}_2^{\mathrm{fcc100}} = \frac{\sqrt{2}}{2} a_{\mathrm{fcc}} \begin{pmatrix} 0 \\ 1 \end{pmatrix} = a_{\mathrm{fcc}}^{100} \begin{pmatrix} 0 \\ 1 \end{pmatrix} \tag{A.10b}$$

Lateral coordinate transformations:

$$\begin{aligned} g_1^{\mathrm{fcc100}}(x,y) &= \frac{1}{4}\left[\cos\left(\boldsymbol{G}_{10}^{\mathrm{fcc100}} \cdot \begin{pmatrix} x \\ y \end{pmatrix}\right) + \cos\left(\boldsymbol{G}_{01}^{\mathrm{fcc100}} \cdot \begin{pmatrix} x \\ y \end{pmatrix}\right)\right] + \frac{1}{2} \\ &= \frac{1}{4}\left[\cos\left(\frac{2\pi}{a_{\mathrm{fcc}}^{100}} x\right) + \cos\left(\frac{2\pi}{a_{\mathrm{fcc}}^{100}} y\right)\right] + \frac{1}{2} \end{aligned} \tag{A.11a}$$

$$\begin{aligned} g_2^{\mathrm{fcc100}}(x,y) &= \frac{1}{4}\left[\cos\left(\boldsymbol{G}_{11}^{\mathrm{fcc100}} \cdot \begin{pmatrix} x \\ y \end{pmatrix}\right) + \cos\left(\boldsymbol{G}_{1\bar{1}}^{\mathrm{fcc100}} \cdot \begin{pmatrix} x \\ y \end{pmatrix}\right)\right] + \frac{1}{2} \\ &= \frac{1}{4}\left[\cos\left(\frac{2\pi}{a_{\mathrm{fcc}}^{100}} x\right) \cdot \cos\left(\frac{2\pi}{a_{\mathrm{fcc}}^{100}} y\right)\right] + \frac{1}{2} \end{aligned} \tag{A.11b}$$

Contour plots of Eqs. (A.11a) and (A.11b) are shown in Fig. A.1.2. Examples for symmetry equivalent points (as given by intersections of contours of g_1^{fcc100} and g_2^{fcc100}) are presented in Fig. A.1.3.

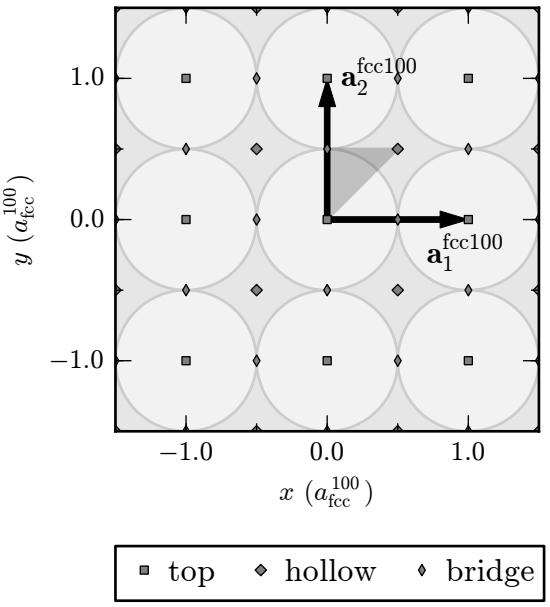

Figure A.1.1.: Structure and symmetry of a fcc(100) surface: The primitive lattice vectors $\boldsymbol{a}_1^{\mathrm{fcc100}}$ and $\boldsymbol{a}_2^{\mathrm{fcc100}}$ as given by Eqs. (A.10) are shown as arrows, high symmetry sites are marked by different symbols, and the irreducible wedge is indicated by the dark gray triangle.

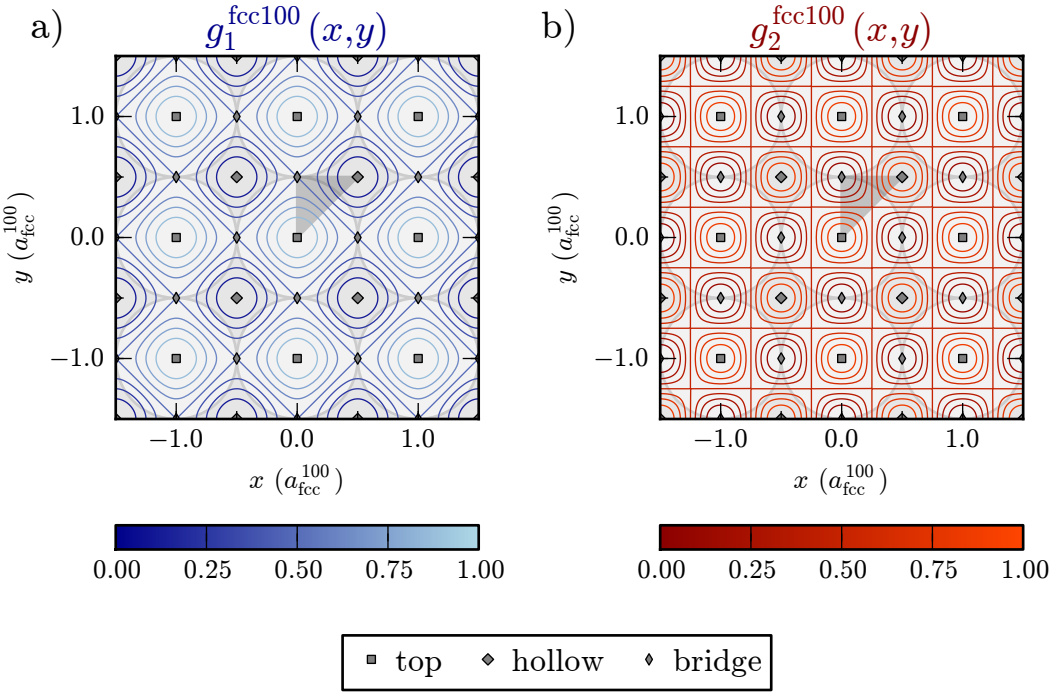

Figure A.1.2.: Contour plots of the coordinate transformations a) g_1^{fcc100} and b) g_2^{fcc100} as defined by Eqs. (A.11) for lateral coordinates (x, y) given in units of the surface lattice constant a_{fcc}^{100}. The spacing of the contour lines is $\frac{1}{8}$.

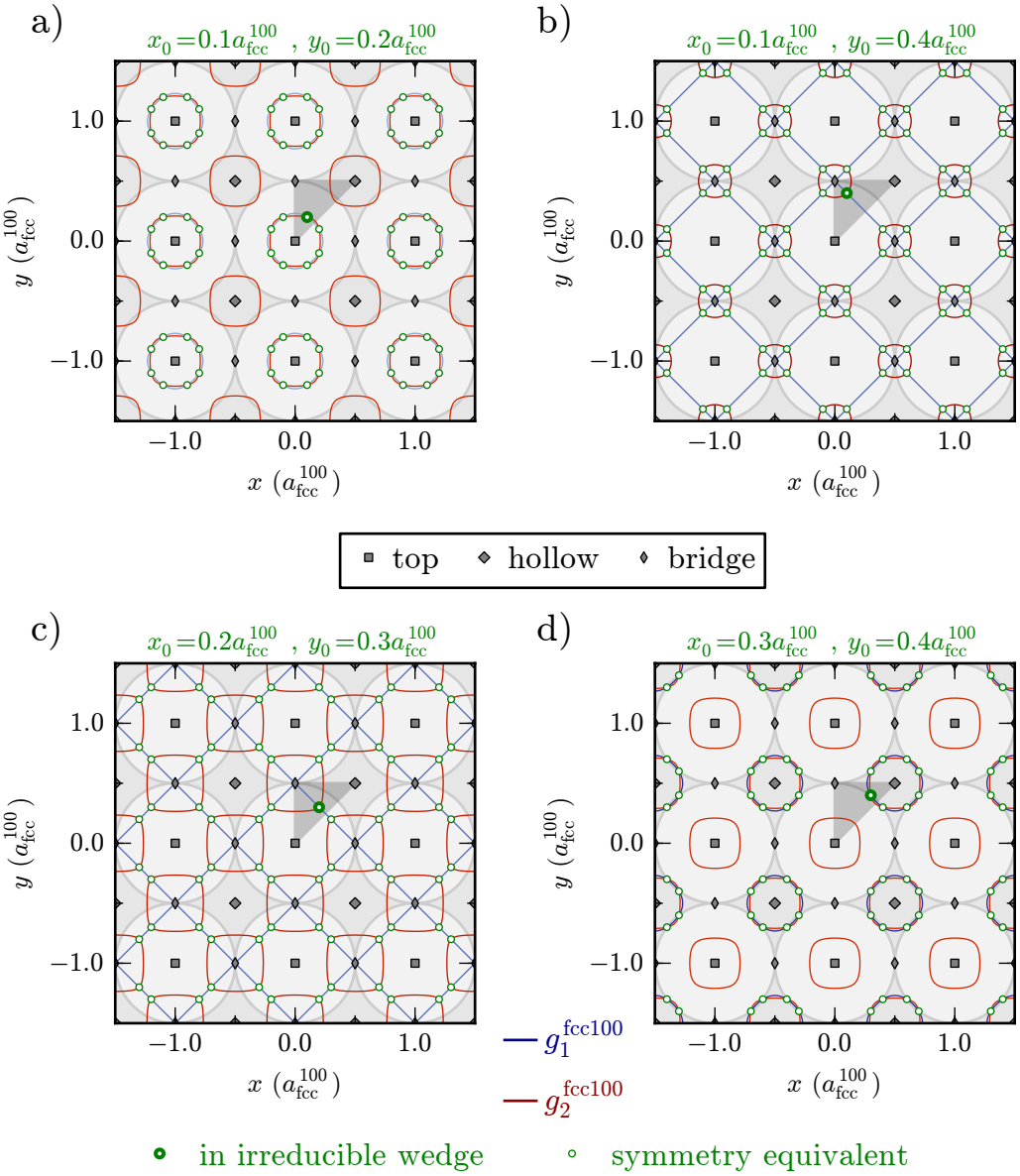

Figure A.1.3.: Examples for symmetry equivalent lateral coordinates given in units of the surface lattice constant a_{fcc}^{100}. In a) to d), for different points (x_0, y_0) in the indicated triangular irreducible wedge (thick green circle), the respective equivalents are the intersection points (thin green circles) of contour lines of g_1^{fcc100} (blue) and g_2^{fcc100} (red) as defined by Eqs. (A.11). Contour values are given by $g_1^{\mathrm{fcc100}}(x_0, y_0)$ and $g_2^{\mathrm{fcc100}}(x_0, y_0)$, respectively.

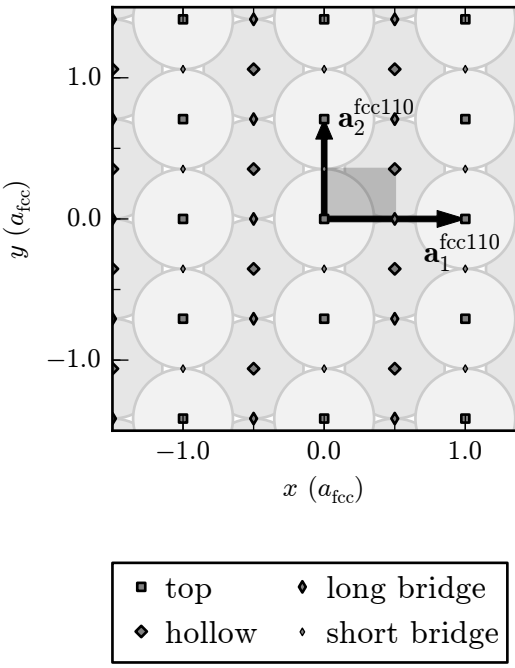

Figure A.2.1.: Structure and symmetry of a fcc(110) surface: The primitive lattice vectors $\boldsymbol{a}_1^{\text{fcc110}}$ and $\boldsymbol{a}_2^{\text{fcc110}}$ as given by Eqs. (A.12) are shown as arrows, high symmetry sites are marked by different symbols, and the irreducible wedge is indicated by the dark gray rectangle.

A.2. fcc(110)

Primitive vectors of the surface lattice (cf Fig. A.2.1 for illustration):

$$\boldsymbol{a}_1^{\text{fcc110}} = a_{\text{fcc}} \begin{pmatrix} 1 \\ 0 \end{pmatrix} \tag{A.12a}$$

$$\boldsymbol{a}_2^{\text{fcc110}} = \frac{\sqrt{2}}{2} a_{\text{fcc}} \begin{pmatrix} 0 \\ 1 \end{pmatrix} \tag{A.12b}$$

Lateral coordinate transformations:

$$\begin{aligned} g_1^{\text{fcc110}}(x,y) &= \frac{1}{4}\left[\cos\left(\boldsymbol{G}_{10}^{\text{fcc110}} \cdot \begin{pmatrix} x \\ y \end{pmatrix}\right) + \cos\left(\boldsymbol{G}_{01}^{\text{fcc110}} \cdot \begin{pmatrix} x \\ y \end{pmatrix}\right)\right] + \frac{1}{2} \\ &= \frac{1}{4}\left[\cos\left(\frac{2\pi}{a_{\text{fcc}}} x\right) + \cos\left(\frac{2\pi}{a_{\text{fcc}}} \sqrt{2} y\right)\right] + \frac{1}{2} \end{aligned} \tag{A.13a}$$

$$\begin{aligned} g_2^{\text{fcc110}}(x,y) &= \frac{1}{4}\left[\cos\left(\boldsymbol{G}_{10}^{\text{fcc110}} \cdot \begin{pmatrix} x \\ y \end{pmatrix}\right) - \cos\left(\boldsymbol{G}_{01}^{\text{fcc110}} \cdot \begin{pmatrix} x \\ y \end{pmatrix}\right)\right] + \frac{1}{2} \\ &= \frac{1}{4}\left[\cos\left(\frac{2\pi}{a_{\text{fcc}}} x\right) - \cos\left(\frac{2\pi}{a_{\text{fcc}}} \sqrt{2} y\right)\right] + \frac{1}{2} \end{aligned} \tag{A.13b}$$

Contour plots of Eqs. (A.13a) and (A.13b) are shown in Fig. A.2.2. Examples for symmetry equivalent points (as given by intersections of contours of g_1^{fcc110} and g_2^{fcc110}) are presented in Fig. A.2.3.

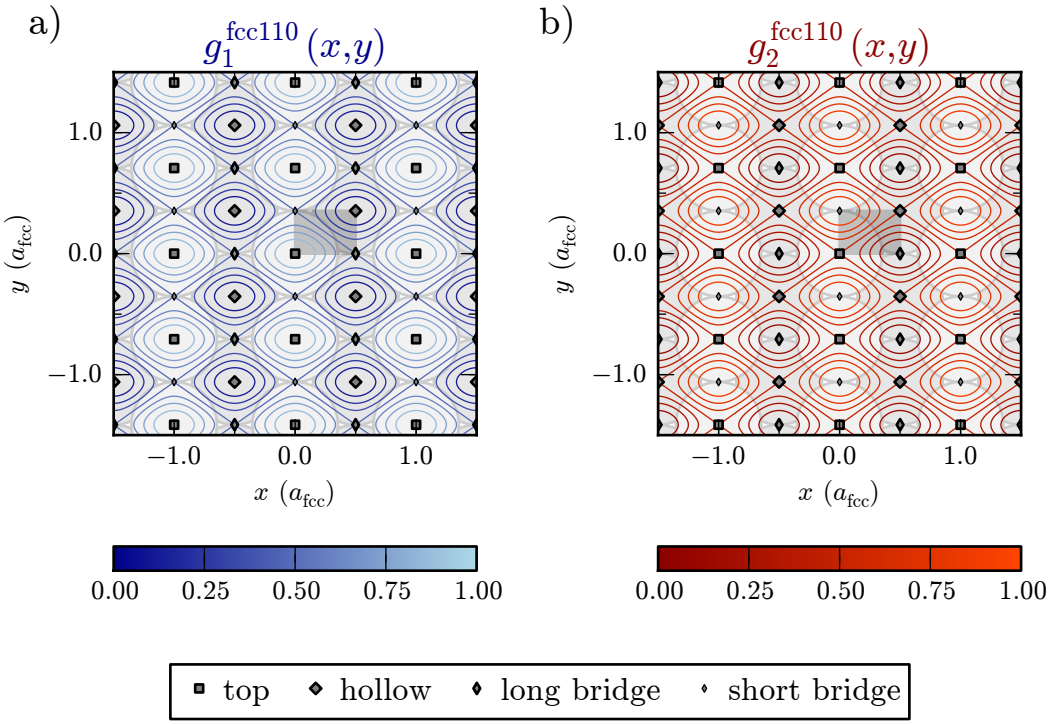

Figure A.2.2.: Contour plots of the coordinate transformations a) g_1^{fcc110} and b) g_2^{fcc110} as defined by Eqs. (A.13) for lateral coordinates (x, y) given in units of the bulk lattice constant a_{fcc}. The spacing of the contour lines is $\frac{1}{8}$.

A.3. fcc(111)

Primitive vectors of the surface lattice (cf Fig. A.3.1 for illustration):

$$\boldsymbol{a}_1^{\mathrm{fcc111}} = \frac{\sqrt{2}}{2} a_{\mathrm{fcc}} \begin{pmatrix} 1 \\ 0 \end{pmatrix} = a_{\mathrm{fcc}}^{111} \begin{pmatrix} 1 \\ 0 \end{pmatrix} \tag{A.14a}$$

$$\boldsymbol{a}_2^{\mathrm{fcc111}} = \frac{\sqrt{2}}{2} a_{\mathrm{fcc}} \begin{pmatrix} \frac{1}{2} \\ \frac{\sqrt{3}}{2} \end{pmatrix} = a_{\mathrm{fcc}}^{111} \begin{pmatrix} \frac{1}{2} \\ \frac{\sqrt{3}}{2} \end{pmatrix} \tag{A.14b}$$

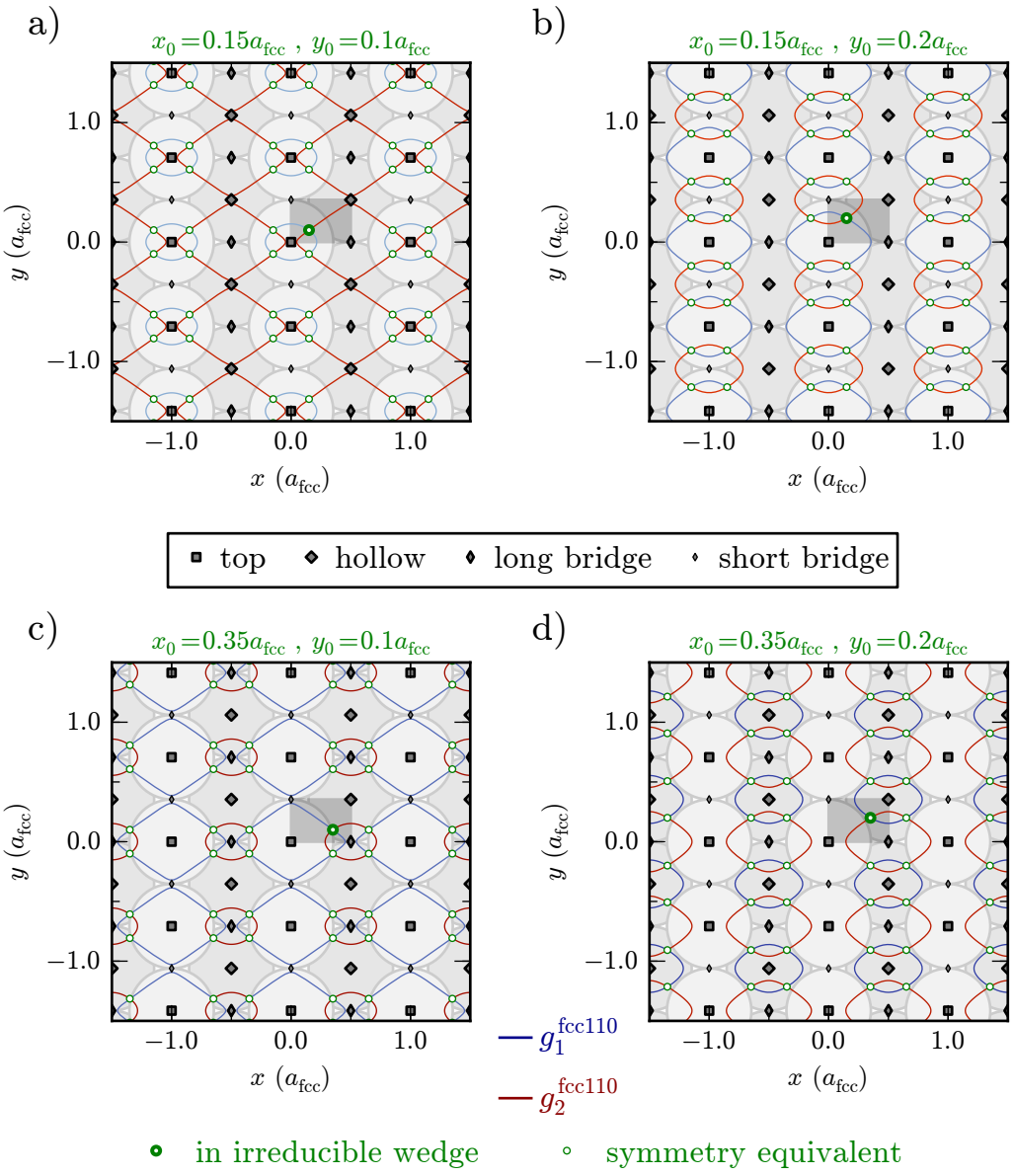

Figure A.2.3.: Examples for symmetry equivalent lateral coordinates given in units of the bulk lattice constant a_{fcc}. In a) to d), for different points (x_0, y_0) in the indicated rectangular irreducible wedge (thick green circle), the respective equivalents are the intersection points (thin green circles) of contour lines of g_1^{fcc110} (blue) and g_2^{fcc110} (red) as defined by Eqs. (A.13). Contour values are given by $g_1^{\mathrm{fcc110}}(x_0, y_0)$ and $g_2^{\mathrm{fcc110}}(x_0, y_0)$ respectively.

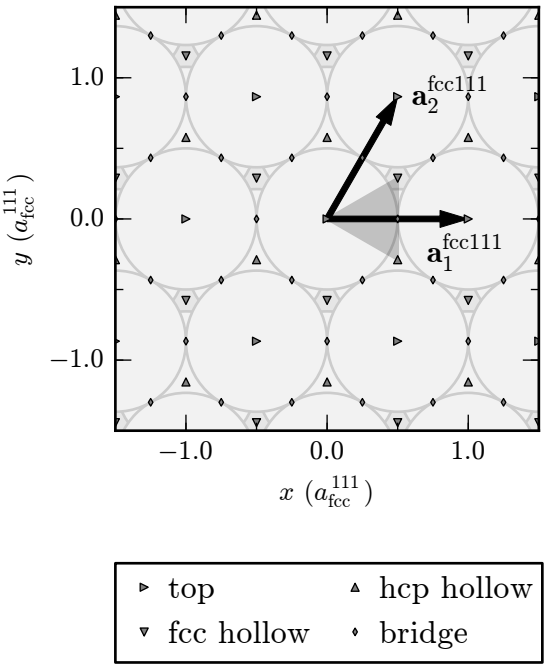

Figure A.3.1.: Structure and symmetry of a fcc(111) surface: The primitive lattice vectors $\boldsymbol{a}_1^{\mathrm{fcc111}}$ and $\boldsymbol{a}_2^{\mathrm{fcc111}}$ as given by Eqs. (A.14) are shown as arrows, high symmetry sites are marked by different symbols, and the irreducible wedge is indicated by the dark gray triangle.

Lateral coordinate transformations (for a "proper" fcc(111) surface):

$$\begin{aligned} g^{\mathrm{fcc111}}(x,y) &= \frac{1}{3\sqrt{3}}\left[\sin\left(\boldsymbol{G}_{10}^{\mathrm{fcc111}}\cdot\begin{pmatrix}x\\y\end{pmatrix}\right)+\sin\left(\boldsymbol{G}_{01}^{\mathrm{fcc111}}\cdot\begin{pmatrix}x\\y\end{pmatrix}\right)+\right. \\ &\qquad \left.\sin\left(\boldsymbol{G}_{11}^{\mathrm{fcc111}}\cdot\begin{pmatrix}x\\y\end{pmatrix}\right)\right]+\frac{1}{2} \\ &= \frac{1}{3\sqrt{3}}\left[\sin\left(\frac{2\pi}{a_{\mathrm{fcc}}^{111}}\left(x-\frac{1}{\sqrt{3}}y\right)\right)+\sin\left(\frac{2\pi}{a_{\mathrm{fcc}}^{111}}\frac{2}{\sqrt{3}}y\right)+\right. \\ &\qquad \left.\sin\left(\frac{2\pi}{a_{\mathrm{fcc}}^{111}}\left(x+\frac{1}{\sqrt{3}}y\right)\right)\right]+\frac{1}{2} \end{aligned} \tag{A.15a}$$

$$g_1^{\mathrm{fcc111}}(x,y) = g^{\mathrm{fcc111}}(x-\tfrac{1}{4}a_{\mathrm{fcc}}^{111}\,,\,y-\tfrac{1}{4\sqrt{3}}a_{\mathrm{fcc}}^{111}) \tag{A.15b}$$

$$g_2^{\mathrm{fcc111}}(x,y) = g^{\mathrm{fcc111}}(x+\tfrac{1}{4}a_{\mathrm{fcc}}^{111}\,,\,y+\tfrac{1}{4\sqrt{3}}a_{\mathrm{fcc}}^{111}) \tag{A.15c}$$

Contour plots of Eqs. (A.15b) and (A.15c) are shown in Fig. A.3.2. Examples for symmetry equivalent points (as given by intersections of contours of g_1^{fcc111} and g_2^{fcc111}) are presented in Fig. A.3.3.

Equations (A.15) are similar to the expressions that have been given by Behler and coworkers.[342,351] In the notation system employed here, these expressions read as follows when linearly trans-

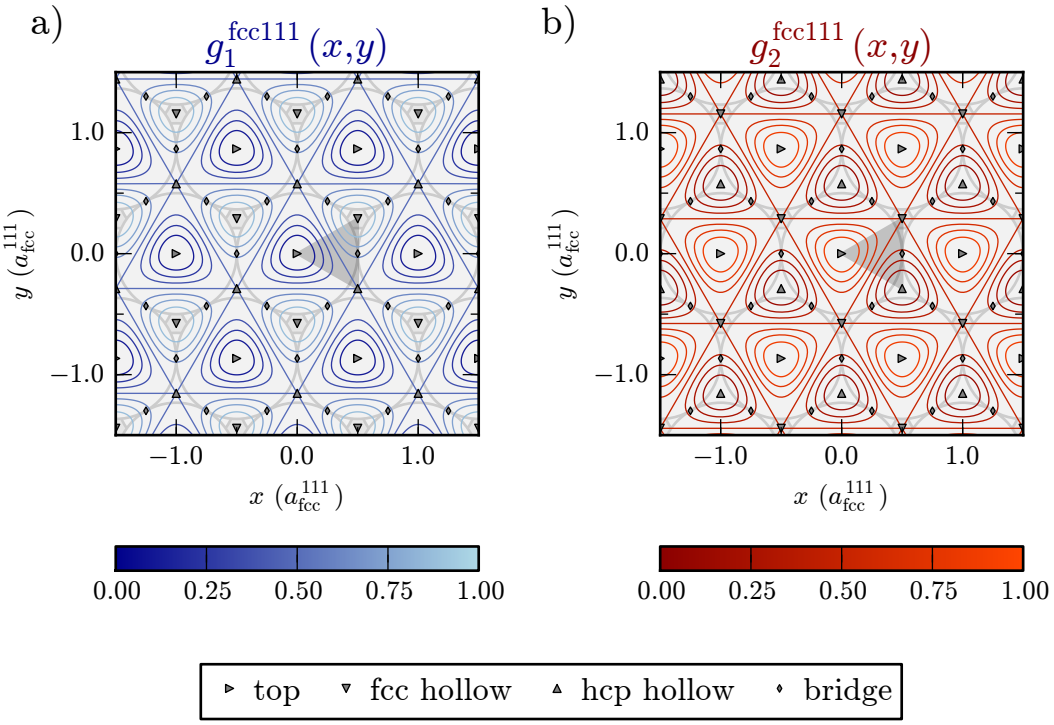

Figure A.3.2.: Contour plots of the coordinate transformations a) g_1^{fcc111} and b) g_2^{fcc111} as defined by Eqs. (A.15) for lateral coordinates (x, y) given in units of the surface lattice constant a_{fcc}^{111}. The spacing of the contour lines is $\frac{1}{8}$.

formed to the range $[0, 1]$ favored here:

$$\tilde{g}^{\mathrm{fcc111}}(x,y) = \frac{2}{9}\left[\cos\left(\boldsymbol{G}_{10}^{\mathrm{fcc111}} \cdot \binom{x}{y}\right) + \cos\left(\boldsymbol{G}_{01}^{\mathrm{fcc111}} \cdot \binom{x}{y}\right) + \cos\left(\boldsymbol{G}_{11}^{\mathrm{fcc111}} \cdot \binom{x}{y}\right)\right] + \frac{1}{3} \tag{A.16a}$$

$$\tilde{g}_{\mathrm{top}}^{\mathrm{fcc111}}(x,y) = \tilde{g}^{\mathrm{fcc111}}(x - \underbrace{0\,a_{\mathrm{fcc}}^{111}}_{\equiv x_{\mathrm{top}}^{\mathrm{fcc111}}}, y - \underbrace{0\,a_{\mathrm{fcc}}^{111}}_{\equiv y_{\mathrm{top}}^{\mathrm{fcc111}}}) \tag{A.16b}$$

$$\tilde{g}_{\mathrm{fcc}}^{\mathrm{fcc111}}(x,y) = \tilde{g}^{\mathrm{fcc111}}(x - \underbrace{\tfrac{1}{2}a_{\mathrm{fcc}}^{111}}_{\equiv x_{\mathrm{fcc}}^{\mathrm{fcc111}}}, y - \underbrace{\tfrac{1}{2\sqrt{3}}a_{\mathrm{fcc}}^{111}}_{\equiv y_{\mathrm{fcc}}^{\mathrm{fcc111}}}) \tag{A.16c}$$

$$\tilde{g}_{\mathrm{bridge}}^{\mathrm{fcc111}}(x,y) = \tilde{g}^{\mathrm{fcc111}}(x - \underbrace{\tfrac{1}{2}a_{\mathrm{fcc}}^{111}}_{\equiv x_{\mathrm{hcp}}^{\mathrm{fcc111}}}, y - \underbrace{\tfrac{-1}{2\sqrt{3}}a_{\mathrm{fcc}}^{111}}_{\equiv y_{\mathrm{hcp}}^{\mathrm{fcc111}}}) \tag{A.16d}$$

Figures A.3.4a to A.3.4c show contour plots of Eqs. (A.16b) to (A.16d), respectively. For the same example points also chosen in Fig. A.3.3 before, those plots show the redundancy of Eqs. (A.16b) to (A.16d): Only two of the originally proposed "Fourier terms" are required in order to describe a point in the irreducible wedge and all its symmetry equivalent replica.

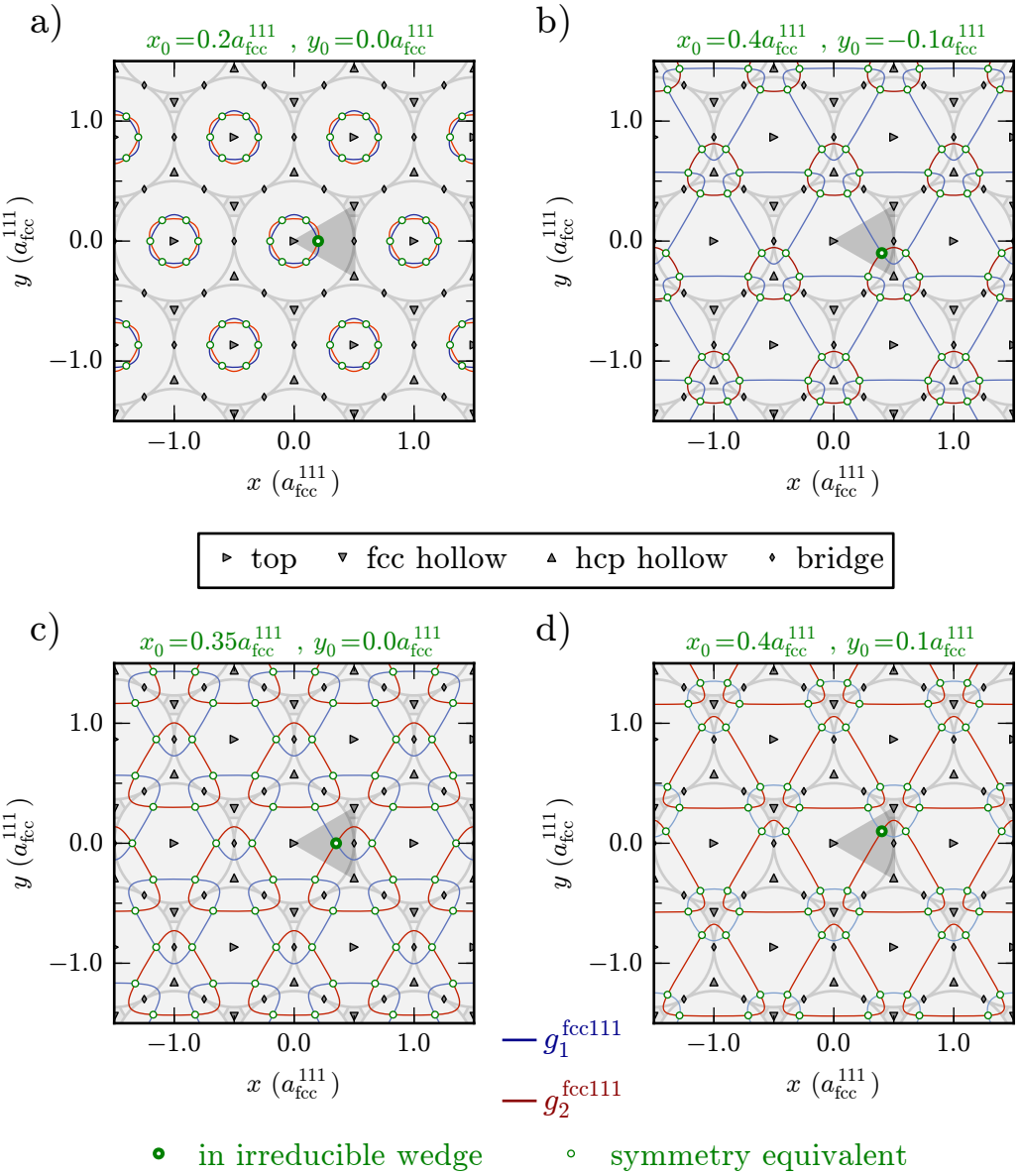

Figure A.3.3.: Examples for symmetry equivalent lateral coordinates given in units of the surface lattice constant a_{fcc}^{111}. In a) to d), for different points (x_0, y_0) in the indicated triangular irreducible wedge (thick green circle), the respective equivalents are the intersection points (thin green circles) of contour lines of g_1^{fcc111} (blue) and g_2^{fcc111} (red) as defined by Eqs. (A.15). Contour values are given by $g_1^{\mathrm{fcc111}}(x_0, y_0)$ and $g_2^{\mathrm{fcc111}}(x_0, y_0)$ respectively.

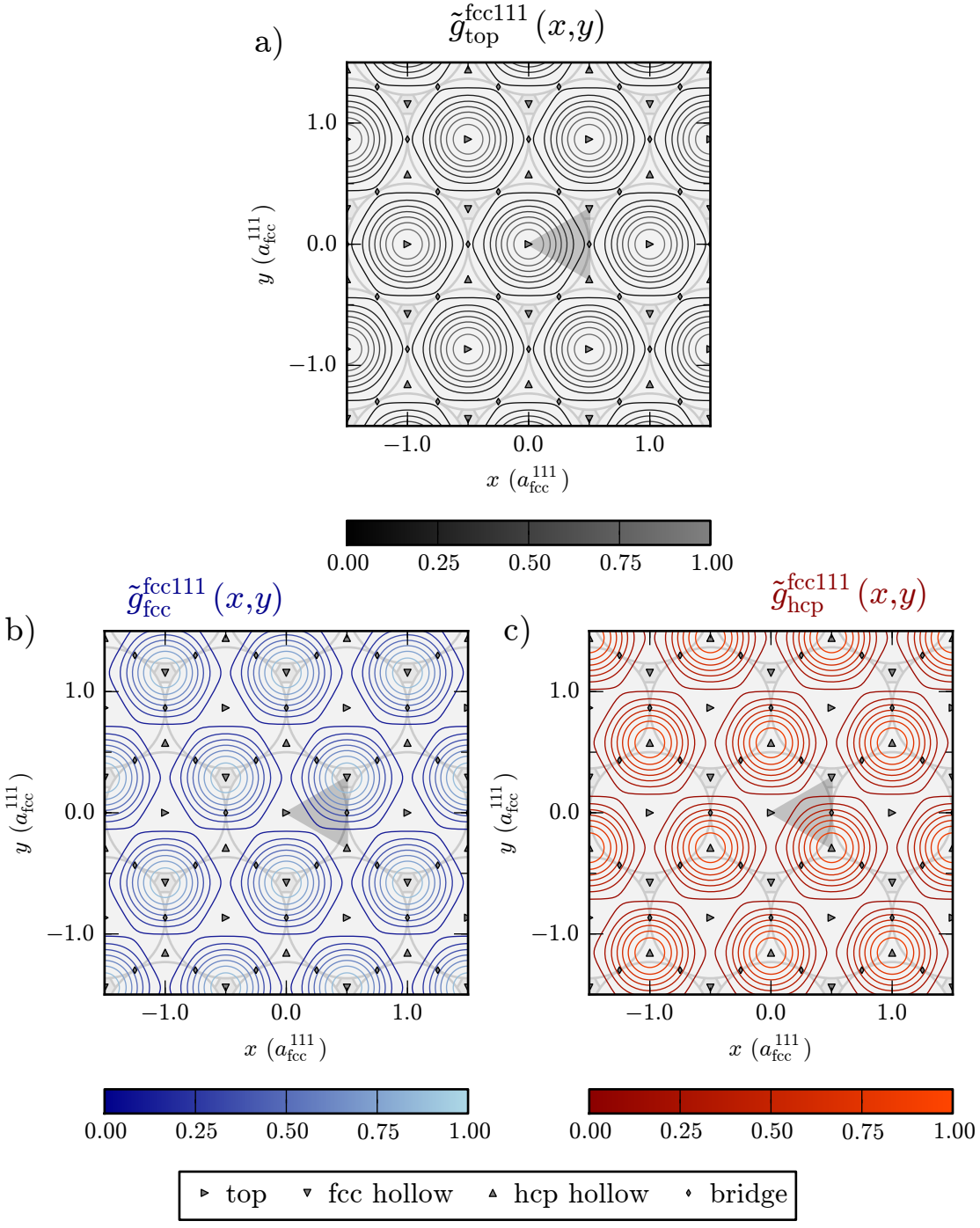

Figure A.3.4.: Contour plots of the "Fourier terms" a) $\tilde{g}^{\mathrm{fcc111}}_{\mathrm{top}}$, b) $\tilde{g}^{\mathrm{fcc111}}_{\mathrm{fcc}}$ and c) $\tilde{g}^{\mathrm{fcc111}}_{\mathrm{hcp}}$ reproduced from the work of Behler and coworkers[342,351] as given by Eqs. (A.16) using the notation employed within this work. Lateral coordinates (x, y) given in units of the surface lattice constant a^{111}_{fcc}. The spacing of the contour lines is $\frac{1}{8}$.

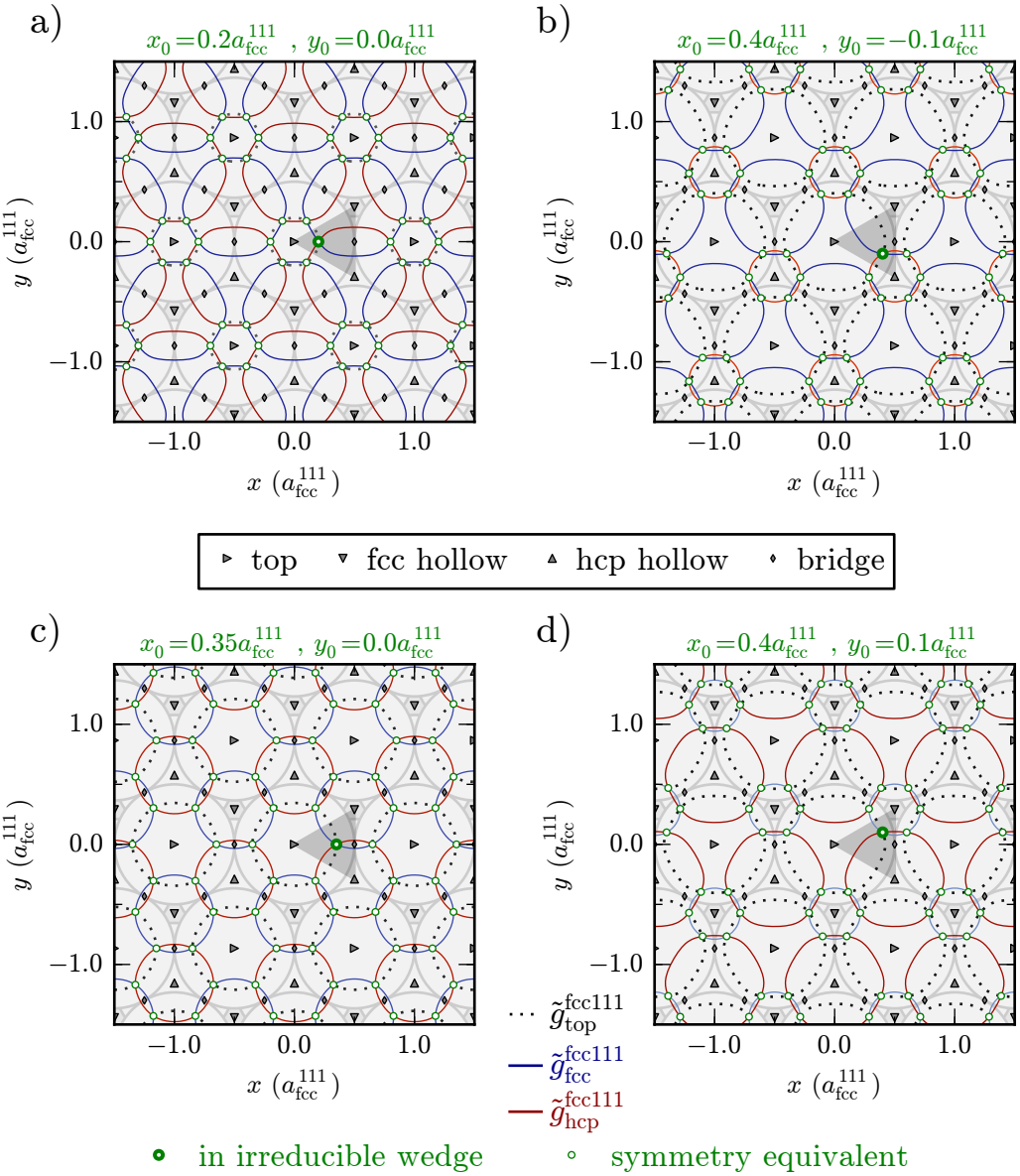

Figure A.3.5.: Same as Fig. A.3.2, but using the "Fourier terms" reproduced from the work of Behler and coworkers[342,351] as given by Eqs. (A.16) and illustrated in Fig. A.3.4. Note that only dotted gray contour lines are given for $\tilde{g}_{\mathrm{top}}^{\mathrm{fcc111}}$ as the present description is redundant: Any two of the three functions $\tilde{g}_{\mathrm{top}}^{\mathrm{fcc111}}$, $\tilde{g}_{\mathrm{fcc}}^{\mathrm{fcc111}}$, $\tilde{g}_{\mathrm{hcp}}^{\mathrm{fcc111}}$ yield the correct symmetry equivalent replica of the points in the irreducible wedge as intersection points of their respective contour lines.

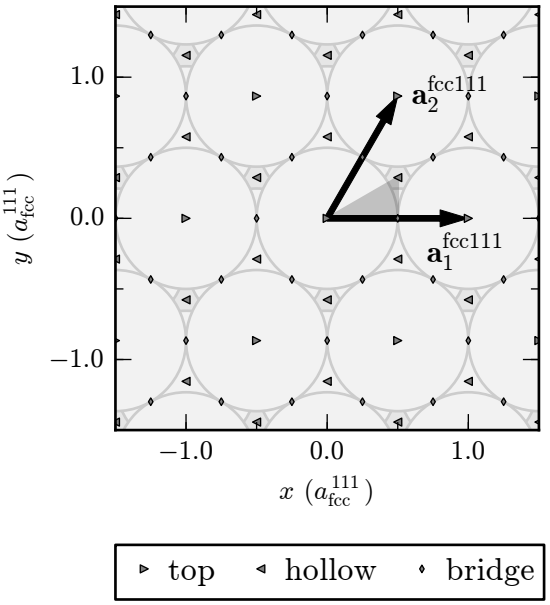

Figure A.3.6.: Structure and symmetry of a derivatice of a fcc(111) surface with six-fold instead of three-fold symmetry: The primitive lattice vectors $\boldsymbol{a}_1^{\mathrm{fcc111}}$ and $\boldsymbol{a}_2^{\mathrm{fcc111}}$ as given by Eqs. (A.14) are shown as arrows, high symmetry sites are marked by different symbols, and the irreducible wedge is indicated by the dark gray triangle.

Apart from transformations g_1^{fcc111} and g_2^{fcc111} given by Eq. (A.15) for "proper" fcc(111) surfaces with threefold symmetry, the following counterparts $\widetilde{g_1^{\mathrm{fcc111}}}$ and $\widetilde{g_2^{\mathrm{fcc111}}}$ (cf Eqs. (A.17)) for an "artificial" fcc(111) derivative with sixfold symmetry as illustrated in Fig. A.3.6 can also prove extremely useful: Very often, fcc-hollow and hcp-hollow are energetically quasi-degenerate, e.g. for H_2 on Pt(111)[324] or O_2 at Ag(111).[ii] Therefore, the interpolation of a six-dimensional PES can greatly benefit from this extended symmetry because the size of irreducible wegde is halfed. By no longer distinguishing between the two

[ii] Work together with I. Goikoetxea, J. Beltrán, M. Alducin and J. I. Juaristi.[52]

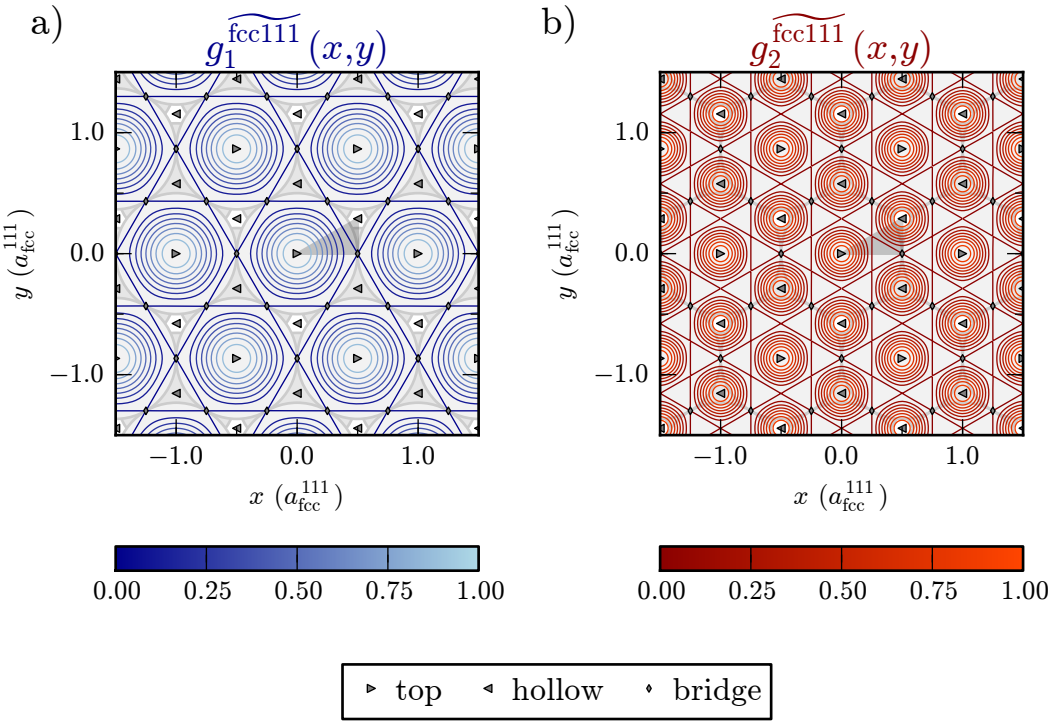

Figure A.3.7.: Contour plots of the coordinate transformations a) $\widetilde{g_1^{\mathrm{fcc111}}}$ and b) $\widetilde{g_2^{\mathrm{fcc111}}}$ as defined by Eq. (A.15) for lateral coordinates (x, y) given in units of the surface lattice constant a_{fcc}^{111}. The spacing of the contour lines is $\frac{1}{8}$.

hollow sites, $\widetilde{g_1^{\mathrm{fcc111}}}$ and $\widetilde{g_2^{\mathrm{fcc111}}}$ do fully take this into account.

$$\begin{aligned}\widetilde{g_1^{\mathrm{fcc111}}}(x,y) &= \frac{1}{4}\left[\cos\left(\boldsymbol{G}_{10}^{\mathrm{fcc111}}\cdot\begin{pmatrix}x\\y\end{pmatrix}\right)+\cos\left(\boldsymbol{G}_{01}^{\mathrm{fcc111}}\cdot\begin{pmatrix}x\\y\end{pmatrix}\right)+\right.\\ &\qquad\left.\cos\left(\boldsymbol{G}_{11}^{\mathrm{fcc111}}\cdot\begin{pmatrix}x\\y\end{pmatrix}\right)\right]+\frac{1}{4}\\ &= \frac{1}{4}\left[\cos\left(\frac{2\pi}{a_{\mathrm{fcc}}^{111}}\left(x-\frac{1}{\sqrt{3}}y\right)\right)+\cos\left(\frac{2\pi}{a_{\mathrm{fcc}}^{111}}\frac{2}{\sqrt{3}}y\right)+\right.\\ &\qquad\left.\cos\left(\frac{2\pi}{a_{\mathrm{fcc}}^{111}}\left(x+\frac{1}{\sqrt{3}}y\right)\right)\right]+\frac{1}{4}\end{aligned} \tag{A.17a}$$

$$\begin{aligned}\widetilde{g_2^{\mathrm{fcc111}}}(x,y) &= \frac{1}{4}\left[\cos\left(\boldsymbol{G}_{1\bar{1}}^{\mathrm{fcc111}}\cdot\begin{pmatrix}x\\y\end{pmatrix}\right)+\cos\left(\boldsymbol{G}_{21}^{\mathrm{fcc111}}\cdot\begin{pmatrix}x\\y\end{pmatrix}\right)+\right.\\ &\qquad\left.\cos\left(\boldsymbol{G}_{12}^{\mathrm{fcc111}}\cdot\begin{pmatrix}x\\y\end{pmatrix}\right)\right]+\frac{1}{4}\\ &= \frac{1}{4}\left[\cos\left(\frac{2\pi}{a_{\mathrm{fcc}}^{111}}\left(x-\sqrt{3}y\right)\right)+\cos\left(\frac{2\pi}{a_{\mathrm{fcc}}^{111}}2x\right)+\right.\\ &\qquad\left.\cos\left(\frac{2\pi}{a_{\mathrm{fcc}}^{111}}\left(x+\sqrt{3}y\right)\right)\right]+\frac{1}{4}\end{aligned} \tag{A.17b}$$

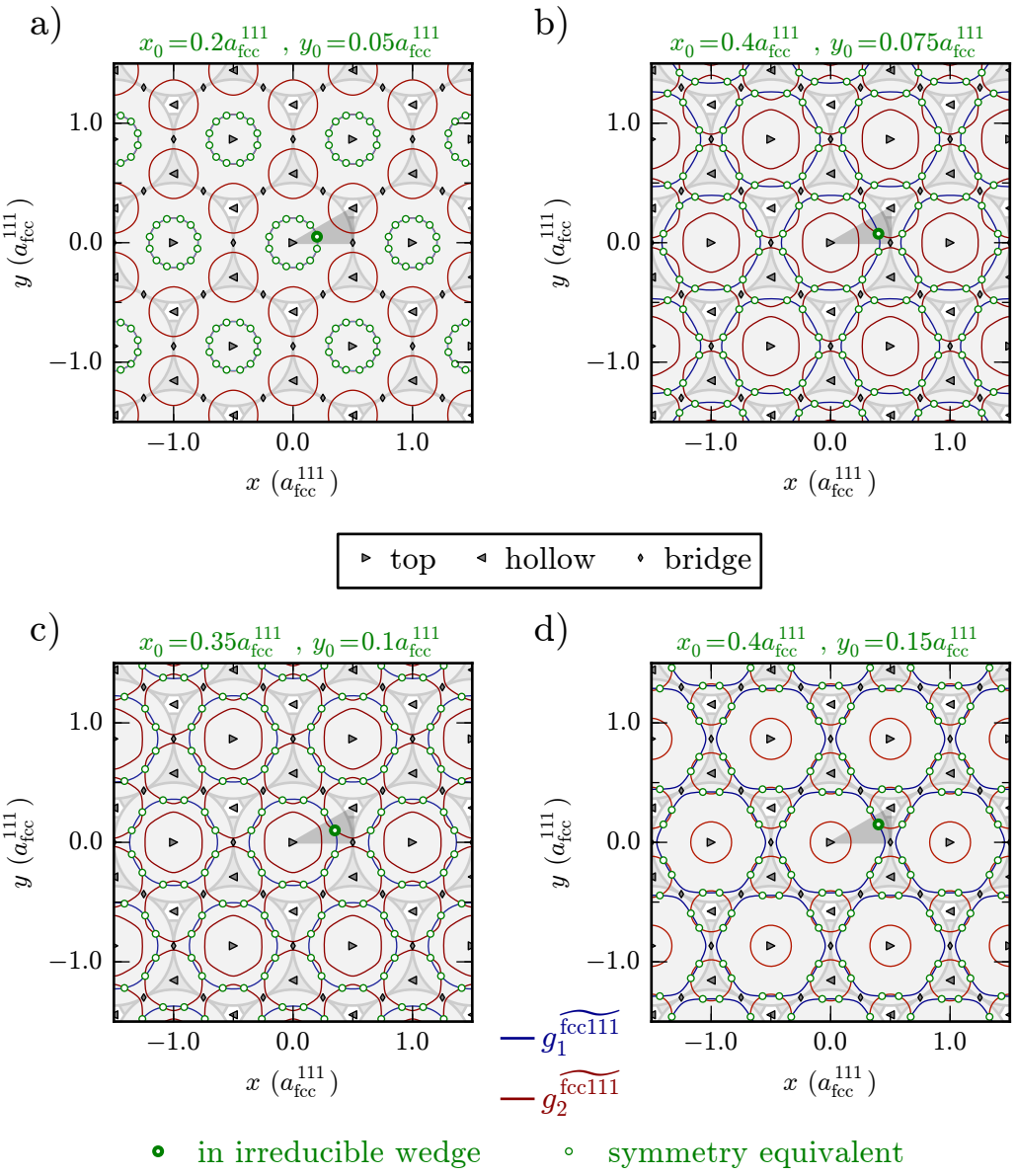

Figure A.3.8.: Examples for symmetry equivalent lateral coordinates given in units of the surface lattice constant a_{fcc}^{111}. In a) to d), for different points (x_0, y_0) in the indicated triangular irreducible wedge (thick green circle), the respective equivalents are the intersection points (thin green circles) of contour lines of $g_1^{\widetilde{\mathrm{fcc111}}}$ (blue) and $g_2^{\widetilde{\mathrm{fcc111}}}$ (red) as defined by Eqs. (A.17). Contour values are given by $g_1^{\widetilde{\mathrm{fcc111}}}(x_0, y_0)$ and $g_2^{\widetilde{\mathrm{fcc111}}}(x_0, y_0)$ respectively.

Contour plots of Eqs. (A.17a) and (A.17b) are shown in Fig. A.3.2. Examples for symmetry equivalent points (as given by intersections of contours of $g_1^{\widetilde{\text{fcc111}}}$ and $g_2^{\widetilde{\text{fcc111}}}$) are presented in Fig. A.3.8. It is noted in passing that $g_1^{\widetilde{\text{fcc111}}}(x,y)$ given in Eq. (A.17a) can also be paired with

$$g_{1'}^{\widetilde{\text{fcc111}}}(x,y) = g_1^{\widetilde{\text{fcc111}}}(2x,2y) \quad , \tag{A.18}$$

thus consisting of cosine terms corresponding to reciprocal lattice vectors $\boldsymbol{G}_{20}^{\text{fcc111}}$, $\boldsymbol{G}_{02}^{\text{fcc111}}$ and $\boldsymbol{G}_{22}^{\text{fcc111}}$. Consequently, two different sets of coordinate transformations for the fcc(111) surface with six-fold symmetry are available.

A.4. bcc(100)

Primitive vectors of the surface lattice:

$$\boldsymbol{a}_1^{\text{bcc100}} = a_{\text{bcc}} \begin{pmatrix} 1 \\ 0 \end{pmatrix} = a_{\text{bcc}}^{100} \begin{pmatrix} 1 \\ 0 \end{pmatrix} \tag{A.19a}$$

$$\boldsymbol{a}_2^{\text{bcc100}} = a_{\text{bcc}} \begin{pmatrix} 0 \\ 1 \end{pmatrix} = a_{\text{bcc}}^{100} \begin{pmatrix} 0 \\ 1 \end{pmatrix} \tag{A.19b}$$

This surface has the same symmetry as a fcc(100) surface with the latter being illustrated in Fig. A.1.1. Accordingly, the transformations given by Eq. (A.11) can be used when substituting $a_{\text{fcc}}^{100} = \frac{\sqrt{2}}{2} a_{\text{fcc}}$ by the surface lattice constant $a_{\text{bcc}}^{100} = a_{\text{bcc}} = \sqrt{2} a_{\text{fcc}}^{100} \frac{a_{\text{bcc}}}{a_{\text{fcc}}}$ of the accordingly more open bcc(100) surface.

A.5. bcc(110)

Primitive vectors of the surface lattice (cf Fig. A.5.1 for illustration):

$$\boldsymbol{a}_1^{\text{bcc110}} = a_{\text{bcc}} \begin{pmatrix} 1 \\ 0 \end{pmatrix} \tag{A.20a}$$

$$\boldsymbol{a}_2^{\text{bcc110}} = a_{\text{bcc}} \begin{pmatrix} \frac{1}{2} \\ \frac{\sqrt{2}}{2} \end{pmatrix} \tag{A.20b}$$

Lateral coordinate transformations:

$$\begin{aligned} g_1^{\text{bcc110}}(x,y) &= \frac{1}{4}\left[\cos\left(\boldsymbol{G}_{10}^{\text{bcc110}} \cdot \begin{pmatrix} x \\ y \end{pmatrix}\right) + \cos\left(\boldsymbol{G}_{11}^{\text{bcc110}} \cdot \begin{pmatrix} x \\ y \end{pmatrix}\right)\right] + \frac{1}{2} \\ &= \frac{1}{4}\left[\cos\left(\frac{2\pi}{a_{\text{bcc}}}\left(x - \frac{1}{\sqrt{2}}y\right)\right) + \right. \\ &\qquad \left. \cos\left(\frac{2\pi}{a_{\text{bcc}}}\left(x + \frac{1}{\sqrt{2}}y\right)\right)\right] + \frac{1}{2} \end{aligned} \tag{A.21a}$$

$$\begin{aligned} g_2^{\text{bcc110}}(x,y) &= \frac{1}{4}\left[\cos\left(\boldsymbol{G}_{01}^{\text{bcc110}} \cdot \begin{pmatrix} x \\ y \end{pmatrix}\right) - \cos\left(\boldsymbol{G}_{21}^{\text{bcc110}} \cdot \begin{pmatrix} x \\ y \end{pmatrix}\right)\right] + \frac{1}{2} \\ &= \frac{1}{4}\left[\cos\left(\frac{2\pi}{a_{\text{bcc}}}\sqrt{2}y\right) - \cos\left(\frac{2\pi}{a_{\text{bcc}}}2x\right)\right] + \frac{1}{2} \end{aligned} \tag{A.21b}$$

Contour plots of Eqs. (A.21a) and (A.21b) are shown in Fig. A.5.2. Examples for symmetry equivalent points (as given by intersections of contours of g_1^{bcc110} and g_2^{bcc110}) are presented in Fig. A.5.3.

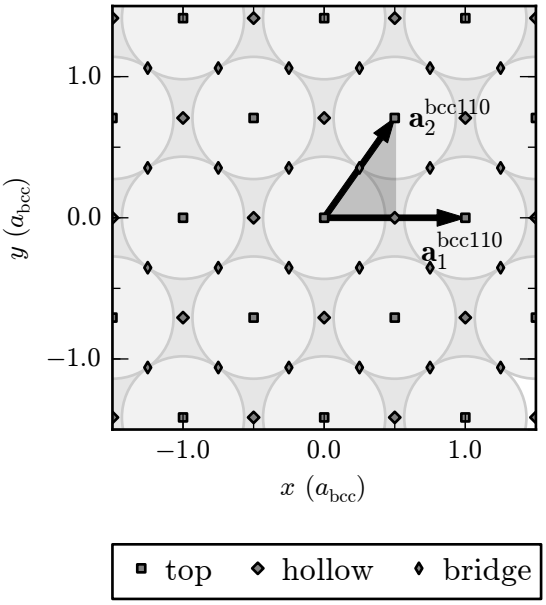

Figure A.5.1.: Structure and symmetry of a bcc(110) surface: The primitive lattice vectors $\boldsymbol{a}_1^{\mathrm{bcc110}}$ and $\boldsymbol{a}_2^{\mathrm{bcc110}}$ as given by Eqs. (A.20) are shown as arrows, high symmetry sites are marked by different symbols, and the irreducible wedge is indicated by the dark gray triangle.

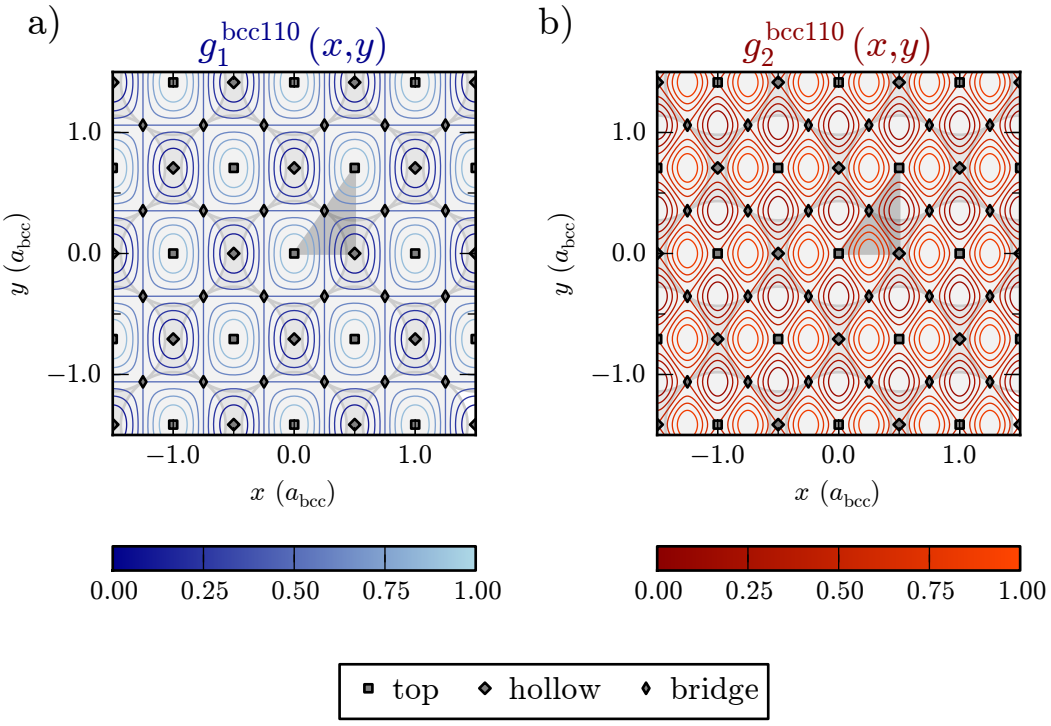

Figure A.5.2.: Contour plots of the coordinate transformations a) g_1^{bcc110} and b) g_2^{bcc110} as defined by Eqs. (A.21) for lateral coordinates (x, y) given in units of the bulk lattice constant a_{bcc}. The spacing of the contour lines is $\frac{1}{8}$.

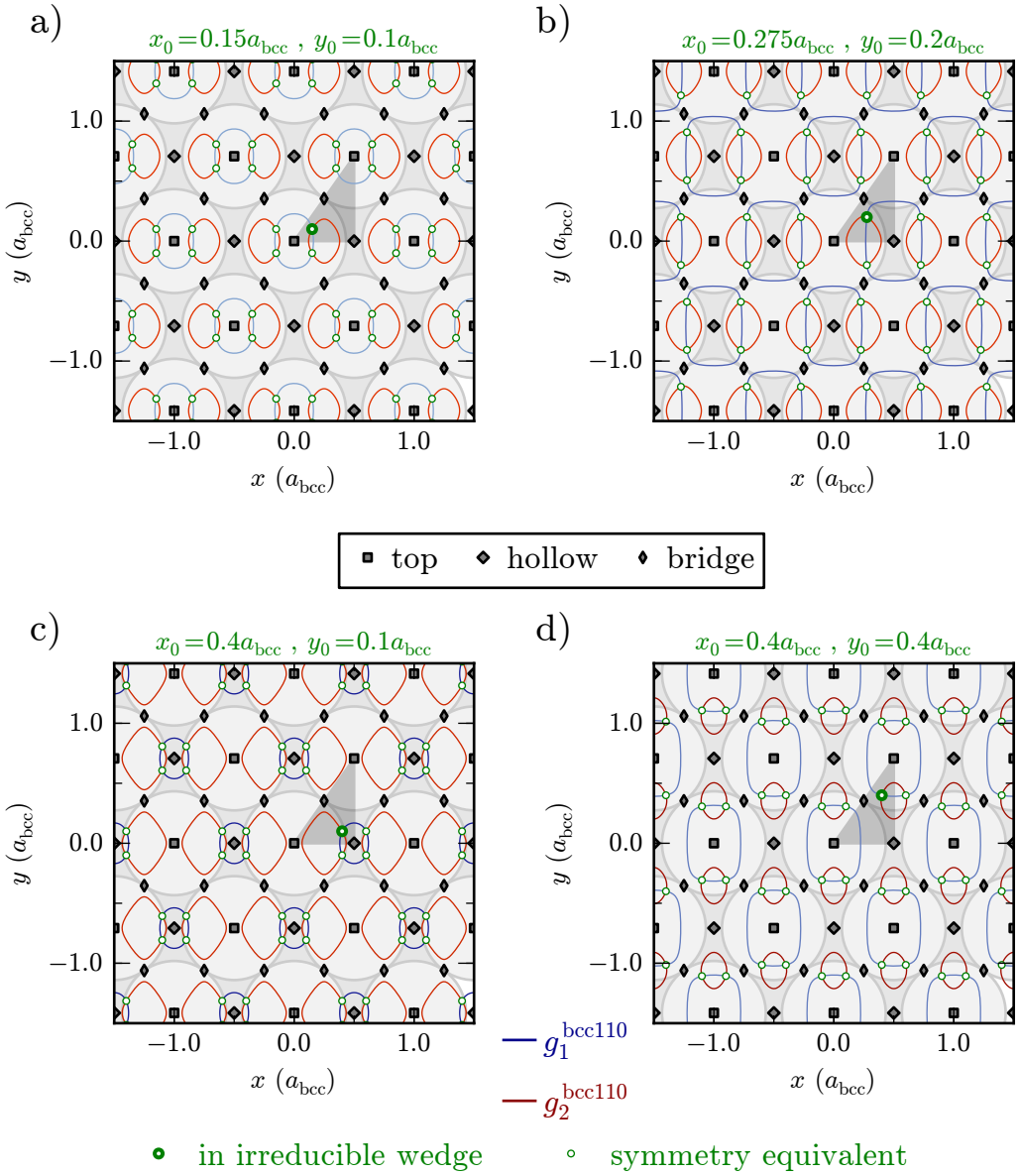

Figure A.5.3.: Examples for symmetry equivalent lateral coordinates given in units of the surface lattice constant a_{bcc}. In a) to d), for different points (x_0, y_0) in the indicated triangular irreducible wedge (thick green circle), the respective equivalents are the intersection points (thin green circles) of contour lines of g_1^{bcc110} (blue) and g_2^{bcc110} (red) as defined by Eqs. (A.21). Contour values are given by $g_1^{\mathrm{bcc110}}(x_0, y_0)$ and $g_2^{\mathrm{bcc110}}(x_0, y_0)$, respectively.

A.6. bcc(111)

Primitive vectors of the surface lattice:

$$\boldsymbol{a}_1^{\mathrm{bcc111}} = \sqrt{2}a_{\mathrm{bcc}} \begin{pmatrix} 1 \\ 0 \end{pmatrix} = a_{\mathrm{bcc}}^{111} \begin{pmatrix} 1 \\ 0 \end{pmatrix} \tag{A.22a}$$

$$\boldsymbol{a}_2^{\mathrm{bcc111}} = \sqrt{2}a_{\mathrm{bcc}} \begin{pmatrix} \frac{1}{2} \\ \frac{\sqrt{3}}{2} \end{pmatrix} = a_{\mathrm{bcc}}^{111} \begin{pmatrix} \frac{1}{2} \\ \frac{\sqrt{3}}{2} \end{pmatrix} \tag{A.22b}$$

This surface has the same symmetry as a fcc(111) surface with the latter being illustrated in Fig. A.3.1. Accordingly, the transformations given by Eq. (A.15) can be used when substituting $a_{\mathrm{fcc}}^{111} = \frac{\sqrt{2}}{2}a_{\mathrm{fcc}}$ by the surface lattice constant $a_{\mathrm{bcc}}^{111} = \sqrt{2}a_{\mathrm{bcc}} = 2a_{\mathrm{fcc}}^{111}\frac{a_{\mathrm{bcc}}}{a_{\mathrm{fcc}}}$ of the accordingly much more open bcc(111) surface.

A.7. Implementation

An implementation in Fortran 90 of all the aforementioned functions is available from the author upon request. The same holds for Python bindings to the former, which have greatly simplified the generation of all the plots.

B. Six-dimensional Potential Energy Surface for O_2on Pd(100)

The six-dimensional potential energy surface (PES) constructed and used in Chapter 6 (based on the techniques both described and developed therein) is characterized in detail by the collection of plots that follows here. They are all based on the finally obtained best NN fit mentioned in Section 6.2.2. Apart from a quantification of the quality of the latter, which is excellent all in all, an impression of the overall shape of the PES can also be obtained.

B.1. Elbow Plots (d-Z-Cuts)

The plots that follow in this section are equivalent to the one shown in Fig. 6.8b, whose caption together with Section 6.2.2 provide more details.

B.1.1. Top Site

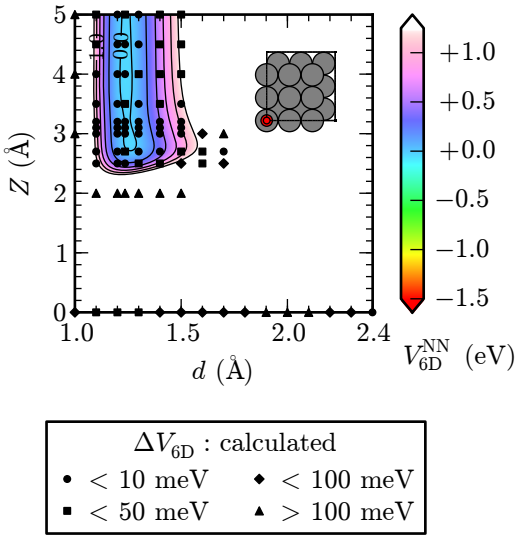

Figure B.1.1.1.:
$X = 0.0\,a_{Pd}^{100}$ $Y = 0.0\,a_{Pd}^{100}$
$\vartheta = 0°$ $\varphi = 0°$

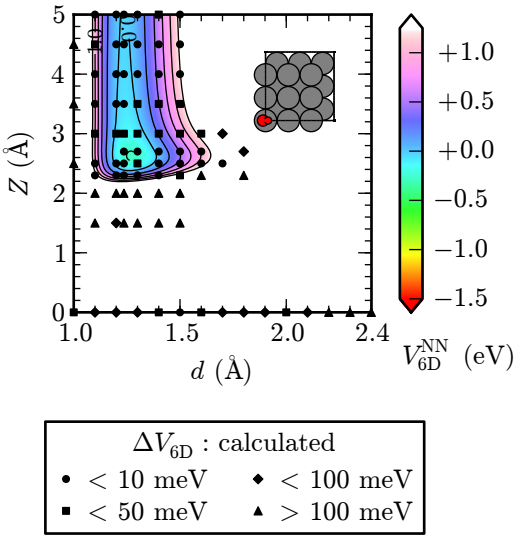

Figure B.1.1.2.:
$X = 0.0\,a_{Pd}^{100}$ $Y = 0.0\,a_{Pd}^{100}$
$\vartheta = 30°$ $\varphi = 0°$

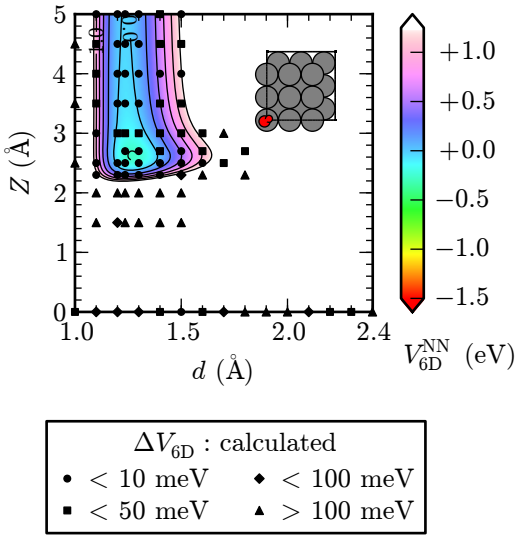

Figure B.1.1.3.:
$X = 0.0\,a_{Pd}^{100}$ $Y = 0.0\,a_{Pd}^{100}$
$\vartheta = 30°$ $\varphi = 30°$

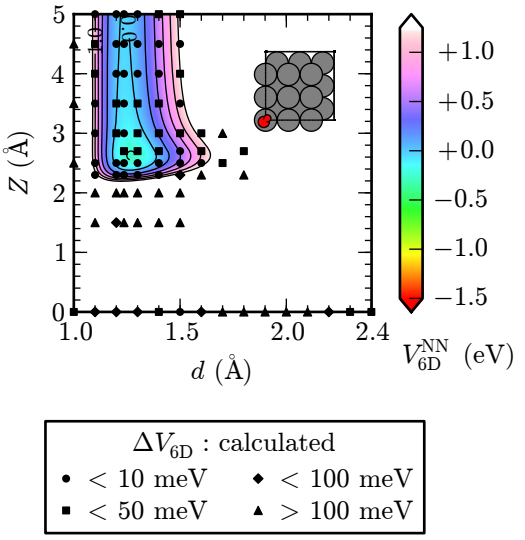

Figure B.1.1.4.:
$X = 0.0\,a_{Pd}^{100}$ $Y = 0.0\,a_{Pd}^{100}$
$\vartheta = 30°$ $\varphi = 45°$

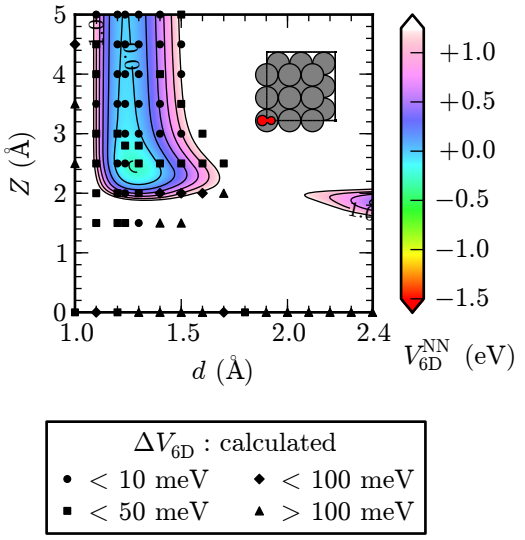

Figure B.1.1.5.:
$X = 0.0\,a_{Pd}^{100}$ $Y = 0.0\,a_{Pd}^{100}$
$\vartheta = 60°$ $\varphi = 0°$

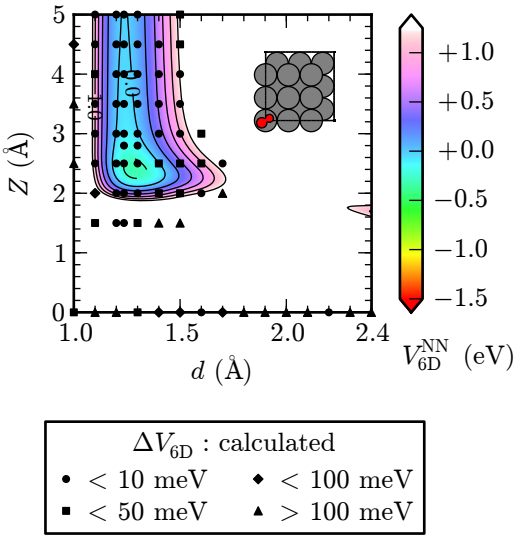

Figure B.1.1.6.:
$X = 0.0\,a_{Pd}^{100}$ $Y = 0.0\,a_{Pd}^{100}$
$\vartheta = 60°$ $\varphi = 30°$

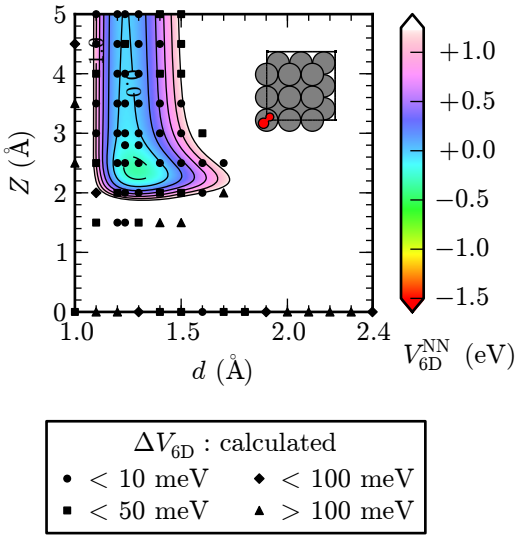

Figure B.1.1.7.:
$X = 0.0\,a_{Pd}^{100}$ $Y = 0.0\,a_{Pd}^{100}$
$\vartheta = 60°$ $\varphi = 45°$

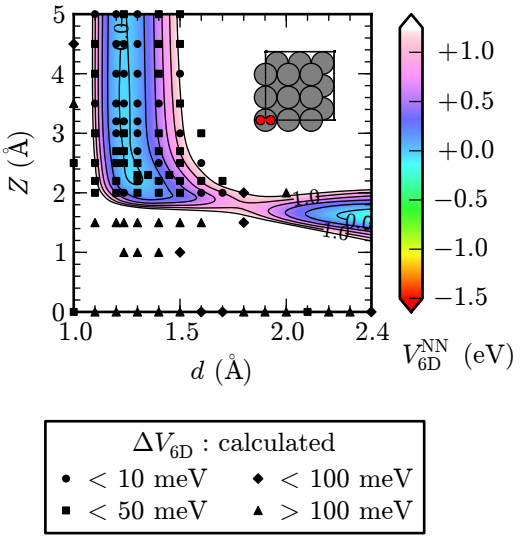

Figure B.1.1.8.:
$X = 0.0\,a_{Pd}^{100}$ $Y = 0.0\,a_{Pd}^{100}$
$\vartheta = 90°$ $\varphi = 0°$

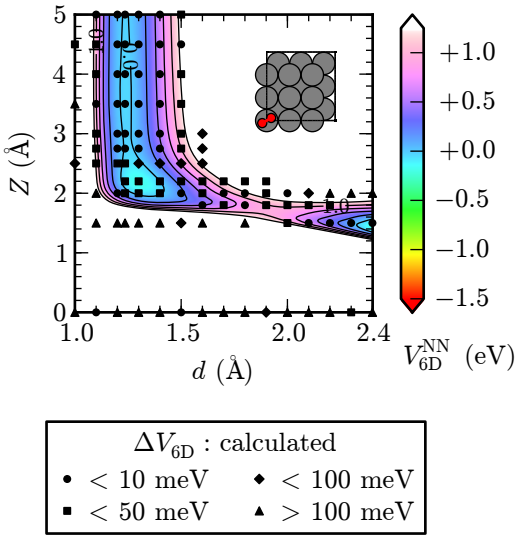

Figure B.1.1.9.:
$X = 0.0\,a_{Pd}^{100}$ $Y = 0.0\,a_{Pd}^{100}$
$\vartheta = 90°$ $\varphi = 30°$

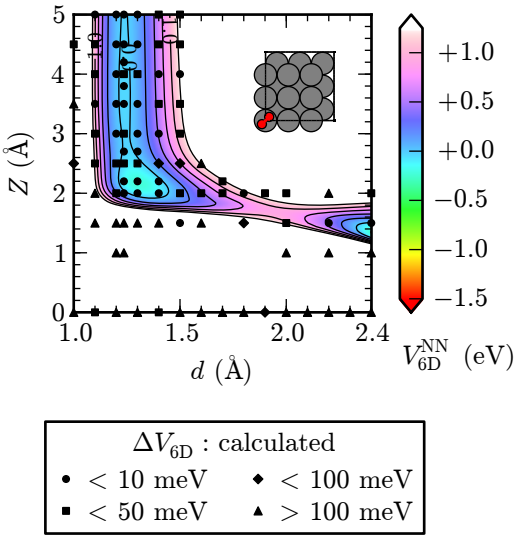

Figure B.1.1.10.:
$X = 0.0\,a_{Pd}^{100}$ $Y = 0.0\,a_{Pd}^{100}$
$\vartheta = 90°$ $\varphi = 45°$

B.1.2. Bridge Site

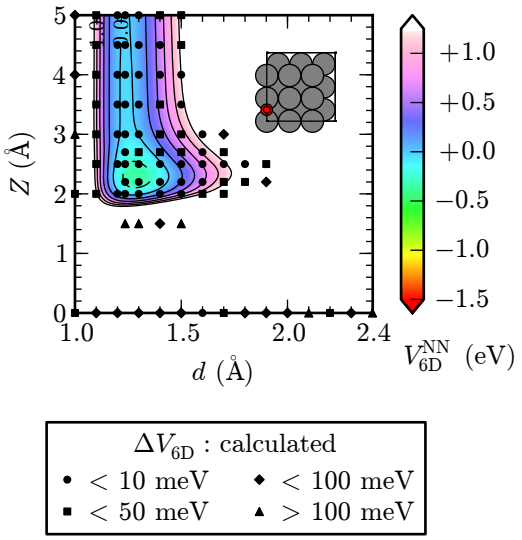

Figure B.1.2.1.:
$X = 0.0\,a_{Pd}^{100}$ $Y = 0.5\,a_{Pd}^{100}$
$\vartheta = 0°$ $\varphi = 0°$

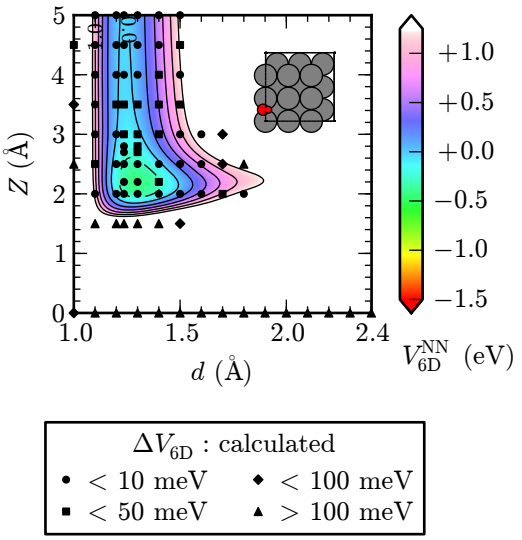

Figure B.1.2.2.:
$X = 0.0\,a_{Pd}^{100}$ $Y = 0.5\,a_{Pd}^{100}$
$\vartheta = 30°$ $\varphi = 0°$

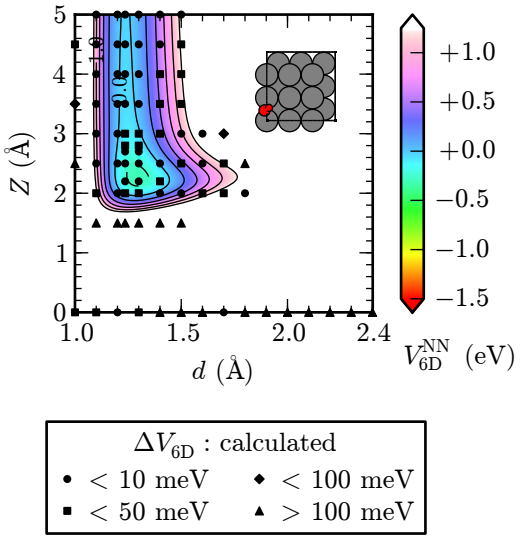

Figure B.1.2.3.:
$X = 0.0\,a_{Pd}^{100}$ $Y = 0.5\,a_{Pd}^{100}$
$\vartheta = 30°$ $\varphi = 30°$

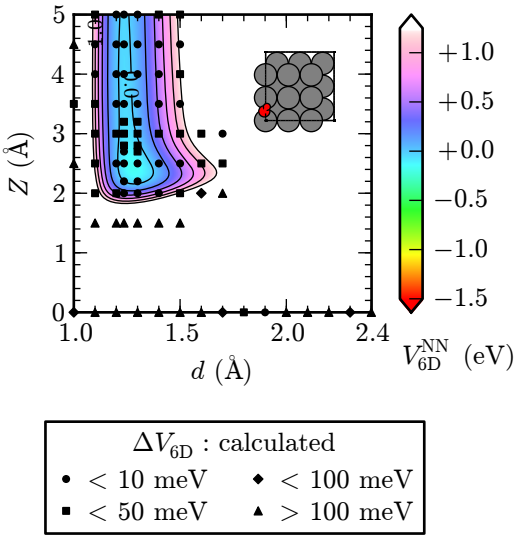

Figure B.1.2.4.:
$X = 0.0\,a_{Pd}^{100}$ $Y = 0.5\,a_{Pd}^{100}$
$\vartheta = 30°$ $\varphi = 60°$

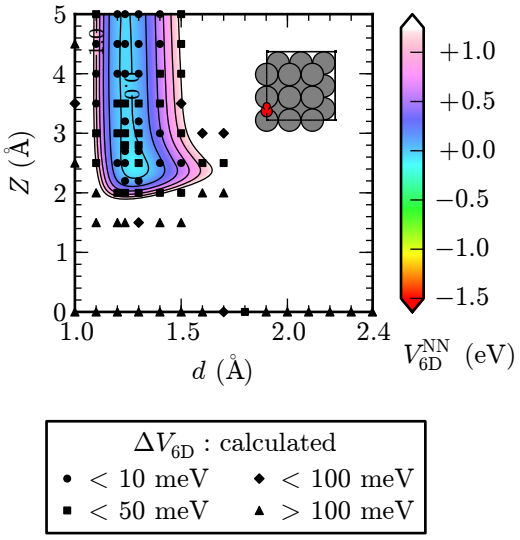

Figure B.1.2.5.:
$X = 0.0\,a_{Pd}^{100}$ $Y = 0.5\,a_{Pd}^{100}$
$\vartheta = 30°$ $\varphi = 90°$

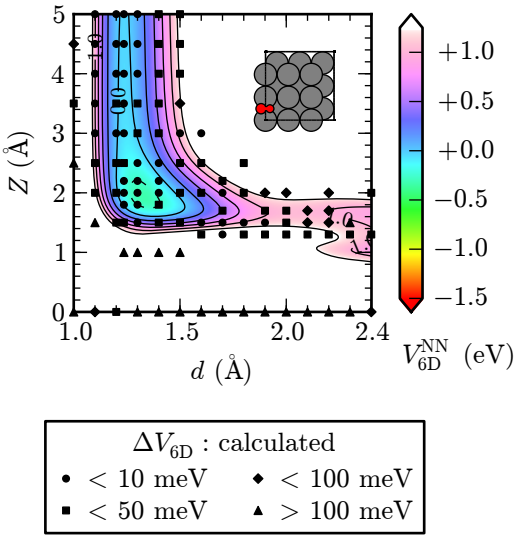

Figure B.1.2.6.:
$X = 0.0\,a_{Pd}^{100}$ $Y = 0.5\,a_{Pd}^{100}$
$\vartheta = 60°$ $\varphi = 0°$

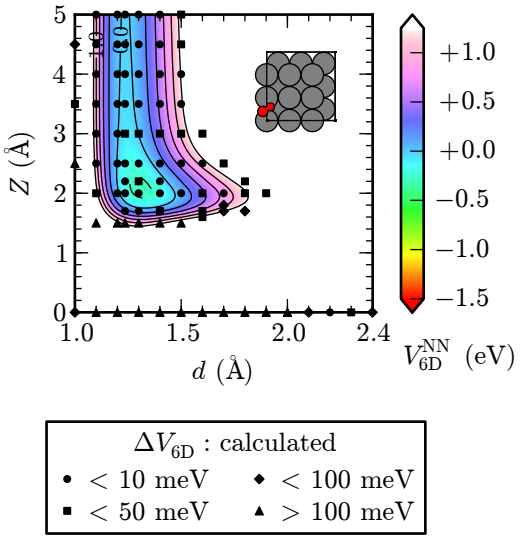

Figure B.1.2.7.:
$X = 0.0\,a_{Pd}^{100}$ $Y = 0.5\,a_{Pd}^{100}$
$\vartheta = 60°$ $\varphi = 30°$

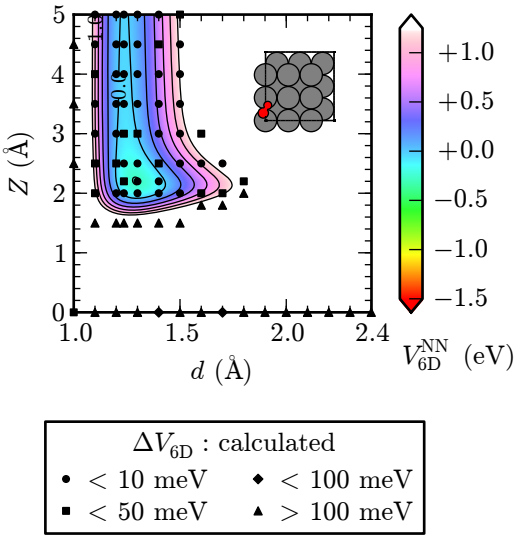

Figure B.1.2.8.:
$X = 0.0\,a_{Pd}^{100}$ $Y = 0.5\,a_{Pd}^{100}$
$\vartheta = 60°$ $\varphi = 60°$

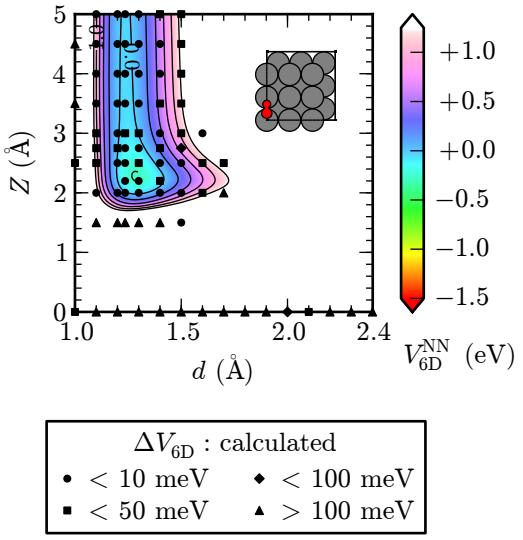

Figure B.1.2.9.:
$X = 0.0\,a_{Pd}^{100}$ $Y = 0.5\,a_{Pd}^{100}$
$\vartheta = 60°$ $\varphi = 90°$

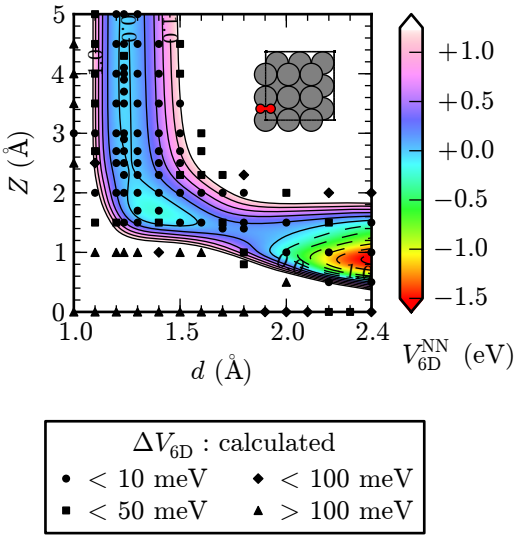

Figure B.1.2.10.:
$X = 0.0\,a_{Pd}^{100}$ $Y = 0.5\,a_{Pd}^{100}$
$\vartheta = 90°$ $\varphi = 0°$

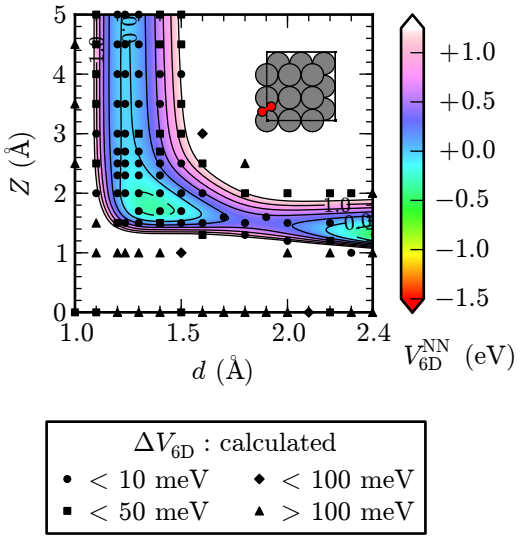

Figure B.1.2.11.:
$X = 0.0\,a_{Pd}^{100}$ $Y = 0.5\,a_{Pd}^{100}$
$\vartheta = 90°$ $\varphi = 30°$

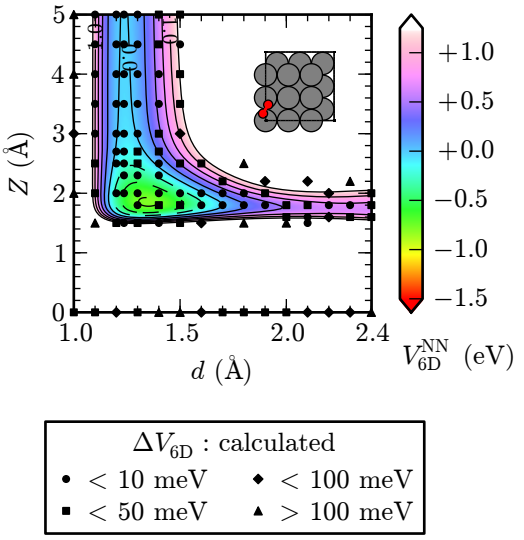

Figure B.1.2.12.:
$X = 0.0\,a_{Pd}^{100}$ $Y = 0.5\,a_{Pd}^{100}$
$\vartheta = 90°$ $\varphi = 60°$

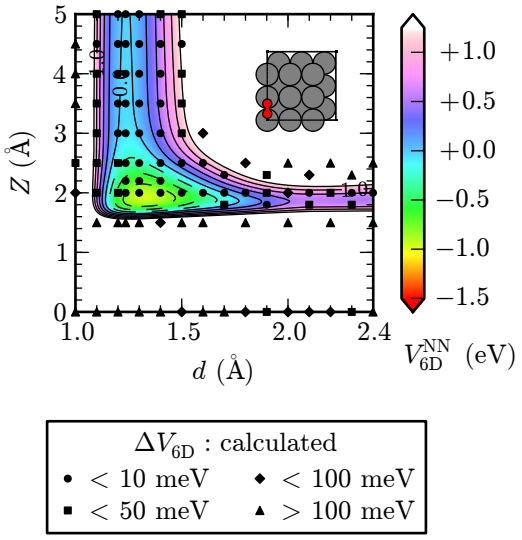

Figure B.1.2.13.:
$X = 0.0\,a_{Pd}^{100}$ $Y = 0.5\,a_{Pd}^{100}$
$\vartheta = 90°$ $\varphi = 90°$

B.1.3. Hollow Site

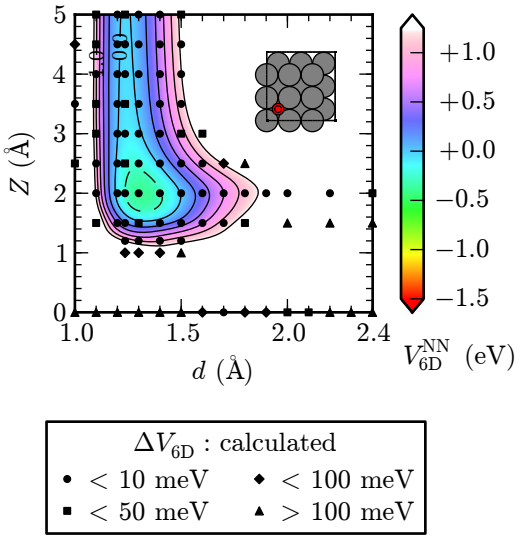

Figure B.1.3.1.:
$X = 0.5\,a_{Pd}^{100}$ $Y = 0.5\,a_{Pd}^{100}$
$\vartheta = 0°$ $\varphi = 0°$

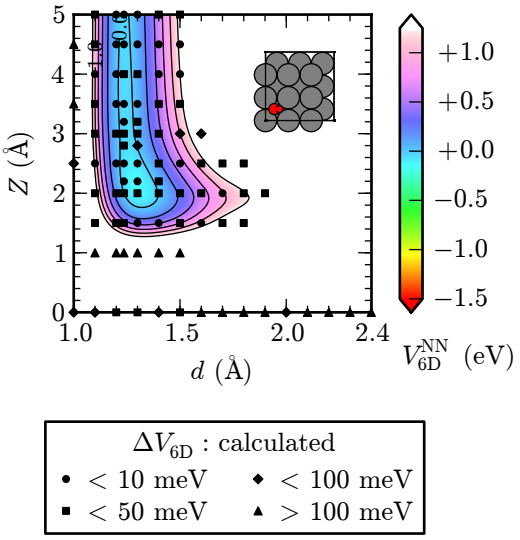

Figure B.1.3.2.:
$X = 0.5\,a_{Pd}^{100}$ $Y = 0.5\,a_{Pd}^{100}$
$\vartheta = 30°$ $\varphi = 0°$

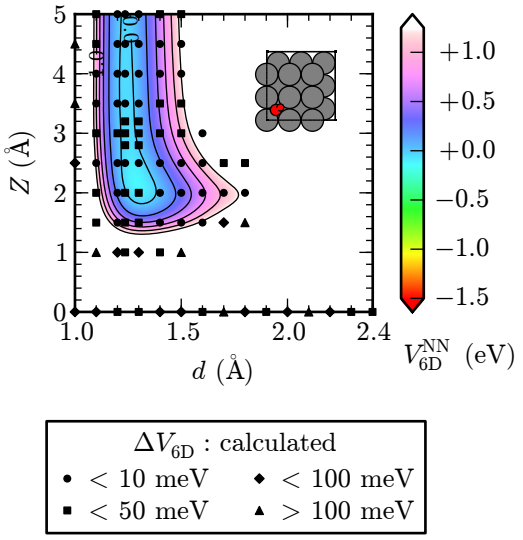

Figure B.1.3.3.:
$X = 0.5\,a_{Pd}^{100}$ $Y = 0.5\,a_{Pd}^{100}$
$\vartheta = 30°$ $\varphi = 30°$

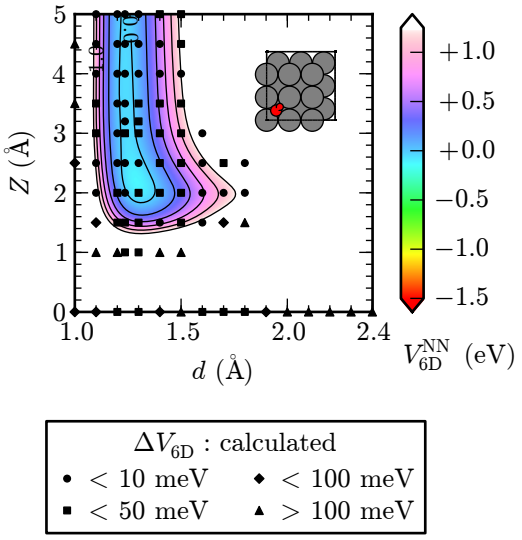

Figure B.1.3.4.:
$X = 0.5\,a_{Pd}^{100}$ $Y = 0.5\,a_{Pd}^{100}$
$\vartheta = 30°$ $\varphi = 45°$

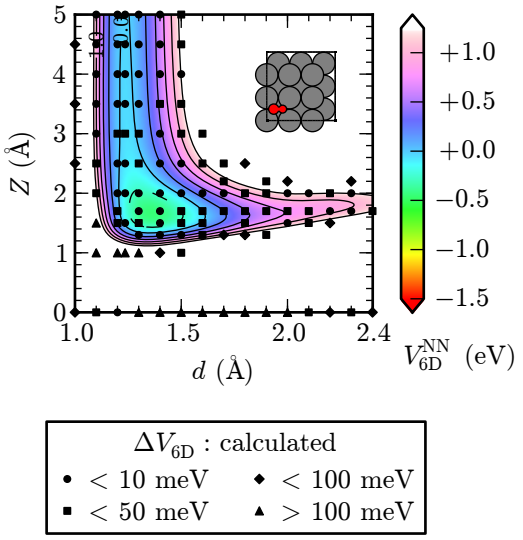

Figure B.1.3.5.:
$X = 0.5\,a_{Pd}^{100}$ $Y = 0.5\,a_{Pd}^{100}$
$\vartheta = 60°$ $\varphi = 0°$

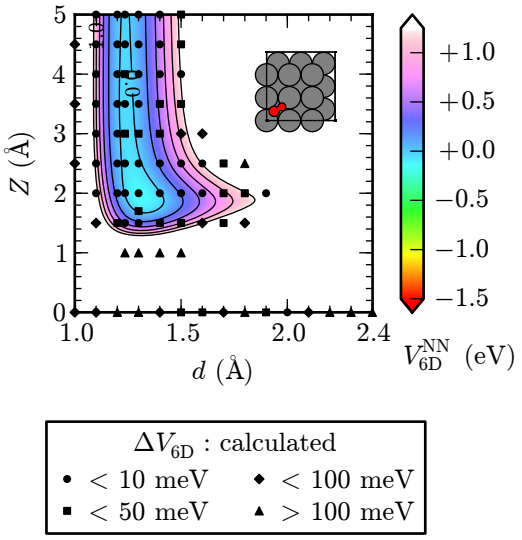

Figure B.1.3.6.:
$X = 0.5\,a_{Pd}^{100}$ $Y = 0.5\,a_{Pd}^{100}$
$\vartheta = 60°$ $\varphi = 30°$

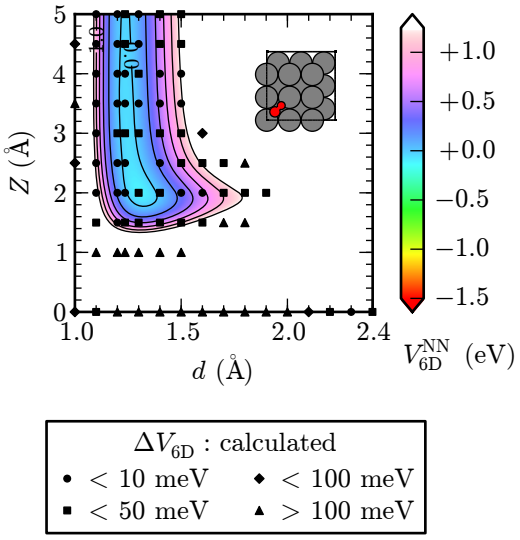

Figure B.1.3.7.:
$X = 0.5\,a_{Pd}^{100}$ $Y = 0.5\,a_{Pd}^{100}$
$\vartheta = 60°$ $\varphi = 45°$

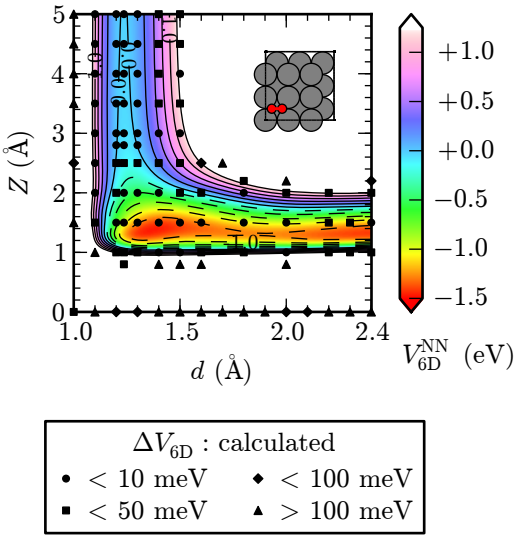

Figure B.1.3.8.:
$X = 0.5\,a_{Pd}^{100}$ $Y = 0.5\,a_{Pd}^{100}$
$\vartheta = 90°$ $\varphi = 0°$

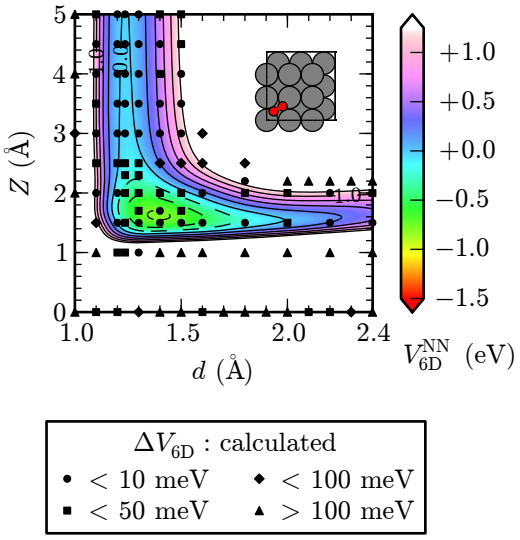

Figure B.1.3.9.:
$X = 0.5\,a_{Pd}^{100}$ $Y = 0.5\,a_{Pd}^{100}$
$\vartheta = 90°$ $\varphi = 30°$

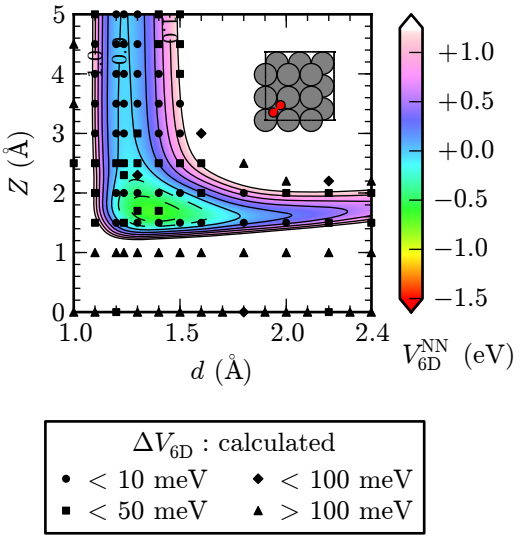

Figure B.1.3.10.:
$X = 0.5\,a_{Pd}^{100}$ $Y = 0.5\,a_{Pd}^{100}$
$\vartheta = 90°$ $\varphi = 45°$

B.2. Lateral Plots (X-Y-Cuts)

The plots that follow in this section are equivalent to the one shown in Fig. 6.9b, whose caption together with Section 6.2.2 provide more details.

B.2.1. Height $Z = 3.5$ Å

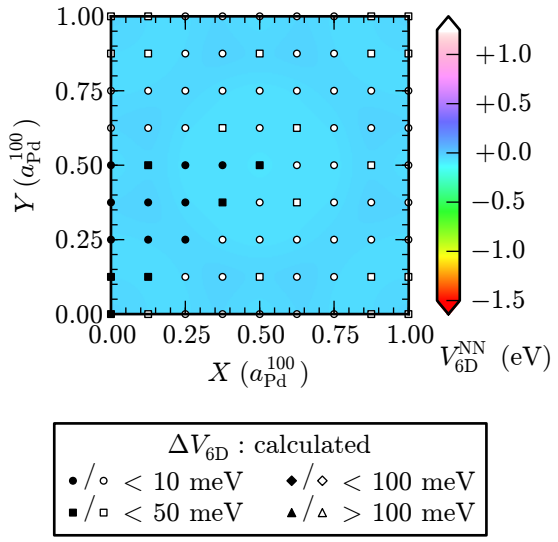

Figure B.2.1.1.:
$Z = 3.5$ Å $d = 1.236$ Å
$\vartheta = 0°$ $\varphi = 0°$

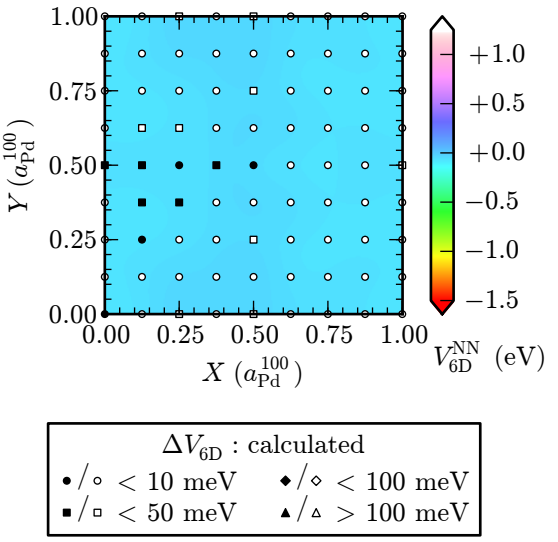

Figure B.2.1.2.:
$Z = 3.5$ Å $d = 1.236$ Å
$\vartheta = 30°$ $\varphi = 0°$

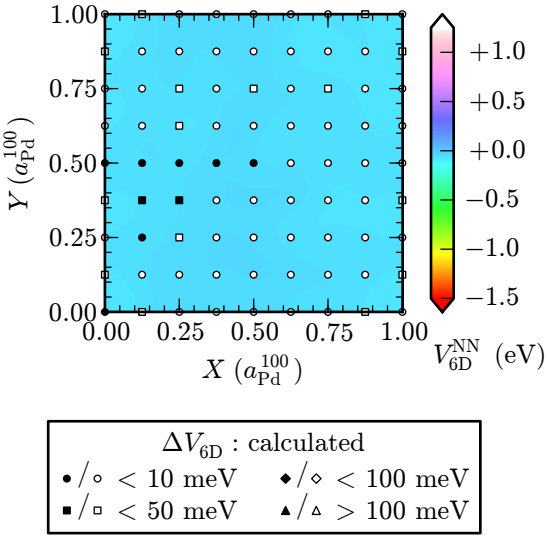

Figure B.2.1.3.:
$Z = 3.5\,\text{Å}$ $d = 1.236\,\text{Å}$
$\vartheta = 30°$ $\varphi = 30°$

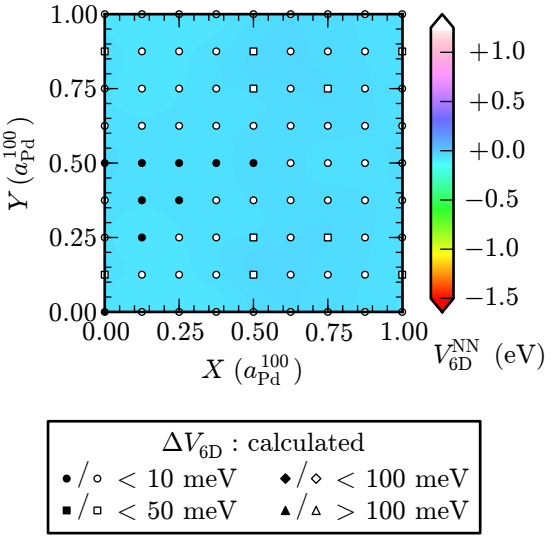

Figure B.2.1.4.:
$Z = 3.5\,\text{Å}$ $d = 1.236\,\text{Å}$
$\vartheta = 60°$ $\varphi = 0°$

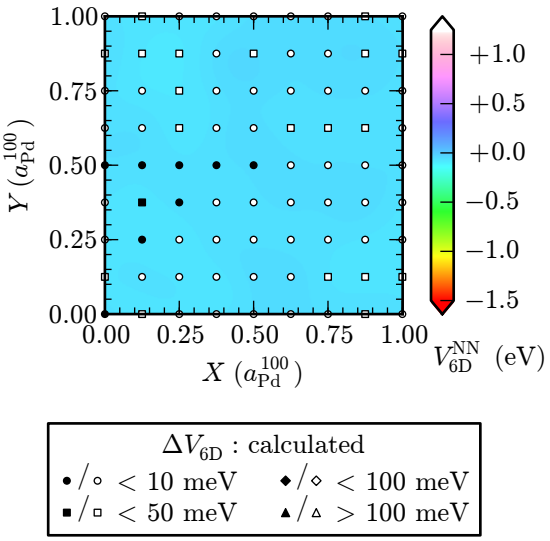

Figure B.2.1.5.:
$Z = 3.5\,\text{Å}$ $d = 1.236\,\text{Å}$
$\vartheta = 60°$ $\varphi = 30°$

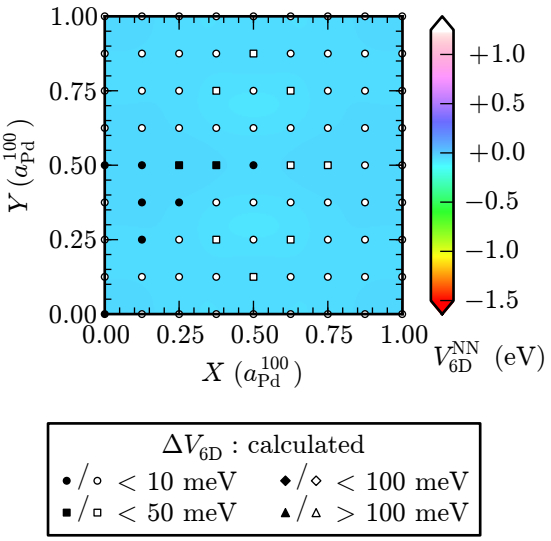

Figure B.2.1.6.:
$Z = 3.5\,\text{Å}$ $d = 1.236\,\text{Å}$
$\vartheta = 90°$ $\varphi = 0°$

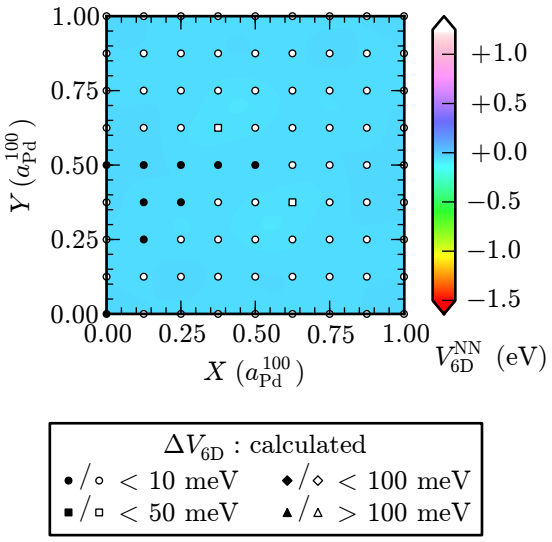

Figure B.2.1.7.:
$Z = 3.5$ Å $\quad d = 1.236$ Å
$\vartheta = 90°$ $\quad \varphi = 30°$

B.2.2. Height $Z = 2.5$ Å

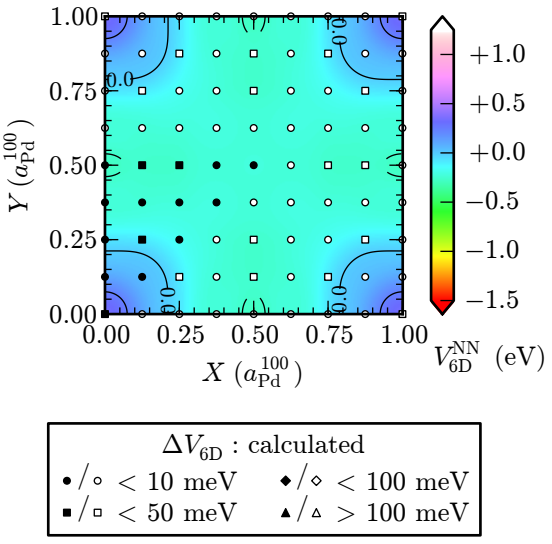

Figure B.2.2.1.:
$Z = 2.5$ Å $\quad d = 1.3$ Å
$\vartheta = 0°$ $\quad \varphi = 0°$

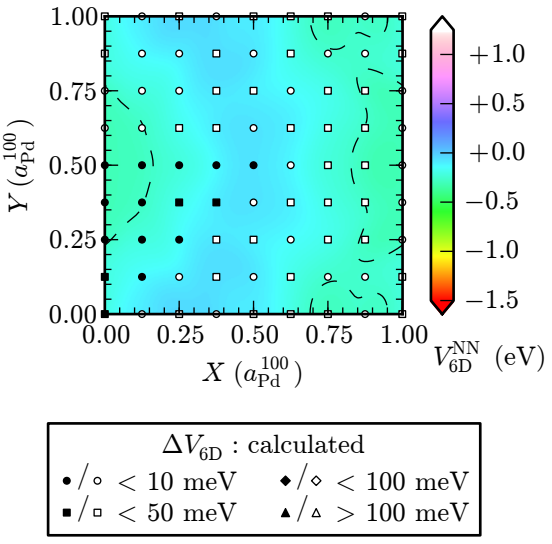

Figure B.2.2.2.:
$Z = 2.5$ Å $\quad d = 1.3$ Å
$\vartheta = 30°$ $\quad \varphi = 0°$

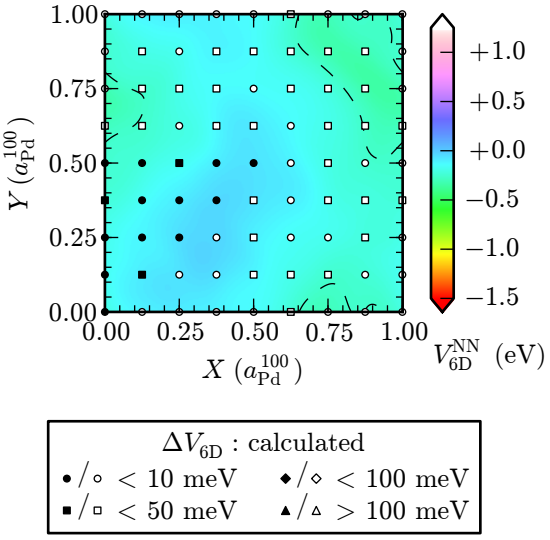

Figure B.2.2.3.:
$Z = 2.5\,\text{Å}$ $d = 1.3\,\text{Å}$
$\vartheta = 30°$ $\varphi = 30°$

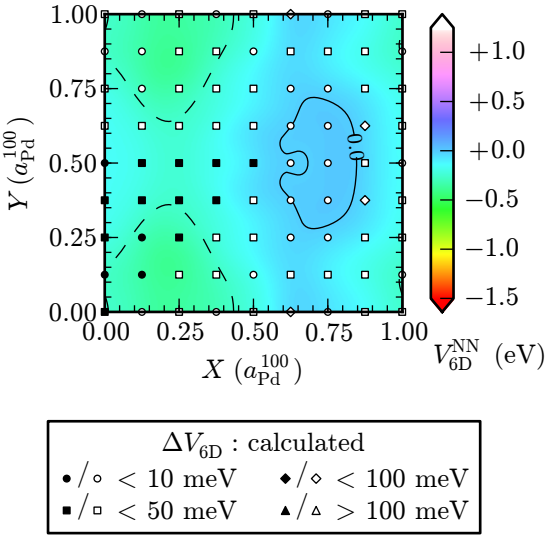

Figure B.2.2.4.:
$Z = 2.5\,\text{Å}$ $d = 1.3\,\text{Å}$
$\vartheta = 60°$ $\varphi = 0°$

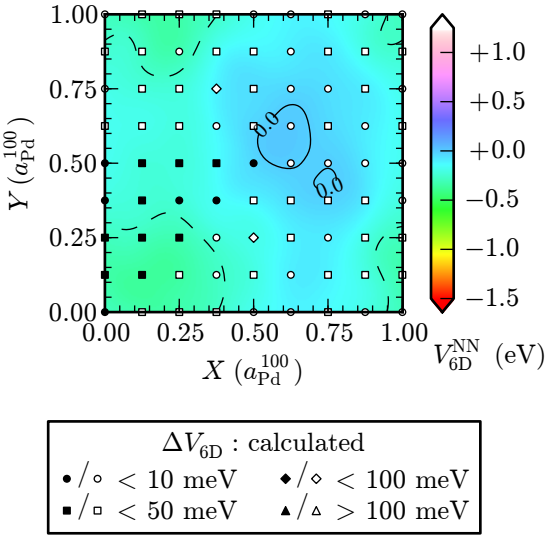

Figure B.2.2.5.:
$Z = 2.5\,\text{Å}$ $d = 1.3\,\text{Å}$
$\vartheta = 60°$ $\varphi = 30°$

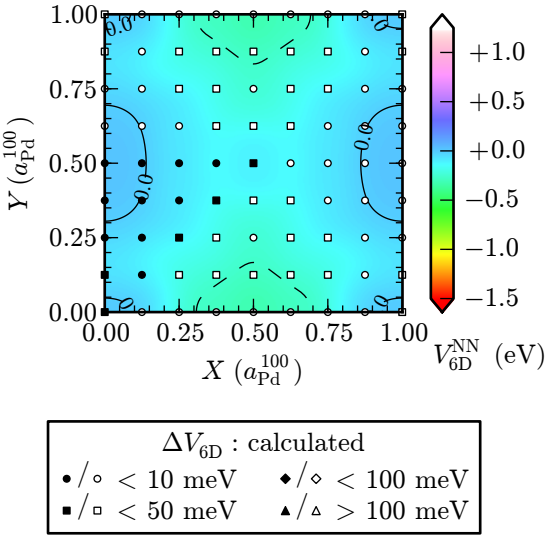

Figure B.2.2.6.:
$Z = 2.5\,\text{Å}$ $d = 1.3\,\text{Å}$
$\vartheta = 90°$ $\varphi = 0°$

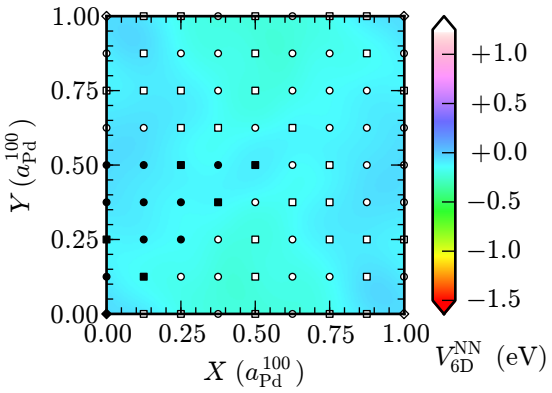

$\Delta V_{6\mathrm{D}}$: calculated	
•/∘ $<$ 10 meV	◆/◇ $<$ 100 meV
■/□ $<$ 50 meV	▲/△ $>$ 100 meV

Figure B.2.2.7.:
$Z = 2.5$ Å $\quad d = 1.3$ Å
$\vartheta = 90°$ $\quad \varphi = 30°$

B.2.3. Height $Z = 2.0$ Å

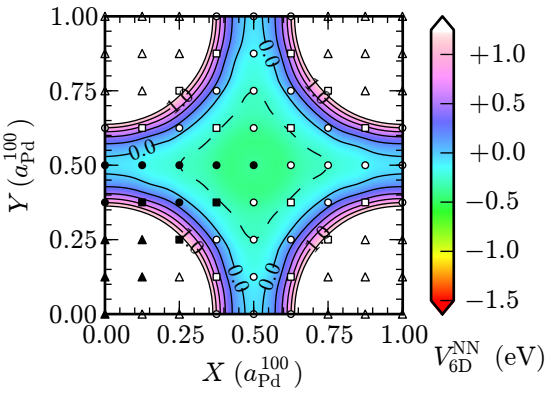

$\Delta V_{6\mathrm{D}}$: calculated	
•/∘ $<$ 10 meV	◆/◇ $<$ 100 meV
■/□ $<$ 50 meV	▲/△ $>$ 100 meV

Figure B.2.3.1.:
$Z = 2.0$ Å $\quad d = 1.3$ Å
$\vartheta = 0°$ $\quad \varphi = 0°$

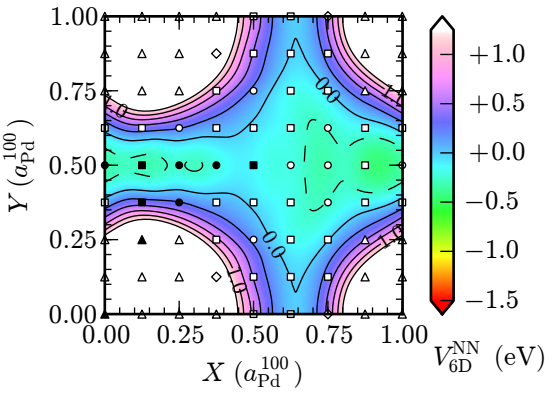

$\Delta V_{6\mathrm{D}}$: calculated	
•/∘ $<$ 10 meV	◆/◇ $<$ 100 meV
■/□ $<$ 50 meV	▲/△ $>$ 100 meV

Figure B.2.3.2.:
$Z = 2.0$ Å $\quad d = 1.3$ Å
$\vartheta = 30°$ $\quad \varphi = 0°$

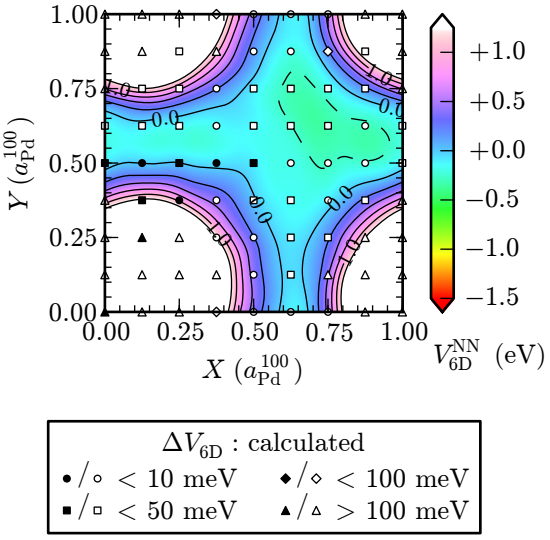

Figure B.2.3.3.:
$Z = 2.0\,\text{Å}$ $d = 1.3\,\text{Å}$
$\vartheta = 30°$ $\varphi = 30°$

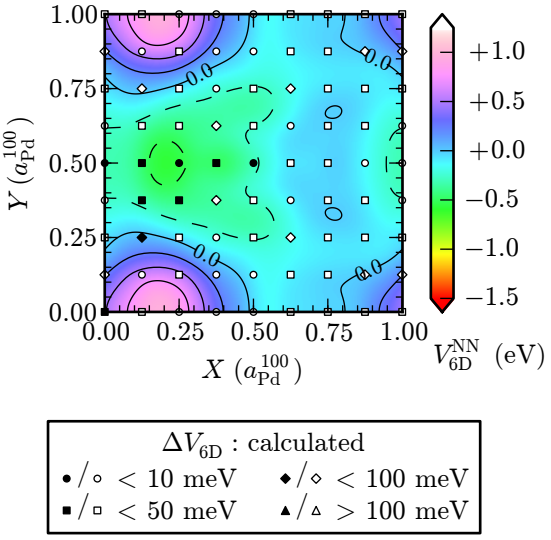

Figure B.2.3.4.:
$Z = 2.0\,\text{Å}$ $d = 1.3\,\text{Å}$
$\vartheta = 60°$ $\varphi = 0°$

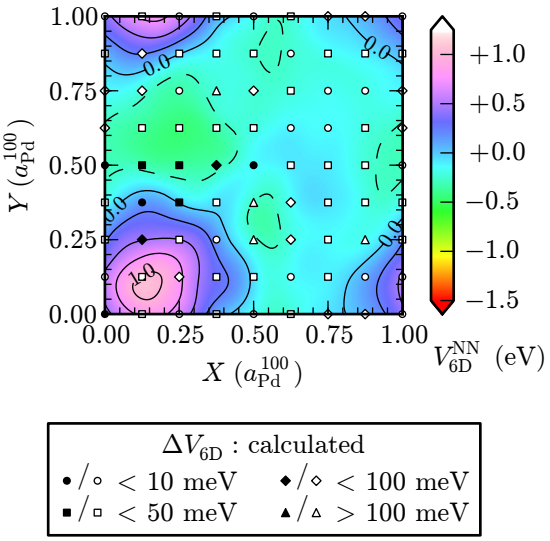

Figure B.2.3.5.:
$Z = 2.0\,\text{Å}$ $d = 1.3\,\text{Å}$
$\vartheta = 60°$ $\varphi = 30°$

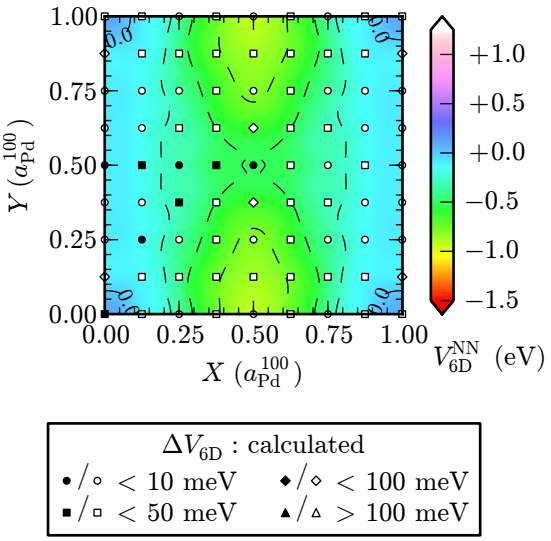

Figure B.2.3.6.:
$Z = 2.0\,\text{Å}$ $d = 1.3\,\text{Å}$
$\vartheta = 90°$ $\varphi = 0°$

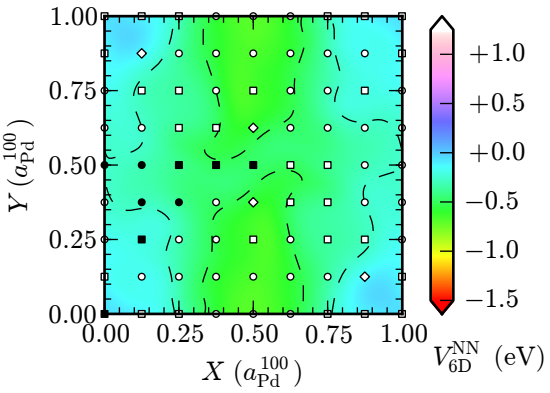

$\Delta V_{6\mathrm{D}}$: calculated	
•/∘ $<$ 10 meV	◆/◇ $<$ 100 meV
■/□ $<$ 50 meV	▲/△ $>$ 100 meV

Figure B.2.3.7.:
$Z = 2.0\,\text{Å}$ $d = 1.3\,\text{Å}$
$\vartheta = 90°$ $\varphi = 30°$

B.2.4. Height $Z = 1.5\,\text{Å}$

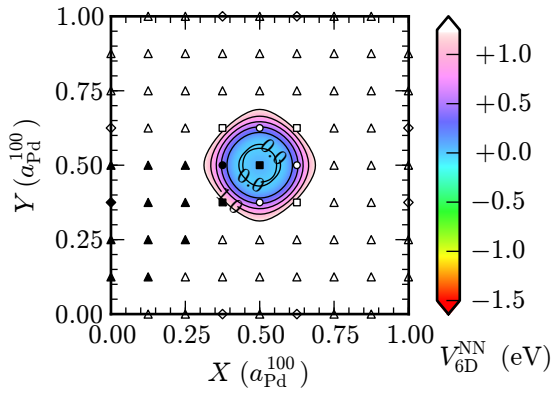

$\Delta V_{6\mathrm{D}}$: calculated	
•/∘ $<$ 10 meV	◆/◇ $<$ 100 meV
■/□ $<$ 50 meV	▲/△ $>$ 100 meV

Figure B.2.4.1.:
$Z = 1.5\,\text{Å}$ $d = 1.3\,\text{Å}$
$\vartheta = 0°$ $\varphi = 0°$

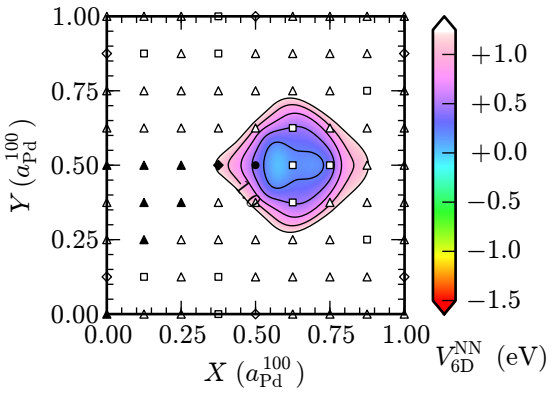

$\Delta V_{6\mathrm{D}}$: calculated	
•/∘ $<$ 10 meV	◆/◇ $<$ 100 meV
■/□ $<$ 50 meV	▲/△ $>$ 100 meV

Figure B.2.4.2.:
$Z = 1.5\,\text{Å}$ $d = 1.3\,\text{Å}$
$\vartheta = 30°$ $\varphi = 0°$

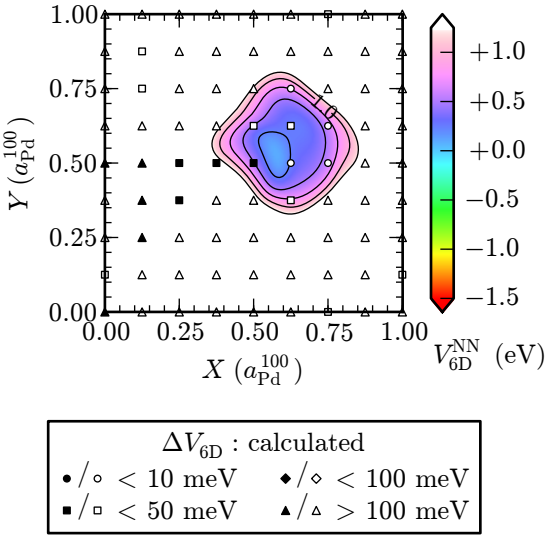

Figure B.2.4.3.:
$Z = 1.5\,\text{Å}$ $d = 1.3\,\text{Å}$
$\vartheta = 30°$ $\varphi = 30°$

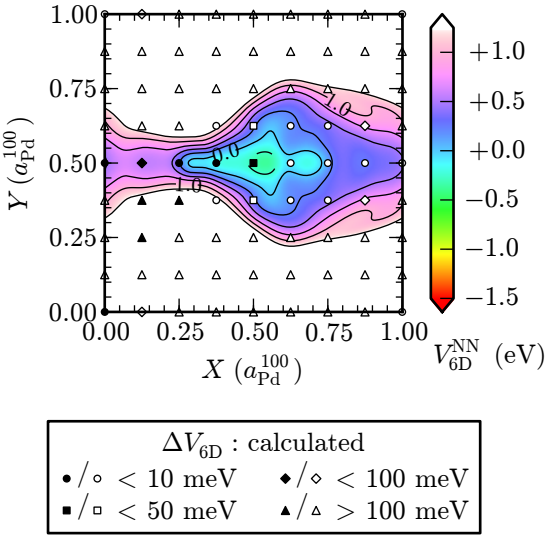

Figure B.2.4.4.:
$Z = 1.5\,\text{Å}$ $d = 1.3\,\text{Å}$
$\vartheta = 60°$ $\varphi = 0°$

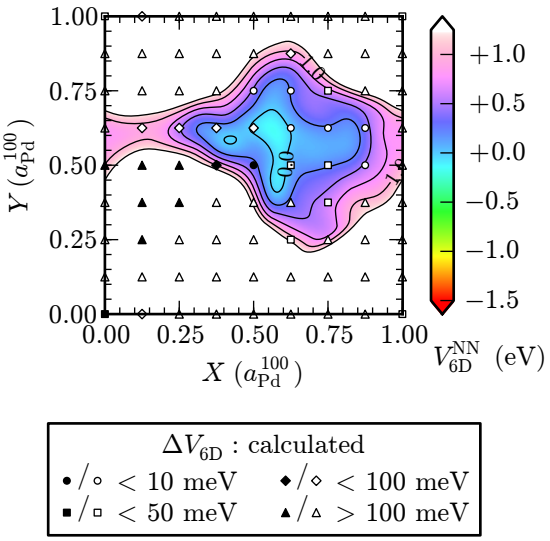

Figure B.2.4.5.:
$Z = 1.5\,\text{Å}$ $d = 1.3\,\text{Å}$
$\vartheta = 60°$ $\varphi = 30°$

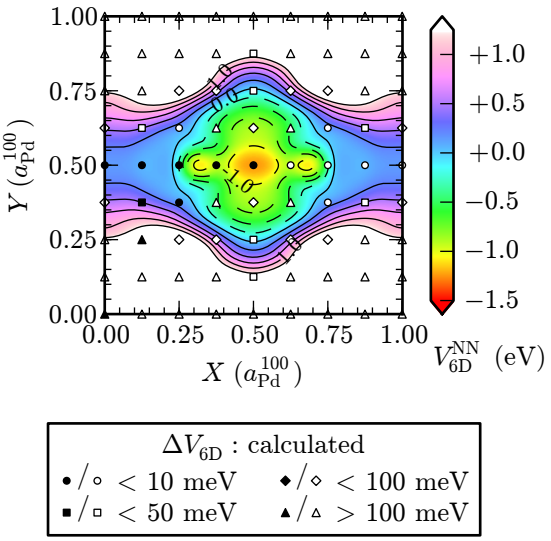

Figure B.2.4.6.:
$Z = 1.5\,\text{Å}$ $d = 1.3\,\text{Å}$
$\vartheta = 90°$ $\varphi = 0°$

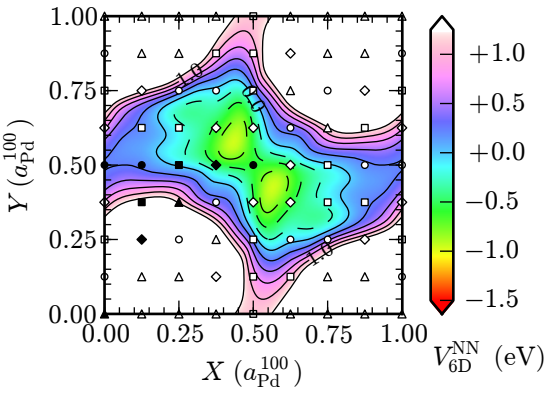

ΔV_{6D} : calculated	
•/∘ $<$ 10 meV	◆/◇ $<$ 100 meV
■/□ $<$ 50 meV	▲/△ $>$ 100 meV

Figure B.2.4.7.:
$Z = 1.5$ Å $\quad d = 1.3$ Å
$\vartheta = 90°$ $\quad \varphi = 30°$

B.3. Angular Plots (ϑ-φ-Cuts)

The plots that follow in this section are equivalent to the one shown in Fig. 6.10b, whose caption together with Section 6.2.2 provide more details.

B.3.1. Height $Z = 3.5\,\text{Å}$

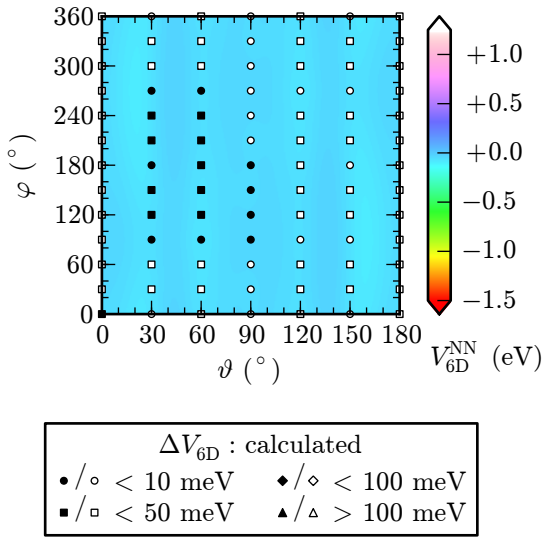

Figure B.3.1.1.:
$X = 0.0\,a_{Pd}^{100}$ $Y = 0.125\,a_{Pd}^{100}$
$Z = 3.5\,\text{Å}$ $d = 1.236\,\text{Å}$

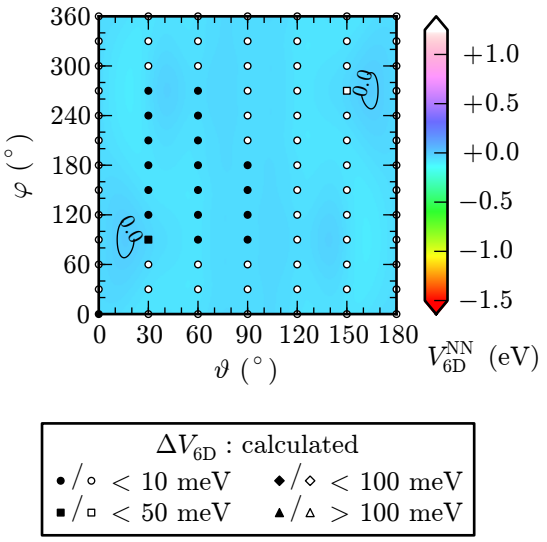

Figure B.3.1.2.:
$X = 0.0\,a_{Pd}^{100}$ $Y = 0.25\,a_{Pd}^{100}$
$Z = 3.5\,\text{Å}$ $d = 1.236\,\text{Å}$

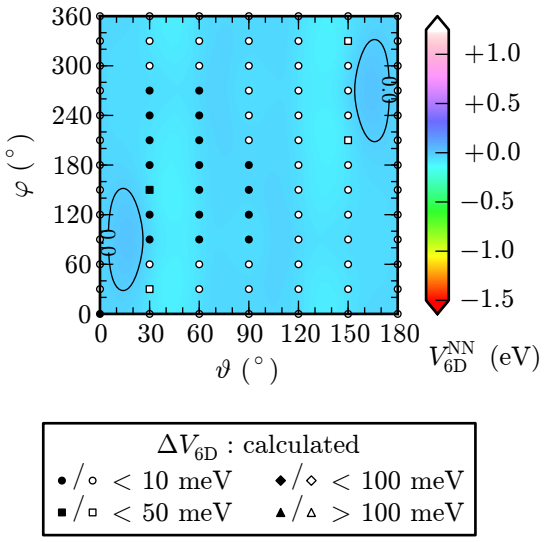

Figure B.3.1.3.:
$X = 0.0\,\mathrm{a}_{\mathrm{Pd}}^{100}$ $Y = 0.375\,\mathrm{a}_{\mathrm{Pd}}^{100}$
$Z = 3.5$ Å $d = 1.236$ Å

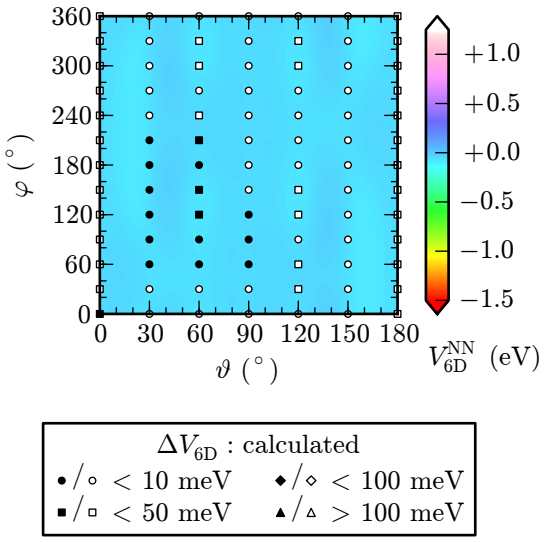

Figure B.3.1.4.:
$X = 0.125\,\mathrm{a}_{\mathrm{Pd}}^{100}$ $Y = 0.125\,\mathrm{a}_{\mathrm{Pd}}^{100}$
$Z = 3.5$ Å $d = 1.236$ Å

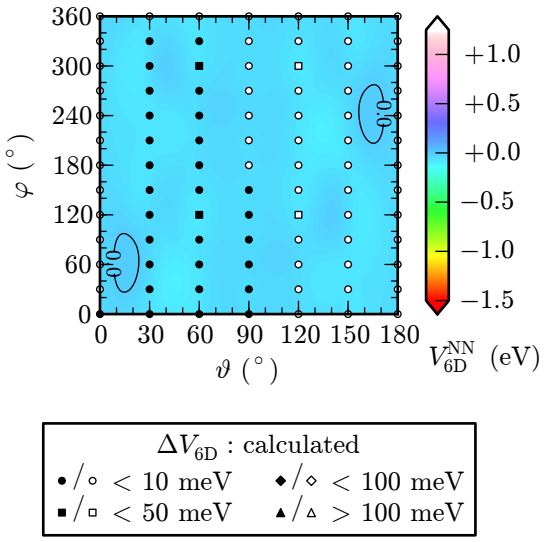

Figure B.3.1.5.:
$X = 0.125\,\mathrm{a}_{\mathrm{Pd}}^{100}$ $Y = 0.25\,\mathrm{a}_{\mathrm{Pd}}^{100}$
$Z = 3.5$ Å $d = 1.236$ Å

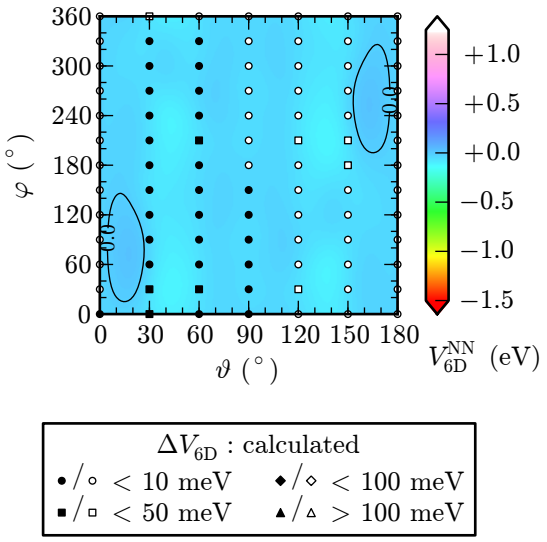

Figure B.3.1.6.:
$X = 0.125\,\mathrm{a}_{\mathrm{Pd}}^{100}$ $Y = 0.375\,\mathrm{a}_{\mathrm{Pd}}^{100}$
$Z = 3.5$ Å $d = 1.236$ Å

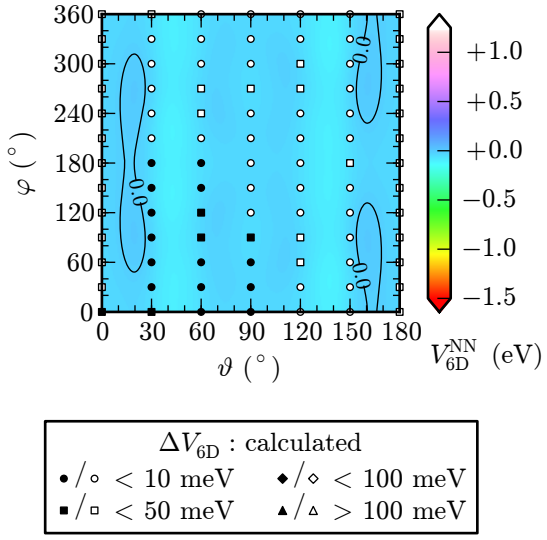

Figure B.3.1.7.:
$X = 0.125\,a_{Pd}^{100}$ $Y = 0.5\,a_{Pd}^{100}$
$Z = 3.5$ Å $d = 1.236$ Å

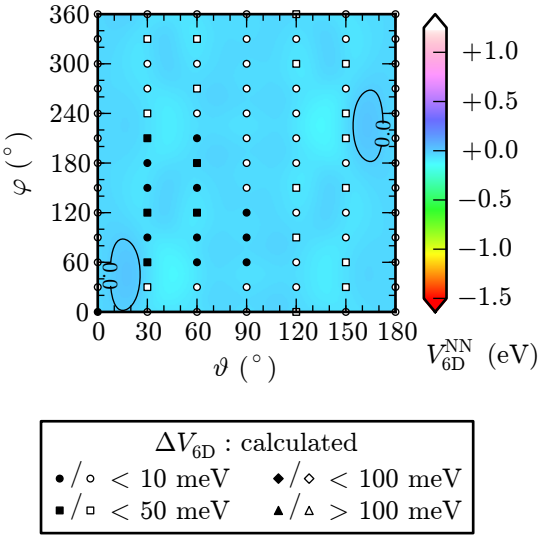

Figure B.3.1.8.:
$X = 0.25\,a_{Pd}^{100}$ $Y = 0.25\,a_{Pd}^{100}$
$Z = 3.5$ Å $d = 1.236$ Å

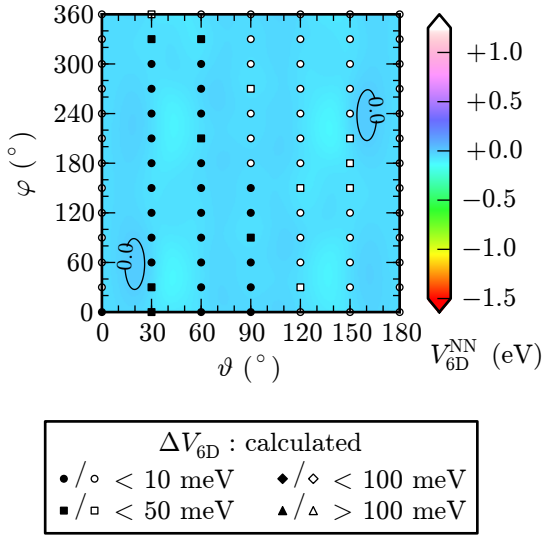

Figure B.3.1.9.:
$X = 0.25\,a_{Pd}^{100}$ $Y = 0.375\,a_{Pd}^{100}$
$Z = 3.5$ Å $d = 1.236$ Å

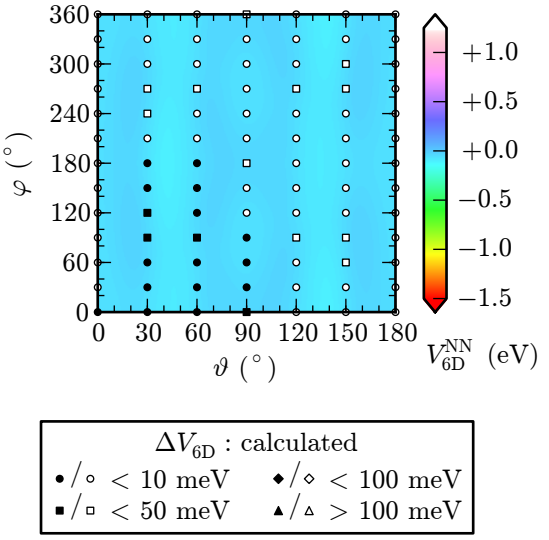

Figure B.3.1.10.:
$X = 0.25\,a_{Pd}^{100}$ $Y = 0.5\,a_{Pd}^{100}$
$Z = 3.5$ Å $d = 1.236$ Å

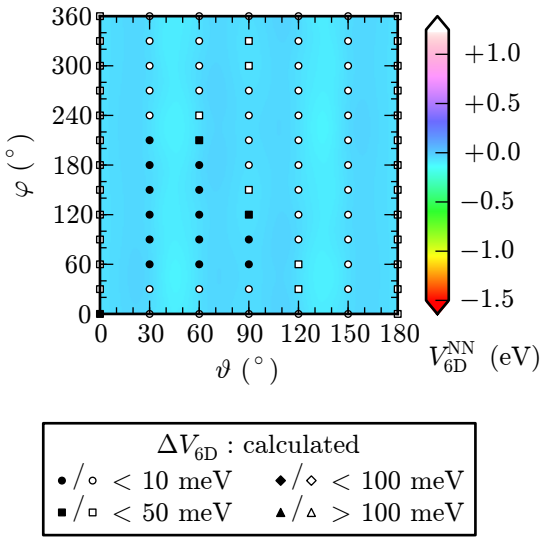

Figure B.3.1.11.:
$X = 0.375\,a_{Pd}^{100}$ $Y = 0.375\,a_{Pd}^{100}$
$Z = 3.5$ Å $d = 1.236$ Å

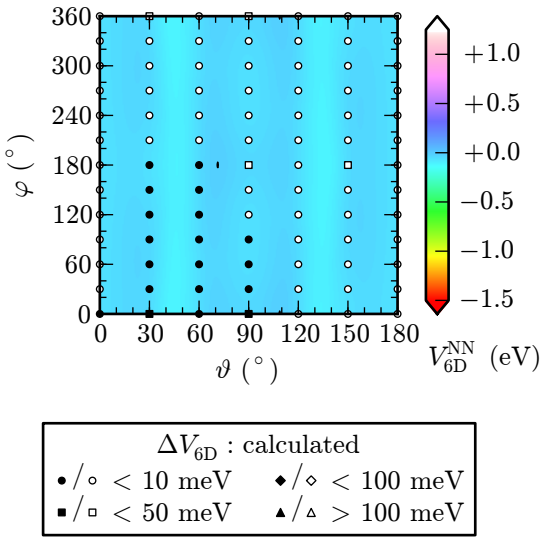

Figure B.3.1.12.:
$X = 0.375\,a_{Pd}^{100}$ $Y = 0.5\,a_{Pd}^{100}$
$Z = 3.5$ Å $d = 1.236$ Å

B.3.2. Height $Z = 2.5$ Å

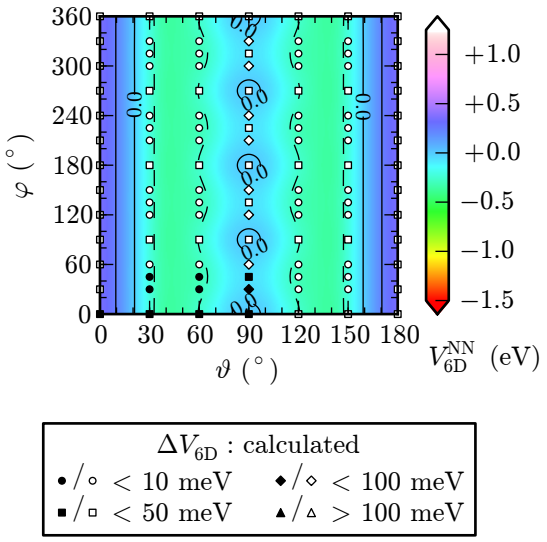

Figure B.3.2.1.:
$X = 0.0\,a_{Pd}^{100}$ $Y = 0.0\,a_{Pd}^{100}$
$Z = 2.5$ Å $d = 1.3$ Å

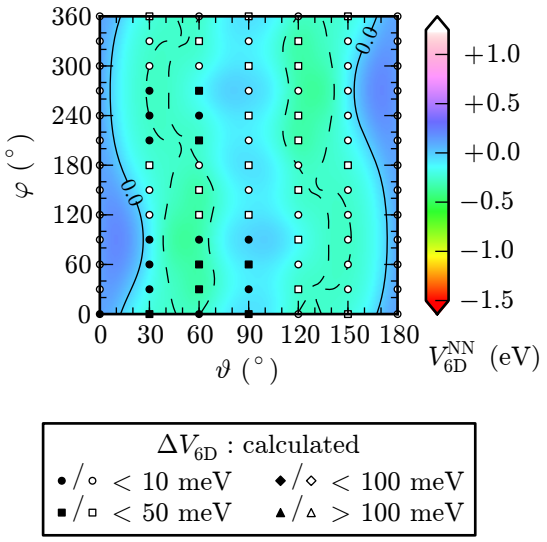

Figure B.3.2.2.:
$X = 0.0\,a_{Pd}^{100}$ $Y = 0.125\,a_{Pd}^{100}$
$Z = 2.5$ Å $d = 1.3$ Å

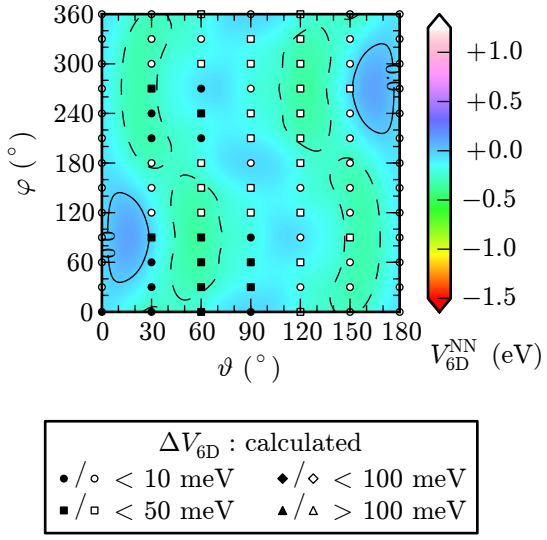

Figure B.3.2.3.:
$X = 0.0\,\mathrm{a}_{\mathrm{Pd}}^{100}$ $Y = 0.25\,\mathrm{a}_{\mathrm{Pd}}^{100}$
$Z = 2.5\,\text{Å}$ $d = 1.3\,\text{Å}$

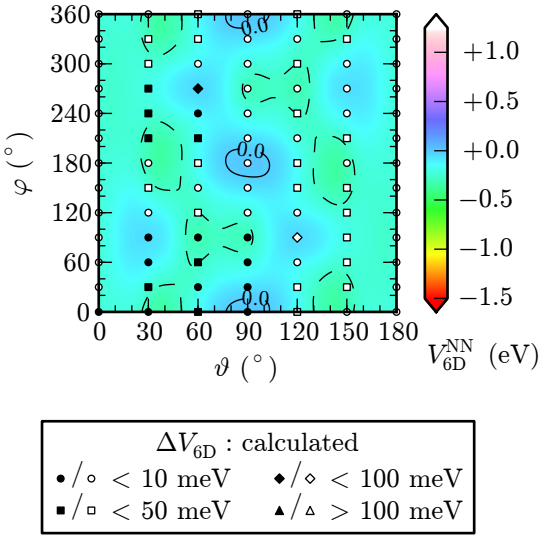

Figure B.3.2.4.:
$X = 0.0\,\mathrm{a}_{\mathrm{Pd}}^{100}$ $Y = 0.375\,\mathrm{a}_{\mathrm{Pd}}^{100}$
$Z = 2.5\,\text{Å}$ $d = 1.3\,\text{Å}$

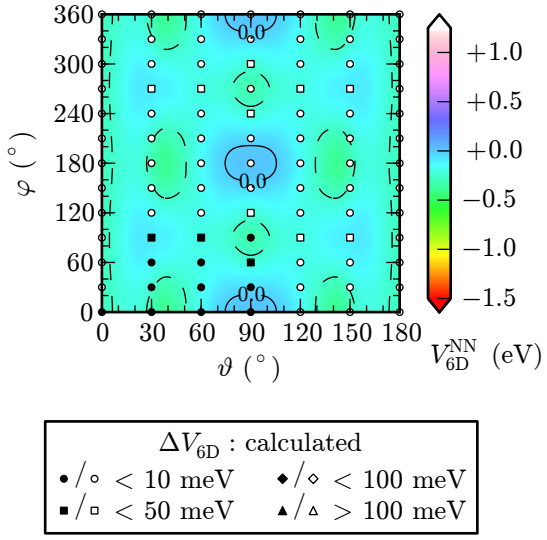

Figure B.3.2.5.:
$X = 0.0\,\mathrm{a}_{\mathrm{Pd}}^{100}$ $Y = 0.5\,\mathrm{a}_{\mathrm{Pd}}^{100}$
$Z = 2.5\,\text{Å}$ $d = 1.3\,\text{Å}$

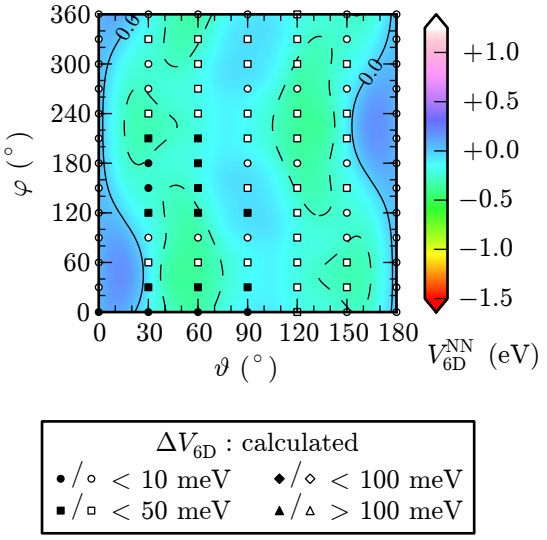

Figure B.3.2.6.:
$X = 0.125\,\mathrm{a}_{\mathrm{Pd}}^{100}$ $Y = 0.125\,\mathrm{a}_{\mathrm{Pd}}^{100}$
$Z = 2.5\,\text{Å}$ $d = 1.3\,\text{Å}$

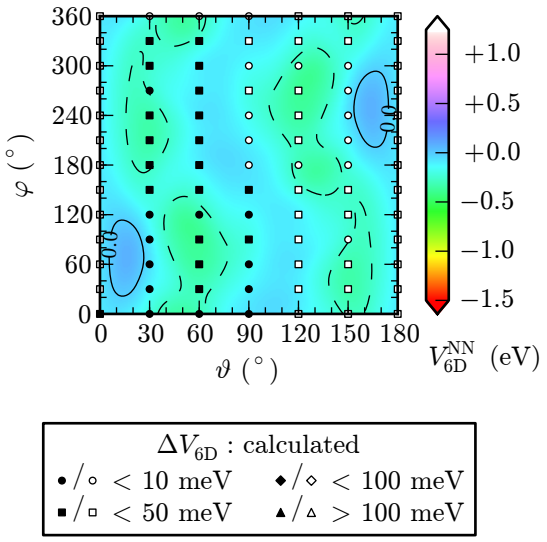

Figure B.3.2.7.:
$X = 0.125\,a_{Pd}^{100}$ $Y = 0.25\,a_{Pd}^{100}$
$Z = 2.5$ Å $d = 1.3$ Å

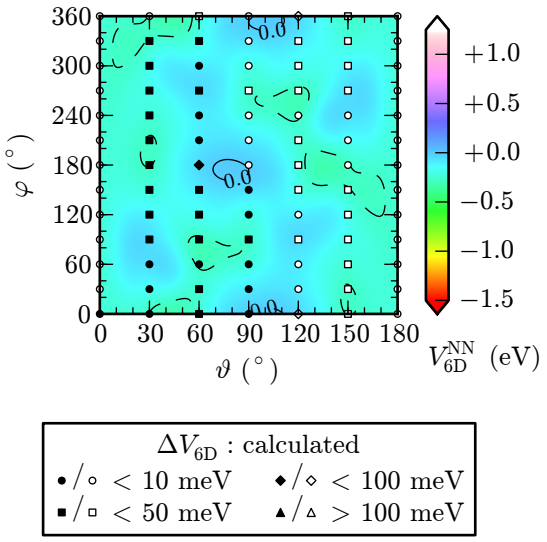

Figure B.3.2.8.:
$X = 0.125\,a_{Pd}^{100}$ $Y = 0.375\,a_{Pd}^{100}$
$Z = 2.5$ Å $d = 1.3$ Å

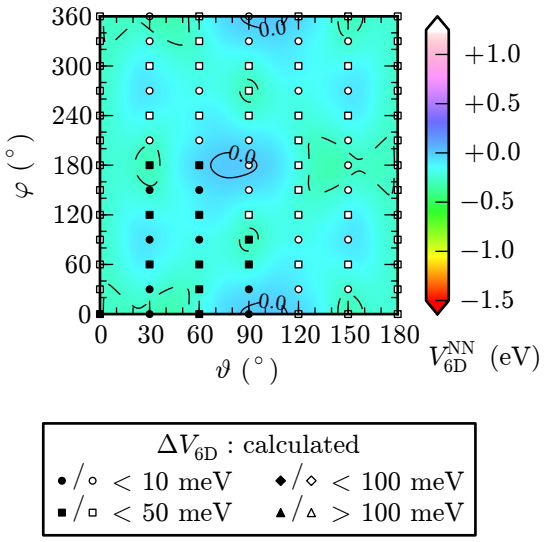

Figure B.3.2.9.:
$X = 0.125\,a_{Pd}^{100}$ $Y = 0.5\,a_{Pd}^{100}$
$Z = 2.5$ Å $d = 1.3$ Å

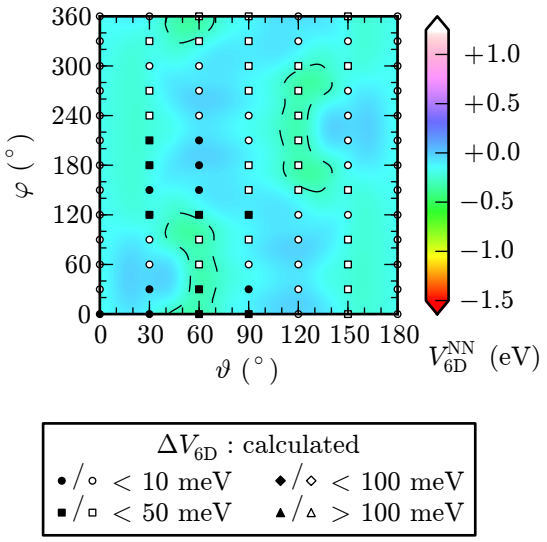

Figure B.3.2.10.:
$X = 0.25\,a_{Pd}^{100}$ $Y = 0.25\,a_{Pd}^{100}$
$Z = 2.5$ Å $d = 1.3$ Å

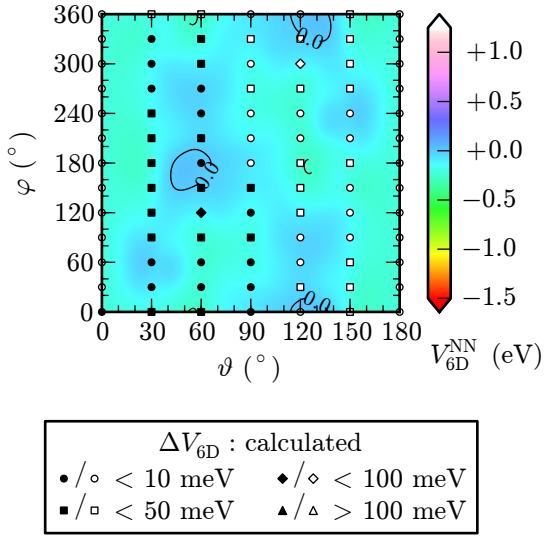

ΔV_{6D} : calculated	
• / ∘ $<$ 10 meV	◆ / ◇ $<$ 100 meV
■ / □ $<$ 50 meV	▲ / △ $>$ 100 meV

Figure B.3.2.11.:
$X = 0.25\,a_{Pd}^{100}$ $Y = 0.375\,a_{Pd}^{100}$
$Z = 2.5$ Å $d = 1.3$ Å

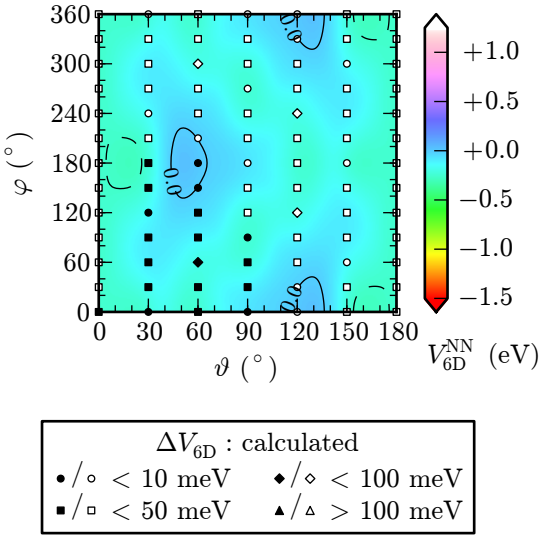

ΔV_{6D} : calculated	
• / ∘ $<$ 10 meV	◆ / ◇ $<$ 100 meV
■ / □ $<$ 50 meV	▲ / △ $>$ 100 meV

Figure B.3.2.12.:
$X = 0.25\,a_{Pd}^{100}$ $Y = 0.5\,a_{Pd}^{100}$
$Z = 2.5$ Å $d = 1.3$ Å

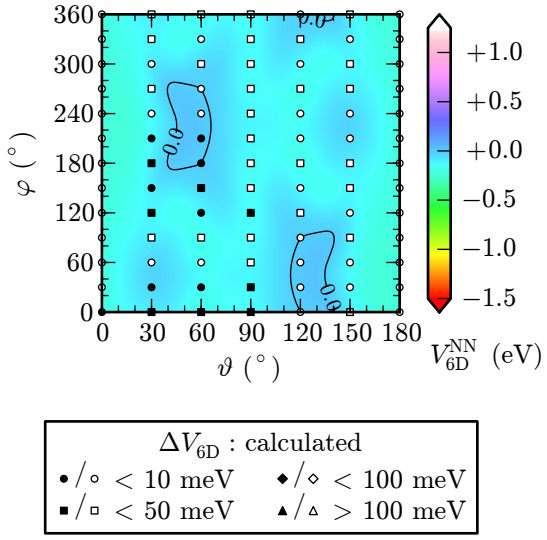

ΔV_{6D} : calculated	
• / ∘ $<$ 10 meV	◆ / ◇ $<$ 100 meV
■ / □ $<$ 50 meV	▲ / △ $>$ 100 meV

Figure B.3.2.13.:
$X = 0.375\,a_{Pd}^{100}$ $Y = 0.375\,a_{Pd}^{100}$
$Z = 2.5$ Å $d = 1.3$ Å

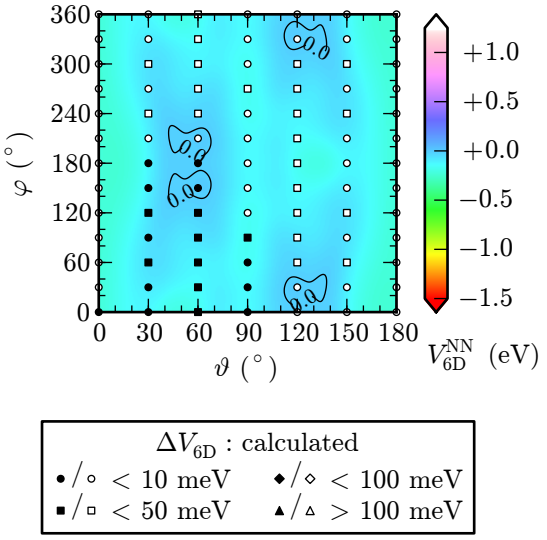

ΔV_{6D} : calculated	
• / ∘ $<$ 10 meV	◆ / ◇ $<$ 100 meV
■ / □ $<$ 50 meV	▲ / △ $>$ 100 meV

Figure B.3.2.14.:
$X = 0.375\,a_{Pd}^{100}$ $Y = 0.5\,a_{Pd}^{100}$
$Z = 2.5$ Å $d = 1.3$ Å

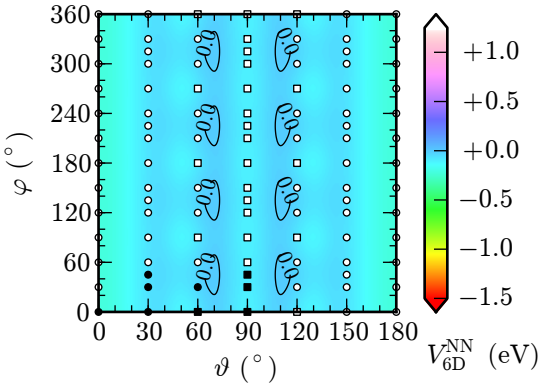

Figure B.3.2.15.:
$X = 0.5\,a_{Pd}^{100}$ $Y = 0.5\,a_{Pd}^{100}$
$Z = 2.5$ Å $d = 1.3$ Å

B.3.3. Height $Z = 2.0$ Å

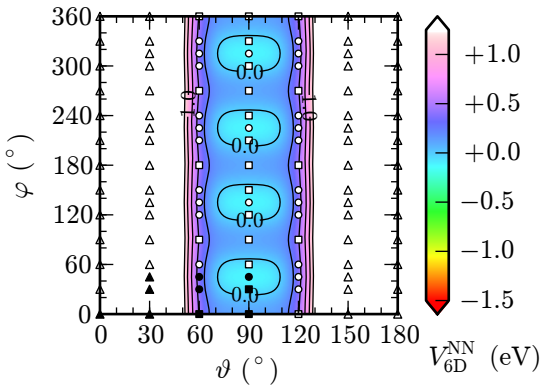

Figure B.3.3.1.:
$X = 0.0\,a_{Pd}^{100}$ $Y = 0.0\,a_{Pd}^{100}$
$Z = 2.0$ Å $d = 1.3$ Å

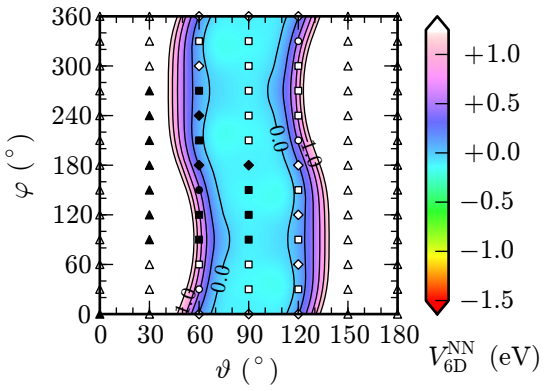

Figure B.3.3.2.:
$X = 0.0\,a_{Pd}^{100}$ $Y = 0.125\,a_{Pd}^{100}$
$Z = 2.0$ Å $d = 1.3$ Å

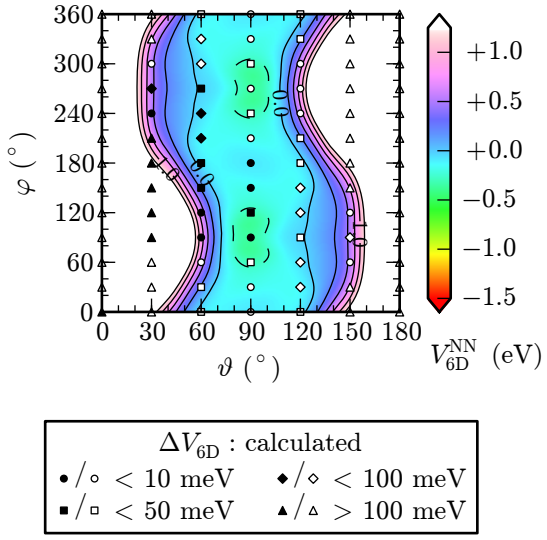

Figure B.3.3.3.:
$X = 0.0\,\mathrm{a}_{\mathrm{Pd}}^{100}$ $Y = 0.25\,\mathrm{a}_{\mathrm{Pd}}^{100}$
$Z = 2.0\,\text{Å}$ $d = 1.3\,\text{Å}$

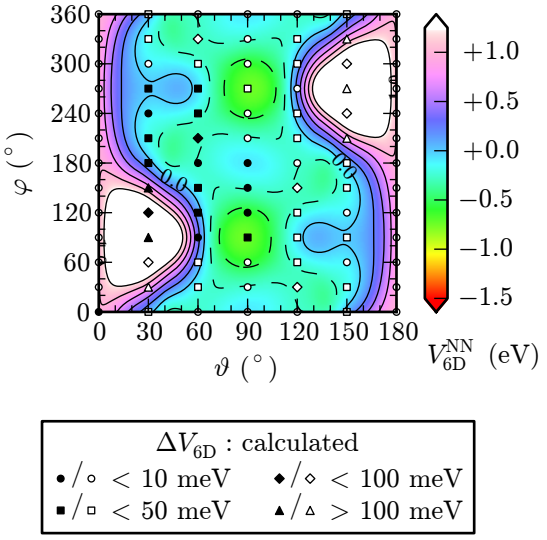

Figure B.3.3.4.:
$X = 0.0\,\mathrm{a}_{\mathrm{Pd}}^{100}$ $Y = 0.375\,\mathrm{a}_{\mathrm{Pd}}^{100}$
$Z = 2.0\,\text{Å}$ $d = 1.3\,\text{Å}$

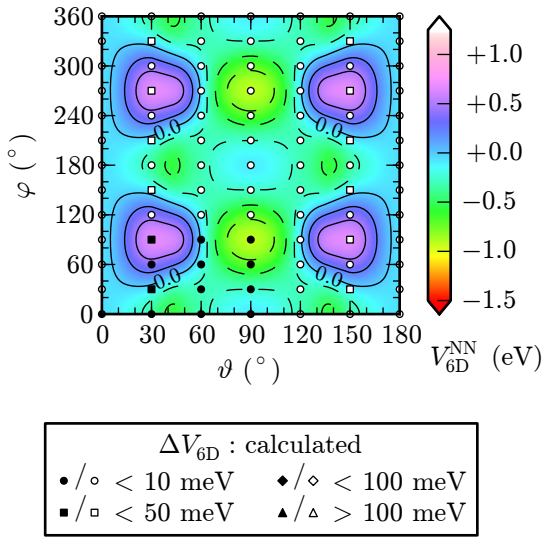

Figure B.3.3.5.:
$X = 0.0\,\mathrm{a}_{\mathrm{Pd}}^{100}$ $Y = 0.5\,\mathrm{a}_{\mathrm{Pd}}^{100}$
$Z = 2.0\,\text{Å}$ $d = 1.3\,\text{Å}$

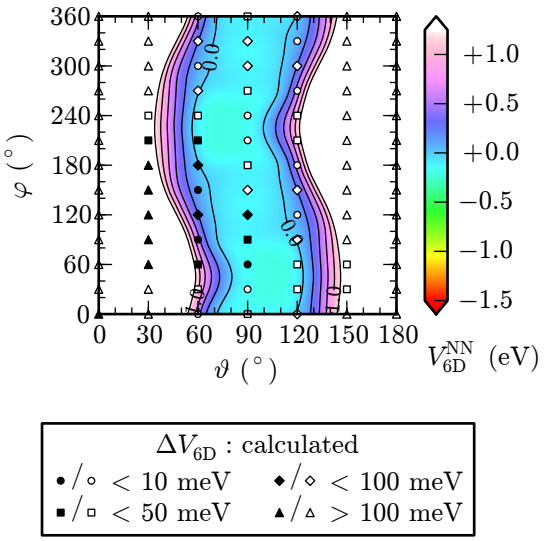

Figure B.3.3.6.:
$X = 0.125\,\mathrm{a}_{\mathrm{Pd}}^{100}$ $Y = 0.125\,\mathrm{a}_{\mathrm{Pd}}^{100}$
$Z = 2.0\,\text{Å}$ $d = 1.3\,\text{Å}$

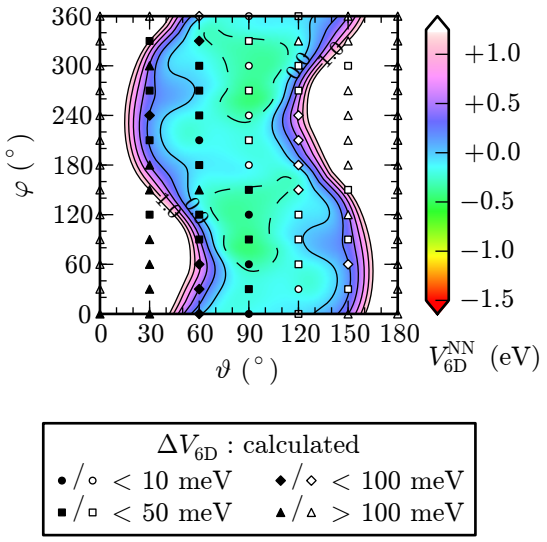

Figure B.3.3.7.:
$X = 0.125\,a_{Pd}^{100}$ $Y = 0.25\,a_{Pd}^{100}$
$Z = 2.0$ Å $d = 1.3$ Å

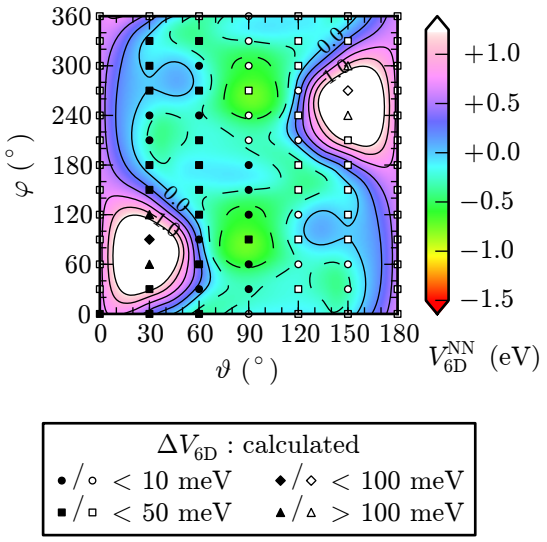

Figure B.3.3.8.:
$X = 0.125\,a_{Pd}^{100}$ $Y = 0.375\,a_{Pd}^{100}$
$Z = 2.0$ Å $d = 1.3$ Å

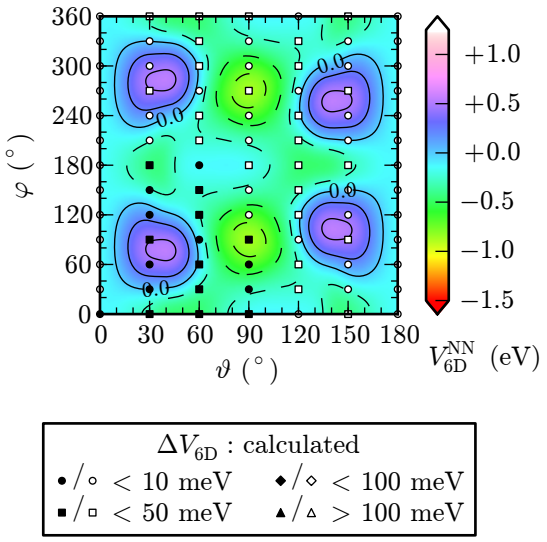

Figure B.3.3.9.:
$X = 0.125\,a_{Pd}^{100}$ $Y = 0.5\,a_{Pd}^{100}$
$Z = 2.0$ Å $d = 1.3$ Å

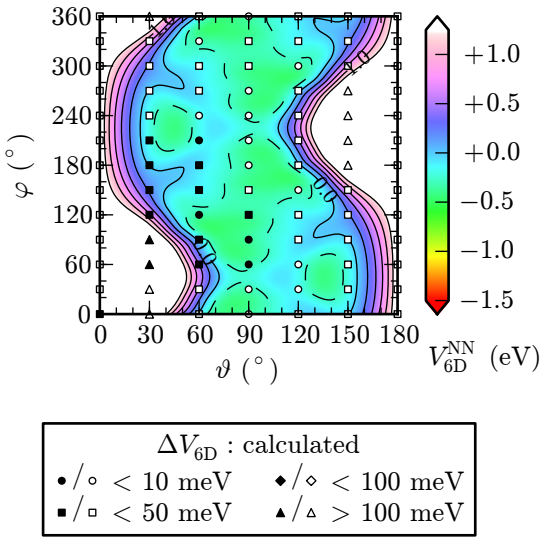

Figure B.3.3.10.:
$X = 0.25\,a_{Pd}^{100}$ $Y = 0.25\,a_{Pd}^{100}$
$Z = 2.0$ Å $d = 1.3$ Å

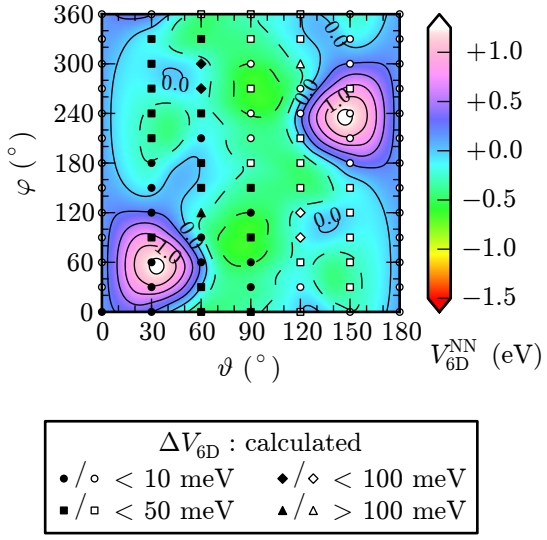

Figure B.3.3.11.:
$X = 0.25\,a_{Pd}^{100}$ $Y = 0.375\,a_{Pd}^{100}$
$Z = 2.0$ Å $d = 1.3$ Å

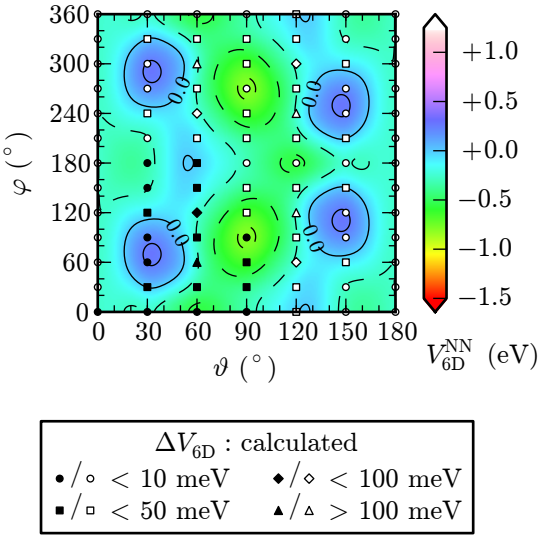

Figure B.3.3.12.:
$X = 0.25\,a_{Pd}^{100}$ $Y = 0.5\,a_{Pd}^{100}$
$Z = 2.0$ Å $d = 1.3$ Å

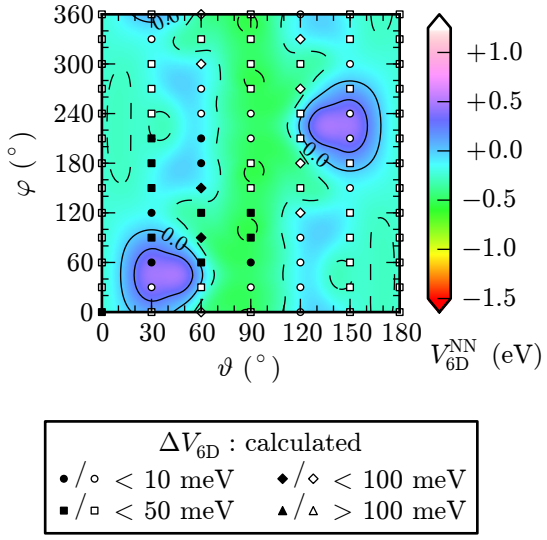

Figure B.3.3.13.:
$X = 0.375\,a_{Pd}^{100}$ $Y = 0.375\,a_{Pd}^{100}$
$Z = 2.0$ Å $d = 1.3$ Å

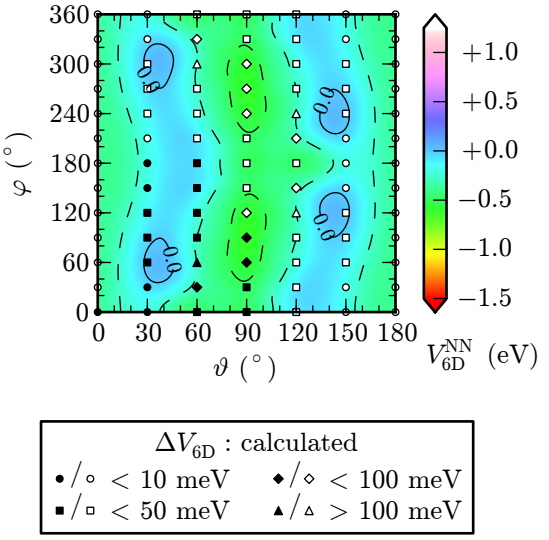

Figure B.3.3.14.:
$X = 0.375\,a_{Pd}^{100}$ $Y = 0.5\,a_{Pd}^{100}$
$Z = 2.0$ Å $d = 1.3$ Å

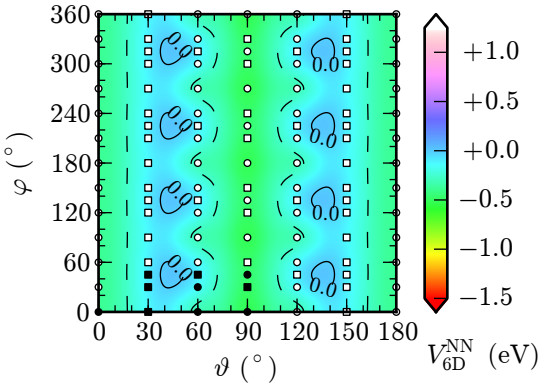

ΔV_{6D} : calculated	
•/∘ $<$ 10 meV	◆/◇ $<$ 100 meV
■/□ $<$ 50 meV	▲/△ $>$ 100 meV

Figure B.3.3.15.:
$X = 0.5\,a_{Pd}^{100}$ $Y = 0.5\,a_{Pd}^{100}$
$Z = 2.0$ Å $d = 1.3$ Å

B.3.4. Height $Z = 1.5$ Å

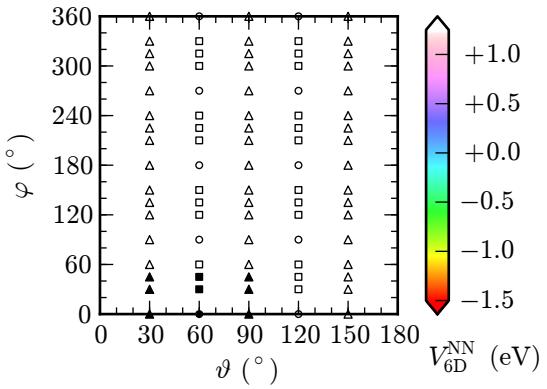

ΔV_{6D} : calculated	
•/∘ $<$ 10 meV	◆/◇ $<$ 100 meV
■/□ $<$ 50 meV	▲/△ $>$ 100 meV

Figure B.3.4.1.:
$X = 0.0\,a_{Pd}^{100}$ $Y = 0.0\,a_{Pd}^{100}$
$Z = 1.5$ Å $d = 1.3$ Å

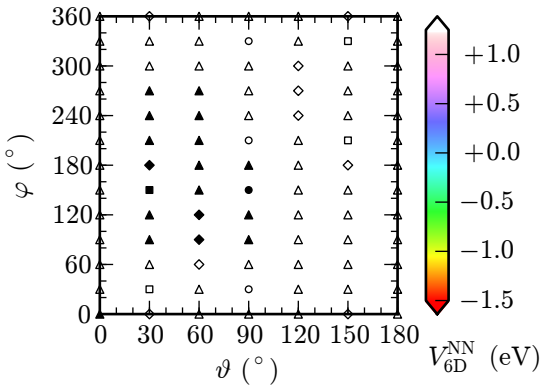

ΔV_{6D} : calculated	
•/∘ $<$ 10 meV	◆/◇ $<$ 100 meV
■/□ $<$ 50 meV	▲/△ $>$ 100 meV

Figure B.3.4.2.:
$X = 0.0\,a_{Pd}^{100}$ $Y = 0.125\,a_{Pd}^{100}$
$Z = 1.5$ Å $d = 1.3$ Å

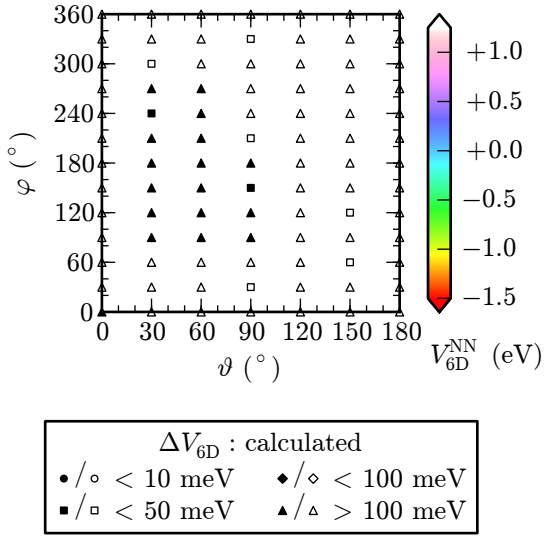

Figure B.3.4.3.:
$X = 0.0\,a_{Pd}^{100}$ $Y = 0.25\,a_{Pd}^{100}$
$Z = 1.5$ Å $d = 1.3$ Å

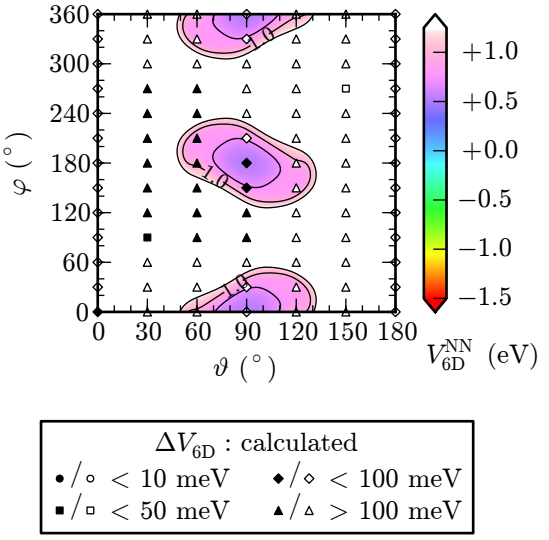

Figure B.3.4.4.:
$X = 0.0\,a_{Pd}^{100}$ $Y = 0.375\,a_{Pd}^{100}$
$Z = 1.5$ Å $d = 1.3$ Å

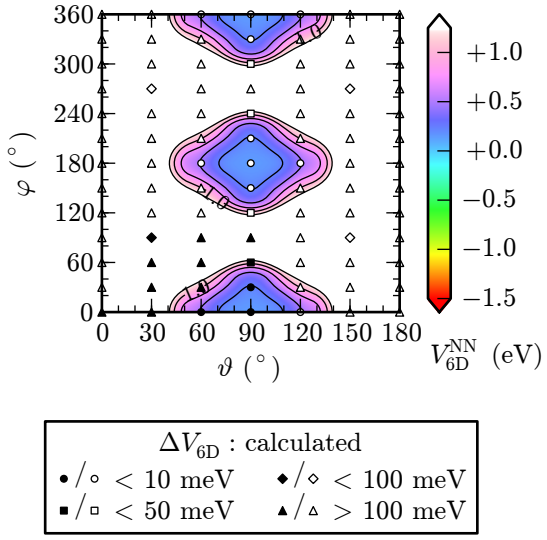

Figure B.3.4.5.:
$X = 0.0\,a_{Pd}^{100}$ $Y = 0.5\,a_{Pd}^{100}$
$Z = 1.5$ Å $d = 1.3$ Å

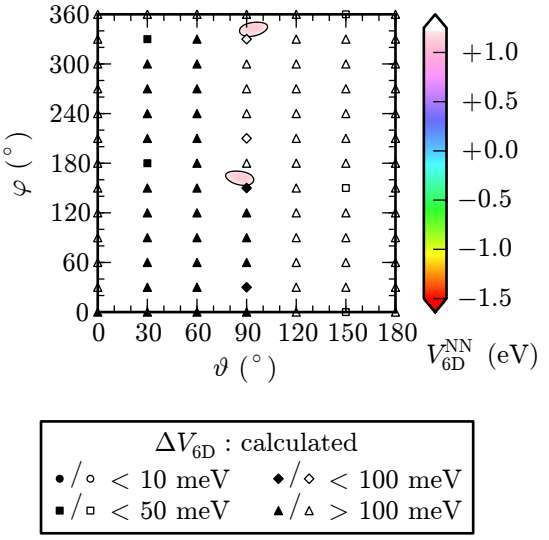

Figure B.3.4.6.:
$X = 0.125\,a_{Pd}^{100}$ $Y = 0.25\,a_{Pd}^{100}$
$Z = 1.5$ Å $d = 1.3$ Å

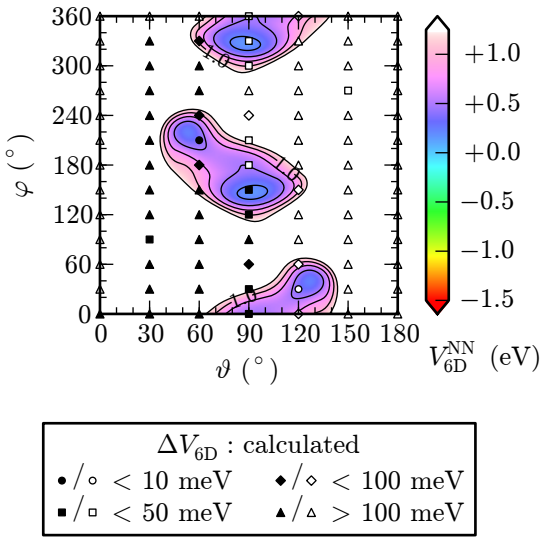

Figure B.3.4.7.:
$X = 0.125\,a_{Pd}^{100}$ $Y = 0.375\,a_{Pd}^{100}$
$Z = 1.5$ Å $d = 1.3$ Å

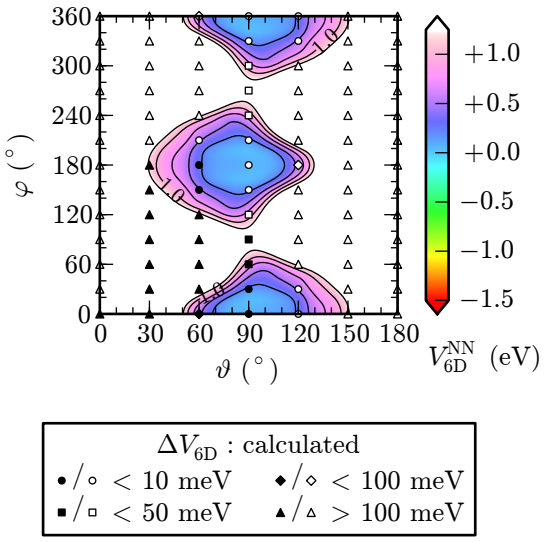

Figure B.3.4.8.:
$X = 0.125\,a_{Pd}^{100}$ $Y = 0.5\,a_{Pd}^{100}$
$Z = 1.5$ Å $d = 1.3$ Å

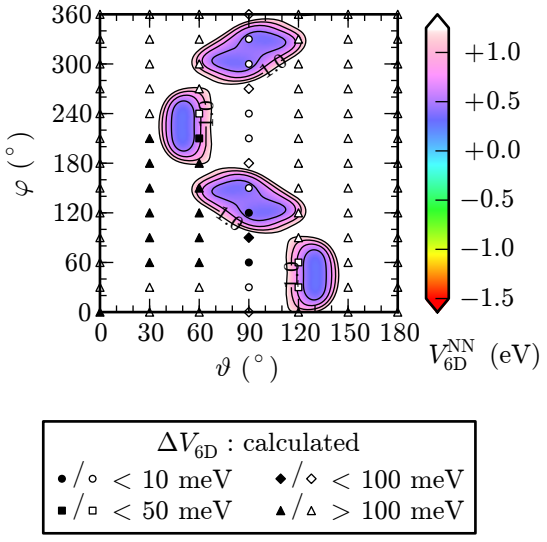

Figure B.3.4.9.:
$X = 0.25\,a_{Pd}^{100}$ $Y = 0.25\,a_{Pd}^{100}$
$Z = 1.5$ Å $d = 1.3$ Å

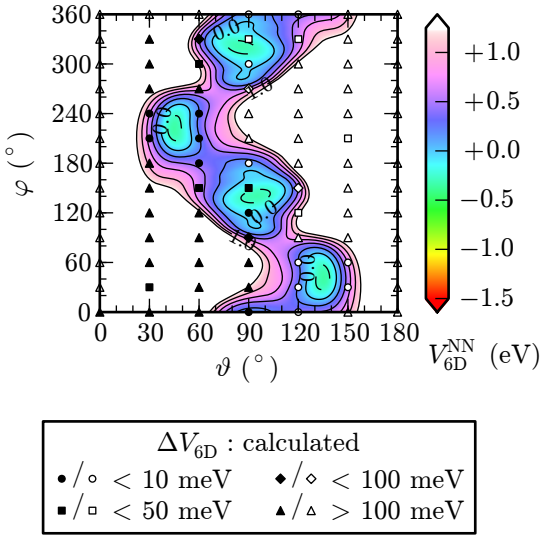

Figure B.3.4.10.:
$X = 0.25\,a_{Pd}^{100}$ $Y = 0.375\,a_{Pd}^{100}$
$Z = 1.5$ Å $d = 1.3$ Å

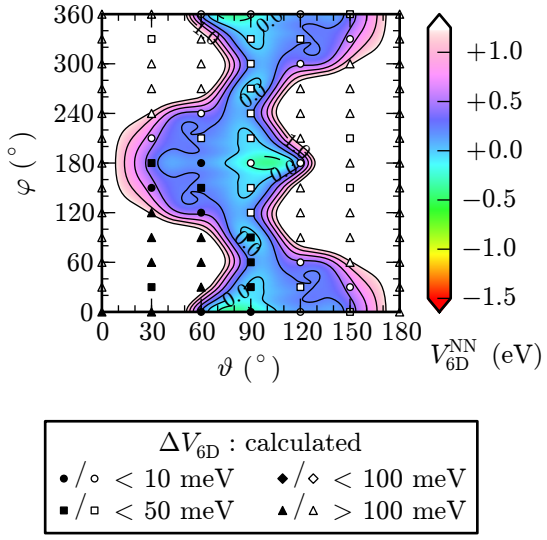

ΔV_{6D} : calculated	
•/◦ $<$ 10 meV	◆/◇ $<$ 100 meV
■/□ $<$ 50 meV	▲/△ $>$ 100 meV

Figure B.3.4.11.:
$X = 0.25\,a_{Pd}^{100}$ $Y = 0.5\,a_{Pd}^{100}$
$Z = 1.5$ Å $d = 1.3$ Å

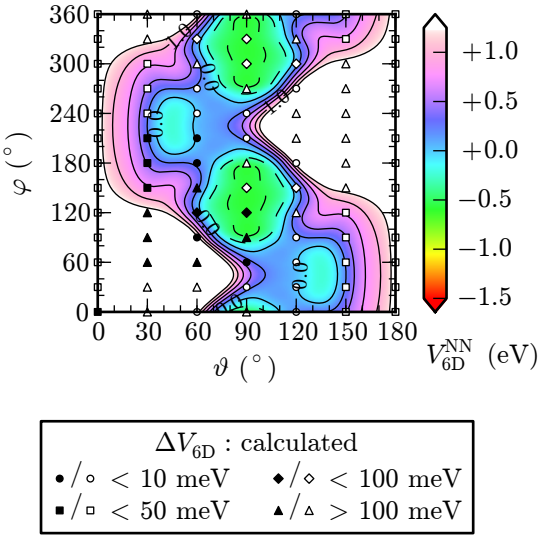

ΔV_{6D} : calculated	
•/◦ $<$ 10 meV	◆/◇ $<$ 100 meV
■/□ $<$ 50 meV	▲/△ $>$ 100 meV

Figure B.3.4.12.:
$X = 0.375\,a_{Pd}^{100}$ $Y = 0.375\,a_{Pd}^{100}$
$Z = 1.5$ Å $d = 1.3$ Å

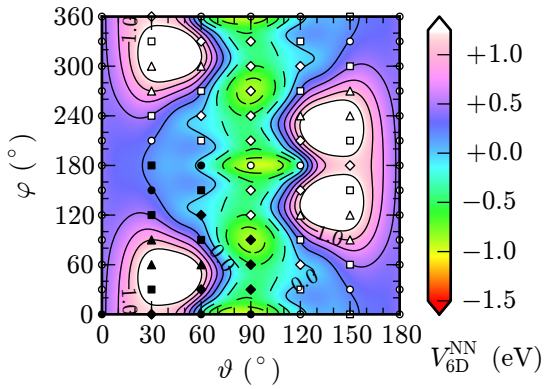

ΔV_{6D} : calculated	
•/◦ $<$ 10 meV	◆/◇ $<$ 100 meV
■/□ $<$ 50 meV	▲/△ $>$ 100 meV

Figure B.3.4.13.:
$X = 0.375\,a_{Pd}^{100}$ $Y = 0.5\,a_{Pd}^{100}$
$Z = 1.5$ Å $d = 1.3$ Å

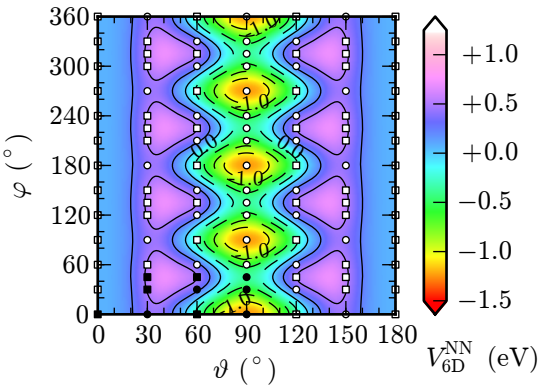

ΔV_{6D} : calculated	
•/◦ $<$ 10 meV	◆/◇ $<$ 100 meV
■/□ $<$ 50 meV	▲/△ $>$ 100 meV

Figure B.3.4.14.:
$X = 0.5\,a_{Pd}^{100}$ $Y = 0.5\,a_{Pd}^{100}$
$Z = 1.5$ Å $d = 1.3$ Å

B.4. Interpolation Errors

The plots that follow here summarize the mean average deviations (MADs) and root mean square errors (RMSEs) of the finally obtained best NN fit for individual groups of data points that are described by the captions below. Plots of this kind have greatly helped to monitor and improve the quality of the NN description as detailed in Section 6.2.2.

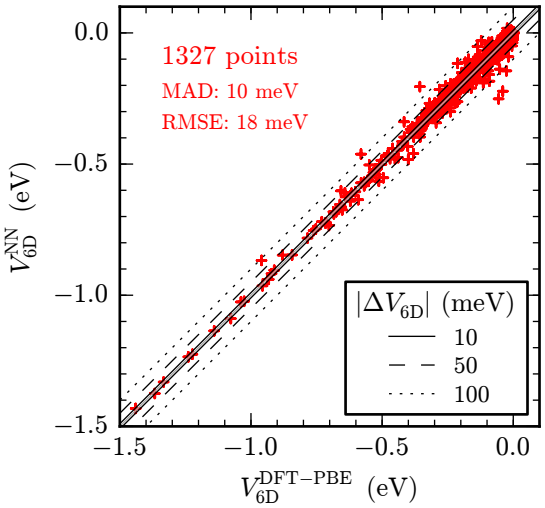

Figure B.4.1.:
$V_{6D} \leq 0\,\text{eV}$

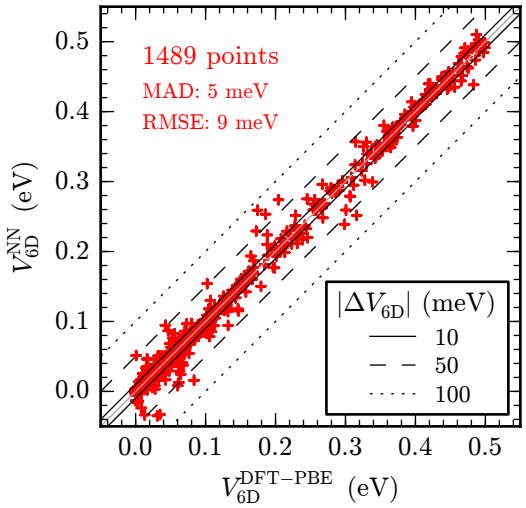

Figure B.4.2.:
$0\,\text{eV} < V_{6D} < 0.5\,\text{eV}$

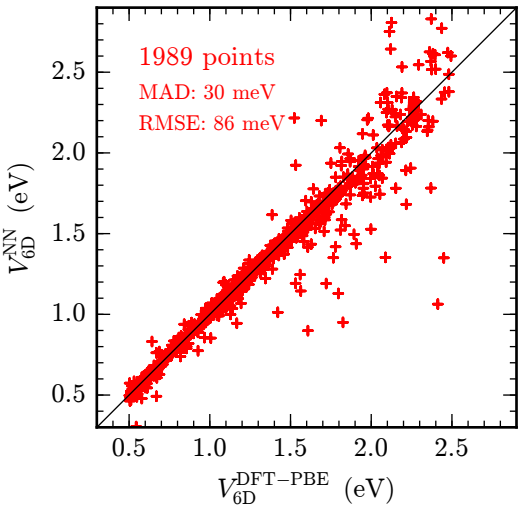

Figure B.4.3.:
$0.5\,\text{eV} < V_{6D} < 2.5\,\text{eV}$

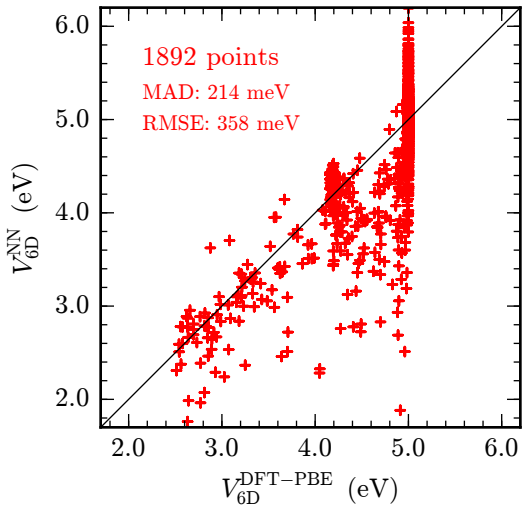

Figure B.4.4.:
$V_{6D} \geq 2.5\,\text{eV}$

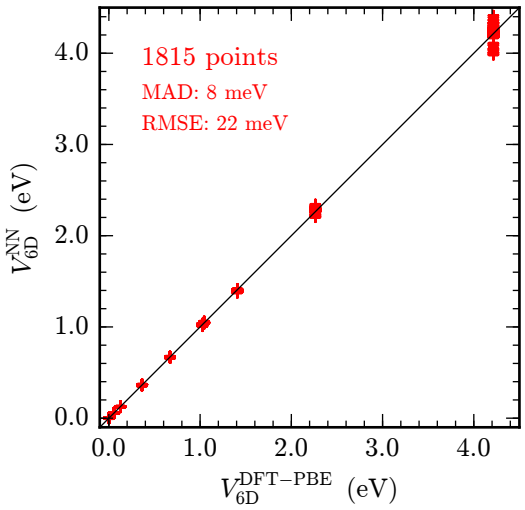

Figure B.4.5.:
$Z > 5\,\text{Å}$,
$1.0\,\text{Å} < d < 1.5\,\text{Å}$

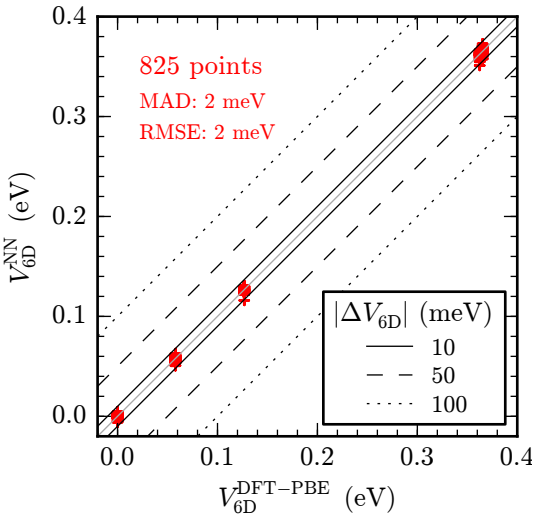

Figure B.4.6.:
$Z > 5\,\text{Å}$,
$1.15\,\text{Å} < d < 1.35\,\text{Å}$

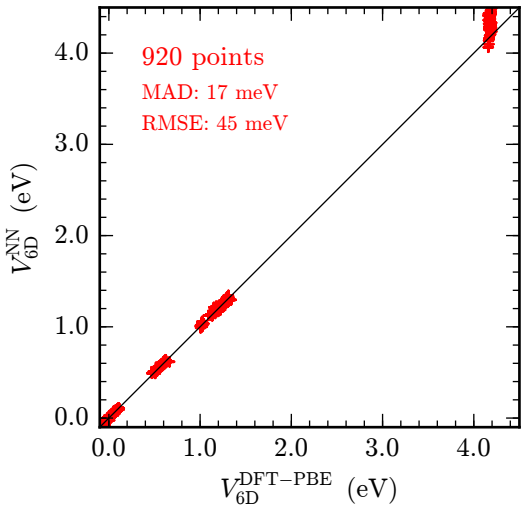

Figure B.4.7.:
$3.5\,\text{Å} \leq Z < 5.0\,\text{Å}$,
$1.0\,\text{Å} < d < 1.5\,\text{Å}$

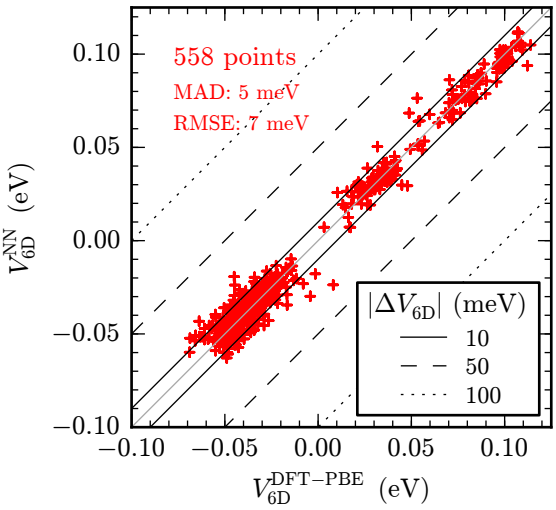

Figure B.4.8.:
$3.5\,\text{Å} \leq Z < 5.0\,\text{Å}$,
$1.2\,\text{Å} < d < 1.3\,\text{Å}$

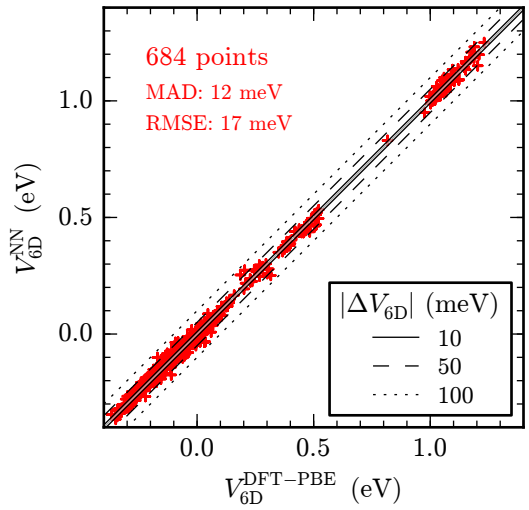

Figure B.4.9.:
$2.5\,\text{Å} \leq Z < 3.5\,\text{Å}$,
$1.1\,\text{Å} < d < 1.4\,\text{Å}$

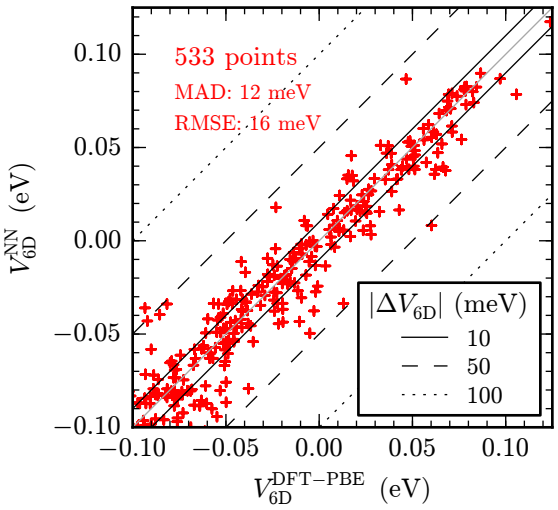

Figure B.4.10.:
$2.5\,\text{Å} \leq Z < 3.5\,\text{Å}$,
$1.2\,\text{Å} < d < 1.3\,\text{Å}$

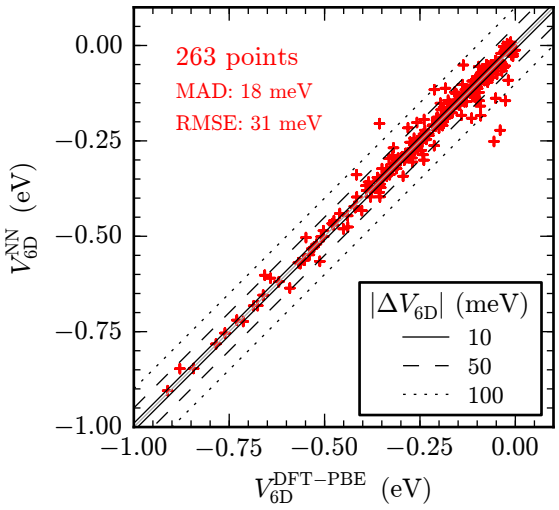

Figure B.4.11.:
$2.0\,\text{Å} \leq Z < 2.5\,\text{Å}$,
$1.1\,\text{Å} < d < 1.4\,\text{Å}$,
$V_{6D} \leq 0\,\text{eV}$

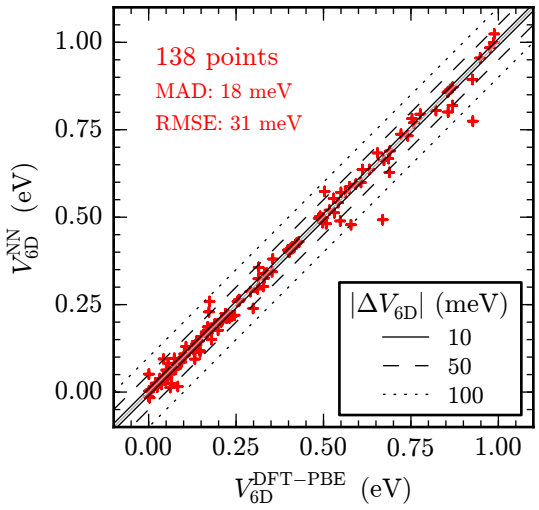

Figure B.4.12.:
$2.0\,\text{Å} \leq Z < 2.5\,\text{Å}$,
$1.1\,\text{Å} < d < 1.4\,\text{Å}$,
$0.0\,\text{eV} < V_{6D} < 1.0\,\text{eV}$

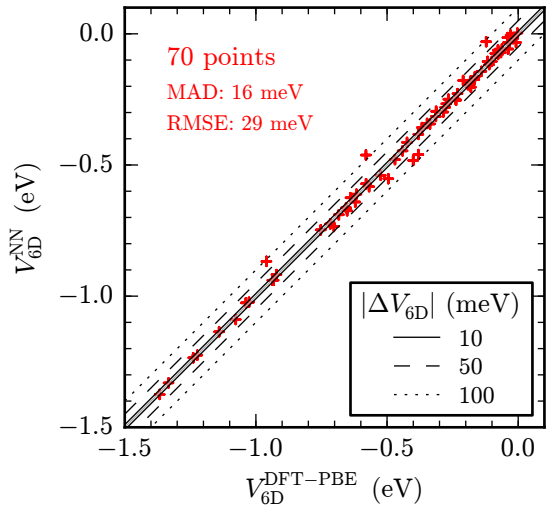

Figure B.4.13.:
$1.5\,\text{Å} \leq Z < 2.0\,\text{Å}$,
$1.1\,\text{Å} < d < 2.4\,\text{Å}$,
$V_{6D} \leq 0\,\text{eV}$

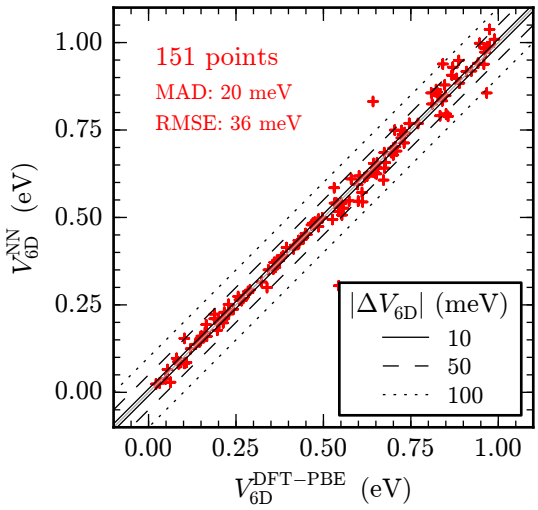

Figure B.4.14.:
$1.5\,\text{Å} \leq Z < 2.0\,\text{Å}$,
$1.1\,\text{Å} < d < 1.4\,\text{Å}$,
$0.0\,\text{eV} < V_{6D} < 1.0\,\text{eV}$

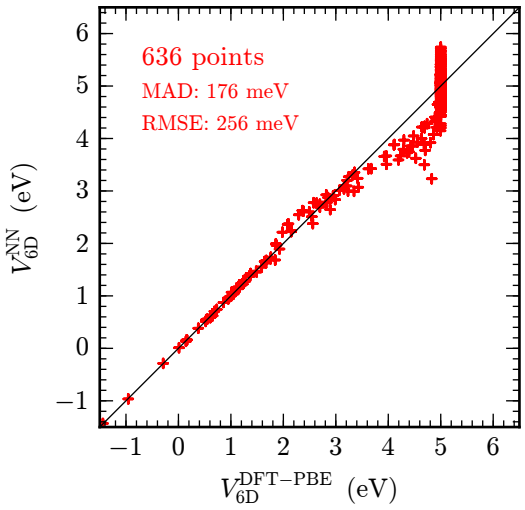

Figure B.4.15.:
$Z \leq 1.5\,\text{Å}$,
$1.0\,\text{Å} < d < 2.4\,\text{Å}$

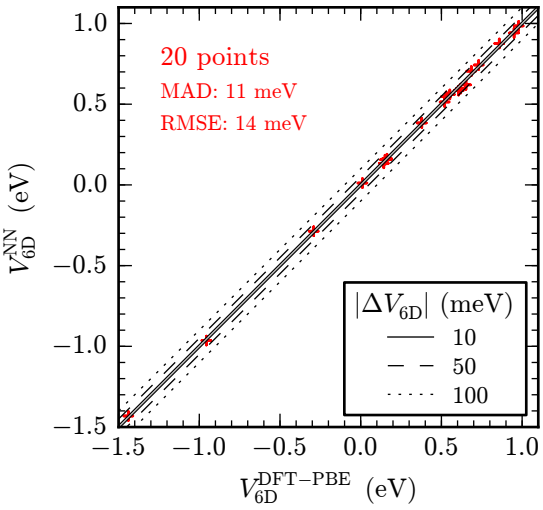

Figure B.4.16.:
$Z \leq 1.5\,\text{Å}$,
$1.0\,\text{Å} < d < 2.4\,\text{Å}$,
$V_{6D} \leq 1.0\,\text{eV}$

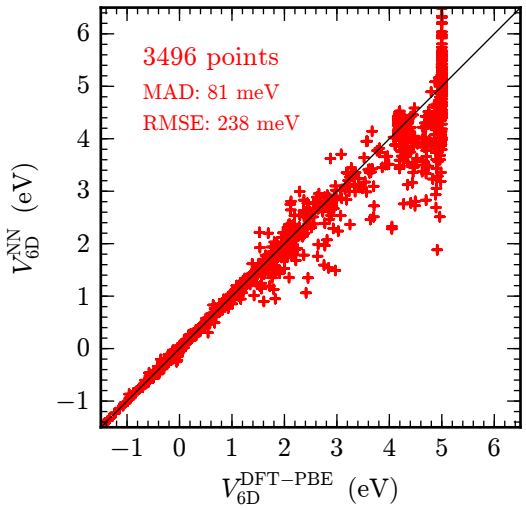

Figure B.4.17.:
DFT points

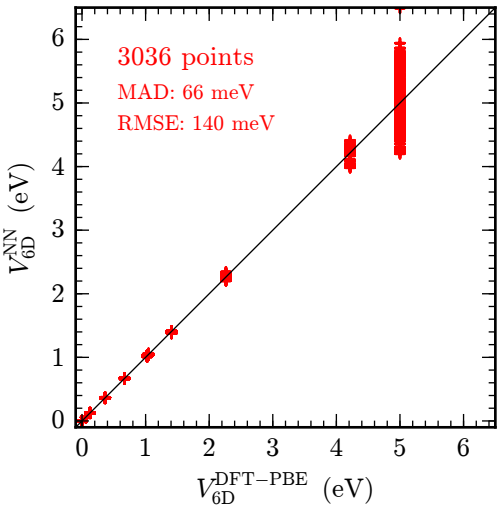

Figure B.4.18.:
added points

C. Electron-Hole Pairs: Supplemental Information

The following sections contain supplemental material to Chapter 7.

C.1. Implementation Details

C.1.1. Numerical Integration and Interpolation

In order to obtain the "dressed" matrix elements described by Eq. (7.12), a huge number of one-dimensional numerical integrations along a trajectory (using reaction coordinate representation in practice) have to be carried out. Details on how to obtain the necessary ingredients for the integrand have just been described in Sections 7.2.1 and 7.2.2. The according to Eq. (7.12) unbounded intervals do not cause any numerical problems, as the interaction of the impinging adsorbate as calculated within DFT rapidly vanishes with increasing distance from the surface. Therefore, "infinite" distance in Eqs. (7.4) and (7.6) is about 5 Å for most systems in practice (cf Chapter 6), so that the integration can be perfectly performed over a finite interval $(\underline{\tau}, \overline{\tau})$. Furthermore, it is worth noting that λ_{ij} are in general complex valued, and that Eq. (7.12) can be rewritten as a sum of four real valued integrals with oscillatory weight functions sin and cos:

$$\begin{aligned}
\lambda_{ij}^{\sigma} \approx & \int_{\underline{\tau}}^{\overline{\tau}} dt \, \mathrm{Re}\left(\frac{\partial}{\partial Q} v_{ij}^{\sigma}(t)\right) \cdot \dot{Q}(t) \cdot \cos\left(\frac{1}{\hbar}(\varepsilon_j^{\sigma} - \varepsilon_i^{\sigma})t\right) - \\
& \int_{\underline{\tau}}^{\overline{\tau}} dt \, \mathrm{Im}\left(\frac{\partial}{\partial Q} v_{ij}^{\sigma}(t)\right) \cdot \dot{Q}(t) \cdot \sin\left(\frac{1}{\hbar}(\varepsilon_j^{\sigma} - \varepsilon_i^{\sigma})t\right) + \\
& i \cdot \int_{\underline{\tau}}^{\overline{\tau}} dt \, \mathrm{Re}\left(\frac{\partial}{\partial Q} v_{ij}^{\sigma}(t)\right) \cdot \dot{Q}(t) \cdot \sin\left(\frac{1}{\hbar}(\varepsilon_j^{\sigma} - \varepsilon_i^{\sigma})t\right) + \\
& i \cdot \int_{\underline{\tau}}^{\overline{\tau}} dt \, \mathrm{Im}\left(\frac{\partial}{\partial Q} v_{ij}^{\sigma}(t)\right) \cdot \dot{Q}(t) \cdot \cos\left(\frac{1}{\hbar}(\varepsilon_j^{\sigma} - \varepsilon_i^{\sigma})t\right) \quad .
\end{aligned} \tag{C.1}$$

This is particularly important as specialized numerical integrators exist for these cases. Examples are those implemented in the `QAWO` and `QAWF` routines in the well-established QUADPACK package.[530]

Furthermore, as already indicated before in Section 7.2.1, matrix elements according to Eq. (7.26) are significantly more computationally expensive to evaluate than the velocities. Less values at potentially different points along a trajectory are hence typically available. Consequently, depending on the applied numerical integration scheme different parts of the integrands need to be interpolated before numerically "smooth" integrations can be carried out. As detailed in Section 7.2.2, the strategy chosen in this work to obtain matrix elements

according to Eq. (7.30) even relies on the (analytical) derivative of a suitable interpolation. In principle, the integrals could even be evaluated by analytical integration of the interpolated integrands. A flexible integration package is hence obviously required altogether. Unfortunately, a lot of well-established spline packages do not come with such functionality available for the interpolation function. Examples are Carl de Boor's Piecewise Polynomial Package PPPACK or John Burkhardt's SPLINE package. On the other hand, both Paul Dierckx's FITPACK package,[i] and its namesake by Alan Cline do provide derivatives and integrals, but only for a limited choice of interpolation functions.

With all that in mind and trying to stick to modern coding and to avoid reinventing the wheel, the GNU Scientific Library (GSL, available under *LGPL*) has been chosen as a convenient stockpile to supply required numerical routines.[531] Written in C, also publicly (under *GPL*) available Fortran wrappers written by Reinhold Bader (FGSL) are employed for it to become usable within the CASTEP code. This can be seen as a technical inconvenience, but Fortran compilers on most major computer architectures are getting more and more adept to offer interoperability with C that even works in practice. However, this is easily outweighed by the advantages for present purposes, in particular during development: Consistent interfaces allow for an easy exchange of different interpolation and integration routines provided within the library. The former encompasses (amongst others) several different flavors of splines, including derivatives and integrals, the latter the rewritten contents of the aforementioned well-established QUADPACK package. Furthermore, a consistent, modern error handling framework facilitates to conveniently monitor numerical integration errors (also if the surrounding code is parallelized). All of this is made proper use of to detect and avoid numerical errors induced by the implementation. Finally, local employment of GSL library routines ensures ease of exchangeability by native Fortran counterparts in the future (based on the experiences from the development collected here).

C.1.2. Parallelization, Output and Restarting

Once all the λ_{ij} according to Eq. (7.12) have been calculated, they are stored in memory for multiple use in the spectra as given by Eqs. (7.14), (7.15a) and (7.15b). A pre-screening of the evaluation of individual λ_{ij} according to thresholds for the Fermi and δ-function factors in those equations as also discussed by Trail and coworkers[389] has been implemented as well. For the same reasons as in case of Timmer and Kratzer, *inter-*$\boldsymbol{k}$ transitions have not been considered. With the application to large systems in mind, parallelism has been added within the (at the point) existing parallel infrastructure of the CASTEP code: Operations required to obtain the matrix elements $\left\langle \varepsilon_j^\sigma \,|\, v^\sigma(\boldsymbol{Q}(t)) \,|\, \varepsilon_i^\sigma \right\rangle$ in Eq. (7.12) are computationally most intense and make use of $\boldsymbol{k}$-point and $\boldsymbol{G}$-vector (i.e. wave function coefficients) parallelism. Integrations for the squared moduli of the fractions involving individual λ_{ij} for different $\boldsymbol{k}$-points (whose indices are hidden together with those for different bands at each $\boldsymbol{k}$-point in the collective indices i and j) in Eqs. (7.14), (7.15a) and (7.15b) are calculated concurrently, only requiring minimal amount of communication for the (final) evaluation of the sums.[ii] Finally, intermediary results are written out to files at different stages, both for potential debugging and restart purposes, including fully parallelized input/ouput (I/O) operations. Results from a previous run are optimally reused automatically, if according files are detected in a subsequent run. Several core

[i] also see http://nalag.cs.kuleuven.be/research/topics/fitpack.shtml

[ii] With the recent advent of bands parallelism in CASTEP 5.5,[148] further parallelization over band indices could be easily added.

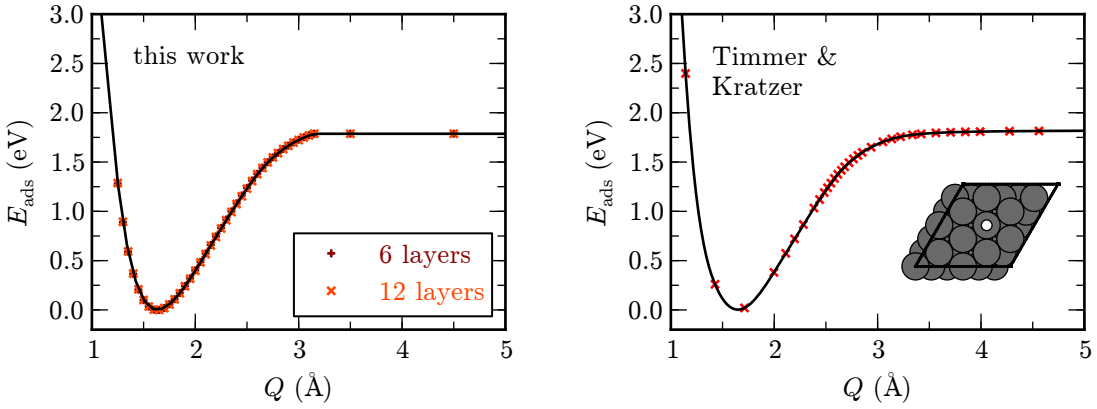

Figure C.1.: Chemisorption potential of a hydrogen atom above the top site on the (111) surface of aluminum (Q denotes distance from the surface). A typical Morse-potential shape is obtained. Left: Details to the results of the present work can be found in the text. Right: Plot reproduced based on Ref. 393, which considers a 12 layer system only. In both cases, points for which DFT total energies have been calculated are indicated by the markers.

routines of the CASTEP code needed to be modified (e.g. for reading of electronic structure input data) as their original design had not envisioned to be used in the present context.

C.2. Tests with H on Al(111)

In order to test the present independent and improved implementation of the perturbative approach to energy dissipation into electron-hole pairs as proposed by Timmer and Kratzer (cf Eqs. (7.14), (7.15a), (7.15b) and (7.19) in Sections 7.1.3 and 7.1.5 of Chapter 7),[393,396] the same system has been considered as in the aforementioned work of the two original authors: Impingement of a single hydrogen atom on a top site of the (111) surface of aluminum.

For this purpose, computational parameters have been synchronized between the two underlying plane-wave DFT-codes CASTEP (this work)[145,146] and PWSCF (Timmer & Krater)[532] wherever possible and reasonable. The exchange-correlation functional due to Perdew, Burke and Enzerhof (PBE)[85,86] has been used in both cases. However, deliberately to both improve convergence with respect to the plane-wave cutoff energy and study the influence on the calculated electron-hole pair properties, ultrasoft pseudopotentials[117,118] supplied within the CASTEP standard library have been used. This is of particular importance for the primary system of interest in this thesis (O_2 on Pd(100)), because a description with norm-conserving pseudopotentials would be very inconvenient in that case and besides would not allow to efficiently reuse calculated data from Chapter 6 besides. At a cutoff energy $E_{\text{cut}}^{\text{Al}} = 250\,\text{eV}$ and with a $12\times12\times12$ Monkhorst-Pack grid,[123] a bulk lattice constant of $a_0 = 4.048\,\text{Å}$ for the fcc-phase of aluminum is obtained (converged with respect to both parameters). This is in close agreement with the value of $a_0^{\text{TK}} = 4.061\,\text{Å}$ reported by Timmer and Kratzer[393,396] and somewhat closer to the tightly converged result of all-electron calculations and the experimental value, $a_0^{\text{AE}} = 4.04\,\text{Å}$ and $a_0^{\text{exp}} = 4.05\,\text{Å}$ respectively.[253]

The Al(111) surface has been modeled with $2\sqrt{3}\times2\sqrt{3}$ supercells of the (primitive) surface unit cell with 12 layers like in case of Timmer and Kratzer. In addition, 6 layer slabs have been constructed as well. They ease the computational burden when evaluating electron-hole

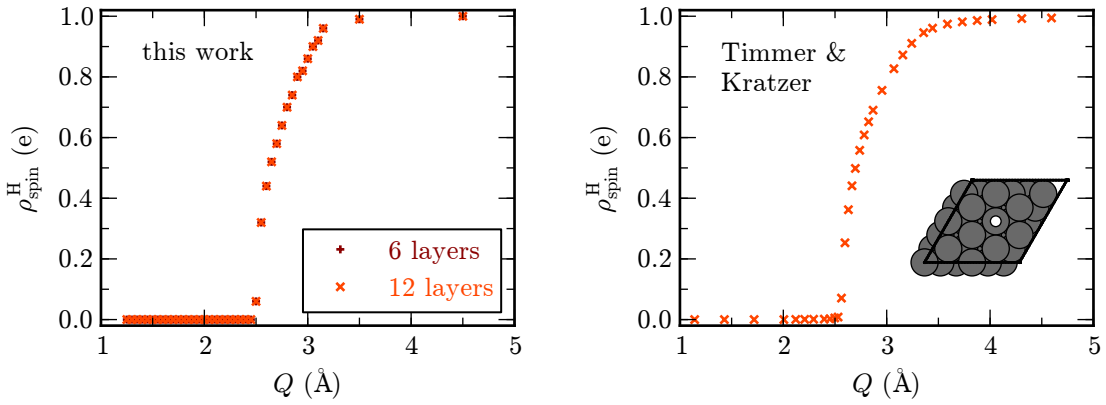

Figure C.2.: Adiabatic spin transition for H perpendiculary approaching the top site of Al(111) with Q denoting the distance from the surface. The spin density projected onto the hydrogen atom $\rho^{\mathrm{H}}_{\mathrm{spin}}$ is shown. Far away from the surface, the single unpaired electron of the "free" hydrogen atom leads to $\rho^{\mathrm{H}}_{\mathrm{spin}}(Q > 4\,\text{Å}) \approx 1\,\mathrm{e}$, whereas the spin is quenched with a typical $\sqrt{Q}$-behavior when approaching the surface. In the present work (left panel), a plane-wave implementation[409,410] of the population analysis scheme due to Mulliken[411] has been used, whereas in the work of Timmer and Kratzer (right panel)[393] the Löwdin approach was employed.[533] This accounts for the slight difference in the spin transition points at 2.5 Å and 2.6 Å, respectively.

pair properties during the development stage of the present implementation, and, in addition, allow to verify that there are no (unphysical!) changes with slab thickness. Relaxed interlayer distances have been obtained by fixing the three bottommost layers within corresponding 1×1 slabs. A vacuum of 12 Å ensures a sufficient decoupling across the periodic boundary conditions even when the adsorbate is included. In all cases, a $6 \times 6 \times 1$ Monkhorst-Pack grid has been employed here, which is the denser grid considered by Timmer and Kratzer,[393] together with a Fermi smearing of 10 meV to improve the convergence of the self-consistency cycles. When adding the hydrogen, whose pseudopotential is harder than the one for aluminum, the cutoff energy was raised to $E_{\mathrm{cut}} = 350\,\mathrm{eV}$, which is between the 286 eV and 544 eV (21 Ry and 40 Ry, respectively) reported in the original work.[393] However, the higher energy cutoff was only used to reveal underconvergence of the hydrogen binding energy by about 30 meV, i.e. all subsequent results have been obtained with the lower. Apart from that, Fig. C.1 shows that the agreement of the chemisorption potential of the hydrogen atom between both works is still excellent. Obviously, the interaction potential is well converged with the 6 layer slabs already. Here and in the following, a strictly one-dimentional trajectory of perpendicular impingement on a top site is considered, described by the coordinate Q, which simply denotes the distance from the surface. Numerical integration using the velocity Verlet algorithm[213] with a starting distance $Q(t=0) = 3.16\,\text{Å}$ and velocity $\dot{Q}(t=0) \approx 34\,\text{Å}\,\mathrm{ps}^{-1}$ corresponding to an initial kinetic energy $E^0_{\mathrm{kin}} = 60\,\mathrm{meV}$ yield a total time of 20 fs for one half round trip. Hence apparently also the same trajectory as in Ref. 393 is obtained when the same initial conditions are used. Of course, this is not surprising, thanks to the good agreement of the chemisorption potential.

Figure C.2 illustrates similarly good agreement for the description of the spin transition in an adiabatic picture. In both cases, the typical[73] $\sqrt{Q}$-behavior is obtained for quenching of the spin when approaching the surface. Again, the 6 and 12 layer slabs employed in this work yield the same results. Two different projection schemes are used to obtain the spin density associated

with the hydrogen atom $\rho^{\mathrm{H}}_{\mathrm{spin}} = \rho^{\mathrm{H}}_{\uparrow} - \rho^{\mathrm{H}}_{\downarrow}$: In this work, a plane-wave implementation[410] of Mulliken's approach[411] is used, whereas Timmer and Kratzer employed the Löwdin scheme[533] implemented in PWSCF. Both are known to give similar results,[409] but nevertheless the slight difference of the spin transition points at 2.5 Å and 2.6 Å, respectively, is attributed to those two the different projections.

Finally, spectra according to Eqs. (7.15a) and (7.15b) and Eq. (7.14) in Section 7.1.3 for one half round trip along the aforementioned trajectory have been evaluated. Matrix elements according to Eq. (7.12) corresponding to excitations with excitation energies $|\hbar\omega| \leq 10\,\mathrm{meV}$ relative to the Fermi level of the aluminum slabs have not been included in the calculations resulting in Figs. C.3 and C.4. As Timmer and Kratzer have already noted,[393] this special care must be taken in the range of the broadening applied during the self-consistency iterations (see above) due to numerical difficulties although the corresponding contributions are analytically well defined. What is of highest importance for present purposes (and hence has been carefully verified) is that it has negligible influence on the energies dissipated into electron-hole pair as calculated by Eq. (7.19). In order to scrutinize the convergence of the matrix elements when evaluated according to Eq. (7.30) and verify the robustness of the employed interpolation and numerical integration techniques as detailed in Section 7.2.2 and Appendix C.1.1, first electronic structure data from only 20 configurations along the trajectory has been calculated and considered. In a second step, 21 more points were added, efficiently exploiting density extrapolation during the self-consistency iterations. Changes to the spectra and dissipated energies were negligible, but the `QAGS` adaptive integrator has been found to be most numerically stable (for details see Appendix C.1.1). Finally, the spectra shown in Figs. C.3 and C.4 have been obtained by using this integrator together with all the available points.

As before, electron and hole pair spectra given by Eqs. (7.15a) and (7.15b) are in good agreement with those in Ref. 393, which is illustrated in Fig. C.3. The hole spectra ($\hbar\omega < 0\,\mathrm{eV}$) match perfectly with results for 6 and 12 layers being almost identical. Tiny differences in the tail towards higher energies for the electron spectra $P^{\sigma}_{\mathrm{ex,el}}(\hbar\omega)$ in case of the 12 layer system are attributed to the fact that the number of empty bands has not been raised sufficiently. More empty states covering a larger energy interval above the Fermi energy have been calculated for the 6 layer system. According to the good agreement in case of the hole spectra, the better agreement of the latter with the 12 layer system considered in Ref. 393 is hence not surprising. By analysing the decay of relevant matrix elements for both systems, this has been confirmed as the reason for the slightly worse agreement. The number of calculated empty bands is hence an important convergence parameter for the spectra to be taken into account which can be verified *a posteriori* by the aforementioned analysis.

Obviously, according to Eq. (7.14), the differences in the tail towards higher energies for the electron spectra of the 12 layer system carry over to the excitation spectra shown in Fig. C.4. Due to the exponential decay of the excitation probabilities, the energy dissipated into electron-hole pair excitations given by Eq. (7.19) (summed over both spin channels) remains largely unaffected – and is in excellent agreement with the result of Ref. 393. It is worth noting that energies dissipated in both individual spin channels are identical to half the total dissipated energies E^{6L}_{eh} and E^{12L}_{eh} given in Fig. C.4 for the electron-hole pair spectra given in 6 layer and 12 layer systems, respectively. Finally, the reader is reminded that this energy is of paramount importance for the purposes of this thesis, and deviations in the order of several millielectron volts are of negligible concern when dissipation of chemisorption energies in the order of several electron volts are considered.

Altogether, the reference results by Timmer and Kratzer for the test case of a H atom

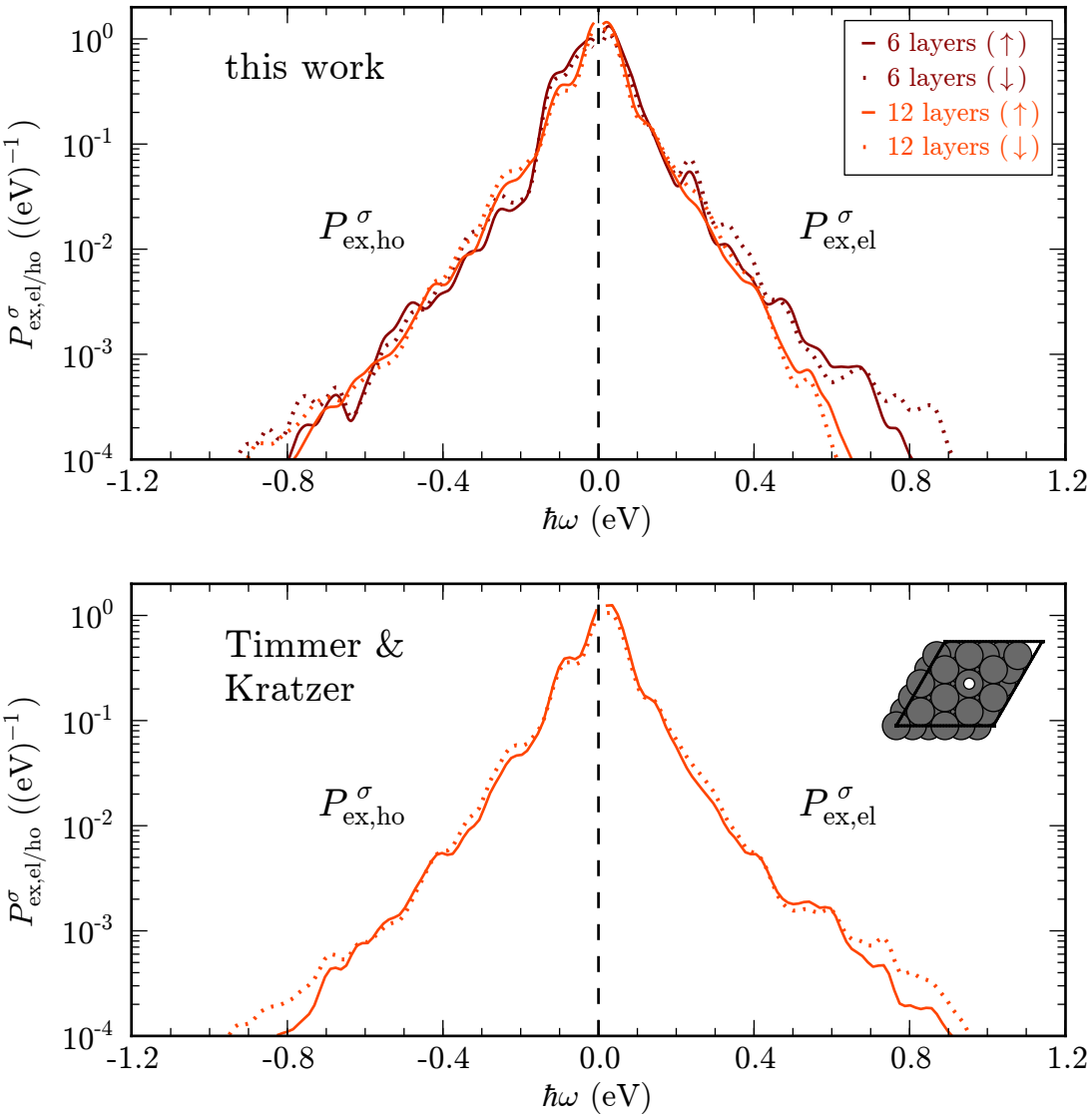

Figure C.3.: Spin dependent excitation spectra for electrons $P^{\sigma}_{\mathrm{ex,el}}(\hbar\omega > 0)$ and holes $P^{\sigma}_{\mathrm{ex,ho}}(\hbar\omega < 0)$ with $\sigma \in \{\uparrow,\downarrow\}$ for H impinging perpendicularly on a top site of Al(111). The former are given by Eqs. (7.15a) and (7.15b) in Section 7.1.3 for excitation energies $\hbar\omega$ relative to the Fermi energy of the aluminum surface. Values in the interval $|\hbar\omega| \leq 10\,\mathrm{meV}$ closely around the latter are not plotted due to numerical inaccuracies. A starting distance $Q(t = 0) = 3.16\,\text{Å}$ and velocity $\dot{Q}(t = 0) \approx 34\,\text{Å}\,\mathrm{ps}^{-1}$ corresponding to a kinetic energy $E^{0}_{\mathrm{kin}} = 60\,\mathrm{meV}$ are the initial conditions of the considered trajectory, a half round trip ending at 20 fs. Differences in the electron spectra in the tail towards higher energies between the present work (top panel) and Ref. 393 (bottom panel) are due insufficent amount of empty bands that have been calculated as detailed in the text.

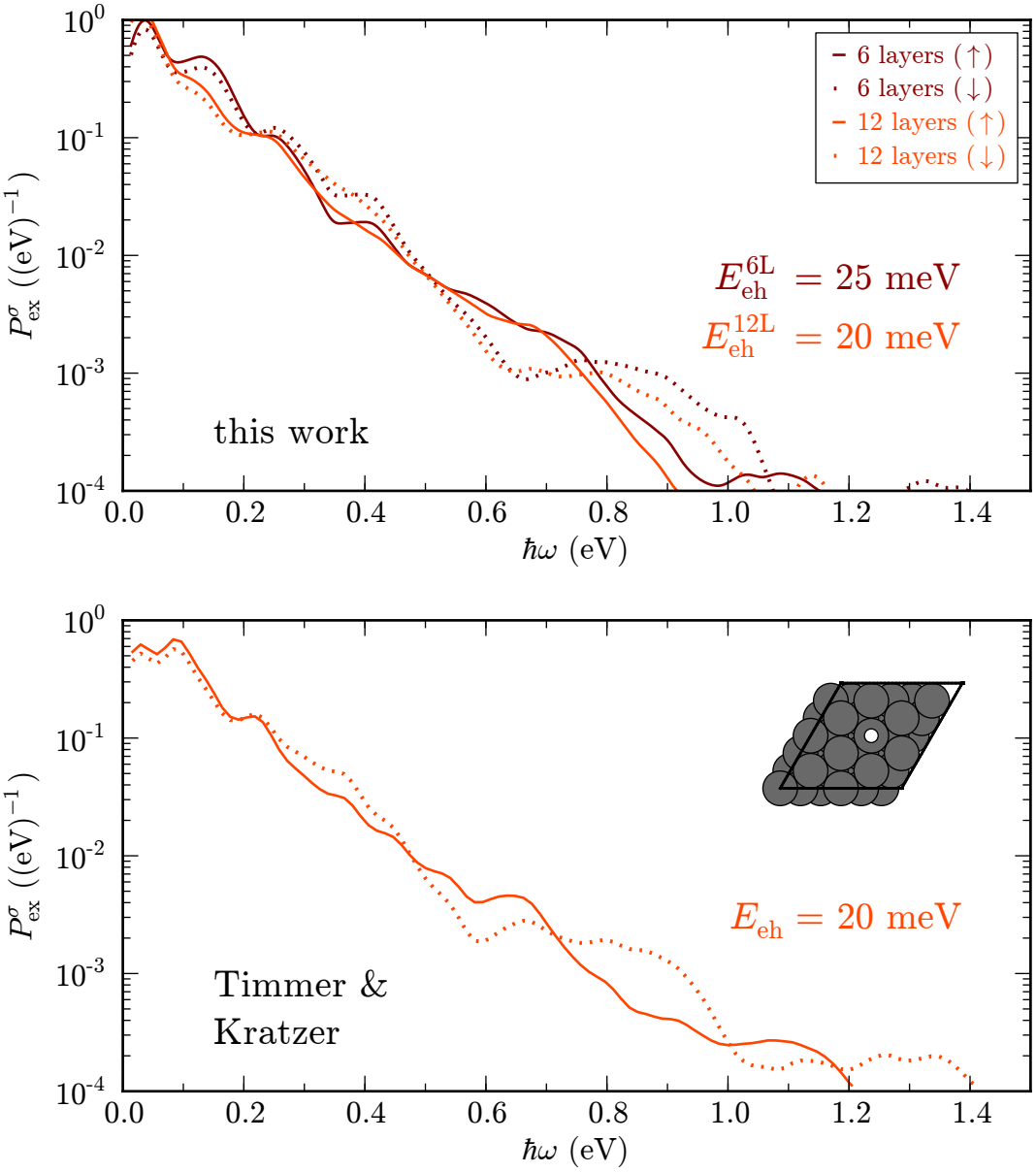

Figure C.4.: Spin dependent electron-hole pair excitation spectra $P_{\mathrm{ex}}^{\sigma}(\hbar\omega > 0)$ with $\sigma \in \{\uparrow, \downarrow\}$ as given by Eq. (7.14) in Section 7.1.3 for H impinging on a on-top site of Al(111). The trajectory is the same as the one considered in Fig. C.3 (see caption for details), and like there no values are plotted for excitation energies $\hbar\omega \leq 10\,\mathrm{meV}$ around the Fermi level of the aluminum surface. Energies dissipated in both individual spin channels are identical to half the total dissipated energies E_{eh}^{6L} and E_{eh}^{12L}. Note that due to their exponential decay differences between this work (top panel) and Ref. 393 (bottom panel) do not affect the good agreement of the latter.

impinging on a top site of the Al(111) surface[393] are excellently reproduced by the present implementation. The use of ultrasoft potentials yields negligible deviations in practice despite potential conceptual difficulties (cf Section 7.2.2),[407] and the same hold for slabs with only 6 layers. Both is important to know for the application to O_2 on Pd(100) described in Section 7.3. Furthermore, thanks to improvements in algorithm (as detailed in Section 7.2.2 and Appendix C.1.2) and parallelism, run times for the evaluation of the spectra could be reduced by about one to two orders of magnitude.[394,396,407]

C.3. Trajectories for O_2 on Pd(100)

Unlike in case of the large number of trajectories obtained for the determination of the initial sticking coefficient here output of coordinates and velocities is obviously required for every integrated time step. Therefore, the corresponding molecular dynamics routines had also to be modified. The reaction coordinate has been constructed according to Eqs. (7.22) and (7.23) such that it describes at the start of each trajectory the center of mass distance from the surface. Comparison has shown that motion is rather rigid for all trajectories considered here, i.e. a corresponding reaction coordinate constructed for the center of mass and concomitant velocities are essentially identical. The employed Bulirsch-Stoer integrator with its varying and possibly large time steps (cf Section 3.3.2 in Part I) has been found to be sufficient for the discretization of reaction coordinate Q and corresponding velocities $\dot{Q}$ as given by Eqs. (7.24) and (7.25) – also thanks to the interpolation described in Section 7.2.1.

D. Extensions to the LAMMPS Code

The results presented in Chapter 9 and Chapter 10 of Part III have been obtained based on the classical molecular dynamics code LAMMPS,[218] which is freely available.[i] While the provided documentation[ii] is exemplary and excellent for a conventional user, only most common entry points for code developers are pointed out therein – as required for straightforward add-ons. More elaborate extensions as required within the scope of this thesis demand intense reading into certain parts of the presently over 170,000 lines of the LAMMPS code in order to grasp the general code structure. Therefore, first, a short overview about the latter is given, focusing on aspects which are of particular relevance in the present context. Here and in the following, the reader is assumed to be familiar with the basic concepts of object oriented programming. Afterwards, the individual extensions are described. In perfect compliance with the paradigm proclaimed by the main developers, they are each capsuled into independent modular pieces – not requiring any further modifications of core parts of the code. They have not been committed back to the main development line yet – despite their apparent maturity and robustness throughout the use for the present work. Of course, should there turn out to be a more general interest in these developments, this will happen supplementary in full compliance with the *GPL*.

D.1. Overview

While low-level parts like IO operations or actual computations are written in a procedural fashion, i.e. "vanilla C-style code", hi-level structures including scientific algorithms are implemented according to an *object-oriented* programing paradigm within C++. This is how the extremely modular design of the LAMMPS code is facilitated in practice. An overview about top-level classes (with no claim of completeness) and others which have been of particular importance for the present thesis and the code extensions crafted therein is given by Fig. D.1. The actual "main" program merely instantiates a `LAMMPS` object and is thus incredibly short *per se*. For this reason, a consequence of the well-thought-out object-oriented design, LAMMPS can be easily coupled to a library in particular to other C++ or also C codes. However, since only very recently, also Python bindings are under "official" development.[iii] This is why the LAMMPS calculator class for the Atomic Simulation Environment (ASE) written by the present author still relies on files to communicate with LAMMPS.[iv]

[i] Licensed under GPL and avialable from `http://lammps.sandia.gov`.

[ii] The source code comes with a manual that is up-to-date, in the sense of being perfectly synchronized with the latter. A version that is continuously updated, following the modifications and extensions due to recent patches, which are individually provided via `http://lammps.sandia.gov/bug.html` or incorporated into recent snapshots obtainable from `http://lammps.sandia.gov/download.html`, is available online under `http://lammps.sandia.gov/doc/Manual.html`.

[iii] See `http://lammps.sandia.gov/doc/Section_howto.html#4_19` and `http://lammps.sandia.gov/doc/Section_python.html` of the on-line manual.

[iv] Further development stimulated after committing this code to the ASE community, see `https://wiki.fysik.dtu.dk/ase/ase/calculators/lammps.html`, now also allows to use `stdin` and `stdout` via pipes to provide

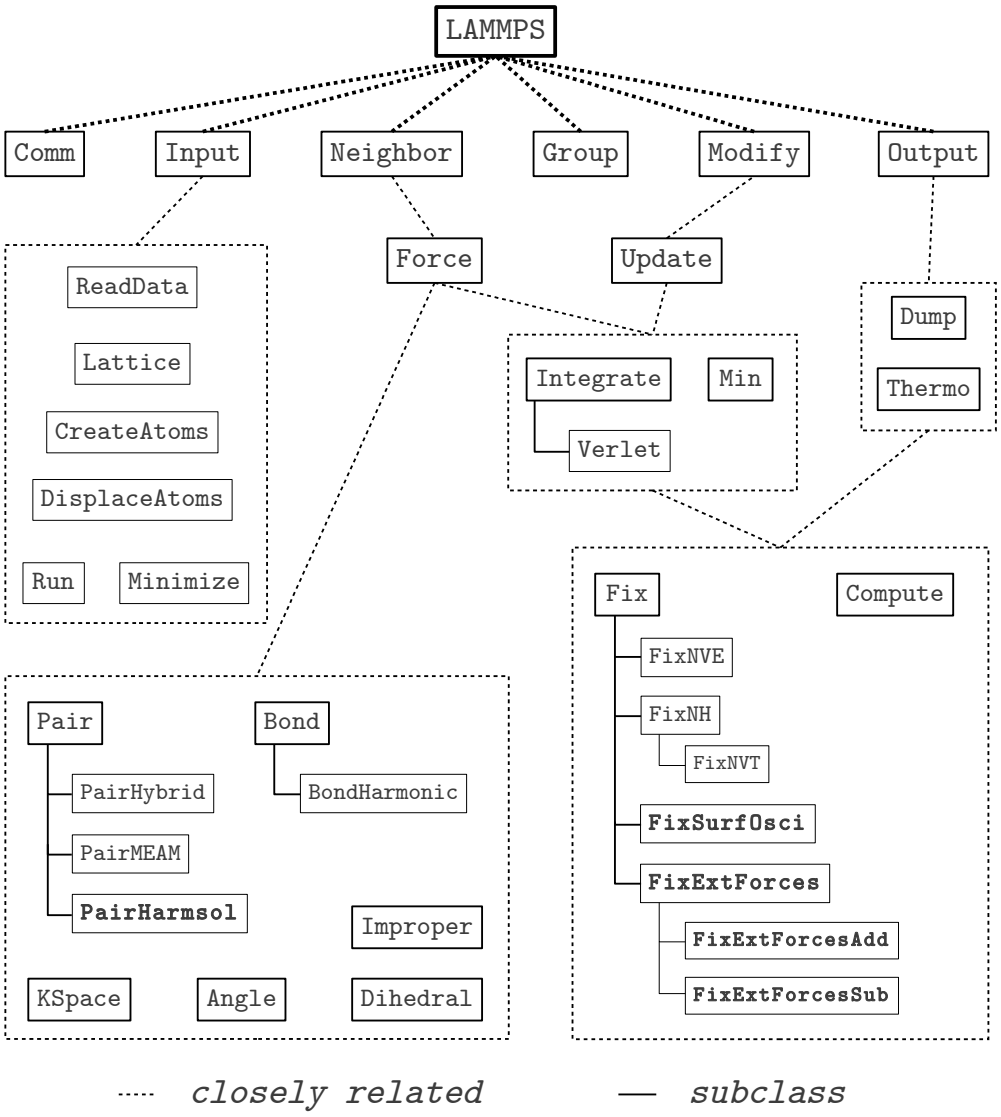

Figure D.1.: LAMMPS classes with particular relevance for this work and their relation to the most top-level layer within the present code design of the former. Classes encompassing code required for this thesis and thus written by the author of the latter as extensions to LAMMPS are highlighted by bold letters.

During instantiation of the `LAMMPS` object, first potential command line arguments are processed, followed by setting up general IO and (even before) the MPI-based communication infra structure[147] to potentially enable parallelism via a spatial-decomposition[218] of the simulation domain. The former is handled and administrated via `Comm` in the following. Input is first processed by an `Input` object, with certain parts potentially being delegated to others. Because the LAMMPS input script language is rather complex, this is not an entirely trivial task. Apart from general simulation parameters, like e.g. the desired boundary conditions, units or overall output options, also the initial "atomic arrangement" is set up at this stage. The input geometry can be read from files using a simple but LAMMPS specific data file format, which is handled by an instance of a `ReadData` and requested in the input script by a `read_data` command. Furthermore, combination of the `lattice` and `create_atoms` input commands is extremely powerful to automatically generate regularly spaced atoms like in a huge surface slab without specifying their individual coordinates explicitly, the latter being handled by a `CreateAtoms` object. Displacements of surfaces layers due to relaxation can then be conveniently adjusted by the `displace_atoms` input command, which hands this job over to an instance of `DisplaceAtoms`. Thanks to the `Group` object, subsets of atoms can be assigned to different groups, for which interaction potentials, properties and details of their structural evolution (i.e. all what is detailed in the following) can be defined and evaluated individually.

For the force calculations, which are centrally managed by the `Force` object, the classical interatomic interaction potentials and their parameters need to be specified. Following common practice in the classical molecular dynamics community, two-body, three-body and four-body contributions are separated into `Pair` and `Bond`, `Angle`, `Dihedral` and `Improper`, respectively. Apart from actual computations, individual subclasses for particular functional forms of these contributions also typically handle the processing of the corresponding input parameters. So-called "hybrid styles" like e.g. `PairHybrid` allow to combine different flavors of the same contribution type in a more or less arbitrary fashion. Different definitions can be made and applied to different groups that have been defined before. As the many-body aspects of the modified embedded atom method (MEAM) are usually accounted for based on nearest neighbors, it is not surprising that `PairMEAM` is derived from `Pair`. It provides the link to the external Fortran code written by Greg Wagner[198] (cf Section 3.2.2). In periodic systems, long range pair interactions can be treated more efficiently with the help of the `KSpace` class and the contents of the `KSPACE` package. This has not been necessary in the present context. The type of interactions determines the neighbor lists and their sizes, which are handled by the `Neighbor` object (cf Section 3.4). In addition, when Newton's third law of actions and reactions is made use of, which has to be supported by the individual respective descendants of `Pair` and `Bond` and can be controlled globally by the input command `newton`, only half neighbor lists are built accordingly.

Very individual output can be tailored and requested via the input script. Overall, it is managed by the `Output` object, with `Thermo` and `Dump` (and the subclasses of the latter) being responsible for outputting intensive and extensive quantities, respectively. Both are internally provided by objects derived from `Compute`, which can be defined individually for each previously defined group.

Most importantly, the input structure can be evolved by the input commands `minimize` and `run`, processed internally by the homonymous classes `Minimize` and `Run`. The former performs relaxations, i.e. energy minimizations of the input geometry according to various

input to and receive results from LAMMPS, respectively.

currently implemented common algorithms (e.g. steepest descent, conjugate gradients), which are all derived from `Min`. The latter command runs molecular dynamics, utilizing integrators descending from the `Integrate` class. The overall responsibility for the structural evolution lies with the `Modify` object, whereas `Update` handles a few detailed preparations and housekeeping tasks (like e.g. setting unit conversion factors), and, most importantly, stores the currently used value for the time step Δt. More precisely, when a `run` command is encountered in the input, `update->integrate->run()` is executed. Here and in the following, attributes and methods are indicated as usual by `->` and `()`, respectively, but arguments of the latter are omitted for the sake of simplicity. Within the scope of this thesis, the `Integrate` object is always an instance of the `Verlet` class.[v] It implements the framework of an integration scheme which is suitable for the velocity Verlet algorithm[213]. Operations which modify properties of the simulation during such a so-called time stepping are referred to as fixes, accordingly derived from the `Fix` class and defined by `fix` command in the input. One very prominent descendant is `FixNVE`, which fits the individual steps of that aforementioned algorithm as given by Eqs. (3.33) in Section 3.3.1 of Part I into the time stepping implemented in the `run()` method of the `Verlet` class in the following way:

- `modify->initial_integrate()`
  This calls the corresponding `initial_integrate()` methods of all registered fixes. In `FixNVE`, an intermediary update of velocities

$$\dot{\boldsymbol{R}}_I\left(t+\frac{\Delta t}{2}\right) = \dot{\boldsymbol{R}}_I(t) \; + \; \frac{\boldsymbol{F}_I(t)}{2\,m_I}\,\Delta t \tag{D.1a}$$

  and the final update of positions

$$\boldsymbol{R}_I(\Delta t) = \boldsymbol{R}_I(t) \; + \; \dot{\boldsymbol{R}}_I\left(t+\frac{\Delta t}{2}\right)\,\Delta t \tag{D.1b}$$

  for the current time step, corresponding to Eqs. (3.33a) and (3.33b), is carried out in the respective method.

- `neighbor->decide()`
  Decides whether a neighbor list rebuild is necessary, exploiting the skin distance (cf Section 3.4), and triggers the latter if it is.

- `modify->pre_force()`
  Just before forces are calculated for the current time step, the corresponding `pre_force()` methods of all registered fixes are called.

- `force->[type]->compute()`
  As described above, the interatomic interactions specified for the current simulation are objects descending of `[type]`, i.e. `Pair` and `Bond`, `Angle`, `Dihedral`, `Improper` or `KSpace`.

[v] For the sake of completeness, another descendant of `Integrate` is the `Respa` class, implementing the reversible reference system propagator algorithm developed by Tuckerman and coworkers.[534] It allows to accelerate molecular dynamics simulations for systems where degrees of freedom performing fast and uninteresting oscillations can be "projected out", thus allowing to use larger time steps for the integration of the dynamics of the "more interesting" degrees of freedoms. Unfortunately, this could not be made use of within the scope of this thesis and is thus not indicated in Fig. D.1.

Their respective `compute()` method gets called by looping over them. This calculates the force contributions at the previously updated positions (cf Eq. (D.1b)):

$$\boldsymbol{F}_I\left(t+\Delta t\right) = -\boldsymbol{\nabla}_{\boldsymbol{R}_I} V_{\mathrm{N}}^{\mathrm{cl}}\left(\{\boldsymbol{R}_I\left(t+\Delta t\right)\}_I\right) \tag{D.1c}$$

Depending on whether Newton's third law is made use of, additional MPI communication might be required afterwards. Potential savings during force field evaluation have thus to be weighed carefully against cost of the latter.

- `modify->post_force()`
  Immediately after the force calculations for the current time step, this is where the corresponding `post_force()` methods of all registered fixes are called.

- `modify->final_integrate()`
  The `final_integrate()` methods of all registered fixes are called here. In `FixNVE`, the respective method performs the final velocity for the current time step

$$\dot{\boldsymbol{R}}_I\left(t+\Delta t\right) = \dot{\boldsymbol{R}}_I\left(t+\frac{\Delta t}{2}\right) + \frac{\boldsymbol{F}_I\left(t+\Delta t\right)}{2\,m_I}\,\Delta t \tag{D.1d}$$

  corresponding Eq. (3.33d) using the previously updated forces.

- `modify->end_of_step()`
  At the very end of each time step, the `end_of_step()` method of all registered fixes are called here, usually in order to update computed quantities stored within the fix.

- `output->write()`
  Finally, the output as requested in the input script is generated and written here, using the `Thermo` and `Dump` together with the respective `Compute` objects. Obviously, depending on the quantities that need to be calculated, this might require a more or less extensive amount of communication.

For extended system approaches like thermostats (cf Section 8.5) or barostats resulting in modified Newtonian equations of motion, other fixes including their own positions and velocity updates (like `FixNVE`) are available.[vi] Thanks to the Liouville operator approach[216,217] discretizations similar to the aforementioned velocity Verlet algorithm in case of the NVE ensemble (cf Section 3.3.3) can also be constructed for NVT based on the equations of motion (cf Eq. (3.6) in Section 3.1) given by Nosé-Hoover chains (NHC).[156] Therefore, the implementation in `FixNVT`, descending from `FixNH`, according to the formulation given by Shinoda and coworkers (also including barostats)[498] perfectly fits into the time stepping framework provided by the `Verlet` class.[vii]

In contrast to simple procedural programs centered around a single "main loop", the well planned and engineered object oriented design of the LAMMPS code facilitates the powerful input

[vi] For the Berendsen thermostat[484] only velocities need to be rescaled at the end of each integration step. Therefore, this is implemented in a corresponding `end_of_step()` method in the `FixTempBerendsen` class, whereas an instance of `FixNVE` is required to perform the actual integration.

[vii] The modern and transparent, i.e. well commented and documented, rewrite of the Nosé-Hoover chains infrastructure centered around `FixNH` and including the NVT integrator in `FixNVT` is only available since April 7th, 2010, due to the patch by Aidan Thompson, see `http://lammps.sandia.gov/bug2010.html`. It has thus become part of the official stale release from September 10th, 2010.

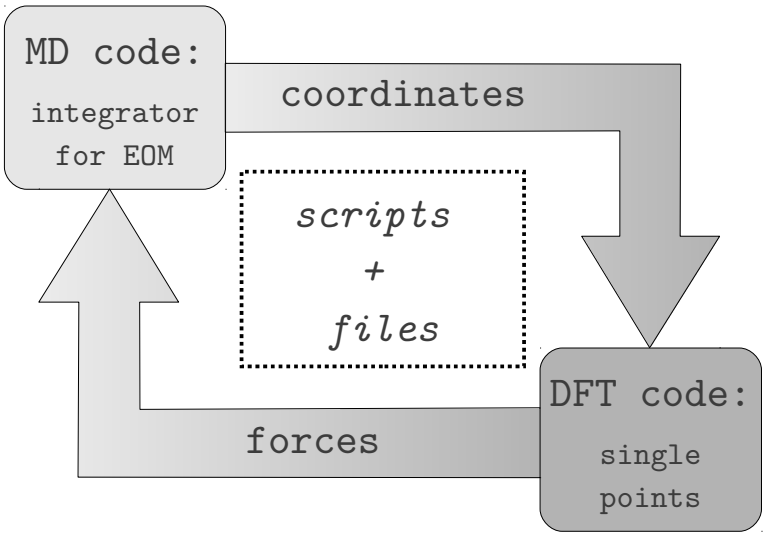

Figure D.1.: Schematic illustration of coupling mechanism provided by the LAMMPS class `FixExtForces`. The LAMMPS code drives the MD integration requests single point calculations from the external (e.g. DFT) code during each step in order to obtain forces calculated by the latter for the chosen number of atoms. Their coordinates as well as the resulting forces are communicated via scripts and files.

script language, already exposing control over many internal parts to the user, thus enabling a remarkable flexibility of potential applications. In addition to what has already been described, also e.g. different structural modifications can be easily combined subsequently in a single run. Nevertheless, for the purposes of this thesis the extensions accentuated in Fig. D.1 and described in more detail in the following sections needed to be developed.

D.2. Coupling Interface: `FixExtForces`

Within the QM/Me embedding approach presented in Chapter 9, molecular dynamics simulations based on forces from both a force field and first-principles need to be obtained during every time step. As detailed in Section 3.2.2, the former is rather complex in order to provide a realistic description of metallic systems (e.g. the modified embedded atom method, MEAM), seamlessly matching the embedding region described on a higher level of theory. In addition, the 10^4 to 10^5 of "force field atoms" acting as bath require an efficient integration based on neighbor lists, potentially even parallelized.[218] As already indicated in Section 3.4, MD routines integrated into many first-principles codes typically do not provide this level of sophistication. A naive and straightforward $\mathcal{O}(N^2)$ implementation is not yet a performance bottleneck for N less than 10^3 atoms which can nowadays be tackled *ab initio* on "interesting" integration time scales. Blinded by the complexity of the quantum mechanical problem, the complexity of classical MD is thus often overlooked in attempts to multiscale modeling. In order to focus efforts first on scientific issues rather than "from-scratch-reimplementation" of existing techniques "from both worlds" into a single code, coupling of different highly specialized packages seems to be a more appealing route at this point.

For the propagation of 10^6 MEAM atoms within LAMMPS the computational cost even on a single CPU is negligible (i.e. less than 5 %) compared to CASTEP calculations underlying the

evaluation of the forces for about 10^2 DFT atoms in the embedding region. The same cost ratio has also been observed for earlier simulations in material science addressing the oxidation of silicon surfaces based on traditional QM/MM embedding.[535,536] Therefore, LAMMPS is suitable to drive the MD integration, thus having the "main" responsibility for an embedding simulation. Using files and (shell) scripts to communicate with *ab initio* codes as depicted schematically in Fig. D.1 provides a flexible interface, easily allowing to switch the latter by adapting the scripts. In fact, other attempts for conventional QM/MM embedding like e.g. ChemShell[viii] have adopted a similar strategy.[537] Tedious technical problems associated with interfacing different programing languages are avoided this way, and potential problems with individual (single point) first-principles calculations in the course of the dynamics can be naturally analyzed in detail by storing the respective outputs. Even a replay mechanism can be easily implemented on the script level, allowing to calculate additional properties for an already "finished" trajectory or to resume an interrupted run. On the other hand, parallel execution of the quantum code and proper book keeping of its input and output files might pose a platform dependent challenge which has to be taken proper care of. Furthermore, within this interfacing strategy, additional overhead is introduced by the input and output (I/O) operations of writing coordinates and reading forces. This, however, is easily mastered by most nowadays file systems, and in light of the dominating computational cost of the first-principles calculations still remains negligible.

According to the structure of the LAMMPS code detailed in Appendix D.1, a coupling interface as described in the previous paragraph, is best implemented in LAMMPS as a fix, i.e. in a class `FixExtForces` derived from `Fix` to obtain *forces* calculated *externally* from the driving LAMMPS simulation. `FixExtForces` provides an input command of the following form (`&` indicating a continuation line):

```
fix <ID> <group-ID> &
    <extforces-style> <forces-file> <script-file> <dump-arguments ...>
```

As usual for `fix` commands, `<ID>` is its user-assigned name[ix], while `<group-ID>` denotes a group of atoms, previously defined in the input script via the `group` command resulting in an instance of `Group`, which the fix is to be applied to. `<extforces-style>` is one of `extforces/set`, `extforces/add` or `extforces/sub`, determining whether the externally calculated forces should replace, be added to or subtracted from other force contribution of the atoms in the group associated with this fix. The corresponding classes `FixExtForcesSet`, `FixExtForcesAdd` and `FixExtForcesAdd`, which are derived from `FixExtForces` (cf Fig. D.1), (only) provide the actual `post_force()` method which is responsible for the according incorporation of the externally calculated forces into the LAMMPS simulation. `<forces-file>` is the name of the file where the latter are tried to be read from by the `read_forces()` method in `FixExtForces`, The expected file format has been inspired by simple `.xyz` files[x] as sketched out in Listing D.1 and can hence be directly read by many visualization tools. It must have been generated as a result by `<script-file>`, which is called in the `run_external()` method of the aforementioned class using a C `system()` command. Apart from calling the desired first-principles code, this script must also take care of setting up all the required input files for the latter, and conveniently perform some clean up afterwards, potentially archiving the results of the single

[viii] ChemShell, a Computational Chemistry Shell, see `www.chemshell.org`

[ix] See `http://lammps.sandia.gov/doc/fix.html`.

[x] See e.g. `http://en.wikipedia.org/wiki/XYZ_file_format`.

N						
`Atoms`						
< `species(1)` >	R_{11}	R_{12}	R_{13}	F_{11}	F_{12}	F_{13}
⋮	⋮	⋮	⋮	⋮	⋮	⋮
< `species(N)` >	R_{N1}	R_{N2}	R_{N3}	F_{N1}	F_{N2}	F_{N3}

Listing D.1: Schematic listing of file from which externally calculated forces $\boldsymbol{F}_I = (F_{I1}, F_{I2}, F_{I3})$ for each atom I of the total number of N atoms marked for external calculation are read from by the `read_forces()` method of the LAMMPS class `FixExtForces`. Respective labels of `<species(I)>` atomic coordinates $\boldsymbol{R}_I = (R_{I1}, R_{I2}, R_{I3})$ are read as well, the latter for proper assignment of forces within LAMMPS as explained in the text. The simple file format has been inspired by `.xyz` files.[x]

point calculation of this iteration. Input coordinates have to be converted from the output requested by the `<dump-arguments ...>`.[xi] In the `do_dump()` method of `FixExtForces` these are handed over to the infrastructure provided by the `Dump` class, which takes proper care of all necessary communication in case of a parallel LAMMPS run, avoiding duplication of rather nasty MPI code here. In contrast, `run_external()` imposes an effective barrier to the LAMMPS parallelism, only having the external script run by the first LAMMPS MPI task while the others wait for its completion. This way, the external first-principles code is only started once, potentially creating its own parallel realm independently. Likewise, the actual file I/O operations in `read_forces()` are also executed only by the first LAMMPS MPI task, communicating the results afterwards. This ensures consistency of the calculated external forces and avoids additional overhead or even file system troubles by having all LAMMPS MPI tasks accessing the same result file simultaneously. Finally, the canonical methods `compute_scalar()` and `compute_vector()` in `FixExtForces` provide access to its contribution to the potential energy, which is also read in by `read_forces()`, and the forces on the atoms of the fix group before the external contributions have been considered. Providing the former method easily facilitates to include the energy contribution in the usual standard ("thermo") output, thus allowing to conveniently monitor energy conservation during an embedding run. In addition to checking the consistency of the intermediary files written for the communication with an external code, this can also be very helpful when testing and debugging the interface, i.e. both the LAMMPS and the script parts.

Obviously, the fix style `extforces/set` directly enables conventional QM/MM embedding. Furthermore, when only the system for which the external first-principles calculations are carried out is modeled within LAMMPS, i.e. no additional environment is included, this effectively also makes all the techniques included therein available to *ab initio* molecular dynamics based on the external code. This is how the selective thermostatting Chapter 9 of only bottom layer atoms in the slab could be easily accomplished, without having to reimplement a common MD technique for very special purpose applications.

The QM/Me approach presented in Chapter 9 is easily obtained by two separate fixes of styles `extforces/add` and `extforces/sub` applied to accordingly different fix groups. In practice, with external codes like CASTEP, which reorder the atoms for internal convenience in

[xi] For details see `http://lammps.sandia.gov/doc/dump.html`.

the output, initial atom numbers of the input geometry can no longer be used in order to assign the external forces to the right atoms in the LAMMPS simulation. In the `post_force()` methods, coordinates from the external output are therefore compared against those within the latter, which is a pragmatic and simpler solution than attaching (and preserving) additional labels. The straightforward implementation of this comparison scales with (N^2), where N is the number of atoms for which external forces have been calculated. Because the motivation for the embedding is N to be small, this is not a bottleneck so that more sophisticated hashing techniques are not required at the moment. Separately for both fixes, the employed shell script also takes care of exploiting the CASTEP reuse mechanism, allowing to restart from density and wave functions as contained in the separate checkpoint files from the last iteration when setting up the input files for the next one. For the QM/Me DFT calculation pairs of Chapter 9 and Chapter 10 tests have shown that this nearly yields the same efficiency as within conventional "internal" CASTEP MD simulations using the extrapolation scheme proposed by Arias and coworkers.[538] In comparison, the calculation without the adsorbate is quite cheap already as a smaller number of self-consistency iterations are required after the first MD step. Therefore, it has not been considered worth the effort to expose the extrapolation functionality to the embedding framework, though the required information could be easily stored alongside the trajectory. Though possible in principle, this is also the reason why the DFT calculations have not been run concurrently – not letting CPUs idle until the calculation with the adsorbate is complete. On the other hand, the replay mechanism indicated in the previous paragraph has shown to be necessary. A script which bypasses the call to CASTEP and extracts archived result files from complete single point calculations instead has therefore been implemented. In this case, it can be beneficial to also run LAMMPS in parallel, mainly in order to accelerate the evaluation of the MEAM forces. Within the scope of this thesis, when CASTEP was run alongside "on-the-fly", the overhead of a serial LAMMPS never was a serious performance bottleneck.

If not being all of a piece, future implementations of QM/Me might rely on tighter coupling strategies of separate packages than the one followed here. This is of particular importance should the file-based I/O operations become a bottleneck in case of small embedding regions or considerably faster external (first-principles) codes. Also, for platforms which might require a single program that manages all the parallelism employed during its execution directly and consistently, this can be a way to rely on a single MPI communicator only. In that respect, the Python developments indicated in Appendix D.1 including the LAMMPS calculator class for ASE in particular are very interesting and promising steps. Not relying on files for communication with LAMMPS any more in its current development version, the latter does already provide a slightly tighter coupling than `FixExtForces` and descendants. However, it is not yet integrated into the molecular dynamics capabilities of ASE, and the "native", i.e. pure Python, versions are by far not efficient enough to deal with a large number of bath atoms as described above. Using the neighbor list based velocity Verlet integrator provided by the ASAP code[xii], which is tightly integrated into ASE, is still by about one order of magnitude slower even with a Lennard-Jones potential (cf Section 3.2.1). In contrast to the LAMMPS solution described above, this makes them similarly expensive as the first-principles calculations. Using the effective medium theory (EMT) implemented in ASAP, which is of course more computationally expensive than Lennard-Jones, but qualitatively similar to MEAM (cf Section 3.2.2), QM/Me embedding based on ASE could become a very powerful alternative – if the performance can be improved significantly. Some ASE calculator classes for first-principles codes do already

[xii] See `https://wiki.fysik.dtu.dk/asap`.

provide a tight coupling. For these, mechanisms discussed in the literature for accelerating conventional *ab initio* MD (cf Section 3.2.3) based on extrapolation techniques[208–211,538] could be easily integrated and tested for their efficiency in this context. Considering these prospects of such tight coupling of "different" codes, it is questionable whether potential future QM/Me implementations in a single monolithic code would actually be advantageous.

D.3. Surface Oscillator: `FixSurfOsci`

In the comparison of QM/Me to energy sinks "from the shelf" (cf Chapter 8) presented in Section 9.2.2 also the surface oscillator model (cf Section 8.2) is included. It only enriches the potential energy surface of an adsorbate with degrees of freedom I based on the frozen surface approximation $V_{\text{fsa}}(\{\boldsymbol{R}_I\}_I)$ by a virtual surface oscillator coupled to the former by rigid shifting (cf Eq. (8.7))

$$V_{\text{fsa+SO}^3}\left(\{\boldsymbol{R}_I\}_I, \boldsymbol{R}_\text{S}\right) = V^{\text{fsa}}\left(\{\boldsymbol{R}_I - \boldsymbol{R}_\text{S}\}_I\right) + \frac{1}{2} m_\text{S} \boldsymbol{R}_\text{S}^\dagger \boldsymbol{\Omega}_\text{S}^2 \boldsymbol{R}_\text{S} \quad , \tag{D.2}$$

with associated displacement coordinate $\boldsymbol{R}_\text{S}$ and the parameters m_S and $\boldsymbol{\Omega}_\text{S}^2$, depicted as mass and matrix of characteristic frequencies, respectively. The corresponding Hamiltonian

$$\begin{aligned} H_{\text{fsa+SO}^3}\left(\{\boldsymbol{R}_I\}_I, \boldsymbol{R}_\text{S}, \left\{\dot{\boldsymbol{R}}_I\right\}_I, \dot{\boldsymbol{R}}_\text{S}\right) = \\ \sum_I \frac{1}{2} m_I \dot{\boldsymbol{R}}_\text{I}^2 + \frac{1}{2} m_S \dot{\boldsymbol{R}}_\text{S}^2 + V_{\text{fsa+SO}^3}(\{\boldsymbol{R}_I\}, \boldsymbol{R}_\text{S}) \end{aligned} \tag{D.3}$$

leads to the following equations of motion

$$\frac{\partial}{\partial t}\boldsymbol{R}_I = \dot{\boldsymbol{R}}_I \tag{D.4a}$$

$$\frac{\partial}{\partial t}\dot{\boldsymbol{R}}_\text{S} = \dot{\boldsymbol{R}}_\text{S} \tag{D.4b}$$

$$\frac{\partial}{\partial t}\dot{\boldsymbol{R}}_I = -\boldsymbol{\nabla}_{\boldsymbol{R}_I} V_{\text{fsa+SO}^3}(\{\boldsymbol{R}_I - \boldsymbol{R}_\text{S}\}_I) \tag{D.4c}$$

$$\frac{\partial}{\partial t}\dot{\boldsymbol{R}}_\text{S} = -\boldsymbol{\nabla}_{\boldsymbol{R}_\text{S}} V_{\text{fsa+SO}^3}(\{\boldsymbol{R}_I - \boldsymbol{R}_\text{S}\}_I) - m_\text{S}\boldsymbol{\Omega}_\text{S}^2 \boldsymbol{R}_\text{S} \quad , \tag{D.4d}$$

formulated using velocities instead of momenta because the former are used internally within LAMMPS. In principle, the neural network interpolation (and associated infrastructure) described in Section 6.1.3 could have been employed. However, for a fair comparison excluding interpolation uncertainties and possible numerical differences in the different integrators used for the molecular dynamics simulations, the frozen surface potential is better also calculated "on-the-fly" as it is done with the first-principles input for the other energy sinks.

This cries for reusing the LAMMPS infrastructure provided by `FixExtForces` as detailed in Appendix D.2. The desired frozen surface slab to be employed by the external first-principles calculations is then also most conveniently represented atomistically within LAMMPS, despite the fact that there are no moving surface atoms appearing in the equations of motion. According to Appendix D.1, a LAMMPS fix is the obvious choice for the integration of Eqs. (D.4), which is why the implementation has been put into a class `FixSurfOsci` derived from `Fix`. The input command associated with this fix expects the following arguments:

`fix <ID> <group-ID> surfosci <surface-group-ID>` m_S Φ_{11} Φ_{22} Φ_{33}

Like for any `fix` command, `<ID>` is its user-assigned name[xiii], while `<group-ID>` denotes the group of actual dynamical atoms with the coordinates $\{\boldsymbol{R}_I\}_I$ and velocities $\left\{\dot{\boldsymbol{R}}_I\right\}_I$. It must have been defined in the input script before via the `group` command resulting in an instance of `Group`. `<surface-group-ID>` denotes another instance of the latter, previously defined in the input for a set of atoms forming the slab to be used in the external DFT calculations. m_S is the fictitious mass parameter of the surface oscillator, and Φ_{11}, Φ_{22} and Φ_{33} are the diagonal elements of the force constant matrix. This implies the following approximation for the matrix of characteristic frequencies

$$m_\mathrm{S}\boldsymbol{\Omega}_\mathrm{S}^2 \approx \begin{pmatrix} \Phi_{11} & 0 & 0 \\ 0 & \Phi_{22} & 0 \\ 0 & 0 & \Phi_{33} \end{pmatrix} \quad , \tag{D.5}$$

which has been commonly used in the literature.[23,24,447] Compared to the original one-dimensional formulation[444,458], this does already allow for both much more flexibility and arbitrariness. An extension of the implementation to a full, non-diagonal 3×3 matrix would be completely straightforward.

`FixSurfOsci` includes its own time stepping. For the actual dynamical atoms, i.e. the adsorbate, coordinates $\{\boldsymbol{R}_I\}_I$ and velocities $\left\{\dot{\boldsymbol{R}}_I\right\}_I$ are updated like in `FixNVE`. As detailed in Appendix D.1 the usual velocity Verlet discretization scheme[213] is employed, implemented in the `initial_integrate()` and `final_integrate()` methods of `FixSurfOsci`. It is also applied in the same fashion to discretize Eqs. (D.4b) and (D.4d), the equations of motion of the surface oscillator degrees of freedom $\boldsymbol{R}_\mathrm{S}$, where the latter are internal variables of the class `FixSurfOsci`. Coordinates of the atoms in the surface group are rigidly shifted in `initial_integrate()`, using the same update value that is also applied to $\boldsymbol{R}_\mathrm{S}$. This way, a fix of style `extforces/set` (cf Appendix D.2) directly passes the right slab geometry to an external first-principles calculation for which forces on the adsorbate atoms I are required in the equations of motion given by Eqs. (D.4c) and (D.4d). Here it is important to emphasize that no `fix` class performing time stepping has been instantiated for the surface group (e.g. by a `fix` style `nve` command including some of its members), unless externally calculated force components for the atoms in that group are explicitly zeroed elsewhere. Otherwise the rigidity of the frozen surface implied by the model could be violated. The actual values of the surface oscillator coordinates $\boldsymbol{R}_\mathrm{S}$ and its contribution to the total energy

$$\begin{aligned} E_{\mathrm{SO}^3} &= E_{\mathrm{SO}^3}^{\mathrm{kin}} \; + \; E_{\mathrm{SO}^3}^{\mathrm{pot}} \\ &= \frac{1}{2} m_\mathrm{S} \dot{\boldsymbol{R}}_\mathrm{S}^2 \; + \; \frac{1}{2} m_\mathrm{S} \boldsymbol{R}_\mathrm{S}^\dagger \, \boldsymbol{\Omega}_\mathrm{S}^2 \, \boldsymbol{R}_\mathrm{S} \end{aligned} \tag{D.6}$$

can be queried and output in a fashion similar to computes, relying on the LAMMPS infrastructure for which the methods `compute_vector()` and `compute_scalar()`, respectively, are defined in `FixSurfOsci`. The latter is also used within the usual LAMMPS machinery to include the aforementioned energy contribution in the total energy output managed by the `Thermo` class, allowing to easily monitor energy conservation according to Eq. (D.3). Using toy potentials for V_fsa, this has also been used to thoroughly test the implementation. For suitable time steps, $H_{\mathrm{fsa}+\mathrm{SO}^3}$ could be excellently preserved, thus providing perfect trust into the former.

[xiii] See `http://lammps.sandia.gov/doc/fix.html`.

D.4. Harmonic Solid: `PairHarmsol`

For the comparison with the harmonic solid in the context of the phonon analysis described in Chapter 10, the pair potential describing the former needed to be implemented within LAMMPS. For a crystalline solid with atoms at positions $\mathcal{R} = \{\boldsymbol{R}_I\}_I$, which are generally displaced from the equilibrium positions $\{\boldsymbol{R}_I^0\}_I$ of the crystal lattice, this potential is given by (cf Eq. (4.2) in Section 4.1):

$$V^{\text{harmsol}}(\mathcal{R}) = \frac{1}{2} \sum_{I,J} \left(\boldsymbol{R}_J - \boldsymbol{R}_J^0\right)^\dagger \boldsymbol{\Phi}_{IJ} \left(\boldsymbol{R}_I - \boldsymbol{R}_I^0\right) \tag{D.7}$$

Here $\boldsymbol{\Phi}_{IJ}$ is a 3×3 matrix of force constants, i.e. the material specific parameters describing the interaction between atoms I and J within the harmonic approximation. These can be obtained from a lattice dynamics calculation, which has been done based on first principles in the present context (cf Section 4.2).

The LAMMPS class `Bond`[xiv] already allows to model harmonic bonds in the simple form which is typically used in force fields for the description of large molecules in the bio-community

$$V^{\text{bond/harmonic}}(\mathcal{R}) = \sum_{I,J} K_n \left(\|\boldsymbol{R}_J - \boldsymbol{R}_I\|_2 - R_n^0\right)^2 \quad , \tag{D.8}$$

where $n = n(I,J)$ and K_n is supposed to include the usual factor $\frac{1}{2}$. Obviously, this is quite different from what is needed here. Both the force constants K_n and the equilibrium bond distances R_n^0 are only scalar, and not matrix and vector valued, respectively. The "self-terms" with $I = J$ in Eq. (D.8) thus only yield a constant energy offset and hence do not contribute to the corresponding forces – quite in contrast to Eq. (D.7). Even worse, $V^{\text{bond/harmonic}}$ is restricted to central forces, which is known to be a limitation in the accurate description of surface phonons[251] as indicated in Section 4.3. Finally, bonds need to be defined one by one in an input data file together with individual parameter definitions K_n and R_n^0 for each declared bond type n and read in via a `read_data` command in the input script as sketched out in Appendix D.1 For the "pair bond topology" of a large slab as required in Eq. (D.7) this is of course very tedious. An automatic generation based on neighbor shells is a much better approach, but an extension of `Bond` along those lines exploiting already existing infrastructure for `Neighbor` and descending classes is not easily possible within the present design of the former class. Alternatively, this could of course be done externally e.g. in the form of scripts, which create the required data input files. But then either very system specific code would have been created or a lot of functionality already existing in the LAMMPS `Neighbor` class and its descendants would have simply been duplicated. Altogether, `Bond` is unfortunately not a helpful starting point in the present context.

In the spirit of generalized Langevin equations (GLEs), the Green's function molecular dynamics (GFMD) approach by Müser and coworkers[450,451] is based on a harmonic solid as well (cf Section 8.1). However, their LAMMPS extensions[452] do not include the latter as a reference system e.g. for testing purposes. It only encompasses the two fixes `FixGFC` and `FixGFMD`. The latter reproduces the effective elastic force on an atom which comes from the bulk that has been integrated out within the GLE ansatz, thereby employing "effective elastic stiffness coefficients". In engineering lingo, these are suitable elements of the dynamical matrix, i.e. the

[xiv] See `http://lammps.sandia.gov/doc/bond_harmonic.html`.

Fourier transforms of the force constants $\boldsymbol{\Phi}_{IJ}$ in Eq. (D.7) (cf Eq. (4.7) in Section 4.1), which can be obtained by the former fix class from preceding molecular dynamics runs. Therefore, this could not be built upon in the context of the present work, either. Starting over from scratch thus turned out to be necessary.

Despite its simple analytic form, the large numbers of (though well determined) parameters occurring in Eq. (D.7) make an implementation of V^{harmsol} for an arbitrarily large simulation cell quite challenging. Only if the latter is restricted to the order of magnitude of the nowadays usually accessible DFT regime, i.e. $N \approx 1000$ atoms, the entries of all 3×3 matrices $\boldsymbol{\Phi}_{IJ}$ for all $\frac{1}{2}\,N^2$ pairs can be straightforwardly kept in memory for a simple direct evaluation of Eq. (D.7).[xv] Quite in contrast, for the huge bath-like slabs consisting of more than 1×10^5 atoms which are of interest in the present work, $\frac{1}{2}(3 \cdot 10^5)^2$ entries would need to be stored. Even when using single-precision floating-point numbers only, each of typically 4 bytes, ≈ 1.5 terabytes of memory would be required only to store the force constants, thus exceeding directly accessible resources even of nowadays supercomputers. Transforming to Eigensystems in order to store only diagonal elements, either in real space or in reciprocal space, the latter along the lines sketched out e.g.by Mueser and coworkers[450,452] or detailed in Section 10.1, is equally or even more expensive in terms of memory since both Eigenvectors and Eigenvalues would need to be stored. However, given the translational invariance of the force constants in periodic directions, a lot of duplicate entries are stored within the previous naive direct approach. Furthermore, force constants go to zero with increasing distance

$$\boldsymbol{\Phi}_{IJ} \xrightarrow{\left\|\boldsymbol{R}_J^0 - \boldsymbol{R}_I^0\right\|_2 \to \infty} 0 \quad , \tag{D.9}$$

with the strength of the decay usually being proportional to a material specific power law. When obtained from first-principles lattice dynamics calculations within the direct method, $\boldsymbol{\Phi}_{IJ}^{\text{cum}} = \mathbf{0}$ even holds exactly for $\left\|\boldsymbol{R}_J^0 - \boldsymbol{R}_I^0\right\|_2 > \boldsymbol{R}_{\text{cut}}$ with a cut-off radius $\boldsymbol{R}_{\text{cut}}$ implicitly imposed by size of the supercells employed for the former (cf Section 4.2). If the latter are sufficiently large, the cumulant force constants (cf Eq. (4.25), in particular for notation)

$$\boldsymbol{\Phi}_{IJ}^{\text{cum}} = \boldsymbol{\Phi}_{\tilde{I}\tilde{J}}^{\text{cum}}\left(\boldsymbol{L}_{\tilde{I}}, \boldsymbol{L}_{\tilde{J}}\right) = \sum_{\boldsymbol{L}^{\text{S}}}^{\substack{\text{supercell} \\ \text{images}}} \boldsymbol{\Phi}_{\tilde{I}\tilde{J}}\left(\boldsymbol{L}_{\tilde{I}}, \boldsymbol{L}_{\tilde{J}} + \boldsymbol{L}^{\text{S}}\right) \tag{D.10}$$

as introduced in the formalism by Parlinski and coworkers[237] are expected to be a good approximation for the $\boldsymbol{\Phi}_{IJ}$ within the principle accuracy limits of the employed *ab initio* theory. Neighbor shells reaching out up $\boldsymbol{R}_{\text{cut}}$ are thus an in this context complete and compact way to input and store the $\boldsymbol{\Phi}_{IJ}$ for the evaluation of $V^{\text{harmsol}}(\mathcal{R})$.

In order to store the force constants of various neighbor shells of inequivalent atoms which are termed centers, the file format sketched out in Listing D.2 has been established and simply suffixed by `.harmsol`. Units of lattice vectors, which are given in absolute coordinates for positions and distances, and force constants are usually in Å and eV Å^{-2}, respectively, but obviously only have to match the corresponding energy units when evaluating Eq. (D.7). All

[xv] In fact, this is done within the present implementation of thermodynamic integration in FHI-AIMS by Christian Carbogno, relying on force constants calculated with `phonopy-FHI-aims`. The latter was contributed to the PHONOPY package by the author of this thesis, who still maintains it, in order to provide a reliable phonon infrastructure based on the direct method (cf Section 4.2) for the former first-principles code.

nine entries of the $\mathbf{\Phi}_{IJ}$ of all neighbors in each shell are expected to be given for every inequivalent "center", i.e. atoms in the primitive cell of the underlying phonon calculation. Within the present work, these are obviously one atom in case of the fcc bulk and one atom per layer in the surface unit cell of the (100) surface of the fcc-crystal. The force constants need to be properly unfolded when symmetry has been used in order to reduce the number of finite displacements and hence the computational costs of the underlying first-principles calculations – as typically done within the Parlinski formalism.[237] In the present work, this is taken care of within the employed Python scripts based on PHONOPY. They center around the Python module `harmsol.py`, defining a class `Harmsol`. In addition to general I/O of `.harmsol` files, it also encompasses replication and linear transformation of force constants. The latter is required when the reference coordinate system changes, like e.g. when switching from the primitive unit cell of a fcc crystal to surface unit cell its (100) surface. For convenience, these operations can also be optionally specified in a `.harmsol` file as indicated in Listing D.2.

```
# optional: comment lines
#           explaining details about force constants in this file

a_11 a_21 a_31   # components of lattice vector a_1 = (a_i1)_i
a_12 a_22 a_32   # components of lattice vector a_2 = (a_i2)_i
a_13 a_23 a_33   # components of lattice vector a_3 = (a_i3)_i


# optional: rotation matrix O = (O_ij)_ij
#           to transform reference coordinate system with
Rotation
   O_11 O_12 O_13
   O_21 O_22 O_23
   O_31 O_32 O_33

# optional: translation vector t = (t_i)_i
#           to shift reference coordinate system with
Translation
   t_1 t_2 t_3


# number of atoms (termed centers)
# for which force constants in neighbor shells follow
N_cent
# maximum neighbors and distances
# between any two of the following neighbor pairs
N_neigh^max  d^max

# in the following:
# R_I = (R_Ii)_i : lattice site of center I
# d_neigh,I^max : maximum distance of neighbors from center I in any shell
# d̄_neigh,I^max : same as before, but in last complete shell
#       (can be set to 0.0 in order to be ignored)
# L_IJ = (L_IJi)_i : lattice vector from center I to its neighbor J
```

```
# Φ_IJ = (Φ_IJij)_ij : force constants for center I and neighbor J
1   R_11  R_12  R_13
N_neigh,1   d^max_neigh,1   d̄^max_neigh,1
  1   L_111  L_112  L_113
      Φ_1111  Φ_1112  Φ_1113
      Φ_1121  Φ_1122  Φ_1123
      Φ_1131  Φ_1132  Φ_1133
  ⋮
  N_neigh,1   L_1N_neigh,1 1  L_1N_neigh,1 2  L_1N_neigh,1 3
      Φ_1N_neigh,1 11  Φ_1N_neigh,1 12  Φ_1N_neigh,1 13
      Φ_1N_neigh,1 21  Φ_1N_neigh,1 22  Φ_1N_neigh,1 23
      Φ_1N_neigh,1 31  Φ_1N_neigh,1 32  Φ_1N_neigh,1 33

⋮

N_cent   R_N_cent 1  R_N_cent 2  R_N_cent 3
N_neigh,N_cent   d^max_neigh,N_cent   d̄^max_neigh,N_cent
  1   L_N_cent 11  L_N_cent 12  L_N_cent 13
      Φ_N_cent 111  Φ_N_cent 112  Φ_N_cent 113
      Φ_N_cent 121  Φ_N_cent 122  Φ_N_cent 123
      Φ_N_cent 131  Φ_N_cent 132  Φ_N_cent 133
  ⋮
  N_neigh,N_cent   L_N_cent N_neigh,N_cent 1  L_N_cent N_neigh,N_cent 2  L_N_cent N_neigh,N_cent 3
      Φ_N_cent N_neigh,N_cent 11  Φ_N_cent N_neigh,N_cent 12  Φ_N_cent N_neigh,N_cent 13
      Φ_N_cent N_neigh,N_cent 21  Φ_N_cent N_neigh,N_cent 22  Φ_N_cent N_neigh,N_cent 23
      Φ_N_cent N_neigh,N_cent 31  Φ_N_cent N_neigh,N_cent 32  Φ_N_cent N_neigh,N_cent 33
```

Listing D.2: Schematic listing of file format used to specify force constants $\mathbf{\Phi}_{IJ}$ for the potential of a harmonic solid V^{harmsol} as given by Eq. (D.7). The usual file suffix is `.harmsol`. Empty lines and lines (or parts thereof) starting with `#` are supposed to be ignored by the respective parser, which holds for the one in the `read_file()` method of the LAMMPS class `PairHarmsol` and `harmsol.Harmsol.read()` in the Python utility module `harmsol.py` both implemented by the author of this thesis. Note that incomplete shells are a consequence of the respective missing neighbors not being captured by the extended supercells used for the finite difference phonon calculations (cf Section 4.2). For more details in particular concerning the use in `PairHarmsol` see text, where the same symbols are used. Explanations for the latter are also provided by comments included in this listing.

Due to the similarities of V^{harmsol} with a conventional pair potential and inadequacy of other parts of LAMMPS outlined before, the present implementation was put into the new class `PairHarmsol` derived from `Pair`. Based on the infrastructure provided by the latter, its associated input commands are

`pair_style harmsol` d^2_{disp} d^2_{lat}

processed within the usual `settings()` method, and (`&` indicating a continuation line)

```
pair_coeff * * <.harmsol-file> <yes or NULL for each atom type> &
   <optional: output-file <optional: .harmsol-output-file>>
```

parsed and evaluated by the expected `coeff()` of `PairHarmsol`. The displacement cut off allows to neglect certain contributions to V^{harmsol} altogether if one of two atoms of a pair is displaced by less than d_{disp}, i.e.

$$\frac{1}{2}\underbrace{\left(\boldsymbol{R}_J - \boldsymbol{R}_J^0\right)^\dagger}_{\equiv \boldsymbol{U}_J^\dagger}\boldsymbol{\Phi}_{IJ}\underbrace{\left(\boldsymbol{R}_I - \boldsymbol{R}_I^0\right)}_{\equiv \boldsymbol{U}_I} \equiv 0 \quad \begin{cases} \|\boldsymbol{U}_I\|_2 < d_{\text{disp}} \\ \quad \text{or} \\ \|\boldsymbol{U}_J\|_2 < d_{\text{disp}} \end{cases} \tag{D.11}$$

in Eq. (D.7), conveniently expressed using the displacement coordinates $\boldsymbol{U}_I$ and $\boldsymbol{U}_J$. It can be set to zero, but 1×10^{-9} Å has been found to give numerically identical results in the present work for greatly reduced computational cost. d_{lat} specifies lattice tolerance, i.e. the acceptable maximum absolute value of differences when determining the associated lattice positions of displaced atoms (vide infra), for which 1.0 Å has been used to reliably carry out the simulations presented in Chapter 10. The syntax of `pair_coeff` has been inspired by the LAMMPS classes `PairMEAM`, `PairSW` and `PairAIREBO`.[xvi] For each atom type the `<yes or NULL>` arguments are used to set the internal masking flags which indicate whether force contributions from `PairHarmsol` are evaluated for that type. The `read_file()` method takes care of reading the specified `<.harmsol-file>` in the format described in Listing D.2. If `<output-file>` is specified, not only debug output but also warnings specific to an instance of `PairHarmsol` are written to the former, which is thus always recommended. Finally, `<.harmsol-output-file>` is written by `write_file()` if it has been optionally specified as last argument to `pair_coeff`, allowing to verify that `<.harmsol-file>` has been read and parsed correctly. Based on the information provided therein, in the `init_style()` method the LAMMPS infrastructure provided by the `Neighbor` class and its descendants is requested to provide a full neighbor list, not relying on Newton's third law. As expected, the necessary cut off distance (cf Eq. (3.8) in Section 3.2.1) is supplied by `init_one()` and chosen to be $N_{\text{neigh}}^{\max} + \sqrt{d_{\text{lat}}}$, where $N_{\text{neigh}}^{\max}$ is the maximum distance of any neighbor in any neighbor shell within the "harmonic force field" read from `<.harmsol-file>` (cf Listing D.2). This way, an external specification of the "pair bond topology" required to evaluate Eq. (D.7) as indicated above is completely avoided and entirely handled internally within LAMMPS.

Most important in `PairHarmsol` is of course the `compute()` method, which gets called during each time step as described in Appendix D.1 in order to evaluate the forces from V^{harmsol} on each atom. This is done according to the following algorithm, which faces the major challenge of assigning the right force constants to the right atoms in a straightforward fashion:

For each atom I do the following:

1. Identify which (equivalent) center at equilibrium position given by the lattice site $\boldsymbol{R}_I^0$ atom I with coordinates $\boldsymbol{R}_I(t)$ at present time step t corresponds to, thereby selecting the right set of neighbor shell force constants to be used in the following.
2. Calculate the displacement vector $\boldsymbol{U}_I(t) = \boldsymbol{R}_I(t) - \boldsymbol{R}_I^0$ of atom I. If $\boldsymbol{U}_I(t) < d_{\text{disp}}$ and thus Eq. (D.11) holds, this (outer) loop is immediately continued by starting over with the first step for the next atom I, which greatly improves performance.

[xvi] Referring to the respective parts of the LAMMPS documentation might thus provide additional insight.

3. Evaluate the "on-site" energy

$$E_{\mathrm{II}}(t) = \frac{1}{2}\,(\boldsymbol{U}_I(t)\,)^{\dagger}\,\boldsymbol{\Phi}_{II}\,\boldsymbol{U}_I(t) \tag{D.12a}$$

and force

$$\boldsymbol{F}_{\mathrm{II}}(t) = -\boldsymbol{\Phi}_{II}\,\boldsymbol{U}_I(t) \tag{D.12b}$$

contributions for atom I due to the displacement of atom I itself, using the force constants $\boldsymbol{\Phi}_{II}$ properly identified before.

4. For each atom J in the neighbor list of the present atom I do the following:

   a) Determine the corresponding equilibrium position of atom J given by the lattice site $\boldsymbol{R}_J^0$, so that the lattice *vector*

$$\boldsymbol{L}_{IJ} = \boldsymbol{R}_J^0 - \boldsymbol{R}_I^0 \tag{D.13}$$

   can be used in order to identify which neighbor of atom I the current atom J corresponds to.

   b) Calculate the displacement vector $\boldsymbol{U}_J(t) = \boldsymbol{R}_J(t) - \boldsymbol{R}_J^0$ of atom J. Like in step 2, if $\boldsymbol{U}_J(t) < d_{\mathrm{disp}}$ and thus Eq. (D.11) holds, this (inner) loop is immediately continued by starting over with the first step for the next atom J in the neighbor list of atom I.

   c) Evaluate the neighbor energy

$$E_{\mathrm{IJ}}(t) = \frac{1}{2}\,(\boldsymbol{U}_J(t))^{\dagger}\;\boldsymbol{\Phi}_{IJ}\,\boldsymbol{U}_I(t) \tag{D.14a}$$

   and force

$$\boldsymbol{F}_{\mathrm{JI}}(t) = -\boldsymbol{\Phi}_{IJ}\,\boldsymbol{U}_I(t) \tag{D.14b}$$

   contributions for atom J due to the displacement of atom I, using the force constants $\boldsymbol{\Phi}_{II}$ properly identified before.

It is important to note that the meaning of the index notation in Eqs. (D.12b) and (D.14b) is completely consistent with Eq. (4.24) in Section 4.2. No explicit checks for LAMMPS atom types are done in `compute()`: It is assumed that force constants are assigned to the right atoms of possibly different species based on their (lattice) coordinates alone.[xvii] In principle, this should also allow applications to multicomponent systems, with the corresponding `.harmsol` files then containing force constants for all atomic species. Of course, when combined with the `hybrid` style from the `PairHybrid` class, the skip list mechanism provided by the latter offers an additional prescreening of neighbor lists. On the other hand, atomic arrangements containing several spatially separated "lattice areas" (like e.g. for a molecule between two surfaces acting as electrodes) would still require some special care.

If the simulation cell is spatially decomposed into different domains within a parallel LAMMPS run,[218] in the present implementation of the above algorithm in `compute()`, the outer loop is

[xvii] This is the reason why the `pair_coeff` command above always needs to be set for all atom types, i.e. followed by `* *`.

over atoms which are local (i.e. "non-ghost") atoms for each parallel process. By using a full neighbor list and enforcing the use of Newton's third law as indicated before, force contributions calculated for ghost atoms are conveniently communicated by the existing LAMMPS infrastructure in the correct way. Consequently, the performance of the present version of `PairHarmsol` could "simply" be improved by running in parallel, which however turned out not to be necessary within the scope of the present work and therefore has not yet been tested extensively.

For the important identification of (equivalent) lattice sites in steps 1 and 4a, the auxiliary method `get_lattice_site()` has been implemented – thus maximizing code reuse and simplifying debugging and maintainability. It makes use of the inverse lattice vectors $\{\boldsymbol{b}_i\}_i = \{(b_{ki})_k\}_i$, which are already calculated in the `read_file()` method according to their definition

$$\boldsymbol{a}_i \cdot \boldsymbol{b}_j = \sum_{k=1}^{3} a_{ki}\, b_{kj} = \delta_{ij} \quad , \tag{D.15}$$

where $\{\boldsymbol{a}_i\}_i = \{(a_{ki})_k\}_i$ are the lattice vectors specified in the `<.harmsol-file>` (cf Listing D.2).[xviii] `get_lattice_site()` iterates over the neighbor shell centers therein, defining the harmonic force field, and compares their absolute coordinates to a position vector $\boldsymbol{R}$ based on the following algorithm:

For each of the N_{cent} centers I do the following:

1. Calculate the difference vector

$$\boldsymbol{d}^{\text{abs}} = \left(d_k^{\text{abs}}\right)_k = \boldsymbol{R} - \boldsymbol{R}_I^0 \tag{D.16}$$

   in absolute coordinates.

2. Obtain its representation in fractional coordinates (cf Eq. (D.15))

$$d_i^{\text{frac}} = \sum_{k=1}^{3} b_{ik}\, d_k^{\text{abs}} \quad . \tag{D.17}$$

3. Determine the displacement from a lattice site

$$u_i^{\text{frac}} = d_i^{\text{frac}} - \text{round}\left(d_i^{\text{frac}}\right) \tag{D.18}$$

   in fractional coordinates, where round defines the usual rounding operation to the nearest integer

$$\text{round}(x) = \begin{cases} \lfloor x \rfloor & \text{if } x - \lfloor x \rfloor < \frac{1}{2} \\ \lceil x \rceil & \text{if } x - \lfloor x \rfloor \geq \frac{1}{2} \end{cases}$$

4. Obtain the aforementioned displacement in absolute coordinates

$$u_i^{\text{abs}} = \sum_{k=1}^{3} a_{ki}\, u_k^{\text{frac}} \quad . \tag{D.19}$$

[xviii] Here, the choice of indices follows the usual crystallographic convention to have lattice vectors as column vectors of the matrix $(\boldsymbol{a}_i)_i = (a_{ki})_{ki}$.

5. If $\left\|\boldsymbol{u}^{\mathrm{abs}}\right\|_2 < d_{\mathrm{lat}}$, where $\boldsymbol{u}^{\mathrm{abs}} = \left(u_i^{\mathrm{abs}}\right)_i$, accept

$$\boldsymbol{R}^0 = \boldsymbol{R} - \boldsymbol{u}^{\mathrm{abs}} \quad . \tag{D.20}$$

as lattice site within the tolerance d_{lat} specified by `pair_style harmsol` command as described above. It is equivalent to $\boldsymbol{R}_I^0$, in the sense of being related to the latter by a lattice vector

$$\boldsymbol{L} = \boldsymbol{R}^0 - \boldsymbol{R}_I^0 \tag{D.21}$$

For slab geometries (cf Fig. 2.1), this algorithm ensures that equivalent centers in different layers can be properly identified due to lateral periodicity while also allowing for relaxation of the surface resulting in deviations from ideal, bulk truncated lattice positions. The only crucial requirement is that the lattice vector encompassing the vacuum separation between slabs given in the `<.harmsol-file>` (cf Listing D.2) and the one used for the actual LAMMPS simulation cell are identical. Thanks to the absolute coordinates used everywhere else in a `.harmsol` file, this can be easily adapted.

In the first algorithm above used in `compute()`, steps 1 and 4a would not have to be done anew during each time step, if the assignment of lattice sites and force constants to atoms and pairs of atoms within LAMMPS, respectively, was stored after having been carried out once. As the comparison operations in `compute()` and `get_lattice_site()` are quite expensive and currently dominate the computational cost, this would be a great performance improvement. Obviously, a direct look-up of the force constants would reduce the poor $\mathcal{O}\left(N_{\mathrm{cent}} N_{\mathrm{neigh}}\right)$ scaling with accordingly large prefactor of the present implementation to $\mathcal{O}(1)$, i.e. like for other potentials with significantly less parameters. Ideally, the force constants could be attached as "tags" within the neighbor lists, which would, however, require significant structural changes at the "heart of LAMMPS", i.e. the `Neighbor` class and its descendants. These are far from being trivial in particular when also supposed to include the communication necessary for the parallel case. Since performance was not a limitation for the present work, also thanks to the introduction of the displacement cut off d_{disp} and the potential parallel use of `PairHarmsol` as indicated above, this has been left to future work where it might become necessary.

Finally, energies V^{harmsol} obtained with the present implementation have been carefully checked against corresponding reference energies for arbitrary displacement patterns, including in particular those from the finite displacement calculations used to determine the underlying force constants. As to be expected from an analytical potential, energy conservation during molecular dynamics runs starting from such displacements patterns is excellent – as long as d_{disp} is not too large as indicated above. But also d_{lat} has to be chosen with proper care. Obviously, it must be big enough to cope with the displacements from lattice sites present in the simulated system, and small enough to avoid wrong assignments by `get_lattice_site()` (cf step Item 5 from the algorithm underlying the latter). Otherwise, with the present implementation, force constants cannot be assigned correctly – a limitation which would also be lifted by the extension sketched out in the previous paragraph. However, by carefully including debug output in both `compute()` and `get_lattice_site()` and monitoring the latter by specifying an `<output-file>` in the `pair_coeff` command as described above, it has been verified that no misassignments occur in the present application for the chosen value of d_{lat}.

Summary

In this work energy dissipation during exothermic chemical reactions in the context of heterogeneous catalysis is investigated in great detail, based on and substantially further developing *ab initio* methodologies. The dissociation of oxygen molecules (O_2) on the Pd(100) surface serves as a representative showcase, involving a release of about 2.6 eV of chemisorption energy. State-of-the-art *ab initio*-based multiscale models implicitly assume an instantaneous equilibration of reaction products. Consequences of this Markov approximation can only be estimated by explicitly time-dependent dynamics without any further simplifying assumptions.

The impingement of O_2 from the gas phase onto the surface occurs with randomly distributed initial molecular orientation and lateral position. The increasing interaction with the surface potential induces a funneling into preferential adsorption channels, which is first investigated based on a frozen surface approximation. Under this assumption, Born-Oppenheimer molecular dynamics needs (at least) a six dimensional potential energy surface representing the molecular degrees of freedom. In order to properly capture the breaking of the oxygen-oxygen bond, the latter is described on the level of density functional theory (DFT) with a semi-local exchange-correlation functional. Following a "divide-and-conquer" strategy, this description is decoupled from the dynamics to reduce the computational cost. The resulting interpolation problem is tackled with the help of neural networks using only a very limited number of data points. In doing so, a suitable transformation of the molecular coordinates is of crucial importance, capturing the complex symmetry of the system. Due to the lack of such a transformation for diatomics on (100) surfaces an approach was developed, which, as opposed to previous concepts, is also demonstrated to be transferable to other low-index surfaces. The initial sticking coefficient resulting from thousands of trajectories shows good agreement with available experimental data. Quite in contrast to Al(111) surfaces, the spin transition of the oxygen molecule ($^3\Sigma_g^-$ spin triplet in gas phase to singlet-like state on the surface) can apparently be described adiabatically.

In order to characterize this further and at the same time assess the relevance of one possible energy dissipation channel, excitations of electron-hole (e-h) pairs in the metal substrate are investigated using time-dependent perturbation theory – based on time-dependent density functional theory (TDDFT) and the Kohn-Sham band structure of the substrate. A new, efficient implementation based on further developed ideas for the evaluation of the required non-adiabatic coupling matrix elements enables the calculation of spin resolved e-h excitation spectra for a variety of trajectories obtained on the previously obtained potential energy surface. The resulting energy losses do vary over several orders of magnitude, but do not exceed 100 meV and thus 5 % of the chemisorption energy mentioned above. On the one hand, this eliminates e-h pair excitations as dominant dissipation channel in this system, in agreement with the lack of detectable chemicurrents in corresponding experiments. On the other, a spin asymmetry identified in the calculated spectra offers a mechanism that could be responsible for the adiabatic spin transition of the oxygen molecule.

As a consequence, focus is inevitably shifted on phonons as major energy dissipation channel. Unfortunately, a detailed discussion reveals the crudeness and inappropriateness of existing schemes to describe the phonon excitation during adsorption at metal surfaces. Within conven-

tional *ab initio* molecular dynamics in particular, phonon propagation is limited by the periodic boundary conditions, that are necessarily used to properly describe the metallic band structure and its influence on the chemical bond with the adsorbate. Therefore, a new embedding scheme called QM/Me was developed, which also offers versatile potential applications beyond the scope of this thesis. In the present context it allows to model realistic (surface) phonons on the level of a "modified embedded atom method" (MEAM) potential, seamlessly adapted to and concurrently with the DFT description of the O_2 dissociation. For the first time, dissipation into a huge environmental bath can be observed directly based on *ab initio* methods. A comparison to previous more approximate approaches shows remarkable differences even with respect to the adsorbate trajectories, which casts severe doubts on prior descriptions achieved with these schemes. Furthermore, the obtained dissociation dynamics yields an extended "hot" translational movement across the surface, with both adsorbed oxygen atoms diffusing in opposite directions away from each other. This coupling of dissociation and diffusion processes through the non-instantaneous dissipation of the released reaction heat invalidates the otherwise unanimously applied Markov assumption for the dynamics of adsorptive processes. Resulting differences in the arrangements of adsorbates might have crucial consequences for many surface functionalities, including the catalytic activity. Finally, a new projection scheme allows to thoroughly characterize the influence of surface phonons and the failure of the harmonic approximation commonly used in models for solids in the context of gas-surface dynamics. These results thus pose a challenge for emerging experimental methods with sufficient time resolution and provide a pioneering foundation for improved multiscale modeling.

Zusammenfassung

In dieser Arbeit wird die Energiedissipation bei exothermen chemischen Reaktionen im Kontext heterogener Katalyse mit Hilfe und unter entscheidender Weiterentwicklung von *ab initio* Methoden eingehend untersucht. Die Dissoziation von molekularem Sauerstoff (O_2) auf der Palladium(100)-Oberfläche dient als repräsentatives Beispiel, welches eine Freisetzung von rund 2.6 eV Chemisorptionsenergie involviert. Multiskalenmodelle, welche dem letzten Stand der Forschung entsprechen und daher ebenfalls auf *ab initio*-Ansätzen basieren, gehen implizit von einer instantanen Equilibrierung der Reaktionsprodukte aus. Konsequenzen dieser Markov-Näherung lassen sich nur durch explizite zeitabhängige Dynamik ohne weitere vereinfachende Annahmen abschätzen.

Sauerstoffmoleküle treffen mit zufällig verteilten Orientierungen und lateralen Positionen über der Oberfläche auf. Die zunehmende Wechselwirkung mit dem Oberflächenpotential steuert Erstere in bevorzugte Adsorptionskanäle, was zunächst ausgehend von einer eingefrorenen Oberfläche untersucht wird. Mit dieser Annahme benötigt Born-Oppenheimer Molekulardynamik eine (mindestens) sechsdimensionale Potentialhyperfläche, welche alle molekularen Freiheitsgrade berücksichtigt. Zur verlässlichen Einbeziehung des Bruches der Sauerstoff-Sauerstoff-Bindung wird diese auf dem Niveau von Dichtefunktionaltheorie (DFT) mit semilokalem Austausch-Korrelationsfunktional beschrieben. Um den notwendigen Rechenaufwand zu verringern, wird dies im Rahmen einer *divide et impera*-Strategie von der Dynamik entkoppelt. Das resultierende Interpolationsproblem lässt sich mit Hilfe von neuronalen Netzen unter Verwendung einer sehr geringen Zahl von Stützpunkten bewältigen. Dabei ist eine geeignete Transformation der Molekülkoordinaten von entscheidender Bedeutung, welche die komplexe Symmetrie des Systems berücksichtigt. Mangels Verfügbarkeit einer solchen Koordinatentransformation für zweiatomige Moleküle auf (100)-Oberflächen wurde ein eigener Ansatz entwickelt, und – im Gegensatz zu bisherigen Konzepten – dessen leichte Übertragbarkeit auf andere niedrigindizierte Oberflächen auch praktisch demonstriert. Der aus tausenden von Trajektorien resultierende Haftkoeffizient auf der sauberen Pd(100)-Oberfläche zeigt bei verschiedenen Einfallsenergien gute Übereinstimmung mit verfügbaren experimentellen Daten. Ganz im Gegensatz zu Aluminium(111)-Oberflächen lässt sich der Spinübergang des Sauerstoffmoleküls ($^3\Sigma_g^-$ Spin-Triplett in der Gasphase zu singlett-artigem Zustand auf der Oberfläche) also offenbar adiabatisch beschreiben.

Um dies und gleichzeitig die Bedeutung eines wichtigen Energiedissipationskanal genauer zu charakterisieren, wird die Anregung von Elektron-Loch-Paaren (eh-Paaren) in der Metalloberfläche mit Hilfe von zeitabhängiger Störungstheorie untersucht, ausgehend von zeitabhängiger Dichtefunktionaltheorie (TD-DFT) und der Kohn-Sham Bandstruktur des Substrats. Eine neuartige, effiziente Implementierung basierend auf weiterentwickelten Ideen zur Auswertung der benötigten nicht-adiabatischen Kopplungsmatrixelemente erlaubt die Berechnung von spinaufgelösten eh-Anregungsspektren erstmals für eine Vielzahl der mit Hilfe vorgenannter Potentialhyperfläche erhaltenen Trajektorien. In der Tat variieren die resultierenden Energieverluste über mehrere Größenordnungen, bleiben aber unterhalb von 100 meV und damit 5 % der oben genannten Chemisorptionsenergie. Einerseits scheiden eh-Paaranregungen damit als Hauptenergiedissipationskanal für dieses System aus, was im Einklang mit nicht detektierbaren

Chemoströmen bei Experimenten für letzteres ist. Andererseits offeriert eine Spin-Asymmetrie in den berechneten Spektren einen Mechanismus, der möglicherweise für den adiabatischen Verlauf des Spinübergangs des Sauerstoffmoleküls verantwortlich ist.

Somit rücken letztlich unweigerlich Phononen als Hauptenergiedissipationskanal in den Vordergrund. Eine detaillierte Diskussion verdeutlicht jedoch leider, dass Phononenanregungen bei der Adsorption auf Metalloberflächen mit bisherigen Ansätze nur äußerst ungenau und unangemessen beschrieben werden. Insbesondere ist bei herkömmlicher *ab initio* Molekulardynamik die Phononenpropagation durch die periodischen Randbedingungen begrenzt, welche zur korrekten Beschreibung der metallischen Bandstruktur mitsamt ihres Einflusses auf die chemische Bindung zum Adsorbat notwendig sind. Daher wurde ein neuartiges Einbettungsverfahren „QM/Me“ entwickelt, welches auch über den Rahmen dieser Arbeit hinaus vielfältige Anwendungsmöglichkeiten bietet. Im Rahmen dieser Arbeit erlaubt es die Modellierung realistischer (Oberflächen-) Phononen auf dem Niveau eines „modified embedded atom method“ (MEAM) Potentials, nahtlos angepasst an die simultane DFT-Beschreibung der O_2 Dissoziation. Erstmalig lässt sich dadurch die Dissipation in ein großes „Umgebungs-Bad“ direkt ausgehend von *ab initio* Methoden beobachten. Ein Vergleich mit vorhergehenden Ansätzen, welche alle starke Näherungen beinhalten, zeigt bemerkenswerte Abweichungen selbst im Hinblick auf Adsorbattrajektorien, welches schwere Zweifel an früheren Beschreibungen mit ebendiesen Ansätzen aufwirft. Weiterhin zeigt die erhaltenen Dissoziationsdynamik eine „heiße“ Translationsbewegung entlang der Oberfläche, bei der sich die beiden adsorbierten Sauerstoffatome in entgegengesetzte Richtungen voneinander weg diffundieren. Diese Verknüpfung von Dissoziation- und Diffusionsprozessen, welche durch die nicht instantane Dissipation der freiwerdenden Reaktionsenergie erfolgt, führt zum Zusammenbruch der sonst einhellig angewendeten Markov-Näherung für die Dynamik von Adsorptionsprozessen. Daraus resultierende Änderungen in der Adsorbatanordnung können wichtige Konsequenzen für viele Funktionalitäten von Oberflächen haben, einschließlich der katalytischen Aktivität. Schließlich erlaubt es ein neu entwickeltes Projektionsschema, den Einfluss von Oberflächenphononen und die in Modellen häufig verwendete harmonische Näherung für den Festkörper sowie ihr Versagen eingehend zu charakterisieren. Diese Ergebnisse stellen damit eine Herausforderung für aufkommende experimenteller Methoden mit ausreichender Zeitauflösung dar und bieten eine zukunftsweisende Grundlage für verbesserte Multiskalenmodellierung.

Publications

Publications which are directly related to this thesis:

7. I. Goikoetxea, J. Meyer, J. I. Juaristi, M. Alducin, and K. Reuter,
   "Scattering Dynamics of O_2 at Ag(111)",
   in preparation

6. J. Meyer and K. Reuter,
   "Symmetry Adapted Coordinates for Diatomics on Low-Index Surfaces",
   in preparation

5. J. Meyer and K. Reuter,
   "First-principles Initial Sticking of O_2 at Pd(100)",
   in preparation

4. J. Meyer and K. Reuter,
   "Chemical Reaction Dynamics on Metal Surfaces – Role of Phonons",
   in preparation

3. J. Meyer and K. Reuter,
   ""QM/Me" - a Novel Embedding Scheme for Adsorbate Dynamics on Metal Surfaces",
   in preparation

2. I. Goikoetxea, J. Beltrán, J. Meyer, M. Alducin, J. I. Juaristi, and K. Reuter,
   "Non-adiabatic effects during the dissociative adsorption of O_2 at Ag(111)? A first-principles divide and conquer study",
   New J. Phys. **14**, 013050 (2012), DOI: 10.1088/1367-2630/14/1/013050, arXiv: 1201.5514 [cond-mat.mtrl-sci]

1. J. Meyer and K. Reuter,
   "Electron-hole pairs during the adsorption dynamics of O_2 on Pd(100): Exciting or not?",
   New J. Phys. **13**, 085010 (2011), DOI: 10.1088/1367-2630/13/8/085010, arXiv: 1104.4212 [cond-mat.mtrl-sci]

For a complete list of publications of the author of this thesis the interested reader is referred to the corresponding part of the former's *curriculum vitae*.

Bibliography

[1] J. Dumesic, D. Rudd, and L. Aparicio, *The Microkinetics of Heterogeneous Catalysis*, in: American Chemical Society, Washington, DC, 1993, ISBN: 978-0841222144, (cit. on pp. 1, 162).

[2] I. Chorkendorff and H. Niemantsverdriet, *Concepts of Modern Catalysis and Kinetics*, in: Wiley-VCH, Weinheim, 2003, ISBN: 978-3527305742, (cit. on pp. 1, 162).

[3] K. Reuter, *First-Principles Kinetic Monte Carlo Simulations for Heterogeneous Catalysis: Concepts, Status and Frontiers*, in: *Modeling Heterogeneous Catalytic Reactions: From the Molecular Process to the Technical System*, ed. by O. Deutschmann, Wiley-VCH, Weinheim, 2011, ISBN: 978-3527321209, (cit. on pp. 1, 70, 165, 182).

[4] O. Deutschmann, *Computational Fluid Dynamics Simulation of Catalytic Reactors*, in: *Handbook of Heterogeneous Catalysis*, ed. by G. Ertl, H. Knözinger, F. Schüth, and J. Weinkamp, 2nd ed., Wiley-VCH, Weinheim, 2008, ISBN: 978-3527312412, (cit. on p. 1).

[5] S. Matera and K. Reuter, *First-Principles Approach to Heat and Mass Transfer Effects in Model Catalyst Studies*, Catal. Lett. **133**, 156 (2009), DOI: 10.1007/s10562-009-0168-8, (cit. on p. 1).

[6] S. Matera and K. Reuter, *Transport limitations and bistability for in situ CO oxidation at RuO_2(110) : First-principles based multiscale modeling*, Phys. Rev. B **82**, 085446 (2010), DOI: 10.1103/PhysRevB.82.085446, (cit. on p. 1).

[7] K. Reuter, D. Frenkel, and M. Scheffler, *The Steady State of Heterogeneous Catalysis, Studied by First-Principles Statistical Mechanics*, Phys. Rev. Lett. **93**, 116105 (2004), DOI: 10.1103/PhysRevLett.93.116105, (cit. on pp. 1, 162, 182).

[8] K. Reuter and M. Scheffler, *First-principles kinetic Monte Carlo simulations for heterogeneous catalysis: Application to the CO oxidation at* RuO_2(110), Phys. Rev. B **73**, 045433 (2006), DOI: 10.1103/PhysRevB.73.045433, (cit. on pp. 1, 70, 162, 182).

[9] J. Rogal, K. Reuter, and M. Scheffler, *First-Principles Statistical Mechanics Study of the Stability of a Subnanometer Thin Surface Oxide in Reactive Environments: CO Oxidation at Pd(100)*, Phys. Rev. Lett. **98**, 046101 (2007), DOI: 10.1103/PhysRevLett.98.046101, (cit. on pp. 1, 162).

[10] J. Rogal, K. Reuter, and M. Scheffler, *CO oxidation on Pd(100) at technologically relevant pressure conditions: First-principles kinetic Monte Carlo study*, Phys. Rev. B **77**, 155410 (2008), DOI: 10.1103/PhysRevB.77.155410, (cit. on pp. 1, 162).

[11] M. Todorova, W. X. Li, M. V. Ganduglia-Pirovano, C. Stampfl, K. Reuter, and M. Scheffler, *Role of Subsurface Oxygen in Oxide Formation at Transition Metal Surfaces*, Phys. Rev. Lett. **89**, 096103 (2002), DOI: 10.1103/PhysRevLett.89.096103, (cit. on pp. 1, 64).

[12] M. Todorova, E. Lundgren, V. Blum, A. Mikkelsen, S. Gray, J. Gustafson, M. Borg, J. Rogal, K. Reuter, J. N. Andersen, and M. Scheffler, *The Pd(100)-($\sqrt{5}\times\sqrt{5}$)R27°-O surface oxide revisited*, Surf. Sci. **541**, 101 (2003), DOI: 10.1016/S0039-6028(03)00873-2, (cit. on pp. 1, 55).

[13] E. Lundgren, J. Gustafson, A. Mikkelsen, J. N. Andersen, A. Stierle, H. Dosch, M. Todorova, J. Rogal, K. Reuter, and M. Scheffler, *Kinetic Hindrance during the Initial Oxidation of Pd(100) at Ambient Pressures*, Phys. Rev. Lett. **92**, 046101 (2004), DOI: 10.1103/PhysRevLett.92.046101, (cit. on p. 1).

[14] M. Todorova, K. Reuter, and M. Scheffler, *Density-functional theory study of the initial oxygen incorporation in Pd(111)*, Phys. Rev. B **71**, 195403 (2005), DOI: 10.1103/PhysRevB.71.195403, (cit. on pp. 1, 64).

[15] Y. Zhang, J. Rogal, and K. Reuter, *Density-functional theory investigation of oxygen adsorption at Pd(11N) vicinal surfaces ($N = 3, 5, 7$) : Influence of neighboring steps*, Phys. Rev. B **74**, 125414 (2006), DOI: 10.1103/PhysRevB.74.125414, (cit. on pp. 1, 55).

[16] Y. Zhang, V. Blum, and K. Reuter, *Accuracy of first-principles lateral interactions: Oxygen at Pd(100)*, Phys. Rev. B **75**, 235406 (2007), DOI: 10.1103/PhysRevB.75.235406, (cit. on pp. 1, 55, 63, 145, 161).

[17] A. Gerbi, L. Savio, L. Vattuone, F. Pirani, D. Cappelletti, and M. Rocca, *Role of rotational alignment in dissociative chemisorption and oxidation: O_2 on bare and CO-precovered Pd(100).* Angew. Chem. Int. Ed. **45**, 6655 (2006), DOI: 10.1002/anie.200602180, (cit. on pp. 1, 64, 96, 99).

[18] L. Vattuone, A. Gerbi, D. Cappelletti, F. Pirani, R. Gunnella, L. Savio, and M. Rocca, *Selective production of reactive and nonreactive oxygen atoms on Pd(001) by rotationally aligned oxygen molecules.* Angew. Chem. Int. Ed. **48**, 4845 (2009), DOI: 10.1002/anie.200900870, (cit. on pp. 1, 64, 99).

[19] L. Vattuone, A. Gerbi, L. Savio, D. Cappelletti, F. Pirani, and M. Rocca, *Stereoselectivity in catalytic reactions: CO oxidation on Pd(100) by rotationally aligned O_2 molecules*, Eur. Phys. J. B **75**, 81 (2010), DOI: 10.1140/epjb/e2010-00112-8, (cit. on pp. 1, 64, 99).

[20] J. E. Lennard-Jones, *Processes of adsorption and diffusion on solid surfaces*, Trans. Faraday Soc. **28**, 333 (1932), DOI: 10.1039/TF9322800333, (cit. on pp. 1, 69).

[21] A. Groß, *Reactions at surfaces studied by ab initio dynamics calculations*, Surf. Sci. Rep. **32**, 291 (1998), DOI: 10.1016/S0167-5729(98)00008-9, (cit. on p. 2).

[22] G.-J. Kroes, A. Groß, E.-J. Baerends, M. Scheffler, and D. A. McCormack, *Quantum Theory of Dissociative Chemisorption on Metal Surfaces*, Acc. Chem. Res. **35**, 193 (2002), DOI: 10.1021/ar010104u, (cit. on pp. 2, 70, 101).

[23] H. F. Busnengo, W. Dong, P. Sautet, and A. Salin, *Surface Temperature Dependence of Rotational Excitation of H_2 Scattered from Pd(111)*, Phys. Rev. Lett. **87**, 127601 (2001), DOI: 10.1103/PhysRevLett.87.127601, (cit. on pp. 2, 135, 151, 156 sq., 263).

[24] H. F. Busnengo, W. Dong, and A. Salin, *Trapping, Molecular Adsorption, and Precursors for Nonactivated Chemisorption*, Phys. Rev. Lett. **93**, 236103 (2004), DOI: 10.1103/PhysRevLett.93.236103, (cit. on pp. 2, 157, 263).

[25] A. Groß, *Ab Initio Molecular Dynamics Simulations of the Adsorption of H2 on Palladium Surfaces*, ChemPhysChem **11**, 1374 (2010), DOI: 10.1002/cphc.200900818, (cit. on pp. 2, 71, 146).

[26] M. Bonfanti, C. Diaz, M. F. Somers, and G.-J. Kroes, *Hydrogen dissociation on Cu(111): The influence of lattice motion. Part I*, Phys. Chem. Chem. Phys. **13**, 4552 (2011), DOI: 10.1039/C0CP01746A, (cit. on pp. 2, 181).

[27] H. Nienhaus, H. S. Bergh, B. Gergen, A. Majumdar, W. H. Weinberg, and E. W. McFarland, *Electron-Hole Pair Creation at Ag and Cu Surfaces by Adsorption of Atomic Hydrogen and Deuterium*, Phys. Rev. Lett. **82**, 446 (1999), DOI: 10.1103/PhysRevLett.82.446, (cit. on pp. 2, 123).

[28] H. Nienhaus, *Electronic excitations by chemical reactions on metal surfaces*, Surf. Sci. Rep. **45**, 1 (2002), DOI: 10.1016/S0167-5729(01)00019-X, (cit. on pp. 2, 103, 123, 181).

[29] Y. Huang, C. T. Rettner, D. J. Auerbach, and A. M. Wodtke, *Vibrational Promotion of Electron Transfer*, Science **290**, 111 (2000), DOI: 10.1126/science.290.5489.111, (cit. on pp. 2, 69, 125, 141).

[30] A. M. Wodtke, J. C. Tully, and D. J. Auerbach, *Electronically non-adiabatic interactions of molecules at metal surfaces: Can we trust the Born-Oppenheimer approximation for surface chemistry?* Int. Rev. Phys. Chem. **23**, 513 (2004), (cit. on pp. 2, 9, 69, 101, 125).

[31] M. Head-Gordon and J. C. Tully, *Vibrational relaxation on metal surfaces: Molecular-orbital theory and application to CO/Cu(100)*, J. Chem. Phys. **96**, 3939 (1992), DOI: 10.1063/1.461896, (cit. on pp. 2, 101, 111).

[32] M. Head-Gordon and J. C. Tully, *Molecular dynamics with electronic frictions*, J. Chem. Phys. **103**, 10137 (1995), DOI: 10.1063/1.469915, (cit. on pp. 2, 101, 103, 133).

[33] X. Li, J. C. Tully, H. B. Schlegel, and M. J. Frisch, *Ab initio Ehrenfest dynamics*, J. Chem. Phys. **123**, 084106 (2005), DOI: 10.1063/1.2008258, (cit. on pp. 2, 101).

[34] H. Cheng, N. Shenvi, and J. C. Tully, *Publisher's Note: Semiclassical Dynamics of Electron Transfer at Metal Surfaces [Phys. Rev. Lett. 99, 053201 (2007)]*, Phys. Rev. Lett. **99**, 069903 (2007), DOI: 10.1103/PhysRevLett.99.069903, (cit. on pp. 2, 101).

[35] H. Cheng, N. Shenvi, and J. C. Tully, *Semiclassical Dynamics of Electron Transfer at Metal Surfaces*, Phys. Rev. Lett. **99**, 053201 (2007), DOI: 10.1103/PhysRevLett.99.053201, (cit. on pp. 2, 101).

[36] S. Roy, N. A. Shenvi, and J. C. Tully, *Model Hamiltonian for the interaction of NO with the Au(111) surface*, J. Chem. Phys. **130**, 174716 (2009), DOI: 10.1063/1.3122989, (cit. on pp. 2, 71, 125, 151, 174).

[37] S. Roy, N. Shenvi, and J. C. Tully, *Dynamics of Open-Shell Species at Metal Surfaces†*, J. Phys. Chem. C **113**, 16311 (2009), DOI: 10.1021/jp811393w, (cit. on pp. 2, 71, 125).

[38] N. Shenvi, S. Roy, and J. C. Tully, *Nonadiabatic dynamics at metal surfaces: Independent-electron surface hopping*, J. Chem. Phys. **130**, 174107 (2009), DOI: 10.1063/1.3125436, (cit. on pp. 2, 101, 125, 141).

[39] N. Shenvi, S. Roy, and J. C. Tully, *Dynamical Steering and Electronic Excitation in NO Scattering from a Gold Surface*, Science **326**, 829 (2009), DOI: 10.1126/science.1179240, (cit. on pp. 2, 71, 101, 125).

[40] J. G. Gay, J. R. Smith, F. J. Arlinghaus, and T. W. Capehart, *Electronic structure of palladium (100)*, Phys. Rev. B **23**, 1559 (1981), DOI: 10.1103/PhysRevB.23.1559, (cit. on pp. 2, 102).

[41] G. S. Elliott, K. E. Smith, and S. D. Kevan, *Surface localized states and the Fermi contour of Pd(001)*, Phys. Rev. B **43**, 3893 (1991), DOI: 10.1103/PhysRevB.43.3893, (cit. on pp. 2, 102).

[42] S. C. Wu, D. M. Poirier, M. B. Jost, and J. H. Weaver, *Inverse-photoemission study of the Pd(001) surface*, Phys. Rev. B **45**, 8709 (1992), DOI: 10.1103/PhysRevB.45.8709, (cit. on pp. 2, 102).

[43] M. Heinrichsmeier, A. Fleszar, W. Hanke, and A. G. Eguiluz, *Nonlocal density-functional calculations of the surface electronic structure of metals: Application to aluminum and palladium*, Phys. Rev. B **57**, 14974 (1998), DOI: 10.1103/PhysRevB.57.14974, (cit. on pp. 2, 102).

[44] J. I. Juaristi, M. Alducin, R. Dìez Muiño, H. F. Busnengo, and A. Salin, *Role of Electron-Hole Pair Excitations in the Dissociative Adsorption of Diatomic Molecules on Metal Surfaces*, Phys. Rev. Lett. **100**, 116102 (2008), DOI: 10.1103/PhysRevLett.100.116102, (cit. on pp. 2, 69, 101, 103, 119, 124, 141, 181).

[45] A. C. Luntz, I. Makkonen, M. Persson, S. Holloway, D. M. Bird, and M. S. Mizielinski, *Comment on "Role of Electron-Hole Pair Excitations in the Dissociative Adsorption of Diatomic Molecules on Metal Surfaces"*, Phys. Rev. Lett. **102**, 109601 (2009), DOI: 10.1103/PhysRevLett.102.109601, (cit. on pp. 2, 69, 101, 103, 124, 181).

[46] J. I. Juaristi, M. Alducin, R. Dìez Muiño, H. F. Busnengo, and A. Salin, *Juaristi et al. Reply:* Phys. Rev. Lett. **102**, 109602 (2009), DOI: 10.1103/PhysRevLett.102.109602, (cit. on pp. 2, 69, 101, 103, 124, 141, 181).

[47] J. Behler, B. Delley, S. Lorenz, K. Reuter, and M. Scheffler, *Dissociation of O_2 at Al(111): The Role of Spin Selection Rules*, Phys. Rev. Lett. **94**, 036104 (2005), DOI: 10.1103/PhysRevLett.94.036104, (cit. on pp. 2, 15, 65, 69, 71, 81, 90, 95, 102).

[48] J. Behler, K. Reuter, and M. Scheffler, *Nonadiabatic effects in the dissociation of oxygen molecules at the Al(111) surface*, Phys. Rev. B **77**, 115421 (2008), DOI: 10.1103/PhysRevB.77.115421, (cit. on pp. 2, 55, 61 sq., 71, 81, 91, 95, 102, 119).

[49] C. Carbogno, J. Behler, A. Groß, and K. Reuter, *Fingerprints for Spin-Selection Rules in the Interaction Dynamics of O_2 at Al(111)*, Phys. Rev. Lett. **101**, 096104 (2008), DOI: 10.1103/PhysRevLett.101.096104, (cit. on pp. 2, 61 sq., 95, 102).

[50] C. Carbogno, J. Behler, K. Reuter, and A. Groß, *Signatures of nonadiabatic O_2 dissociation at Al(111): First-principles fewest-switches study*, Phys. Rev. B **81**, 035410 (2010), DOI: 10.1103/PhysRevB.81.035410, (cit. on pp. 2, 61 sq., 65, 71, 95, 102).

[51] H. Schwarz, *On the spin-forbiddeness of gas-phase ion-molecule reactions: A fruitful intersection of experimental and computational studies*, Int. J. Mass Spectrom. **237**, 75 (2004), DOI: 10.1016/j.ijms.2004.06.006, (cit. on pp. 2, 102).

[52] I. Goikoetxea, J. Beltrán, J. Meyer, M. Alducin, J. I. Juaristi, and K. Reuter, *Non-adiabatic effects during the dissociative adsorption of O_2 at Ag(111)? A first-principles divide and conquer study*, New J. Phys. **14**, 013050 (2012), DOI: 10.1088/1367-2630/14/1/013050, (cit. on pp. 2 sq., 88, 96, 99, 181, 200).

[53] F. Schwabl, *Quantum Mechnanics*, in: 4th ed., Springer, Berlin, 2007, ISBN: 978-3540719328, (cit. on pp. 7, 105).

[54] M. Born and R. Oppenheimer, *Zur Quantentheorie der Molekeln*, Annalen der Physik **389**, 457 (1927), DOI: 10.1002/andp.19273892002, (cit. on p. 9).

[55] R. P. Feynman, *Forces in Molecules*, Phys. Rev. **56**, 340 (1939), DOI: 10.1103/PhysRev.56.340, (cit. on p. 10).

[56] L. H. Thomas, *The calculation of atomic fields*, Proc. Cambridge Phil. Soc. **23**, 542 (1927), DOI: 10.1017/S0305004100011683, (cit. on pp. 10, 14).

[57] E. Fermi, *Un Metodo Statistico per la Determinazione di alcune Prioprietà dell'Atomo*, Rend. Accad. Naz. Lincei **6**, 602 (1927), (cit. on pp. 10, 14).

[58] E. Fermi, *Eine statistische Methode zur Bestimmung einiger Eigenschaften des Atoms und ihre Anwendung auf die Theorie des periodischen Systems der Elemente*, Zeitschrift für Physik A **48**, 73 (1928), DOI: 10.1007/BF01351576, (cit. on pp. 10, 14).

[59] P. Hohenberg and W. Kohn, *Inhomogeneous Electron Gas*, Phys. Rev. **136**, B864 (1964), DOI: 10.1103/PhysRev.136.B864, (cit. on pp. 10 sq.).

[60] J. Chayes, L. Chayes, and M. Ruskai, *Density functional approach to quantum lattice systems*, Journal of Statistical Physics **38**, 497 (1985), DOI: 10.1007/BF01010474, (cit. on p. 11).

[61] M. Levy, *Electron densities in search of Hamiltonians*, Phys. Rev. A **26**, 1200 (1982), DOI: 10.1103/PhysRevA.26.1200, (cit. on p. 11).

[62] E. H. Lieb, *Density functionals for coulomb systems*, Int. J. Quantum Chem. **24**, 243 (1983), DOI: 10.1002/qua.560240302, (cit. on p. 11).

[63] M. Levy, *Universal Variational Functionals of Electron Densities, First-Order Density Matrices, and Natural Spin-Orbitals and Solution of the v-Representability Problem*, Proc. Natl. Acad. Sci. USA **76**, 6062 (1979), (cit. on p. 11).

[64] N. Choly and E. Kaxiras, *Kinetic energy density functionals for non-periodic systems*, Solid State Commun. **121**, 281 (2002), DOI: 10.1016/S0038-1098(01)00500-2, (cit. on p. 11).

[65] G. Lu, E. B. Tadmor, and E. Kaxiras, *From electrons to finite elements: A concurrent multiscale approach for metals*, Phys. Rev. B **73**, 024108 (2006), DOI: 10.1103/PhysRevB.73.024108, (cit. on p. 11).

[66] W. Kohn and L. J. Sham, *Self-Consistent Equations Including Exchange and Correlation Effects*, Phys. Rev. **140**, A1133 (1965), DOI: 10.1103/PhysRev.140.A1133, (cit. on p. 12).

[67] R. Stowasser and R. Hoffmann, *What Do the Kohn-Sham Orbitals and Eigenvalues Mean?* J. Am. Chem. Soc. **121**, 3414 (1999), DOI: 10.1021/ja9826892, (cit. on p. 12).

[68] E. Runge and E. K. U. Gross, *Density-Functional Theory for Time-Dependent Systems*, Phys. Rev. Lett. **52**, 997 (1984), DOI: 10.1103/PhysRevLett.52.997, (cit. on pp. 13, 104).

[69] C. F. Craig, W. R. Duncan, and O. V. Prezhdo, *Trajectory Surface Hopping in the Time-Dependent Kohn-Sham Approach for Electron-Nuclear Dynamics*, Phys. Rev. Lett. **95**, 163001 (2005), DOI: 10.1103/PhysRevLett.95.163001, (cit. on p. 13).

[70] S. A. Fischer, B. F. Habenicht, A. B. Madrid, W. R. Duncan, and O. V. Prezhdo, *Regarding the validity of the time-dependent Kohn–Sham approach for electron-nuclear dynamics via trajectory surface hopping*, J. Chem. Phys. **134**, 024102 (2011), DOI: 10.1063/1.3526297, (cit. on p. 13).

[71] A. Abedi, N. T. Maitra, and E. K. U. Gross, *Exact Factorization of the Time-Dependent Electron-Nuclear Wave Function*, Phys. Rev. Lett. **105**, 123002 (2010), DOI: 10.1103/PhysRevLett.105.123002, (cit. on pp. 13, 101, 124).

[72] U. von Barth and L. Hedin, *A local exchange-correlation potential for the spin polarized case. I*, Journal of Physics C: Solid State Physics **5**, 1629 (1972), DOI: 10.1088/0022-3719/5/13/012, (cit. on pp. 14, 104).

[73] J. R. Trail, D. M. Bird, M. Persson, and S. Holloway, *Electron–hole pair creation by atoms incident on a metal surface*, J. Chem. Phys. **119**, 4539 (2003), DOI: 10.1063/1.1593631, (cit. on pp. 14, 103, 107 sqq., 113, 248).

[74] M. Lindenblatt and E. Pehlke, *Ab Initio Simulation of the Spin Transition during Chemisorption: H/Al(111)*, Phys. Rev. Lett. **97**, 216101 (2006), DOI: 10.1103/PhysRevLett.97.216101, (cit. on pp. 14, 103, 105, 108 sq., 112, 118 sq., 123 sq., 136, 141).

[75] F. L. Hirshfeld, *Bonded-atom fragments for describing molecular charge densities*, Theoret. Chim. Acta **44**, 129 (1977), DOI: 10.1007/BF00549096, (cit. on p. 15).

[76] J. Behler, *Dissociation of Oxygen Molecules on the Al(111) Surface*, PhD thesis, Technische Universität Berlin, 2004, (cit. on pp. 15, 55, 60 sqq., 77 sq., 91, 119).

[77] J. Behler, B. Delley, K. Reuter, and M. Scheffler, *Nonadiabatic potential-energy surfaces by constrained density-functional theory*, Phys. Rev. B **75**, 115409 (2007), DOI: 10.1103/PhysRevB.75.115409, (cit. on pp. 15, 77, 102).

[78] D. M. Ceperley and B. J. Alder, *Ground State of the Electron Gas by a Stochastic Method*, Phys. Rev. Lett. **45**, 566 (1980), DOI: 10.1103/PhysRevLett.45.566, (cit. on p. 15).

[79] J. P. Perdew and A. Zunger, *Self-interaction correction to density-functional approximations for many-electron systems*, Phys. Rev. B **23**, 5048 (1981), DOI: 10.1103/PhysRevB.23.5048, (cit. on pp. 15, 55).

[80] J. P. Perdew and Y. Wang, *Accurate and simple analytic representation of the electron-gas correlation energy*, Phys. Rev. B **45**, 13244 (1992), DOI: 10.1103/PhysRevB.45.13244, (cit. on pp. 15, 55).

[81] R. O. Jones and O. Gunnarsson, *The density functional formalism, its applications and prospects*, Rev. Mod. Phys. **61**, 689 (1989), DOI: 10.1103/RevModPhys.61.689, (cit. on p. 15).

[82] M. Scheffler and C. Stampfl, *Theory of adsorption on metal substrates*, in: *Handbook of Surface Science*, Handbook of Surface Science, Vol. 2, ed. by K. Horn and M. Scheffler, Elsevier, Amsterdam, 2000, ISBN: 978-0444892911, pp. 286–356, (cit. on pp. 15, 19, 70, 137, 143).

[83] J. P. Perdew, J. A. Chevary, S. H. Vosko, K. A. Jackson, M. R. Pederson, D. J. Singh, and C. Fiolhais, *Atoms, molecules, solids, and surfaces: Applications of the generalized gradient approximation for exchange and correlation*, Phys. Rev. B **46**, 6671 (1992), DOI: 10.1103/PhysRevB.46.6671, (cit. on p. 15).

[84] J. P. Perdew, J. A. Chevary, S. H. Vosko, K. A. Jackson, M. R. Pederson, D. J. Singh, and C. Fiolhais, *Erratum: Atoms, molecules, solids, and surfaces: Applications of the generalized gradient approximation for exchange and correlation*, Phys. Rev. B **48**, 4978 (1993), DOI: 10.1103/PhysRevB.48.4978.2, (cit. on p. 15).

[85] J. P. Perdew, K. Burke, and M. Ernzerhof, *Generalized Gradient Approximation Made Simple*, Phys. Rev. Lett. **77**, 3865 (1996), DOI: 10.1103/PhysRevLett.77.3865, (cit. on pp. 15, 55, 89, 247).

[86] J. P. Perdew, K. Burke, and M. Ernzerhof, *Generalized Gradient Approximation Made Simple [Phys. Rev. Lett. 77, 3865 (1996)]*, Phys. Rev. Lett. **78**, 1396 (1997), DOI: 10.1103/PhysRevLett.78.1396, (cit. on pp. 15, 55, 89, 247).

[87] Y. Zhang and W. Yang, *Comment on "Generalized Gradient Approximation Made Simple"*, Phys. Rev. Lett. **80**, 890 (1998), DOI: 10.1103/PhysRevLett.80.890, (cit. on p. 15).

[88] J. P. Perdew, K. Burke, and M. Ernzerhof, *Perdew, Burke, and Ernzerhof Reply:* Phys. Rev. Lett. **80**, 891 (1998), DOI: 10.1103/PhysRevLett.80.891, (cit. on p. 15).

[89] B. Hammer, L. B. Hansen, and J. K. Nørskov, *Improved adsorption energetics within density-functional theory using revised Perdew-Burke-Ernzerhof functionals*, Phys. Rev. B **59**, 7413 (1999), DOI: 10.1103/PhysRevB.59.7413, (cit. on pp. 15, 55).

[90] Q.-M. Hu, K. Reuter, and M. Scheffler, *Erratum: Towards an Exact Treatment of Exchange and Correlation in Materials: Application to the "CO Adsorption Puzzle" and Other Systems [Phys. Rev. Lett. 98, 176103 (2007)]*, Phys. Rev. Lett. **99**, 169903 (2007), DOI: 10.1103/PhysRevLett.99.169903, (cit. on p. 15).

[91] Q.-M. Hu, K. Reuter, and M. Scheffler, *Towards an Exact Treatment of Exchange and Correlation in Materials: Application to the "CO Adsorption Puzzle" and Other Systems*, Phys. Rev. Lett. **98**, 176103 (2007), DOI: 10.1103/PhysRevLett.98.176103, (cit. on p. 15).

[92] M. Rohlfing and T. Bredow, *Binding Energy of Adsorbates on a Noble-Metal Surface: Exchange and Correlation Effects*, Phys. Rev. Lett. **101**, 266106 (2008), DOI: 10.1103/PhysRevLett.101.266106, (cit. on p. 15).

[93] X. Ren, P. Rinke, and M. Scheffler, *Exploring the random phase approximation: Application to CO adsorbed on Cu(111)*, Phys. Rev. B **80**, 045402 (2009), DOI: 10.1103/PhysRevB.80.045402, (cit. on p. 15).

[94] L. Schimka, J. Harl, A. Stroppa, A. Grüneis, M. Marsman, F. Mittendorfer, and G. Kresse, *Accurate surface and adsorption energies from many-body perturbation theory*, Nature Materials **9**, 741 (2010), DOI: 10.1038/nmat2806, (cit. on p. 15).

[95] M. Dion, H. Rydberg, E. Schröder, D. C. Langreth, and B. I. Lundqvist, *Van der Waals Density Functional for General Geometries*, Phys. Rev. Lett. **92**, 246401 (2004), DOI: 10.1103/PhysRevLett.92.246401, (cit. on p. 15).

[96] M. Dion, H. Rydberg, E. Schröder, D. C. Langreth, and B. I. Lundqvist, *Erratum: Van der Waals Density Functional for General Geometries [Phys. Rev. Lett. 92, 246401 (2004)]*, Phys. Rev. Lett. **95**, 109902 (2005), DOI: 10.1103/PhysRevLett.95.109902, (cit. on p. 15).

[97] J. Klimeš, D. R. Bowler, and A. Michaelides, *Chemical accuracy for the van der Waals density functional*, J. Phys.: Condens. Matter **22**, 022201 (2010), DOI: 10.1088/0953-8984/22/2/022201, (cit. on p. 15).

[98] O. A. Vydrov and T. V. Voorhis, *Improving the accuracy of the nonlocal van der Waals density functional with minimal empiricism*, J. Chem. Phys. **130**, 104105 (2009), DOI: 10.1063/1.3079684, (cit. on p. 15).

[99] O. A. Vydrov and T. V. Voorhis, *Nonlocal van der Waals Density Functional Made Simple*, Phys. Rev. Lett. **103**, 063004 (2009), DOI: 10.1103/PhysRevLett.103.063004, (cit. on p. 15).

[100] O. A. Vydrov and T. V. Voorhis, *Implementation and assessment of a simple nonlocal van der Waals density functional*, J. Chem. Phys. **132**, 164113 (2010), DOI: 10.1063/1.3398840, (cit. on p. 15).

[101] O. A. Vydrov and T. V. Voorhis, *Nonlocal van der Waals density functional: The simpler the better*, J. Chem. Phys. **133**, 244103 (2010), DOI: 10.1063/1.3521275, (cit. on p. 15).

[102] O. A. Vydrov and T. V. Voorhis, *Vydrov and Van Voorhis Reply:* Phys. Rev. Lett. **104**, 099304 (2010), DOI: 10.1103/PhysRevLett.104.099304, (cit. on p. 15).

[103] G. Román-Pérez and J. M. Soler, *Efficient Implementation of a van der Waals Density Functional: Application to Double-Wall Carbon Nanotubes*, Phys. Rev. Lett. **103**, 096102 (2009), DOI: 10.1103/PhysRevLett.103.096102, (cit. on p. 15).

[104] F. Ortmann, F. Bechstedt, and W. G. Schmidt, *Semiempirical van der Waals correction to the density functional description of solids and molecular structures*, Phys. Rev. B **73**, 205101 (2006), DOI: 10.1103/PhysRevB.73.205101, (cit. on pp. 15, 28).

[105] S. Grimme, *Semiempirical GGA-type density functional constructed with a long-range dispersion correction*, J. Comput. Chem. **27**, 1787 (2006), DOI: 10.1002/jcc.20495, (cit. on pp. 15, 28).

[106] A. Tkatchenko and M. Scheffler, *Accurate Molecular Van Der Waals Interactions from Ground-State Electron Density and Free-Atom Reference Data*, Phys. Rev. Lett. **102**, 073005 (2009), DOI: 10.1103/PhysRevLett.102.073005, (cit. on pp. 15, 29).

[107] E. R. McNellis, J. Meyer, and K. Reuter, *Azobenzene at coinage metal surfaces: Role of dispersive van der Waals interactions*, Phys. Rev. B **80**, 205414 (2009), DOI: 10.1103/PhysRevB.80.205414, (cit. on pp. 15, 22, 29).

[108] G. Mercurio, E. R. McNellis, I. Martin, S. Hagen, F. Leyssner, S. Soubatch, J. Meyer, M. Wolf, P. Tegeder, F. S. Tautz, and K. Reuter, *Structure and Energetics of Azobenzene on Ag(111): Benchmarking Semiempirical Dispersion Correction Approaches*, Phys. Rev. Lett. **104**, 036102 (2010), DOI: 10.1103/PhysRevLett.104.036102, (cit. on pp. 15, 22).

[109] C. Carbogno, *Non-Adiabatic Effects in the Dissociative Adsorption of O_2 on Aluminum (111) Surfaces*, PhD thesis, Universität Ulm, 2009, (cit. on pp. 15, 60, 102, 119).

[110] F. Bloch, *Über die Quantenmechanik der Elektronen in Kristallgittern*, Z. Phys. A **52**, 555 (1929), DOI: 10.1007/BF01339455, (cit. on p. 16).

[111] W. E. Pickett, *Pseudopotential methods in condensed matter applications*, Computer Physics reports **9**, 115 (1989), DOI: 10.1016/0167-7977(89)90002-6, (cit. on p. 17).

[112] M. Fuchs and M. Scheffler, *Ab initio pseudopotentials for electronic structure calculations of poly-atomic systems using density-functional theory*, Comput. Phys. Commun. **119**, 67 (1999), DOI: 10.1016/S0010-4655(98)00201-X, (cit. on p. 17).

[113] L. Kleinman and D. M. Bylander, *Efficacious Form for Model Pseudopotentials*, Phys. Rev. Lett. **48**, 1425 (1982), DOI: 10.1103/PhysRevLett.48.1425, (cit. on p. 17).

[114] D. D. Koelling and B. N. Harmon, *A technique for relativistic spin-polarised calculations*, Journal of Physics C: Solid State Physics **10**, 3107 (1977), DOI: 10.1088/0022-3719/10/16/019, (cit. on p. 17).

[115] D. R. Hamann, M. Schlüter, and C. Chiang, *Norm-Conserving Pseudopotentials*, Phys. Rev. Lett. **43**, 1494 (1979), DOI: 10.1103/PhysRevLett.43.1494, (cit. on p. 17).

[116] N. Troullier and J. Martins, *Efficient pseudopotentials for plane-wave calculations*, Phys. Rev. B **43**, 1993 (1991), DOI: 10.1103/PhysRevB.43.1993, (cit. on p. 17).

[117] D. Vanderbilt, *Soft self-consistent pseudopotentials in a generalized eigenvalue formalism*, Phys. Rev. B **41**, 7892 (1990), DOI: 10.1103/PhysRevB.41.7892, (cit. on pp. 19, 247).

[118] K. Laasonen, R. Car, C. Lee, and D. Vanderbilt, *Implementation of ultrasoft pseudopotentials in ab initio molecular dynamics*, Phys. Rev. B **43**, 6796 (1991), DOI: 10.1103/PhysRevB.43.6796, (cit. on pp. 19, 247).

[119] N. Lorente and M. Persson, *Theoretical aspects of tunneling-current-induced bond excitation and breaking at surfaces*, Faraday Discuss. **117**, 277 (2000), DOI: 10.1039/B002826F, (cit. on pp. 19, 111, 113, 120, 181).

[120] E. McNellis, J. Meyer, A. D. Baghi, and K. Reuter, *Stabilizing a molecular switch at solid surfaces: A density functional theory study of azobenzene on Cu(111), Ag(111), and Au(111)*, Phys. Rev. B **80**, 035414 (2009), DOI: 10.1103/PhysRevB.80.035414, (cit. on pp. 19, 122).

[121] K. Laasonen, A. Pasquarello, R. Car, C. Lee, and D. Vanderbilt, *Car-Parrinello molecular dynamics with Vanderbilt ultrasoft pseudopotentials*, Phys. Rev. B **47**, 10142 (1993), DOI: 10.1103/PhysRevB.47.10142, (cit. on p. 19).

[122] D. J. Chadi and M. L. Cohen, *Special Points in the Brillouin Zone*, Phys. Rev. B **8**, 5747 (1973), DOI: 10.1103/PhysRevB.8.5747, (cit. on p. 19).

[123] H. J. Monkhorst and J. D. Pack, *Special points for Brillouin-zone integrations*, Phys. Rev. B **13**, 5188 (1976), DOI: 10.1103/PhysRevB.13.5188, (cit. on pp. 19, 247).

[124] M. C. Payne, M. P. Teter, D. C. Allan, T. A. Arias, and J. D. Joannopoulos, *Iterative minimization techniques for ab initio total-energy calculations: Molecular dynamics and conjugate gradients*, Rev. Mod. Phys. **64**, 1045 (1992), DOI: 10.1103/RevModPhys.64.1045, (cit. on pp. 19 sq., 24).

[125] C. G. Broyden, *A Class of Methods for Solving Nonlinear Simultaneous Equations*, Mathematics of Computation **19**, 577 (1965), (cit. on p. 20).

[126] P. Pulay, *Convergence acceleration of iterative sequences. The case of scf iteration*, Chem. Phys. Lett. **73**, 393 (1980), DOI: 10.1016/0009-2614(80)80396-4, (cit. on p. 20).

[127] G. P. Kerker, *Efficient iteration scheme for self-consistent pseudopotential calculations*, Phys. Rev. B **23**, 3082 (1981), DOI: 10.1103/PhysRevB.23.3082, (cit. on p. 20).

[128] G. P. Srivastava, *Broyden's method for self-consistent field convergence acceleration*, J. Phys. A: Math. Gen. **17**, L317 (1984), DOI: 10.1088/0305-4470/17/6/002, (cit. on p. 20).

[129] D. D. Johnson, *Modified Broyden's method for accelerating convergence in self-consistent calculations*, Phys. Rev. B **38**, 12807 (1988), DOI: 10.1103/PhysRevB.38.12807, (cit. on p. 20).

[130] R. Car and M. Parrinello, *Unified Approach for Molecular Dynamics and Density-Functional Theory*, Phys. Rev. Lett. **55**, 2471 (1985), DOI: 10.1103/PhysRevLett.55.2471, (cit. on pp. 20, 34).

[131] M. P. Teter, M. C. Payne, and D. C. Allan, *Solution of Schrödinger's equation for large systems*, Phys. Rev. B **40**, 12255 (1989), DOI: 10.1103/PhysRevB.40.12255, (cit. on pp. 20, 24, 61).

[132] W. H. Press, S. A. Teukolsky, W. T. Vetterling, and B. P. Flannery, *Numerical Recipes in Fortran 77 : The Art of Scientific Computing*, in: *Fortran Numerical Recipes*, Vol. 1, 2nd ed., Cambridge University Press, Cambridge, 1992, ISBN: 0-521-43064-X, (cit. on pp. 20, 36 sq., 59).

[133] G. Kresse and J. Furthmüller, *Efficiency of ab-initio total energy calculations for metals and semiconductors using a plane-wave basis set*, Computational Materials Science **6**, 15 (1996), DOI: 10.1016/0927-0256(96)00008-0, (cit. on pp. 20, 24, 61).

[134] G. Kresse and J. Furthmüller, *Efficient iterative schemes for ab initio total-energy calculations using a plane-wave basis set*, Phys. Rev. B **54**, 11169 (1996), DOI: 10.1103/PhysRevB.54.11169, (cit. on pp. 20, 24).

[135] C.-L. Fu and K.-M. Ho, *First-principles calculation of the equilibrium ground-state properties of transition metals: Applications to Nb and Mo*, Phys. Rev. B **28**, 5480 (1983), DOI: 10.1103/PhysRevB.28.5480, (cit. on pp. 21 sq.).

[136] S. de Gironcoli, *Lattice dynamics of metals from density-functional perturbation theory*, Phys. Rev. B **51**, 6773 (1995), DOI: 10.1103/PhysRevB.51.6773, (cit. on p. 21).

[137] M. J. Gillan, *Calculation of the vacancy formation energy in aluminium*, J. Phys.: Condens. Matter **1**, 689 (1989), DOI: 10.1088/0953-8984/1/4/005, (cit. on p. 21).

[138] N. D. Mermin, *Thermal Properties of the Inhomogeneous Electron Gas*, Phys. Rev. **137**, A1441 (1965), DOI: 10.1103/PhysRev.137.A1441, (cit. on p. 21).

[139] J. A. White, D. M. Bird, and M. C. Payne, *Dissociation of H_2 on W(100)*, Phys. Rev. B **53**, 1667 (1996), DOI: 10.1103/PhysRevB.53.1667, (cit. on p. 22).

[140] M. Methfessel and A. T. Paxton, *High-precision sampling for Brillouin-zone integration in metals*, Phys. Rev. B **40**, 3616 (1989), DOI: 10.1103/PhysRevB.40.3616, (cit. on p. 22).

[141] N. Marzari, *Ab-initio Molecular Dynamics for Metallic Systems*, PhD thesis, Pembroke College, University of Cambridge, 1996, (cit. on p. 22).

[142] B. G. Walker, C. Molteni, and N. Marzari, *Ab initio molecular dynamics of metal surfaces*, J. Phys.: Condens. Matter **16**, S2575 (2004), DOI: 10.1088/0953-8984/16/26/028, (cit. on pp. 22, 24, 61, 65).

[143] F. Wagner, T. Laloyaux, and M. Scheffler, *Errors in Hellmann-Feynman forces due to occupation-number broadening and how they can be corrected*, Phys. Rev. B **57**, 2102 (1998), DOI: 10.1103/PhysRevB.57.2102, (cit. on p. 22).

[144] N. Marzari, D. Vanderbilt, and M. C. Payne, *Ensemble Density-Functional Theory for Ab Initio Molecular Dynamics of Metals and Finite-Temperature Insulators*, Phys. Rev. Lett. **79**, 1337 (1997), DOI: 10.1103/PhysRevLett.79.1337, (cit. on pp. 22, 24, 61).

[145] M. D. Segall, P. J. D. Lindan, M. J. Probert, C. J. Pickard, P. J. Hasnip, S. J. Clark, and M. C. Payne, *First-principles simulation: Ideas, illustrations and the CASTEP code*, J. Phys.: Condens. Matter **14**, 2717 (2002), DOI: 10.1088/0953-8984/14/11/301, (cit. on pp. 22, 24, 247).

[146] S. J. Clark, M. D. Segall, C. J. Pickard, P. J. Hasnip, M. I. J. Probert, K. Refson, and M. C. Payne, *First principles methods using CASTEP*, Z. Kristallogr. **220**, 567 (2009), DOI: 10.1524/zkri.220.5.567.65075, (cit. on pp. 22, 247).

[147] *MPI: A Message-Passing Interface Standard*, 1994, URL: http://www.mcs.anl.gov/research/projects/mpi/standard.html, (cit. on pp. 24, 39, 255).

[148] P. J. Hasnip, M. I. J. Probert, K. Refson, M. Plummer, and M. Ashworth, *Band Parallelism in CASTEP: Scaling to More Than 1000 Cores*, in: *Cray User Group 2009 Proceedings*, 2009, pp. 1–5, (cit. on pp. 24, 246).

[149] D. Frenkel and B. Smit, *Understanding Molecular Simulation – From Algorithms to Applications*, in: Computational Science Series, Vol. 1, Academic Press, San Diego, 2002, ISBN: 978-0122673511, (cit. on pp. 25, 28, 36, 139, 156).

[150] D. Marx and J. Hutter, *Ab Initio Molecular Dynamics – Basic Theory and Advanced Methods*, in: 1st ed., Cambridge University Press, Cambridge, 2009, ISBN: 978-0521898638, (cit. on p. 25).

[151] R. van Harrevelt, K. Honkala, J. K. Nørskov, and U. Manthe, *The reaction rate for dissociative adsorption of N_2 on stepped Ru(0001): Six-dimensional quantum calculations*, J. Chem. Phys. **122**, 234702 (2005), DOI: 10.1063/1.1927513, (cit. on pp. 25, 101).

[152] S. Nosé, *A unified formulation of the constant temperature molecular dynamics methods*, J. Chem. Phys. **81**, 511 (1984), DOI: 10.1063/1.447334, (cit. on pp. 26, 139).

[153] S. Nosé, *A molecular dynamics method for simulations in the canonical ensemble*, Mol. Phys. **52**, 255 (1984), DOI: 10.1080/00268978400101201, (cit. on pp. 26, 139).

[154] S. Nosé, *A molecular dynamics method for simulations in the canonical ensemble*, Mol. Phys. **100**, 191 (2002), DOI: 10.1080/00268970110089108, (cit. on pp. 26, 139).

[155] W. G. Hoover, *Canonical dynamics: Equilibrium phase-space distributions*, Phys. Rev. A **31**, 1695 (1985), DOI: 10.1103/PhysRevA.31.1695, (cit. on pp. 26, 139).

[156] G. J. Martyna, M. L. Klein, and M. Tuckerman, *Nosé–Hoover chains: The canonical ensemble via continuous dynamics*, J. Chem. Phys. **97**, 2635 (1992), DOI: 10.1063/1.463940, (cit. on pp. 26, 37, 139 sq., 156, 257).

[157] M. Parrinello and A. Rahman, *Crystal Structure and Pair Potentials: A Molecular-Dynamics Study*, Phys. Rev. Lett. **45**, 1196 (1980), DOI: 10.1103/PhysRevLett.45.1196, (cit. on p. 27).

[158] M. Parrinello and A. Rahman, *Polymorphic transitions in single crystals: A new molecular dynamics method*, J. Appl. Phys. **52**, 7182 (1981), DOI: 10.1063/1.328693, (cit. on p. 27).

[159] J. E. Jones, *On the Determination of Molecular Fields. II. From the Equation of State of a Gas*, Proc. R. Soc. Lond A **106**, 463 (1924), DOI: 10.1098/rspa.1924.0082, (cit. on p. 28).

[160] A. Rahman, *Correlations in the Motion of Atoms in Liquid Argon*, Phys. Rev. **136**, A405 (1964), DOI: 10.1103/PhysRev.136.A405, (cit. on p. 28).

[161] S. Zhen and G. J. Davies, *Calculation of the Lennard-Jones n–m potential energy parameters for metals*, phys. stat. sol. (a) **78**, 595 (1983), DOI: 10.1002/pssa.2210780226, (cit. on p. 29).

[162] R. E. Allen, G. P. Alldredge, and F. W. de Wette, *Surface Modes of Vibration in Monatomic Crystals*, Phys. Rev. Lett. **23**, 1285 (1969), DOI: 10.1103/PhysRevLett.23.1285, (cit. on pp. 29 sq., 50).

[163] R. E. Allen and F. W. de Wette, *Calculation of Dynamical Surface Properties of Noble-Gas Crystals. I. The Quasiharmonic Approximation*, Phys. Rev. **179**, 873 (1969), DOI: 10.1103/PhysRev.179.873, (cit. on pp. 29 sq., 50).

[164] R. E. Allen and F. W. de Wette, *Mean-Square Amplitudes of Vibration at a Surface*, Phys. Rev. **188**, 1320 (1969), DOI: 10.1103/PhysRev.188.1320, (cit. on pp. 29 sq., 50).

[165] R. E. Allen, F. W. de Wette, and A. Rahman, *Calculation of Dynamical Surface Properties of Noble-Gas Crystals. II. Molecular Dynamics*, Phys. Rev. **179**, 887 (1969), DOI: 10.1103/PhysRev.179.887, (cit. on pp. 29 sq., 50, 133).

[166] R. E. Allen, G. P. Alldredge, and F. W. de Wette, *Surface Modes Within the Bulk Continua*, Phys. Rev. Lett. **24**, 301 (1970), DOI: 10.1103/PhysRevLett.24.301, (cit. on pp. 29 sq., 50).

[167] G. P. Alldredge, R. E. Allen, and F. W. de Wette, *Studies of Vibrational Surface Modes. III. Effect of an Adsorbed Layer*, Phys. Rev. B **4**, 1682 (1971), DOI: 10.1103/PhysRevB.4.1682, (cit. on pp. 29 sq., 50).

[168] R. E. Allen, G. P. Alldredge, and F. W. de Wette, *Studies of Vibrational Surface Modes. I. General Formulation*, Phys. Rev. B **4**, 1648 (1971), DOI: 10.1103/PhysRevB.4.1648, (cit. on pp. 29 sq., 50).

[169] R. E. Allen, G. P. Alldredge, and F. W. de Wette, *Studies of Vibrational Surface Modes. II. Monatomic fcc Crystals*, Phys. Rev. B **4**, 1661 (1971), DOI: 10.1103/PhysRevB.4.1661, (cit. on pp. 29 sq., 50).

[170] P. M. Morse, *Diatomic Molecules According to the Wave Mechanics. II. Vibrational Levels*, Phys. Rev. **34**, 57 (1929), DOI: 10.1103/PhysRev.34.57, (cit. on p. 29).

[171] L. A. Girifalco and V. G. Weizer, *Application of the Morse Potential Function to Cubic Metals*, Phys. Rev. **114**, 687 (1959), DOI: 10.1103/PhysRev.114.687, (cit. on pp. 29 sq.).

[172] M. S. Daw and M. I. Baskes, *Semiempirical, Quantum Mechanical Calculation of Hydrogen Embrittlement in Metals*, Phys. Rev. Lett. **50**, 1285 (1983), DOI: 10.1103/PhysRevLett.50.1285, (cit. on pp. 30, 138).

[173] M. W. Finnis and J. E. Sinclair, *A simple empirical N-body potential for transition metals*, Philos. Mag. A **50**, 45 (1984), DOI: 10.1080/01418618408244210, (cit. on p. 30).

[174] E. Shustorovich, *Chemisorption phenomena: Analytic modeling based on perturbation theory and bond-order conservation*, Surf. Sci. Rep. **6**, 1 (1986), DOI: 10.1016/0167-5729(86)90003-8, (cit. on p. 30).

[175] M. S. Daw and M. I. Baskes, *Embedded-atom method: Derivation and application to impurities, surfaces, and other defects in metals*, Phys. Rev. B **29**, 6443 (1984), DOI: 10.1103/PhysRevB.29.6443, (cit. on pp. 30, 69, 138, 153).

[176] K. W. Jacobsen, J. K. Nørskov, and M. J. Puska, *Interatomic interactions in the effective-medium theory*, Phys. Rev. B **35**, 7423 (1987), DOI: 10.1103/PhysRevB.35.7423, (cit. on pp. 30, 69, 153).

[177] K. W. Jacobsen, P. Stoltze, and J. K. Nørskov, *A semi-empirical effective medium theory for metals and alloys*, Surf. Sci. **366**, 394 (1996), DOI: 10.1016/0039-6028(96)00816-3, (cit. on pp. 30, 153).

[178] F. Ercolessi, M. Parrinello, and E. Tosatti, *Simulation of gold in the glue model*, Philos. Mag. A **58**, 213 (1988), DOI: 10.1080/01418618808205184, (cit. on pp. 30, 153).

[179] S. M. Foiles, M. I. Baskes, and M. S. Daw, *Embedded-atom-method functions for the fcc metals Cu, Ag, Au, Ni, Pd, Pt, and their alloys*, Phys. Rev. B **33**, 7983 (1986), DOI: 10.1103/PhysRevB.33.7983, (cit. on p. 30).

[180] S. M. Foiles, M. I. Baskes, and M. S. Daw, *Erratum: Embedded-atom-method functions for the fcc metals Cu, Ag, Au, Ni, Pd, Pt, and their alloys*, Phys. Rev. B **37**, 10378 (1988), DOI: 10.1103/PhysRevB.37.10378, (cit. on p. 30).

[181] M. S. Daw, S. M. Foiles, and M. I. Baskes, *The embedded-atom method: A review of theory and applications*, Materials Science Reports **9**, 251 (1993), DOI: 10.1016/0920-2307(93)90001-U, (cit. on pp. 30, 69, 138).

[182] M. J. Stott and E. Zaremba, *Quasiatoms: An approach to atoms in nonuniform electronic systems*, Phys. Rev. B **22**, 1564 (1980), DOI: 10.1103/PhysRevB.22.1564, (cit. on p. 30).

[183] J. Behler and M. Parrinello, *Generalized Neural-Network Representation of High-Dimensional Potential-Energy Surfaces*, Phys. Rev. Lett. **98**, 146401 (2007), DOI: 10.1103/PhysRevLett.98.146401, (cit. on pp. 30, 34, 71, 78, 81 sq., 95, 147, 182).

[184] A. P. Bartók, M. C. Payne, R. Kondor, and G. Csányi, *Gaussian Approximation Potentials: The Accuracy of Quantum Mechanics, without the Electrons*, Phys. Rev. Lett. **104**, 136403 (2010), DOI: 10.1103/PhysRevLett.104.136403, (cit. on pp. 30, 34, 71, 82, 147, 182).

[185] F. Ercolessi and J. B. Adams, *Interatomic Potentials from First-Principles Calculations: The Force-Matching Method*, Europhys. Lett. **26**, 583 (1994), DOI: 10.1209/0295-5075/26/8/005, (cit. on p. 31).

[186] P. Brommer and F. Gähler, *Potfit: Effective potentials from ab initio data*, Modell. Simul. Mater. Sci. Eng. **15**, 295 (2007), DOI: 10.1088/0965-0393/15/3/008, (cit. on pp. 31, 153).

[187] P. van Beurden and G. J. Kramer, *Parametrization of modified embedded-atom-method potentials for Rh, Pd, Ir, and Pt based on density functional theory calculations, with applications to surface properties*, Phys. Rev. B **63**, 165106 (2001), DOI: 10.1103/PhysRevB.63.165106, (cit. on pp. 31, 150, 153).

[188] P. van Beurden, H. G. J. Verhoeven, G. J. Kramer, and B. J. Thijsse, *Atomistic potential for adsorbate/surface systems: CO on Pt*, Phys. Rev. B **66**, 235409 (2002), DOI: 10.1103/PhysRevB.66.235409, (cit. on pp. 31, 33).

[189] M. I. Baskes, *Application of the Embedded-Atom Method to Covalent Materials: A Semiempirical Potential for Silicon*, Phys. Rev. Lett. **59**, 2666 (1987), DOI: 10.1103/PhysRevLett.59.2666, (cit. on pp. 31, 144).

[190] M. I. Baskes, J. S. Nelson, and A. F. Wright, *Semiempirical modified embedded-atom potentials for silicon and germanium*, Phys. Rev. B **40**, 6085 (1989), DOI: 10.1103/PhysRevB.40.6085, (cit. on pp. 31, 144).

[191] M. I. Baskes, *Modified embedded-atom potentials for cubic materials and impurities*, Phys. Rev. B **46**, 2727 (1992), DOI: 10.1103/PhysRevB.46.2727, (cit. on pp. 31, 33, 144, 150 sq., 153).

[192] M. I. Baskes, *Determination of modified embedded atom method parameters for nickel*, Mater. Chem. Phys. **50**, 152 (1997), DOI: 10.1016/S0254-0584(97)80252-0, (cit. on p. 31).

[193] M. I. Baskes, *Atomistic potentials for the molybdenum-silicon system*, Mater. Sci. Eng., A **261**, 165 (1999), DOI: 10.1016/S0921-5093(98)01062-4, (cit. on p. 32).

[194] M. I. Baskes, J. E. Angelo, and C. L. Bisson, *Atomistic calculations of composite interfaces*, Modell. Simul. Mater. Sci. Eng. **2**, 505 (1994), DOI: 10.1088/0965-0393/2/3A/006, (cit. on p. 32).

[195] J. H. Rose, J. R. Smith, F. Guinea, and J. Ferrante, *Universal features of the equation of state of metals*, Phys. Rev. B **29**, 2963 (1984), DOI: 10.1103/PhysRevB.29.2963, (cit. on p. 33).

[196] B.-J. Lee and M. I. Baskes, *Second nearest-neighbor modified embedded-atom-method potential*, Phys. Rev. B **62**, 8564 (2000), DOI: 10.1103/PhysRevB.62.8564, (cit. on p. 33).

[197] B.-J. Lee, J.-H. Shim, and M. I. Baskes, *Semiempirical atomic potentials for the fcc metals Cu, Ag, Au, Ni, Pd, Pt, Al, and Pb based on first and second nearest-neighbor modified embedded atom method*, Phys. Rev. B **68**, 144112 (2003), DOI: 10.1103/PhysRevB.68.144112, (cit. on p. 33).

[198] A. S. P. M. Gullet, G. Wagner, *Numerical Tools for Atomistic Simulations*, Sandia National Laboratories, 8782, 2003, URL: http://infoserve.sandia.gov/sand_doc/2003/038782.pdf, (cit. on pp. 33, 39, 255).

[199] M. S. Daw and R. D. Hatcher, *Application of the embedded atom method to phonons in transition metals*, Solid State Commun. **56**, 697 (1985), DOI: 10.1016/0038-1098(85)90781-1, (cit. on p. 33).

[200] J. S. Nelson, E. C. Sowa, and M. S. Daw, *Calculation of Phonons on the Cu(100) Surface by the Embedded-Atom Method*, Phys. Rev. Lett. **61**, 1977 (1988), DOI: 10.1103/PhysRevLett.61.1977, (cit. on p. 33).

[201] J. S. Nelson, M. S. Daw, and E. C. Sowa, *Cu(111) and Ag(111) surface-phonon spectrum: The importance of avoided crossings*, Phys. Rev. B **40**, 1465 (1989), DOI: 10.1103/PhysRevB.40.1465, (cit. on p. 33).

[202] J. S. Nelson, M. S. Daw, and E. C. Sowa, *Embedded atom calculations of the Cu (001), (111), and (110) surface phonon spectra*, Superlattices Microstruct. **7**, 259 (1990), DOI: 10.1016/0749-6036(90)90304-P, (cit. on p. 33).

[203] J. Behler, R. Martoňák, D. Donadio, and M. Parrinello, *Pressure-induced phase transitions in silicon studied by neural network-based metadynamics simulations*, phys. stat. sol. (b) **245**, 2618 (2008), DOI: 10.1002/pssb.200844219, (cit. on p. 34).

[204] J. Behler, R. Martoňák, D. Donadio, and M. Parrinello, *Metadynamics Simulations of the High-Pressure Phases of Silicon Employing a High-Dimensional Neural Network Potential*, Phys. Rev. Lett. **100**, 185501 (2008), DOI: 10.1103/PhysRevLett.100.185501, (cit. on pp. 34, 71).

[205] H. Eshet, R. Z. Khaliullin, T. D. Kühne, J. Behler, and M. Parrinello, *Ab initio quality neural-network potential for sodium*, Phys. Rev. B **81**, 184107 (2010), DOI: 10.1103/PhysRevB.81.184107, (cit. on pp. 34, 71).

[206] R. Z. Khaliullin, H. Eshet, T. D. Kühne, J. Behler, and M. Parrinello, *Graphite-diamond phase coexistence study employing a neural-network mapping of the ab initio potential energy surface*, Phys. Rev. B **81**, 100103R (2010), DOI: 10.1103/PhysRevB.81.100103, (cit. on pp. 34, 71).

[207] M. C. Payne, J. D. Joannopoulos, D. C. Allan, M. P. Teter, and D. H. Vanderbilt, *Molecular Dynamics and ab initio Total Energy Calculations*, Phys. Rev. Lett. **56**, 2656 (1986), DOI: 10.1103/PhysRevLett.56.2656, (cit. on p. 34).

[208] A. M. N. Niklasson, C. J. Tymczak, and M. Challacombe, *Time-Reversible Born-Oppenheimer Molecular Dynamics*, Phys. Rev. Lett. **97**, 123001 (2006), DOI: 10.1103/PhysRevLett.97.123001, (cit. on pp. 34, 72, 182, 262).

[209] A. M. N. Niklasson, *Extended Born-Oppenheimer Molecular Dynamics*, Phys. Rev. Lett. **100**, 123004 (2008), DOI: 10.1103/PhysRevLett.100.123004, (cit. on pp. 34, 72, 182, 262).

[210] J. L. Alonso, X. Andrade, P. Echenique, F. Falceto, D. Prada-Gracia, and A. Rubio, *Efficient Formalism for Large-Scale Ab Initio Molecular Dynamics based on Time-Dependent Density Functional Theory*, Phys. Rev. Lett. **101**, 096403 (2008), DOI: 10.1103/PhysRevLett.101.096403, (cit. on pp. 34, 72, 182, 262).

[211] X. Andrade, A. Castro, D. Zueco, J. L. Alonso, P. Echenique, F. Falceto, and A. Rubio, *Modified Ehrenfest Formalism for Efficient Large-Scale ab initio Molecular Dynamics*, J. Chem. Theory Comput. **5**, 728 (2009), DOI: 10.1021/ct800518j, (cit. on pp. 34, 262).

[212] L. Verlet, *Computer "Experiments" on Classical Fluids. I. Thermodynamical Properties of Lennard-Jones Molecules*, Phys. Rev. **159**, 98 (1967), DOI: 10.1103/PhysRev.159.98, (cit. on pp. 35, 38).

[213] W. C. Swope, H. C. Andersen, P. H. Berens, and K. R. Wilson, *A computer simulation method for the calculation of equilibrium constants for the formation of physical clusters of molecules: Application to small water clusters*, J. Chem. Phys. **76**, 637 (1982), DOI: 10.1063/1.442716, (cit. on pp. 35, 156, 248, 256, 263).

[214] R. Bulirsch and J. Stoer, *Numerical treatment of ordinary differential equations by extrapolation methods*, Numerische Mathematik **8**, 1 (1966), (cit. on pp. 36, 156).

[215] R. Bulirsch and J. Stoer, *Fehlerabschätzungen und Extrapolation mit rationalen Funktionen bei Verfahren vom Richardson-Typus*, Numerische Mathematik **6**, 413 (1964), (cit. on p. 37).

[216] G. J. Martyna, M. E. Tuckerman, D. J. Tobias, and M. L. Klein, *Explicit reversible integrators for extended systems dynamics*, Mol. Phys. **87**, 1117 (1996), DOI: 10.1080/00268979600100761, (cit. on pp. 37 sq., 156, 257).

[217] M. E. Tuckerman, J. Alejandre, R. López-Rendón, A. L. Jochim, and G. J. Martyna, *A Liouville-operator derived measure-preserving integrator for molecular dynamics simulations in the isothermal–isobaric ensemble*, J. Phys. A: Math. Gen. **39**, 5629 (2006), DOI: 10.1088/0305-4470/39/19/S18, (cit. on pp. 37 sq., 156, 257).

[218] S. Plimpton, *Fast Parallel Algorithms for Short-Range Molecular Dynamics*, J. Comput. Phys. **117**, 1 (1995), DOI: 10.1006/jcph.1995.1039, (cit. on pp. 39, 154, 253, 255, 258, 269).

[219] J. Yang, Y. Wang, and Y. Chen, *GPU accelerated molecular dynamics simulation of thermal conductivities*, J. Comput. Phys. **221**, 799 (2007), DOI: 10.1016/j.jcp.2006.06.039, (cit. on p. 39).

[220] J. E. Stone, J. C. Phillips, P. L. Freddolino, D. J. Hardy, L. G. Trabuco, and K. Schulten, *Accelerating molecular modeling applications with graphics processors*, J. Comput. Chem. **28**, 2618 (2007), DOI: 10.1002/jcc.20829, (cit. on p. 39).

[221] J. A. van Meel, A. Arnold, D. Frenkel, S. F. P. Zwart, and R. G. Belleman, *Harvesting graphics power for MD simulations*, Molecular Simulation **34**, 259 (2008), DOI: 10.1080/08927020701744295, (cit. on p. 39).

[222] J. A. Anderson, C. D. Lorenz, and A. Travesset, *General purpose molecular dynamics simulations fully implemented on graphics processing units*, J. Comput. Phys. **227**, 5342 (2008), DOI: 10.1016/j.jcp.2008.01.047, (cit. on p. 39).

[223] W. Liu, B. Schmidt, G. Voss, and W. Müller-Wittig, *Accelerating molecular dynamics simulations using Graphics Processing Units with CUDA*, Comput. Phys. Commun. **179**, 634 (2008), DOI: 10.1016/j.cpc.2008.05.008, (cit. on p. 39).

[224] C. Díaz, E. Pijper, R. A. Olsen, H. F. Busnengo, D. J. Auerbach, and G. J. Kroes, *Chemically Accurate Simulation of a Prototypical Surface Reaction: H2 Dissociation on Cu(111)*, Science **326**, 832 (2009), DOI: 10.1126/science.1178722, (cit. on p. 41).

[225] N. W. Ashcroft and N. D. Mermin, *Solid State Physics*, in: 1st ed., Brooks Cole, South Melbourne, 1976, ISBN: 978-0030839931, (cit. on pp. 41, 44, 102).

[226] K. Esfarjani and H. T. Stokes, *Method to extract anharmonic force constants from first principles calculations*, Phys. Rev. B **77**, 144112 (2008), DOI: 10.1103/PhysRevB.77.144112, (cit. on p. 42).

[227] A. A. Maradudin and S. H. Vosko, *Symmetry Properties of the Normal Vibrations of a Crystal*, Rev. Mod. Phys. **40**, 1 (1968), DOI: 10.1103/RevModPhys.40.1, (cit. on p. 44).

[228] S. K. Estreicher, D. Backlund, and T. M. Gibbons, *Non-equilibrium dynamics for impurities in semiconductors*, Physica B **404**, 4337 (2009), DOI: 10.1016/j.physb.2009.09.024, (cit. on p. 45).

[229] S. K. Estreicher, D. Backlund, T. M. Gibbons, and A. Doçaj, *Vibrational properties of impurities in semiconductors*, Modell. Simul. Mater. Sci. Eng. **17**, 084006 (2009), DOI: 10.1088/0965-0393/17/8/084006, (cit. on pp. 45, 166, 170).

[230] T. M. Gibbons and S. K. Estreicher, *Erratum: Impact of Impurities on the Thermal Conductivity of Semiconductor Nanostructures: First-Principles Theory [Phys. Rev. Lett. 102, 255502 (2009)]*, Phys. Rev. Lett. **103**, 099904 (2009), DOI: 10.1103/PhysRevLett.103.099904, (cit. on pp. 45, 166, 170).

[231] T. M. Gibbons and S. K. Estreicher, *Impact of Impurities on the Thermal Conductivity of Semiconductor Nanostructures: First-Principles Theory*, Phys. Rev. Lett. **102**, 255502 (2009), DOI: 10.1103/PhysRevLett.102.255502, (cit. on pp. 45, 166, 170).

[232] K.-M. Ho, C. L. Fu, B. N. Harmon, W. Weber, and D. R. Hamann, *Vibrational Frequencies and Structural Properties of Transition Metals via Total-Energy Calculations*, Phys. Rev. Lett. **49**, 673 (1982), DOI: 10.1103/PhysRevLett.49.673, (cit. on p. 46).

[233] W. Frank, C. Elässer, and M. Fähnle, *Ab initio Force-Constant Method for Phonon Dispersions in Alkali Metals*, Phys. Rev. Lett. **74**, 1791 (1995), DOI: 10.1103/PhysRevLett.74.1791, (cit. on p. 47).

[234] W. Kohn, *Density Functional and Density Matrix Method Scaling Linearly with the Number of Atoms*, Phys. Rev. Lett. **76**, 3168 (1996), DOI: 10.1103/PhysRevLett.76.3168, (cit. on pp. 47, 145, 148).

[235] E. Prodan and W. Kohn, *Nearsightedness of electronic matter*, Proc. Natl. Acad. Sci. USA **102**, 11635 (2005), DOI: 10.1073/pnas.0505436102, (cit. on pp. 47, 145, 148).

[236] G. Kresse, J. Furthmüller, and J. Hafner, *Ab initio Force Constant Approach to Phonon Dispersion Relations of Diamond and Graphite*, Europhys. Lett. **32**, 729 (1995), DOI: 10.1209/0295-5075/32/9/005, (cit. on p. 47).

[237] K. Parlinski, Z. Q. Li, and Y. Kawazoe, *First-Principles Determination of the Soft Mode in Cubic ZrO2*, Phys. Rev. Lett. **78**, 4063 (1997), DOI: 10.1103/PhysRevLett.78.4063, (cit. on pp. 47, 51, 57, 265 sq.).

[238] K. Parlinski, Z. Q. Li, and Y. Kawazoe, *Parlinski, Li, and Kawazoe Reply:* Phys. Rev. Lett. **81**, 3298 (1998), DOI: 10.1103/PhysRevLett.81.3298, (cit. on p. 48).

[239] F. Detraux, P. Ghosez, and X. Gonze, *Long-Range Coulomb Interaction in ZrO2*, Phys. Rev. Lett. **81**, 3297 (1998), DOI: 10.1103/PhysRevLett.81.3297, (cit. on p. 48).

[240] Y. Wang, J. J. Wang, W. Y. Wang, Z. G. Mei, S. L. Shang, L. Q. Chen, and Z. K. Liu, *A mixed-space approach to first-principles calculations of phonon frequencies for polar materials*, J. Phys.: Condens. Matter **22**, 202201 (2010), DOI: 10.1088/0953-8984/22/20/202201, (cit. on p. 48).

[241] S. Baroni, P. Giannozzi, and A. Testa, *Elastic Constants of Crystals from Linear-Response Theory*, Phys. Rev. Lett. **59**, 2662 (1987), DOI: 10.1103/PhysRevLett.59.2662, (cit. on p. 48).

[242] S. Baroni, S. de Gironcoli, A. D. Corso, and P. Giannozzi, *Phonons and related crystal properties from density-functional perturbation theory*, Rev. Mod. Phys. **73**, 515 (2001), DOI: 10.1103/RevModPhys.73.515, (cit. on pp. 48, 110).

[243] K. Refson, P. R. Tulip, and S. J. Clark, *Variational density-functional perturbation theory for dielectrics and lattice dynamics*, Phys. Rev. B **73**, 155114 (2006), DOI: 10.1103/PhysRevB.73.155114, (cit. on pp. 48, 111).

[244] L. Rayleigh, *On Waves Propagated along the Plane Surface of an Elastic Solid*, Proc. London Math. Soc. **s1 - 17**, 4 (1885), DOI: 10.1112/plms/s1-17.1.4, (cit. on p. 48).

[245] G. Brusdeylins, R. B. Doak, and J. P. Toennies, *Observation of Surface Phonons in Inelastic Scattering of He Atoms from LiF(001) Crystal Surfaces*, Phys. Rev. Lett. **44**, 1417 (1980), DOI: 10.1103/PhysRevLett.44.1417, (cit. on p. 49).

[246] G. Brusdeylins, R. B. Doak, and J. P. Toennies, *Measurement of the Dispersion Relation for Rayleigh Surface Phonons of LiF(001) by Inelastic Scattering of He Atoms*, Phys. Rev. Lett. **46**, 437 (1981), DOI: 10.1103/PhysRevLett.46.437, (cit. on p. 49).

[247] R. B. Doak, U. Harten, and J. P. Toennies, *Anomalous Surface Phonon Dispersion Relations for Ag(111) Measured by Inelastic Scattering of He Atoms*, Phys. Rev. Lett. **51**, 578 (1983), DOI: 10.1103/PhysRevLett.51.578, (cit. on p. 49).

[248] S. Lehwald, J. M. Szeftel, H. Ibach, T. S. Rahman, and D. L. Mills, *Surface Phonon Dispersion of Ni(100) Measured by Inelastic Electron Scattering*, Phys. Rev. Lett. **50**, 518 (1983), DOI: 10.1103/PhysRevLett.50.518, (cit. on p. 49).

[249] L. Chen and L. L. Kesmodel, *Surface phonon dispersion along $\Gamma\bar{X}$ on Pd(100)*, Surf. Sci. **320**, 105 (1994), DOI: 10.1016/0039-6028(94)00510-9, (cit. on pp. 49, 51).

[250] R. Heid and K.-P. Bohnen, *Ab initio lattice dynamics of metal surfaces*, Physics Reports **387**, 151 (2003), DOI: 10.1016/j.physrep.2003.07.003, (cit. on pp. 50 sq., 171).

[251] S. W. Musser and K. H. Rieder, *Influence of Surface Force-Constant Changes on Surface-Mode Frequencies*, Phys. Rev. B **2**, 3034 (1970), DOI: 10.1103/PhysRevB.2.3034, (cit. on pp. 50, 264).

[252] I. Y. Sklyadneva, G. G. Rusina, and E. V. Chulkov, *Vibrational states on Pd surfaces*, Surf. Sci. **377 - 379**, 313 (1997), DOI: 10.1016/S0039-6028(96)01391-X, (cit. on p. 51).

[253] J. L. F. D. Silva, C. Stampfl, and M. Scheffler, *Converged properties of clean metal surfaces by all-electron first-principles calculations*, Surf. Sci. **600**, 703 (2006), DOI: 10.1016/j.susc.2005.12.008, (cit. on pp. 51, 55 sq., 59 sq., 247).

[254] K.-P. Bohnen, R. Heid, and O. de la Peña Seaman, *Ab initio lattice dynamics and thermodynamics of RuO_2 (110) surfaces*, Phys. Rev. B **81**, 081405 (2010), DOI: 10.1103/PhysRevB.81.081405, (cit. on p. 51).

[255] K.-P. Bohnen, R. Heid, and O. de la Peña Seaman, *Erratum: Ab initio lattice dynamics and thermodynamics of RuO_2 (110) surfaces [Phys. Rev. B 81, 081405(R) (2010)]*, Phys. Rev. B **81**, 209902 (2010), DOI: 10.1103/PhysRevB.81.209902, (cit. on p. 51).

[256] H. Yildirim, A. Kara, T. S. Rahman, R. Heid, and K.-P. Bohnen, *Surface vibrational thermodynamics from ab initio calculations for fcc(100)*, Surf. Sci. **604**, 308 (2010), DOI: 10.1016/j.susc.2009.11.022, (cit. on p. 51).

[257] J. Fritsch and U. Schröder, *Density functional calculation of semiconductor surface phonons*, Physics Reports **309**, 209 (1999), DOI: 10.1016/S0370-1573(98)00034-9, (cit. on p. 51).

[258] W. Kress and F. W. de Wette, *Surface Phonons*, in: *Springer Series in Surface Sciences*, Vol. 21, 1st ed., Springer, Berlin, 1991, ISBN: 978-3540527213, (cit. on p. 51).

[259] G. Benedek, M. Bernasconi, V. Chis, E. Chulkov, P. M. Echenique, B. Hellsing, and J. P. Toennies, *Theory of surface phonons at metal surfaces: Recent advances*, J. Phys.: Condens. Matter **22**, 084020 (2010), DOI: 10.1088/0953-8984/22/8/084020, (cit. on p. 51).

[260] D. Alfè, *PHON: A program to calculate phonons using the small displacement method*, Comput. Phys. Commun. **180**, 2622 (2009), DOI: 10.1016/j.cpc.2009.03.010, (cit. on p. 51).

[261] A. Togo, F. Oba, and I. Tanaka, *First-principles calculations of the ferroelastic transition between rutile-type and $CaCl_2$ -type SiO_2 at high pressures*, Phys. Rev. B **78**, 134106 (2008), DOI: 10.1103/PhysRevB.78.134106, (cit. on p. 51).

[262] Y. Zhang, *First-principles Statistical Mechanics Approach to Step Decoration at Solid Surfaces*, PhD thesis, Freie Universität Berlin, 2008, (cit. on pp. 55 sq., 59 sq., 63).

[263] M. Todorova, *Oxidation of Palladium Surfaces*, PhD thesis, Technische Universität Berlin, 2004, (cit. on pp. 55 sq., 59 sq.).

[264] J. Rogal and K. Reuter, *Ab Initio Atomistic Thermodynamics for Surfaces: A Primer*, in: *Experiment, Modeling and Simulation of Gas-Surface Interactions for Reactive Flows in Hypersonic Flights*, Vol. 14, NATO, 2007, pp. 2–1 –2–18, (cit. on p. 55).

[265] E. R. McNellis, *First-Principles Modeling of Molecular Switches at Surfaces*, PhD thesis, Freie Universität Berlin, 2009, (cit. on pp. 55, 122).

[266] H. W. King and F. D. Manchester, *A low-temperature X-ray diffraction study of Pd and some Pd-H alloys*, Journal of Physics F: Metal Physics **8**, 15 (1978), DOI: 10.1088/0305-4608/8/1/007, (cit. on p. 55).

[267] A. K. Giri and G. B. Mitra, *Extrapolated values of lattice constants of some cubic metals at absolute zero*, J. Phys. D: Appl. Phys. **18**, L75 (1985), DOI: 10.1088/0022-3727/18/7/005, (cit. on p. 55).

[268] M. Todorova, K. Reuter, and M. Scheffler, *Oxygen Overlayers on Pd(111) Studied by Density Functional Theory*, J. Phys. Chem. B **108**, 14477 (2004), DOI: 10.1021/jp040088t, (cit. on p. 55).

[269] J. A. Rayne, *Elastic Constants of Palladium from 4.2-300° K*, Phys. Rev. **118**, 1545 (1960), DOI: 10.1103/PhysRev.118.1545, (cit. on pp. 55 sq., 59, 129).

[270] D. K. Hsu and R. G. Leisure, *Elastic constants of palladium and β-phase palladium hydride between 4 and 300 K*, Phys. Rev. B **20**, 1339 (1979), DOI: 10.1103/PhysRevB.20.1339, (cit. on pp. 56, 129).

[271] F. D. Murnaghan, *The Compressibility of Media under Extreme Pressures*, Proc. Natl. Acad. Sci. **30**, 244 (1944), (cit. on p. 56).

[272] B. G. Pfrommer, M. Côté, S. G. Louie, and M. L. Cohen, *Relaxation of Crystals with the Quasi-Newton Method*, J. Comput. Phys. **131**, 233 (1997), DOI: 10.1006/jcph.1996.5612, (cit. on pp. 56, 59).

[273] A. P. Miiller and B. N. Brockhouse, *Anomalous Behavior of the Lattice Vibrations and the Electronic Specific Heat of Palladium*, Phys. Rev. Lett. **20**, 798 (1968), DOI: 10.1103/PhysRevLett.20.798, (cit. on pp. 57 sq., 129).

[274] A. P. Miiller and B. N. Brockhouse, *Crystal Dynamics and Electronic Specific Heats of Palladium and Copper*, Can. J. Phys. **49**, 704 (1971), DOI: 10.1139/p71-087, (cit. on pp. 57 sq.).

[275] B. W. Veal and J. A. Rayne, *Heat Capacity of Palladium and Dilute Palladium: Iron Alloys from 1.4 To 100° K*, Phys. Rev. **135**, A442 (1964), DOI: 10.1103/PhysRev.135.A442, (cit. on pp. 58 sq.).

[276] R. Rajput, *Phonon Dispersion in Platinum and Palladium*, Phys. Status Solidi B **128**, 411 (1985), DOI: 10.1002/pssb.2221280206, (cit. on p. 58).

[277] S. Y. Savrasov and D. Y. Savrasov, *Electron-phonon interactions and related physical properties of metals from linear-response theory*, Phys. Rev. B **54**, 16487 (1996), DOI: 10.1103/PhysRevB.54.16487, (cit. on pp. 57, 59, 181).

[278] T. Takezawa, H. Nagara, and N. Suzuki, *Ab initio calculations of superconductivity in palladium under pressure*, Phys. Rev. B **71**, 012515 (2005), DOI: 10.1103/PhysRevB.71.012515, (cit. on pp. 57, 59).

[279] D. A. Stewart, *Ab initio investigation of phonon dispersion and anomalies in palladium*, New Journal of Physics **10**, 043025 (2008), DOI: 10.1088/1367-2630/10/4/043025, (cit. on pp. 57, 59, 64).

[280] S. Y. Savrasov, *Linear-response theory and lattice dynamics: A muffin-tin-orbital approach*, Phys. Rev. B **54**, 16470 (1996), DOI: 10.1103/PhysRevB.54.16470, (cit. on p. 57).

[281] F. E. Hoare and B. Yates, *The Low-Temperature (2 to 4 · 2 ° K) Specific Heats of Palladium-Silver Alloys*, Proc. R. Soc. London, Ser. A **240**, 42 (1957), DOI: 10.1098/rspa.1957.0065, (cit. on p. 59).

[282] T. W. Orent and S. D. Bader, *LEED and ELS study of the initial oxidation of Pd(100)*, Surf. Sci. **115**, 323 (1982), DOI: 10.1016/0039-6028(82)90412-5, (cit. on p. 60).

[283] T. E. Felter, E. C. Sowa, and M. A. V. Hove, *Location of hydrogen adsorbed on palladium (111) studied by low-energy electron diffraction*, Phys. Rev. B **40**, 891 (1989), DOI: 10.1103/PhysRevB.40.891, (cit. on p. 60).

[284] A. Barbieri, M. A. V. Hove, and G. A. Somorjai, *Benzene coadsorbed with CO on Pd(111) and Rh(111): Detailed molecular distortions and induced substrate relaxations*, Surf. Sci. **306**, 261 (1994), DOI: 10.1016/0039-6028(94)90070-1, (cit. on p. 60).

[285] V. Blum, R. Gehrke, F. Hanke, P. Havu, V. Havu, X. Ren, K. Reuter, and M. Scheffler, *Ab initio molecular simulations with numeric atom-centered orbitals*, Comput. Phys. Commun. **180**, 2175 (2009), DOI: 10.1016/j.cpc.2009.06.022, (cit. on pp. 60, 66).

[286] G. Herzberg, *Molecular Spectra and Molecular Structure: I. Spectra of Diatomic Molecules*, in: 2nd ed., Krieger, Malabar, FL, 1950, ISBN: 978-0894642685, (cit. on p. 61).

[287] G. Herzberg, *Forbidden transitions in diatomic molecules: Ii. The absorption bands of the oxygen molecule*, Can. J. Phys. **30**, 185 (1952), DOI: 10.1139/p52-019, (cit. on pp. 60 sq.).

[288] *CRC Handbook of Chemistry and Physics*, in: ed. by W. M. Haynes, 92nd ed., CRC Press, Boca Raton, FL, 2011, ISBN: 978-1439855119, (cit. on pp. 60 sq.).

[289] J. Neugebauer and M. Scheffler, *Adsorbate-substrate and adsorbate-adsorbate interactions of Na and K adlayers on Al(111)*, Phys. Rev. B **46**, 16067 (1992), DOI: 10.1103/PhysRevB.46.16067, (cit. on p. 63).

[290] Y. Zhang, WIEN2K *Calculations for Pd bulk and O_2 on Pd(100)*, private communication, Fritz-Haber-Institut, Berlin, 2006, (cit. on pp. 63 sq.).

[291] S. S. Alexandre, E. Anglada, J. M. Soler, and F. Yndurain, *Magnetism of two-dimensional defects in Pd: Stacking faults, twin boundaries, and surfaces*, Phys. Rev. B **74**, 054405 (2006), DOI: 10.1103/PhysRevB.74.054405, (cit. on p. 64).

[292] S. S. Alexandre, M. Mattesini, J. M. Soler, and F. Yndurain, *Comment on "Magnetism in Atomic-Size Palladium Contacts and Nanowires"*, Phys. Rev. Lett. **96**, 079701 (2006), DOI: 10.1103/PhysRevLett.96.079701, (cit. on p. 64).

[293] N. Marzari, D. Vanderbilt, A. D. Vita, and M. C. Payne, *Thermal Contraction and Disordering of the Al(110) Surface*, Phys. Rev. Lett. **82**, 3296 (1999), DOI: 10.1103/PhysRevLett.82.3296, (cit. on p. 65).

[294] V. Havu, V. Blum, P. Havu, and M. Scheffler, *Efficient O(N) integration for all-electron electronic structure calculation using numeric basis functions*, J. Comput. Phys. **228**, 8367 (2009), DOI: 10.1016/j.jcp.2009.08.008, (cit. on p. 66).

[295] J. R. Manson, *Energy Transfer to Phonons in Atom and Molecule Collisions with Surfaces*, in: *Dynamics*, Handbook of Surface Science, Vol. 3, ed. by E. Hasselbrink and B. I. Lundqvist, 1st ed., Elsevier, Amsterdam, 2008, ISBN: 978-0444520562, Chap. 3, pp. 53 –94, (cit. on pp. 69, 130, 165).

[296] J. R. Manson, *Including Chemical Reactions in Desciption of Energy Transfer by Scattering Theory*, private communication, Fritz-Haber-Institut, Berlin, 2010, (cit. on pp. 69, 130).

[297] G. R. Darling and S. Holloway, *The dissociation of diatomic molecules at surfaces*, Rep. Prog. Phys. **58**, 1595 (1995), DOI: 10.1088/0034-4885/58/12/001, (cit. on pp. 69 sq.).

[298] X. L. Fan, W. M. Lau, and Z. F. Liu, *Comment on "Dissociation of O_2 at Al(111): The Role of Spin Selection Rules"*, Phys. Rev. Lett. **96**, 079801 (2006), DOI: 10.1103/PhysRevLett.96.079801, (cit. on pp. 69, 71, 81).

[299] J. Behler, K. Reuter, and M. Scheffler, *Behler, Reuter, and Scheffler Reply:* Phys. Rev. Lett. **96**, 079802 (2006), DOI: 10.1103/PhysRevLett.96.079802, (cit. on pp. 69, 71, 81, 95).

[300] A. C. Luntz and M. Persson, *How adiabatic is activated adsorption/associative desorption?* J. Chem. Phys. **123**, 074704 (2005), DOI: 10.1063/1.2000249, (cit. on pp. 69, 103, 124, 133).

[301] J. H. McCreery and G. W. Jr, *A model potential for chemisorption: H_2+W(001)*, J. Chem. Phys. **63**, 2340 (1975), DOI: 10.1063/1.431663, (cit. on pp. 69, 72, 133).

[302] J. H. McCreery and G. W. Jr, *Erratum: A model potential for chemisorption: H_2+W(001)*, J. Chem. Phys. **65**, 2922 (1976), DOI: 10.1063/1.433601, (cit. on pp. 69, 72, 133).

[303] J. H. McCreery and G. W. Jr, *Dynamics of adsorption on covered surfaces*, J. Chem. Phys. **66**, 2316 (1977), DOI: 10.1063/1.434266, (cit. on p. 69).

[304] J. H. McCreery and G. W. Jr, *Atomic recombination dynamics on a solid surface: H_2+W(001)*, J. Chem. Phys. **64**, 2845 (1976), DOI: 10.1063/1.432584, (cit. on pp. 69, 134, 136, 144).

[305] J. H. McCreery and G. W. Jr, *Atomic recombination dynamics on solid surfaces: Effect of various potentials*, J. Chem. Phys. **67**, 2551 (1977), DOI: 10.1063/1.435222, (cit. on p. 69).

[306] C. Engdahl and G. Wahnström, *Transient hyperthermal diffusion following dissociative chemisorption: A molecular dynamics study*, Surf. Sci. **312**, 429 (1994), DOI: 10.1016/0039-6028(94)90734-X, (cit. on p. 69).

[307] T. N. Truong, D. G. Truhlar, and B. C. Garrett, *Embedded diatomics-in-molecules: A method to include delocalized electronic interactions in the treatment of covalent chemical reactions at metal surfaces*, J. Phys. Chem. **93**, 8227 (1989), DOI: 10.1021/j100362a017, (cit. on p. 69).

[308] T. N. Truong and D. G. Truhlar, *The effects of steps, coupling to substrate vibrations, and surface coverage on surface diffusion rates and kinetic isotope effects: Hydrogen diffusion on Ni*, J. Chem. Phys. **93**, 2125 (1990), DOI: 10.1063/1.459038, (cit. on p. 69).

[309] T. N. Truong and D. G. Truhlar, *Effect of steps and surface coverage on rates and kinetic isotope effects for reactions catalyzed by metallic surfaces: Chemisorption of hydrogen on nickel*, J. Phys. Chem. **94**, 8262 (1990), DOI: 10.1021/j100384a052, (cit. on p. 69).

[310] J. Dai and J. Z. H. Zhang, *Quantum adsorption dynamics of a diatomic molecule on surface: Four-dimensional fixed-site model for H_2 on Cu(111)*, J. Chem. Phys. **102**, 6280 (1995), DOI: 10.1063/1.469074, (cit. on p. 69).

[311] A. Forni, G. Wiesenekker, E. J. Baerends, and G. F. Tantardini, *A dynamical study of the chemisorption of molecular hydrogen on the Cu(111) surface*, J. Phys.: Condens. Matter **7**, 7195 (1995), DOI: 10.1088/0953-8984/7/36/009, (cit. on p. 69).

[312] G. Wiesenekker, G. J. Kroes, and E. J. Baerends, *An analytical six-dimensional potential energy surface for dissociation of molecular hydrogen on Cu(100)*, J. Chem. Phys. **104**, 7344 (1996), DOI: 10.1063/1.471402, (cit. on pp. 69 sq., 81).

[313] D. A. McCormack, G.-J. Kroes, R. A. Olsen, J. A. Groeneveld, J. N. P. van Stralen, E. J. Baerends, and R. C. Mowrey, *Quantum dynamics of the dissociation of H2 on Cu(100): Dependence of the site-reactivity on initial rovibrational state*, Faraday Discuss. **117**, 109 (2000), DOI: 10.1039/B002507K, (cit. on pp. 69 sq., 81).

[314] S. Caratzoulas, B. Jackson, and M. Persson, *Eley–Rideal and hot-atom reaction dynamics of H(g) with H adsorbed on Cu(111)*, J. Chem. Phys. **107**, 6420 (1997), DOI: 10.1063/1.474302, (cit. on pp. 69, 81).

[315] M. Persson, J. Strömquist, L. Bengtsson, B. Jackson, D. V. Shalashilin, and B. Hammer, *A first-principles potential energy surface for Eley–Rideal reaction dynamics of H atoms on Cu(111)*, J. Chem. Phys. **110**, 2240 (1999), DOI: 10.1063/1.477836, (cit. on pp. 69, 81).

[316] A. Groß, S. Wilke, and M. Scheffler, *Six-Dimensional Quantum Dynamics of Adsorption and Desorption of H2 at Pd(100): Steering and Steric Effects*, Phys. Rev. Lett. **75**, 2718 (1995), DOI: 10.1103/PhysRevLett.75.2718, (cit. on pp. 70, 81, 96, 136).

[317] C. T. Rettner and D. J. Auerbach, *Comment on "Six-Dimensional Quantum Dynamics of Adsorption and Desorption of H2 at Pd(100): Steering and Steric Effects"*, Phys. Rev. Lett. **77**, 404 (1996), DOI: 10.1103/PhysRevLett.77.404, (cit. on pp. 70, 81, 136).

[318] A. Groß and M. Scheffler, *Groß and Scheffler Reply:* Phys. Rev. Lett. **77**, 405 (1996), DOI: 10.1103/PhysRevLett.77.405, (cit. on pp. 70, 81, 136).

[319] A. Groß and M. Scheffler, *Role of zero-point effects in catalytic reactions involving hydrogen*, in: Vol. 15, AVS, 1997, pp. 1624 –1629, (cit. on p. 70).

[320] A. Groß and M. Scheffler, *Ab initio quantum and molecular dynamics of the dissociative adsorption of hydrogen on Pd(100)*, Phys. Rev. B **57**, 2493 (1998), DOI: 10.1103/PhysRevB.57.2493, (cit. on pp. 70, 81, 96, 101).

[321] R. C. Mowrey, G. J. Kroes, and E. J. Baerends, *Dissociative adsorption of H_2 on Cu(100): Fixed-site calculations for impact at hollow and top sites*, J. Chem. Phys. **108**, 6906 (1998), DOI: 10.1063/1.476105, (cit. on p. 70).

[322] G. Kresse, *Dissociation and sticking of H_2 on the Ni(111), (100), and (110) substrate*, Phys. Rev. B **62**, 8295 (2000), DOI: 10.1103/PhysRevB.62.8295, (cit. on pp. 70, 81).

[323] H. F. Busnengo, A. Salin, and W. Dong, *Representation of the 6D potential energy surface for a diatomic molecule near a solid surface*, J. Chem. Phys. **112**, 7641 (2000), DOI: 10.1063/1.481377, (cit. on pp. 70, 80 sq., 187).

[324] R. A. Olsen, H. F. Busnengo, A. Salin, M. F. Somers, G. J. Kroes, and E. J. Baerends, *Constructing accurate potential energy surfaces for a diatomic molecule interacting with a solid surface: H_2 + Pt(111) and H_2 + Cu(100)*, J. Chem. Phys. **116**, 3841 (2002), DOI: 10.1063/1.1446852, (cit. on pp. 70, 80 sq., 200).

[325] M. A. D. Césare, H. F. Busnengo, W. Dong, and A. Salin, *Role of dynamic trapping in H_2 dissociation and reflection on Pd surfaces*, J. Chem. Phys. **118**, 11226 (2003), DOI: 10.1063/1.1575208, (cit. on p. 70).

[326] N. Pineau, H. F. Busnengo, J. C. Rayez, and A. Salin, *Relaxation of hot atoms following H_2 dissociation on a Pd(111) surface*, J. Chem. Phys. **122**, 214705 (2005), DOI: 10.1063/1.1924550, (cit. on pp. 70, 133, 136, 144).

[327] M. Alducin, R. D. e. Mui, H. F. Busnengo, and A. Salin, *Dissociative adsorption of N2 on W(110): Theoretical study of the dependence on the incidence angle*, Surf. Sci. **601**, 3726 (2007), DOI: 10.1016/j.susc.2007.04.016, (cit. on p. 70).

[328] M. Alducin, H. F. Busnengo, and R. D. Muiño, *Dissociative dynamics of spin-triplet and spin-singlet O_2 on Ag(100)*, J. Chem. Phys. **129**, 224702 (2008), DOI: 10.1063/1.3012354, (cit. on pp. 70, 164).

[329] C. Arasa, H. F. Busnengo, A. Salin, and R. Sayos, *Classical dynamics study of atomic oxygen sticking on the β-cristobalite (100) surface*, Surf. Sci. **602**, 975 (2008), DOI: 10.1016/j.susc.2007.12.034, (cit. on p. 70).

[330] M. A. Collins, *Molecular potential-energy surfaces for chemical reaction dynamics*, Theoretical Chemistry Accounts: Theory, Computation, and Modeling (Theoretica Chimica Acta) **108**, 313 (2002), DOI: 10.1007/s00214-002-0383-5, (cit. on pp. 70, 80).

[331] C. Crespos, M. A. Collins, E. Pijper, and G. J. Kroes, *Multi-dimensional potential energy surface determination by modified Shepard interpolation for a molecule-surface reaction: H2+Pt(111)*, Chem. Phys. Lett. **376**, 566 (2003), DOI: 10.1016/S0009-2614(03)01033-9, (cit. on pp. 70, 80).

[332] C. Crespos, M. A. Collins, E. Pijper, and G. J. Kroes, *Application of the modified Shepard interpolation method to the determination of the potential energy surface for a molecule–surface reaction: H_2 + Pt(111)*, J. Chem. Phys. **120**, 2392 (2004), DOI: 10.1063/1.1637337, (cit. on pp. 70, 80).

[333] P. N. Abufager, C. Crespos, and H. F. Busnengo, *Modified Shepard interpolation method applied to trapping mediated adsorption dynamics*, Phys. Chem. Chem. Phys. **9**, 2258 (2007), DOI: 10.1039/B617209A, (cit. on pp. 70, 80, 181).

[334] C. Díaz, J. K. Vincent, G. P. Krishnamohan, R. A. Olsen, G. J. Kroes, K. Honkala, and J. K. Nørskov, *Multidimensional Effects on Dissociation of N_2 on Ru(0001)*, Phys. Rev. Lett. **96**, 096102 (2006), DOI: 10.1103/PhysRevLett.96.096102, (cit. on p. 70).

[335] C. Díaz, R. A. Olsen, H. F. Busnengo, and G. J. Kroes, *Dynamics on Six-Dimensional Potential Energy Surfaces for H2/Cu(111): Corrugation Reducing Procedure versus Modified Shepard Interpolation Method and PW91 versus RPBE*, J. Phys. Chem. C **114**, 11192 (2010), DOI: 10.1021/jp1027096, (cit. on p. 70).

[336] A. Groß, A. Eichler, J. Hafner, M. J. Mehl, and D. A. Papaconstantopoulos, *Unified picture of the molecular adsorption process: O_2/Pt(111)*, Surf. Sci. **539**, L542 (2003), DOI: 10.1016/S0039-6028(03)00791-X, (cit. on p. 71).

[337] A. Groß, A. Eichler, J. Hafner, M. J. Mehl, and D. A. Papaconstantopoulos, *Ab initio based tight-binding molecular dynamics simulation of the sticking and scattering of O_2/Pt(111)*, J. Chem. Phys. **124**, 174713 (2006), DOI: 10.1063/1.2192512, (cit. on pp. 71, 96, 136).

[338] S. Lorenz, A. Groß, and M. Scheffler, *Representing high-dimensional potential-energy surfaces for reactions at surfaces by neural networks*, Chem. Phys. Lett. **395**, 210 (2004), DOI: 10.1016/j.cplett.2004.07.076, (cit. on pp. 71, 77 sq., 81, 87).

[339] S. Lorenz, M. Scheffler, and A. Groß, *Descriptions of surface chemical reactions using a neural network representation of the potential-energy surface*, Phys. Rev. B **73**, 115431 (2006), DOI: 10.1103/PhysRevB.73.115431, (cit. on pp. 71, 77 sq., 81, 87, 90).

[340] J. Ludwig and D. G. Vlachos, *Ab initio molecular dynamics of hydrogen dissociation on metal surfaces using neural networks and novelty sampling*, J. Chem. Phys. **127**, 154716 (2007), DOI: 10.1063/1.2794338, (cit. on pp. 71, 80 sq., 87 sq.).

[341] J. Ludwig and D. G. Vlachos, *Molecular dynamics of hydrogen dissociation on an oxygen covered Pt(111) surface*, J. Chem. Phys. **128**, 154708 (2008), DOI: 10.1063/1.2902981, (cit. on pp. 71, 81, 87 sq.).

[342] J. Behler, S. Lorenz, and K. Reuter, *Representing molecule-surface interactions with symmetry-adapted neural networks*, J. Chem. Phys. **127**, 014705 (2007), DOI: 10.1063/1.2746232, (cit. on pp. 71, 77 sq., 80 sqq., 87 sq., 90, 195, 198 sq.).

[343] E. D. German, A. M. Kuznetsov, and M. Sheintuch, *Predicting the kinetics of the dissociative adsorption of homonuclear molecules on metal surfaces in gas phase and solution: I. Rate constant of the elementary step of adiabatic reaction*, Surf. Sci. **554**, 159 (2004), DOI: 10.1016/j.susc.2004.01.033, (cit. on p. 71).

[344] E. D. German, A. M. Kuznetsov, and M. Sheintuch, *Predicting the kinetics of the dissociative adsorption of homonuclear molecules on metal surfaces in gas phase and solution II. Numerical calculations of the molecular oxygen dissociative adsorption on the Pd(111) surface*, Surf. Sci. **554**, 170 (2004), DOI: 10.1016/j.susc.2004.01.061, (cit. on p. 71).

[345] Z. Wang, X. Jia, and R. Wang, *Dynamic Study of O2 Adsorption and Dissociation on Pd Low-Index Surfaces*, J. Phys. Chem. A **108**, 5424 (2004), DOI: 10.1021/jp0377174, (cit. on p. 71).

[346] S. Chen, D. Wang, and S. Yu, *Adsorption and Dissociation of O/O_2 on flat and stepped Palladium surfaces*, Surf. Rev. Lett. **5**, 669 (2006), DOI: 10.1142/S0218625X06008645, (cit. on p. 71).

[347] L. Martin-Gondre, C. Crespos, P. Larrégaray, J. C. Rayez, B. van Ootegem, and D. Conte, *Is the LEPS potential accurate enough to investigate the dissociation of diatomic molecules on surfaces?* Chem. Phys. Lett. **471**, 136 (2009), DOI: 10.1016/j.cplett.2009.01.046, (cit. on p. 71).

[348] L. Martin-Gondre, C. Crespos, P. Larrégaray, J. C. Rayez, B. van Ootegem, and D. Conte, *Dynamics simulation of N_2 scattering onto W(100,110) surfaces: A stringent test for the recently developed flexible periodic London–Eyring–Polanyi–Sato potential energy surface*, J. Chem. Phys. **132**, 204501 (2010), DOI: 10.1063/1.3389479, (cit. on p. 71).

[349] M. Malshe, R. Narulkar, L. M. Raff, M. Hagan, S. Bukkapatnam, P. M. Agrawal, and R. Komanduri, *Development of generalized potential-energy surfaces using many-body expansions, neural networks, and moiety energy approximations*, J. Chem. Phys. **130**, 184102 (2009), DOI: 10.1063/1.3124802, (cit. on p. 71).

[350] J. Behler, *Atom-centered symmetry functions for constructing high-dimensional neural network potentials*, J. Chem. Phys. **134**, 074106 (2011), DOI: 10.1063/1.3553717, (cit. on pp. 71, 81 sq.).

[351] J. Behler, *Neural network potential-energy surfaces in chemistry: A tool for large-scale simulations*, Phys. Chem. Chem. Phys. **13**, 17930 (2011), DOI: 10.1039/C1CP21668F, (cit. on pp. 71, 195, 198 sq.).

[352] C. M. Handley and P. L. A. Popelier, *Potential Energy Surfaces Fitted by Artificial Neural Networks*, J. Phys. Chem. A **114**, 3371 (2010), DOI: 10.1021/jp9105585, (cit. on pp. 71, 75).

[353] A. Groß and A. Dianat, *Hydrogen Dissociation Dynamics on Precovered Pd Surfaces: Langmuir is Still Right*, Phys. Rev. Lett. **98**, 206107 (2007), DOI: 10.1103/PhysRevLett.98.206107, (cit. on pp. 71, 136).

[354] A. Groß, *Ab Initio Molecular Dynamics Study of Hot Atom Dynamics after Dissociative Adsorption of H_2 on Pd(100)*, Phys. Rev. Lett. **103**, 246101 (2009), DOI: 10.1103/PhysRevLett.103.246101, (cit. on pp. 71, 136, 161, 165).

[355] A. Lozano, A. Groß, and H. F. Busnengo, *Adsorption dynamics of H2 on Pd(100) from first principles*, Phys. Chem. Chem. Phys. **11**, 5814 (2009), DOI: 10.1039/B905432B, (cit. on p. 71).

[356] A. Lozano, A. Groß, and H. F. Busnengo, *Molecular dynamics study of H_2 dissociation on H-covered Pd(100)*, Phys. Rev. B **81**, 121402 (2010), DOI: 10.1103/PhysRevB.81.121402, (cit. on p. 71).

[357] T. D. Kühne, M. Krack, F. R. Mohamed, and M. Parrinello, *Efficient and Accurate Car-Parrinello-like Approach to Born-Oppenheimer Molecular Dynamics*, Phys. Rev. Lett. **98**, 066401 (2007), DOI: 10.1103/PhysRevLett.98.066401, (cit. on pp. 72, 182).

[358] S. Lorenz, *Reactions on Surfaces with Neural Networks*, PhD thesis, Technische Universität Berlin, 2001, (cit. on pp. 76 sqq.).

[359] G. Cybenko, *Approximation by superpositions of a sigmoidal function*, Mathematics of Control, Signals, and Systems (MCSS) **2**, 303 (1989), DOI: 10.1007/BF02551274, (cit. on p. 77).

[360] K. Hornik, M. Stinchcombe, and H. White, *Multilayer feedforward networks are universal approximators*, Neural Networks **2**, 359 (1989), DOI: 10.1016/0893-6080(89)90020-8, (cit. on p. 77).

[361] A. Groß, *Electronic Convergence in ab-initio Molecular Dynamics used to obtain Statistics in Simulations of Gas-Surface Dynamics*, private communication, Universität Ulm, 2010, (cit. on pp. 77, 136, 165).

[362] J. B. Witkoskie and D. J. Doren, *Neural Network Models of Potential Energy Surfaces: Prototypical Examples*, J. Chem. Theory Comput. **1**, 14 (2005), DOI: 10.1021/ct049976i, (cit. on p. 78).

[363] A. Groß, *Coverage effects in the adsorption of H2 on Pd(100) studied by ab initio molecular dynamics simulations*, J. Chem. Phys. **135**, 174707 (2011), DOI: 10.1063/1.3656765, (cit. on pp. 87, 96, 146).

[364] Richard and Franke, *Smooth interpolation of scattered data by local thin plate splines*, Comp. & Maths. with Appls. **8**, 273 (1982), DOI: 10.1016/0898-1221(82)90009-8, (cit. on p. 92).

[365] S.-L. Chang and P. A. Thiel, *Formation of a Metastable Ordered Surface Phase Due to Competitive Diffusion and Adsorption Kinetics: Oxygen on Pd(100)*, Phys. Rev. Lett. **59**, 1171 (1987), DOI: 10.1103/PhysRevLett.59.1171.2, (cit. on pp. 95, 162).

[366] M. Rocca, *Initial Sticking Coefficient for O_2 on Pd(100) as obtained by Molecular Beam Experiments with an incidence Energy of 400 meV*, private communication, 25th European Conference on Surface Science (ECOSS-25), Liverpool, UK, 2008, (cit. on p. 95).

[367] A. C. Luntz, M. D. Williams, and D. S. Bethune, *The sticking of O_2 on a Pt(111) surface*, J. Chem. Phys. **89**, 4381 (1988), DOI: 10.1063/1.454824, (cit. on p. 96).

[368] P. Sjövall and P. Uvdal, *Oxygen sticking on Pd(111): Double precursors, corrugation and substrate temperature effects*, Chem. Phys. Lett. **282**, 355 (1998), DOI: 10.1016/S0009-2614(97)01293-1, (cit. on p. 96).

[369] P. Sjövall and P. Uvdal, *Adsorption of oxygen on Pd(111): Precursor kinetics and coverage-dependent sticking*, J. Vac. Sci. Technol. A **16**, 943 (1998), DOI: 10.1116/1.581216, (cit. on p. 96).

[370] C. Nyberg and C. G. Tengstål, *Vibrational excitations of p(2×2) oxygen and c(2×2) hydrogen on Pd(100)*, Solid State Commun. **44**, 251 (1982), DOI: 10.1016/0038-1098(82)90442-2, (cit. on p. 96).

[371] C. Nyberg and C. G. Tengstål, *Vibrational excitations of hydrogen and oxygen on Pd(100)*, Surf. Sci. **126**, 163 (1983), DOI: 10.1016/0039-6028(83)90705-7, (cit. on p. 96).

[372] E. M. Stuve, R. J. Madix, and C. R. Brundle, *CO oxidation on Pd(100): A study of the coadsorption of oxygen and carbon monoxide*, Surf. Sci. **146**, 155 (1984), DOI: 10.1016/0039-6028(84)90235-8, (cit. on p. 96).

[373] H. F. Busnengo, E. Pijper, M. F. Somers, G. J. Kroes, A. Salin, R. A. Olsen, D. Lemoine, and W. Dong, *Six-dimensional quantum and classical dynamics study of H2(ν=0,J=0) scattering from Pd(111)*, Chem. Phys. Lett. **356**, 515 (2002), DOI: 10.1016/S0009-2614(02)00404-9, (cit. on p. 101).

[374] L. S. Cederbaum, *Born–Oppenheimer approximation and beyond for time-dependent electronic processes*, J. Chem. Phys. **128**, 124101 (2008), DOI: 10.1063/1.2895043, (cit. on p. 101).

[375] P. Nieto, E. Pijper, D. Barredo, G. Laurent, R. A. Olsen, E.-J. Baerends, G.-J. Kroes, and D. Farias, *Reactive and Nonreactive Scattering of H2 from a Metal Surface Is Electronically Adiabatic*, Science **312**, 86 (2006), DOI: 10.1126/science.1123057, (cit. on p. 101).

[376] A. C. Luntz, *The dynamics of dissociative adsorption on metal surfaces: "First principles" theory - Experiment confrontations*, Surf. Sci. **603**, 1557 (2009), DOI: 10.1016/j.susc.2008.11.044, (cit. on pp. 101, 124).

[377] J. C. Tully, *Molecular dynamics with electronic transitions*, J. Chem. Phys. **93**, 1061 (1990), DOI: 10.1063/1.459170, (cit. on p. 102).

[378] F. J. Arlinghaus, J. G. Gay, and J. R. Smith, *Surface states on d-band metals*, Phys. Rev. B **23**, 5152 (1981), DOI: 10.1103/PhysRevB.23.5152, (cit. on p. 102).

[379] M. S. Mizielinski, D. M. Bird, M. Persson, and S. Holloway, *Electronic nonadiabatic effects in the adsorption of hydrogen atoms on metals*, J. Chem. Phys. **122**, 084710 (2005), DOI: 10.1063/1.1854623, (cit. on p. 103).

[380] M. S. Mizielinski, D. M. Bird, M. Persson, and S. Holloway, *Erratum: "Spectrum of electronic excitations due to the adsorption of atoms on metal surfaces" [J. Chem. Phys. **126**, 034705 (2007)]*, J. Chem. Phys. **126**, 229901 (2007), DOI: 10.1063/1.2741541, (cit. on p. 103).

[381] M. S. Mizielinski, D. M. Bird, M. Persson, and S. Holloway, *Spectrum of electronic excitations due to the adsorption of atoms on metal surfaces*, J. Chem. Phys. **126**, 034705 (2007), DOI: 10.1063/1.2431362, (cit. on p. 103).

[382] M. S. Mizielinski, D. M. Bird, M. Persson, and S. Holloway, *Newns-Anderson model of chemicurrents in H/Cu and H/Ag*, Surf. Sci. **602**, 2617 (2008), DOI: 10.1016/j.susc.2008.06.015, (cit. on pp. 103, 118).

[383] M. Lindenblatt and E. Pehlke, *Time-dependent density-functional molecular-dynamics study of the isotope effect in chemicurrents*, Surf. Sci. **600**, 5068 (2006), DOI: 10.1016/j.susc.2006.08.034, (cit. on pp. 103, 105, 108 sq., 112, 123 sq., 136).

[384] M. Lindenblatt, J. van Heys, and E. Pehlke, *Molecular dynamics of nonadiabatic processes at surfaces: Chemisorption of H/Al(111)*, Surf. Sci. **600**, 3624 (2006), DOI: 10.1016/j.susc.2006.01.066, (cit. on pp. 103, 105, 108 sq., 112, 118, 123 sq., 136, 141).

[385] H. Appel, *Combining TD-DFT with QM/Me*, private communication, March Meeting of the American Physical Society (APS), Portland, OR, USA, 2010, (cit. on p. 103).

[386] E. G. d'Agliano, P. Kumar, W. Schaich, and H. Suhl, *Brownian motion model of the interactions between chemical species and metallic electrons: Bootstrap derivation and parameter evaluation*, Phys. Rev. B **11**, 2122 (1975), DOI: 10.1103/PhysRevB.11.2122, (cit. on pp. 103, 107, 111).

[387] M. Persson and B. Hellsing, *Electronic Damping of Adsorbate Vibrations on Metal Surfaces*, Phys. Rev. Lett. **49**, 662 (1982), DOI: 10.1103/PhysRevLett.49.662, (cit. on pp. 103, 107, 111, 124).

[388] B. Hellsing and M. Persson, *Electronic Damping of Atomic and Molecular Vibrations at Metal Surfaces*, Phys. Scr. **29**, 360 (1984), DOI: 10.1088/0031-8949/29/4/014, (cit. on pp. 103, 107, 111, 124).

[389] J. R. Trail, M. C. Graham, and D. M. Bird, *Electronic damping of molecular motion at metal surfaces*, Comput. Phys. Commun. **137**, 163 (2001), DOI: 10.1016/S0010-4655(01)00177-1, (cit. on pp. 103, 111 sq., 246).

[390] M. Persson, *Theory of elastic and inelastic tunnelling microscopy and spectroscopy: CO on Cu revisited*, Phil. Trans. R. Soc. Lond. A **362**, 1173 (2004), DOI: 10.1098/rsta.2004.1370, (cit. on pp. 103, 111).

[391] A. C. Luntz, M. Persson, S. Wagner, C. Frischkorn, and M. Wolf, *Femtosecond laser induced associative desorption of H_2 from Ru(0001): Comparison of "first principles" theory with experiment*, J. Chem. Phys. **124**, 244702 (2006), DOI: 10.1063/1.2206588, (cit. on pp. 103, 133).

[392] J. R. Trail, M. C. Graham, D. M. Bird, M. Persson, and S. Holloway, *Energy Loss of Atoms at Metal Surfaces due to Electron-Hole Pair Excitations: First-Principles Theory of "Chemicurrents"*, Phys. Rev. Lett. **88**, 166802 (2002), DOI: 10.1103/PhysRevLett.88.166802, (cit. on pp. 103, 107 sqq., 113).

[393] M. Timmer and P. Kratzer, *Electron-hole spectra created by adsorption on metals from density functional theory*, Phys. Rev. B **79**, 165407 (2009), DOI: 10.1103/PhysRevB.79.165407, (cit. on pp. 103 sqq., 107 sqq., 112 sq., 118 sq., 123 sq., 141, 247–252).

[394] M. Timmer and P. Kratzer, *Theoretical investigation of the influence of isotope mass on chemicurrents during adsorption of H on K(110)*, Surf. Sci. **604**, 1452 (2010), DOI: 10.1016/j.susc.2010.05.008, (cit. on pp. 107, 109, 113, 141, 252).

[395] M. S. Mizielinski and D. M. Bird, *Accuracy of perturbation theory for nonadiabatic effects in adsorbate-surface dynamics*, J. Chem. Phys. **132**, 184704 (2010), DOI: 10.1063/1.3424765, (cit. on pp. 107, 109, 124).

[396] M. Timmer, *Ab initio theory of electronic excitations at surfaces*, PhD thesis, Universität Duisburg-Essen, 2010, (cit. on pp. 108, 110, 113, 123 sq., 247, 252).

[397] K. Schönhammer and O. Gunnarsson, *Localized dynamic perturbations in metals*, Z. Phys. B **38**, 127 (1980), DOI: 10.1007/BF01598752, (cit. on p. 108).

[398] S. Baroni, P. Giannozzi, and A. Testa, *Green's-function approach to linear response in solids*, Phys. Rev. Lett. **58**, 1861 (1987), DOI: 10.1103/PhysRevLett.58.1861, (cit. on p. 110).

[399] N. Lorente and M. Persson, *Theory of Single Molecule Vibrational Spectroscopy and Microscopy*, Phys. Rev. Lett. **85**, 2997 (2000), DOI: 10.1103/PhysRevLett.85.2997, (cit. on pp. 111, 181).

[400] N. Lorente, M. Persson, L. J. Lauhon, and W. Ho, *Symmetry Selection Rules for Vibrationally Inelastic Tunneling*, Phys. Rev. Lett. **86**, 2593 (2001), DOI: 10.1103/PhysRevLett.86.2593, (cit. on p. 111).

[401] N. Lorente, *Mode excitation induced by the scanning tunnelling microscope*, Applied Physics A: Materials Science & Processing **78**, 799 (2004), DOI: 10.1007/s00339-003-2434-8, (cit. on p. 111).

[402] N. Lorente, R. Rurali, and H. Tang, *Single-molecule manipulation and chemistry with the STM*, J. Phys.: Condens. Matter **17**, S1049 (2005), DOI: 10.1088/0953-8984/17/13/003, (cit. on p. 111).

[403] G. Teobaldi, M. Peñalba, A. Arnau, N. Lorente, and W. A. Hofer, *Including the probe tip in theoretical models of inelastic scanning tunneling spectroscopy: CO on Cu(100)*, Phys. Rev. B **76**, 235407 (2007), DOI: 10.1103/PhysRevB.76.235407, (cit. on p. 111).

[404] M. Alducin, D. Sanchez-Portal, A. Arnau, and N. Lorente, *Mixed-Valency Signature in Vibrational Inelastic Electron Tunneling Spectroscopy*, Phys. Rev. Lett. **104**, 136101 (2010), DOI: 10.1103/PhysRevLett.104.136101, (cit. on p. 111).

[405] S. Monturet, M. Alducin, and N. Lorente, *Role of molecular electronic structure in inelastic electron tunneling spectroscopy: O_2 on Ag(110)*, Phys. Rev. B **82**, 085447 (2010), DOI: 10.1103/PhysRevB.82.085447, (cit. on p. 111).

[406] M. Head-Gordon and J. C. Tully, *Molecular-orbital calculations of the lifetimes of the vibrational modes of CO on Cu(100)*, Phys. Rev. B **46**, 1853 (1992), DOI: 10.1103/PhysRevB.46.1853, (cit. on p. 111).

[407] M. Timmer and P. Kratzer, *Implementation Details of Time-Dependent Perturbative Approach to Electron-Hole Pair Spectra*, private communication, Spring Meeting of the German Physical Society (DPG), Dresden, 2009, (cit. on pp. 113, 252).

[408] P. E. Blöchl, *Projector augmented-wave method*, Phys. Rev. B **50**, 17953 (1994), DOI: 10.1103/PhysRevB.50.17953, (cit. on p. 113).

[409] M. D. Segall, C. J. Pickard, R. Shah, and M. C. Payne, *Population analysis in plane wave electronic structure calculations*, Mol. Phys. **89**, 571 (1996), DOI: 10.1080/00268979609482494, (cit. on pp. 115, 122, 248 sq.).

[410] M. D. Segall, R. Shah, C. J. Pickard, and M. C. Payne, *Population analysis of plane-wave electronic structure calculations of bulk materials*, Phys. Rev. B **54**, 16317 (1996), DOI: 10.1103/PhysRevB.54.16317, (cit. on pp. 115, 122, 248 sq.).

[411] R. S. Mulliken, *Electronic Population Analysis on LCAO[Single Bond]MO Molecular Wave Functions. I*, J. Chem. Phys. **23**, 1833 (1955), DOI: 10.1063/1.1740588, (cit. on pp. 115, 122, 248 sq.).

[412] H. Nienhaus, *Chemicurrents are not detectable during Adsorption of Molecular Oxygen on Palladium Surfaces*, private communication, Gordon Research Conference "Dynamics at Surfaces", Proctor Academy, Andover, New Hampshire, 2009, (cit. on pp. 123, 129).

[413] B. Gergen, H. Nienhaus, W. H. Weinberg, and E. W. McFarland, *Chemically Induced Electronic Excitations at Metal Surfaces*, Science **294**, 2521 (2001), DOI: 10.1126/science.1066134, (cit. on p. 123).

[414] H. Nienhaus, H. S. Bergh, B. Gergen, A. Majumdar, W. H. Weinberg, and E. W. McFarland, *Direct detection of electron-hole pairs generated by chemical reactions on metal surfaces*, Surf. Sci. **445**, 335 (2000), DOI: 10.1016/S0039-6028(99)01078-X, (cit. on p. 123).

[415] B. Gergen, S. J. Weyers, H. Nienhaus, W. H. Weinberg, and E. W. McFarland, *Observation of excited electrons from nonadiabatic molecular reactions of NO and O2 on polycrystalline Ag*, Surf. Sci. **488**, 123 (2001), DOI: 10.1016/S0039-6028(01)01124-4, (cit. on p. 123).

[416] M. Grotemeyer and E. Pehlke, *Ab-initio Molecular Dynamics Simulation of Electronic Energy Dissipation: HCl/Al(111)*, private communication, Spring Meeting of the German Physical Society (DPG), Regensburg, 2010, (cit. on p. 124).

[417] *Handbook of the physicochemical properties of the elements*, in: ed. by G. V. Samsonov, IFI/Plenum, New York, NY, 1968, (cit. on p. 129).

[418] G. D. Billing, *On a semiclassical approach to energy transfer by atom/molecule-surface collisions*, Chem. Phys. **70**, 223 (1982), DOI: 10.1016/0301-0104(82)88091-9, (cit. on p. 130).

[419] G. D. Billing, *Semiclassical theory for atom–surface scattering: Calculations on Ar + W(110)*, Chem. Phys. **74**, 143 (1983), DOI: 10.1016/0301-0104(83)80017-2, (cit. on p. 130).

[420] G. D. Billing, *The dynamics of molecule-surface interaction*, Computer Physics Reports **12**, 383 (1990), DOI: 10.1016/0167-7977(90)90001-M, (cit. on p. 130).

[421] G. D. Billing, *Semiclassical Formulation of Molecule-Surface Scattering Using an Embedded Diatomics in Molecules Potential*, J. Phys. Chem. **99**, 15378 (1995), DOI: 10.1021/j100042a009, (cit. on p. 130).

[422] R. W. Zwanzig, *Collision of a Gas Atom with a Cold Surface*, J. Chem. Phys. **32**, 1173 (1960), DOI: 10.1063/1.1730869, (cit. on p. 130).

[423] R. Zwanzig, *Time-Correlation Functions and Transport Coefficients in Statistical Mechanics*, Annu. Rev. Phys. Chem. **16**, 67 (1965), DOI: 10.1146/annurev.pc.16.100165.000435, (cit. on p. 130).

[424] H. Mori, *Transport, Collective Motion, and Brownian Motion*, Progress of Theoretical Physics **33**, 423 (1965), DOI: 10.1143/PTP.33.423, (cit. on pp. 130, 132).

[425] R. Kubo, *The fluctuation-dissipation theorem*, Rep. Prog. Phys. **29**, 255 (1966), DOI: 10.1088/0034-4885/29/1/306, (cit. on pp. 130, 132).

[426] S. A. Adelman and J. D. Doll, *Generalized Langevin equation approach for atom/solid-surface scattering: Collinear atom/harmonic chain model*, J. Chem. Phys. **61**, 4242 (1974), DOI: 10.1063/1.1681723, (cit. on p. 131).

[427] S. A. Adelman and J. D. Doll, *Erratum: Generalized Langevin equation approach for atom/solid-surface scattering: Collinear atom/harmonic chain model*, J. Chem. Phys. **62**, 2518 (1975), DOI: 10.1063/1.431022, (cit. on p. 131).

[428] S. A. Adelman and J. D. Doll, *Generalized Langevin equation approach for atom/solid-surface scattering: General formulation for classical scattering off harmonic solids*, J. Chem. Phys. **64**, 2375 (1976), DOI: 10.1063/1.432526, (cit. on pp. 131 sqq.).

[429] S. A. Adelman, *Generalized Langevin theory for many-body problems in chemical dynamics: General formulation and the equivalent harmonic chain representation*, J. Chem. Phys. **71**, 4471 (1979), DOI: 10.1063/1.438200, (cit. on p. 131).

[430] S. A. Adelman and J. D. Doll, *Brownian Motion and Chemical Dynamics on Solid Surfaces*, Acc. Chem. Res. **10**, 378 (1977), DOI: 10.1021/ar50118a005, (cit. on p. 131).

[431] J. C. Tully, *Dynamics of chemical processes at surfaces*, Acc. Chem. Res. **14**, 188 (1981), DOI: 10.1021/ar00066a004, (cit. on p. 131).

[432] L. Kantorovich, *Generalized Langevin equation for solids. I. Rigorous derivation and main properties*, Phys. Rev. B **78**, 094304 (2008), DOI: 10.1103/PhysRevB.78.094304, (cit. on pp. 131 sqq.).

[433] M. Shugard, J. C. Tully, and A. Nitzan, *Dynamics of gas–solid interactions: Calculations of energy transfer and sticking*, J. Chem. Phys. **66**, 2534 (1977), DOI: 10.1063/1.434249, (cit. on p. 132).

[434] J. C. Tully, *Dynamics of gas–surface interactions: 3D generalized Langevin model applied to fcc and bcc surfaces*, J. Chem. Phys. **73**, 1975 (1980), DOI: 10.1063/1.440287, (cit. on pp. 133, 151, 160, 174).

[435] J. C. Tully, G. H. Gilmer, and M. Shugard, *Molecular dynamics of surface diffusion. I. The motion of adatoms and clusters*, J. Chem. Phys. **71**, 1630 (1979), DOI: 10.1063/1.438490, (cit. on p. 133).

[436] J. C. Tully, *Dynamics of gas–surface interactions: Reaction of atomic oxygen with adsorbed carbon on platinum*, J. Chem. Phys. **73**, 6333 (1980), DOI: 10.1063/1.440097, (cit. on p. 133).

[437] R. R. Lucchese and J. C. Tully, *Trajectory studies of rainbow scattering from the reconstructed Si(100) surface*, Surf. Sci. **137**, 570 (1984), DOI: 10.1016/0039-6028(84)90530-2, (cit. on p. 133).

[438] C.-Y. Lee and A. E. DePristo, *Dissociative chemisorption dynamics of H_2 on Ni and Cu surfaces: Morphology and surface temperature effects*, J. Chem. Phys. **85**, 4161 (1986), DOI: 10.1063/1.450889, (cit. on pp. 133 sq.).

[439] C.-Y. Lee and A. E. DePristo, *Erratum: Dissociative chemisorption dynamics of H_2 on Ni and Cu surfaces: Morphology and surface temperature effects [J. Chem. Phys. [Bold 8][bold 5], 4161 (1986)]*, J. Chem. Phys. **86**, 6568 (1987), DOI: 10.1063/1.452791, (cit. on pp. 133 sq.).

[440] A. E. DePristo, *Memory function parametrization in the GLE-Ghost atom formalism: A microscopic approach*, Surf. Sci. **141**, 40 (1984), DOI: 10.1016/0039-6028(84)90195-X, (cit. on p. 133).

[441] A. E. DePristo and H. Metiu, *Molecular dynamics simulations of energy flow at a solid surface. New methods using a small number of atoms*, J. Chem. Phys. **90**, 1229 (1989), DOI: 10.1063/1.456128, (cit. on p. 133).

[442] A. E. DePristo and H. Metiu, *Erratum: Molecular dynamics simulations of energy flow at a solid surface: New methods using a smaller number of atoms [J. Chem. Phys.* **90**, *1229 (1989)]*, J. Chem. Phys. **91**, 1385 (1989), DOI: 10.1063/1.457686, (cit. on p. 133).

[443] J. T. Kindt, J. C. Tully, M. Head-Gordon, and M. A. Gomez, *Electron-hole pair contributions to scattering, sticking, and surface diffusion: CO on Cu(100)*, J. Chem. Phys. **109**, 3629 (1998), DOI: 10.1063/1.476960, (cit. on p. 133).

[444] J. C. Polanyi and R. J. Wolf, *Dynamics of simple gas–surface interaction. II. Rotationally inelastic collisions at rigid and moving surfaces*, J. Chem. Phys. **82**, 1555 (1985), DOI: 10.1063/1.448431, (cit. on pp. 133, 135, 160, 263).

[445] M. Dohle, P. Saalfrank, and T. Uzer, *The dissociation of diatomic molecules on vibrating surfaces: A semiclassical generalized Langevin approach*, J. Chem. Phys. **108**, 4226 (1998), DOI: 10.1063/1.475821, (cit. on pp. 133 sqq.).

[446] M. Dohle, P. Saalfrank, and T. Uzer, *Dissociative sticking of diatomic molecules on cold, nonrigid surfaces: Comparison of quantal and semiclassical surface oscillator models*, Surf. Sci. **409**, 37 (1998), DOI: 10.1016/S0039-6028(98)00194-0, (cit. on pp. 133 sqq.).

[447] H. F. Busnengo, M. A. D. Césare, W. Dong, and A. Salin, *Surface temperature effects in dynamic trapping mediated adsorption of light molecules on metal surfaces: H2 on Pd(111) and Pd(110)*, Phys. Rev. B **72**, 125411 (2005), DOI: 10.1103/PhysRevB.72.125411, (cit. on pp. 133, 135, 156, 263).

[448] N. Perron, N. Pineau, E. Arquis, J. C. Rayez, and A. Salin, *Adsorption of atomic oxygen on the Cu(100) surface*, Surf. Sci. **599**, 160 (2005), DOI: 10.1016/j.susc.2005.09.044, (cit. on pp. 133, 136, 144, 151, 174).

[449] W. Cai, M. de Koning, V. V. Bulatov, and S. Yip, *Minimizing Boundary Reflections in Coupled-Domain Simulations*, Phys. Rev. Lett. **85**, 3213 (2000), DOI: 10.1103/PhysRevLett.85.3213, (cit. on pp. 133, 146).

[450] C. Campañá and M. H. Müser, *Practical Green's function approach to the simulation of elastic semi-infinite solids*, Phys. Rev. B **74**, 075420 (2006), DOI: 10.1103/PhysRevB.74.075420, (cit. on pp. 133, 264 sq.).

[451] C. Campañá, M. H. Müser, C. Denniston, Y. Qic, and T. A. Perry, *Elucidating the contact mechanics of aluminum silicon surfaces with Green's function molecular dynamics*, J. Appl. Phys. **102**, 113511 (2007), DOI: 10.1063/1.2815640, (cit. on pp. 133, 264).

[452] L. T. Kong, G. Bartels, C. Campañá, C. Denniston, and M. H. Müser, *Implementation of Green's function molecular dynamics: An extension to LAMMPS*, Comput. Phys. Commun. **180**, 1004 (2009), DOI: 10.1016/j.cpc.2008.12.035, (cit. on pp. 133, 264 sq.).

[453] W. E and Z. Huang, *A Dynamic Atomistic-Continuum Method for the Simulation of Crystalline Materials*, J. Comput. Phys. **182**, 234 (2002), DOI: 10.1006/jcph.2002.7164, (cit. on pp. 133, 146).

[454] X. Li and W. E, *Variational boundary conditions for molecular dynamics simulations of crystalline solids at finite temperature: Treatment of the thermal bath*, Phys. Rev. B **76**, 104107 (2007), DOI: 10.1103/PhysRevB.76.104107, (cit. on pp. 133, 146).

[455] M. Moseler, J. Nordiek, and H. Haberland, *Reduction of the reflected pressure wave in the molecular-dynamics simulation of energetic particle-solid collisions*, Phys. Rev. B **56**, 15439 (1997), DOI: 10.1103/PhysRevB.56.15439, (cit. on p. 133).

[456] L. Kantorovich and N. Rompotis, *Generalized Langevin equation for solids. II. Stochastic boundary conditions for nonequilibrium molecular dynamics simulations*, Phys. Rev. B **78**, 094305 (2008), DOI: 10.1103/PhysRevB.78.094305, (cit. on pp. 133 sq., 141, 160).

[457] D. Toton, C. D. Lorenz, N. Rompotis, N. Martsinovich, and L. Kantorovich, *Temperature control in molecular dynamic simulations of non-equilibrium processes*, J. Phys.: Condens. Matter **22**, 074205 (2010), DOI: 10.1088/0953-8984/22/7/074205, (cit. on pp. 134, 141).

[458] M. Hand and J. Harris, *Recoil effects in surface dissociation*, J. Chem. Phys. **92**, 7610 (1990), DOI: 10.1063/1.458198, (cit. on pp. 134, 263).

[459] W. Brenig, T. Brunner, A. Groß, and R. Russ, *Numerically stable solution of coupled channel equations: The local reflection matrix*, Zeitschrift für Physik B Condensed Matter **93**, 91 (1993), DOI: 10.1007/BF01308812, (cit. on p. 134).

[460] A. Groß and W. Brenig, *Vibrational excitation in the scattering from an almost rigid surface: NO/diamond(110)*, Surf. Sci. **302**, 403 (1994), DOI: 10.1016/0039-6028(94)90844-3, (cit. on p. 134).

[461] M. Dohle and P. Saalfrank, *Surface oscillator models for dissociative sticking of molecular hydrogen at non-rigid surfaces*, Surf. Sci. **373**, 95 (1997), DOI: 10.1016/S0039-6028(96)01143-0, (cit. on pp. 134 sq.).

[462] Z. S. Wang, G. R. Darling, and S. Holloway, *Surface Temperature Dependence of the Inelastic Scattering of Hydrogen Molecules from Metal Surfaces*, Phys. Rev. Lett. **87**, 226102 (2001), DOI: 10.1103/PhysRevLett.87.226102, (cit. on p. 134).

[463] C. Bach and A. Groß, *Semiclassical treatment of reactions at surfaces with electronic transitions*, Faraday Discuss. **117**, 99 (2000), DOI: 10.1039/B002632H, (cit. on p. 134).

[464] C. Bach, T. Klüner, and A. Groß, *Simulation of laser-induced desorption of NO from NiO(100)*, Chem. Phys. Lett. **376**, 424 (2003), DOI: 10.1016/S0009-2614(03)01023-6, (cit. on p. 134).

[465] C. Bach, T. Klüner, and A. Groß, *Multi-dimensional mixed quantum–classical description of the laser-induced desorption of molecules*, Appl. Phys. A **78**, 231 (2004), DOI: 10.1007/s00339-003-2307-1, (cit. on pp. 134, 157, 174).

[466] C. Bach, C. Carbogno, and A. Groß, *Mixed quantum—classical treatment of reactions at surfaces with electronic transitions*, Isr. J. Chem. **45**, 45 (2005), DOI: 10.1560/T4CN-FWAG-YYXE-L7G7, (cit. on pp. 134 sq.).

[467] C. Carbogno, A. Groß, and M. Rohlfing, *Ab initio investigation of the laser induced desorption of iodine from KI(100)*, Appl. Phys. A **88**, 579 (2007), DOI: 10.1007/s00339-007-4046-1, (cit. on pp. 134 sq.).

[468] A. Groß, *Surface temperature effects in dissociative adsorption: D_2/Cu(111)*, Surf. Sci. **314**, L843 (1994), DOI: 10.1016/0039-6028(94)90205-4, (cit. on pp. 135, 157, 174).

[469] G.-J. Kroes, *Frontiers in Surface Scattering Simulations*, Science **321**, 794 (2008), DOI: 10.1126/science.1157717, (cit. on pp. 135, 141).

[470] M. Svensson, S. Humbel, R. D. J. Froese, T. Matsubara, S. Sieber, and K. Morokuma, *ONIOM: A Multilayered Integrated MO + MM Method for Geometry Optimizations and Single Point Energy Predictions. A Test for Diels-Alder Reactions and Pt(P(t-Bu)3)2 + H2 Oxidative Addition*, The Journal of Physical Chemistry **100**, 19357 (1996), DOI: 10.1021/jp962071j, (cit. on pp. 138, 145).

[471] I. Solt, P. Kulhánek, I. Simon, S. Winfield, M. C. Payne, G. Csányi, and M. Fuxreiter, *Evaluating Boundary Dependent Errors in QM/MM Simulations*, J. Phys. Chem. B **113**, 5728 (2009), DOI: 10.1021/jp807277r, (cit. on pp. 138, 147).

[472] G. Csányi, T. Albaret, M. C. Payne, and A. D. Vita, *"Learn on the Fly": A Hybrid Classical and Quantum-Mechanical Molecular Dynamics Simulation*, Phys. Rev. Lett. **93**, 175503 (2004), DOI: 10.1103/PhysRevLett.93.175503, (cit. on p. 138).

[473] G. Csányi, T. Albaret, G. Moras, M. C. Payne, and A. D. Vita, *Multiscale hybrid simulation methods for material systems*, J. Phys.: Condens. Matter **17**, R691 (2005), DOI: 10.1088/0953-8984/17/27/R02, (cit. on p. 138).

[474] M. C. Payne, G. Csányi, T. Albaret, and A. D. Vita, *A novel quantum/classical hybrid simulation technique.* ChemPhysChem **6**, 1731 (2005), DOI: 10.1002/cphc.200400585, (cit. on p. 138).

[475] G. Moras, G. Csányi, M. C. Payne, and A. D. Vita, *A novel molecular dynamics approach to large semiconductor systems*, Physica B: Condensed Matter **376 - 377**, 936 (2006), DOI: 10.1016/j.physb.2005.12.233, (cit. on p. 138).

[476] K. Morokuma, *ONIOM and its applications to material chemistry and catalyses*, Bull. Korean Chem. Soc. **24**, 797 (2003), (cit. on p. 138).

[477] C. Bo and F. Maseras, *QM/MM methods in inorganic chemistry*, Dalton Transactions, 2911 (2008), DOI: 10.1039/B718076D, (cit. on p. 138).

[478] H. Lin and D. Truhlar, *QM/MM: What have we learned, where are we, and where do we go from here?* Theor Chem Acc **117**, 185 (2007), DOI: 10.1007/S00214-006-0143-z, (cit. on p. 138).

[479] H.-R. Tang and K.-N. Fan, *Application of ONIOM to cluster modeling of the metal surface*, Chem. Phys. Lett. **330**, 509 (2000), DOI: 10.1016/S0009-2614(00)01133-7, (cit. on p. 138).

[480] N. Choly, G. Lu, W. E, and E. Kaxiras, *Multiscale simulations in simple metals: A density-functional-based methodology*, Phys. Rev. B **71**, 094101 (2005), DOI: 10.1103/PhysRevB.71.094101, (cit. on p. 138).

[481] Y. Liu, G. Lu, Z. Chen, and N. Kioussis, *An improved QM/MM approach for metals*, Modell. Simul. Mater. Sci. Eng. **15**, 275 (2007), DOI: 10.1088/0965-0393/15/3/006, (cit. on p. 138).

[482] N. Bernstein, J. R. Kermode, and G. Csányi, *Hybrid atomistic simulation methods for materials systems*, Rep. Prog. Phys. **72**, 026501 (2009), DOI: 10.1088/0034-4885/72/2/026501, (cit. on pp. 138, 147).

[483] H. C. Andersen, *Molecular dynamics simulations at constant pressure and/or temperature*, J. Chem. Phys. **72**, 2384 (1980), DOI: 10.1063/1.439486, (cit. on p. 139).

[484] H. J. C. Berendsen, J. P. M. Postma, W. F. van Gunsteren, A. DiNola, and J. R. Haak, *Molecular dynamics with coupling to an external bath*, J. Chem. Phys. **81**, 3684 (1984), DOI: 10.1063/1.448118, (cit. on pp. 139, 257).

[485] G. Bussi, D. Donadio, and M. Parrinello, *Canonical sampling through velocity rescaling.* J. Chem. Phys. **126**, 014101 (2007), DOI: 10.1063/1.2408420, (cit. on p. 140).

[486] J. Jellinek, *Dynamics for nonconservative systems: Ergodicity beyond the microcanonical ensemble*, J. Phys. Chem. **92**, 3163 (1988), DOI: 10.1021/j100322a027, (cit. on p. 140).

[487] J. Jellinek and R. S. Berry, *Generalization of Nosé's isothermal molecular dynamics*, Phys. Rev. A **38**, 3069 (1988), DOI: 10.1103/PhysRevA.38.3069, (cit. on p. 140).

[488] W. G. Hoover, *Generalization of Nosé's isothermal molecular dynamics: Non-Hamiltonian dynamics for the canonical ensemble*, Phys. Rev. A **40**, 2814 (1989), DOI: 10.1103/PhysRevA.40.2814, (cit. on p. 140).

[489] J. Jellinek and R. S. Berry, *Generalization of Nosé's isothermal molecular dynamics: Necessary and sufficient conditions of dynamical simulations of statistical ensembles*, Phys. Rev. A **40**, 2816 (1989), DOI: 10.1103/PhysRevA.40.2816, (cit. on p. 140).

[490] F. Müller-Plathe, *A simple nonequilibrium molecular dynamics method for calculating the thermal conductivity*, J. Chem. Phys. **106**, 6082 (1997), DOI: 10.1063/1.473271, (cit. on p. 141).

[491] T. A. Baker, B. Xu, X. Liu, E. Kaxiras, and C. M. Friend, *Nature of Oxidation of the Au(111) Surface: Experimental and Theoretical Investigation*, J. Phys. Chem. C **113**, 16561 (2009), DOI: 10.1021/jp9052192, (cit. on p. 141).

[492] T. A. Baker, C. M. Friend, and E. Kaxiras, *Local Bonding Effects in the Oxidation of CO on Oxygen-Covered Au(111) from Ab Initio Molecular Dynamics Simulations*, J. Chem. Theory Comput. **6**, 279 (2010), DOI: 10.1021/ct9004596, (cit. on p. 141).

[493] I. Goikoetxea, J. I. Juaristi, M. Alducin, and R. Dìez Muiño, *Dissipative effects in the dynamics of N_2 on tungsten surfaces*, J. Phys.: Condens. Matter **21**, 264007 (2009), DOI: 10.1088/0953-8984/21/26/264007, (cit. on p. 141).

[494] S. Goedecker, *Decay properties of the finite-temperature density matrix in metals*, Phys. Rev. B **58**, 3501 (1998), DOI: 10.1103/PhysRevB.58.3501, (cit. on p. 145).

[495] M. R. Fellinger, H. Park, and J. W. Wilkins, *Force-matched embedded-atom method potential for niobium*, Phys. Rev. B **81**, 144119 (2010), DOI: 10.1103/PhysRevB.81.144119, (cit. on p. 153).

[496] F. Römer, S. Braun, and T. Kraska, *Development of an EAM potential for zinc and its application to the growth of nanoparticles.* Phys. Chem. Chem. Phys. **11**, 4039 (2009), DOI: 10.1039/b820278h, (cit. on p. 153).

[497] C. Kanzow, N. Yamashita, and M. Fukushima, *Levenberg–Marquardt methods with strong local convergence properties for solving nonlinear equations with convex constraints*, Journal of Computational and Applied Mathematics **172**, 375 (2004), DOI: 10.1016/j.cam.2004.02.013, (cit. on p. 153).

[498] W. Shinoda, M. Shiga, and M. Mikami, *Rapid estimation of elastic constants by molecular dynamics simulation under constant stress*, Phys. Rev. B **69**, 134103 (2004), DOI: 10.1103/PhysRevB.69.134103, (cit. on pp. 157, 257).

[499] S.-L. Chang and P. A. Thiel, *Formation of a metastable ordered surface phase due to competitive diffusion and adsorption kinetics: Oxygen on Pd(100)*, Phys. Rev. Lett. **59**, 296 (1987), DOI: 10.1103/PhysRevLett.59.296, (cit. on pp. 160, 162).

[500] H. Brune, J. Wintterlin, R. J. Behm, and G. Ertl, *Surface migration of "hot" adatoms in the course of dissociative chemisorption of oxygen on Al(111)*, Phys. Rev. Lett. **68**, 624 (1992), DOI: 10.1103/PhysRevLett.68.624, (cit. on pp. 160, 162, 165).

[501] H. Brune, J. Wintterlin, J. Trost, G. Ertl, J. Wiechers, and R. J. Behm, *Interaction of oxygen with Al(111) studied by scanning tunneling microscopy*, J. Chem. Phys. **99**, 2128 (1993), DOI: 10.1063/1.465278, (cit. on pp. 162, 165).

[502] J. Wintterlin, R. Schuster, and G. Ertl, *Existence of a "Hot" Atom Mechanism for the Dissociation of O_2 on Pt(111)*, Phys. Rev. Lett. **77**, 123 (1996), DOI: 10.1103/PhysRevLett.77.123, (cit. on pp. 162, 165).

[503] S. Schintke, S. Messerli, K. Morgenstern, J. Nieminen, and W.-D. Schneider, *Far-ranged transient motion of "hot" oxygen atoms upon dissociation*, J. Chem. Phys. **114**, 4206 (2001), DOI: 10.1063/1.1346687, (cit. on pp. 162, 164 sq.).

[504] M.-F. Hsieh, D.-S. Lin, H. Gawronski, and K. Morgenstern, *Hard repulsive barrier in hot adatom motion during dissociative adsorption of oxygen on Ag(100)*, J. Chem. Phys. **131**, 174709 (2009), DOI: 10.1063/1.3258849, (cit. on pp. 162, 164 sq.).

[505] K. Yagyu, X. Liu, Y. Yoshimoto, K. Nakatsuji, and F. Komori, *Dissociative Adsorption of Oxygen on Clean Cu(001) Surface*, J. Phys. Chem. C **113**, 5541 (2009), DOI: 10.1021/jp808542z, (cit. on pp. 162, 165).

[506] F. Komori, *Distance Distributions of dissociatively adsorbed O_2 on Cu(100) at low Temperatures*, Gordon Reasearch Conference: Dynamics on Surfaces, Newport, RI, USA, 2011, (cit. on pp. 162, 165).

[507] S.-L. Chang and P. A. Thiel, *Oxygen on Pd(100): Order, reconstruction, and desorption*, J. Chem. Phys. **88**, 2071 (1988), DOI: 10.1063/1.454084, (cit. on p. 162).

[508] D.-J. Liu and J. W. Evans, *Lattice-gas modeling of the formation and ordering of oxygen adlayers on Pd(100)*, Surf. Sci. **563**, 13 (2004), DOI: 10.1016/j.susc.2004.06.165, (cit. on p. 163).

[509] A. J. H. McGaughey and M. Kaviany, *Quantitative validation of the Boltzmann transport equation phonon thermal conductivity model under the single-mode relaxation time approximation*, Phys. Rev. B **69**, 094303 (2004), DOI: 10.1103/PhysRevB.69.094303, (cit. on pp. 166, 169, 182).

[510] A. J. H. McGaughey and M. Kaviany, *Erratum: Quantitative validation of the Boltzmann transport equation phonon thermal conductivity model under the single-mode relaxation time approximation [Phys. Rev. B 69, 094303 (2004)]*, Phys. Rev. B **79**, 189901 (2009), DOI: 10.1103/PhysRevB.79.189901, (cit. on p. 166).

[511] J. E. Turney, E. S. Landry, A. J. H. McGaughey, and C. H. Amon, *Predicting phonon properties and thermal conductivity from anharmonic lattice dynamics calculations and molecular dynamics simulations*, Phys. Rev. B **79**, 064301 (2009), DOI: 10.1103/PhysRevB.79.064301, (cit. on p. 166).

[512] A. S. Henry and G. Chen, *Spectral Phonon Transport Properties of Silicon Based on Molecular Dynamics Simulations and Lattice Dynamics*, Journal of Computational and Theoretical Nanoscience **5**, 141 (2008), DOI: 10.1166/jctn.2008.001, (cit. on pp. 166, 169, 182).

[513] A. Henry and G. Chen, *High Thermal Conductivity of Single Polyethylene Chains Using Molecular Dynamics Simulations*, Phys. Rev. Lett. **101**, 235502 (2008), DOI: 10.1103/PhysRevLett.101.235502, (cit. on pp. 166, 169, 182).

[514] A. Henry and G. Chen, *Anomalous heat conduction in polyethylene chains: Theory and molecular dynamics simulations*, Phys. Rev. B **79**, 144305 (2009), DOI: 10.1103/PhysRevB.79.144305, (cit. on pp. 166, 169, 182).

[515] K. K. Kohli, G. Davies, N. Q. Vinh, D. West, S. K. Estreicher, T. Gregorkiewicz, I. Izeddin, and K. M. Itoh, *Isotope Dependence of the Lifetime of the $1136-cm^{-1}$ Vibration of Oxygen in Silicon*, Phys. Rev. Lett. **96**, 225503 (2006), DOI: 10.1103/PhysRevLett.96.225503, (cit. on pp. 166, 170).

[516] D. West and S. K. Estreicher, *Isotope dependence of the vibrational lifetimes of light impurities in Si from first principles*, Phys. Rev. B **75**, 075206 (2007), DOI: 10.1103/PhysRevB.75.075206, (cit. on pp. 166, 170).

[517] S. K. Estreicher and T. M. Gibbons, *Non-equilibrium molecular-dynamics for impurities in semiconductors: Vibrational lifetimes and thermal conductivities*, Physica B **404**, 4509 (2009), DOI: 10.1016/j.physb.2009.08.102, (cit. on pp. 166, 170).

[518] N. de Koker, *Thermal Conductivity of MgO Periclase from Equilibrium First Principles Molecular Dynamics*, Phys. Rev. Lett. **103**, 125902 (2009), DOI: 10.1103/PhysRevLett.103.125902, (cit. on p. 167).

[519] N. de Koker, *Thermal conductivity of MgO periclase at high pressure: Implications for the D" region*, Earth. Planet. Sci. Lett. **292**, 392 (2010), DOI: 10.1016/j.epsl.2010.02.011, (cit. on p. 167).

[520] M. D. Stiles and J. W. Wilkins, *Sticking Probability of H2 and HD on Noble-Metal Surfaces*, Phys. Rev. Lett. **54**, 595 (1985), DOI: 10.1103/PhysRevLett.54.595, (cit. on p. 172).

[521] M. D. Stiles, J. W. Wilkins, and M. Persson, *Inelastic gas-surface scattering. I. Formalism*, Phys. Rev. B **34**, 4490 (1986), DOI: 10.1103/PhysRevB.34.4490, (cit. on p. 172).

[522] B. Jackson, *Reduced density matrix approach for gas-solid scattering*, Chem. Phys. Lett. **270**, 484 (1997), DOI: 10.1016/S0009-2614(97)00404-1, (cit. on p. 172).

[523] B. Jackson, *Reduced density matrix description of gas–solid interactions: Scattering, trapping, and desorption*, J. Chem. Phys. **108**, 1131 (1998), DOI: 10.1063/1.475475, (cit. on p. 172).

[524] B. Jackson, *Dissociative adsorption at finite temperature: Multiconfiguration vector description of the reduced density matrix*, Chem. Phys. Lett. **308**, 456 (1999), DOI: 10.1016/S0009-2614(99)00637-5, (cit. on p. 172).

[525] B. Lepetit and B. Jackson, *Sticking of Hydrogen on Supported and Suspended Graphene at Low Temperature*, Phys. Rev. Lett. **107**, 236102 (2011), DOI: 10.1103/PhysRevLett.107.236102, (cit. on p. 172).

[526] T. A. Arias, M. C. Payne, and J. D. Joannopoulos, *Ab initio molecular-dynamics techniques extended to large-length-scale systems*, Phys. Rev. B **45**, 1538 (1992), DOI: 10.1103/PhysRevB.45.1538, (cit. on p. 182).

[527] N. Artrith, T. Morawietz, and J. Behler, *High-dimensional neural-network potentials for multicomponent systems: Applications to zinc oxide*, Phys. Rev. B **83**, 153101 (2011), DOI: 10.1103/PhysRevB.83.153101, (cit. on p. 182).

[528] T. C. Castonguay and F. Wang, *Kinetic Monte Carlo modeling of chemical reactions coupled with heat transfer.* J. Chem. Phys. **128**, 124706 (2008), DOI: 10.1063/1.2877443, (cit. on p. 182).

[529] I. Goikoetxea, J. I. Juaristi, and M. Alducin, *Comparison of Accuracy and Efficiency of six-dimensional Interpolation of Gas-Surface Dynamics Systems based on Neural Networks and the Corrugation Reducing Procedure*, private communication, Fritz-Haber-Institut, Berlin, 2010, (cit. on p. 187).

[530] R. Piessens, E. deDoncker Kapenga, C. Ueberhuber, and D. Kahaner, *QUADPACK: A Subroutine Package for Automatic Integration*, in: Springer Series in Computational Mathematics, Springer, 1983, ISBN: 978-0387125534, (cit. on p. 245).

[531] M. Galassi, J. Davies, J. Theiler, B. Gough, G. Jungman, P. Alken, M. Booth, and F. Rossi, *GNU Scientific Library Reference Manual*, in: 3rd ed., Network Theory Ltd., Bristol, 2009, ISBN: 978-0954612078, (cit. on p. 246).

[532] P. Giannozzi, S. Baroni, N. Bonini, M. Calandra, R. Car, C. Cavazzoni, D. Ceresoli, G. L. Chiarotti, M. Cococcioni, I. Dabo, A. D. Corso, S. de Gironcoli, S. Fabris, G. Fratesi, R. Gebauer, U. Gerstmann, C. Gougoussis, A. Kokalj, M. Lazzeri, L. Martin-Samos, N. Marzari, F. Mauri, R. Mazzarello, S. Paolini, A. Pasquarello, L. Paulatto, C. Sbraccia, S. Scandolo, G. Sclauzero, A. P. Seitsonen, A. Smogunov, P. Umari, and R. M. Wentzcovitch, *QUANTUM ESPRESSO: A modular and open-source software project for quantum simulations of materials*, J. Phys.: Condens. Matter **21**, 395502 (2009), DOI: 10.1088/0953-8984/21/39/395502, (cit. on p. 247).

[533] P.-O. Löwdin, *On the Non-Orthogonality Problem Connected with the Use of Atomic Wave Functions in the Theory of Molecules and Crystals*, J. Chem. Phys. **18**, 365 (1950), DOI: 10.1063/1.1747632, (cit. on pp. 248 sq.).

[534] M. Tuckerman, B. J. Berne, and G. J. Martyna, *Reversible multiple time scale molecular dynamics*, J. Chem. Phys. **97**, 1990 (1992), DOI: 10.1063/1.463137, (cit. on p. 256).

[535] S. Ogata, E. Lidorikis, F. Shimojo, A. Nakano, P. Vashishta, and R. K. Kalia, *Hybrid finite-element/molecular-dynamics/electronic-density-functional approach to materials simulations on parallel computers*, Comput. Phys. Commun. **138**, 143 (2001), DOI: 10.1016/S0010-4655(01)00203-X, (cit. on p. 259).

[536] S. Ogata, F. Shimojo, R. K. Kalia, A. Nakano, and P. Vashishta, *Hybrid quantum mechanical/molecular dynamics simulation on parallel computers: Density functional theory on real-space multigrids*, Comput. Phys. Commun. **149**, 30 (2002), DOI: 10.1016/S0010-4655(02)00612-4, (cit. on p. 259).

[537] P. Sherwood, A. H. de Vries, M. F. Guest, G. Schreckenbach, C. R. A. Catlow, S. A. French, A. A. Sokol, S. T. Bromley, W. Thiel, A. J. Turner, S. Billeter, F. Terstegen, S. Thiel, J. Kendrick, S. C. Rogers, J. Casci, M. Watson, F. King, E. Karlsen, M. Sjøvoll, A. Fahmi, A. Schäfer, and C. Lennartz, *QUASI: A general purpose implementation of the QM/MM approach and its application to problems in catalysis*, J. Mol. Struct. (Theochem) **632**, 1 (2003), DOI: 10.1016/s0166-1280(03)00285-9, (cit. on p. 259).

[538] T. A. Arias, M. C. Payne, and J. D. Joannopoulos, *Ab initio molecular dynamics: Analytically continued energy functionals and insights into iterative solutions*, Phys. Rev. Lett. **69**, 1077 (1992), DOI: 10.1103/PhysRevLett.69.1077, (cit. on pp. 261 sq.).

Curriculum Vitae

For reasons of data protection, my résumé is not published in the electronic version of this thesis.

Mein Lebenslauf wird aus Gründen des Datenschutzes in der elektronischen Fassung meiner Arbeit nicht veröffentlicht.

Acknowledgements

First of all and most important, I want to express my sincere gratitude towards my parents for our strong company in these very difficult and fateful last years: Mama und Papa, ich danke Euch für Eure Unterstützung in den vergangenen Jahren, trotz aller widrigen Umstände.

Prof. Dr. Karsten Reuter, formerly at the Fritz-Haber-Insitut der Max-Planck-Gesellschaft (FHI), now at the Technische Universität München (TUM), I thank for any supervision that might have gone both unnoticed and unappreciated, and his generosity concerning conference participations and funding, which allowed this work as well as several sidetracks to prosper.

Prof. Dr. Daniel Sebastiani from the Freie Universität Berlin (FU Berlin) I am very grateful for taking the time to act as second referee and thus help me through the graduation process.

Furthermore, without my collaborator, colleague at FHI and dear friend Dr. Erik McNellis I might have given up much earlier: Our discussions, both 'hands-on' at the computers and in good old scientific tradition at the (black or white) board and/or with paper and pencil, have helped me quite a lot to keep my fascination about science. That experience I have also shared with my former colleagues Dr. Felix Hanke, Dr. Luca Ghiringhelli, Dr. Elizabeth C. Beret, Dr. Heiko Appel and, last but by no means least, Dr. Christian Carbogno – both during the time he spent at FHI and at the many conferences where we met.

Despite our so far limited contact during regular office hours here at theoretical chemistry at TUM, Dr. Christoph Scheurer, Dr. Harald Oberhofer and PD Dr. Sergy Dr. Sergy Grebenshchikov have already provided me with similar opportunities and new perspectives.

Similarly, Prof. Dr. Karina Morgenstern I was lucky to get to know during my studies and Diploma thesis at the university of university of Hannover (now officially called "Leibniz Universität Hannover") has also provided very encouraging advice and valuable guidance at several occasions, combined and mixed with her perspective as an experimentalist, for both of which I am very grateful.

Prof. Dr. Axel Gross, without whom this project would probably have turned out quite differently, I would like to acknowledge for his invitation to Ulm and our stimulating discussions.

Itziar Goikoetxea together with her official and unofficial supervisors, Prof. Dr. Iñaki Juaristi and Dr. Maite Alducin, I would like to thank for our nice collaboration that developed out of Itziar's extended stay at FHI. I really enjoyed the few days I was allowed to spent in San Sebastian in turn, also together with Dr. Fabio Busnengo.

Prof. Dr. Matthias Scheffler and Dr. Volker Blum I want to thank for their lectures that I (loosely) followed. The same holds for Prof. Dr. Klaus Hermann from FHI, whose very interesting manuscript of his recently published book "Crystallography and Surface Structure" I enjoyed proof-reading.

From the numerous and interesting visitors at FHI and/or scientists that I have met at conferences I have kept the following in particularly good memory – probably due to the very interesting and inspiring discussions I could enjoy together with them: Prof. Dr. Mats Persson, Dr. Gábor Csányi, Dr. Matt Probert, Dr. Keith Refson, Prof. Dr. Ben Leimkuehler, Prof. Dr. Roberto Car, Prof. Dr. Annabella Selloni-Car and Prof. Dr. David Tománek, who has the additional fascinating gift to make science appear as interesting as a (good) soccer game.

Abbas Ali Deghan, Michael Rieger, Hannes Guhl, Juan Beltrán, Claudia Mangold, Jelena

Jelic, Xin Tan and Itziar Goikoetxea, who have had the strange pleasure of sharing office 1.03 at building T of the theory department of FHI with me, I want to thank for their patience with the often impatient and frustrated myself.

Finally, the administrative and technical staff at FHI, in particular Gaby Tysper, Julia Pach, Wolfram Zieger and Steffen Kangowski, as well as Christoph Herrmann, the external IT support from science + computing, shall be mentioned and appreciated for fulfilling my sometimes probably quite difficult wishes of administrative or computational nature. Here at TUM, Ruth Mösch has been incredibly helpful and supportive both when moving from Berlin to Munich and during the whole time that has passed thereafter. Special thanks goes to Mrs Angelika Pasanec for here extremely reassuring and accommodating support when facing the PhD formalities at FU Berlin.

In the end, credit is definitely due to the open source spirit and all the excellent software it has produced and hence could be made use of for this thesis - starting from an operating system like GNU/Linux, desktop environments like KDEor GNOME, programming languages and related tools (gcc, gfortran, GAWK, Python, GNUMake), plotting, graphic and text utilities (gnuplot, grace, matplotlib, matplotlib, GIMP, Inkscape, OpenOffice, LaTeX) and scientific libraries, visualizers and software – some of them very specific to this field (GSL, FGSL, XCrysDen, GDIS, Jmol, ASE, phonopy). During this work, within the aforementioned spirit, contributions have been made to those packages which are underlined.